AD-A271 458

Global Monitoring

PROCEEDINGS

Geophysics

15th ANNUAL

SEISMIC RESEARCH SYMPOSIUM

8-10 September 1993
Westin Conference Center
Vail, Colorado

DTIC
ELECTE
OCT 0 4 1993
S D
B

Basic Research

PHILLIPS LABORATORY
29 Randolph Road
Hanscom AFB, Massachusetts 01731-3010

AIR FORCE OFFICE OF SCIENTIFIC RESEARCH
110 Duncan Avenue, Suite B-115
Bolling AFB, DC 20332-0001

ADVANCED RESEARCH PROJECTS AGENCY
3701 North Fairfax Drive
Arlington, Virginia 22203-1714

Technology

DISTRIBUTION STATEMENT A
Approved for public release;
Distribution Unlimited

THE VIEWS AND CONCLUSIONS CONTAINED IN THIS DOCUMENT ARE THOSE OF THE AUTHORS AND SHOULD NOT BE INTERPRETED AS REPRESENTING THE OFFICIAL POLICIES, EITHER EXPRESSED OR IMPLIED, OF THE ADVANCED RESEARCH PROJECTS AGENCY OR THE U.S. AIR FORCE

DISCLAIMER NOTICE

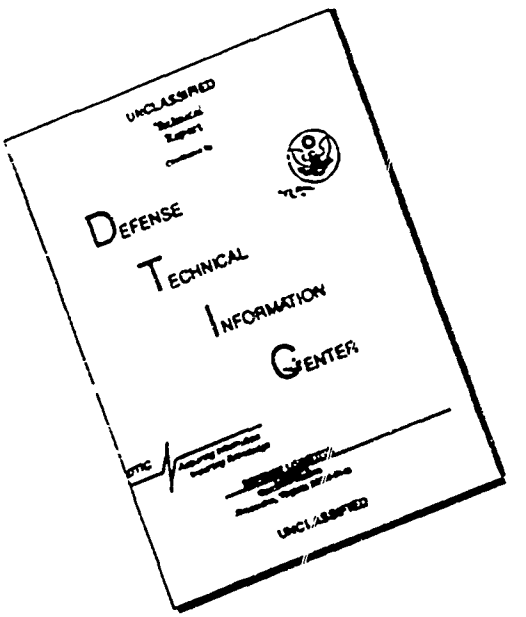

THIS DOCUMENT IS BEST QUALITY AVAILABLE. THE COPY FURNISHED TO DTIC CONTAINED A SIGNIFICANT NUMBER OF PAGES WHICH DO NOT REPRODUCE LEGIBLY.

PL-TR-93-2160
Environmental Research Papers, No. 1125

PROCEEDINGS OF THE 15TH ANNUAL SEISMIC RESEARCH SYMPOSIUM 8-10 SEPTEMBER 1993

Editors:
James F. Lewkowicz
Jeanne M. McPhetres

August 1993

APPROVED FOR PUBLIC RELEASE; DISTRIBUTION UNLIMITED

PHILLLIPS LABORATORY
Directorate of Geophysics
AIR FORCE MATERIEL COMMAND
HANSCOM AIR FORCE BASE, MA 01731-3010

93-22974

4447P0

83 0 117

"This technical report has been reviewed and is approved for publication."

JAMES F. LEWKOWICZ
Branch Chief
Solid Earth Geophysics Branch
Earth Sciences Division

DONALD H. ECKHARDT
Director
Earth Sciences Division

This report has been reviewed by the ESC Public Affairs Office (PA) and is releasable to the National Technical Information Service (NTIS).

Qualified requestors may obtain additional copies from the Defense Technical Information Center. All others should apply to the National Technical Information Service.

If your address has changed, or if you wish to be removed from the mailing list, or if the addressee is no longer employed by your organization, please notify PL/TSI, 29 Randolph Road, Hanscom AFB, MA 01731-3010. This will assist us in maintaining a current mailing list.

Do not return copies of this report unless contractual obligations or notices on a specific document requires that it be returned.

REPORT DOCUMENTATION PAGE

Form Approved
OMB No. 0704-0188

Public reporting burden for this collection of information is estimated to average hour per response, including the time for reviewing instructions, searching existing data sources, gathering and maintaining the data needed, and completing and reviewing the collection of information. Send comments regarding this burden estimate or any other aspect of this collection of information, including suggestions for reducing this burden, to Washington Headquarters Services, Directorate for information Operations and Reports, 1215 Jefferson Davis Highway, Suite 1204, Arlington, VA 22202-4302, and to the Office of Management and Budget, Paperwork Reduction Project (0704-0188), Washington, DC 20503.

1. AGENCY USE ONLY (Leave blank)	2. REPORT DATE	3. REPORT TYPE AND DATES COVERED
	3 August 1993	Scientific, Final

4. TITLE AND SUBTITLE
Proceedings of the 15th Annual Seismic Research Symposium, 8-10 September 1993

5. FUNDING NUMBERS
PE 61102F
PR 2309
TA G2
WU 10

6. AUTHOR(S)
Editors: James F. Lewkowicz
Jeanne M. McPhetres

7. PERFORMING ORGANIZATION NAME(S) AND ADDRESS(ES)
Phillips Laboratory /GPEH
29 Randolph Road
Hanscom AFB, MA 01731-3010

8. PERFORMING ORGANIZATION REPORT NUMBER
PL-TR-93-2160
ERP, No. 1125

9. SPONSORING/MONITORING AGENCY NAME(S) AND ADDRESS(ES)
ARPA/NMRO
3701 North Fairfax Drive
Arlington, VA 22203-1714

AFOSR/NL
110 Duncan Avenue, Suite B115
Bolling AFB, DC 20332-0001

10. SPONSORING/MONITORING AGENCY REPORT NUMBER

11. SUPPLEMENTARY NOTES
This research was supported by ARPA under PE 62301E and AFOSR, PE 61102F.

12a. DISTRIBUTION/AVAILABILITY STATEMENT
Approved for Public Release; distribution unlimited

12b. DISTRIBUTION CODE

13. ABSTRACT *(Maximum 200 words)*

These Proceedings contain papers presented at the Fifteenth Annual Seismic Research Symposium held 8–10 September 1993, in Vail, Colorado. This Symposium represents the combined annual review for the seismic verification research programs funded by the Air Force Phillips Laboratory, PL/GPEH, the Air Force Office of Scientific Research, AFOSR/NL, and the Advanced Research Projects Agency, ARPA/NMRO. The scientific objectives of the research programs are to improve the Air Force's capability to seismically detect, locate, identify, and estimate the yield of underground nuclear explosions. The purpose of these Symposia, organized annually by GPEH, is to provide the sponsoring agencies an opportunity to review research, particularly contractor research, accomplished during the preceding year and to outline areas of investigation for the coming year. For the researchers, it provides a forum for the exchange of scientific information to help achieve program goals, and an opportunity to meet PL, AFOSR, and NMRO staff to

14. SUBJECT TERMS
underground nuclear explosions, discrimination, intelligent processing of seismic signals, regional seismology, sources, yield estimation, laboratory measurements of rock properties

15. NUMBER OF PAGES
444

16. PRICE CODE

17. SECURITY CLASSIFICATION OF REPORT	18. SECURITY CLASSIFICATION OF THIS PAGE	19. SECURITY CLASSIFICATION OF ABSTRACT	20. LIMITATION OF ABSTRACT
UNCLASSIFIED	UNCLASSIFIED	UNCLASSIFIED	UL

discuss results and future plans. In addition, the Symposium and the technical presentations serve as an important avenue for technology transition to the Air Force user. The papers include studies of the identification and characterization of seismic explosion sources (discrimination), intelligent processing of regional seismic signals, the acquisition and processing of seismic data including data from the Commonwealth of Independent States, regional seismic wave propagation from both an empirical and theoretical viewpoint, yield estimation, and laboratory studies of rock properties appropriate to test sites.

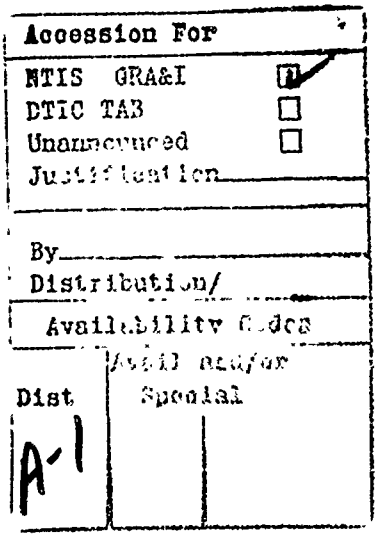

DTIC QUALITY INSPECTED 3

TABLE OF CONTENTS

PAGE

Anderson, William W.; **Zhao**, Yusheng and **Ahrens**, Thomas J.
Large Variations in Shock Energy Coupling in Different Sedimentary Rocks 1

Baker, G. Eli; **Burdick**, Lawrence J. and **Minster**, J. Bernard
Regional Broadband Waveforms: Individual Station and Three Component Array Analysis of Nuclear Explosion Sources Crossing a Southern California Path 8

Barker, T.G.; **Stevens**, J.L. and **McLaughlin**, K.L.
XNICE - A System for Evaluation of the Identification Capabilities of Regional and Global Networks 15

Baumgardt, Douglas R. and **Der**, Zoltan
Investigation of Regional Seismic Discriminants Using Visualization and Statistical Analysis Methods in the Intelligent Seismic Event Identification System 22

Bennett, T.J.; **Murphy**, J.R.; **Marshall**, M.E. and **Barker**, B.W.
Seismic Discrimination of Rockbursts and Cavity Decoupled Explosions 29

Boitnott, G.N.
Nonlinear Rheology of Rock at Moderate Strains: Fundamental Observations of Hysteresis in the Deformation of Rock 36

Cansi, Y. and **Bottero**, A.
Automatic Processing of Seismic Events Recorded on a Mini-Array (Signal Analysis Combined with Neural Networks) 43

Chapman, Martin C.; **Huang**, Shaosong and **Snoke**, J. Arthur
Comparison of Single-Station Backazimuth Estimates with Regional Event Locations in the Central Appalachians 51

Chen, Xiaofei and **Aki**, Keiiti
Energy Transfer Theory of Seismic Surface Waves in a Random Scattering and Absorption Half-Space Medium 58

PAGE

Clouser, Robert H. and **Langston**, Charles A.
Scattering of Broadband Regional Waves from Sinusoidal Layer Interfaces 65

Crusem, René and **Massot**, Jean-Pierre
The Giat Mini-Array in Central France: Preliminary Detection and Phase Identification Results 72

Ecker, Christine and **Langston**, Charles A.
Source Parameters From Near Regional Earthquake Data Recorded at Garm, Tadjikistan 79

Ekström, Göran; **Dziewonski**, Adam M.; **Tromp**, Jeroen and **Su**, Wei-Jia
Elastic and Anelastic Structure Beneath Eurasia 86

Fielding, Eric; **Barazangi**, Muawia and **Isacks**, Bryan
A Network-Accessible Geological and Geophysical Database for Eurasia, North Africa, and the Middle East 93

Fisk, Mark D.; **Gray**, Henry L. and **McCartor**, Gary D.
Applications of a Robust Statistical Framework for Seismic Event Identification 100

Frohlich, Cliff and **Kadinsky-Cade**, Katharine
An Investigation of the Practical Limits of Accuracy for Relative Seismic Event Locations 107

Grant, Lori; **Ryall**, Floriana and **Coyne**, John
CSS Ground-Truth Database: Update and Case Study 114

Gray, H.L.; **Woodward**, W.A.; **McCartor**, G.D. and **Fisk**, M.D.
A Bootstrap Generalized Likelihood Rat io Test in Discriminant Analysis 121

Gurrola, H. and **Minster**, J. Bernard
Resolution of Velocity Structure Determined by Velocity Spectrum Stacking of Receiver Functions 125

Hanson, J.A.; **Minster**, J.B. and **Vernon**, F.L.
Characteristics of Frequency Dependent Polarizations for Local Events Recorded on Surface and Borehole Instruments 132

PAGE

Harjes, H.-P.; **Jost**, M.L. and **Schweitzer**, J.
GERESS - A Key Station in a Future Global Monitoring Network 139

Hedlin, Michael A.H.; **Minster**, J. Bernard and **Orcutt**, John A.
Resolution of Prominent Crustal Scatterers Using a Small Aperture Array 146

Helmberger, D.V.; **Zhao**, L.S. and **Woods**, B.
Source Estimation, Energy Levels, and a New Discriminant 154

Henson, Ivan and **Coyne**, John
The Geotool Seismic Analysis System 162

Herrin, Eugene and **Golden**, Paul
Design, Evaluation and Construction of Two Nine Element Experimental Arrays TEXESS and LUXESS 169

Herrmann, R.B.
Automated Analysis of Regional Wave Propagation 177

Jih, R.-S.; **Wagner**, R.A. and **Shumway**, R.H.
Statistical Analysis of Soviet Nuclear Explosions 186

Kennett, B.L.N.
Location and Phase Association for Seismic Events at Regional and Teleseismic Distances 193

Kim, Won-Young and **Richards**, Paul G.
Seismological Studies Using Borovoye Data 200

Koch, Karl and **Stump**, Brian W.
Constraints from Surface Wave Inversion for Upper Mantle Shear Structure of the Basin and Range 207

Kohler, Werner; **Papanicolaou**, George C. and **White**, Benjamin S.
Pulse Reflection From Locally Layered Random Media 214

Kværna, Tormod and **Ringdal**, Frode
Continuous Seismic Threshold Monitoring 221

PAGE

Lawson, James Edward Jr.
An International Data Exchange System of Open Stations Using Two Standard Internet Tools: Gopher Plus and NFS Remote Mount 228

Lay, Thorne; **Xie**, Xiao-bi and **Zhang**, Tianrun
LG Propagation in Eurasia 234

Lay, Thorne and **Wu**, Ru-Shan
Analysis of 3D Complex Structure and Heterogeneity Effects on Formation and Propagation of Regional Phases in Eurasia 241

Leonard, S.K.
Automatic Global Seismic Event Association and Location Estimation Using a Knowledge Based Approach to Generalized Beaforming 248

Magnier, Sophie-Adélaïde; **Donzé**, Frédéric; **Hanson**, Jeff; **Minster**, Bernard and **Orcutt**, John
Analysis of the SAA2 Experiment, Piñon Flat California 256

McLaughlin, K.L.; **Barker**, T.G.; **Stevens**, J.L. and **Day**, S.M.
Numerical Simulation of Quarry Blast Sources..... 263

McQuarrie, Allan D.R. and **Shumway**, Robert H.
Parametric and Nonparametric Discriminators for Regional Earthquakes and Explosions 269

Mitchell, B.J.; **Xie**, J.K.; **Pan**, Y. and **Ni**, J.
Lg Q, Lg Coda Q, and Yield Estimation in Eurasia 277

Murphy, J.R.; **Marshall**, M.E. and **Barker**, B.W.
Application of Network-Averaged Teleseismic P Wave Spectra to Seismic Yield Estimation of Soviet PNE Explosions 284

Mykkeltveit, Svein; **Kværna**, Tormod; **Fyen**, Jan and **Ringdal**, Frode
Array Research at NORSAR 291

Priestley, Keith and **Cipar**, John J.
Central Siberian Upper Mantle Structure and the Structure of the South Caspian Basin 298

PAGE

Pulli, Jay J. and **Dysart**, Paul S.
Regional Seismic Event Identification in Eurasia: A Hybrid Machine Learning Approach 305

Pulli, Jay J. and **Dysart**, Paul S.
Two-Dimensional Signal Processing and Machine Learning for Regional Seismic Event Identification 312

Rivière-Barbier, F.; **Baumgardt**, D.; and **Rodi**, W.
Using Groups of Similar Events at the Scandinavian Arrays to Identify and to Relocate Events 318

Ruud, B.O.; **Husebye**, E.S. and **Hestholm**, S.O.
Modelling and Analysis of Seismic Wave Propagation in the Lithosphere Using 2D Finite Difference Synthetics 326

Saikia, Chandan K.; **Woods**, Bradley B.; **Zhao**, L-S. and **Helmberger**, Donald V.
Discrimination of Low-Yield Events Using Regional Seismograms: A Semi-Automated System 334

Sammis, Charles G.
Incorporating Damage Mechanics into Explosion Source Models 349

Schwartz, Susan Y. and **Mandel**, Ron
Characterization of Regional Phase Propagation in Eurasia Using Data From Historic Nuclear Explosions in the U.S.S.R. 356

Sereno, Thomas J. Jr.; **Swanger**, Henry J. and **Bache**, Thomas C.
Progress in Automated Processing and Interpretation of Seismic Data 363

Stump, Brian and **Min**, Gyungsik
Resolution of Explosion Source Model Parameters by the Nonlinear Inversion of Near-Source Data: Synthetic Tests and Observational Applications 370

Suteau-Henson, A.; **Ryaboy**, V. Z.; **Israelsson**, H. and **Carter**, J. A.
Station Evaluation and Accurate Event Locations for Global Monitoring 377

PAGE

Sykes, Lynn R.
Partially Decoupled and Enhanced-Coupled Nuclear Explosions Detonated in Cavities at Azgir, Kazakhstan: Implications for Identifying Decoupled Nuclear Explosions in Salt 384

Teng, Yu-Chiung and **Kuo**, John T.
Finite-Element Modeling of the Blockage and Scattering of Lg Wave Propagation 391

Toksöz, M.N.; **Li**, Y. and **Rodi**, W.
Seismic Source Characterization with Empirical Green's Function and Relative Location Techniques 398

Toksöz, M.N.; **Mandal**, B.; **Dong**, W. and **Schultz**, C.
Seismic Scattering From Non-Spherical Cavities and Rough Interfaces 405

Wallace, Terry C. and **Beck**, Susan L.
Characterization of Broadband, Regional Distance Seismograms in Eurasia and Other Regions of Potential Underground Testing: Preliminary Results from the Arabian Shield, Kamchatka and South America 412

Walter, William R.; **Patton**, Howard J.; **Mayeda**, Kevin; **Goldstein**, Peter; **Dowla**, Farid and **Smith**, Albert T.
Seismic Discrimination Studies of Little Skull Mountain Earthquakes and NTS Explosions 419

Zeilhuis, A.
A Preliminary Model for the S Wave Velocity Below Central Asia 426

Zhang, Zhao-Qing; **White**, Benjamin; **Sheng**, Ping and **Jeanloz**, Raymond
Statistical Inversion of Layered Media with Physical Boundary Conditions 430

LARGE VARIATIONS IN SHOCK ENERGY COUPLING IN DIFFERENT SEDIMENTARY ROCKS

William W. Anderson, Yusheng Zhao, and Thomas J. Ahrens

Lindhurst Laboratory of Experimental Geophysics
Seismological Laboratory
California Institute of Technology
Pasadena, CA 91125

Contract No F49620-92-J-0402
DNA Contract No. 001-92-C-0128

OBJECTIVE

The shock Hugoniot and adiabatic release curves of sedimentary rocks display a range of different behaviors that affect the decay of shock waves propagating away form a confined source. Many of the minerals making up sandstones, shales, and limestones undergo phase transitions when shocked to pressures of interest to studies of coupling of energy from explosive sources into far field seismic waves. Both sandstones and limestones have been observed to exhibit elastic precursors and multiple wave behavior at shock velocities up to 3.7 km/s and 5.7 km/s, respectively [*Ahrens and Gregson, 1964*]. Hysteresis in the shock-release paths of materials results in irreversible energy deposition, thus depriving the shock wave of energy required to drive its propagation and resulting in a more rapid decay and less efficient coupling to far field waves than expected from geometrical effects alone. Thus, data constraining this behavior in rocks are essential for determining the cavity volumes for various degrees of decoupling for different lithologies.

The behavior of most sedimentary rocks during adiabatic release has not been experimentally investigated to a significant extent. Our objective was to obtain experimental data for shock and release behaviors of clastic and carbonate sedimentary rocks and use those data along with data from other sources, to develop a theoretical model of the hysteretic shock-release paths of these rocks. We use this model to constrain the energy deposited irreversibly in these rocks by the passage of shock and release waves. The release model we use is a modification of that used by *Sekine et al.* [*1993, submitted*] for granite.

RESEARCH ACCOMPLISHED

We have studied the shock compression and adiabatic release behavior of Coconino sandstone with an initial density $\rho_{00} = 2.329\ Mg/m^3$, Solenhofen limestone with initial density $\rho_{00} = 2.613\ Mg/m^3$, and a calcareous shale with initial density $\rho_{00} = 2.574\ Mg/m^3$. The sandstone is essentially quartz with only minor amounts of other constituents and the limestone is essentially pure calcite with very minor amounts of other constituents. The shale, based on a modified CIPW normative mineral calculation, is composed of subequal amounts of quartz, clays, and calcite.

The features of the Coconino sandstone Hugoniot (figure 1) can be identified with those of the quartz Hugoniot. At very low pressures, there is an elastic shock wave which precedes the plastic deformation shock wave. The

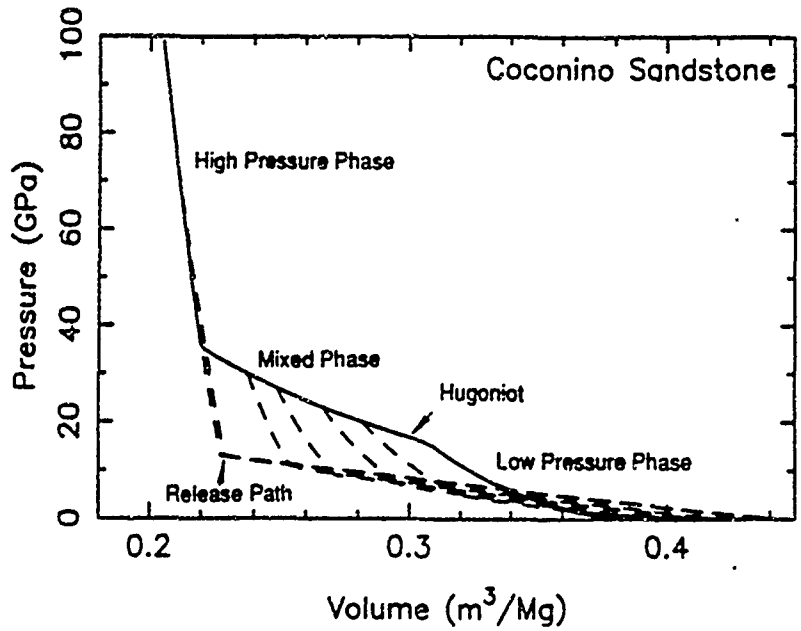

Figure 1. Hugoniot curve and adiabatic release paths for Coconino sandstone.

limiting stress of this elastic wave is the Hugoniot elastic limit (HEL). Above the HEL, the Hugoniot may be broken down into low pressure phase (LPP) and high pressure phase (HPP) stability regions, with an intervening mixed phase (MP) region where insufficient energy is provided by the shock wave to drive the formation of the HPP to completion. Based on the data of *Ahrens and Gregson [1964]*, the HEL of sandstones seems very strongly dependent on the initial density of the rock. The elastic wave velocity, which has no systematic dependence on strain rate at a given initial density, varies from 2.8±.2 km/s for ρ_{00} = 1.961 Mg/m³ to 3.6±.1 km/s for ρ_{00} = 2.141 Mg/m³.

Above the HEL, the sandstone LPP and HPP can be identified with quartz and stishovite. The sandstone Hugoniot is well modelled using the equation of state (EOS) parameters of quartz for the LPP region and stishovite for the HPP region. The MP region is modelled by a volume weighted average of the HPP and LPP Hugoniot curves in the *P-V* plane:

$$V_{MP} = fV_{HPP} + (1-f)V_{LPP} \qquad (1)$$

where f is the mass fraction of HPP. We assume that f varies linearly with pressure from 0 at the lower bound to the MP region, where HPP formation begins, to 1 at the upper bound of the MP region, where HPP formation is complete. Consideration of the present data and data from *Van Thiel [1977]* suggests that HPP formation begins at a Rankine-Hugoniot energy of $E_{RH} \approx$ 0.95±.05 MJ/kg and is complete at $E_{RH} \approx$ 3.8±.2 MJ/kg, independent of the initial density of the sample. E_{RH} is given by

$$E_{RH} = \tfrac{1}{2}P_H(V_H - V_{00}) \qquad (2)$$

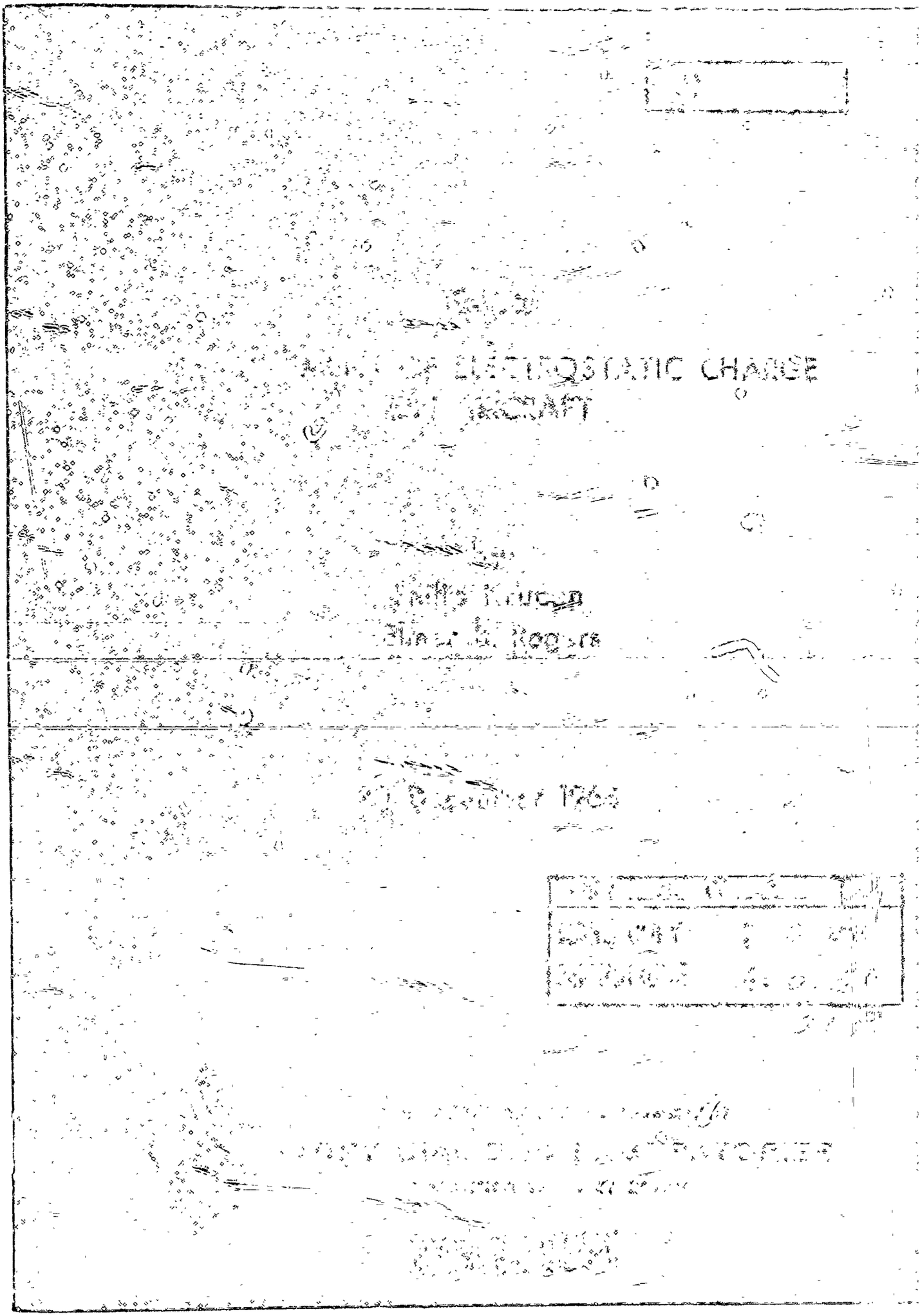

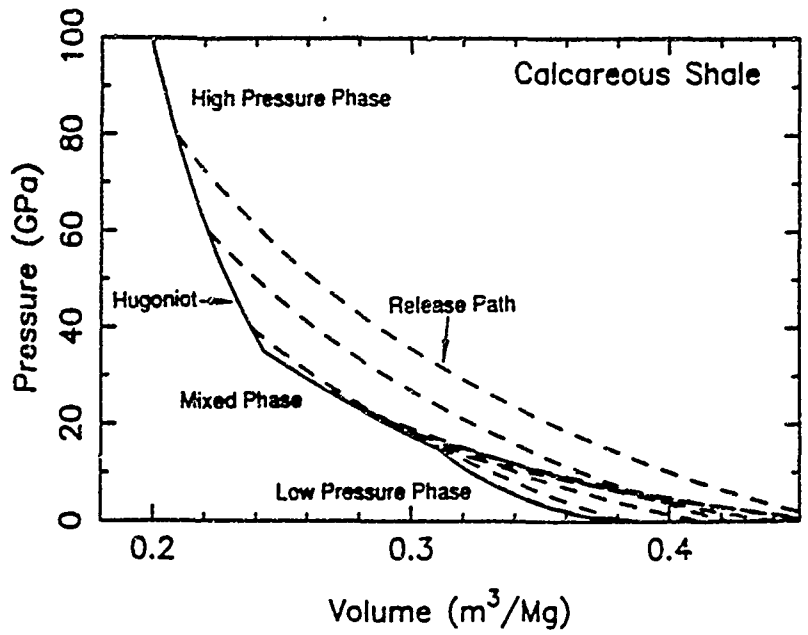

Figure 2. Hugoniot curve and adiabatic release paths for calcareous shale. The large expansions from the low pressure phase region above 14 GPa is also observed in pure carbonates. The release paths above ~50 GPa are not well constrained by the available data.

Murnaghan parameters K_{S0} = 66 GPa and K_S' = 1. Interestingly, the HPP release paths do not show as rapid expansion as the LPP release paths from P_H > 14 GPa. Similar behavior is shown by the release data of *Vizgirda and Ahrens [1982]* for aragonite, suggesting that this behavior in the shale can be attributed to the presence of calcite, suggesting that evolution of CO_2 may be important in this region. The MP release paths are well modelled by a mixture of the HPP and LPP release paths according to equation (1), with f frozen at the Hugoniot value.

The limestone Hugoniot is complicated at low pressures by an elastic wave and several phase transitions, causing a multiple wave structure with as many as five separate shock fronts observed in some experiments [*Ahrens and Gregson, 1964*]. The multiple wave structure does not disappear until shock pressures above ~20 GPa, corresponding to a shock wave velocity of ~5.9 km/s, are attained. Above 20 GPa (figure 3), the Hugoniot becomes much less complicated. A single high pressure phase region extends from 31 GPa to over 100 GPa. Based on the results of *Vizgirda and Ahrens [1982]*, we model this phase with EOS parameters ρ_0 = 3.05 Mg/m³, K_{S0} = 85.5 GPa, K_S' = 3.75, γ_0 = 1.43, n = 0.6, and E_{tr} = 0.1 MJ/kg. Between 10 GPa and 31 GPa, the final shock state is modelled as a mixture of this high pressure phase and a lower pressure phase that has ρ_0 = 2.985 Mg/m³, K_{S0} = 110 GPa, K_S' = 4, γ_0 = 1.44, n = 0.6, and E_{tr} = 0. These parameters are not a true equation of state, but provide a convenient estimate of the Hugoniot of the lower pressure phase. As with the mixed phase regions of the shale and sandstone, we model this mixture by equation (1) with the fraction f of the higher pressure phase varying linearly

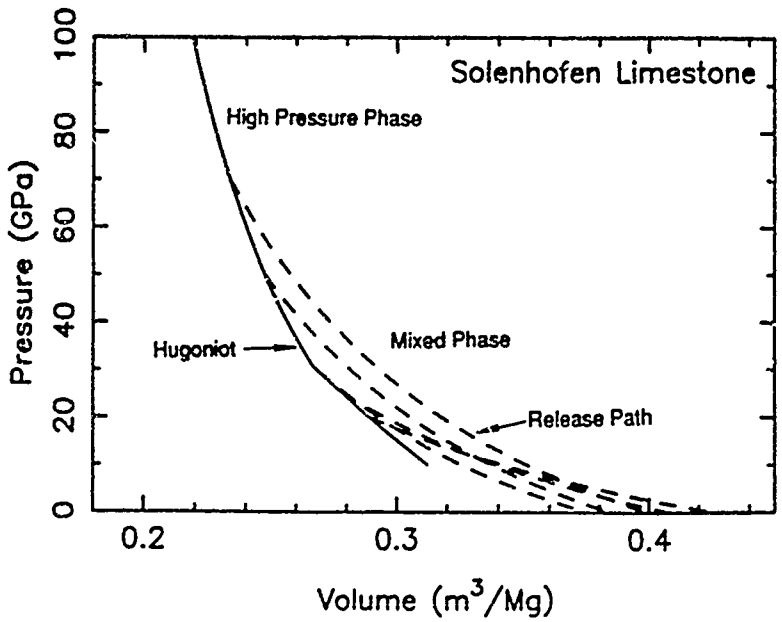

Figure 3. Hugoniot curve and adiabatic release paths for Solenhofen limestone. The shock behavior below 20 GPa is very complicated. The release paths are constrained by the new data obtained in this study and by the data of *Vizgirda and Ahrens [1982]*.

with pressure between the phase transition onset at 10 GPa and completion at 31 GPa.

Release paths from the single phase region of the Hugoniot are tentatively modelled as isentropes with Murnaghan equation parameters K_{S0} = 66 GPa and K_S' = 2.3, based on our results and those of *Vizgirda and Ahrens [1982]* for aragonite. For the purposes of calculating the mixed phase release paths from Hugoniot states between 14 GPa and 31 GPa, we model the lower pressure phase release paths as isentropes with Murnaghan equation parameters K_{S0} = 30 GPa and K_S' = 1.

CONCLUSIONS AND RECOMMENDATIONS

We apply the results for the hysteretic shock-release paths of the rocks studied to calculate the fraction f' of the energy E_{RH} that is irreversibly deposited in the material for a given shock pressure using the equation

$$f' = 1 - (E_{Rel}/E_{RH}) \tag{5}$$

where

$$E_{Rel} = \int_{V_R}^{V_H} P dV \tag{6}$$

where the subscripts H and R on V denote the Hugoniot and release volumes, respectively. The resulting estimates for f' are presented in figure 4. For

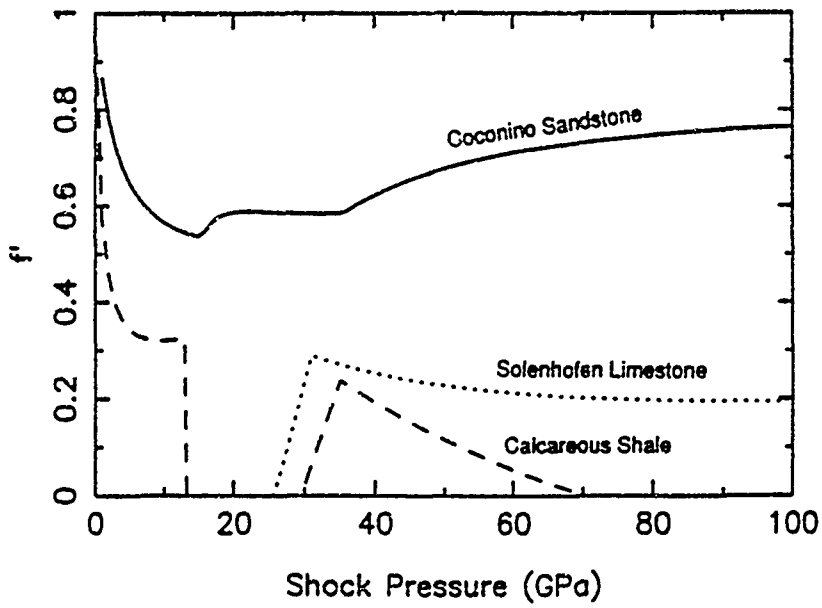

Figure 4. Fraction f' of the Rankine-Hugoniot energy irreversibly deposited in sandstone, shale, and limestone, as a function of shock pressure. The low values for the limestone and shale can apparently be attributed to the release behavior of calcite.

the sandstone, f' approaches 1 at low shock pressures because of pore collapse, but rapidly drops to ~0.53 at 14 GPa, rising slowly thereafter to ~0.77 at 100 GPa. Because the release paths for both the shale and the limestone show large expansions, the value of E_{Rel} is close to E_{RH}. As a result, f' is small for both of these materials, falling below 0.4 for $P_H > 3$ GPa. At shock pressures below ~30 GPa, both shale and limestone show regions where $f' \approx 0$, reflecting the large expansion of calcite on release from the low pressure region of the Hugoniot. The shale shows similar behavior above 70 GPa in the calculations, but this behavior is not well constrained by the data presently in hand. These results suggest that shock waves from sources confined in volatile-rich rocks, especially those rocks rich in carbonates, will decay more slowly (by a factor of ~3) than those in volatile-poor rocks such as sandstones. As a result coupling of explosions is expected to be more efficient in volatile-rich rocks.

References.

Ahrens, T. J., and V. G. Gregson, Shock compression of crustal rocks: data for quartz, calcite, and plagioclase rocks, *J. Geophys. Res.*, *69*, 4839-4874, 1964.

Lyzenga, G. A., T. J. Ahrens, and A. C. Mitchell, Shock temperatures of SiO_2 and their geophysical implications, *J. Geophys. Res.*, *88*, 2431-2444, 1983.

Sekine, T., T. S. Duffy, A. M. Rubin, W. W. Anderson, and T. J. Ahrens, Shock compression and isentropic release of granite, *Geophys. J. Int*, submitted.

Swegle, J. W., Irreversible phase transitions and wave propagation in silicate geologic materials, *J. Appl. Phys.*, *68*, 1563-1579, 1990.

Van Thiel, M., *Compendium of Shock Wave Data*, Lawrence Livermore Laboratory, UCRL-50108, 1977.

Vizgirda, J., and T. J. Ahrens, Shock compression of aragonite and implications for the equation of state of carbonates, *J. Geophys. Res.*, *87*, 4747-4758, 1982.

Regional Broadband Waveforms: Individual Station and Three Component Array Analysis of Nuclear Explosion Sources Crossing a Southern California Path.

G. Eli Baker, Lawrence J. Burdick, and J. Bernard Minster (IGPP, UCSD)

DARPA Contract No. F19628-93-K-0010 and AF F29601-91-K-DB13

Objective:

The prediction of source parameters from seismic waveforms is dependent on the separation of source and propagation effects. Understanding the physics of propagation effects has ramifications for the transportability of discrimination techniques, particularly those dependent on waveforms. The purpose of this research is to understand better the relation of path structure to broad-band waveforms.

Research Accomplished:

Previous Work: Modeling of regional broad-band (BB) earthquake and explosion waveforms for source retrieval (eg Zhao and Helmberger, 1993) and lithospheric modeling (eg Helmberger et al, 1993; Helmberger et al, 1992) has grown extensively in the last several years, as such data have become available and synthetic seismogram techniques are improved. The techniques used include modeling with generalized ray (Helmberger, 1973) and frequency-wavenumber (FK) (Bouchon, 1981) synthetics. These efforts are extensions of techniques developed for modeling the simpler long period waveforms of, first, teleseismic events (eg Muller, 1969; Langston and Helmberger, 1975), and later, of regional events (Helmberger and Engen, 1980).

BB regional waveforms contain a large amount of information and so are quite difficult to model. Much of the work on regional propagation has been done in southern California. For earthquakes, source finiteness as well as mechanism are important, as is scattering all along the laterally heterogeneous path. Nuclear explosions at the Nevada Test Site (NTS) have been an invaluable source of data for understanding regional propagation as they have well known source locations and origin times, and simple source mechanisms, permitting the isolation of propagation effects. In a study to assess the utility of regional BB Pn for discrimination of nuclear explosions, significant variation of the Pn/Pg amplitude ratio south of NTS was interpreted as evidence of a rapid velocity increase or discontinuity within the lid (Burdick et al, 1991). Our research tests and extends work done studying propagation from NTS to southern California.

Data: We have collected 3-component seismograms of nuclear explosions from the Nevada Test Site (NTS) recorded at three broad-band stations in southern California, Landers (LAC), operated by Lawrence Livermore National Laboratories), Pasadena (PAS), part of the California Institute of Technology Terrascope network), and Piñon Flat Observatory (PFO), part of the IDA/IRIS network operated by the Institute of Geophysics and Planetary Physics at University of California, San Diego (figure 1). For the nuclear explosions, source parameters are well constrained. That and the range of distances available from the source distribution enable us to observe the development of phases with distance. Furthermore, as the sources are all similar, we may attribute many of the differences we see between different events recorded at a single station as being due to structure along the propagation path and so generate an opportunity to test the hypothesis of a triplication due to upper mantle structure (Burdick et al, 1991). We also have recordings from three of the explosions from a temporary 28

station broad-band 3-component array, located at PFO which enables us to distinguish the direction of arrival and wave type of various phases using both array and three component analysis techniques. This ability complements our modeling of the broad-band source array records by corroborating our interpretations of phases

Results: The variation of the Pn/Pg amplitude ratio with distance provided the primary impetus for the hypothesis of a gradient or discontinuity in the upper mantle (Burdick, et al, 1991). We first reproduced the results of Burdick et al with our expanded dataset. That is, we plotted the Pn/Pg ratios measured at LAC, PAS, and PFO, as a function of distance (figure 2). On the left side of figure 2, Pn amplitude is the rms value of the first 5 seconds after onset. Our initial assumption is that the Pg variation will be small compared to Pn, and so can be used to normalize the Pn amplitudes for different events and distances. For Pg amplitude, we use the rms value of the first 20 seconds after the predicted PmP time relative to Pn, using the Helmberger and Engen (1980) layer over a half space model developed for the western US. We used a passband of 0.4 to 2 hz. At LAC, we see some trend to increasing amplitude ratio with distance and significantly lower amplitude ratios than at the more distant PAS and PFO stations. Contrary to the trend observed using the initial fewer data of Burdick et al (1991), there is no significant difference between PAS and PFO, or trend within the data from either station individually. However, when we use just the initial peak amplitude of Pn (the right side of figure 2), the amplitude ratio for every event recorded at PFO drops to approximately half the value at PAS (figure 2b). This is due to a difference in the initial Pn waveforms at the 2 stations. While the initial peak at PAS dominates Pn, most of the Pn energy at PFO is in a secondary phase arriving one second after the initial peak. This is illustrated in record sections made up of different events at each station (figure 3). We have plotted 2-sided envelope functions (excluding some records for clarity) for the first 15 seconds of each event. Note that the distance scales are not equal. The zero line is at the first arrival. The second line, moving out with distance, is the predicted (Helmberger and Engen, 1980) PmP arrival time. This figure illustrates several important differences between the records at different distances and stations. The small initial peak at PFO, contrasting with the large one at PAS is clear. This could be interpreted as supportive of the triplication hypothesis, where PAS is at the distance of intersection of 2 phases, and so has a large initial peak. Then, at the slightly greater distance of PFO, the phases separate. Some lateral variation is indicated however, at least in the depth of the discontinuity or gradient, as the relative amplitude variation is sustained throughout the distances for which PAS and PFO overlap. The crustal phases also vary significantly from station to station. The PmP phase arrives precisely at the predicted time at LAC. At PAS however, it is approximately 3 seconds early. At PFO, PmP is indiscernible. These last 2 observations are seen more clearly in figure 4.

Synthetic Seismogram Modeling: We are employing the generalized ray code of Helmberger (1983) and the FK code of Saikia and Burdick (1992). The advantage of generalized ray synthetics is the insight gained regarding the phases which make up various portions of a seismogram. The trade-off is that ray paths must be specified, making complete solutions impractical to obtain for any but the simplest structure. FK synthetics on the other hand include all phases, for a complete solution, although with this technique we cannot tell which path the propagating energy has traversed. In figure 4, synthetic seismograms for the two models of figure 6 are plotted above the vertical P waveforms of a single NTS explosion recorded at all three stations. We note again the differences in Pn/Pg amplitudes between stations. Here we can identify specific Pg arrivals in the data by comparison to synthetics. Major phases are noted above the top trace (C Gr is the converted group of PmPPmS, PmPSmP, etc.). Pasadena is the only station where PmP is large and distinct, as in the synthetics. That the PAS PmP arrival is earlier than the synthetics while the LAC PmP (recall figure 3 as well) matches their timing indicates lateral variations along either the respective crustal or upper mantle paths. The virtual disappearance of PmP at PFO and its diminution at LAC argue for variation in the crust be-

tween the NTS-LAC-PAS and the NTS-PAS path. The variation in Pn waveforms, further highlighted in figure 5, may indicate lateral variation or complicated 1-D structure in the upper mantle. Figure 5 is arranged like figure 4, but for Pn only. We can clearly see a secondary phase at about 1 second, moving in with distance (indicated by the upward arrows). There is a similar phase moving in with distance in the southern California model synthetics (figure 6), due to reflection off the top of the LVZ (indicated by the downward arrow at LAC; it merges with the initial peak at PAS and PFO). Furthermore, in the data there are 3 similar phases after the initial Pn peak at LAC, one at PAS, and 2 at PFO. These will be critical phases to understand,and will be the target of further study.

Figure 6 shows the models used to produce the synthetics of figure 5. At top is the model of Helmberger and Engen 1980), and below is a composite southern California model. The average crustal slowness and thickness matches Helmberger and Engen's. The average lid slowness is slightly greater than Helmberger and Engen's, to match the lower Pn velocity observed by Hearn and Clayton (1986) for southern California. The lid thickness is consistent with that found by Cara (1979). The velocity of the low velocity zone is consistent with P and S models developed by Helmberger (1973) and Grand and Helmberger (1984) respectively. The Moho and lid gradients were arrived at by forward modeling to approximate Pn and Pg relative amplitudes.

Conclusions and Recommendations:

The observed variation of both Pn/Pg ratios with distance and Pn waveforms is suggestive of lateral variations in the crust and upper mantle structure of southern California. The importance of understanding the secondary Pn phases to enable the distinction of depth phases points to the direction future work should take. Specifically, more detailed modeling of the Pn waveform should be performed to distinguish triplication phases, LVZ reflected phases, or other path effects, from depth phases. This should be complemented by array and 3-component analyses, both to distinguish the previously mentioned phases, as well as to separate out multipathing and near receiver scattering effects.

Bibliography:

Bouchon, M., Bull. Seism. Soc. Am., 71, 959-971, 1981

Burdick, L.J., C. K. Saikia, and N. F. Smith, Explosion Source Phenomenology, Geophys. Monog. 65, Am. Geophys. Un., 197-209, 1991

Cara, M., J.B. Minster, and R. LeBras, Bull. Seism. Soc. Am., 71, 985-1002, 1981

Grand, S.P. and D.V. Helmberger, Geophys. J. R. astr. Soc., 76, 399-438, 1984

Hearn, T.M. and R.W. Clayton, Bull. Seism. Soc. Am., 76, 511-520, 1986

Helmberger, D. V., Geophys. J. R. astr. Soc., 34, 251-263, 1973

Helmberger, D. V. and G. R. Engen, Bull. Seism Soc. Am., 70, 1699-1714, 1980

Helmberger, D. V., Proc. of the Intl. School of Phys. <<Enrico Fermi>> Course, LXXXV, Earthquakes: Observation, Theory and Interpretation, Ed. Kanamori, H. and E. Boshi, North-Holland Pub. Co., 1983

Helmberger, D. V., R. Stead, P. Ho-Liu, and D. Dreger, Geophys. J. Int., 110, 42-54, 1992

Helmberger, D. V., L.S. Zhao, D. Dreger and V. LeFevre, Exploration of the Lower Lithosphere; Northeastern United States, (pre-print) 1993

Langston, C. A. and D. V. Helmberger, Geophys. J. R. Astr. Soc., 42, 117-130, 1975

Muller, G., Z. Geophys., 35, 347-371, 1969

Saikia, C. K. and L. J. Burdick, Phillips Laboratory, WCCP-R-93-01, Sci. Report, 1993

Zhao, L. S., and D. Helmberger, Source Estimation from Broadband Regional Seismograms, (pre-print) 1993

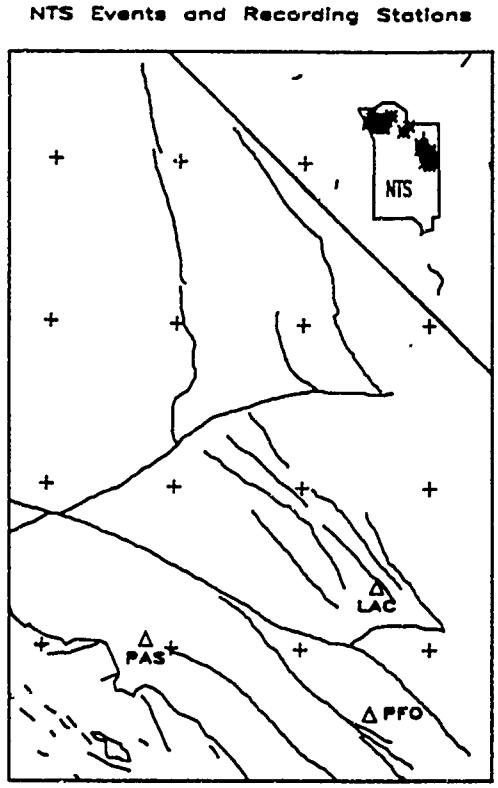

Figure 1: Nevada Test Site (NTS) event locations (asterisks) and seismic stations (triangles).

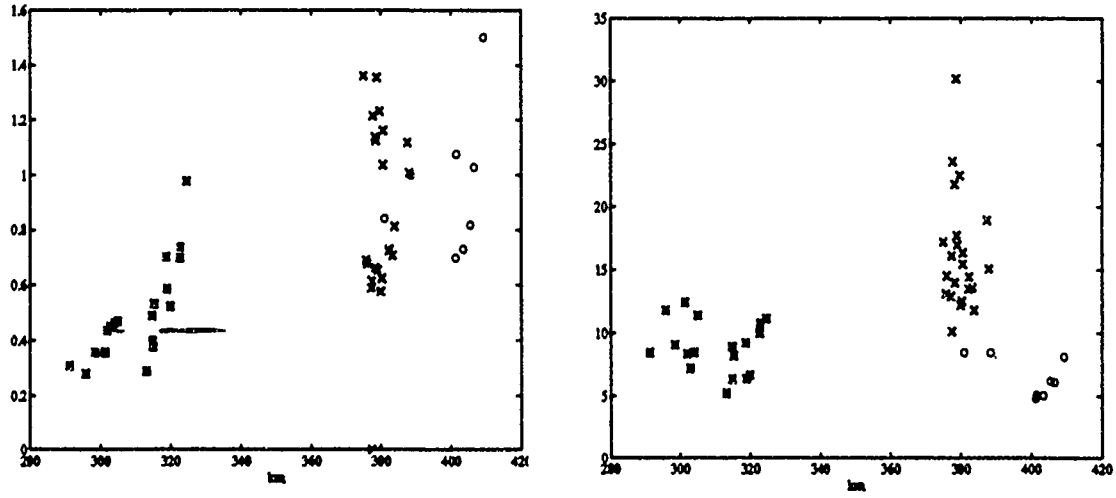

Figure 2: Pn/Pg amplitude ratios plotted as a function of distance for LAC (asterisks), PAS (x's), and PFO (circles), using Pn rms amplitude (left) and Pn peak amplitude (right).

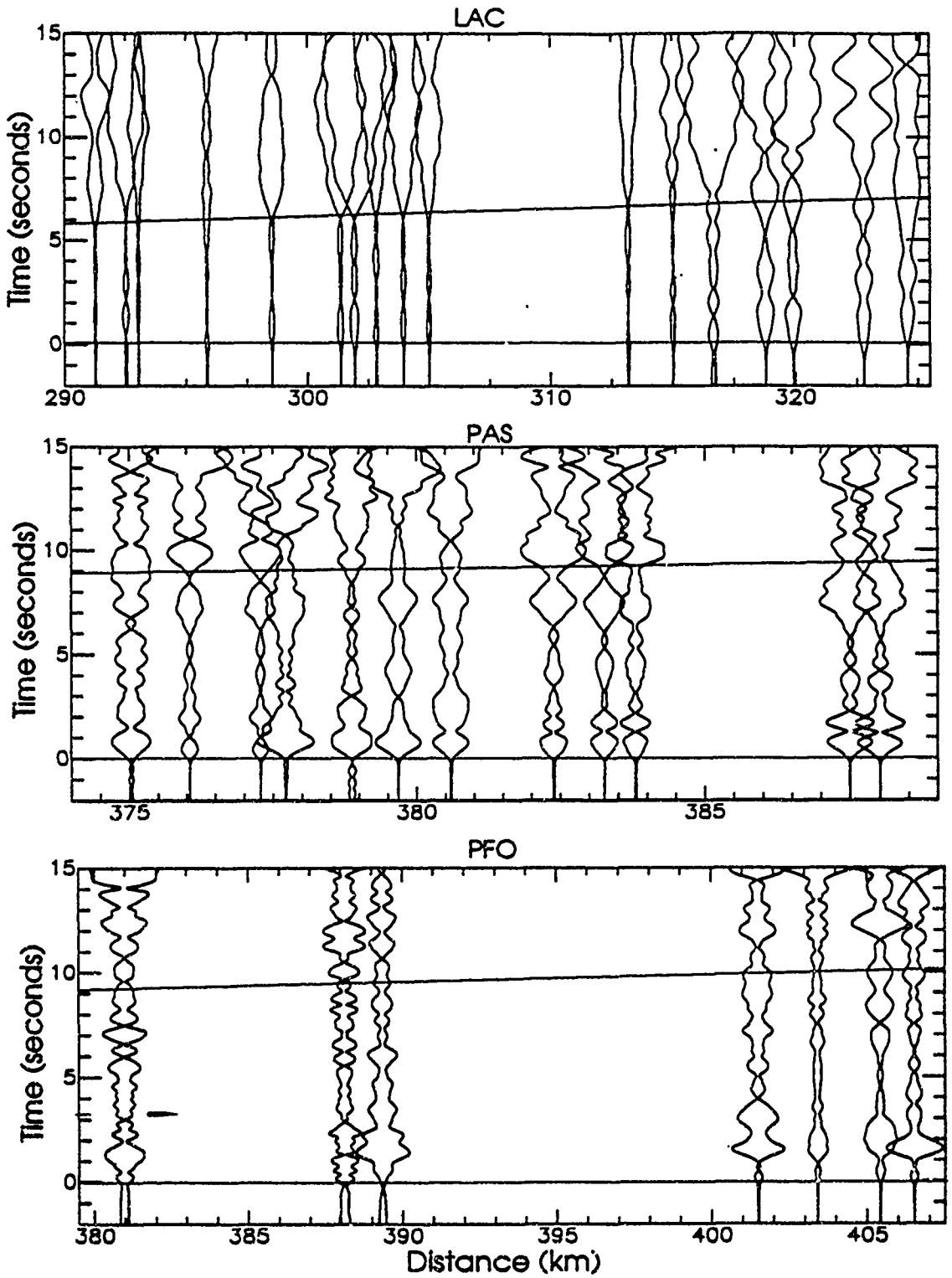

Figure 3: Envelope record sections for NTS events recorded at LAC, PAS, and PFO. Note that distance scales vary.

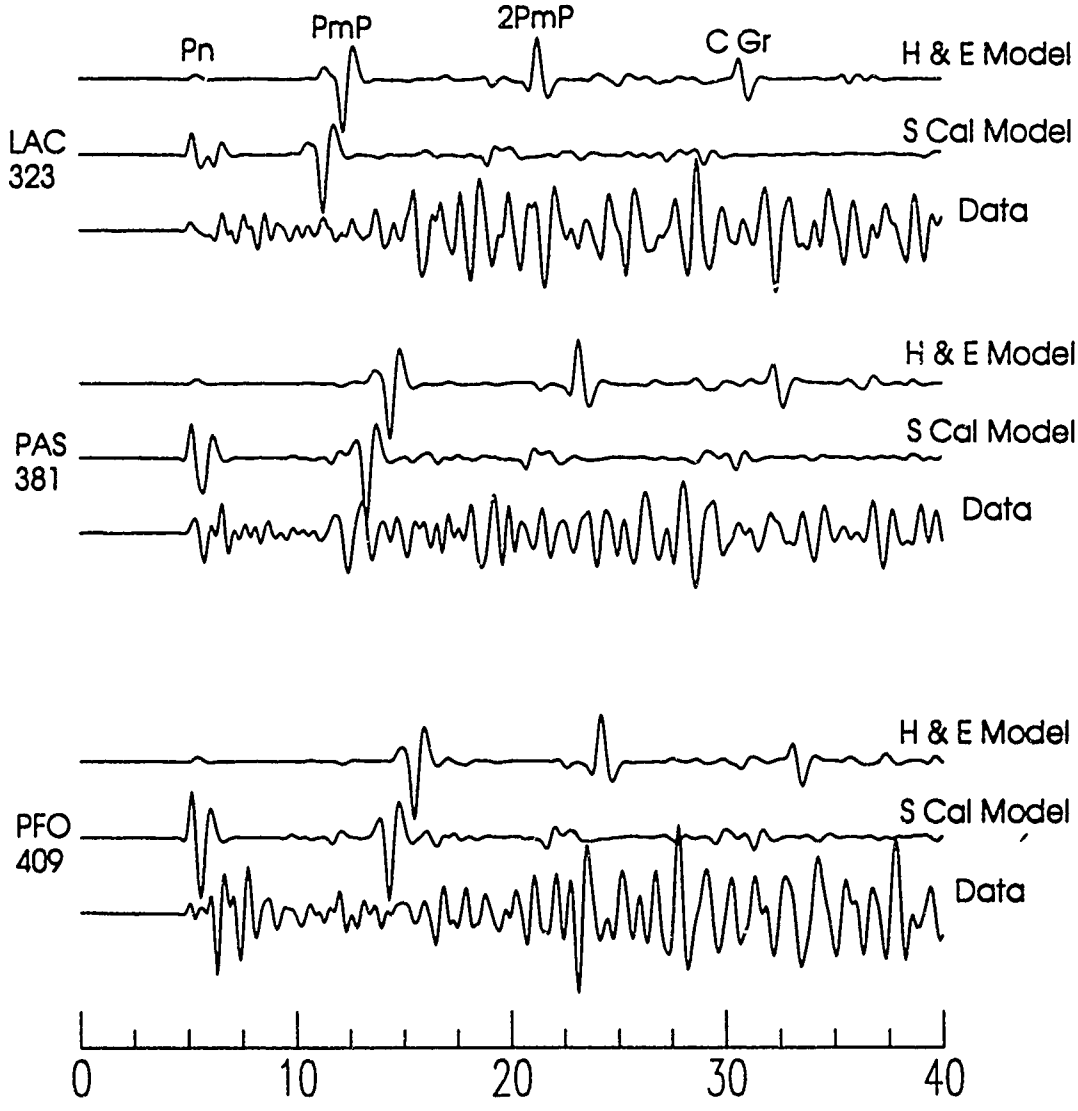

Figure 4: Synthetic and observed vertical P waveforms at LAC (top), PAS (middle), and PFO (bottom) for the April 4, 1991 NTS event (BEXAR). The top trace in each set of three is a synthetic for the Helmberger and Engen Model (1980), the middle trace is a synthetic for the composite southern California model, and the lower trace is data. Numbers to the left are NTS to station distances. The major P phases are indicated above the uppermost synthetic seismogram using the terminology of Saikia and Burdick (1991).

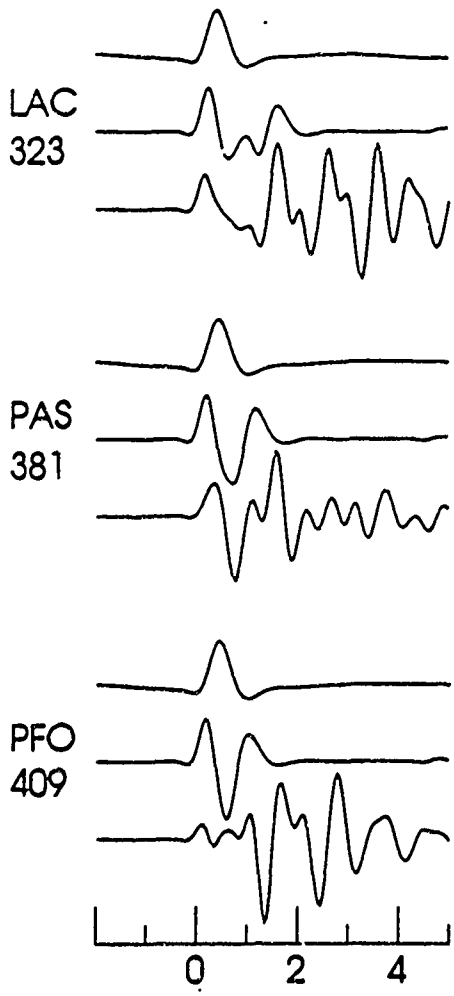

Figure 5 (above): Synthetic and observed Pnl waveforms at LAC (top), PAS (middle), and PFO (bottom) for the April 4, 1991 NTS event (BEXAR).Numbers to left are NTS to stationdistances.

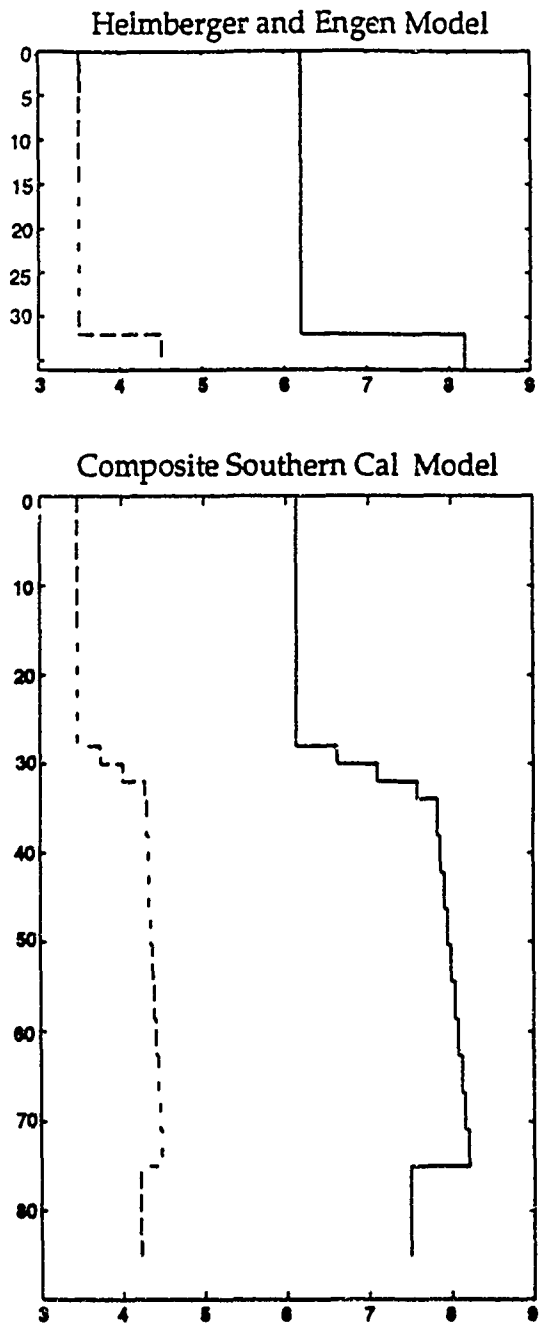

Figure 6: Models used in constructing synthetic seismograms of figures 4 and 5.

XNICE - A System for Evaluation of the Identification Capabilities of Regional and Global Networks

T. G. Barker, J. L. Stevens, and K.L. McLaughlin

Contract Pending
S-CUBED, A Division of Maxwell Laboratories

1. OBJECTIVE

The ability to identify underground nuclear explosions in a non-proliferation environment is critically dependent on the capability of the network of seismic stations to detect a sufficient number and quality of seismic signals from suspicious events. In this paper, we describe a system to evaluate the capability of networks to identify events. This system will be derived from the NICE program, which was developed under DARPA support and installed at the Center for Seismic Studies. NICE (Network Identification Capability Evaluation) is a set of computer programs which evaluate the ability of either existing or potential networks of seismic stations to identify events as nuclear explosions or earthquakes. NICE makes this assessment based on analysis of teleseismic body waves and surface waves using identification criteria established by AFTAC.

The objective of the project is to enhance and expand the capabilities of the NICE programs, to evaluate the system using data and NMRD software at the Center for Seismic Studies and to use the system to evaluate the capabilities of existing and hypothetical networks to monitor areas where there is real concern about the possibility of clandestine underground nuclear testing programs. NICE will be enhanced (to XNICE) by adding a modern Graphical User Interface (X/Motif) and linking with the Center 3.0 Oracle database; capabilities will be expanded by adding the capability to evaluate networks that include arrays and use regional seismic signals; the system will be evaluated by linking directly with the IMS to use the capabilities of the IMS together with the ability of NICE to generate a realistic arrival stream, and by using the GSETT data to evaluate the capabilities and limitations of a worldwide network of stations. Finally, XNICE will be applied to determine network capability and optimal network configuration in four specific areas: the Middle East (Pakistan, Iran, Iraq), South America (Brazil, Argentina), North-Central Africa (Algeria, Libya), and Korea.

2. RESEARCH ACCOMPLISHED

The original version of NICE was completed under an earlier DARPA contract, while the contract to write the enhanced version, XNICE, is pending. In the following, we describe the current version of the program and discuss an initial analysis of the capabilities of the ISC and GSETT networks using the program. Finally, we discuss our plans for applying XNICE to selected geographic regions.

2.1 NICE – Network Identification Capability Evaluation

The NICE program (Barker, *et al.*, 1986) was developed by S-CUBED under DARPA support and installed at CSS in 1986. The version of NICE installed at CSS is designed to model the process used by AFTAC to identify events recorded at teleseismic distances. It uses a Monte Carlo approach in which a sequence of events are generated, propagated to the stations in a network, then analyzed to extract relevant parameters and given discrimination scores. This is accomplished by four modules, which are shown in a flow chart in Figure 1, and which we describe briefly below. The modular design allows one to examine independently the effects of the source region, the wave propagation, the seismic network (both location of stations and sensitivity) and discrimination rules on identification of events. The parameters of each module can be verified by direct comparison with observations.

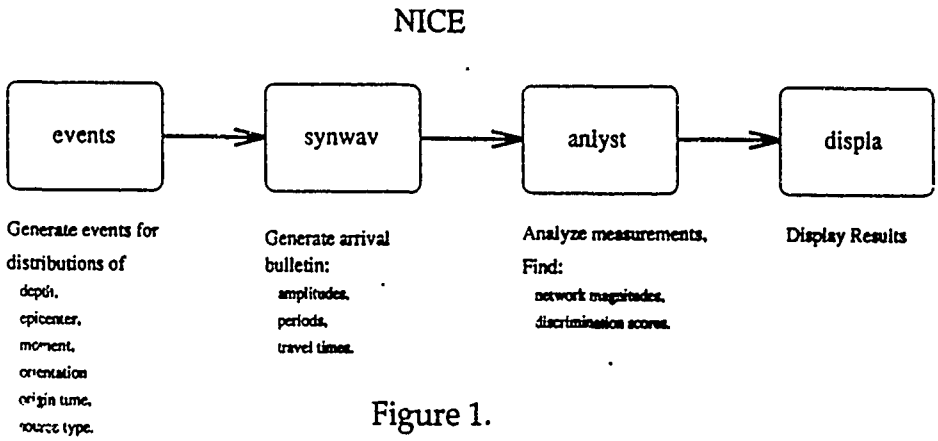

Figure 1.

events module

The **events module** computes the source properties of a sequence of events which are realizations of probability distributions derived from observations of the source region. The distributions describe the epicenter, depth, moment, orientation and recurrence interval of the events. The program currently computes explosion and earthquake sources, but can be easily extended to include quarry blasts, mine implosions, rock bursts, and decoupled explosions. The **events module** generates an events bulletin appropriate for a particular geographic region.

synwav module

The **synwav module** generates a synthetic stream of arrivals. **Synwav** reads the events catalogue generated by the **events module** along with station locations and detection parameters from a station file and computes synthetic body wave (P, pP and S phases) and fundamental-mode surface wave seismograms (LR) for all stations in the network. The signals are measured for amplitude, period and travel time after which a station-specific noise estimate is added to the measurements. Signals which do not meet a specified signal-to-noise ratio are classified as non-detections. The parameters of wave

propagation can be regionalized and verified by comparison with observations. The results are summarized in an arrival bulletin.

Modeling teleseismic signals can be done reliably once the propagation parameters are derived. Realistic regional waveforms cannot, in general, be generated by synthetic methods. However, amplitudes, arrival times, and other features of regional phases can be generated reliably by a combination of theoretical and empirical methods.

anlyst module

The **anlyst module** reads the arrival bulletin made by the **synwav module** and calculates network averaged magnitudes (currently m_b and M_S) and discrimination scores. **Anlyst** is currently coded to compute the scores for these discriminants: epicentral location, depth by pP, depth by travel times and ratio of m_b to M_S. The program uses rules similar to those of AFTAC for censoring bad data (rejection of signals based on signal-to-noise ratios and number of quadrants reporting) and for assigning discrimination scores, which indicate the degree of confidence that the event can be considered an earthquake. Although **anlyst** was designed specifically to model AFTAC discriminants, it is easily extended to add additional discriminants such as those discussed by Bennett, *et al.* (1989,1992) and can be used as a testbed for potential discriminants. The results of the calculations by the **anlyst module** are written to a discrimination bulletin.

displa module

The **displa module** makes lists and plots which show the identification performance of the net. A sophisticated command line processor allows the user to view not only the overall performance, but also features of the process which contributed to the performance. For example, one may determine the identification rate as function of m_b. The program can be used to answer questions such as: What discriminants were credited with the identification? What range of m_b, M_S or depth contained the events which were responsible for identification? What role did the detection threshold play? In addition, discrimination bulletins can be compared with this module. Thus, the results of a Monte Carlo simulation can be compared with a bulletin derived directly from observations so that the program can be calibrated for a particular seismic area and network.

2.2 Evaluation of the GSETT Network

As an illustration of the NICE software capabilities we have exercised the existing software using the GSETT arrival database available on CDROM from CSS (GSETT, 1992). We compare the detection and depth location capabilities of the GSETT network with that of a hypothetical ISC network as analyzed by Ringdal (1986). We chose as an example, to estimate the uncertainty in teleseismic depth determination as a function of m_b and location for a 10 km deep earthquake in the region of North Africa and the Middle East (15-40 deg N., 10-80 deg E.). This exercise illustrates some of the existing capabilities of the current existing software.

In order to predict teleseismic P detections, we first estimated detection thresholds for the GSETT stations. We used only those GSETT stations that reported 20 or more P arrivals with amplitudes given in nm. The Kelly & Lacoss (1969) maximum likelihood estimation facility was used within NICE for estimating the 50% detection threshold and variance. Figure 2 shows plots of cumulative detections as a function of log-amplitude for a subset of the GSETT network. The stations are labeled on the plot in order of detection threshold level. The average detection threshold for the GSETT network was 20 times lower than thresholds derived by Ringdal (1986) for the ISC network. This is in some measure due to the use of arrays in the GSETT network.

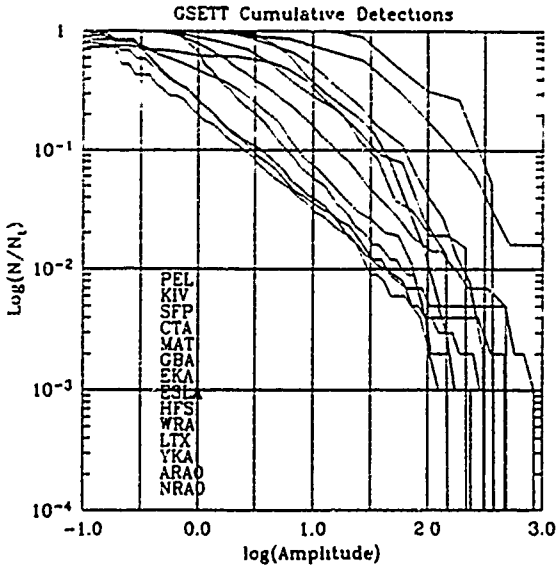

Figure 2. Normalized cumulative number of detections for 14 selected GSETT stations.

Next, NICE was instructed to generate an ensemble of earthquakes with depths of 10 km, located on a grid of latitudes and longitudes with m_b's between 3.83 and 4.83. Detection thresholds (noise levels), and variances for log-amplitude and travel-time were input for each station. NICE then generated P waveforms for each station-event pair, determined which waveforms would have been detected, and measured each waveform. The events were then located and classified. The process was repeated for an ISC network of 115 stations analyzed by Ringdal (1986).

Figure 3 compares some of the summary statistics of the GSETT and ISC networks. At the bottom plots, the median number of stations detecting and the 50% quantiles are plotted as a function of magnitude. In the middle plots, the median formal depth uncertainty and 50% quantiles are plotted versus magnitude. In the upper plots, the network m_b bias due to censoring is plotted as a function of magnitude. Note that the detection threshold of the GSETT network is substantially better than the hypothetical ISC network.

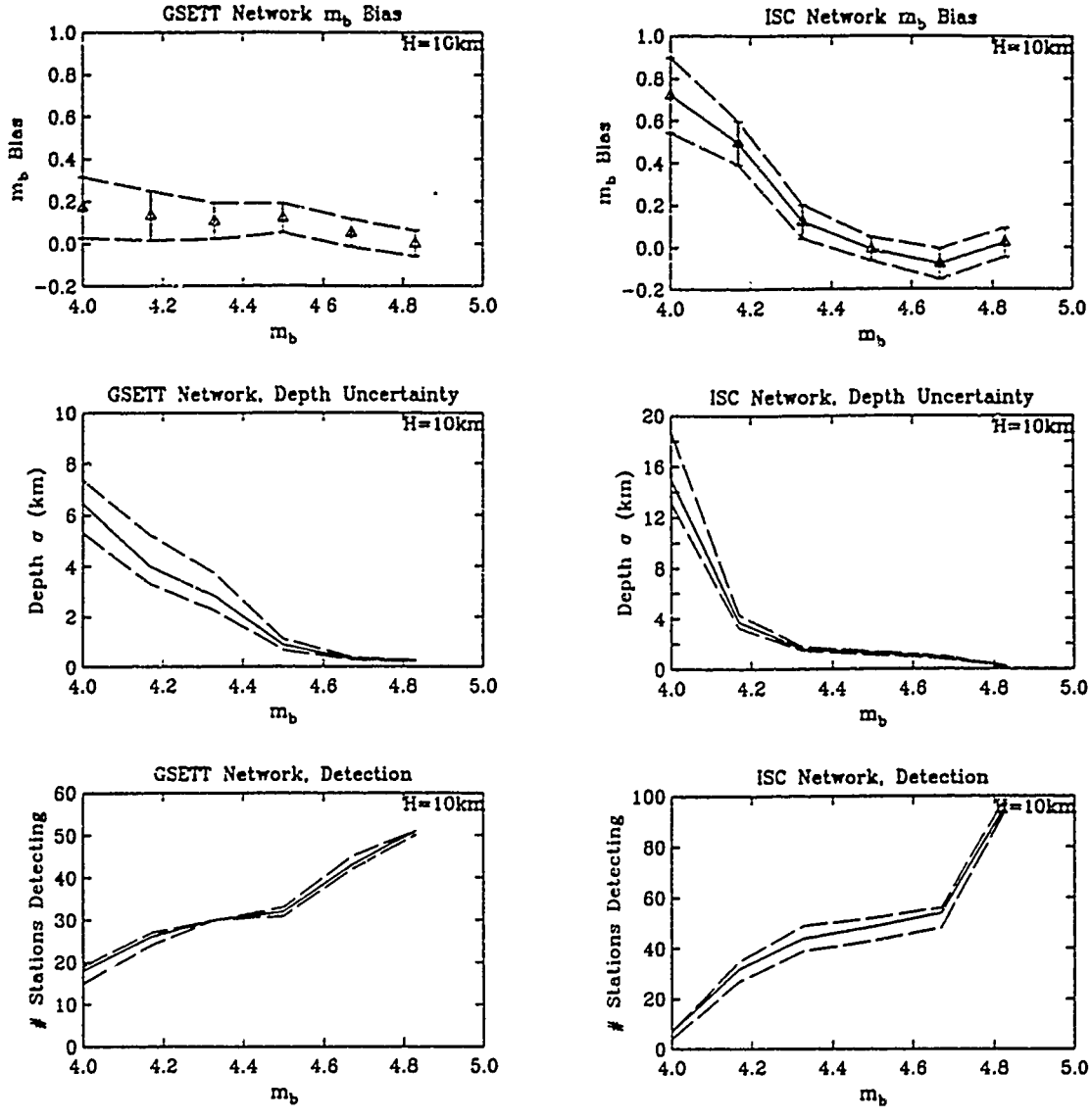

Figure 3. Comparison of GSETT and ISC network bias, depth uncertainty, and detections as a function of m_b.

Depth determination is an important discriminant. In particular, if an event can be located at depth such that the error in depth precludes the event from having a location at the surface, we can consider the event an earthquake. In analyzing the capability of each network, we can use NICE to estimate the magnitude at which a nominal earthquake at 10 km will with some certainty be located at 10 km plus or minus 5 km. This "identification" detection threshold is in the neighborhood of 4.1 to 4.3 for both networks, but we see that the GSETT depth uncertainties increase more slowly as the magnitude is decreased. This is largely due to the somewhat larger ISC network offsetting the lower GSETT detection thresholds.

Figure 4 shows the projected GSETT teleseismic detection and location capabilities as a function of latitude and longitude for an m_b = 4.0 earthquake at a depth of 10 km. The maps cover parts of Northern Africa and the Middle East (15-40 deg N., 10-80 deg E.). The top map shows contours of the number of stations detecting for the

GSETT network and the middle map shows contours of depth location uncertainty in km. For comparison, the bottom map shows contours of stations detecting for the ISC network. Note that the formal depth uncertainty for the GSETT network has significant dependence on latitude and longitude. To the south and east of the region under study, the network .vould not be able to identify a 10 km earthquake by depth location alone. The GSETT network should be able to identify an earthquake at deptl. at this magnitude level for some of the region of interest. Depth uncertainty is greater than the earthquake depth over the entire region for the ISC network.

This analysis could have included evaluation of other discriminants such as M_S:m_b. Furthermore, with the inclusion of regional modeling capabilities, NICE will be able to evaluate the effectiveness of regional 3-component stations and arrays in monitoring any region of interest.

RECOMMENDATIONS AND RESEARCH PLANS

The NICE program will be enhanced to include stations at regional distances. A graphical user interface (using Xwindows) will be added and the program will be connected to the Center relational database management system. We will then apply XNICE to regions where there is concern about the possibility of clandestine nuclear testing to evaluate existing networks and identify network improvements to optimize identification capability.

REFERENCES

Bratt, S.R., G.W. Beall, H.J. Swanger. F.K. Dashiell and T.C. Bache (1991), "A Knowledge-Based System for Automatic Interpretation of Seismic Data to Associate Signals and Locate Events", Science Applications International Corporation Quarterly Report to DARPA, SAIC 91/1281.

Ringdal, F. (1986). "Study of Magnitudes, Seismicity, and Earthquake Detectability Using a Global Network," *BSSA 76*, 1641-1659.

Gupta, I. N., and K. L. McLaughlin (1987). "Attenuation of Ground Motion in the Eastern United States", *BSSA 77*, 366-383.

Gupta, I. N., K. L. McLaughlin, R.A. Wagner, R.S. Jih, and T.W. McElfresh (1989). "Seismic Wave Attenuation in Eastern North America", Teledyne Geotech Report NP-6304 to EPRI.

Kelly, E. J., and R. T. Lacoss (1969). "Estimation of Seismicity and Network Detection Capability", Lincoln Laboratory Technical Note 1969-41, MIT.

Sereno, T. J., Jr. (1989), "Numerical Modeling of Pn Geometric Spreading and Empirically Determined Attenuation of Pn and Lg Phases Recorded in Eastern Kazakh", Science Applications International Corporation Semiannual Report to DARPA, SAIC 89/1555.

Number of GSETT Network Teleseismic Stations Detecting

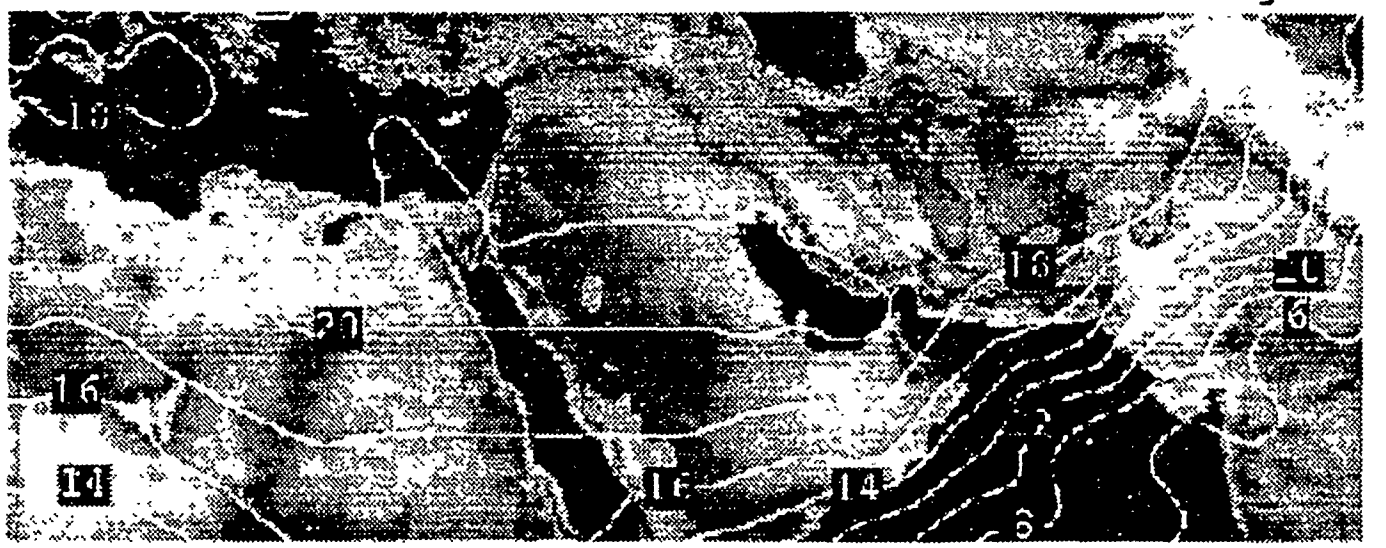

GSETT Network Teleseismic Depth Uncertainty (km)

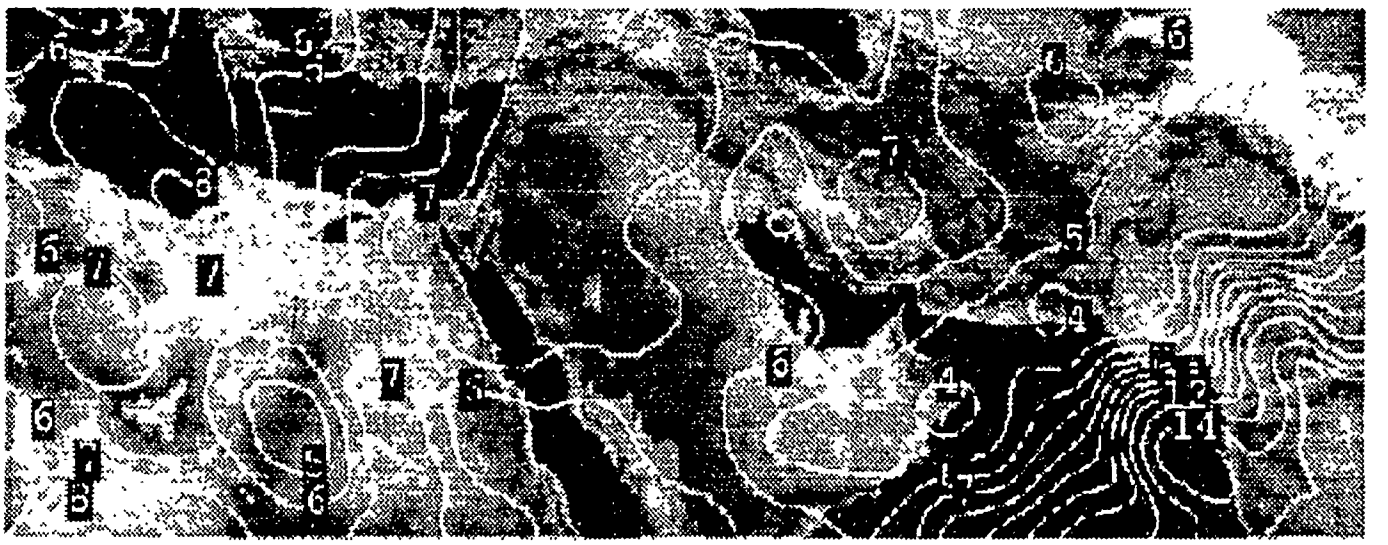

Number of ISC Network Teleseismic Stations Detecting

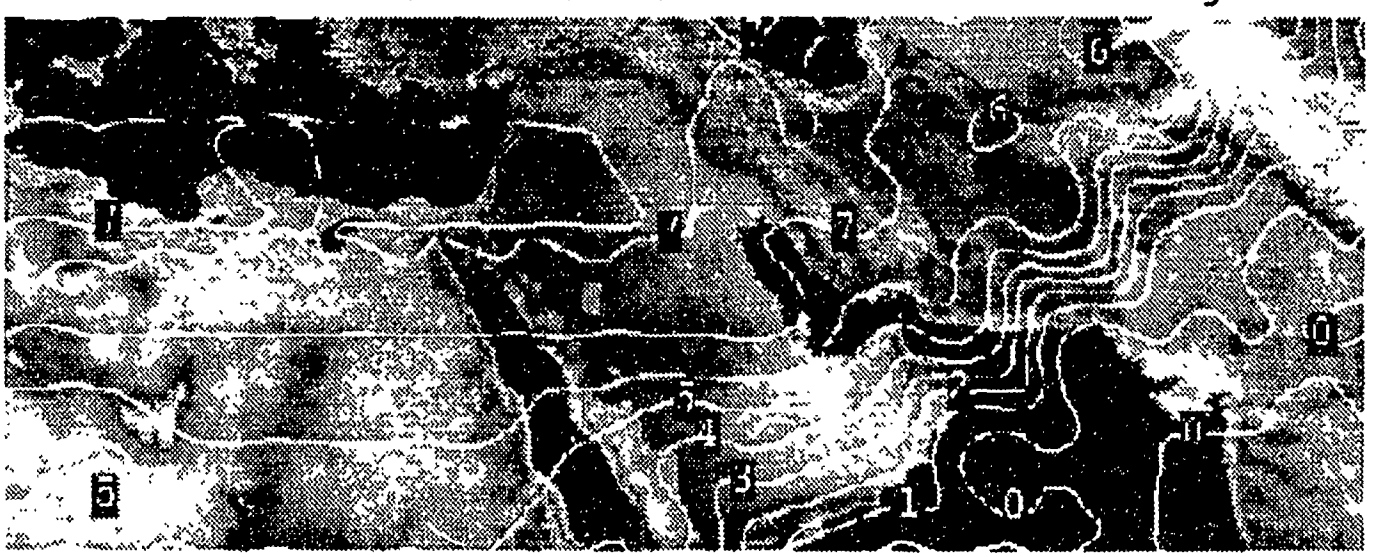

Figure 4.

Investigation of Regional Seismic Discriminants Using Visualization and Statistical Analysis Methods in the Intelligent Seismic Event Identification System

Douglas R. Baumgardt
Zoltan Der

ENSCO, Inc., 5400 Port Royal Road
Springfield, Virginia 22151
Contract No. F29601-92-C-0009
Contract No. F19628-93-C-0103

OBJECTIVES

This paper reports on the progress of a continuing project, dealing with discrimination analysis research of a large number of regional events processed by the Intelligent Monitoring System (IMS), and a new project concerned with issues involved with porting discriminants from known geographic regions, such as Scandinavia and the U.S., to other regions of the world, like the Middle East. In both studies, a seismic discrimination research system, called the Intelligent Seismic Event Identification System or ISEIS, developed under an earlier project (Baumgardt et al, 1991) has been used to process events formed by the IMS to extract discrimination waveform features and to view the processing results. Our goals have been to analyze the promising waveform discriminants; to examine the variabilities of performance of waveform discriminants for identifying nuclear explosions, chemical explosions, and earthquakes; to determine the possible causes of these variabilities; and to study effects of propagation path which will affect the porting of discriminants to other regions of the world.

RESEARCH ACCOMPLISHED

ISEIS Processing of IMS Data

The ISEIS system has been successfully installed at the Center for Seismic Studies (CSS) and interfaced with the CSS databases in order to process, either automatically or interactively, regional seismic waveforms formed by the IMS (Baumgardt et al , 1993). Figure 1 shows a schematic diagram of the processing methods used. Since ISEIS was designed to be a research system, much effort was given to provide numerous options for extracting a variety of waveform features (e.g., regional multifrequency *P/S* ratios, spectral features) which are all stored in an Oracle database. These features can then be extracted from this database, either by ISEIS or by other algorithms, such as, for example, SPLUS, in order to do subsequent statistical analysis and visualization studies of the features for discrimination purposes.

ISEIS also includes interfaces for a rule-based expert system which contains rules for the identification of events based on waveform features. Currently, discrimination rules have been implemented for identification of explosions and earthquakes based on regional high-frequency (8-16 Hz) *P/S* amplitude ratios, single-phase spectral ratios, and ripple-fire detection in mine blasts based on time-independent spectral modulations. The system is sufficiently modular to allow the modification of discriminants and the easy incorporation of new ones. Our statistical visualization studies of multivariate *Pn/Sn* and *Pn/Lg* ratios in different frequency bands (Baumgardt et al, 1993) revealed that discrimination information is contained in all the frequency bands. Thus, in order to utilize these multivariate features, a *three-layer perceptron neural network* simulator, trained by *back-propagation*, has been implemented for event identification using ISEIS-derived phase-amplitude-ratio features.

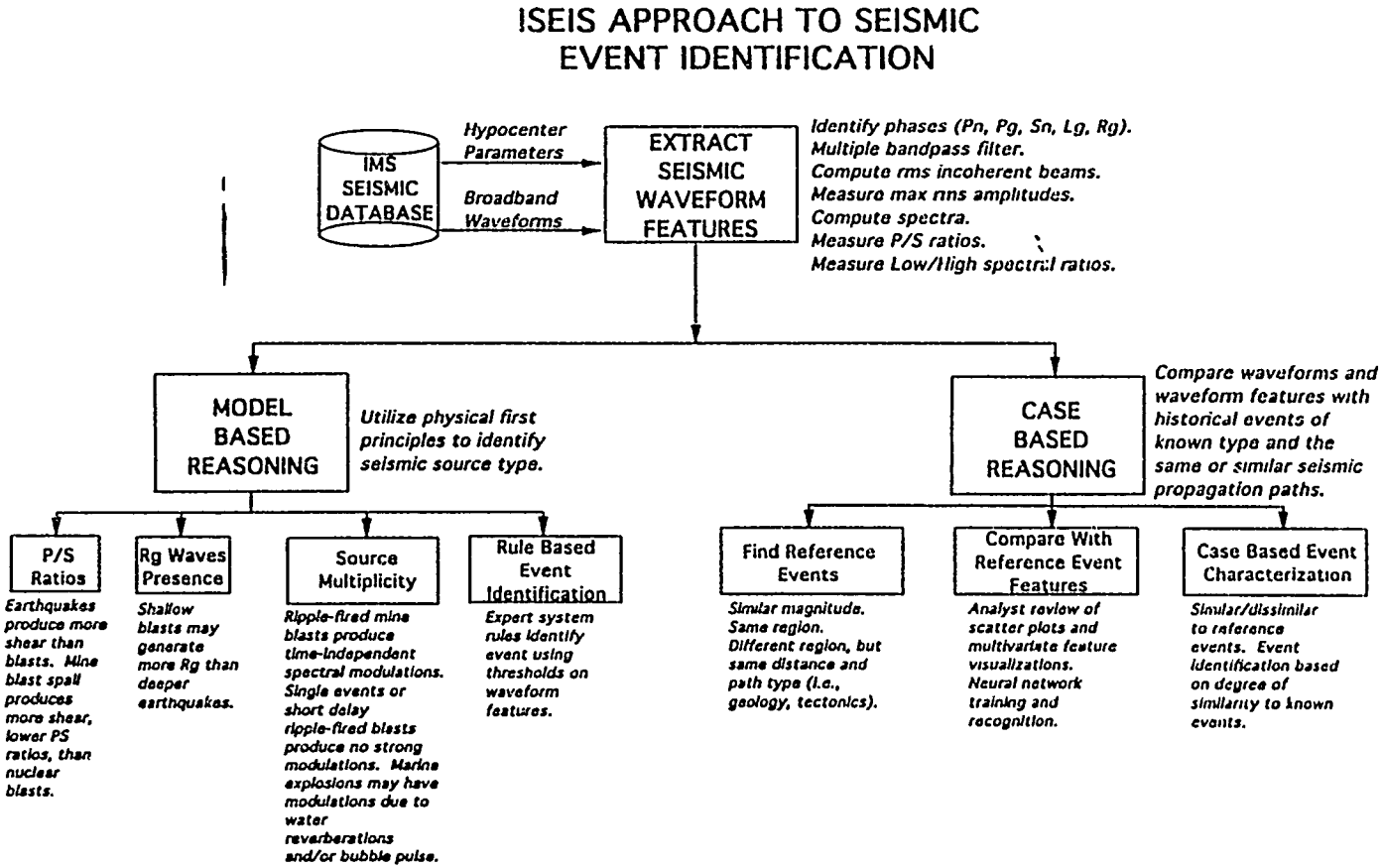

Figure 1: Schematic diagram of the ISEIS approach and interface to the IMS at the CSS.

The performance of these rule-based and neural-network identification procedures are now being evaluated on a large database of presumed known events recorded by the Scandinavian arrays, NORESS, ARCESS, and FINESA (Riviere-Barbier et al., 1993) and on events in the ground-truth database (Grant et al, 1993).

Discriminant Evaluation On the Ground Truth Database and Other Known Events

Data for selected events in the Ground-Truth Database (GTD) at the CSS (Grant et al., 1993) and other presumed known events have been processed by ISEIS and the amplitude-ratio and spectral-ratio features have been studied in detail (Baumgardt et al, 1993). Most of the events in the GDT consist of mine blasts, earthquakes, and mine tremors in mining districts of Germany (Vogtland) and Poland (Lubin, Upper Silesia) recorded at the GERESS array and the Steigen earthquake swarm in northern Norway, recorded at ARCESS and NORESS. Other events studied have included earthquakes and mine blasts in southern Norway recorded at NORESS and ARCESS recordings of Spitzbergen region earthquakes and mine blasts on the Kola Peninsula.

Figure 2 shows a summary of *Pn/Lg* amplitude ratios results for mine blasts and earthquakes recorded at the three arrays, GERESS, NORESS, ARCESS, for three different geographic regions. Although the distance ranges of the events from these three arrays and tectonic characteristics of the three geographic areas varied considerably, the high-frequency *Pn/Lg* were very consistent. As found in other studies (e.g., Bennett et al, 1989), high-frequency *P/S* ratios separate explosions and earthquakes, with explosions having higher values. However, our studies have shown that the mine blast populations have much greater variance in these ratios than earthquakes, which is clear in the larger error bars for the blasts evident in Figure 2. Mine blasts can generate significant shear waves, perhaps due to spall, induced fracturing of rock, or associated mine tremors, and thus cannot be considered to be pure explosions.

Figure 3a shows a plot versus distance of *Pn/Lg* in the 8 to 10 Hz band for mine blasts and earthquakes in the Vogtland region of Germany and mine tremors in the Lubin region of Poland. Clearly, mine tremors resemble earthquakes in that they have low *Pn/Lg* ratios. Some of these events may be associated with blasting activity. Thus, the low *Pn/Lg* ratios we have observed for blasts in other regions may be a result of their being associated with induced mine tremors.

Bennett and Murphy (1986) showed that spectral ratio between low and high frequency bands of the *Lg* spectrum effectively separated explosions and nuclear explosions in the western U.S. Figure 3b shows a plot of the *Lg* spectral ratios (2-4 Hz/4-6 Hz) for the same events in Germany and Poland shown in Figure 3a. We find that this ratio separates the Vogtland mine blasts and earthquakes, with earthquakes having lower ratios (higher frequencies) than blasts, although the mine blasts have larger variance that the earthquakes. However, Figure 3b shows that the induced events at Lubin are very scattered and overlap both populations. Baumgardt et al (1993) found this discriminant to be completely ineffective in the Scandinavian shield. We suggest that this discriminant may be due to depth differences between earthquakes and explosions and may be strongly affected by tectonic region.

Tectonic Effects on Discriminants - Portability Issues

As mentioned above, waveform discriminants will be strongly affected by differences in propagation path which must be taken into account when porting discriminants from one geographic region, such as Scandinavia or western U.S., to other regions, like the Middle East. We have begun a study to investigate these effects in detail.

We expect that regional propagation across the Middle East will be much more complicated by tectonic features, such as the Red Sea and Jordan rifts, than the simpler shield regions of Scandinavia. As an analogy to this region, we have investigated

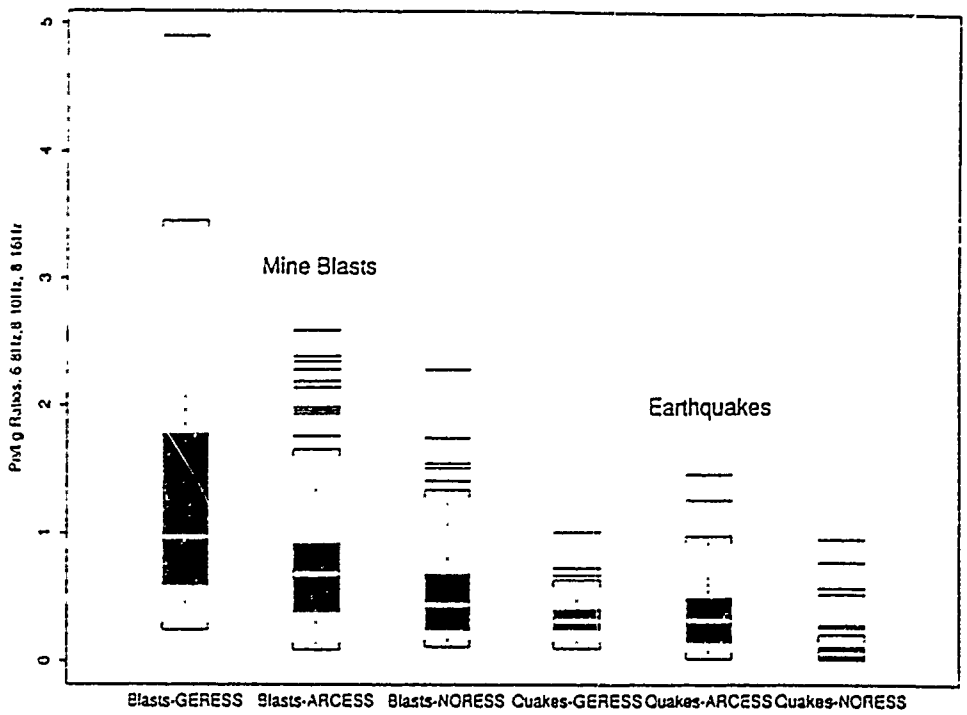

Figure 2: Boxplot diagram of *Pn/Lg* ratios in the 6-8 Hz and 8-10 Hz band for mine blasts and earthquakes recorded by three regional arrays in three different geographic regions.

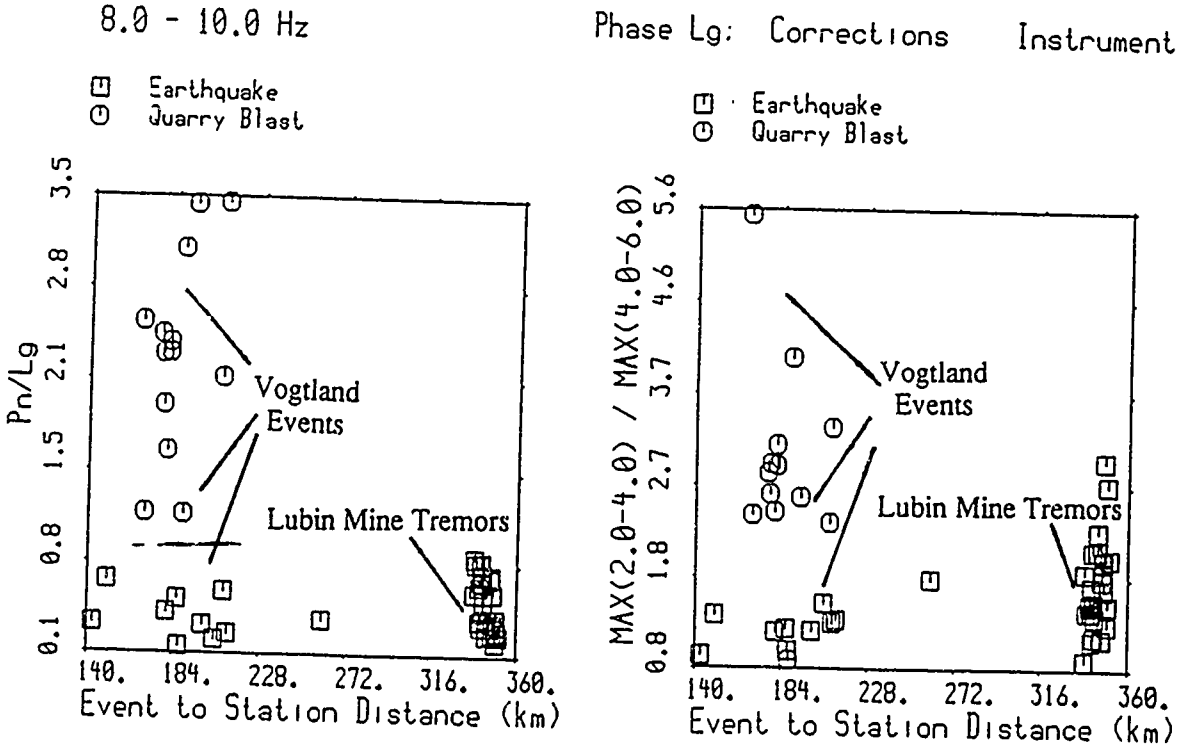

Figure 3: (a) Plot of 8-10 Hz*Pn/Lg* ratios, measured at GERESS, versus distance for mine blasts and earthquakes at Vogtland, Germany, and mine tremors in the Lubin region of Poland; (b) Plot of 2-4Hz/4-8Hz *Lg* spectral ratios of the same events as in 3(a).

variations in *Pn/Sn* ratios for earthquakes in the Spitzbergen and Greenland Sea regions, associated with the northern part of the Mid-Atlantic ridge, compared with nuclear explosions at Novaya Zemlya, continental earthquakes, and mine blasts on the Kola Peninsula.

Figure 4 shows a plot versus distance of *Pn/Sn* ratios in the 8-10 Hz band, measured at ARCESS, for these events. The events plotted as triangles are events from the Greenland Sea. They exhibit large scatter and some of the events have large *Pn/Sn* ratios, associated with low *Sn* excitation compared with *Pn* which overlaps the nuclear explosion values. Figures 5a and 5b show plots of the locations of the events which had high and low *Pn/Sn* ratios, respectively. These plots show that the events with high *Pn/Sn* ratio occurred on or near the east flank of the Mohns Ridge, whereas the events with low *Pn/Sn* ratio occurred well to the east of the Ridge. It has long been known (e.g., Molnar and Oliver, 1969) that *Sn* wave propagation inefficiently across rift zones and our results show that inefficient *Sn* propagation will produce explosion-like *Pn/Sn* ratios.

CONCLUSIONS AND RECOMMENDATIONS

Discrimination studies of Scandinavian and European explosions and earthquakes processed by the IMS and ISEIS have demonstrated that regional waveform features, most notably, high-frequency *P/S* ratios, can provide useful discrimination capability. Nuclear explosions can be clearly identified based on high *Pn/Sn* ratios (Baumgardt, 1993). However, many mine blasts may be confused with earthquakes because the former can generate significant shear waves due to associated spalling and induced mine tremors. Hopefully, many such events can be identified from observed ripple fire or context. However, when considering evasion scenarios in mines, it should be recognized that earthquake-like features can be produced by shallow explosions.

With respect to porting discriminants, we have seen clear indication of propagation path effects on *Pn/Sn* ratios and possible tectonic region effects on *Sn* and *Lg* spectral ratios. Future research for nonproliferation monitoring will be directed towards a closer examination of these effects and to developing methods for utilizing geologic and tectonic knowledge of propagation paths to properly calibrate waveform discriminants in regions of extreme tectonic complexity, such as in the Middle East.

REFERENCES

Baumgardt, D.R., S. Carter, M. Maxson, J. Carney, K. Ziegler, and N. Matson (1991). Design and development of the intelligent event identification system, *PL-TR-91-2298(I)*, Final Report, Volumes I,II, and III, ENSCO, Inc., Springfield, Va. ADA248381

Baumgardt, D.R., J. Carney, M. Maxson, and S. Carter (1993). Evaluation of regional seismic discriminants using the Intelligent Seismic Event Identification System, SAS-TR-93-38, ENSCO, Inc., Springfield, Va.

Bennett, T.J. and J.R. Murphy (1986). Analysis of seismic discrimination capabilities using regional data from western United States events, *Bull. Seism. Soc. Am.*, **76**, 1069-1086.

Bennett, T.J., B.W. Barker, K.L. McLaughlin, and J.R. Murphy (1989). Regional discrimination of quarry blasts, earthquakes, and underground nuclear explosions, Final Report, *GL-TR-89-0114*, S-Cubed, La Jolla, Ca. ADA223148

Grant, L., J. Coyne, F. Ryall (1993). CSS Ground-Truth Database: Version 1 Handbook SAIC Scientific Report No. C93-05, August, 1993.

Molnar, P. and J. Oliver (1969). Lateral variations of attenuation in the upper mantle and discontinuities in the lithosphere, *J. Geophys. Res.*, 74, 2648-2682.

Riviere-Barbier, F., D. Baumgardt, and W. Rodi (1993). Using groups of similar events at the Scandinavian arrays to identify and to relocate events, 15th Annual PL/ARPA Seismic Research Symposium, Vail, Co.

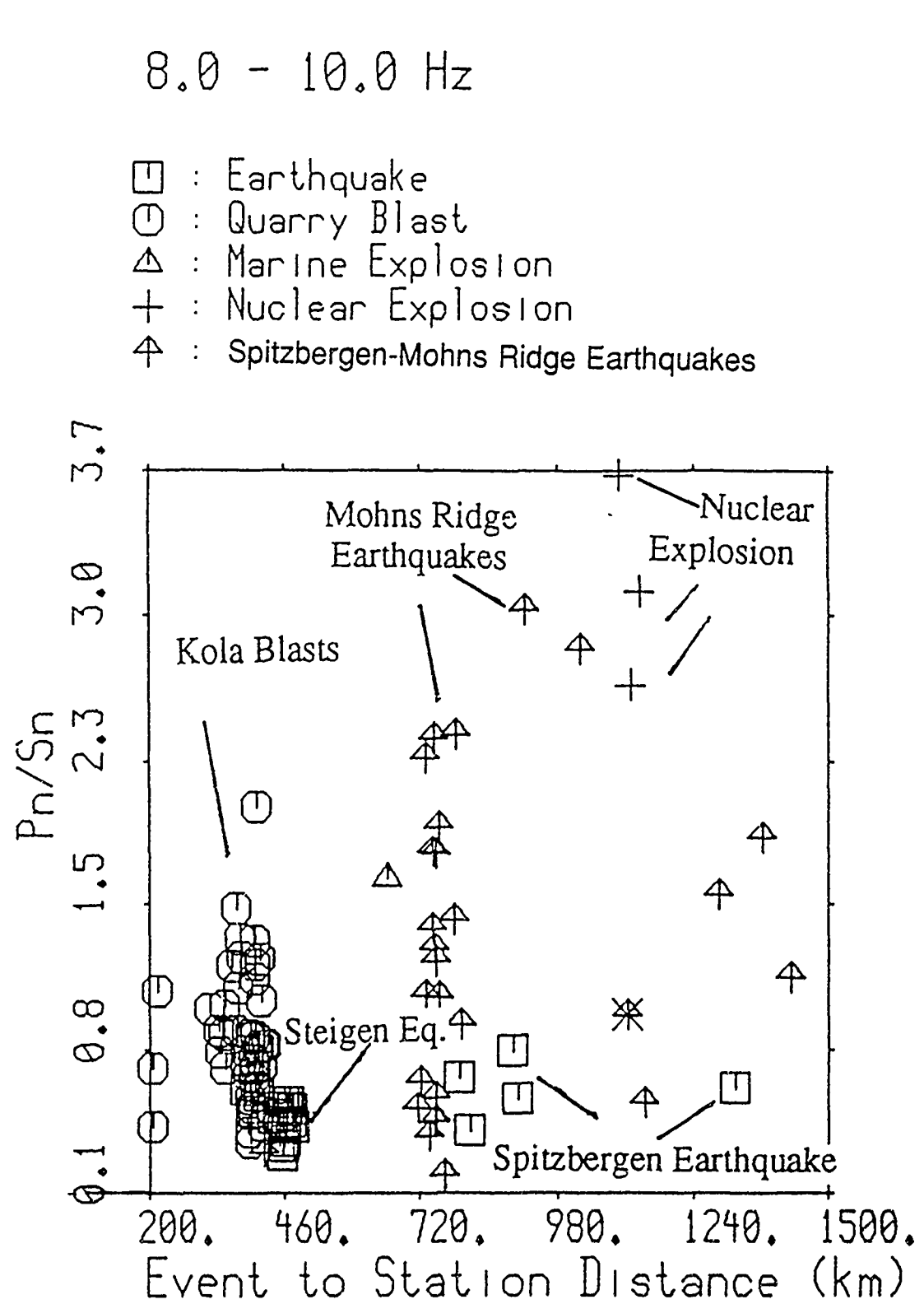

Figure 4: Plot of 8-10 Hz *Pn/Lg* ratios vs. distance for continental earthquakes (squares), Kola mine blasts (circles), nuclear explosions (plus signs), and earthquakes in the Spitzbergen and Mohns Ridge regions (triangles).

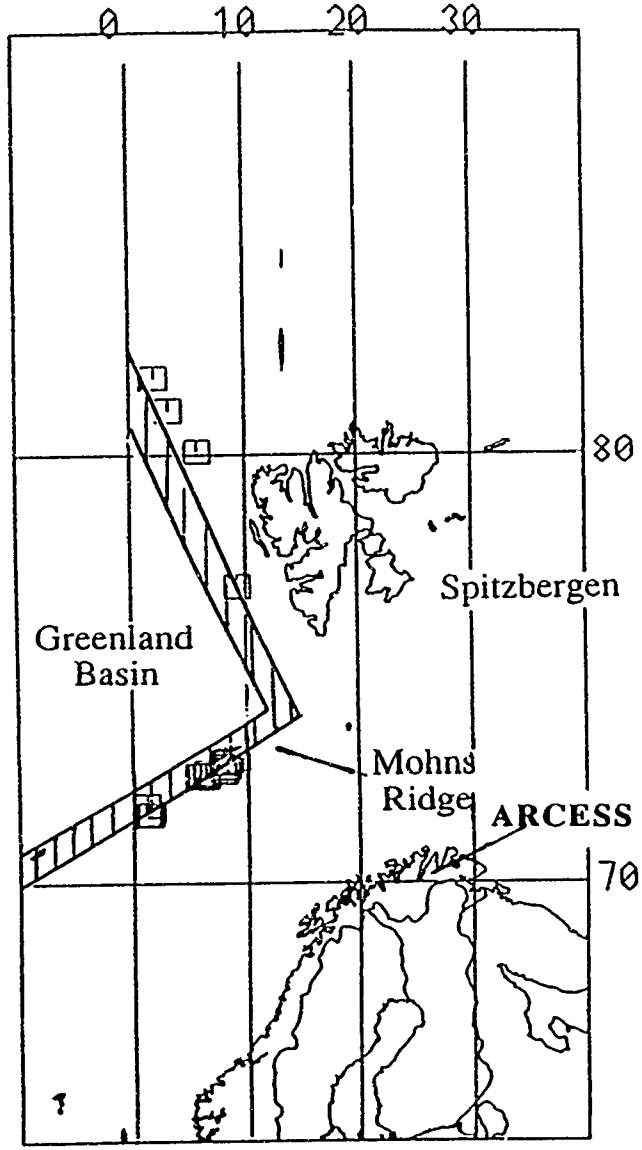

HIGH P/S RATIO

(a)

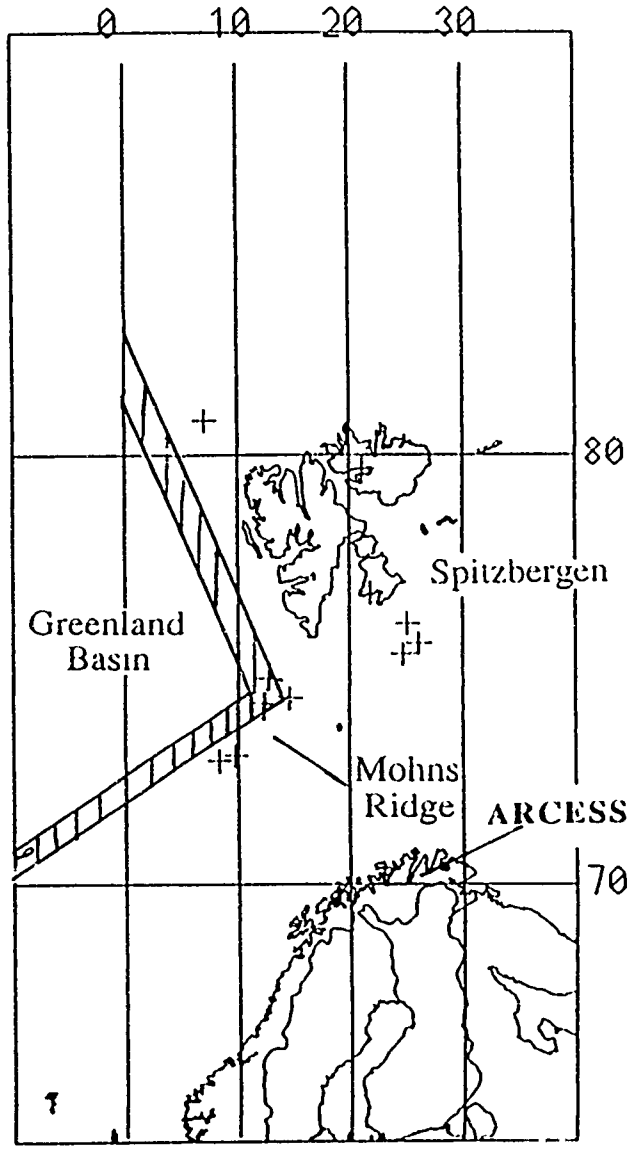

LOW P/S RATIO

(b)

Figure 5: (a) Map showing locations of earthquakes which produce high *Pn/Sn* ratios, indicating strong attenuation of *Sn*. These events occurred near the Mohns Ridge rift. (b) Locations of events which produce higher *Pn/Sn* ratios, which show less attenuation of *Sn*. Most of these events occurred more east of the Ridge or on Spitzbergen.

Seismic Discrimination of Rockbursts and Cavity Decoupled Explosions

T. J. Bennett, J. R. Murphy, M. E. Marshall and B. W. Barker
S-CUBED
11800 Sunrise Valley Dr., Suite 1212
Reston, Virginia 22091
Contract No. F 19628-91-C-0186

Objective

The research described here deals with two types of seismic events (viz. rockbursts and decoupled nuclear explosions) which are important to the discussions of nuclear weapons proliferation and more comprehensive limitations on nuclear weapons tests. However, over the past several years these event types have received only limited attention in seismic research and remain problems for seismic identification. Since the last review meeting, S-CUBED has continued research on the seismic identification of rockburst events and related mine tremors. The frequent occurrence of these types of events in mining areas throughout the world (cf. Figure 1) and the problems which they pose for standard teleseismic discriminants indicate that alternative methods of signal measurements and event discrimination (primarily based on regional signal analyses) would be useful to facilitate their identification. We have been exploring the characteristics of the mechanisms and seismic signals from these mine-related events and attempting to find features which will aid in their discrimination. Interest in lower discrimination thresholds also directs attention at decoupled or partially decoupled nuclear explosion tests. For these latter events we have been seeking to determine regional signal characteristics which will be useful in distinguishing this type of event from small chemical explosions. In these analyses we have used recently acquired seismic data from decoupled explosions and nearby mine blasts in the former Soviet Union as well as prior U. S. experience.

Research Accomplishments

Our investigation of rockburst events has been directed at review of the characteristics of rockburst mechanisms from different source areas and discrimination analyses of seismic waveform data from rockbursts events in varied source environments around the world. Published reports on the mechanisms of mining-induced seismic events indicate several distinct source types may be experienced and that the mechanism is to some degree controlled by mining practice. Hasegawa et al. (1989) identified six distinct models for induced seismic events associated with mining: (1) cavity collapse, (2) pillar burst, (3) tensile failure of cap rock, (4) normal faulting above the stope face, (5) thrust faulting on pre-existing fractures above or below the excavation, and (6) shallow, near-horizontal thrusting along layer boundaries above the mine roof. These various models would be expected to differ with regards to energy release and the mechanism of seismic wave generation (cf. Bennett et al., 1993). Individual rockfalls or pillar bursts would be expected to normally release only small amounts of seismic energy and to have simple vertical force or dipole mechanisms unlike double-couple mechanisms experienced in typical earthquakes. On the other hand, many large mining-induced events throughout the world appear to be associated with the release of tectonic stress on pre-existing faults or fractures in the vicinity of the mine opening. These triggered events normally have mechanisms and produce seismic signals similar to

Figure 1. Locations of Mining Areas with Reported Rockbursts or Tremors

those of double-couple earthquakes. Examples of this latter case are seen in the mechanisms of most large rockbursts in South Africa which typically appear to be associated with shear failure on faults or planes of weakness near the excavation (cf. McGarr et al., 1979). These South African mine tremors have magnitudes which frequently exceed 5 m_b with most of their seismic energy derived from the release of the tectonic stress. However, with regard to the influence of rockburst mechanism on the signal spectrum, McGarr et al. (1990) and Battis (1992) found evidence that the observed spectral decay rate for body waves from these South African mine tremors could not always be explained by a simple double-couple rupture model but might instead be represented as a multiple rupture. Thus, many rockburst might be expected to have mechanisms distinct from other source types.

A particularly interesting example of a large rockburst (m_b = 5.4) is the event which occurred in Central Europe on March 13, 1989 near Völkershausen, Germany. Unlike the South African tremors, the Völkershausen rockburst is thought to have been produced by the nearly simultaneous collapse of multiple mine pillars (cf. Ahorner, 1989; Minkley, 1993). The proposed model for this event is illustrated schematically in Figure 2. Observations in the mine and at the surface above indicate that the area above the mine, extending for several square kilometers, subsided within 1-2 seconds by an amount averaging between 0.5-1 meter. We estimated the potential energy loss corresponding to this down-dropped block and the radiated seismic energy based on the Gutenberg-Richter relation between energy and magnitude. The calculated seismic efficiency of about 0.5 % seems reasonable for this type of event and suggests that an event of this magnitude could have been generated by the multiple-pillar-collapse model without the need to draw on tectonic stress release. The corresponding seismic mechanism has been represented as an implosion by Ahorner (1989). This mechanism appears to be corroborated by the observation of dilatational P-wave first motions at all azimuths for all the nearby seismic stations (about 50 stations to distances of 380 km; Ahorner, 1989). However, it should be noted that many first motions (nearly half) reported to ISC for this event are compressional, including most of the teleseismic observations. This would be inconsistent with a simple implosional source mechanism for the Völkershausen event but could just represent erroneous first motion determinations by the varying analysts reporting to ISC for low signal-to-noise recordings. We are continuing to investigate this discrepancy.

The waveform database developed for this study currently includes digital waveforms for more than 100 events from known rockburst source regions. To date we have focussed our data collection efforts on two areas: South Africa and Central Europe. The South African events include mine tremors from the deep gold-mining area in the Witwatersrand basin and presumed earthquakes scattered throughout the remainder of the country. The Central European events include rockbursts from several parts of the region but are concentrated mainly in the Lubin and Upper Silesia areas of Poland. For comparison we have included in the database a few of the larger earthquakes from the region for which good regional recordings are available. For events in these areas we have tried to collect all available waveform data from GDSN, IRIS, and ARPA array stations. We have performed a variety of measurements on the time-domain signals comparing relative amplitudes of P, S, and L_g between events of similar and contrasting source types. The L_g/P or S/P ratios observed at regional stations tend to be larger for rockbursts than for all other types of events. We plan to investigate the spectral behavior of this observation in more detail.

For the Völkershausen, Germany rockburst described above, we have been comparing the regional seismic signals recorded at several common stations with those for a large European earthquake (German/Netherlands border, April 13, 1992, 5.5 m_b) and another large rockburst in Germany (May 16, 1991, 4.4 m_b) at a different mine. In comparison to the earthquake, the Völkershausen rockburst produced much stronger L_g (relative to other phases) at these common stations even though the epicentral distances and azimuths were comparable. This is illustrated quite nicely in the band-pass filter analysis shown in Figure 3 where we show the vertical-component record for the NORESS center element unfiltered and in three narrow frequency bands. For the earthquake the S signal is the most prominent phase at all frequencies; while for the

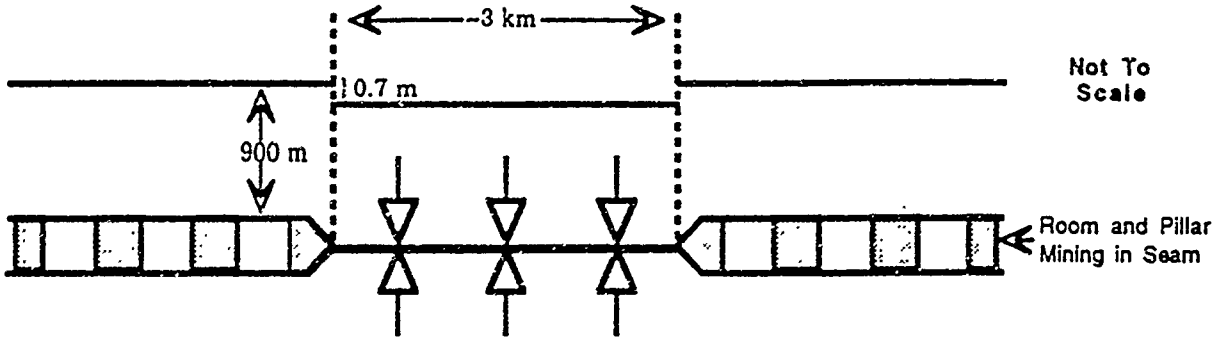

Potential Energy: $E_p = 1.1 \times 10^{21}$ ergs

Seismic Energy: $E_s = 10^{5.8 + 2.4 m_b}$ (Gutenberg - Richter)

$= 10^{18.76} = 5.7 \times 10^{18}$ ergs

Seismic Efficiency: $e_s = \frac{E_s}{E_p} = \frac{5.7 \times 10^{18}}{1.1 \times 10^{21}} = 0.52\ \%$

Figure 2. Schematic model of the 1989 Völkershausen, Germany rockburst (5.4 mb) approximating an implosional source (produced by simultaneous failure of multiple pillars) and the associated energy relations.

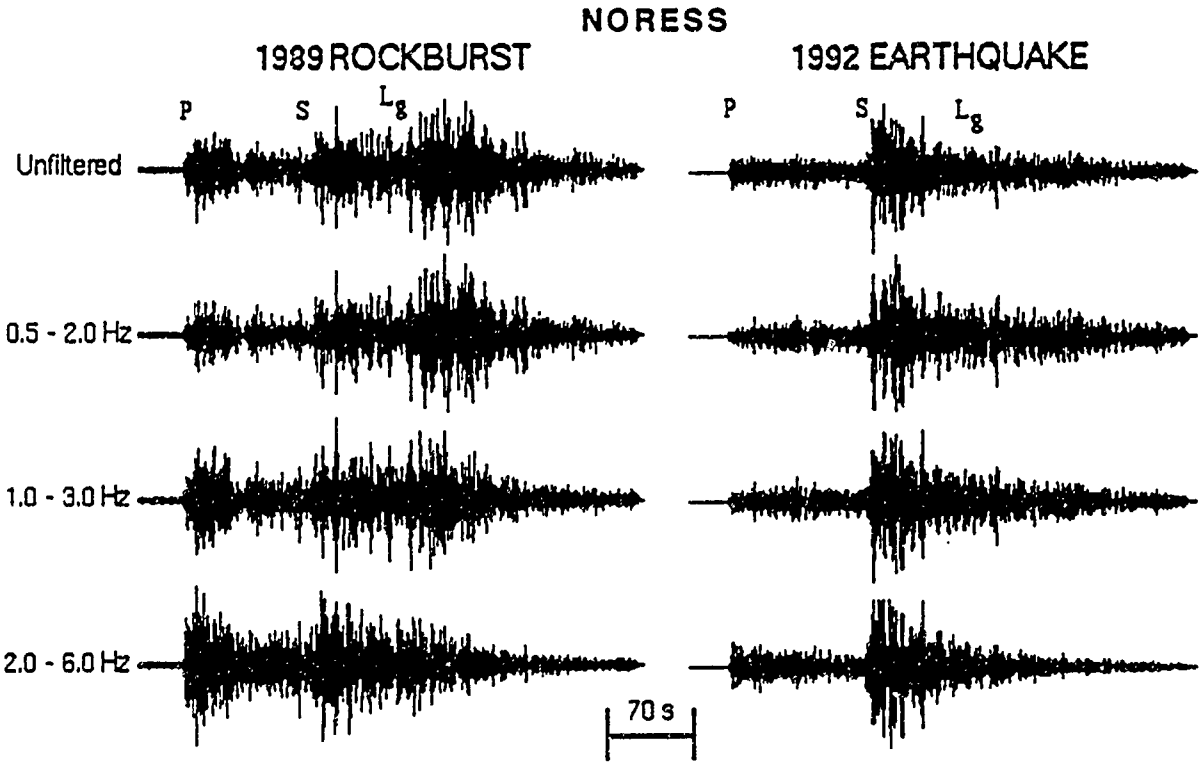

Figure 3. Comparison of band-pass filter analysis of NORESS vertical-component waveforms from the 1989 German rockburst and 1992 German/Netherlands border earthquake. Note relatively stronger Lg signals for the rockburst at all frequencies.

rockburst L_g and P signals are predominant with L_g enhanced at low frequencies and P at higher frequencies. The preliminary indication from the second German rockburst is that the S phase is stronger across the frequency band, making this latter event look more like an earthquake. Harjes (1993) has suggested that the Völkershausen rockburst is atypical of Central European events for which mechanisms are normally associated with a fault rupture process. Thus, the strong differences seen in Figure 3 between the rockburst and earthquake may not be representative. It is interesting to note then that some variations in the regional signals are to be anticipated from rockbursts within relatively confined source regions and the variations may be influenced to some degree by mining practice.

As interest increases in lower nuclear weapons testing thresholds, comprehensive test bans, or nuclear weapons proliferation, the use of cavity decoupling to conceal possible tests takes on increased significance. For identification of such tests, regional seismic discrimination will be extremely important. However, we have only very limited experience in regional seismic monitoring of decoupled nuclear explosions. The U.S. experience in this areas is limited to the STERLING nuclear explosion. Therefore, seismic data recently made available from a cavity-decoupled nuclear explosion test in the north Caspian area of the former Soviet Union is viewed as important to assessing regional seismic monitoring for such events. Our research under this contract has been directed to the analysis and comparison of near-regional and regional seismic data recorded from cavity-decoupled nuclear explosions and nearby chemical explosion sources. The ability to discriminate these event types is viewed as critical to a comprehensive nuclear weapons test monitoring effort.

We are using available near-regional seismic data from the STERLING and the nearly collocated STERLING HE chemical explosion and the newly acquired data from the Soviet Azgir decoupled explosion of March 29, 1976 (4.4 m_b) and from some mine blasts in the same general region recorded at similar distance ranges. We also have similar recordings from a tamped nuclear explosion at the same Azgir location on December 22, 1971 (6.0 m_b). The common near-regional stations which recorded useful signals from STERLING and STERLING HE were at ranges of 16 km and 32 km. The broad-band recordings from the two Azgir events were obtained at station ranges between about 1 km and 150 km. The mineblasts from the former Soviet Union occurred in a region southwest of the north Caspian area in the vicinity of station KIV (cf. Rivière-Barbier, 1993) and were recorded on broad-band instruments at ranges between 28 km and 117 km.

For STERLING and STERLING HE we have compared the time-domain and spectral characteristics of the P and S waves recorded at the two common stations from the nearly collocated sources. The principal difference between the signals observable in the time domain was the enhancement of S relative to P for the HE chemical blast compared to the decoupled nuclear explosion. In the spectral domain both P and S waves were found to be enhanced at high frequencies for the decoupled nuclear explosion versus the HE chemical blast. The effect on the S/P ratio in the frequency domain is seen as a larger value over a broad range of frequencies for the HE chemical blast versus the decoupled nuclear explosion.

We are currently analyzing the amplitude and spectral characteristics of the regional signals observed from the Azgir decoupled and tamped nuclear explosions and from the Russian mineblasts. Comparisons of the signal characteristics at similar epicentral distance ranges from the different source types should help identify distinguishing features which may be useful for discrimination. For the moment we are assuming there are no major differences in regional phase propagation characteristics between the area around Azgir and that near KIV; this assumption will need to be tested in future investigations. Future plans also include development and application of appropriate scaling relations to minimize effects related to differences in the explosion yields between source types. Figure 4 shows expanded P-wave segments recorded on the broad-band vertical components at similar near-regional distance ranges for the Azgir decoupled nuclear explosion and for selected chemical blasts from the Russian mines. The onsets of the P waves are approximately alligned about 1 second after the start of the records. To illustrate the complexity of the regional discrimination problem, we invite you to test your visual discrimination capability on this record sample. Correct answers will be made available to those visiting our poster display.

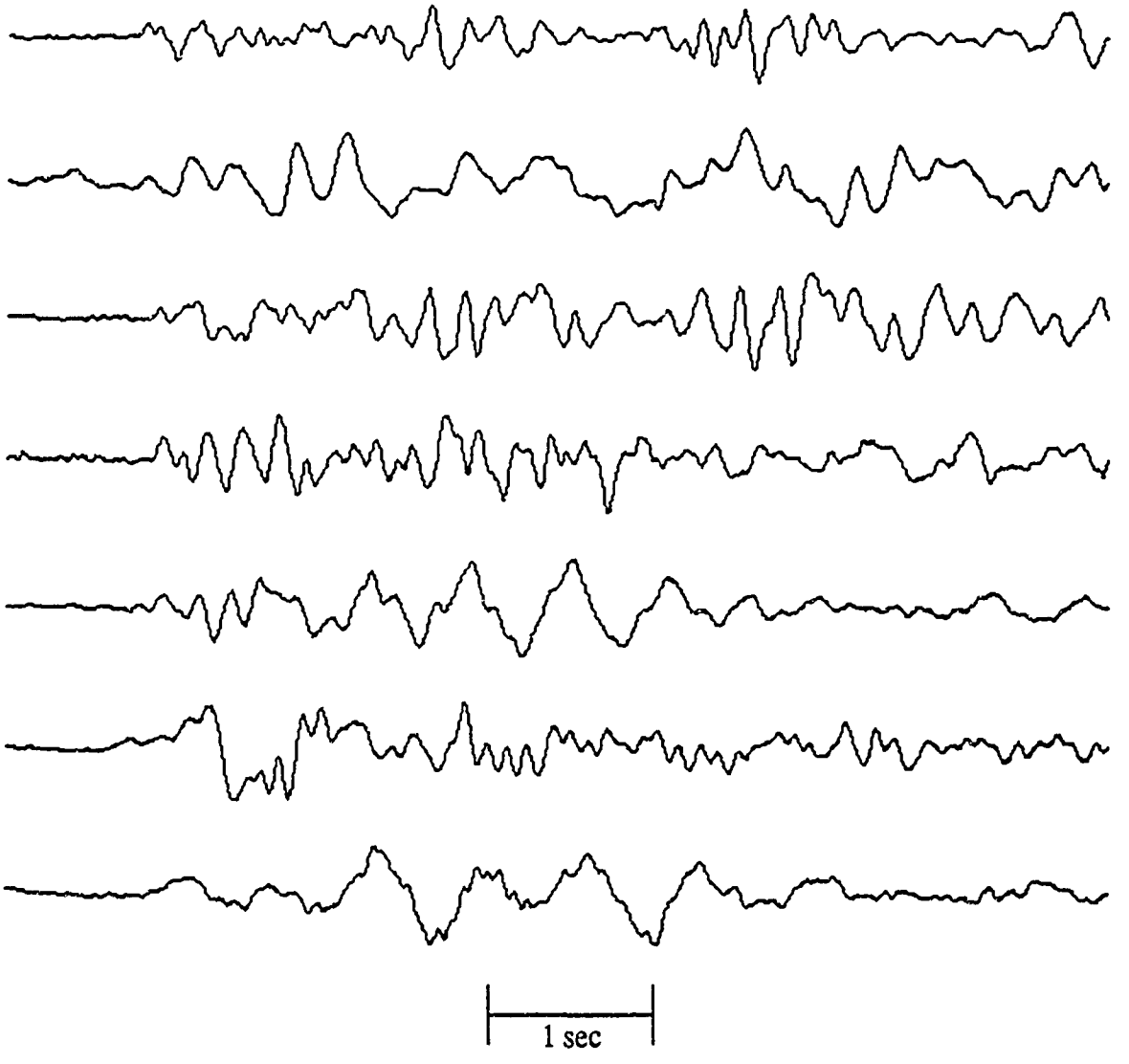

Figure 4. How good is your visual discrimination capability? This figure shows selected near-regional P waveforms recorded from the Azgir decoupled nuclear explosion and nearby quarry blasts in the 45 to 85 km distance range. Come to our poster to receive your score!

Conclusions and Recommendations

With regard to rockbursts our observations indicate that these mining induced events occur throughout the world and cover a large range in magnitude. Rockburst mechanisms and the associated behavior of the regional seismic signals vary between source regions and to some degree between sources within a region. The latter is affected and may be controlled by mining practice. The characteristics of rockbursts and their associated regional signals need to be developed for other areas to facilitate their future identification; and the potential for using rockbursts to conceal covert nuclear weapons testing should be assessed.

On the topic of cavity-decoupled nuclear explosions, careful analyses of near-regional signals from STERLING and STERLING HE suggests there may be differences in the relative excitation of P and S phases as well as spectral differences in the individual phases. Preliminary observations comparing time-domain character of near-regional P phases from recently acquired seismic data for an Azgir decoupled nuclear explosion reveals little obvious difference compared to nearby mineblasts recorded at similar epicentral distances. Thorough analyses of these new Soviet data need to be completed and compared to U.S. experience to define an optimum strategy for the seismic identification of small cavity decoupled explosions in these and other source environments.

References

Ahorner, L. (1989). "Seismologische Untersuchung des Gebirgsschlages am 13. März 1989 im Kalisalzbergbau bei Völkershausen, DDR," Glückauf-Forschungshefte, 50, pp. 224-230.

Battis, J. C. (1992). "Source Modelling of South African Mine Tremors," (Abstract), Seismological Research Letters, 63, p. 20.

Bennett, T. J., J. F. Scheimer, A. K. Campanella, and J. R. Murphy (1993). "Seismic Characteristics of Rockbursts for Use in Discrimination," PL Report No. PL-TR-93-2059, ADA266063

Harjes, Hans-Peter (1993). Personal Communication.

Hasegawa, H. S., R. J. Wetmiller, and D. J. Gendzwill (1989). "Induced Seismicity in Mines in Canada - An Overview," Pageoph, 129, pp. 513-521.

McGarr, A., S. M. Spottiswoode, and N. C. Gay (1979). "Observations Relevant to Seismic Driving Stress, Stress Drop and Efficiency," J. Geophys. Res., 84, pp. 2251-2261.

McGarr, A., J. Bicknell, J. Churcher, and S. Spottiswoode (1990). "Comparison of Ground Motion from Tremors and Explosions in Deep Gold Mines," J. Geophys. Res., 95, pp. 21,777-21,792.

Minkley, W. (1993). "Zum Herdmechanismus von großen seismischen Ereignissen im Kalibergbau," Jahrestagung der Deutschen Geophysikalischen Gesellschaft, Kiel.

Rivière-Barbier, F. (1993). "Status Report on the Cooperative Research Program Between the EME and the CSS for Exchange and Analysis of Seismic Data from Quarry Blasts in Russia and in the U.S.," CSS Technical Report C93-01.

Nonlinear Rheology of Rock at Moderate Strains: Fundamental Observations of Hysteresis in the Deformation of Rock

G. N. BOITNOTT
New England Research, Inc.
contract F29601-91-C-DB26

OBJECTIVES

In order to discriminate between underground nuclear explosions and other seismic sources, it is necessary to have confidence in derived source spectra based on regional and teleseismic signals. While it is generally accepted that a considerable amount of attenuation and resultant waveform distortion occurs due to deformation near the source, an area that has received little attention is the broad enveloping region of nonlinear deformation where moderate stress perturbations occur. Owing to its great extent, the moderate strain regime has the potential to influence the entire frequency band of the regional and teleseismic signals and thus may be central to the problem of inferring source characteristics from far-field signals.

The objectives of this project have been to characterize the fundamental aspects of the rheology of rock subjected to moderate perturbations in strain. We present the results of experiments designed to characterize the intrinsic loading path dependence of the deformation of rock subjected to moderate strains. Cyclic loading tests in unconfined uniaxial compression have been performed on intact and jointed Sierra White granite and Berea sandstone. Fundamental aspects of the hysteresis are identified and a general rheological model is constructed which embodies the effects of mean load, amplitude of the stress perturbations, as well as some aspects of previous loading history. The model is parameterized in terms of hysteresis in the modulus, and thus can be easily incorporated into numerical models of wave propagation. The success of the model in predicting the hysteresis in the deformation for arbitrary loading history illustrates that realistic rheologies are tractable for the moderate strain regime. Extension of this work to other rock types and other modes of deformation is needed in order to constrain realistic models of wave propagation from underground explosions.

RESEARCH ACCOMPLISHED

Introduction

There are three regimes pertinent to discrimination, detection, and yield estimation:

- a **near source** region where hydrodynamic and rock failure models dominate the rheology.
- a **moderate strain** regime where rock deformation is known to be nonlinear, inelastic, and hysteretic, yet realistic rheological models are lacking.
- a **far field** regime where rock deformation is linear and traditional seismological techniques can be applied.

Previous studies have shown that nonlinearities have a significant effect on spectral character and amplitude decay of the elastic waves propagating through the moderate strain regime (i.e. *Minster et al.* [1991]; *Wortman and McCarter* [1991]). In this study, we concentrate on studying fundamental issues concerning the deformation of rock in the moderate strain regime. Understanding the fundamentals of the rheology of rock in this regime are required before developing wave propagation models to assess its importance to discrimination and detection.

When rock is subjected to moderate perturbations in strain (10^{-6} to 10^{-3}), the resulting deformation is strongly dependent on the loading history. This loading history dependence is referred to as "hysteresis". The consequences of hysteresis to problems of wave propagation are largely unknown. Little experimental data is available to construct realistic rheological descriptions which can be used to model wave propagation in this moderate strain regime. Recent studies by *Minster et al.*, [1991], *Wortman and McCarter* [1991], and *Day et al.*, [1993] indicate that detailed rheological descriptions which include the intrinsic loading path dependence of the deformation are required. Their conclusions stress that:

- simulations must embody realistic rheologies in order to be helpful in assessing the importance of the nonlinearities expected in the moderate strain regime on the resulting seismic signal.
- more laboratory data on rheology of rock in the moderate strain regime is essential before model simulations can be reliably used to study the effects of the observed nonlinearity.
- the moderate strain regime has the potential to influence the entire frequency band of the regional and teleseismic signals and thus is central to the problem of inferring source characteristic from these seismic signals.

Experimental Results

An experimental study has been initiated to characterize hysteresis in the deformation of rock subject to the conditions expected in the moderate strain regime [*Boitnott,* 1992a,b; 1993]. A data set on intact and jointed samples of Sierra White granite and Berea sandstone has been collected which sheds light on some fundamental aspects of hysteresis in the deformation of rock subject to moderate strains. These results, along with the results due to *Holcomb* [1981] and *Scholz and Hickman* [1983], demonstrate that these rheologies obey important simplifying principles.

Holcomb [1981] and *Scholz and Hickman* [1983] demonstrated that deformation of intact and jointed rock in the moderate strain regime exhibits end-point memory. This means that the deformation path will revisit the stress-strain states previously attained at local extrema in the loading history. For complex loading, multiple reversal points can be "remembered" simultaneously. Although simply stated, the notion that a rock will "remember" all local extrema in the loading history leads to a somewhat cumbersome and unusual requirement for a general rheology.

Recent tests on Sierra White granite and Berea sandstone have produced further simplifications to the notion of "memory". Examples of some of these tests are shown in Figures 1 and 2. Note that for the case reported in Figure 1, the local Young's modulus during loading is to first order independent of the previous local maximum. The modulus vs. load paths during the multiple loading segments all overlay, yet each segment was preceded by a different local stress maximum. Similar experiments looking to see if the local modulus during unloading "remembers" the previous minimum in stress produce similar results. In such experiments, we see that the modulus during unloading is to first order independent of the previous minimum. Thus, the modulus versus load relationship during both loading and unloading are simple functions of the

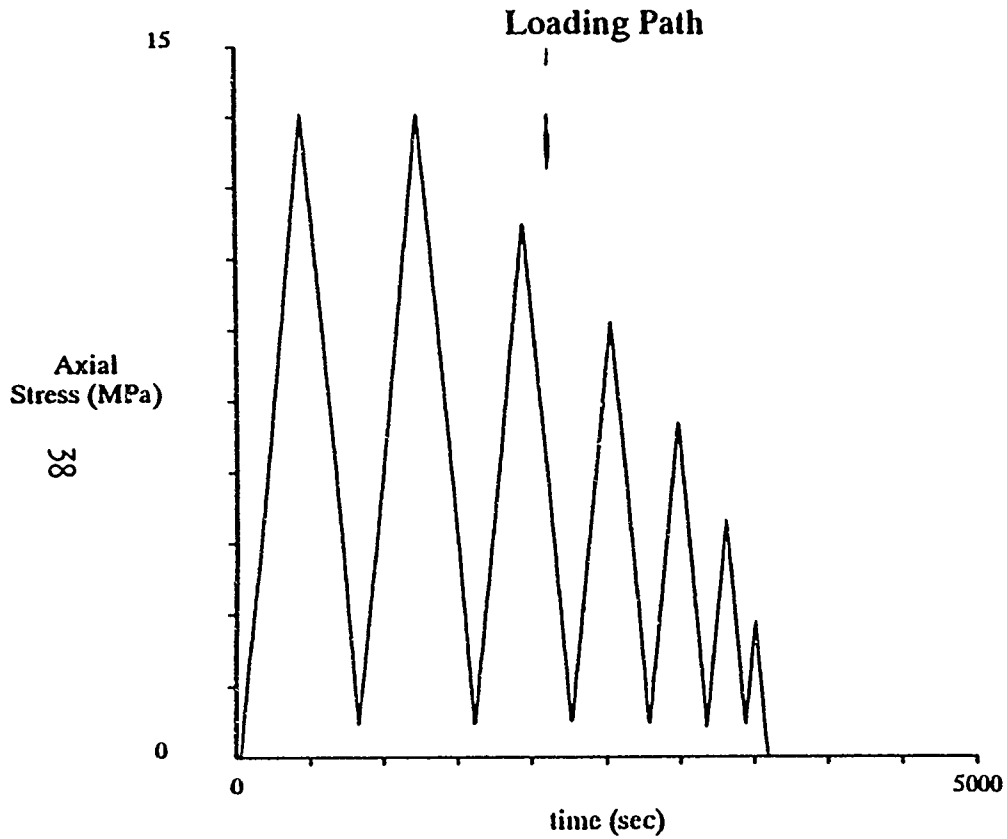

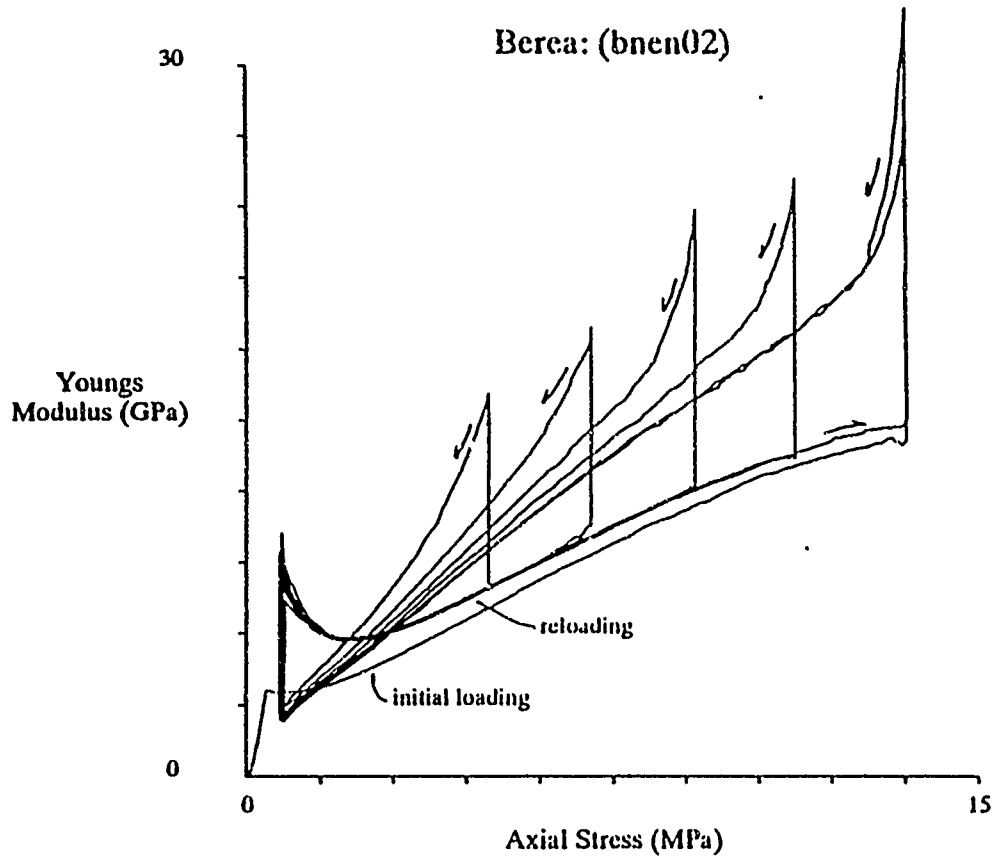

Fig. 1:

a) Stress history of an experiment designed to test the "memory" of a rock subject to uniaxial stress perturbations. In this experiment we were particularly interested in whether the modulus versus load relationship during loading was a function of the previous local maximum in stress.

b) Local Youngs modulus ($\partial\sigma/\partial\varepsilon$) versus axial stress for the experiment shown in (a) on an intact sample of Berea sandstone. Note that Youngs modulus during loading is independent of the previous local maximum. This suggests the the rheology may be parameterized in a way which does not require long term memory of the loading history.

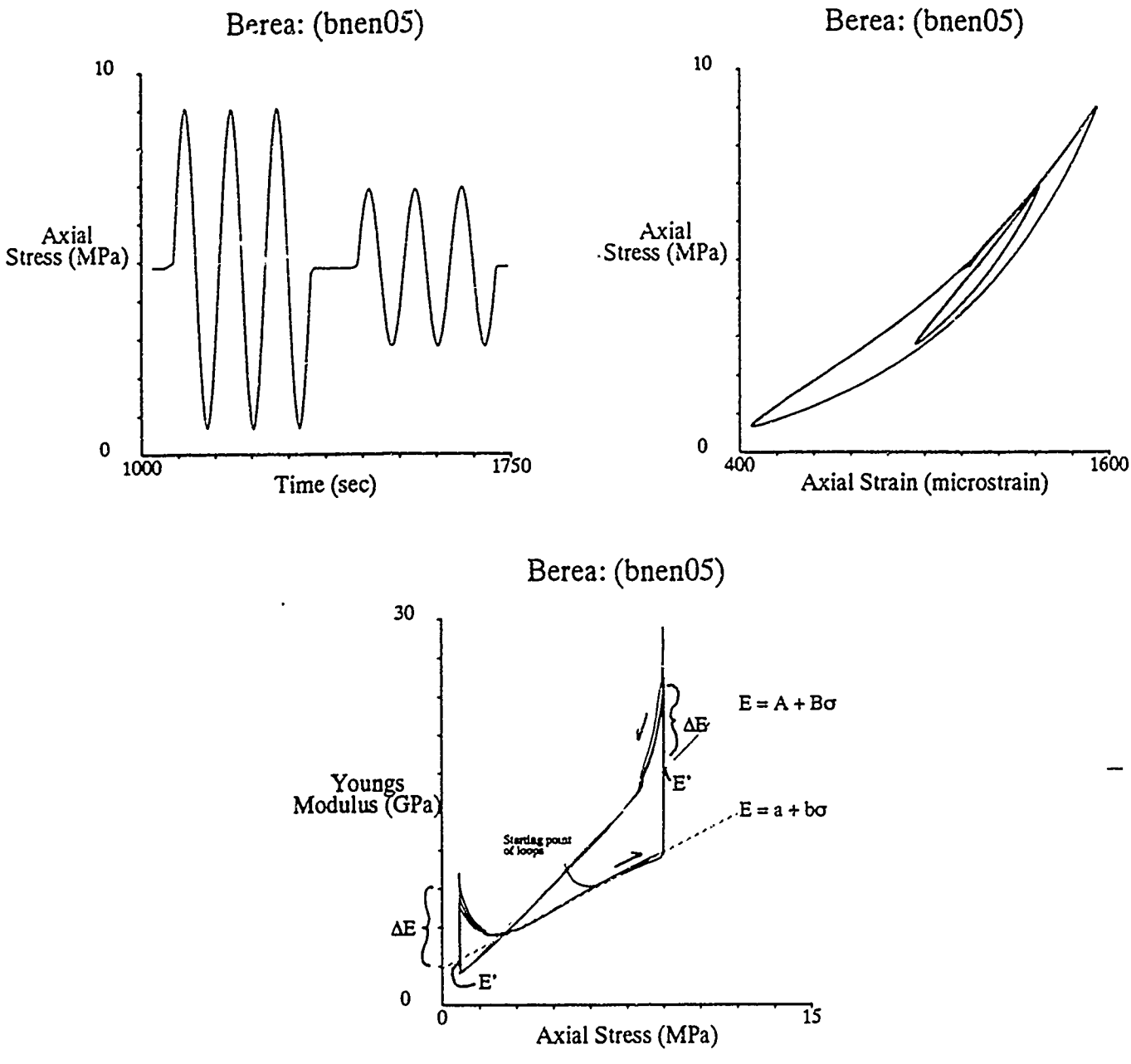

Fig. 2:

a) Time history ~~of a portion~~ of an experiment which involves sinusoidal oscillations of stress about a given mean stress. Note each set of oscillations begins and ends at a zero-crossing of the perturbation. Different amplitudes of the stress perturbation and different mean stresses are used.

b) Stress - Strain response for an intact sample of Berea sandstone during the portion of the loading history shown in (a). Note that the stress strain relation for each successive cycle overlay after the first quarter cycle. Thus the hysteresis loops are to first order closed and repeatable. This is found for both Berea sandstone and Sierra White granite.

c) Local Youngs modulus versus axial stress for Berea sandstone during the three consecutive 4.25 MPa amplitude cycles shown in (a) and (b). At each reversal in the direction of loading, there is a rapid increase (discontinuity) in the local modulus. During the unloading portion of the cycles, the modulus versus load relationship is approximately linear ($E = A + B\sigma$). Similarly, during the loading portion a linear relationship is also seen. The modulus E', which is defined by extending the line ($E = a + b\sigma$) to the maximum and minimum stresses, appears to be a rheological parameter of the material. The extra stiffening ΔE near each reversal in stress direction is found to be a unique function of the amplitude of the local stress perturbation. The effect of this stiffening decreases during the first MPa or so of loading or unloading from a reversal. The unloading parameter B is constrained by the local stress maximum and the global extrema. With these observations, we can generate a general rheology for cyclic loading which includes the effects of loading history, stress amplitude, and mean stress.

last load extremum and require little memory of previous extrema. This important result indicates that the rheology may not require detailed memory of previous loading history prior to the previous local extremum in the stress-time history.

Figure 2 shows an additional experiment which illustrates some other important features of hysteresis in rock. In the test shown in Figure 2, the loading history consisted of a series of sinusoidal load variations at a given mean stress. In Figure 2c, the local Young's modulus for a portion of the experiment is shown plotted against stress. Here we see a similar modulus-stress relationship to that in the stress cycling experiments shown in Figure 1. Note that there are a number of features of the modulus-stress relationship which can easily be exploited in formulating an empirical rheology. Some aspects of the developed parameterization are shown graphically in Figure 2c and can be briefly summarized as follows.

- The deformation exhibits long term memory of the global extrema in stress and strain. The rheology does not require memory of local extrema.
- With the exception of some complications in the immediate vicinity of a reversal in load, the modulus-load relationship during both loading and unloading are well defined by simple linear functions of stress.
- The modulus E' defined graphically in Figure 2 is found to be a material property which defines the modulus upon load reversal in the absence of the ΔE effect. For Berea sandstone, E' is found to be slightly different for loading and unloading.
- The parameter B which describes the decrease in modulus with decrease in stress is found to be a simple function of the previous peak stress and the global extrema of the loading history.
- Transient stiffening at reversals in load direction (defined graphically in Figure 2 as ΔE) is found to be a simple function of the amplitude of the local stress perturbation and decays with stress during loading or unloading.
- Once E', B, and ΔE have been constrained, the parameter b defined in Figure 2 is uniquely specified by the constraint that deformation must revisit the global extrema. Additionally, the parameters A and a are in effect arbitrary for the problem at hand and come out directly through integration.

Note that the rheology described here is slightly different from that described in *Boitnott* [1993]. The previous version of this model involved the "closed loop" assumption, which required memory of all local extrema and thus limited the rheology to restricted loading histories. Here we have modified the rheology to only require memory of the *global* extrema in the loading history. The "closed loop" behavior becomes a result of the model, not a part of its foundation. We have found that the model parameters are independent of the loading history of the test from which they are constrained, indicating that the parameters describe fundamental material properties. Thus, with these few observations, a general rheology has been formulated which embodies the essential features of hysteresis for the case of variations in uniaxial stress.

Model Results

Comparisons of the predicted deformation with measured stress-strain paths are shown in Figure 3. Note that the effects of loading history, mean stress, and the amplitude of the stress perturbations are well preserved by the rheological description. These figures serve as an illustration that a general rheology is tractable. The same

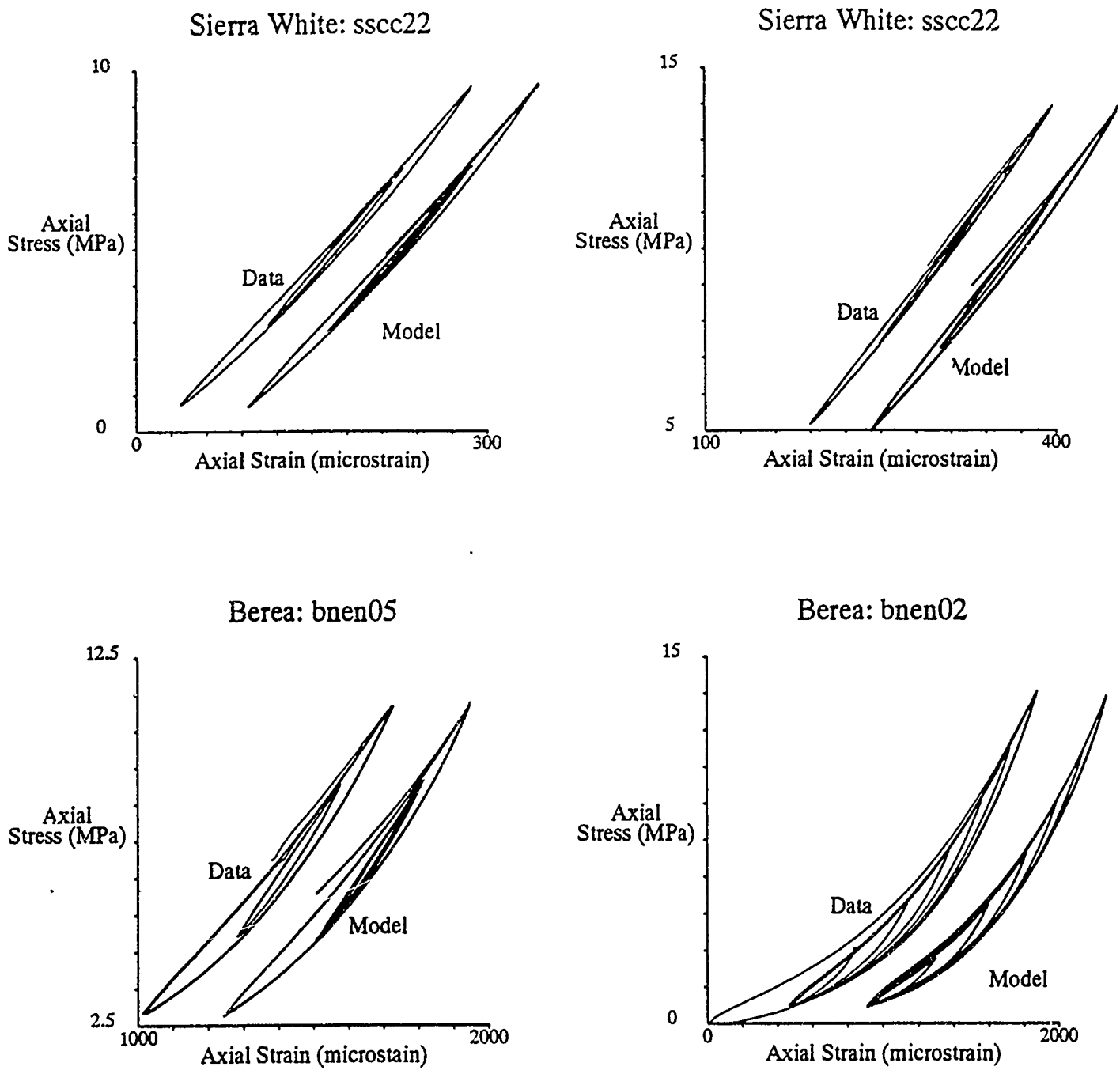

Fig. 3:

Comparisons of model predictions with data for portions of experiments on Sierra White granite and Berea sandstone. In each figure, the model results have been offset for comparison.

a) Stress - strain path for Sierra White granite during the loading shown in Figure 2a. Note that the gross features of the deformation are well described by the model. Refinement of model parameters should improve the fit.

b) Simular comparison as in (a) for another portion of an experiment. In this case the mean stress was approximately 9.5 MPa. The same parameters were used as in the comparison in (a). Thus the empirical rheology includes the effects of both the mean stress and the amplitude of the stress perturbation.

c) Simular comparison of measured and modeled hysteresis loops in Berea sandstone. Note that the same parameterization can be used for both granite and sandstone.

d) Comparison of model predictions with data for the experiment shown in Figure 1. The same model parameters have been used in both (c) and (d). Note that the model does well even for this more complex loading history.

parameterization can be used for both Sierra White granite and Berea sandstone, two rocks with very different microstructure and mechanical properties. In addition, the rheology is formulated in a differential form which can be fully parameterized in terms of the stress history, and thus should be well suited for incorporation into numerical models of wave propagation. Most notably, the "memory" of previous loading history is limited and thus will not add a substantial amount of overhead when incorporated into numerical simulations.

CONCLUSIONS AND RECOMMENDATIONS

We have developed a model which incorporates the fundamental features of hysteresis in intact rock for the case of perturbation in uniaxial stress. The model successfully includes the effects rock type, mean load, and load history. Based on this work, there are a few aspects of the uniaxial stress tests which must be studied in more detail. There is a need to develop a better understanding of the nature and characteristics of the ΔE effect illustrated in Figure 2. Some of this effect may be related to a "visco-elastic like" relaxations. We also recommend experiments on both dry and saturated samples.

In addition, we recommend shear oscillation experiments on the same rock types. Understanding hysteresis in the shear modulus is essential for constraining simulations of shear wave propagation. Since spectral ratios of compressional and shear phases are commonly used as a discriminant as well as an indicator of important details of the source physics, including shear modulus in this study is very important. Experiments should also be conducted in a triaxial apparatus to include the effects of ambient confining pressure and allow greater flexibility in control of the mode of deformation.

REFERENCES

Boitnott, G. N., The role of rock joints in non-linear attenuation in moderate strain amplitude regimes, Semi-annual Report, DARPA/PL contract F29601-91-C-DB26, August, 1992.

Boitnott, G. N., Nonlinear attenuation in the near source region: characterization of hysteresis in the deformation of rock joints, *in* Proceedings of the 14th annual PL/DARPA Seismic Research Symposium, J. F. Lewkowicz and J. M. McPhetres eds., PL-TR-92-2210, September 16, 1992, ADA256711

Boitnott, G. N., Fundamental Observations concerning hysteresis in the deformation of rock with applications to nonlinear attenuation in the near source region, Proceedings of the Numerical Modeling of Underground Nuclear Test Monitoring Symposium, DOE-OACN, Durango, March 23, 1993 (in press).

Day S. M., J. B. Minster, M. Tryon, and L. Yu, Nonlinear Hysteresis in an Endochronic Solid, Proceedings of the Numerical Modeling of Underground Nuclear Test Monitoring Symposium, DOE-OACN, Durango, March 23, 1993 (in press).

Holcomb, D. J., Memory, relaxation, and microfracturing in dilatant rock, *J. Geophys, Res., 86,* 6235-6248, 1981.

Minster, J. B., S. M. Day, and P. M. Shearer, The transition to the elastic regime in the vicinity of an underground explosion, *in* Explosion Source Phenomenology, S. Taylor, H. Patton, P. Richards, eds., *Geophysical Monograph 65,* Amer. Geophys. Union, 1991.

Scholz, C. H., and S. H. Hickman, Hysteresis in the closure of a nominally flat crack, *J. Geophys. Res., 88,* 6501-6504, 1983.

Wortman, W. R., and G. D. McCartor, Review of attenuation in salt at moderate strains, *in* Explosion Source Phenomenology, S. Taylor, H. Patton, P. Richards, eds., *Geophysical Monograph 65,* Amer. Geophys. Union, 1991.

AUTOMATIC PROCESSING OF SEISMIC EVENTS RECORDED ON A MINI-ARRAY (SIGNAL ANALYSIS COMBINED WITH NEURAL NETWORKS)

Y. CANSI and A. BOTTERO
Radiomana
27 Rue C. Bernard
75005 PARIS
No 90-0356

OBJECTIVES

Among the different methods used to automatically locate earthquakes recorded on a mini-array, the method based on the broad band F-k analysis is the most common (e.g. . Mykkeltveit et al., 1990). However, this method assumes that the propagation of the considered wave front can be modeled by a plane-wave at the scale of the array. Furthermore, in the case of local model variations (e.g. . station anomalies) the resulting precision is very low because of the large wavelength compared to the array extension. To take into account these difficulties, we have tested another method based on a high precision determination of the arrival-times, from which the event location is derived by a classical Husebye's method which computes the velocity and the azimuth of the wave. Each time-window is processed by this method in different frequency bands and activated only if the arrival-time delay set is consistent. Furthermore, this consistency is used as a signal detector and leads to three time-frequency functions, representing first the consistency, and second the velocity and azimuth when they are available. In the case of teleseismic events, the event location is strictly derived from the determinations of the velocity and the azimuth. But for regional events a phase identification is needed. This task is performed by a neural network which uses the three time-frequency functions as inputs and which leads to an estimate of each phase occurrence possibility as a function of time.

Processing of a set of 28 regional events recorded on the 5-station mini-array worked by the Laboratoire de Détection et de Géophysique of the french Commissariat à l'Energie Atomique led to the following results :

- a very precise determination of the azimuth : standard error is less than 4 degrees;
- a good phase identification capability (especially for P-waves) which leads to an estimation of the distance with a relative error lower than 20%.

RESEARCH ACCOMPLISHED

In 1992, the french Laboratoire de Détection et de Géophysique of the Commissariat à l'Energie Atomique has installed in Central France a temporary mini-array composed of 5 vertical short-period seismometers (Figure 1). Numerical signals are digitized at a rate of 50 cycles per second with a 12-bit dynamic.

This mini-array has recorded more than 100 teleseismic events and about 28 regional events during its 4-months operating period. This experience has provided a useful database for testing different automatic

location methods (Cansi et al., 1992). We have shown that better results are obtained when we use the two-step correlation-method which computes first the arrival-time differences with a high precision (less than the sampling interval 0.02s), and second the azimuth and propagation velocity corrected for statistically determined station anomalies.

1) Data Processing :

For regional events, the correlation functions which define the arrival-time differences often have several relative maxima with comparable amplitudes. This leads to an ambiguity in the arrival-time computation, which can be removed by testing the consistency of the time-delay set, using the Chasles relationship :

$$\Delta t_{ij} + \Delta t_{jk} + \Delta t_{ki} = 0$$

Furthermore, this consistency can be used as a signal detector. When the studied time-window contains a seismic signal, the Root Mean Square of the residuals of the Chasles relations is low (i.e. : less than the sampling interval : it is an estimate of the measurement accuracy). On the opposite, when it contains only noise, no consistency can be found (i.e. : the RMS of Chasles relations is high), because of its low correlation at the scale of the array.

Then, for each 4.5s-time window and for different frequency-bands, we can estimate a probability of signal occurrence, and, in the case of high probability, the corresponding velocity and azimuth. Some examples of these time-frequency functions are displayed on figures 3 and 4. For each time step and for each frequency-band, the velocity is shown (grey scale) only when the consistency is better than 0.02s.

We can see clearly that most of the seismic phases lead to consistent signals whose velocity is well defined for all the available frequency-bands. Nevertheless, some cases are more ambiguous :

- a phase cannot be precisely recognized because the velocity is not clearly defined (see Sn-phase on figure 4),
- a false detection is obtained because a part of the record contains consistent noise with a velocity compatible with the regional phases velocity (see noise on figures 3 and 4 as an example).

Since these two kinds of problems cannot be easily modeled, we have used a "learning system" approach based on a neural network to identify the different phases of each event without ambiguity.

2) Phase Identification :

For neuromimetic applications, the classical programming efforts are transposed to the determination of the various authorised degrees of freedom described as follows :

- the data structure : the first step is to extract from the database the information that are strictly necessary for phase identification. Furthermore, those data have to be invariant by translation, rotation and dilatation, which precludes the analysis on a variable period. The solution we chose is thus to present as inputs and for each time sample the signal velocity for 5 frequency bands (from 0 to 12 Hz). The data whose corresponding Chasles RMS is greater than an arbitrary threshold (i.e. : 0.02 s) are set to 0.

- the network structure : we only used multi-layered perceptrons, with a sigmoïd tranfer function. They are indeed capable of building complex decision hyper-volumes in the hyper-space of the input data, thus realising an accurate classifier. Several tests led to choose a 2 hidden-layer perceptron. The complexity of the system is due to the high non-linearity of the problem.

- the learning function . we chose as a learning function the"back propagation with momentum" method, which uses a gradient method to minimize the quadratic error between the expected and the observed results. Despite a long computing time, this allows a reliable and accurate learning convergence.

- the example database : it was made of all the available events, excepted 3 of them on which the tests were made. In order to avoid incoherencies, the arrival time of each phase was picked on the time-frequency diagrams , a phase is thus declared present over the whole time-window between its arrival time and the arrival time of the following phase. Each sample is presented 50000 times in a random order.

- the network topology : the number of nodes in the hidden layers was determinated empirically. Several networks were designed . in order to avoid over-training, we chose for each phase the simplest one which did not degrade the results. Finally, the Pn phase requires 24+9 units, the Pg phase 20+6, the Sn phase 16+6 and the Sn phase 20+6 (Figure 2).

All the designing, learning and testing operations were performed using the neural simulator SNNS, developed by the Stuttgart University. The middle diagrams of figures 3 and 4 show the neural outputs as a function of time for two events which were not in the learning database.

3) Distance estimation :

In order to remove the last false detections due to consistent noise, a post data processing is needed to test the consistency of the results on the whole signal, by using the azimuthal information as described as follows:

- the first step is to compute an azimuth histogram with the possibility functions previously determined and to choose the more probable 20° wide interval. The average azimuth can then be calculated.

- the second step is to refine this approximation by determining the most probable 5° wide sub-interval for each phase. For each time sample, the probability of existence of a phase is set to 0 if the corresponding azimuth is out of those sub-intervals.

The bottom diagrams in figures 3 and 4 show the phase characterization curves after this azimuthal filtering.

At this step, in the function describing the possibility of occurrence of each phase as a function of time, all the information which do not belong to the detected event have been removed. The last step - the distance evaluation - can now be performed.

Each function is differentiated to allow an easy detection of each phase by identifying the times where the derivative is greater than an arbitrary threshold (i.e. . 0.7). When only two phases are detected, the resulting distance is computed using the two times for which the product of the corresponding possibility functions is at its maximum. When more than two phases are detected, a least-squares estimation of the distance is performed for each set of possible arrival-times. The best one is retained as the event distance.

4) Results :

We have processed 28 regional events which occurred in Western Europe during the experiment. Their magnitudes ranged from Ml=2.2 to Ml=5.3, and their epicentral distances from 40 to 1200 km.

The azimuth error is shown as a function of azimuth on figure 5. It is clearly that this method leads to a very precise azimuth estimation : the mean value of the error bars is roughly 3 degrees.

For the 21 events for which a distance can be computed (i.e. : at least two phases have been recognized), the computed distance is shown versus the bulletin distance on figure 6. Excepted for two events for which confusions occurred between Sn and Lg-phases, a good agreement is obtained in the full distance range : the relative standard error is less than 20%. This results are illustrated on a regional map showing the location errors (Figure 7).

CONCLUSIONS AND RECOMMENDATIONS

We have tested a new method for automatic location of regional seismic events recorded on a mini-array. This method includes first a signal analysis process in order to evaluate the consistency of the relative time delays computed from the correlation functions, and second a neural network analysis to identify the different phases and compute the distance of the event.

The standard error of the azimuth estimation is less than 4 degrees for a set of events with distances ranging from 40 to 1200 km. Most of the P-phases are clearly identified by the system, but some confusion between Sn and Lg phases can be observed. When the cases of misidentification are removed, the method leads to an estimate of the distance with an uncertainty of about 20%.

We have shown that this method is able to produce an estimation of the location of regional events with a reasonable error. Further studies will be devoted to testing the method on a larger dataset including the new design of the mini-array which is now composed of 10 stations, and for lower SNR ratios. Comparisons with azimuthal and velocity determinations computed from the new 3 components station and from the broad band F-k analysis will also be performed.

REFERENCES

CANSI, Y.; PLANTET, J.L.; and MASSOT, J.P., "Epicentral azimuth determination by mini-array processing", DARPA, September 1992.

MYKKELTVEIT, S., F. RINGDAL, T. KVAERNA and R. W. ALEWINE, "Application of regional arrays in seismic verification", Bull. Seism. Soc. Am., 80, 1777-1800, 1990.

LACOSS, R.T., CURTIS, S.R., CUNNINGHAM, R.K. and SIBERT, M., "Seismic phase and event labeling using artificial neural network", DARPA, August 1991.

UNIVERSITÄT STUTTGART, "SNNS User Manual, Version 2.0", 1992, ftp- anonymous : 129.69.21.11.

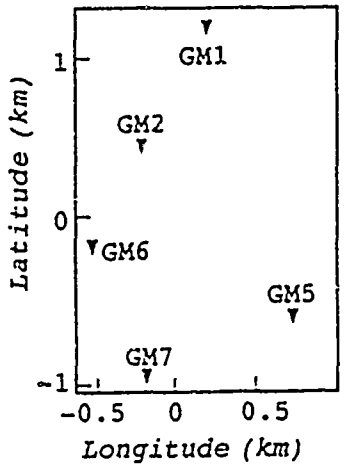

Figure 1 : Network map. It is centred on the point 45.7411N-2.0133E.

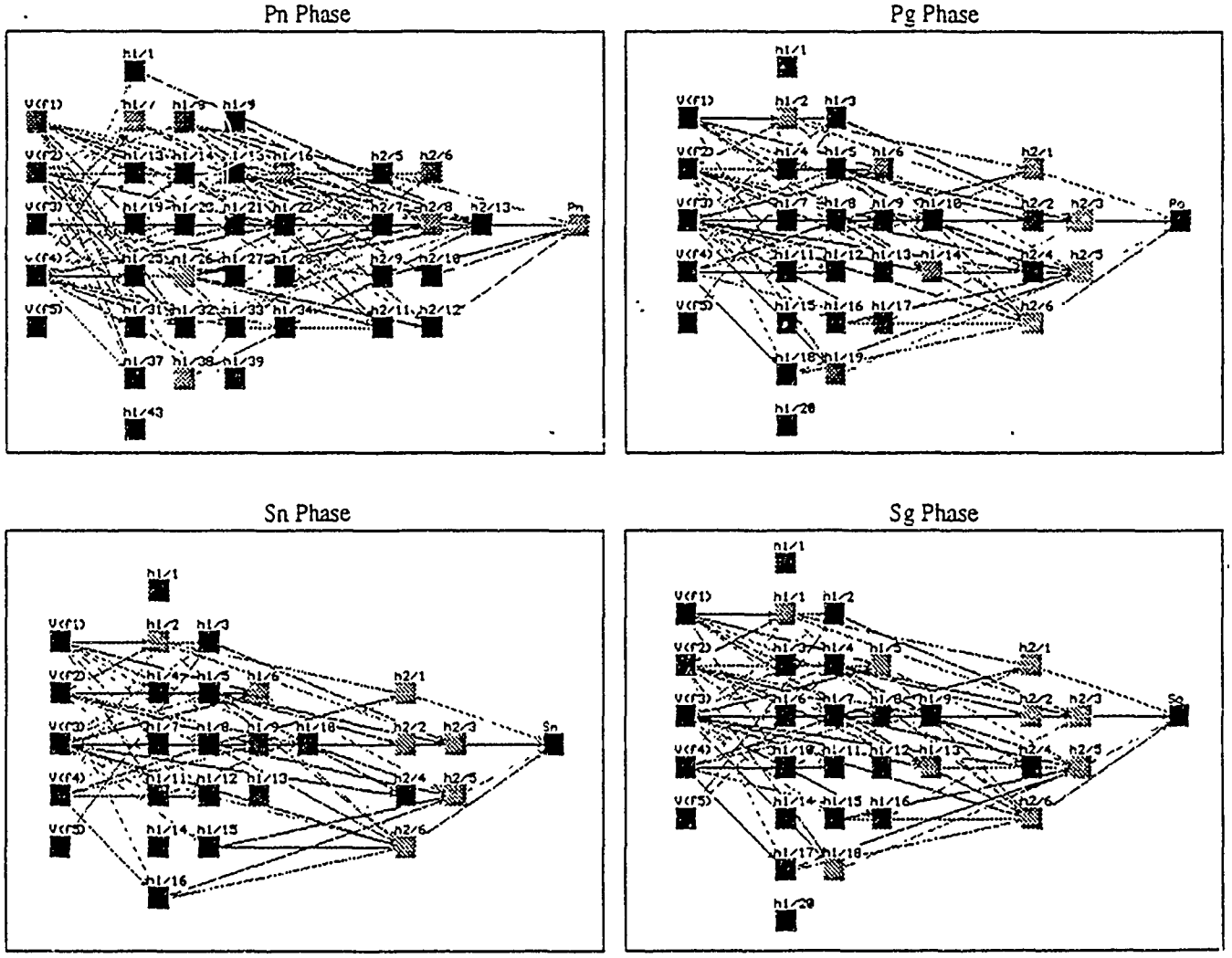

Figure 2 : Design of the neural networks.

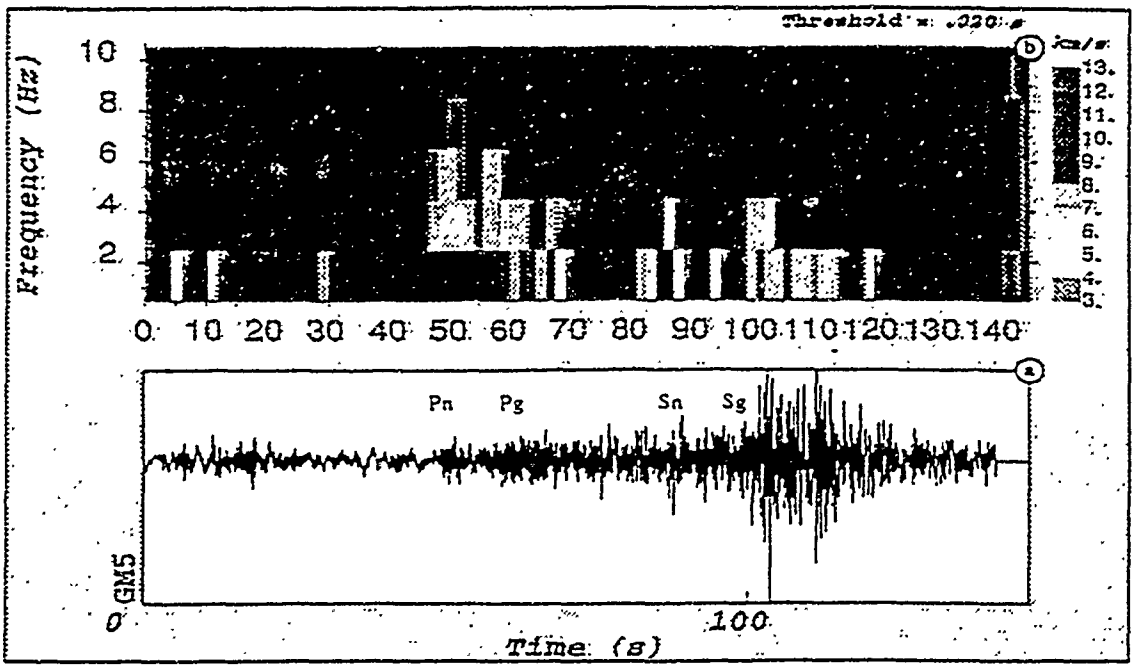

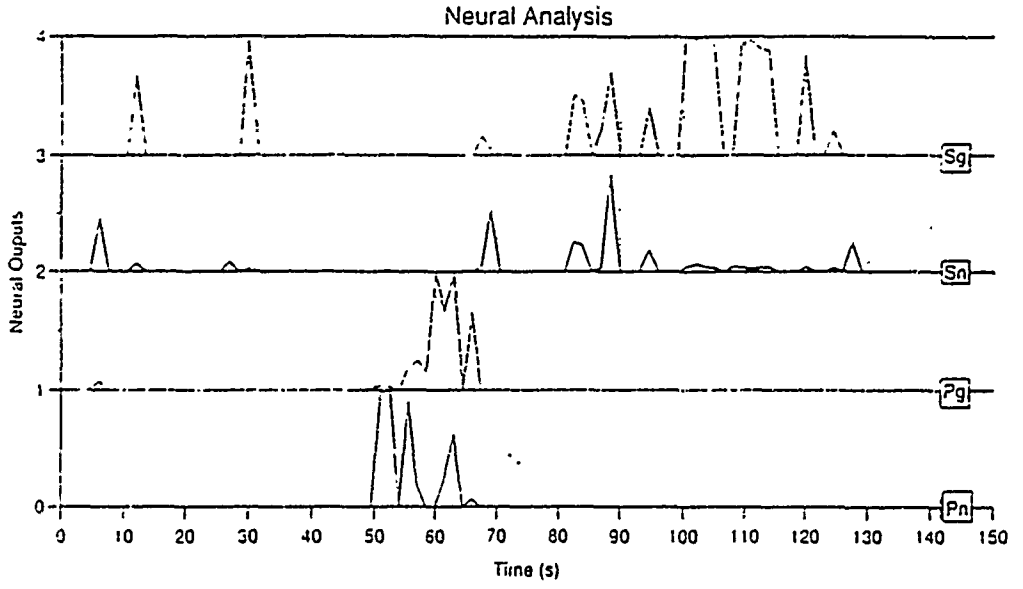

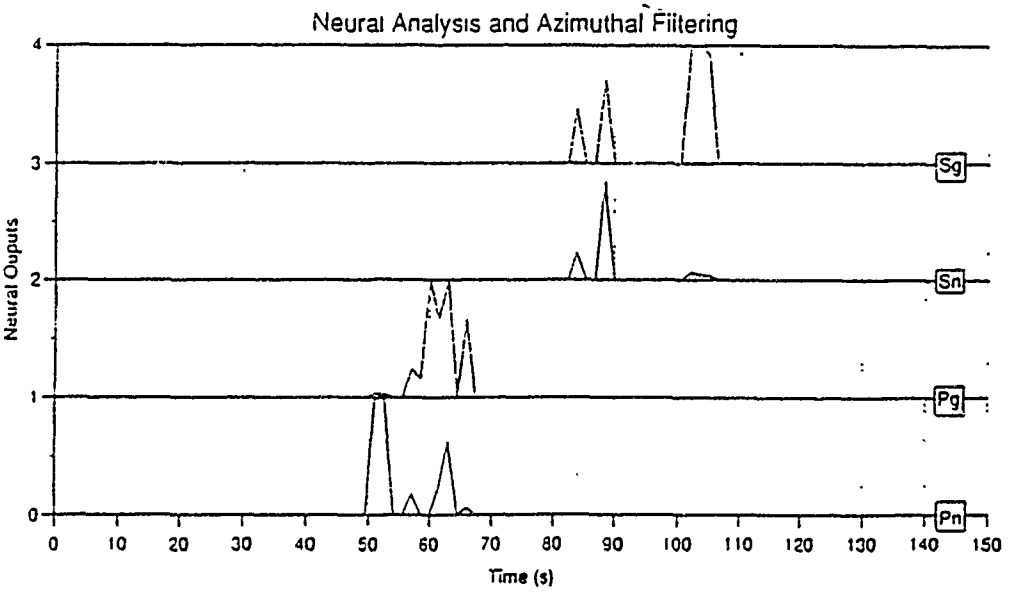

Figure 3 . Example of an event at the different processing levels : the time-frequency plot of the velocity (top), the 4 phase probability functions (middle), and the same after azimuth filtering (bottom).

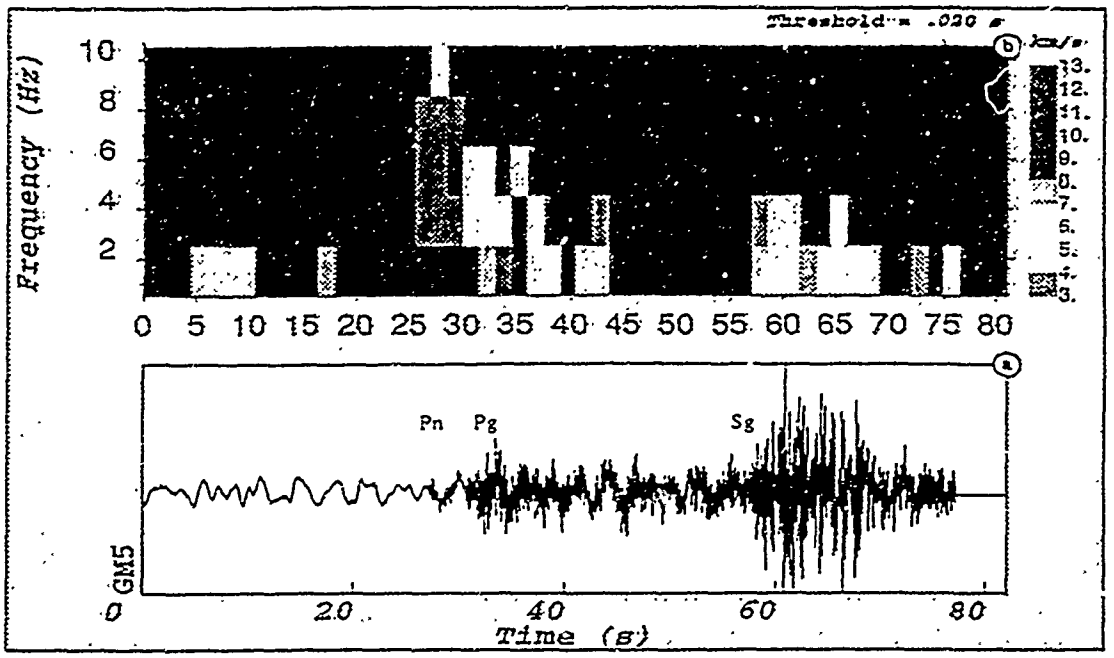

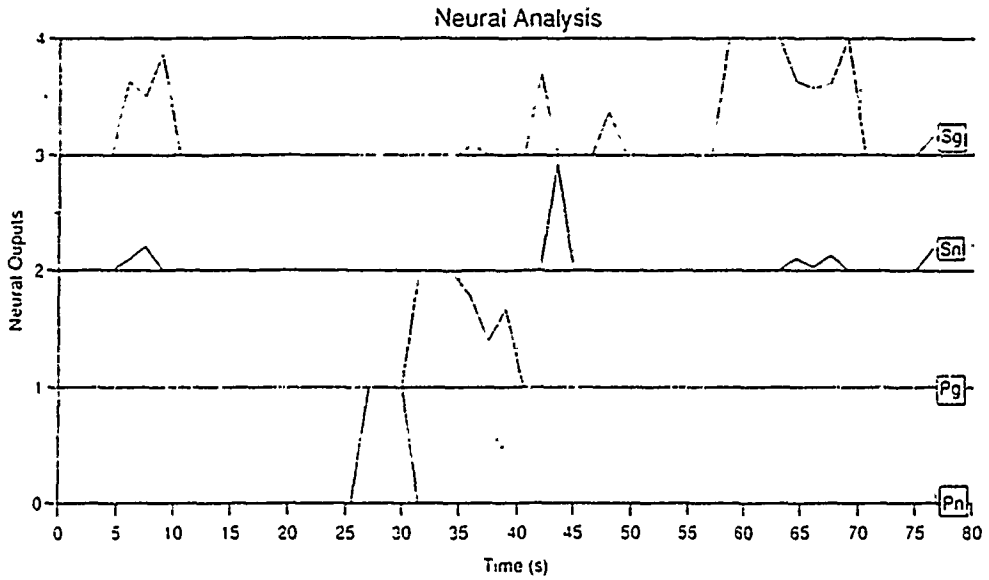

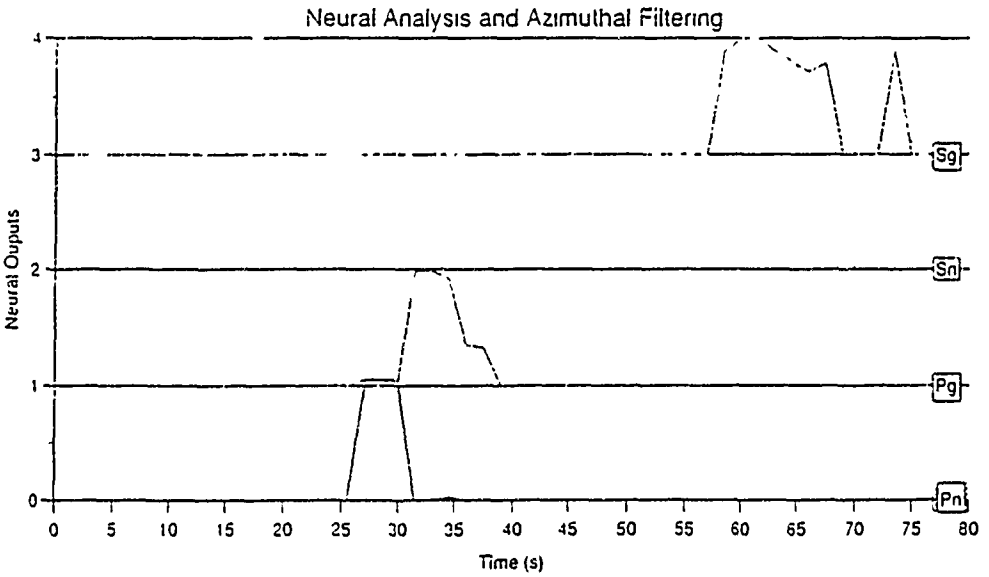

Figure 4 . Example of an event at the different processing levels : the time-frequency plot of the velocity (top), the 4 phase probability functions (middle), and the same after azimuth filtering (bottom).

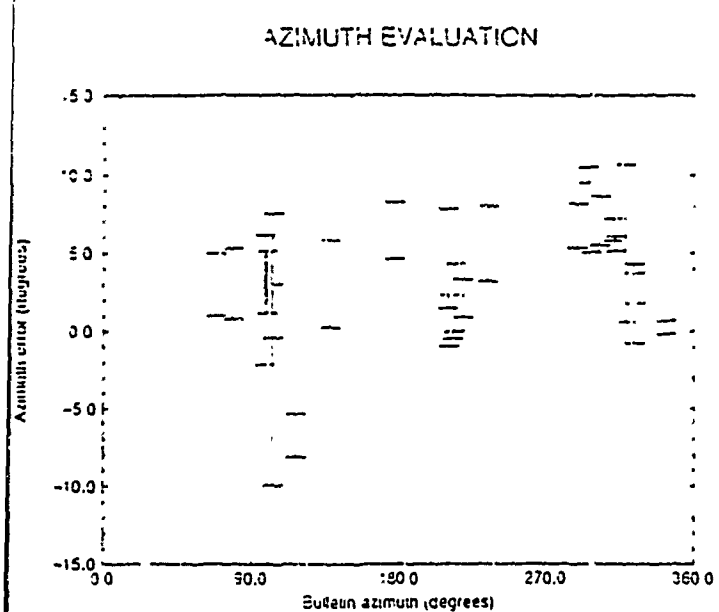

Figure 5 . Azimuth results . azimuth errors versus bulletin azimuths (reference)

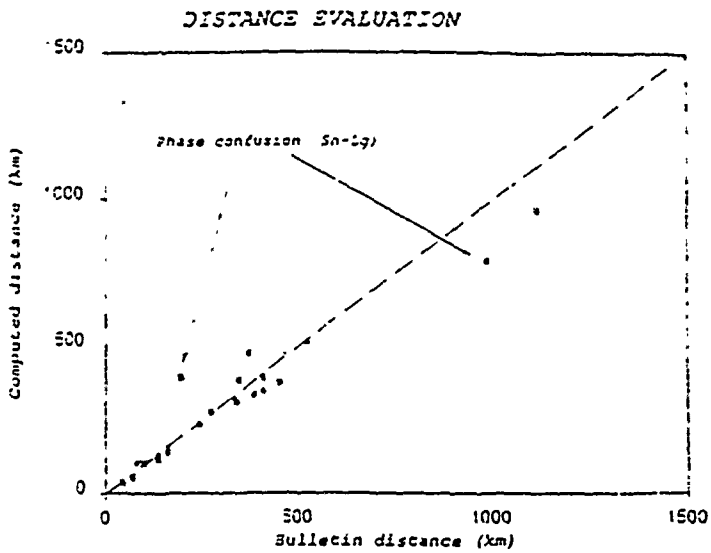

Figure 6 : computed distance (this study) versus bulletin distance (reference).

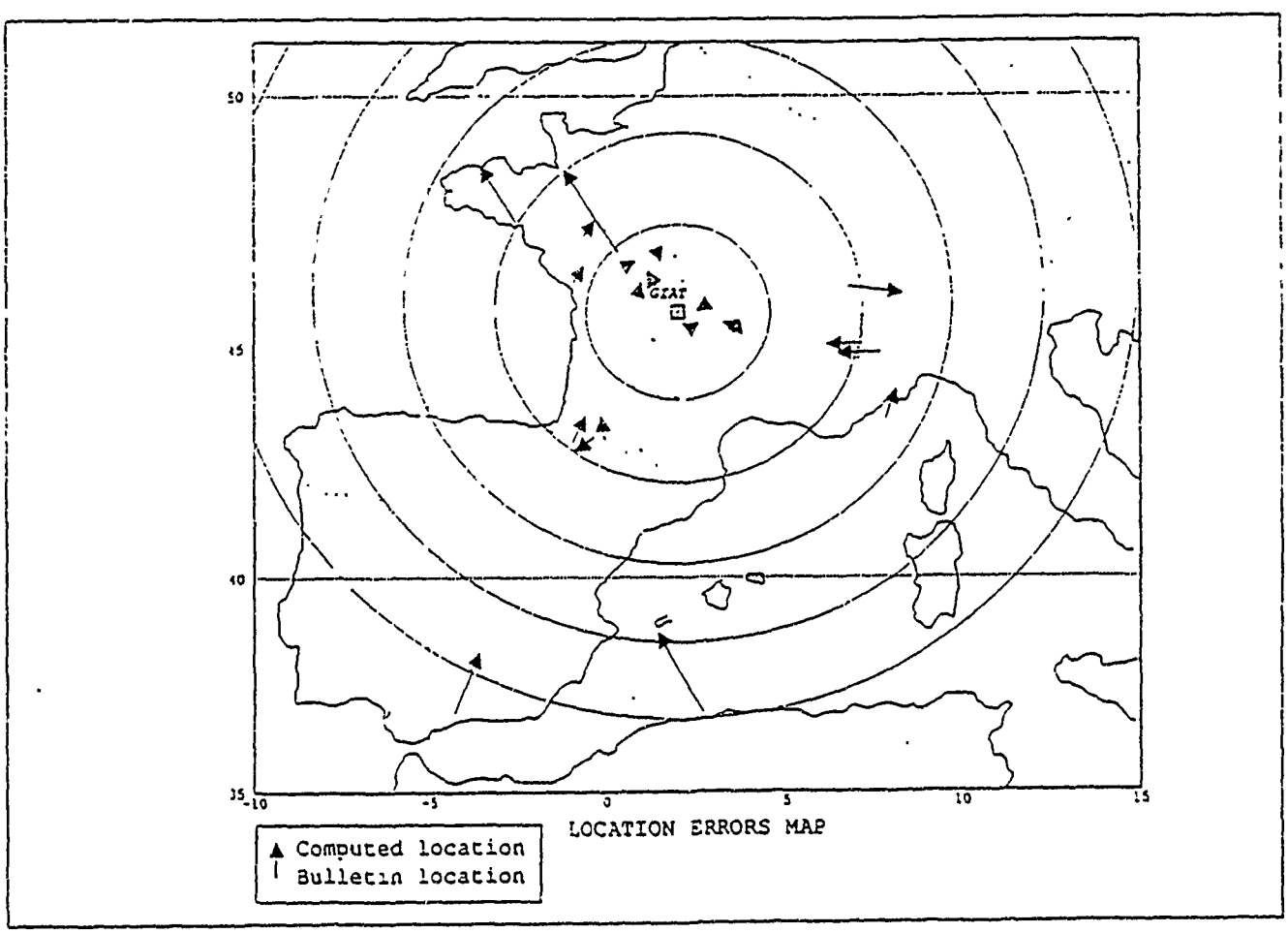

Figure 7 : Regional map showing the location errors for all the events.

COMPARISON OF SINGLE-STATION BACKAZIMUTH ESTIMATES WITH REGIONAL EVENT LOCATIONS IN THE CENTRAL APPALACHIANS

Martin C. Chapman, Shaosong Huang and J. Arthur Snoke
Department of Geological Sciences
Virginia Polytechnic Institute and State University
Blacksburg, Virginia 24061-0421

Contract No. F19628-92-K-0029

OBJECTIVE

The study examines the accuracy with which the source-station backazimuth can be determined from single-station polarization analysis of mining explosion generated P and Rg wave signals at near-regional distances.

RESEARCH ACCOMPLISHED

Station BLA:

The Blacksburg, Virginia, GSETT-2 station was installed in January, 1990 in the WWSSN vault on the campus of Virginia Tech. The station is equipped with Teledyne Geotech GS-13 short-period and BB-13 broadband sensors. Digitization, multiplexing and calibration are performed by a Teledyne-Geotech RDAS-200 unit, and time synchronization is obtained via a Kinemetrics, Inc. Omega receiver/clock. The short-period and broadband sample rates are 40 and 10 samples/sec, respectively. The data are demultiplexed, event-detected and archived by a Science Horizons, Inc. NOMAD workstation.

Location of the Mining Explosions:

Figure 1 shows the locations of 36 mining explosions, along with the regional network stations used for epicenter determination. The data set consists of multiple explosions at nine mine sites plus single explosions at nine additional sites. Confirmation of the geographic locations of the explosions through contact with the mine operators has been achieved for three mines.

The epicenters of the explosions were located using HYPOELLIPSE (Lahr, 1980), with a three layer crustal velocity model (Bollinger et al., 1980). In cases where the event epicenter was not known from independent information and where multiple events were recorded from the same location, the network location with smallest statistical uncertainty was adopted as the epicenter of the group of explosions.

Figure 2 shows the location error ellipses for the events in the data set. With the exception of one event in Kentucky, the error ellipse semi-major axes are all less than 25 km. The horizontal angles subtended by the error ellipses as viewed from station BLA were calculated: the maximum uncertainty (defined by the angular extent of the error ellipse), is ±4.6 degrees. This error estimate does not account for any systematic bias due to inaccuracy of the velocity model. However, this latter source of error appears to be small, because the calculated locations are within 10 km of the confirmed mine locations in Kentucky and West Virginia.

Method of P wave Polarization Analysis:

The backazimuth estimates from P wave arrivals at BLA were derived using the method developed by Jurkevics (1988). The short-period data were corrected for minor differences in system response of the three component channels (Chapman et al., 1988).

Fourier amplitude spectra of the P wave and pre-P wave data segments were calculated using 10 sec time windows. Explosions with signal/noise ratios less than 2 in the frequency range 1 to 10 Hz were rejected. The three component data were then bandpass filtered with corner frequencies 1.0 and 10.0 Hz. The duration of the moving time window used in the polarization analysis is a critical parameter. Testing showed that a window duration of 0.5 seconds generally provided the best backazimuth determination. Given the data bandwidth of 1 to 10 Hz and a sample rate of 40 samples/second, windows less that 0.5 seconds in duration gave unstable results due to the small number of sample points, whereas larger windows tended to reduce resolution because of the non-stationary polarization character of the coda immediately following the initial P wave arrival.

An example showing the processing procedure is shown in Figures 3 and 4. In Figure 3 the data have been rotated into vertical, radial and transverse components, on the basis of the independently determined location. Figure 4 shows a 5 second duration sequence of the data centered near the time of P wave onset, with continuous estimates of backazimuth, rectilinearity and signal/noise ratio. The signal/noise quantity was calculated as the ratio of the average three-component amplitude in the 5 second moving window to the average long-term three-component amplitude using a 10 second data segment prior to P wave onset.

The polarization analysis was performed in an automated manner, with the best-estimate of the backazimuth determined on the basis of maximum rectilinearity near the time of the P wave onset.

Results from the P wave analysis:

The backazimuth errors, defined as the differences in the network derived estimates and the results from the three-component polarization measurements, are plotted as a function of signal/noise ratio in Figure 5. Figure 5 shows that ratios less than 2 can, but do not always, result in very unstable estimates of the polarization parameters, as evidenced by the two points with backazimuth errors in excess of 90 degrees.

Large signal/noise ratios do not guarantee accurate backazimuth estimates, at least for BLA and this mine explosion data set. Figure 5 shows no evidence for the backazimuth error to decrease with increasing signal/noise ratio, in the range 2 to 10. Deleting the two observations with errors in excess of 100 degrees results in a mean azimuth error of -6 degrees; the standard deviation is 21 degrees.

Figure 6 shows the backazimuth error plotted as a function of rectilinearity. Again, there is no tendency in this data set for the errors to decrease with increasing values of this parameter in the range 0.8 to 1.0. Thus, it appears that the initial P wave arrivals from some of the mine explosions are arriving from off-azimuth directions, probably due to refraction from laterally heterogeneous velocity structure.

As a rule, the explosion data set exhibits very emergent and complex P wave arrivals. The emergent character of the signal may be due to the extended nature of the delay-fired source-time function (Chapman, et al., 1992). Off-azimuth arrivals consisting of converted and scattered energy appear at a very early stage in the coda: rarely can accurate estimates of the P wave backazimuth be obtained from portions of the coda at times greater than 1.0 second following the initial onset time. Also, the P wave angles of incidence with the vertical are small, averaging 22 degrees with a standard deviation of 9 degrees. This results in a reduced signal/noise ratio on the horizontal components. This phenomenon, which may be station dependent, tends to further reduce the accuracy of the backazimuth determination for low S/N events.

Rg Wave Analysis:

The complications discussed above make accurate backazimuth determination difficult for this delay-fired explosion data set. In an effort to extract more information from the single-station data, we have examined the potential for using the Rg phase to determine source direction.

Several of the explosion signals exhibit Rg phases. At BLA, Rg is a Rayleigh wave with group velocities in the range 1.8 to 2.3 km/sec. It is apparent on short period recordings which have been bandpass filtered for the range 0.2 to 1.0 Hz. A typical example is shown in Figure 7.

The backazimuth of the source was estimated from the Rg wave by noting that for a laterally homogeneous, isotropic earth, the phase angles of the Rg radial component Fourier harmonics lead those of the vertical by 90 degrees. In the presence of noise and other seismic phases, this phase difference can be used to estimate the backazimuth if energy on the transverse component in the Rg frequency band is sufficiently incoherent with respect to that on the vertical and radial components. The approach we have used is described below.

Let $z(\omega)$, $n(\omega)$ and $e(\omega)$ be the Fourier transforms of the windowed time series containing the Rg arrival on the vertical, north-south and east-west components. For an arbitrary rotation angle ϕ, representing a trial source-station azimuth, the radial component of motion is given by

$$r(\omega) = n(\omega) \cos(\phi) + e(\omega) \sin(\phi),$$

and the phase spectrum is

$$\Theta_r(\omega) = \arg r(\omega).$$

Similarly, for the vertical component, the phase is

$$\Theta_z(\omega) = \arg z(\omega).$$

Because the Rg signal is bandlimited, we define ω_j to represent the j'th discrete Fourier frequency in the range $\omega_n \le \omega_j \le \omega_m$, j =n, n+1....m, where ω_n and ω_m are the lower and upper bandlimits of the signal.

Let

$$A_j = \sqrt{|z(\omega_j)|^2 + |r(\omega_j)|^2}, \text{ if } |[\Theta_r(\omega_j) - \Theta_z(\omega_j)] - \pi/2| \le \alpha$$

$$A_j = 0, \text{ if } |[\Theta_r(\omega_j) - \Theta_z(\omega_j)] - \pi/2| > \alpha$$

where α is a pre-selected phase difference tolerance. By summing over the frequency band of interest, we obtain a measure of the coherent signal amplitude in the vertical-radial plane. This sum is normalized by the total 3-component amplitude in the frequency band to yield

$$P = \sum_{j=n}^{m} A_j \Big/ \sqrt{|z(\omega_j)|^2 + |n(\omega_j)|^2 + |e(\omega_j)|^2}$$

This quantity is unity when the rotation angle ϕ is such that all horizontal motion is in the radial direction, and the phase differences between radial and vertical Fourier harmonics in the chosen frequency band are in the range $\pi/2 \pm \alpha$. In practice, P is evaluated with ϕ ranging from 0 to 359 degrees, in 1 degree increments, with a phase difference tolerance of 10 degrees. The value of ϕ resulting in a maximum value of P is the estimated Rg azimuth of approach.

Figure 8 shows P plotted as a function of trial backazimuth for the time series data shown in Figure 7. In this case, the estimated backazimuth differs by 16 degrees from the true value.

Results from the Rg wave analysis:

Figure 9 compares the backazimuths estimated from the Rg phase with those derived from the P wave, using 27 explosions featuring discernible Rg phases. For Rg, the mean error is -2 degrees: the standard deviation is 26 degrees, which is only 5 degrees larger than the result obtained from the P wave arrivals.

CONCLUSIONS AND RECOMMENDATIONS

We have compared the single-station backazimuth estimates at BLA with independently derived locations for a set of mining explosions and find that for sources in the northwest quadrant, polarization analysis of the P wave arrival gives an essentially unbiased estimate of the source direction (mean error 6 degrees), but that the scatter in the results is substantial, with a standard deviation for 35 measurements of 21 degrees.

Characteristics of the P wave signal which contribute to the errors in the estimates include: (1) emergent initial motions from the delay-fired explosions; (2) off-azimuth arrivals and/or converted phases arriving early in the P coda; (3) steep angles of incidence, averaging 22 degrees from vertical, which tend to reduce the signal/noise ratios on the horizontal components. Optimum data segments for reliable backazimuth estimates are restricted to short time intervals (1 second or less) beginning with the initial P wave motion.

The Rg phase is present in many of the explosion signals at BLA. Analysis of this arrival using a phase difference criterion results in backazimuth estimates of approximately the same reliability as those derived from the initial P wave motion. These results are encouraging, and methods for combining the two estimates are being pursued.

REFERENCES

Bollinger, G. A., M. C. Chapman and T. P. Moore, (1980), Central Virginia regional seismic network: Crustal velocity structure in central and southwestern Virginia, NUREG/CR-1217, (R6, RA), U.S. NRC, Div. of Reactor Safety Res., Contract No. NRC-04-77-134, 187 pp.

Chapman, M. C., G. A. Bollinger and M. S. Sibol, (1992), Modeling delay-fired explosion spectra at regional distances, Bull. Seism. Soc. Am., 82, pp. 2430-2447.

Chapman, M. C., J. A. Snoke and G. A. Bollinger, (1988), A procedure for calibrating short-period telemetered seismograph systems, Bull. Seism. Soc. Am., 78, pp. 2077-2088.

Jurkevics, A., (1988), Polarization analysis of three-component array data, Bull. Seism. Soc. Am., 78, pp. 1725-1743.

Lahr, J. C., (1980), Hypoellipse/Vax: A computer program for determining local earthquake hypocentral parameters, magnitude and first motion pattern, U.S. Geol. Survey Open-File Report 80-59, 67 pp.

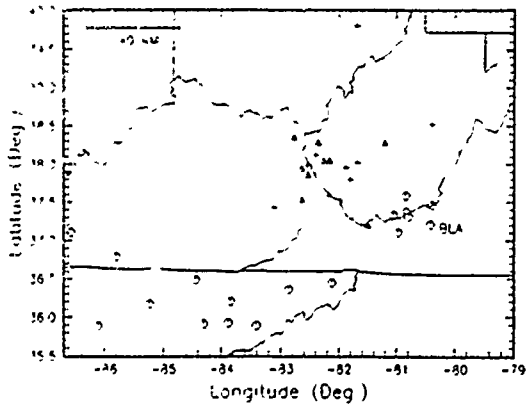

Figure 1 Network stations (including three-component station BLA) are shown by circles. Crosses indicate mine locations yielding multiple explosion signals. Mines for which only a single explosion was recorded are shown by triangles

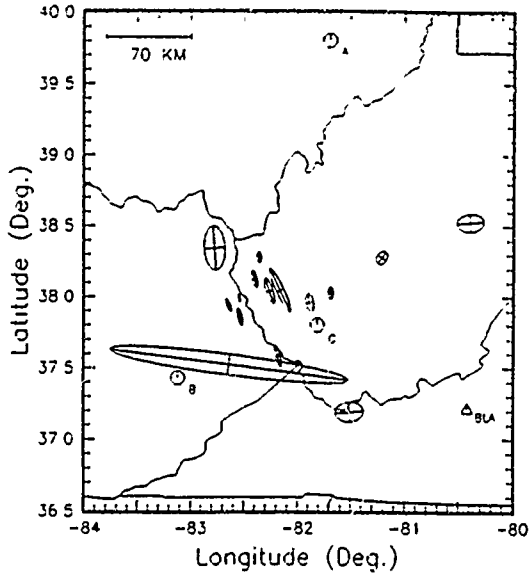

Figure 2 Confirmed mine locations are shown by the circles with associated letters. The location of three-component station BLA is shown by the triangle. The ellipses indicate 68% chi-square confidence regions for mine locations

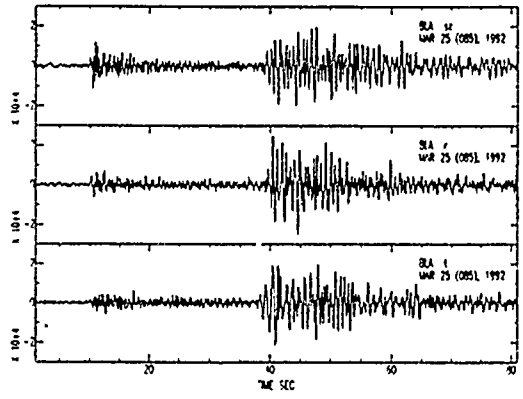

Figure 3 Time series data for explosion in Kentucky (mine B in Fig. 2). The data have been rotated into vertical (top), radial (center), and transverse (bottom) components

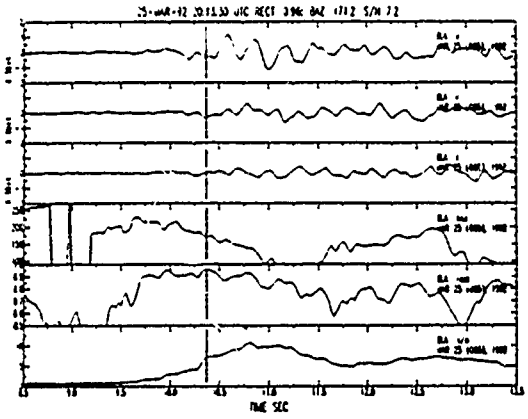

Figure 4 Example of P wave polarization processing for the signal shown in Fig. 3. From the top, the traces are: (1) Vertical, (2) radial, (3) transverse, (4) station-source backazimuth (deg), (5) rectilinearity, and (6) three-component signal/noise ratio. Note that for rotated components, the true backazimuth angle is 180 degrees. Vertical lines indicate time at which the rectilinearity is maximum. The duration of the moving window for polarization analysis is 0.5 seconds.

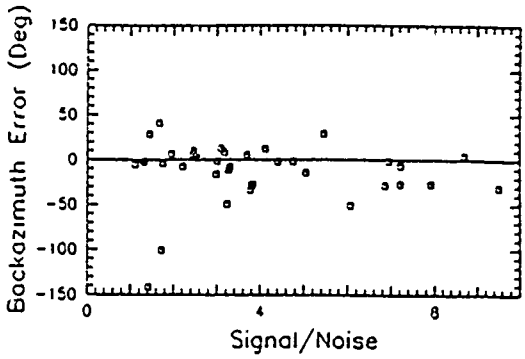

Figure 5. Backazimuth error versus signal/noise ratio, from P wave polarization analysis.

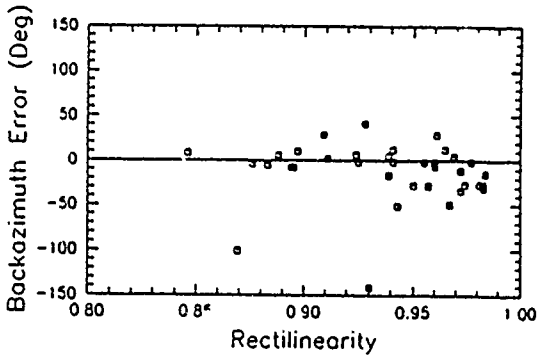

Figure 6 Backazimuth error versus rectilinearity, from P wave polarization analysis

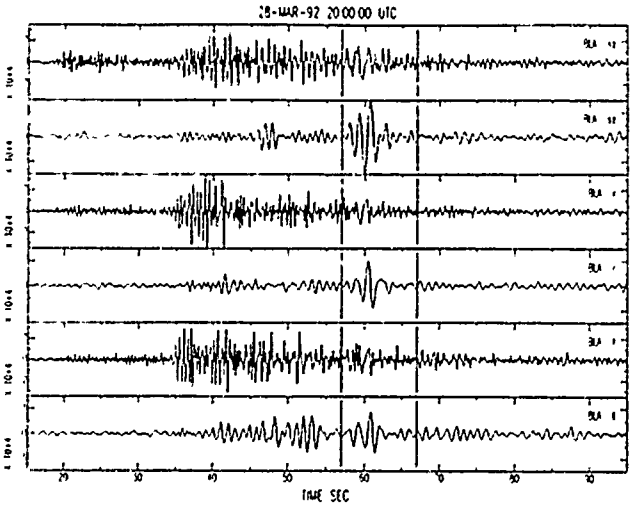

Figure 7 A typical Rg phase The 1st, 3rd and 5th traces from the top are unfiltered short-period recordings of the vertical, radial and transvertse co.iponents. The 2nd, 4th and 6th traces are bandpass filtered from 0 2 to 1.0 Hz.

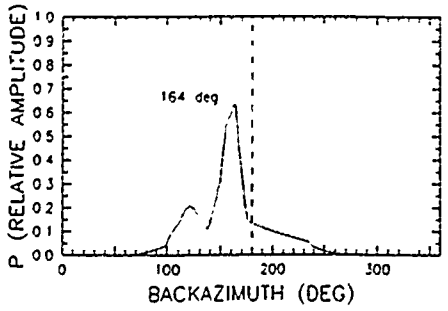

Figure 8 Results of the Rg analysis, using the signal in Fig 7 The backazimuth estimate is 164 degrees, versus the true value of 180

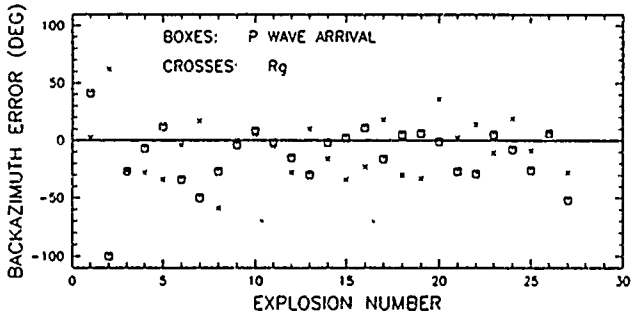

Figure 9. Comparison of backazimuth estimates from Rg and P wave polarization analysis.

ENERGY TRANSFER THEORY OF SEISMIC SURFACE WAVES IN A RANDOM SCATTERING AND ABSORPTION HALF-SPACE MEDIUM

Xiaofei Chen and Keiiti Aki

Department of Geological Sciences, University of Southern California, Los Angeles, CA90089-740

Contract Number: F49620-93-1-0016

OBJECTIVE

The objective of this study is to develop an energy transfer theory for seismic surface waves in a random scattering and absorption half-space medium. Su and Aki (1991) found a significant difference in coda attenuation, Q_c^{-1}, for quarry blasts and earthquakes for lower frequencies of 1.5 and 3 Hz for lapse time less than 30 seconds, and they suggested that such a significant difference in Q_c^{-1} may be attributed to the seismic surface wave's contributions. To interpret the observed seismic coda waves we need to consider the seismic surface wave scattering. As shown in Wu (1985) and Zeng et al. (1991), the energy transfer theory can successfully describe the seismic body wave propagation in a random scattering and absorption full-space medium. In this paper, we establish the energy transfer theory for seismic surface wave propagation in a random half-space medium.

RESEARCH ACCOMPLISHED

1. Energy transfer theory for Rayleigh wave

In this section, we shall consider a simple case in which the background medium is a homogeneous half-space. The only surface wave in this case is the Rayleigh wave. For simplicity, we neglect the conversions between the body waves and the Rayleigh wave. Then the energy distribution of Rayleigh wave in an absorption and scattering medium at an arbitrary point $\mathbf{x}$ for frequency ω can be written as,

$$E^R(\mathbf{x},\omega) = G(\mathbf{x},\mathbf{x}_s)\exp[-\eta^R|\mathbf{r}-\mathbf{r}_s|]\varepsilon_0^R(\mathbf{x}_s,\omega) + \sum_j \sigma(\mathbf{x}_j)G(\mathbf{x},\mathbf{x}_s)\exp[-\eta^R|\mathbf{r}-\mathbf{r}_j|]E^R(\mathbf{x}_j,\omega), \quad (1)$$

Where, $\mathbf{r}= \mathbf{x}-\hat{\mathbf{e}}_z(\mathbf{x}\cdot\hat{\mathbf{e}}_z)$ is a horizontal vector, and η^R is the attenuation coefficient that includes the intrinsic (η_i^R) and scattering attenuation (η_s^R), i.e., $\eta^R = \eta_i^R + \eta_s^R$. In eq.(1), $E^R(\mathbf{x},\omega)$ is the seismic energy per unit volume carried by Rayleigh wave at point $\mathbf{x}$ and frequency ω. The first term in the right-hand-side of (1) represents the direct Rayleigh wave energy radiated from source, and the second term in the right-hand-side of (1) describes the total scattering energy from all scatters ($\mathbf{x}_j$). Where σ is the scattering cross-section, $G(\mathbf{x},\mathbf{x}_j)$ and $\exp[-\eta^R|\mathbf{r}-\mathbf{r}_j|]$ describes the geometrical spreading and attenuation, respectively. It should be noted that the attenuation is caused only by the horizontal propagation, since the surface wave only propagates horizontally. For weak scattering case, the scattering cross-section σ can be analytically derived by using Born approximation (Aki and Richards, 1980). Here, for simplicity, we assume that σ is a constant. The geometrical spreading function $G(\mathbf{x},\mathbf{x}')$, however, can be determined by the consideration of energy conservation.

Geometrical Spreading Function of Rayleigh Wave:

The direct Rayleigh wave (Rayleigh wave in the background medium) has the following form (Aki and Richards, 1980),

$$U^R(x,\omega) = \frac{P_R(x)[P_R(x_s)\cdot F(x_s)]}{\sqrt{(\pi/2)k_R|r-r_s|}} \exp\{i[k_R|r-r_s|+\pi/4]\}. \qquad (2)$$

Where,

$$P_R(x) = r_1(z,\omega)\hat{e}_r + ir_2(z,\omega)\hat{e}_z\,, \qquad (2a)$$

with $\hat{e}_r = (r-r_s)/|r-r_s|$. The corresponding energy density is

$$E_o^R(x,\omega) = \frac{1}{2}\rho\omega^2|U^R(x,\omega)|^2 = \frac{\rho\omega^2}{\pi k_R}\frac{|P_R(z)|^2}{|r-r_s|}|P_R(x_s)\cdot F(x_s)|^2\,. \qquad (3)$$

For steady state, the energy rate should be a constant for any closed-surface that encloses the source, namely,

$$\oint_S \{E_o^R(x,\omega)v_R\}\cdot\hat{s}\,dS = \text{constant}, \qquad \text{for } x_s \text{ inside S.} \qquad (4)$$

Where, $\hat{s}$ is the normal vector of the surface element dS, and v_R is the velocity vector of the Rayleigh wave. Since the surface wave propagates along the horizontal direction, we consider a cylindrical surface that leads to a simple surface integration,

$$\oint_S \{E_o^R(x,\omega)v_R\}\cdot\hat{s}\,dS = \int_0^{+\infty} dz \int_0^{2\pi} Rd\theta\; E_o^R(x,\omega)v_R\,.$$

Where, $R = |r-r_s|$. Substituting (3) in (4), we find

$$\varepsilon_o^R(x_s) = \frac{1}{v_R}\oint_S \{E_o^R(x,\omega)v_R\}\cdot\hat{s}\,dS = \frac{2\omega^2\rho}{k_R}\int_0^{+\infty}|P_R(z)|^2dz\,|P_R(x_s)\cdot F(x_s)|^2$$

$$= \frac{2\rho\omega^2}{k_R}\cdot|F(x_s)|^2\{|r_1(z_s)n_r|^2 + |r_2(z_s)n_z|^2\}\int_0^{+\infty}\{|r_1(z)|^2 + |r_2(z)|^2\}\,dz\,. \qquad (5)$$

Using the above result, eq. (3) can be rewritten as

$$E_o^R(x,\omega) = \frac{g_R(z,\omega)}{2\pi|r\text{-}r_s|}\varepsilon_o^R(x_s). \qquad (6)$$

Where,

$$g_R(z,\omega) = \frac{|P_R(z)|^2}{\int_0^{+\infty}|P_R(z')|^2dz'} = \frac{[r_1(z,\omega)^2 + r_2(z,\omega)^2]}{\int_0^{+\infty}[r_1(z',\omega)^2 + r_2(z',\omega)^2]dz'}\,. \qquad (6a)$$

Thus, we obtain the geometrical spreading function of Rayleigh wave energy propagation as

$$G(x,x') = \frac{g_R(z,\omega)}{2\pi|r-r'|}. \tag{7}$$

From equation(6a), we can verify the following identity,

$$\int_0^{+\infty} g_R(z,\omega)dz = 1. \tag{7a}$$

Integral equation of scattering Rayleigh wave in random medium:

We are now ready to set up the basic integral equation for Rayleigh wave scattering in random medium. Substituting eq.(7) in (1), and assuming that the random scatters are uniformly distributed and can be described by a continuous distribution n_o(density of scatters), we obtain the following integral equation,

$$E^R(x,\omega) = \frac{g_R(z,\omega)e^{-\eta^R|r-r_s|}}{2\pi|r-r_s|}\varepsilon_o^R(x,\omega) + \int_V \eta_s^R \frac{g_R(z,\omega)}{2\pi|r-r'|} e^{-\eta^R|r-r'|}E^R(x,\omega)dV(x'). \tag{8}$$

Where, $\eta_s^R = n_o\sigma$. Eq.(8) is similar to the energy transfer equation for body wave (Wu, 1985; Zeng et al., 1991), but with different geometrical spreading functions and the attenuation factors that are caused by the characterizations of surface wave propagation. The dependence of $|r-r'|$ indicates the horizontal propagation property of the surface wave, whereas, the $g_R(z,\omega)$ explores the depth distribution of surface wave energy. Integral equation (8) can be solved by using spatial domain Fourier transform method. First, we note that equation (8) can be rewritten as

$$E^R(x,\omega) = g_R(z,\omega)E_2^R(r,\omega). \tag{9}$$

Inserting equation (9) into (8) and using the identity (7a), we obtain

$$E_2^R(r,\omega) = \frac{e^{-\eta^R|r-r_s|}}{2\pi|r-r_s|}\varepsilon_o^R(x_s,\omega) + \int_\Sigma \eta_s^R \frac{e^{-\eta^R|r-r'|}}{2\pi|r-r'|} E_2^R(r',\omega)\, d\Sigma(r'). \tag{10}$$

Where, $\Sigma(r) = \{(x,y)|-\infty<x<+\infty, -\infty<y<+\infty\}$. The corresponding Fourier transform is

$$\tilde{E}_2^R(k,\omega) = \tilde{G}_2^R(k)\tilde{\varepsilon}_o^R(x_s,\omega) + \eta_s^R\tilde{G}_2^R(k)\tilde{E}_2^R(k,\omega). \tag{11}$$

Where, we assumed $r_s = 0$, and $\tilde{G}_2^R(k,\omega)$ is given by

$$\tilde{G}_2^R(k,\omega) = \iint_{-\infty}^{+\infty} dxdy\, \frac{e^{-\eta^R r}}{2\pi r}\exp(ik\cdot r) = \int_0^{+\infty} J_o(kr)e^{-\eta^R r}dr = \frac{1}{\sqrt{k^2+(\eta^R)^2}}. \tag{11a}$$

Substituting this result in eq.(11), then taking the inverse Fourier transform over k, we finally obtain

$$E^R(x,\omega) = g_R(z,\omega)P_R(r,\eta^R,\eta_s^R)\,\varepsilon_o^R(x_s,\omega)\,. \tag{12}$$

Where $P_R(r,\eta^R,\eta_s^R)$ is the inverse Fourier transform of $\tilde{G}_2^R(k,\omega)$,

$$P_R(r,\eta^R,\eta_s^R) = \frac{1}{2\pi}\int_0^{+\infty} J_0(kr)\frac{kdk}{\sqrt{k^2+(\eta^R)^2}-\eta_s^R}\,. \tag{12a}$$

Solution (12) has a clear physical meaning. The term $\varepsilon_o^R(x_s,\omega)$, as defined earlier, contains the seismic source information. Function $g_R(z,\omega)$ represents the depth dependence of Rayleigh wave energy, whereas the function $P_R(r,\eta^R,\eta_s^R)$ describes the propagation and attenuation processes of the Rayleigh wave energy. $P_R(r,\eta^R,\eta_s^R)$ can be obtained by evaluating integral (12a). For a pure absorption medium ($\eta_s^R=0$), we find $P_R(r,\eta^R,0) = e^{-\eta^R r}/2\pi r$. This is consistent with our direct Rayleigh wave (solution in background medium). For general absorption and scattering media, we can numerically evaluate the propagation and attenuation function $P_R(r,\eta^R,\eta_s^R)$.

2. Energy transfer theory for Rayleigh and Love waves

For a general vertically heterogeneous background medium, both Rayleigh waves and Love waves exist. The randomly distributed scatters will cause the conversions between these two independent types of surface waves. For simplicity, we shall still neglect the conversions between body waves and surface waves as we did above. Then the energy transfer processes of Rayleigh and Love waves can be described by,

$$E^R(x,\omega) = G^R(x,x_s)e^{-\eta^R|r-r_s|}\varepsilon_o^R(x,\omega) \tag{13a}$$
$$+\int_V G^R(x,x')e^{-\eta^R|r-r'|}\{\eta_s^{RR}E^R(x',\omega)+\eta_s^{LR}E^L(x',\omega)\}dV(x')$$

$$E^L(x,\omega) = G^L(x,x_s)e^{-\eta^L|r-r_s|}\varepsilon_o^L(x,\omega)$$
$$+\int_V G^L(x,x')e^{-\eta^R|r-r'|}\{\eta_s^{RL}E^R(x',\omega)+\eta_s^{LL}E^L(x',\omega)\}dV(x')\,.$$

Where,

$E^L(x,\omega)$: seismic energy carried by Love wave per unit volume at x;

η^R : total attenuation coefficient for Rayleigh wave, $\eta^R = \eta_i^R + \eta_s^{RR} + \eta_s^{LR}$;

η_s^{RR}: Rayleigh to Rayleigh waves scattering coefficient;

η_s^{LR} : Love to Rayleigh waves scattering coefficient;

η^L : total attenuation coefficient for Love wave, $\eta^L = \eta_i^L + \eta_s^{RL} + \eta_s^{LL}$;

η_i^L : absorption coefficient for Love wave;

η_s^{RL} : Rayleigh to Love waves scattering coefficient;

η_s^{LL} : Love to Love waves scattering coefficient;

$\varepsilon_0^L(x_s,\omega)$: total Love wave energy rate radiated from source divided by the velocity of Love wave;

$G^L(x,x')$: the geometrical spreading function for Love wave.

Neglecting all the contributions from higher modes, we can determine $G^R(x,x')$ and $G^L(x,x')$ for a steady state in the same manner as that for Rayleigh wave above, and find,

$$G^R(x,x') = \frac{g_R(z,\omega)}{2\pi|r-r'|} \quad \text{and} \quad G^L(x,x') = \frac{g_L(z,\omega)}{2\pi|r-r'|}, \tag{14}$$

$$g_R(z,\omega) = \frac{\{[r_1^{(0)}(z,\omega)]^2 + [r_2^{(0)}(z,\omega)]^2\}}{\int_0^{+\infty} \{[r_1^{(0)}(z',\omega)]^2 + [r_2^{(0)}(z',\omega)]^2\}dz'}, \tag{15}$$

and

$$g_L(z,\omega) = \frac{[l^{(0)}(z,\omega)]^2}{\int_0^{+\infty} \{l^{(0)}(z',\omega)\}^2 dz'}. \tag{16}$$

Where,

$r_1^{(o)}(z,\omega)$: is vertical displacement component of the fundamental Rayleigh mode;

$r_2^{(o)}(z,\omega)$: horizontal displacement component of the fundamental Rayleigh mode;

$l^{(o)}(z,\omega)$: displacement of the fundamental Love mode.

Inserting eqs. (14), (15) and (16) into eqs. (13a) and (13b) yields

$$\begin{cases} E^R(x,\omega) = g_R(z,\omega)E_2^R(r,\omega) \\ E^L(x,\omega) = g_L(z,\omega)E_2^L(r,\omega) \end{cases} \tag{17}$$

and

$$E_2^R(r,\omega) = \frac{e^{-\eta^R|r-r_s|}}{2\pi|r-r_s|}\varepsilon_0^R(x_s,\omega) + \int_\Sigma \frac{e^{-\eta^R|r-r'|}}{2\pi|r-r'|}\{\eta_s^{RR}E_2^R(r',\omega) + \eta_s^{LR}E_2^L(r',\omega)\}d\Sigma(r'), \tag{18a}$$

$$E_2^L(r,\omega) = \frac{e^{-\eta^L|r-r_s|}}{2\pi|r-r_s|}\varepsilon_0^L(x_s,\omega) + \int_\Sigma \frac{e^{-\eta^L|r-r'|}}{2\pi|r-r'|}\{\eta_s^{RL}E_2^R(r',\omega) + \eta_s^{LL}E_2^L(r',\omega)\}d\Sigma(r'). \tag{18b}$$

Similar to the Rayleigh wave energy scattering problem discussed above, eqs. (18a) and (18b) can be solved by using the Fourier transform method. In horizontal wave-number domain, eqs. (18a) and (18b) can be reduced to,

$$\begin{cases} \tilde{E}_2^R(k,\omega) = \tilde{G}_2^R(k)\varepsilon_0^R(z_s,\omega) + \tilde{G}_2^R(k)\{\eta_s^{RR}\tilde{E}_2^R(k,\omega) + \eta_s^{LR}\tilde{E}_2^L(k,\omega)\} \\ \tilde{E}_2^L(k,\omega) = \tilde{G}_2^L(k)\varepsilon_0^L(z_s,\omega) + \tilde{G}_2^L(k)\{\eta_s^{RL}\tilde{E}_2^R(k,\omega) + \eta_s^{LL}\tilde{E}_2^L(k,\omega)\} \end{cases} \tag{19}$$

with, $\tilde{G}_2^R(k) = \dfrac{1}{\sqrt{k^2+(\eta^R)^2}}$ and $\tilde{G}_2^L(k) = \dfrac{1}{\sqrt{k^2+(\eta^L)^2}}$.

In equation (19), we have assumed $r_s = 0$. Using compact matrix form, equation (19) can be solved as

$$\tilde{E}_2(k,\omega) = \{I-\eta_s\tilde{G}_2(k)\}^{-1}\,\tilde{G}_2(k)\varepsilon_o(z_s,\omega) \tag{20}$$

where,

$$\tilde{E}_2(k,\omega) = [\tilde{E}_2^R(k,\omega),\ \tilde{E}_2^L(k,\omega)]^T,\quad \varepsilon_o(z_s,\omega) = [\varepsilon_o^R(z_s,\omega),\ \varepsilon_o^L(z_s,\omega)],$$

$$\tilde{G}_2(k) = \begin{bmatrix} \tilde{G}_2^R(k) & 0 \\ 0 & \tilde{G}_2^L(k) \end{bmatrix},\ \eta_s = \begin{bmatrix} \eta_s^{RR} & \eta_s^{RL} \\ \eta_s^{LR} & \eta_s^{LL} \end{bmatrix} \text{ and } I = \begin{bmatrix} 1 & 0 \\ 0 & 1 \end{bmatrix}.$$

By taking the inverse Fourier transform, we finally obtain the spatial domain solution as follows,

$$E(x,\omega) = g(z,\omega)P(r;\eta^R;\eta^L;\eta_s)\varepsilon_o(z_s,\omega) \tag{21}$$

Where,

$$E(x,\omega) = [E^R(x,\omega),\ E^L(x,\omega)]^T$$

$$g(z,\omega) = \begin{bmatrix} g_R(z,\omega) & 0 \\ 0 & g_L(z,\omega) \end{bmatrix},$$

and

$$P(r;\eta^R;\eta^L;\eta_s) = \frac{1}{2\pi}\int_0^{+\infty} \{I-\eta_s\tilde{G}_2(k)\}^{-1}\tilde{G}_2(k)kJ_o(kr)dk\,. \tag{21a}$$

Solution (21) has a similar form as that of the Rayleigh waves scattering problem discussed earlier. $g(z, \omega)$ gives rise to the depth dependence of the energies for Rayleigh and Love waves, $\varepsilon_0(z_s,\omega)$ represents the source energies of Rayleigh and Love waves; and $P(r;\eta^R;\eta^L;\eta_s)$ describes the horizontal propagation and attenuation of the Rayleigh and Love waves in a scattering and absorption medium.

CONCLUSIONS AND RECOMMENDATIONS

To date, we have developed the energy transfer theory for seismic surface wave propagation in a random medium. Using Fourier transform method we have solved these surface wave's energy transfer problems. Our solutions for both the Rayleigh wave case and the Rayleigh-Love wave case have an elegant form: the energy of Rayleigh or Love wave can be decomposed into three factors, namely, the depth-dependence factor determined by the fundamental normal mode, the source factor determined by seismic source parameters, and the horizontal propagation factor determined by the horizontal distance and the absorption and scattering coefficients of the random medium. These solutions can be applied to interpret some observed seismic coda wave that is believed due to the surface waves such as those for quarry blasts and shallow earthquakes. We are now working on this problem.

By neglecting the surface waves, Wu (1985) and Zeng et al. (1991) developed the energy transfer theory for seismic body wave. In this study we set up the energy transfer theory for seismic surface waves by neglecting the body waves. In some cases, both the body waves and surface waves have significant contributions, we therefore need to consider the energy transfer process for both body waves and surface waves simultaneously. We will work on this problem in the future.

REFERENCES

Aki, K. and P. G. Richards (1980). *Quantitative Seismology: Theory and Methods*, W. H. Freeman, San Francisco.

Su, F. , K. Aki, and N. N. Biswas (1991). Discriminating quarry blasts from earthquakes using coda waves, *Bull. Seism. Soc. Am.*, **81**, 161-178.

Wu, R. S. (1985). Multiple scattering and energy transfer of seismic waves--seperation of scattering effect from intrinsic attenuation, I. Theoretical modeling, *Geophys. J. R. Astr. Soc.*, **82**, 57-80.

Zeng, Y. H., F. Su, and K. Aki (1991). Scattering wave energy propagation in a random isotropic scattering medium, 1. Theory, *J. Geophys. Res.*, **96**, 607-620.

Scattering of Broadband Regional Waves from Sinusoidal Layer Interfaces

Robert H. Clouser
Charles A. Langston
Department of Geosciences
Pennsylvania State University
University Park, PA 16802

Contract F29601-91-K-DB12

Objective

The propagation of regional seismic phases is influenced by gross aspects of lithospheric structure, such as layer interfaces and average layer velocities, as well as velocity heterogeneity along the path. Velocity heterogeneity serves to scatter the wavefield giving rise to apparent phase attenuation and excitation of significant coda waves. Our objective in this research is to investigate the role of interface irregularities in the formation of coda and its effect in scattering regional seismic phases. We approach this problem using the T-matrix formalism to construct solutions to the wave equation for ideal crustal models consisting of a layer over halfspace. The free surface and Moho in these models are allowed to take on sinusoidal topography. Line source solutions are computed to investigate the nature of scattering in the waveguide and outside the waveguide within the mantle halfspace. Assumed topography simulates topography found in the Basin and Range province of the western U.S. These models are evaluated to determine whether interface irregularity may be a major factor in the propagation of various regional phases.

Research Accomplished

SH and isotropic line source problems have been formulated and solved using the T-matrix method (Clouser, 1993). Figure 1 shows the geometry of the source and structure considered. A line source is situated within a layer over halfspace structure where the free surface and, possibly, the Moho are allowed to have topography with wavelength "L" and amplitude "b". Topography is assumed to be sinusoidal. Theory and numerical methods are developed in Clouser (1993) and are too extensive to be summarized here. A final report to the sponsor is currently being prepared and will be available.

The first problem considered is a SH line source imbedded in the crustal layer. Both the free surface and Moho may have the same topography. Figure 2 shows synthetic seismograms for a distance of 500 km and a source depth of 15 km. Only the free surface has topography with wavelength 43 km. Topographic amplitude is given by b which changes from 0 to 0.75 km. The synthetics are dominated by small Sn phases and a large amplitude wavetrain of crustal multiples which can be considered to be the Lg wavetrain. Surprisingly, the effect of scattering from the free surface is to not create coda in the regional wavetrain. Progressive multiples are scattered and lose energy as topographic amplitude increases. Thus, there is an apparent coda attenuation where the wavetrain has progressively larger amplitude decays with time. Figure 3 demonstrates that this energy scatters out of the crustal waveguide into teleseismic S waves. The effect of free surface and Moho topography on Sn is shown in Figure 4. Higher order Sn multiples are somewhat affected by free surface irregularity but Moho topography has little effect on any Sn phase.

Results for the isotropic line source are shown in the remainder of the figures. Only the free surface is allowed to have topography. Figure 5 displays broad band regional waveforms for a layer over halfspace model with no topography for reference. Pn, a series of P multiples and then the fundamental mode Rg wave comprises the seismograms. With topography, however, significant energy gets efficiently scattered into the Rg wave from the crustal multiples. This produces a nearly monochromatic wavetrain with time that has the appearance of a well dispersed Rayleigh wavetrain. Figure 7 shows the variation of these scattered waves with topography amplitude, b. Figure 8 shows that only a narrow frequency band is affected in the seismogram spectra. At closer ranges scattering seems to be roughly proportional to topographic amplitude. At larger ranges, scattering is saturated for the amplitudes considered. Figure 9 shows the effect of changing source depth. Fundamental mode Rg decreases as expected as source depth increases. Scattered Rg remains roughly constant. This effect is also topography wavelength dependent as shown in Figure 10. Scattered waves are higher frequency for shorter wavelength topography, which may be intuitively expected.

Conclusions and Recommendations

The SH line source results show that topographic scattering serves to attenuate the Lg wavetrain by scattering energy out of higher order multiples in the crust into teleseismic waves. This serves to cause a coda attenuation but with little effect on maximum amplitudes. Sn is not affected by scattering from a sinusoidal Moho boundary.

The P-SV system behaves differently as shown by the isotropic line source results. Energy from the higher order multiples and conversions gets pumped into a long duration Rg wavetrain. Conversion of P and SV waves in Rg is an efficient process in the regional wavetrain.

Topographic scattering in 3D is undoubtedly more complicated resulting in coupling between the SH and P-SV systems. Thus, there will be competition between these two mechanisms in scattering energy into and out of the regional wavetrain.

References

Clouser, R.H. (1993). *Scattering of seismic waves by irregular interfaces*, Ph.D. Thesis, The Pennsylvania State University, University Park, PA 16802.

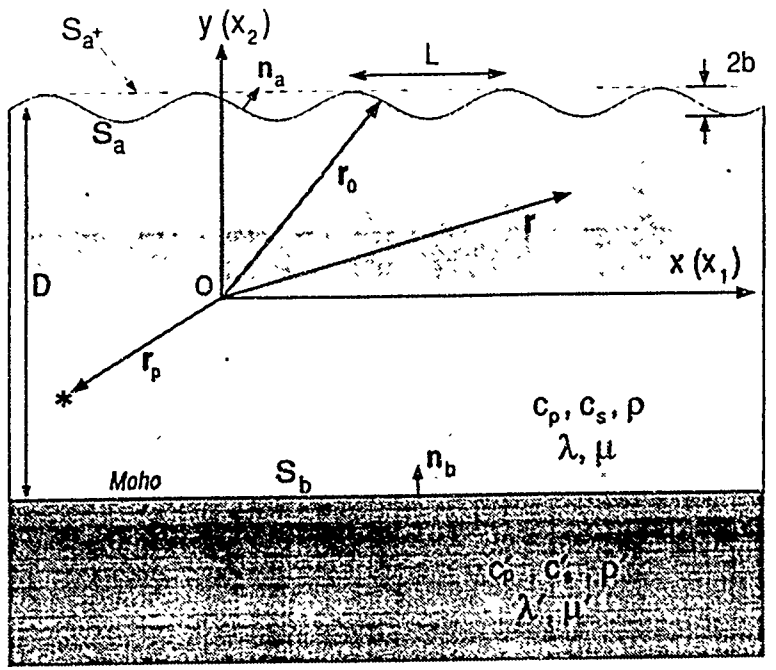

Figure 1. Geometry and parameters for the line source problem. Both the Moho and free surface are allowed to have a sinusoidal undulation with the same amplitude and period for the SH line source problem. Only a sinusoidal free surface is considered for the P-SV problem.

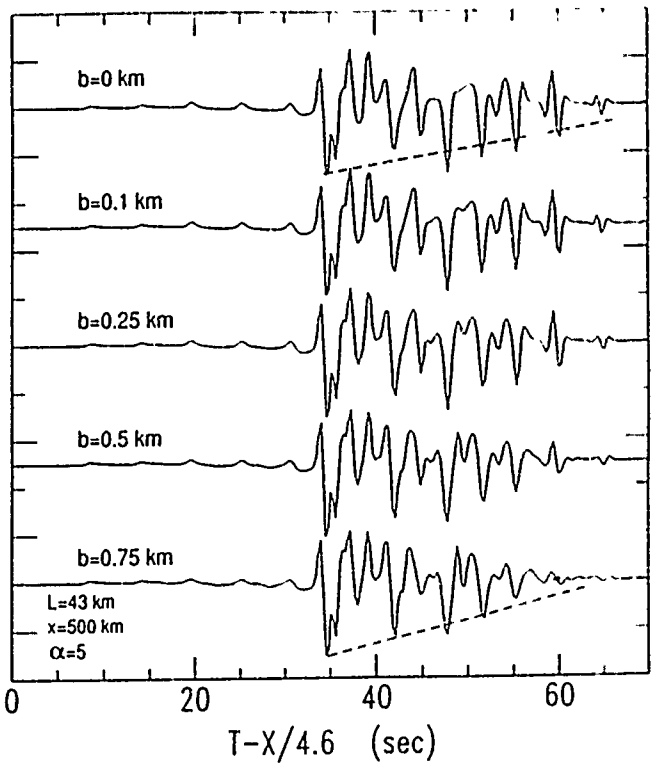

Figure 2. Comparison of the temporal decay rates of the Lg wavetrain as the surface roughness increases. Receiver distance is 500 km and L=43 km. The time function is a Gaussian derivative, with peak response at 0.5 Hz. Note how the wavetrain decays more rapidly as "b" increases.

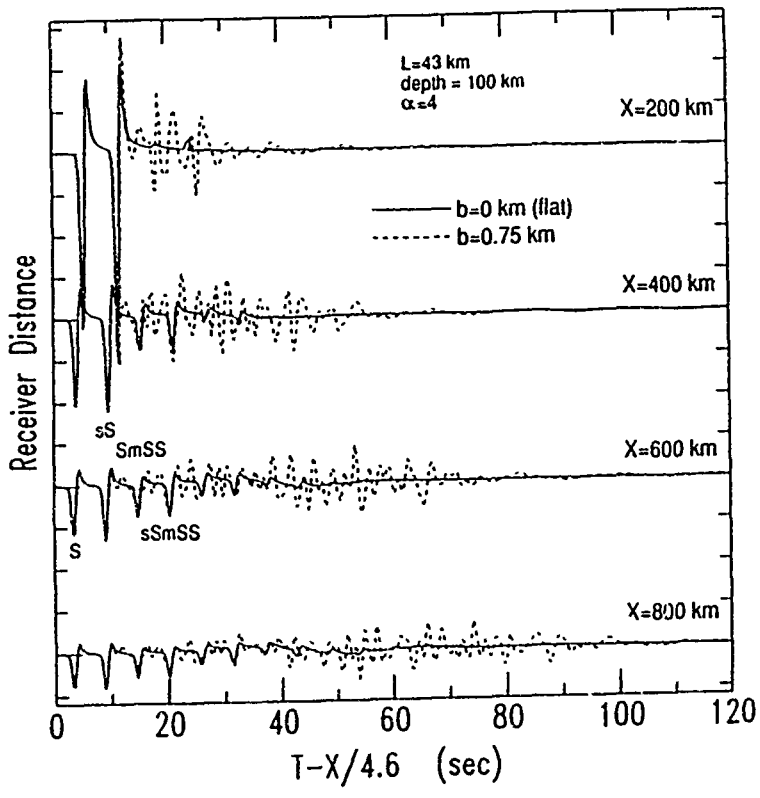

Figure 3. Displacement field in the halfspace 100 km below the surface at various distances. The Gaussian derivative time function has a peak response at 0.45 Hz. Notice the additional scattered energy in the halfspace when the free surface is rough. The amplitude scales are the same for all traces.

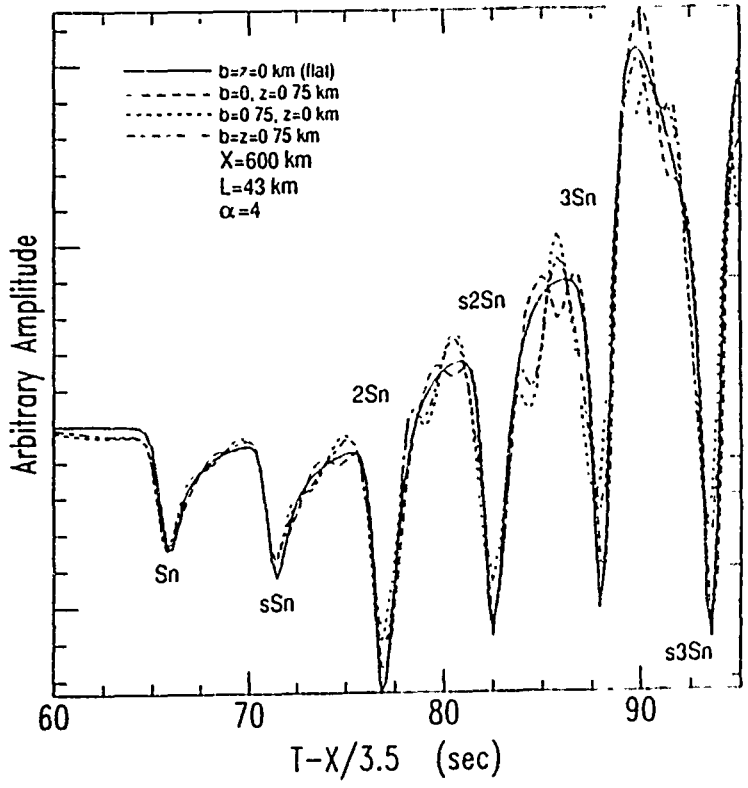

Figure 4. Sn window of the synthetics for the four possible combinations of flat and sinusoidal interfaces. Receiver distance is 600 km, and the Gaussian derivative time function peaks at 0.45 Hz. Successive Sn-type phases have SmS bounces in their raypaths, so 2Sn=SmSSn, and so forth. Models with a sinusoidal free surface are much better at diminishing the amplitudes of the crustal multiples producing the Sn phases; note the approximately 30% amplitude reduction in 3Sn for these models. Also, notice that the sinusoidal Moho does not reduce the amplitude of Sn.

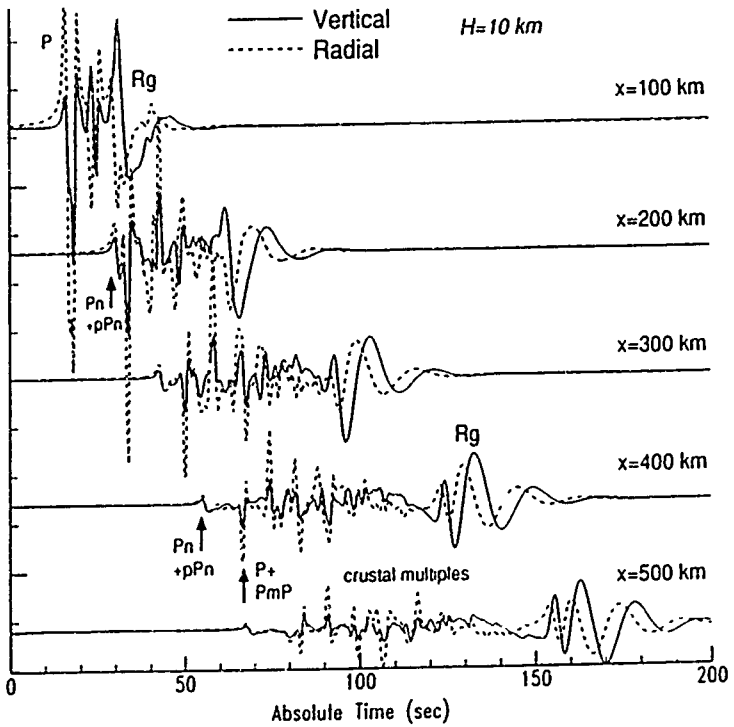

Figure 5. Vertical and radial component record section for a flat free surface model, isotropic source depth at 10 km. Peak response of the time function is 0.32 Hz. Note the Pn arrival (and its depth phase pPn), direct P, PmP and Rg. Arrivals after PmP are crustal P-S and S-P converted reverberations.

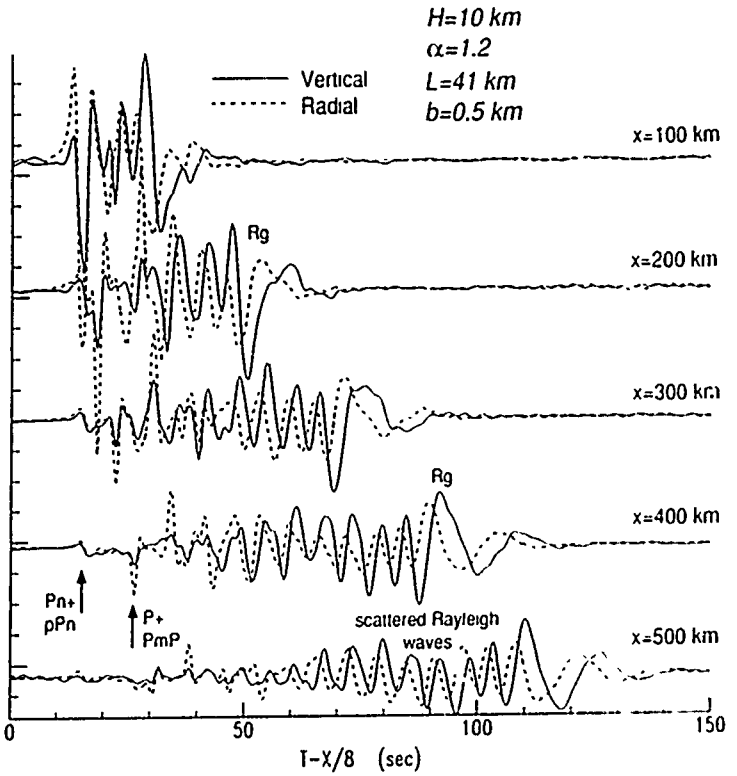

Figure 6. Vertical and radial component record section, plotted in reduced time, for a model with L=41 km and b=0.5 km and a source depth of 10 km. Note the large-amplitude, monochromatic scattered Rayleigh waves (period of about 8 sec). Compare to Figure 5.

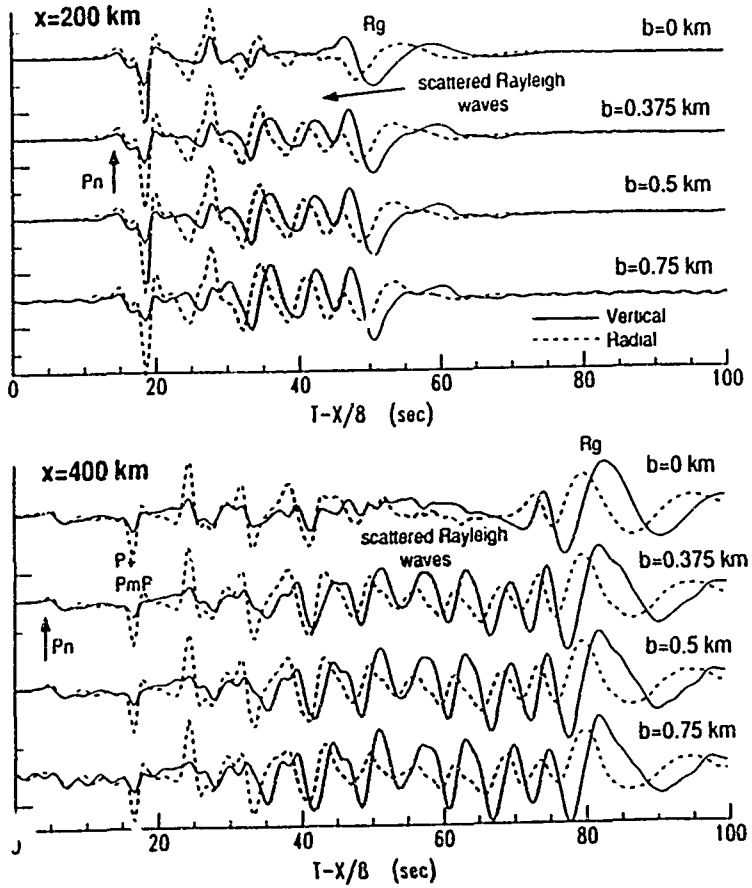

Figure 7. Vertical and redial synthetics for two distances (200 km and 400 km) showing the effect of increasing b for L=41 km, H=10 km. The scattered Rayleigh waves are shaded. These waves have retrograde elliptical particle motion like the source-generated Rg-wave. Note that the scattered wave amplitudes are not highly sensitive to roughness.

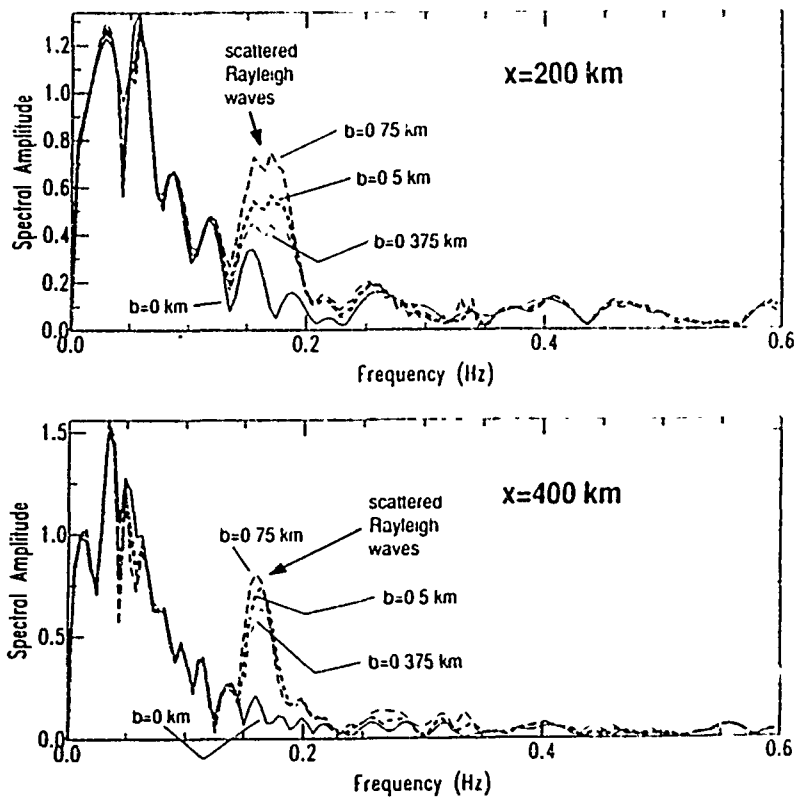

Figure 8. Vertical component impulse response amplitude spectra for distances of 200 and 400 km, for different b values, L=41 km, H=10 km Note the decreased sensitivity to roughness at larger distances At X=200 km, the scattered Rayleigh wave anomaly amplitude varies roughly linearly with b.

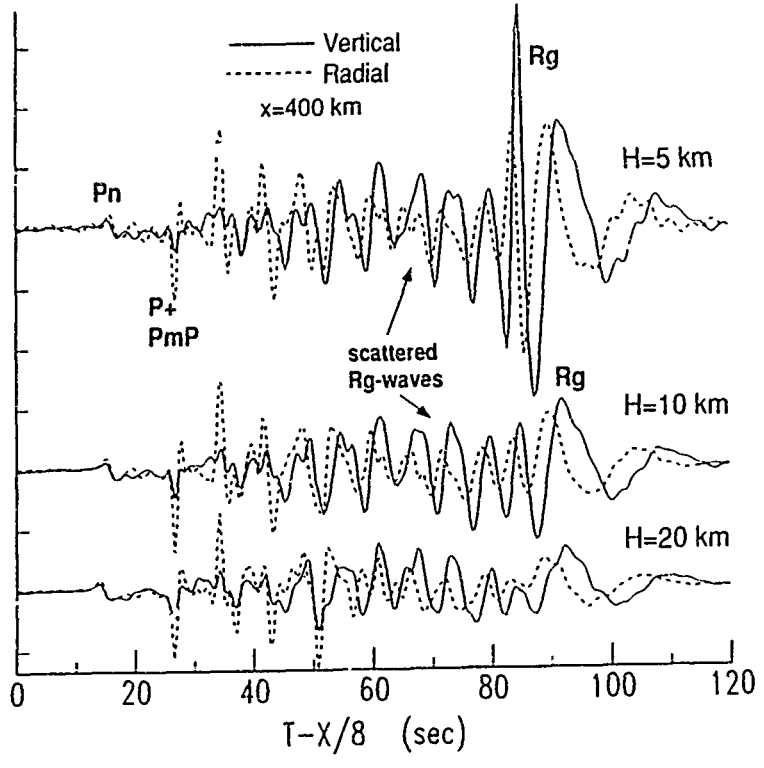

Figure 9. Vertical and radial component synthetics for different source depths H within the crust. Receiver distance is 400 km, and free surface parameters are L=41 km, b=0.5 km. The source-generated Rg wave amplitude decreases with increasing source depth, but the scattered Rg wave remains fairly constant.

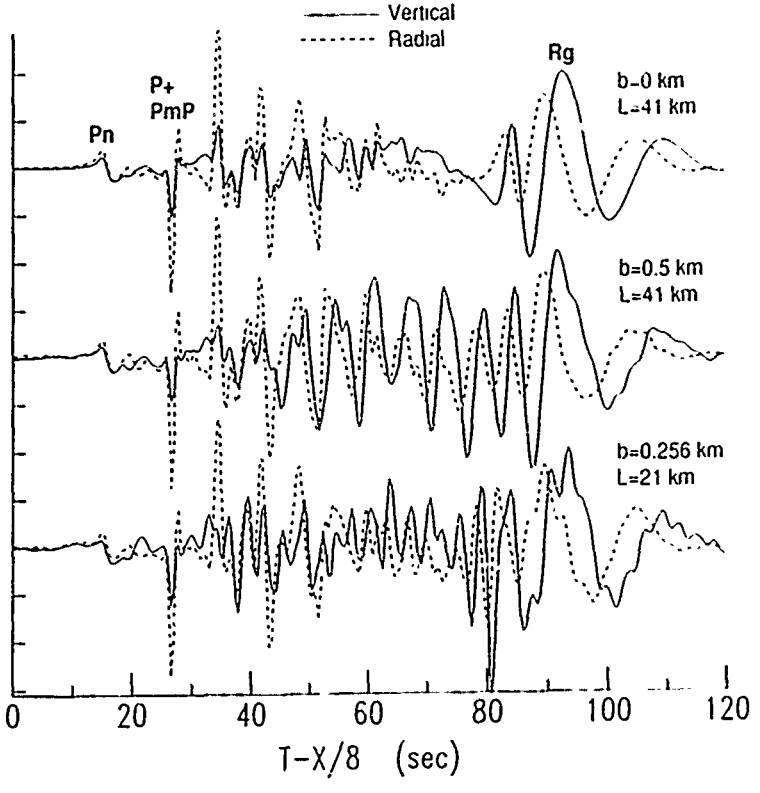

Figure 10. Vertical and radial component synthetics illustrating the effect of changing L on the scattered Rg waves. Upper traces are for a flat free surface, the lower two are for fixed b/L=0.0122. Receiver distance is 400 km, source depth is 10 km. Note the shorter period of the scattered Rg waves for L=21 km (at about 3-4 seconds) than for L=41 km (at about 8 seconds).

THE GIAT MINI-ARRAY IN CENTRAL FRANCE: PRELIMINARY DETECTION AND PHASE IDENTIFICATION RESULTS

René Crusem and Jean-Pierre Massot
Laboratoire de Géophysique
BP 12
91680 Bruyères-le-Châtel
FRANCE

Contract No:
90-0356

OBJECTIVE

The French LDG (Laboratoire de Géophysique) has been installing and operating an experimental mini-array in Central France (GIAT) for seismic Verification and Monitoring purposes, since March, 1993. The objective of the work presented here was to adapt and use the software developed at Norsar, in order to assess the detection capabilities of the GIAT array, both for regional and teleseismic events.

RESEARCH ACCOMPLISHED

Data acquisition and processing:

The French GIAT mini-array presently consists of 9 vertical seismometers, and one 3-components station. It's size is about 3 kilometres (figure 1). The data are digitised at a rate of 50 samples a second, and are stored locally on a personal computer in files containing each about 17 mn of data. Once a file is completed, it is sent to the distant processing centre via phone, where it is automatically written to a Norsar type diskloop. The detection software recognises the arrival of new data, computes a set of filtered beams, and then uses a classical STA/LTA detector on each beam.

Detection configuration:

The results reported here were obtained over a 57 day period, between May 5 and June 30, 1993. During this period, a set of 83 beams was deployed, at different velocities (for regional phases) and for many azimuths. These beams were also attached to different sub-arrays, which were empirically and qualitatively determined according to the frequency content and correlation characteristics of the different wave types and the background noise (Kvaerna,

1989). STA/LTA thresholds were between 4.4 and 7.1 for coherent beams, and between 3.6 and 4.4 for incoherent beams. No horizontal beams could be used, since only one 3 components station was available.

Detection results:

During the period considered, an average of 161 detections was observed each day. Deviations from this mean can be very high (figure 2), due to transient noise occurring on one or more stations (it's origin can be cultural, meteorological, traffic, etc.). The smallest numbers of detections are sometimes observed on Saturdays or Sundays, but this is not always true.

As a reference for estimating detection capabilities, we used the LDG regional and teleseismic bulletins, which are obtained from the whole LDG network (about 40 stations covering France), and which are available and distributed once a week.

Only events for which both a location and a magnitude were reported in these bulletins were used for the comparisons. Thus, 184 regional events and 186 teleseismic events were selected, i.e. an average of about 3 regional events and 3 teleseismic events every day.

An event was declared to be detected by the mini-array if at least one phase was detected by at least one beam. Note that this does NOT mean that such an event could be located or identified automatically by the mini-array.

Results indicate that less than 5 % of all detections can be associated with natural seismic events. Another 5 to 10 % can be attributed to artificial sources such as quarry or rock blasts. In fact, from Mondays to Fridays, the mini-array detected an average of 5 quarry-blasts per day during working hours. Thus, nearly 90 % of all detections were never attributed to a known seismic source.

Detectability of regional events:

Figures 3 and 4 display the preliminary results obtained for regional events. It can be concluded from these figures that the 75% confidence threshold for detection is about Ml = 3.4 (Ml is the LDG local magnitude).

This value is about 0.7 magnitude units higher than the value obtained for the whole LDG network, which can be estimated as Ml = 2.7 (LDG local magnitude), for distances up to 6 to 8 degrees.

It is instructive to compare this threshold with those reported for the fennoscandian arrays (Mykkeltveit et al. 1990; Uski, 1990), which are close to Ml = 2.3 to 2.7 (where Ml is the local magnitude computed for Norway) at the 90% confidence level.

Thus, the difference between the detection capabilities at both sites is presently close to one unit of local magnitude. This is apparently due to the different calibrations used for these local magnitudes, which should be further investigated in the future. Also, there is about a factor two difference in Lg wave attenuation coefficients between Norway and France (Alsaker et al. 1991; Plantet et al. 1991).

Detectability for teleseismic events:

Figures 5 and 6 display the results obtained for the detectability of teleseismic events. The 75% confidence threshold can presently be estimated at mb = 4.9, which is close to the whole LDG network threshold, though the LDG bulletin can probably no longer be used as a reference in the teleseismic case. Anyway, only one event with a magnitude above 5.4 was missed.

These results are close to those reported for GERESS (Gestermann et al. 1991).

Regional phase identification:

Regional phases observed in central France are mainly Pn, Pg, Sg and Lg, while Sn is rarely detected. For Fennoscandian arrays, Norsar uses both phase velocity (obtained from the f-k analysis) and polarisation results in order to identify regional phases. However, this is more difficult for GIAT, since only one (very noisy) 3 components station is available. So, presently, we only use velocities for identifying regional phases.

An analysis of 38 such phases, carefully checked by the analyst, led to the following preliminary rules (velocities are given in km/sec):

if VEL < 3.1 then phase is Noise
else: if VEL < 5.8 then phase is S
if VEL > 3.1 and VEL < 4.2 then phase is Lg
if VEL > 4.2 and VEL < 5.8 then phase is Sn
else: if VEL > 5.8 then phase is P
if VEL > 5.8 and VEL < 7.4 then phase is Pg
if VEL > 7.4 and VEL < 10.5 then phase is Pn
else: if VEL > 10.5 then phase is teleseismic

The main ambiguity which may appear is for Sg-Lg versus Sn discrimination, for velocities between 4.2 and 5.2. More experience is now needed before evaluating the performances of these phase identification rules.

CONCLUSIONS AND RECOMMENDATIONS

Despite the fact that the GIAT mini-array consists of only 10 stations, detection results for both regional and teleseismic events are encouraging: the 75 % confidence threshold is ML=3.4 for regional and mb=4.9 for teleseismic events.

Such figures could only be obtained due to the high false detection rate (nearly 90%) that was allowed. It is expected that these false detections will be eliminated during the phase association procedure included in the RONAPP software, and that no or little spurious events will be found in the final automatic bulletin.

We are presently trying to further reduce the STA/LTA thresholds, to ameliorate the spike elimination algorithm, and to increase the total number of beams. We plan to run with an average of perhaps 400 detections a day, among

which less than 5% would be associated with real seismic events. We hope that this will further reduce the detection thresholds by about 0.2 to 0.3 magnitude units. However, it is not yet sure weather regional events with such low magnitudes (say 3.1 local LDG magnitude) could be automatically located, since for that purpose at least two phases must be detected.

A longer period of observation, and comparisons with other reference bulletins (for teleseismic events) should confirm these results.

Of course, adding more stations, especially 3-component stations, would also improve the results.

The next step is now to investigate in more details the phase identification and location capabilities of the GIAT mini-array. This will be done using both the classical RONAPP algorithm provided by Norsar, and a novel approach for phase picking and classification based on coherency analysis and neural networks (Cansi et al., 1993).

Finally, before distributing automatic bulletins, it will be necessary to address the important issue of discriminating between quarry blasts and natural seismic events.

Acknowledgement

We want to acknowledge the NORSAR staff, especially Svein Mykkeltveit, Tormod Kvaerna and Jan Fyen, for their hospitality and support during the stay of one of us (R.C.) in October-November 1992, and for kindly providing the NORSAR software package.

References

Kvaerna, Tormod (1989) - On exploitation of small-aperture Noress type arrays for enhanced P-wave detectability, Bull. Seismol. Soc. Am., 79, 888-900.

Mykkeltveit, S., F. Ringdal, T. Kvaerna, and R. Alewine (1990) - Application of regional arrays in seismic verification research, Bull. Seismol. Soc. Am., 80, 1777-1800.

Uski, Marja (1990) - Event detection and location performance of the Finessa array in Finland, Bull. Seismol. Soc. Am., 80, 1818-1832.

Alsaker,A., L.B. Kvamme, R.A. Hansen, A. Dahle and H. Bungum (1991) - The ML scale in Norway, Bull. Seismol. Soc. Am., 81, 379-398.

Plantet, J.L., Y. Cansi, and M. Campillo (1991) - Regional seismic wave attenuation and evaluation of seismic sources; in Recent Advances in Earthquake Engineering and Structural Dynamics, Ouest Editions, France, ISBN 2-908261-22-7.

Gestermann, N., H.-P. Harjes, M. Jost, J. Schweitzer, and J. Würster - Analysis of Geress-recordings during GSETT-2, 13th annual PL/DARPA seismic research symposium, 204-210, PL-TR-91-2208, ADA241325.

Cansi, Y., and A. Bottero (1993) - Automatic processing of seismic events recorded on a mini-array (signal analysis combined with neural networks); 15th PL/ARPA seismic research symposium, this volume.

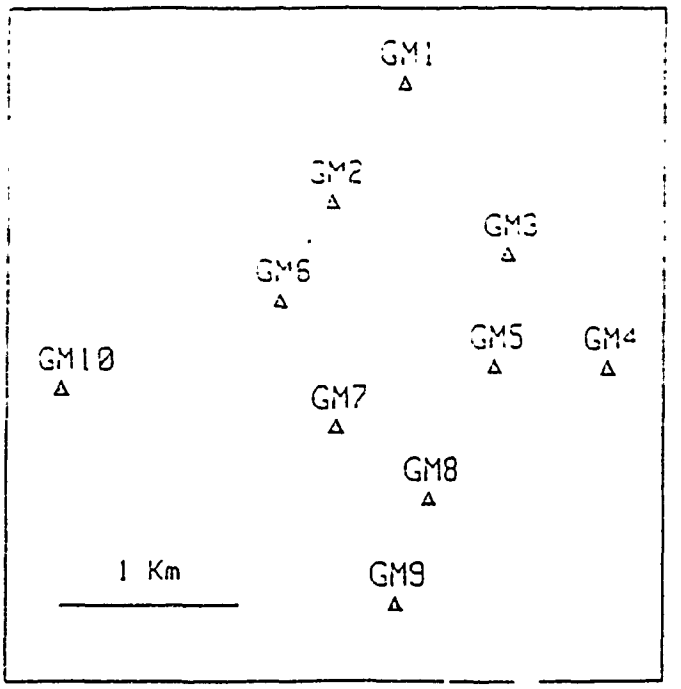

FIGURE 1. Location and geometry of the French GIAT mini-array in central France. The array consists of 9 vertical seismometers, and one "central" 3-components station (GM5). GM5 is located at 45°44 N and 2°01 E.

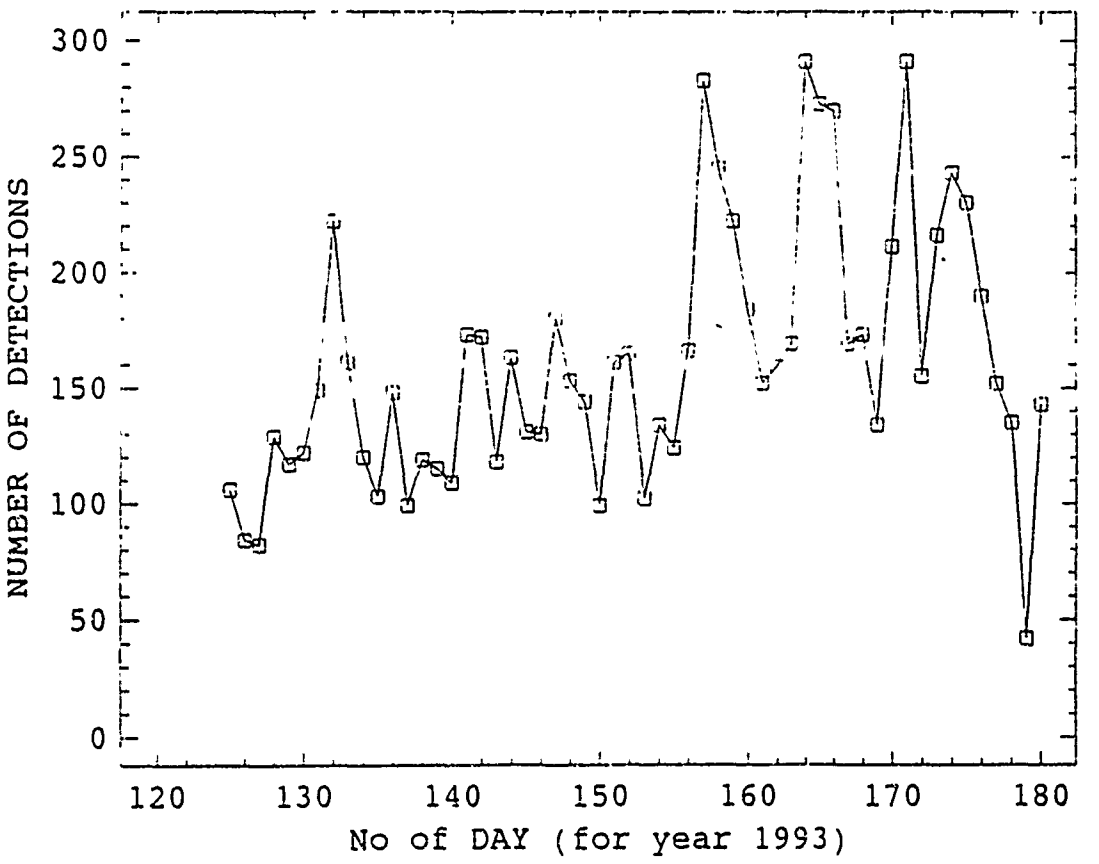

FIGURE 2. Number of detections per day at GIAT, from May 5 to June 30, 1993, deploying a set of 83 beams. Mean is 161. Deviations from the mean by more than a factor 2 are not rare. The effect of weekends does not appear clearly.

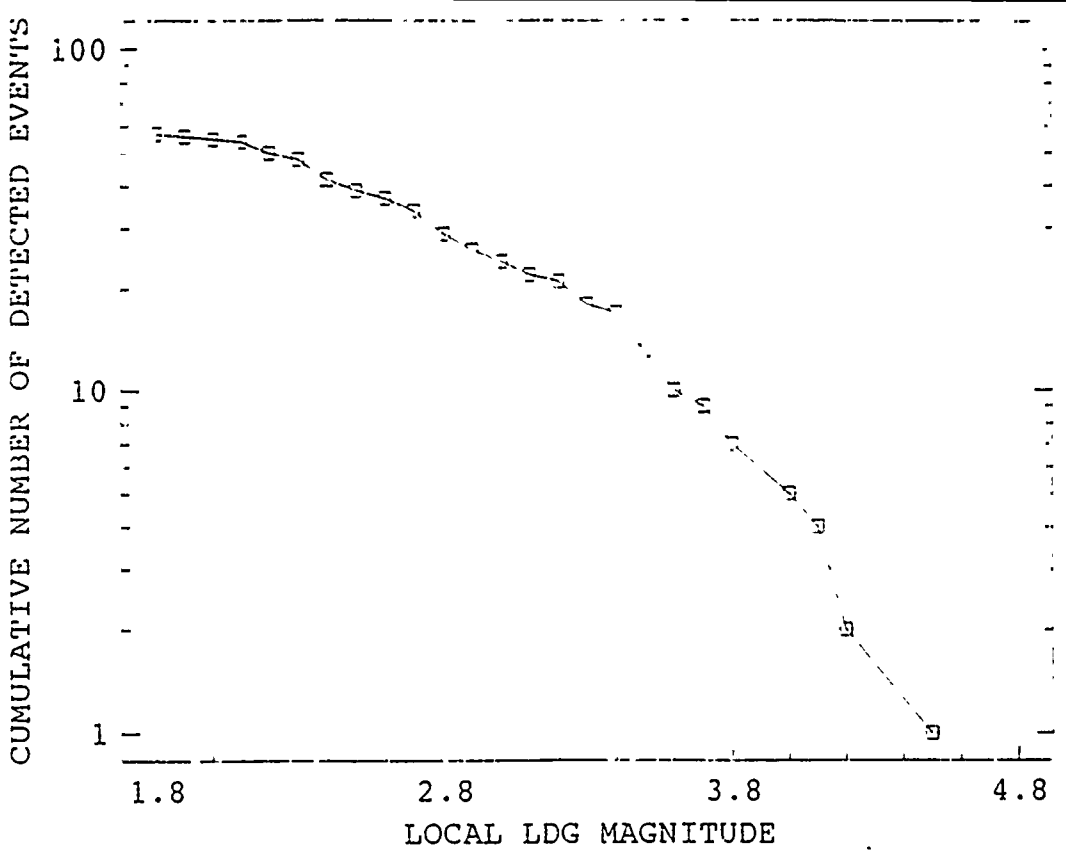

FIGURE 3. Regional event detectability at GIAT. The Y-axis displays the cumulated number of detected events, whose local LDG magnitude is higher than the value specified on the X-axis. Reference is the LDG regional bulletin.

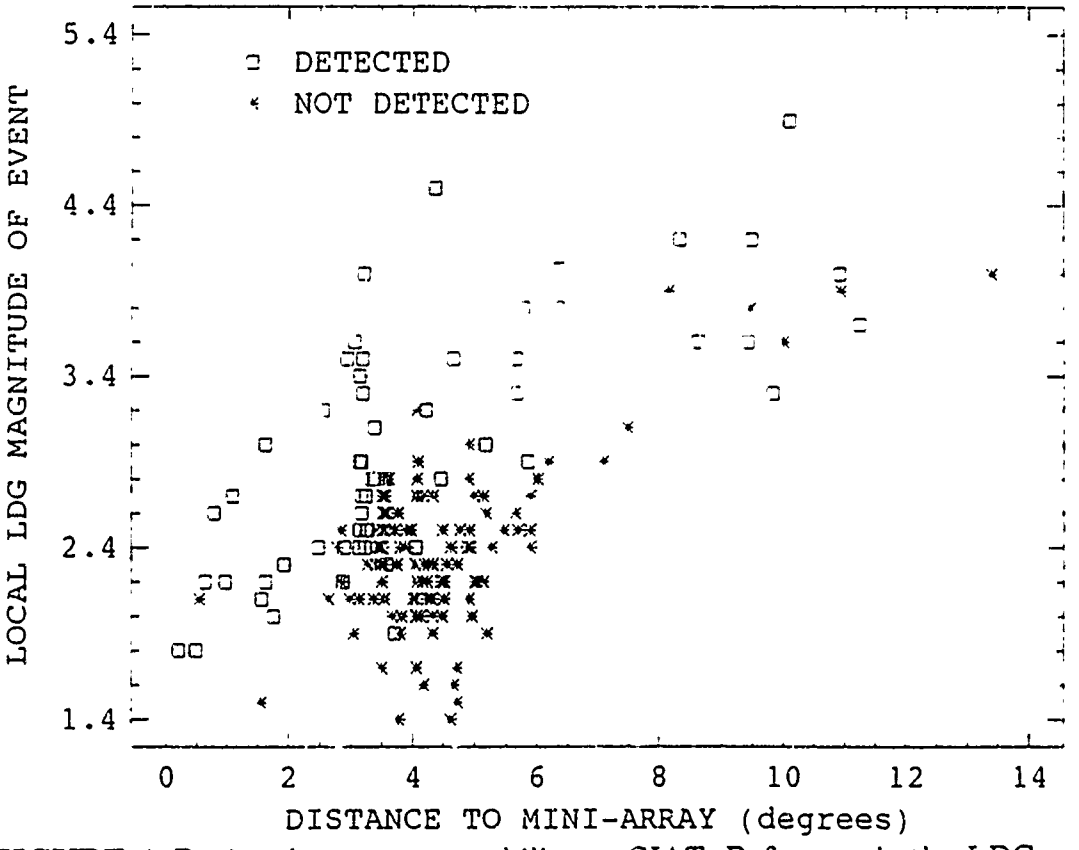

FIGURE 4. Regional event detectability at GIAT. Reference is the LDG regional bulletin. The 75% confidence threshold for detection is 3.4. Up to a distance of 8 degrees, no event with local magnitude greater than 3.2 was missed.

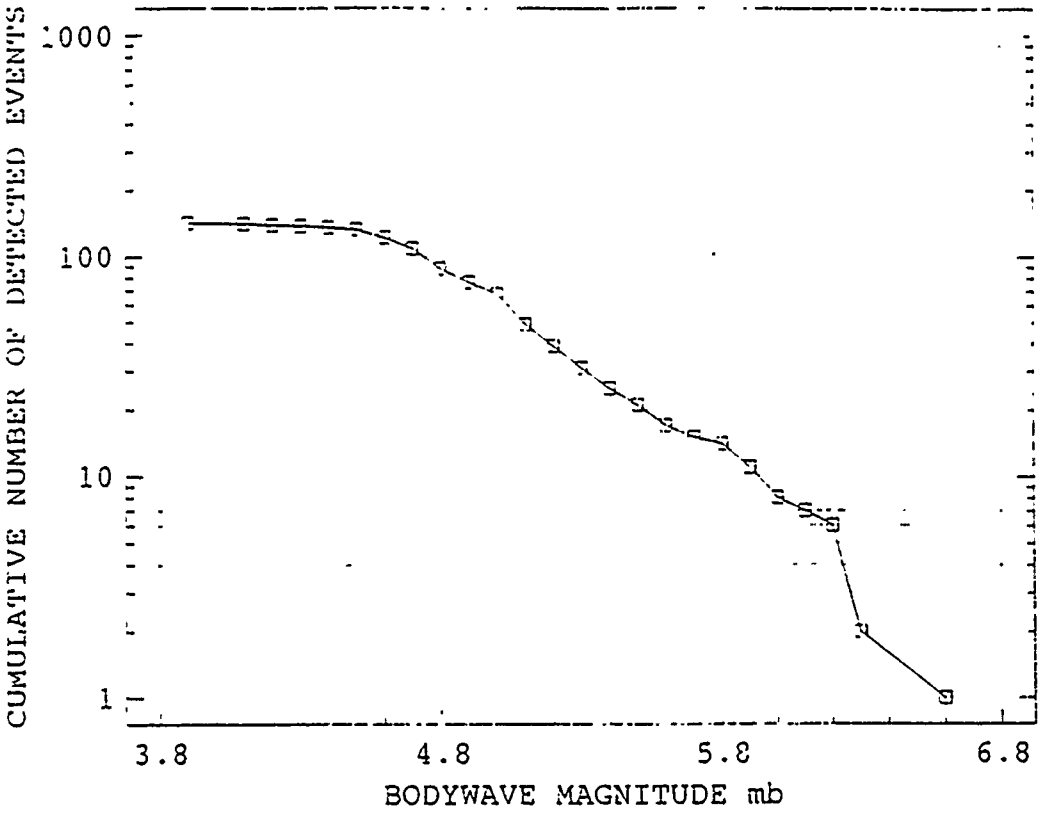

FIGURE 5. Teleseismic event detectability at GIAT. The Y-axis displays the cumulated number of detected events, whose body wave magnitude mb is higher than the value specified on the X-axis. Reference is the LDG teleseismic bulletin. Theoretical relation is linear with a slope equal to -1. Deviation from linearity is observed for an mb of about 4.8 and points out the detection threshold.

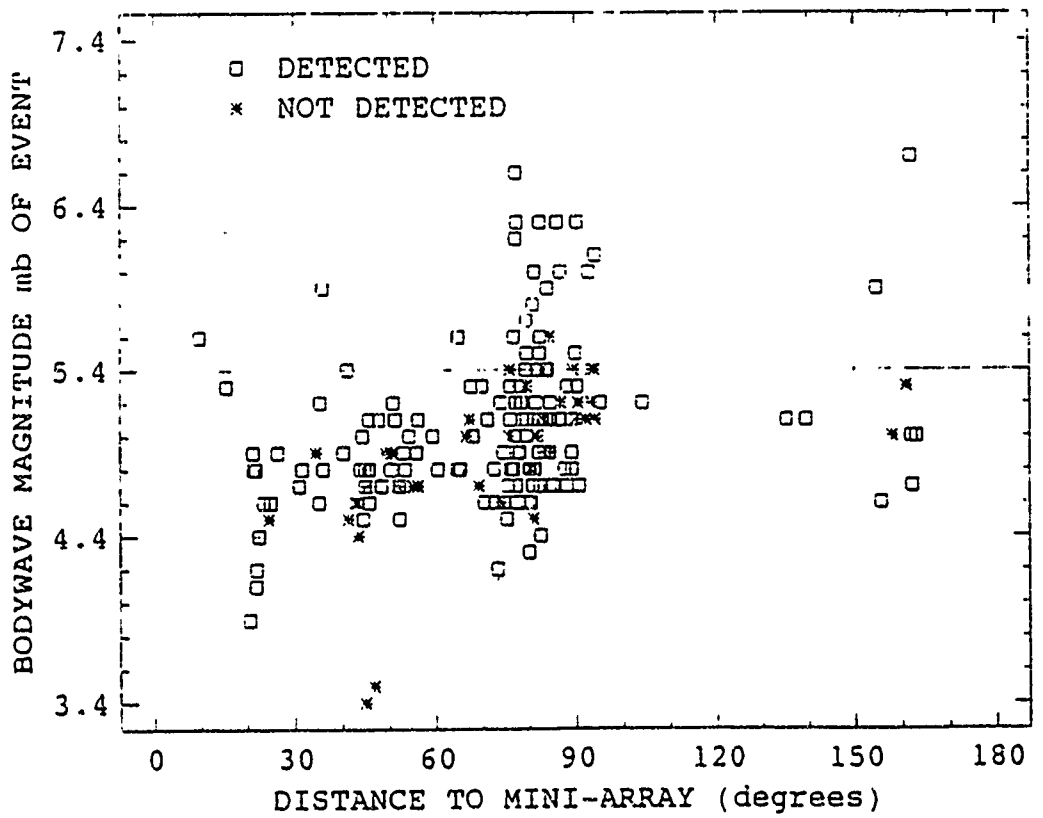

FIGURE 6. Teleseismic event detectability at GIAT. Reference is the LDG teleseismic bulletin. The 75% confidence threshold for detection is 4.9. Up to a distance of 60 degrees, no event with mb greater than 4.9 was missed.

Source Parameters From Near Regional Earthquake Data Recorded at Garm, Tadjikistan

Christine Ecker
Charles A. Langston
Department of Geosciences
Pennsylvania State University
University Park, PA 16802

Contract F29601-91-K-DB12
and F49620-93-1-0207

Objective

Discrimination of small seismic events in an area of sparse station coverage requires knowledge of the regional wave propagation so that source parameters may be usefully estimated from the waveform data. Event location, including source depth, and focal mechanism may be estimated from single station data with synthetic seismogram techniques provided wave propagation conforms to fairly simple plane-layered structure models. In this research we explore a regional data set of broad-band seismograms recorded at the IRIS station at Garm, Tadjikistan. Our objectives include first using robust properties of the data waveforms to infer major wave propagation effects in the crust and mantle of central Asia. Secondly, we use arrival times and relative amplitudes of observed phases to infer event location and focal mechanism. Additional constraint on the nature of the crust and mantle under Garm was investigated using the receiver function technique.

Research Accomplished

The Garm area of southern Tadjikistan (Figure 1) has been the locus of geophysical studies in the Soviet Union. Structure is known primarily from Soviet Deep Seismic Sounding surveys (DSS) (Belyaevsky et al, 1973; Alekseev et al, 1973; Khamrabayev, 1986; Alekseev et al, 1988) which indicate crustal thickness of approximately 70 km. Aside from an anomalously thickened crust, crustal P-wave velocities are typical ranging from 5.3 km/s near the surface to about 6.9 km/s above the Moho. Several midcrust reflectors were also identified in these surveys. These important parameters of the crust in the region are expected to play a major role in defining the character of wave propagation from regional events around Garm.

In an attempt to verify structure from these past studies, we performed a study of teleseismic receiver functions for the Garm station. Four teleseismic events with good signal-to-noise ratios were found that were usable. Other events were found in the IRIS data archives but were of poor quality because of apparent polarity reversals on horizontal components or mis-identified channels. Receiver functions were computed using the standard technique (Langston, 1979) and are shown in Figure 2. The radial receiver functions show very large secondary phases for events from the northeast. An event from the southeast shows few secondary phases. Tangential motions are also large and complex for all backazimuths. Such data suggest immediately that structure under Garm is heavily influenced by large velocity contrasts, lateral heterogeneity and possible topographic scattering of teleseismic body waves.

Topography is extreme in the area, so a study of topographic scattering was performed to test the assertion that the large secondary phase seen in the northeast azimuth data is due to P-to-Rg conversion. Particle motions for this phase seen in the raw data from an impulsive event show elliptical particle motions suggestive of Rayleigh

wave propagation. However, the ellipticity is dominated by horizontal motions which is more suggestive of complex P-to-SV conversion. The T-matix method was used to compute the effect of plane wave scattering from a simple 2D shape that was an approximation to the immediate topography around Garm. Resulting P-to-Rg conversions were not large enough to explain the data nor the near-horizontal ellipticity. Thus, these large secondary phases have a complex genesis through P-wave interaction with extreme lateral heterogeneity.

Figure 3 is a warning to those who believe in 1D inversion results based on good waveform fits. 1D structure was found using the technique of Ammon et al (1990) on the receiver function of the 7/05/91 event. The synthetic fit is remarkably good but the resulting 1D velocity model shows geophysically absurd velocity constrasts and magnitudes throughout the crust and upper mantle. This result, combined with the obvious azimuthal changes seen in the data of Figure 2 suggest the effects of lateral heterogeneity and wave scattering from 3D structure in the lithosphere around Garm. We were unable to verify structures found in DSS studies or determine much information important to regional wave propagation.

Although our experience with near-vertical wave propagation near Garm was inconclusive, the regional waveform data from three intermediate depth earthquakes in the Hindu Kush indicates that much can be learned about first-order wave propagation effects from near-horizontally propagating waves. Figure 4 shows the PDE locations of the three events studied here. Body wave magnitudes ranged from 4.7 to 5.1. We discuss results from the largest event here. Although intermediate depth events have little use in the discrimination problem because of their great depth, the apparent simplicity of the waveform data, compared to shallow crustal events, was thought to offer the greatest chance for understanding the nuances of regional wave propagation in an unknown area.

The goal of studying these events at a single station was to use major phases to locate and then to determine focal mechanisms. If these relatively simple data can be used successfully, then it may be possible to do similar studies with shallow events. Figure 5 shows rotated raw and filtered waveform data from the magnitude 5.1 4/16/91 earthquake. Because of subcrustal depth, surface waves are not obvious in the data and the primary body waves dominate the waveforms. P and S are clear phases and the P wave was used to determine event backazimuth using horizontal particle motion.

The most interesting aspect of these data is the large arrival before direct SV denoted by SsPxp on Figure 5. Clearly, particle motion is of the P type and is quite large compared to direct SV. This phase has been seen in other regional data from intermediate depth earthquakes (Langston and Clouser, 1992) and is due to conversion of direct SV at the free surface to P which then reflects from a crustal interface. The "x" denotes the unknown crustal reflector depth. Because the amplitude of this phase is sensitive to whether the P reflection is pre- or post-critical, SsPxp can be used as another phase in earthquake location. This event was located by assuming the DSS crustal structure and computing S-P and S-SsPxp arrival times for various source distances and depths. Figure 6a shows the travel time curves for a source depth of 110 km, the final inferred depth. Synthetic seismograms (Figure 8) show that the only major phase of this type is SsPmp, the Moho reflection. Reflections from midcrust have very small amplitudes since the ray parameter is usually precritical for crustal velocities. The moveout of SsPmp with source depth and distance allows its use in location. The precision of the location, assuming the DSS model and a ± 1 s time reading error for the phase picks, is 110 ± 5 km in depth and 320 ± 2 km in distance. Assuming only a 50 km thick crust changes the location by 10 km. Our location is within 16 km for depth and 24 km in distance from the PDE location. It is well known that PDE locations have typical errors of 50 km for small events in remote areas of sparse station coverage.

Relative amplitudes of S, P and SsPmp were then used to model the possible source mechanism through a grid search procedure. The result is shown in Figure 6b and is remarkably well constrained. Comparisons of synthetics and data waveforms are

shown in Figure 7. Synthetic seismograms were constructed using a robust wavenumber integration code for plane layered media for the entire wave field. Note that the synthetics are very simple and show little of character of the coda behind P and S. We found that the coda presented major problems with modeling individual phases particularly when the P or S phase was comparable in size to later arriving coda waves. We appeal to the standard model that most coda is set up by incident S and consists of backscattered S waves scattered from 3D heterogeneity in the regional lithosphere. If scattering is severe, then direct arrivals are degraded by superimposed coda waves. Degradation becomes a significant problem for ideal synthetic seismogram models when the direct waves on a particular ground motion component are small. Coda is presumably at a constant level for any component.

Conclusions and Recommendations

Teleseismic receiver function analysis of the IRIS station at Garm shows that near-vertical P-wave propagation is dominated by severe scattering effects of 3D geologic structure and, possibly, topography. The data show large secondary phases in radial components which vary azimuthally and large tangential motions. Previously determined DSS profile results could not be substantiated with the receiver function data. 1D inversion models were geophysically unreasonable even though waveform fits were quite good.

The SsPmp phase is a new regional phase which can be used in conjunction with S and P to locate intermediate depth events provided the crustal model is known. This new phase is large and can arrive before or after the direct S wave. Its large amplitude is due to both efficient S-to-P conversion at the free surface and post-critical P reflection from the Moho.

Three regional events recorded at the Garm station were modeled to determine location and mechanism. Results for two events were quite good but a third event was indeterminant because of small S arrivals compared to coda. S wave coda from heterogeneity degrades interpretations using synthetic seismograms and is a major limiting factor in waveform modeling.

References

Alekseev, A.S., A.V. Belonosova, I.A. Burnakov, G.V. Krasnopevtseva, N.N. Matreeva, G.L. Nersessov, N.I. Pavlenkov, V.G. Ramanov and V.Z. Ryaboy (1973). Seismic studies of low-velocity layers and horizontal inhomogeneities within the crust and upper mantle on the territory of the U.S.S.R., *Tectonophysics, 20,* 47-56.

Alekseev, A.S., A.V. Egorkin and N.I. Pavlenkova (1988). Shear waves in lithosphere studies on the territory of the U.S.S.R., *Tectonophysics, 154,* 227-239.

Ammon, C.J., G.E. Randall and G. Zandt (1990). On the nonuniqueness of receiver function inversion, *J. Geophys. Res., 95,* 15,303-15,313.

Belyaevsky, N.A., A.A. Borisov, V.V. Fedynsky, E.E. Fotiadi, S.I. Subbotin and I.S. Volvovsky (1973). Structure of the earth's crust on the territory of the U.S.S.R., *Tectonophysics, 20,* 35-45.

Khamrabayev, I.K. (1986). The deep-level structure of the lithosphere of the Pamirs and the Tien Shan, *Int. Geol. Rev., 28,* 1401-1416.

Langston, C.A. (1979). Structure under Mount Rainier, Washington, inferred from teleseismic body waves, *J. Geophys. Res., 84,* 2749-4762.

Langston, C.A., and R.H. Clouser (1992). SV-to-P conversions in regional intermediate depth and deep earthquake waveforms (Abstract). Presented at the 1992 meeting of the Seismological Society of America.

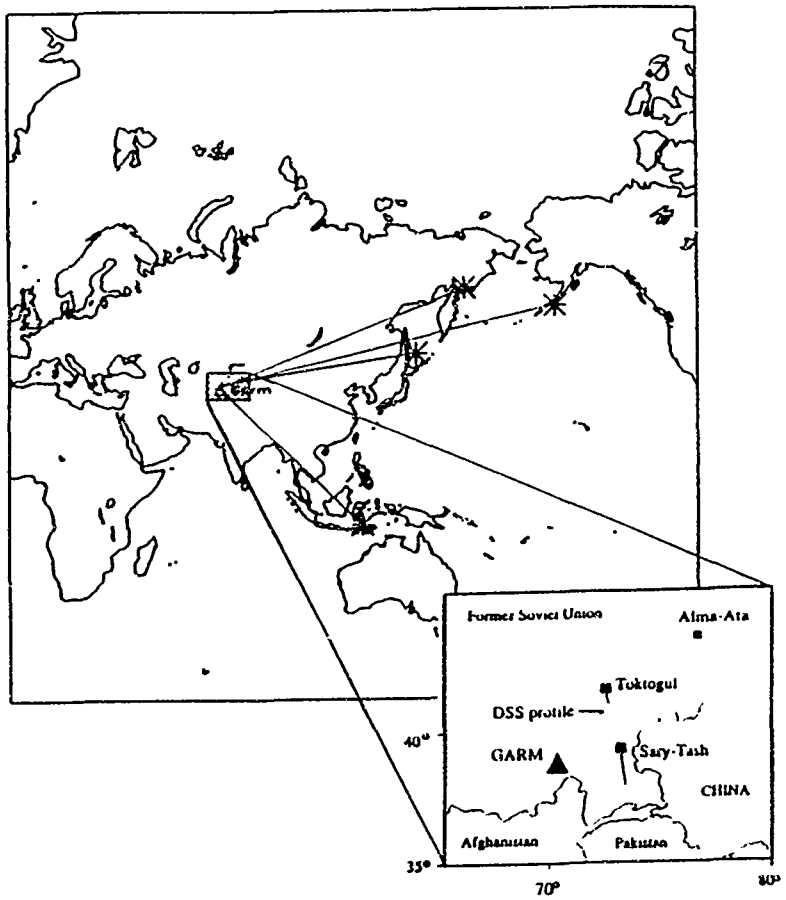

Figure 1 Teleseismic events (stars) used in the receiver function study. The small square is an enlargement of the Garm area and shows the location of a DSS profile. The earth model inferred from this profile was used in both receiver function and regional waveform studies.

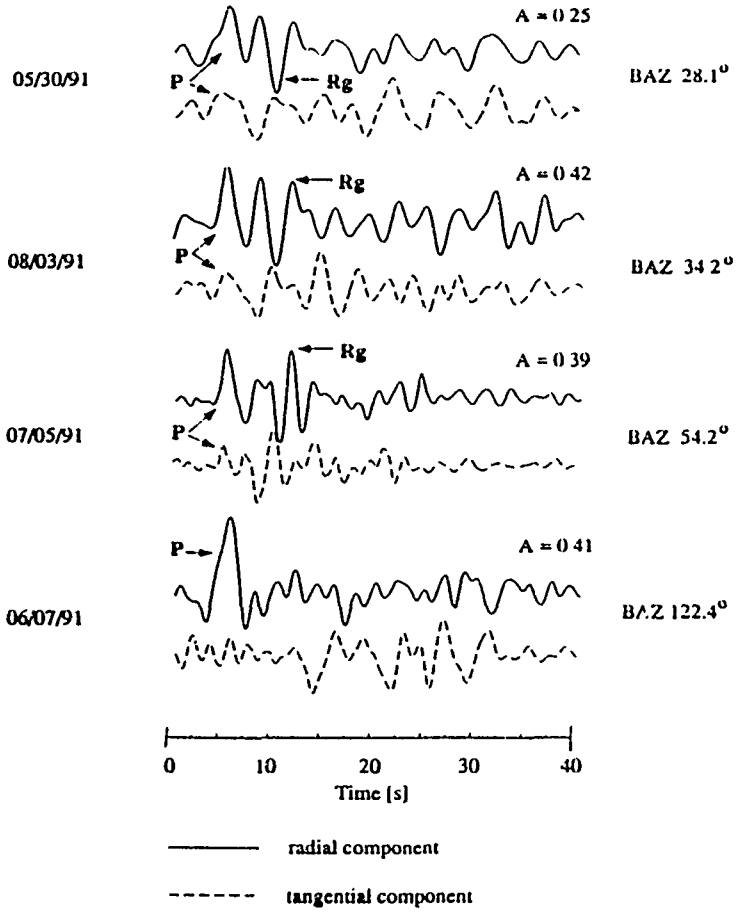

Figure 2. Processed radial (solid line) and tangential (dashed line) receiver functions for the four teleseismic events. The maximum radial to vertical ratio is give by "A". First arriving P and a secondary phase denoted by "Rg" are annotated. Note that this secondary phase is azimuthally dependent and very large, relative to P.

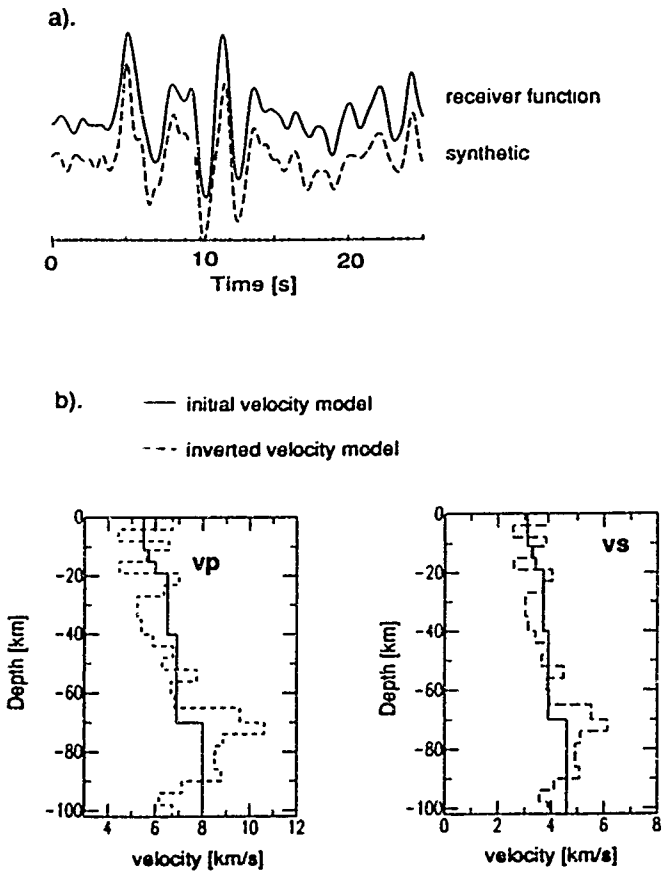

Figure 3. Inversion result using the receiver function of the 7/05/91 event and assuming a plane layered earth model. Panel (a) shows the waveform fit and (b) shows starting and final inversion velocity models. Note the large and unrealistic velocity variations throughout the crust and mantle required to fit the waveform data. This result strongly implies significant lateral heterogeneity in the crust under Garm.

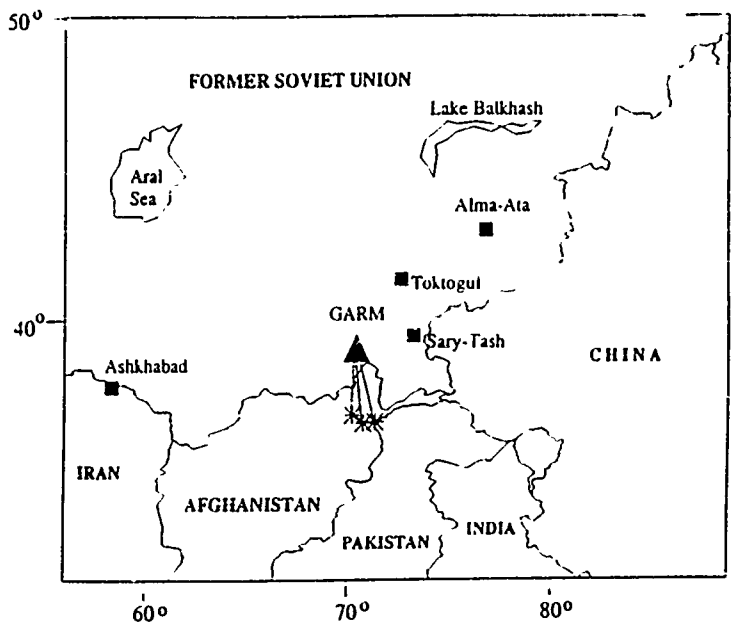

Figure 4. Location of three intermediate depth earthquakes within 300 km of Garm station.

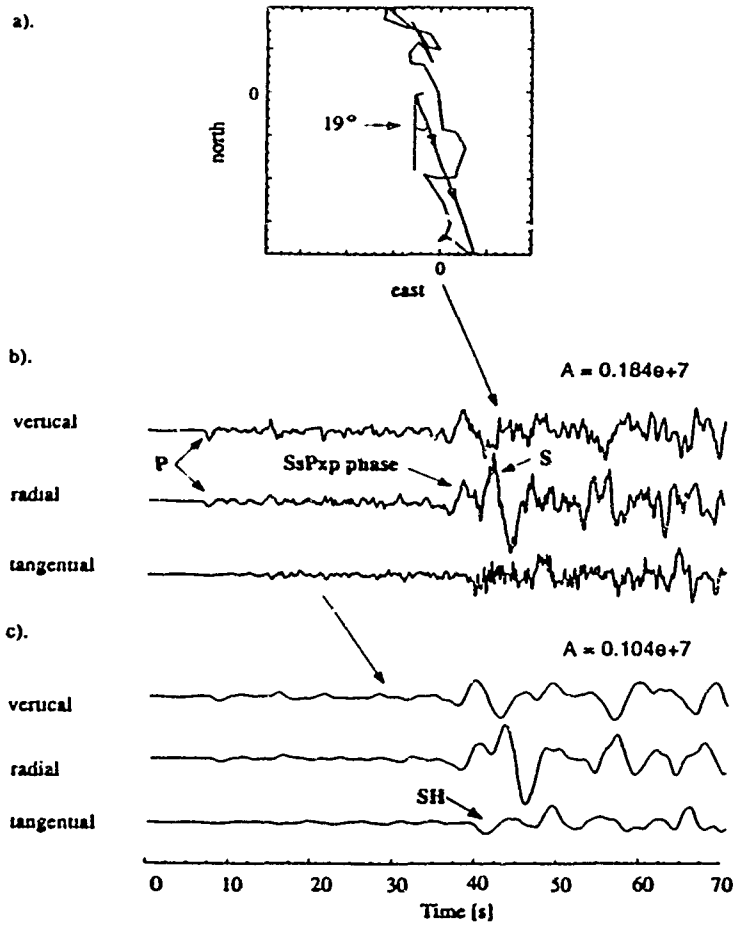

Figure 5. Raw and filtered waveform data from the 4/16/91 event. Panel (a) shows the particle motion of the first five seconds of the direct P wave in the horizontal plane which yields an estimate of event back azimuth. Panel (b) displays the raw data with amplitude in digital counts. Note the obvious and large SsPxp phase before direct SV. Panel (c) shows low-passed filtered data.

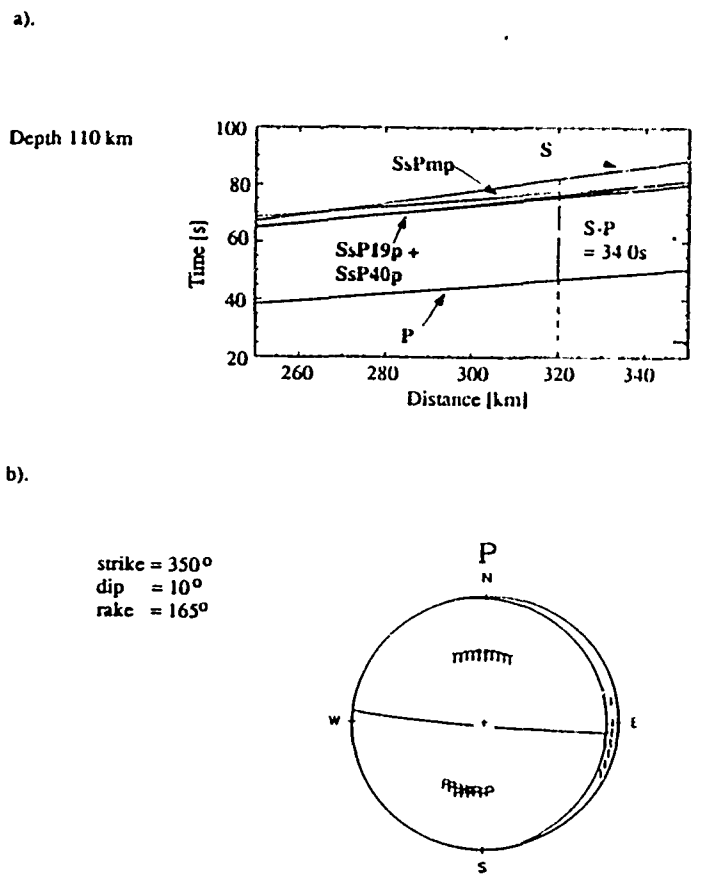

Figure 6. Panel (a) shows the travel time curves for various possible SsPxp phases. These include SsPmp in which SV converts at the free surface to P and reflects from the Moho, SsP19p which reflects from a reflector at 19 km, and SsP40p which reflects in mid crust. Synthetic computations show that SsPmp is the only significant phase since the P reflection is post critical. Panel (b) shows the result of grid test focal mechanisms using P, SV, SH and SsPmp relative amplitudes for the 4/16/91 event. T, P and I denote the tension, compression and intermediate axes of viable mechanisms. Only one set of focal planes are shown.

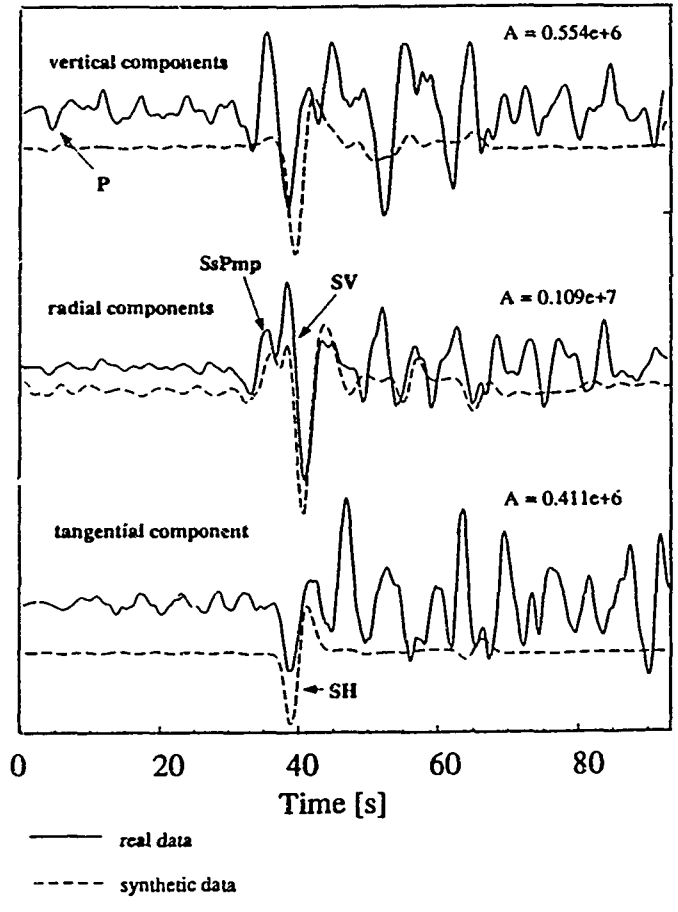

Figure 7. Comparison of lowpassed data (solid lines) and synthetics (dashed lines) for the 4/16/91 event. Large amplitude phases, like radial SV and SsPmp are fit well but lower amplitude vertical and tangential components show long codas. Polarities and relative amplitudes are well fit by the grid test mechanism. Amplitudes are in digitial counts.

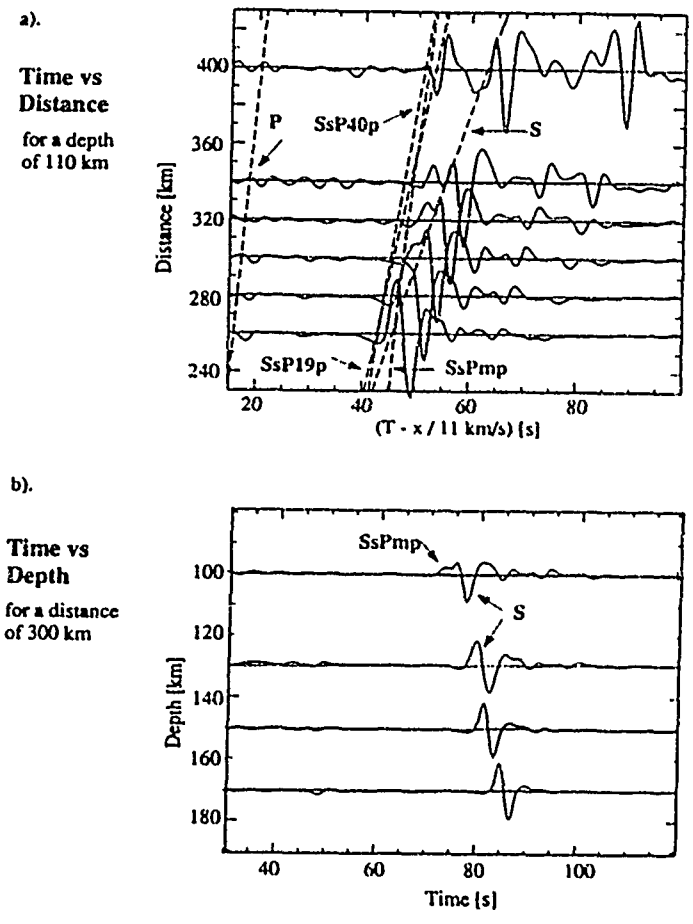

Figure 8. Sensitivity study of the timing and interference of SsPmp and direct SV. Panel (a) shows a synthetic distance section for an assumed source depth of 110 km. Panel (b) shows a synthetic depth section for an assumed distance of 300 km. Phase interference is a sensitive function of both depth and distance.

Elastic and Anelastic Structure Beneath Eurasia

Göran Ekström, Adam M. Dziewonski, Jeroen Tromp, and Wei-jia Su

Department of Earth and Planetary Sciences
Harvard University
Cambridge, MA 02138

Contract No. F49620-92-J-0392

Objective

We are adapting the seismic tomographic techniques developed in global scale studies to the regional scale problem of mapping the elastic and anelastic material properties beneath Eurasia. The abundance of earthquake sources and seismic stations in the northern hemisphere provides a dense ray coverage across Eurasia, making it possible to achieve greater resolution in this part of the world than is currently possible in global structure inversions of uniform resolution. The maximum angular degree l in the spherical harmonic expansion of lateral structure is 12 for our new preferred P and S global models. The objective for the research presented here is a tomographic seismic velocity model for structure beneath Eurasia with a horizontal resolution corresponding to at least $l = 20$ consistent with the widest possible range of seismological observations.
In this paper we present the results from the first year of effort on our two year project.

Research Accomplished

Our work on the seismic structure beneath Eurasia builds on the methods developed and experiences gained over more than a decade of research into the large scale seismic structure of the whole Earth. We are collecting new data and developing new methods to be able to achieve improved resolution of the structure beneath Eurasia, while at the same time satisfying global observations with structure with less detailed resolution. In practice, we can then use data from sources and seismic stations both inside and outside the region of immediate interest, while making propagation corrections for both regional and global structure. With this approach, progress is incremental in that each new model, with higher resolution, builds on a previous model. We have derived a new degree 12 S and a preliminary P model which will form the starting models for the planned degree 20 models for Eurasia. Our model inversions include several large datasets: travel times from the ISC bulletin, differential travel times (SS-S, ScS-S, etc.) and absolute travel times (S, SS, SSS, etc.) measured from waveform correlation, complete long-period ($T > 32$ s) body wave seismograms, and long-period ($T > 135$ s) mantle wave seismograms. A large effort has been devoted to building and reorganizing these datasets in preparation for analysis and inversion. The waveform data sets are the most crucial for constraining the shallower structures beneath Eurasia, and we have expanded this dataset, making extensive use of data from the IRIS/USGS and IRIS/IDA stations in the former USSR, as well as from the DARPA funded CDSN stations. We have also pre-processed the ISC bulletin data from 1964 through August 1990, and performed preliminary inversions with this new data set.

In order to better constrain the vertical resolution of crustal and upper mantle structure we are developing a new set of fundamental mode dispersion observations in the period range 50–200 seconds, as well as methods to interpret these observation.

Degree 12 S model - Derivation of S12/WM13 (Su, Woodward and Dziewonski, 1993) - a degree-12 model of shear velocity anomalies in the mantle– is an intermediate step between a decade old degree-6 and -8 representations (Dziewonski, 1984; Woodhouse and Dziewonski, 1984) and, what we believe to be a realistic goal, a degree-20 model. Because of the higher density of the stations and sources, we expect that this resolution can be fully achieved in Eurasia. An even more detailed (degree-36) model of the uppermost 300 km, or so, of the upper mantle, based on surface wave dispersion measurements, have been proposed (Zhang and Tanimoto, 1992; Anderson et al., 1992), but it shows serious discrepancies with observations (Su et al., 1992) and must undergo further evaluation. Our objective is to map anomalies at all depth in the mantle. The experience so far shows that there is no natural cut-off depth below which the structure can be assumed to be uniform.

Model S12 is based on a very large set of data – all of which were derived from digitally recorded waveforms. The data set consists of roughly 25,000 low-pass filtered waveforms spanning a period range from 45 to about 500 seconds. Some 10,000 differential travel times (SS-S and ScS-S of Woodward and Masters, 1991a, b) and absolute times (SS and S; Su and Dziewonski, 1991) provide important constraints on the structure near the surface as well as near the core-mantle boundary. An important element in achieving the higher resolution has been the addition in the mid-80's of new seismographic networks such as the CDSN, French GEOSCOPE, and the improvement of some existing stations due to the joint effort of IRIS and USGS.

In addition to showing good correlation with shallow geologic and tectonic structures (Figure 1), model S12 reveals new features at all levels in the mantle. Of particular interest are: 1) the details of low velocity anomalies in the oceanic mid-upper mantle which may be indicative of the influx of hot material from the lower mantle; 2) resolution of smaller scale structure in the transition zone at the eastern edge of Eurasia; 3) the change in the character of the spectrum of the heterogeneity across the 670 km discontinuity; 4) another, rather sudden, change in the spectrum at a depth of about 1700 km. The last two features seem to be consistent with the predictions of 3-D mantle convection modeling by Tackley et al. (1993).

Degree 12 P model - With the improvement in representation of the shear velocity anomalies, it became desirable to take another look at the P-velocities. The traditional source of data is the ISC Bulletin, although Woodward and Masters (1991) report differential PP-P travel times measured from digitally recorded waveforms. This is our fourth attempt at extracting information from this data source. The first study (Dziewonski, 1975; Dziewonski et al., 1977) showed the existence of velocity anomalies in the lower mantle with very large spatial dimensions. The second (Dziewonski, 1984), provided maps of the lower mantle that conceptually remain valid today. In the third we have shown that the inner core may be anisotropic (Morelli et al., 1986) and provided the first global maps of the CMB topography (Morelli and Dziewonski, 1987). In the preliminary stages of the current work we use our knowledge of the S-velocity patterns to fill in the gaps in the very uneven sampling of the upper mantle by the P-wave data.

It has been known for some time that the P- and S-velocity anomalies are correlated (Doyle

and Hales, 1967; Souriau and Woodhouse, 1985; Woodward and Masters, 1991). We assume that the ratios $\delta v_S/v_S$ and $\delta v_P/v_P$ are proportional; a proportionality factor of 1.85 seems to be consistent with most of the data.

In the first stage we relocate some 23,000 shallow earthquakes, using corrections for lateral heterogeneity predicted by the scaled S12 model. The average relocation vectors in 5° spherical caps are shown for Eurasia in Figure 1. There is an important trade-off between the lateral heterogeneity and earthquake location, so the studies in which this effect was not considered are likely to provide biased results. We then project some 2,500,000 travel time residuals into about 90,000 summary residuals (Dziewonski, 1984) which then are used as the data in inversion. In addition to the P travel time residuals we use also PKIKP and PKP (AB and BC branch) data, which provide additional coverage of the lowermost mantle. To control the upper mantle structure, we use the 9,000 mantle wave waveforms, maintaining our assumption of the proportionality of the relative P- and S-velocity perturbations. The resulting model shows that in the lower mantle there is good overall correlation between the P12 and S12 models (in the upper mantle this relationship is largely a forced one). It is not clear yet whether the dissimilarities are demanded by the data or are an artifact of the different coverage by the P- and S-wave ray sampling.

This will be investigated in the next stage where an inversion will be performed simultaneously for P- and S-velocities using the full data set developed in the context of the S12 study, P and PKP data obtained here as well as other data extracted from the ISC Bulletins (PcP, S, ScS, PP, SS and possibly others). We expect that we shall attempt to establish a penalty function for departures from the proportionality assumption, to minimize the differences resulting from the sampling bias.

The fact that P12 model can provide substantial variance reduction is illustrated in Figure 2 in which the 'observed' summary residuals for a summary source on the coast of Kamchatka are compared with those predicted by the model. There is a satisfactory overall similarity in the pattern. The size of the residuals is quite substantial.

Dispersion measurements – We have developed a matched filter technique for measuring the amplitude and phase of fundamental mode surface waves. The model dispersed surface wave $a(\omega)\exp[i\Phi(\omega)]$ is calculated for an initial Earth model (in our case PREM plus SH8WM13), and a non-linear minimization is made for incremental perturbations to both $a(\omega)$ and $\Phi(\omega)$. Both $a(\omega)$ and $\Phi(\omega)$ are represented by smooth functions parameterized by cubic B-splines. A misfit function, based on the windowed and weighted difference between the autocorrelation of the dispersed model pulse and the cross-correlation of the observed and model pulses has been found to be very suitable for rapid and robust convergence. Using CMT solutions for 1992 and data from the Global Seismic Network we have been able to collect more than 5000 good quality $R1$ dispersion and amplitude measurements.

Initially we are focusing on the period range 50–200 seconds. The amplitude measurements, which are collected at the same time as the phase observations, can be interpreted in terms of polarization. Amplitude and polarization measurements will be important when in the next phase of this work we will attempt to separate elastic focusing from the amplitude effects due to intrinsic attenuation.

Higher order effects of local structure on surface waves – The phase anomaly measurements will be combined with existing travel time and waveform data in an inversion

for elastic lateral heterogeneity up to degree 20. The amplitude anomalies will be used in an attempt to resolve large scale lateral variations in attenuation. To do this, we need to correct the amplitude anomalies for the effects of focusing and defocusing, changes in the takeoff angle and arrival azimuth, and local structure at the source and receiver. Synthetic seismograms are constructed based upon the JWKB approximation. In this approximation we trace surface wave trajectories and calculate amplitude variations due to focusing and defocusing along such trajectories. At the source we excite the appropriate local mode based upon the local radial structure and takeoff angle. Similarly, at the receiver we observe the same mode based upon the local radial structure and arrival azimuth. As shown in Figure 3, perturbations in the excitation amplitude relative to that in PREM are often as large as 20% and therefore play a significant role in explaining observed amplitude anomalies.

Conclusions and Recommendations

By combining a large number of diverse seismological observations, we are making progress towards higher resolutions tomographic images of the regional scale elastic and anelastic structure beneath Eurasia. The models are constructed in such a way that globally distributed observations are satisfied. We show that well-constrained global heterogeneities produce significant effects on the teleseismic locations of events within Eurasia.

References

Anderson, D. L., Tanimoto, T. & Zhang, Y.-S., Plate tectonics and hotspots: the third dimension, *Science*, **256**, 1645-1651 (1992).

Dziewonski, A.M., Resolution of large scale velocity anomalies in the mantle, *EOS, Trans. Am. Geophys. Un.*, **56**, 395, 1975.

Dziewonski, A. M., B. H. Hager and R. J. O'Connell, Large scale heterogeneity in the lower mantle, *J. Geophys. Res.*, **82**, 239-255, 1977.

Dziewonski, A. M., Mapping the lower mantle: Determination of lateral heterogeneity in P velocity up to degree and order 6, *J. Geophys. Res.*, **89**, 5929-5952, 1984.

Hales, A.L. and Doyle, A., P and S travel time anomalies and their interpretation, *Geophys. J. R. Astron. Soc.*, **13**, 403-415, 1967.

Morelli, A., A. M. Dziewonski and J. H. Woodhouse, Anisotropy of the inner core inferred from PKIKP travel times, *Geophys. Res. Lett.*, **13**, 1545-1548, 1986.

Morelli, A. and A. M. Dziewonski, Topography of the core-mantle boundary and lateral homogeneity of the liquid core, *Nature*, **325**, 678-683, 1987.

Souriau, A. and J. H. Woodhouse, A worldwide comparison of predicted S-wave delays from a three-dimensional upper mantle model with P-wave station corrections, *Phys. Earth Planet. Int.*, **39**, 75-88, 1985.

Su, W.-J. and A. M. Dziewonski, Predominance of long-wavelength heterogeneity in the mantle, *Nature*, **352**, 121-126, 1991.

Su, W.-J., R. L. Woodward and A. M. Dziewonski, Deep origin of mid-oceanic ridge velocity anomalies, *Nature*, **360**, 149-152, 1992.

Su, W.-J., R. L. Woodward and A. M. Dziewonski, Degree-12 Model of Shear Velocity Heterogeneity in the Mantle, *J. Geophys. Res.*, submitted, 1993.

Tackley, P. J., D. J. Stevenson, G. A. Glatzmaier and G. Schubert, Effects of an endothermic phase transition at 670 km depth in a spherical model of convection in the Earth's mantle, *Nature*, **361**, 699, 1993.

Woodhouse, J. H., and A. M. Dziewonski, Mapping the upper mantle: three-dimensional modeling of Earth structure by inversion of seismic waveforms, *J. Geophys. Res.*, 89, 5953-5986, 1984.
Woodward, R. L. and G. Masters, Global upper mantle structure from long-period differential travel-times *J. Geophys. Res.*, 96, 6351-6377, 1991a.
Woodward, R. L. and G. Masters, Lower-mantle structure from long-period differential travel times, *Nature*, 352, 231-233, 1991b.
Zhang, Y.-S. and Tanimoto, T., Ridges, hotspots and their interpretation as observed in seismic velocity maps, *Nature*, 355, 45-49, 1992.

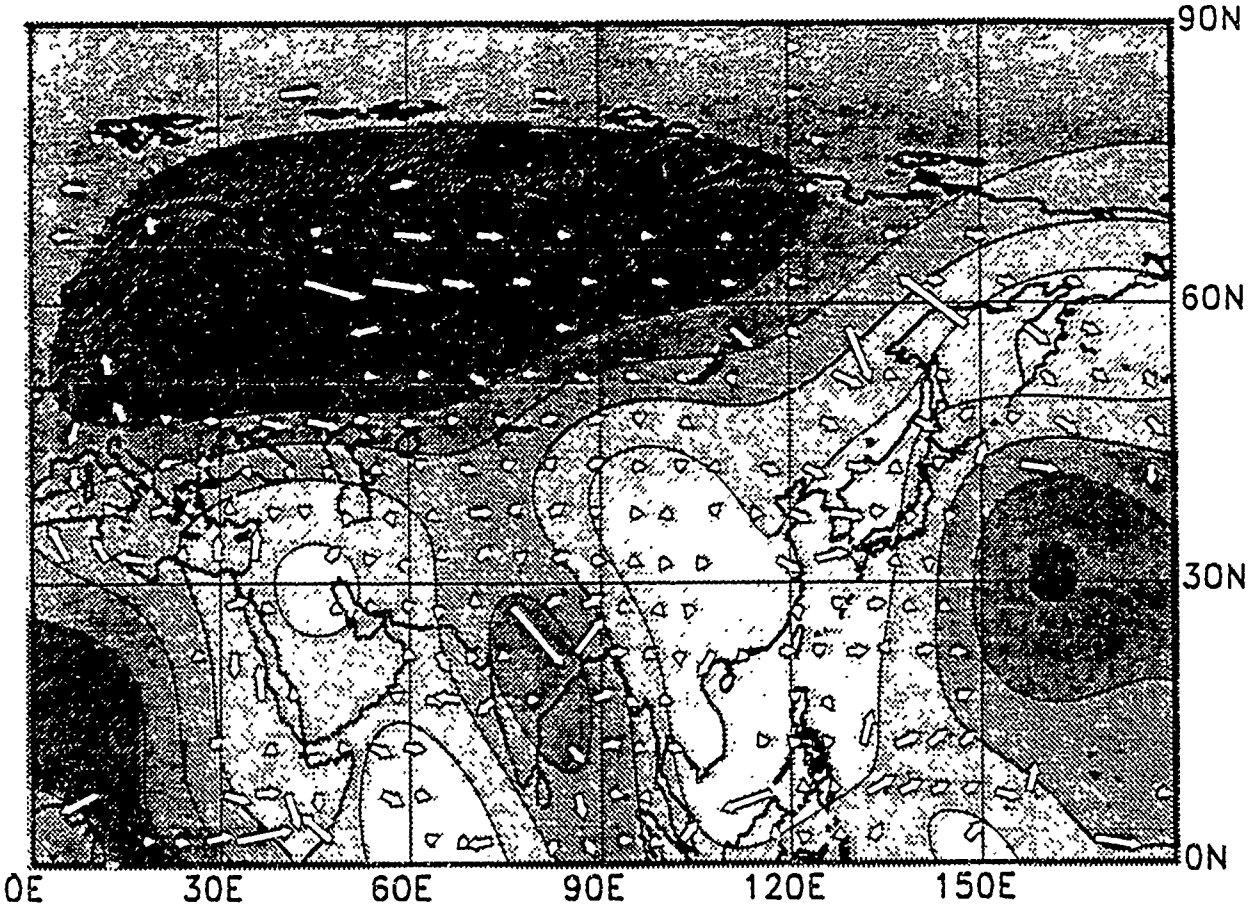

Figure 1. Background shading shows shear velocity perturbations at 100 km depth beneath Eurasia as imaged in the model S12/WM13. The thick line represents the zero contour. The contour inverval is 1% and faster than average velocities are shown by darker shading and slower velocities are shown by lighter shading. Superimposed on the map are vectors representing the average relocation of events in 5° caps with respect to ISC locations after locating the events in the scaled S12/WM13 model. The longest arrow corresponds to a horizontal relocation of 43 km.

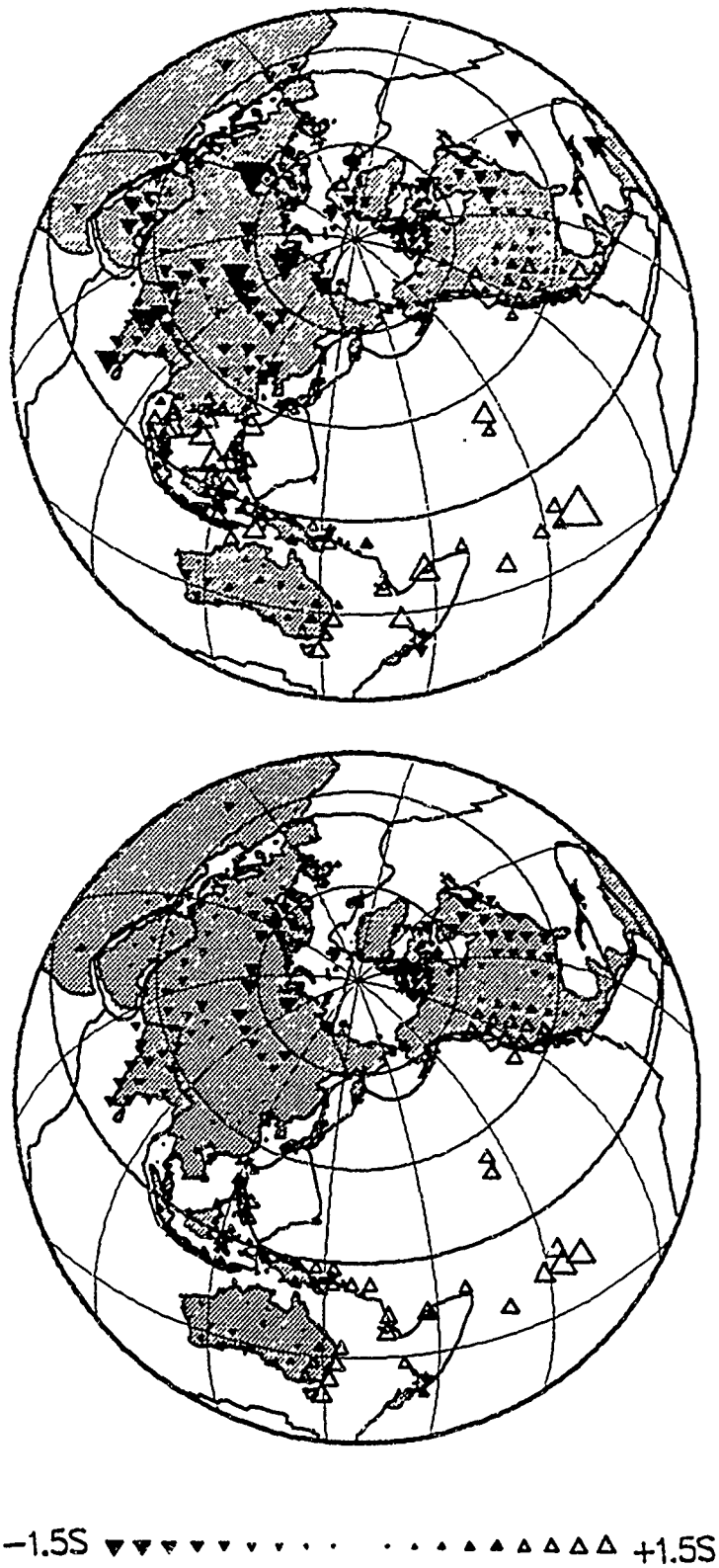

Figure 2. The observed summary residuals (top) for a source region near Kamchatka. The negative residuals are indicated by solid inverted triangles, and positive ones are represent by open triangles pointing up. The predicted residuals (bottom), based on our new P model, shows good agreement with the observations, in particular in the longer wavelength pattern of residuals. In Eurasia, predicted residuals are generally smaller than observed ones.

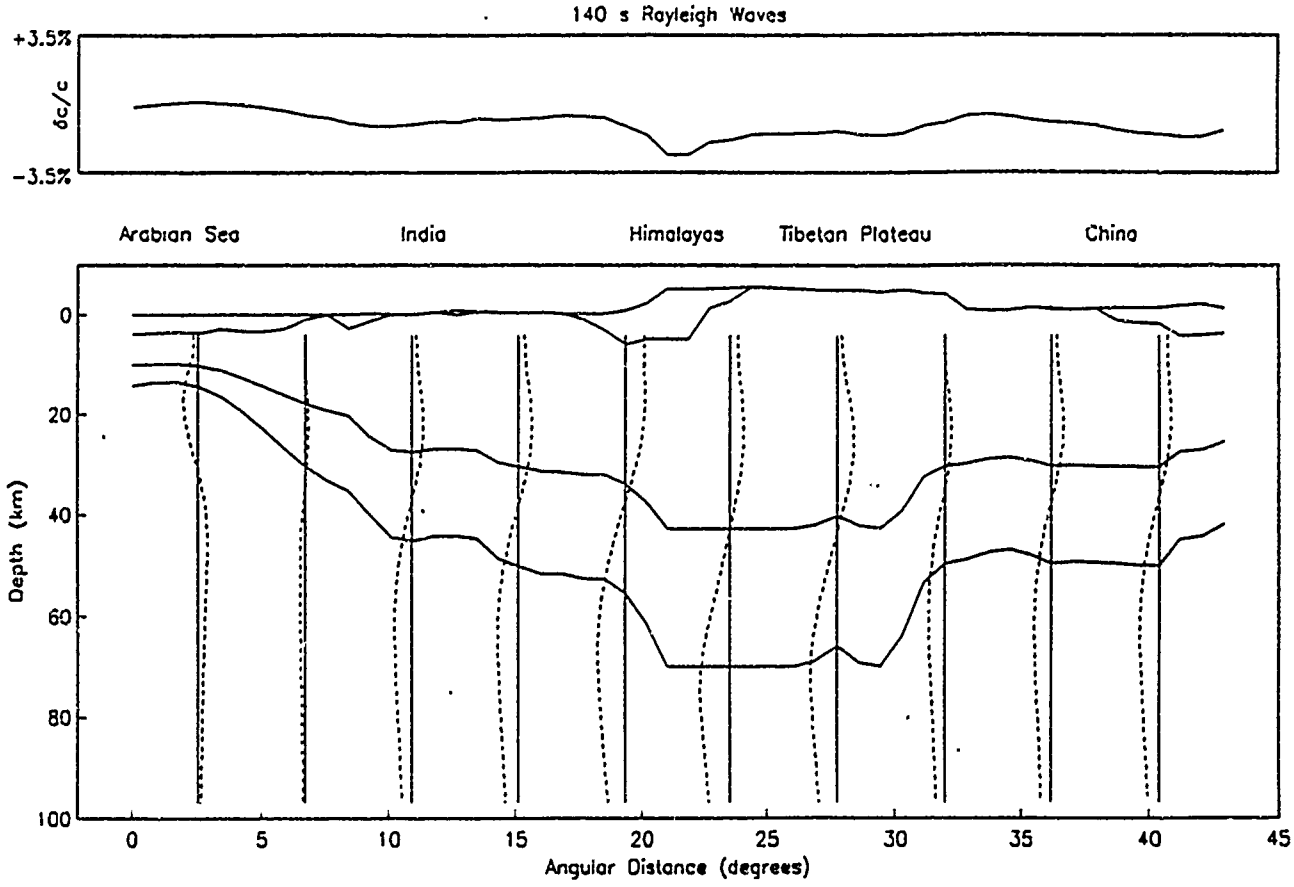

Figure 3. *Top*: Relative phase velocity perturbation $\delta c/c$ for 140 s Rayleigh waves along the cross section shown in the bottom panel. The phase velocity perturbations are a result of mantle heterogeneity, crustal structure, topography, and ellipticity. *Bottom*: Model cross section from the Arabian Sea over India through the Himalayas to China. Shown are the surface, ocean floor where present, sedimentary basement where present, middle crust, and Moho. Where available, the the information on the crust was extracted from the Cornell Eurasian database. At ten selected locations the relative perturbation in excitation amplitude, for a particular source mechanism and takeoff azimuth, as a function of depth is shown by the dashed lines. The spacing between the solid vertical lines corresponds to a 100% change in the excitation amplitude relative to PREM, indicating that variations of 20–30% are not uncommon.

A Network-Accessible Geological and Geophysical Database for Eurasia, North Africa, and the Middle East

Eric Fielding, Muawia Barazangi, and Bryan Isacks

Institute for the Study of the Continents (INSTOC)
Cornell University, Ithaca, New York 14853
E-mail: "eric@geology.cornell.edu" -or- "fielding@seismo.css.gov"

Contract #F29601-91-K-DB08

OBJECTIVE

Topography and variations in crustal structure along seismic propagation paths and at the source and receiver sites are crucial information to understand the excitation and propagation of regional seismic phases and other aspects of the problems of detection, verification, and estimation of the yield of nuclear explosions. Our objective is to collect and organize available topographical, remote-sensing, geological, and geophysical datasets for Eurasia, North Africa, and the Middle East into a digital information system that can be accessed by display programs running at the Center for Seismic Studies (CSS) and by other ARPA researchers. We are expanding the area of data coverage to include China, the Middle East and North Africa in addition to continuing our work in Europe and Central Asia. We store the data in an information system (GIS) with a network-accessible server to which can connect X Window System client modules of future versions of the Intelligent Monitoring System (IMS) running at CSS and other ARPA researchers. The information system is organized to extract and usefully display the information most relevant to verification and detection, such as maps and profiles of crustal thickness and depth to basement. The work includes assembly of available digital datasets such as topography, satellite imagery, and crustal reflection and refraction profiles and digitization of available geological and geophysical map information on sedimentary basins and crustal thicknesses and other details of crustal structure.

RESEARCH ACCOMPLISHED

Work in progress has now realized useful datasets for Eurasia, including a vast digital topographic database and digitization of several sets of crustal seismic structure maps, at scales from 1:15,000,000 for the entire continent to 1:500,000 for selected areas. These include maps of crustal thicknesses (depth to Moho) and sedimentary basin depths (depth to seismic or "metamorphic" basement). We have created regularly spaced grids of the crustal and sediment thickness values from these maps that can be used to create profiles of crustal structure. These profiles can be compared with the crustal seismic phases received along the propagation path to better understand and predict the path effects on phase amplitudes, predominant frequencies, and delay times, which are keys to estimating event magnitudes and yields. The gridded data could also be used to model propagation of crustal phases in three dimensions.

We are utilizing the rapidly accelerating Internet (formerly ARPAnet) network to share datasets with CSS and other ARPA researchers. We have developed a "server" system at Cornell to allow "client" modules of the IMS to directly connect to databases that we are generating and improving. This allows IMS users to utilize data as soon as it is available. Our network "raster server" program that allows "client" programs, such as the "Xgbm" program (Davis and Henson, 1992; 1993) to access our crustal structure datasets over the Internet, extracting a profile along a great circle path and then using the structure for seismic propagation modeling. Datasets are also available via the time-honored method of "anonymous ftp" from Cornell. We encourage researchers to contact us about gaining access to our databases at the computer mail addresses listed on the first page of this paper. Due to data access restrictions imposed by the DMA, we are not able to provide network access to our digital topography databases, but we encourage ARPA and Air Force researchers to contact us about access to processed versions of the topography for use in their seismic research.

We continue to expand our database of digital topography for Eurasia, North Africa, and the Middle East. We have processed and analyzed a huge volume, nearly 15 gigabytes (GB), of high-resolution Digital Terrain Elevation Data (DTED—Level 1) that we have received for Asia, Europe, the Middle East and North Africa (Figure 1). Coverage is complete for Europe, central and southern Asia, and most of the Middle East and North Africa. The basic processing of the raw DTED into an accessible format included the creation of mosaics of the full resolution data for each 5° by 5° block, a file of manageable size for manipulation on a workstation and storage on optical media.

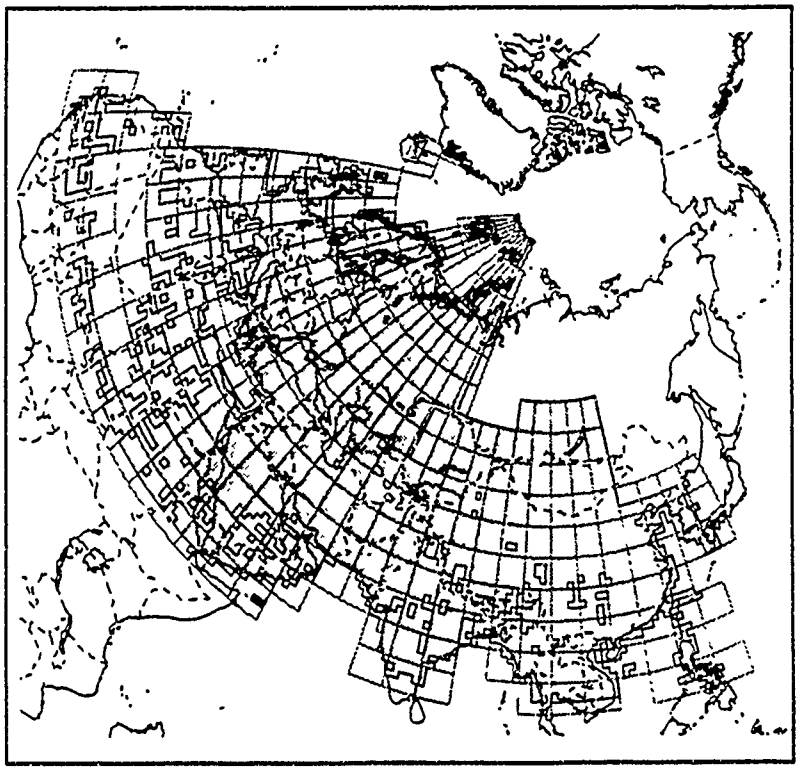

Figure 1: Map of Eurasia, the Middle East and North Africa showing area covered by our present databases of digital topography. Coastlines of oceans, seas, and major lakes are *solid lines* and country borders are *dashed lines*. Acquired and processed DTED cells are *filled light gray* and outlined with a *black line*. Missing and "unavailable" cells are *irregular white holes*. Blocks 5° by 5° of DTED are outlined with *dark gray lines*. Map is an azimuthal equidistant projection centered in north central Eurasia.

All of our topography, including both the reduced resolution mosaics and the full resolution topography blocks, and other archived datasets are being stored in our Epoch-1. The network-based Epoch file server includes an optical disk jukebox system with a library unit that contains 60 GB of "semi-online" storage and unlimited off-line storage of

rewritable optical cartridges. The Epoch-1 provides unattended access, usually within less than a minute to any of the disks in the library unit. Our server program is able to load any part of the dataset in a short time, when the necessary optical cartridges are available inside the jukebox.

The digital topography is stored with "georeferencing" or geographic coordinates, and can be easily projected into a map projection and overlain with other datasets, such as seismic events. Figure 2 shows the full resolution DTED for the nuclear test site at Matochkin Shar, central Novaya Zemlya, portrayed as shaded relief, overlain with the locations of known nuclear tests as 250m radius circles and the 95% confidence error ellipse of an event that occurred on 92/12/31(both obtained courtesy of Dr. Hans Israelsson at CSS). The "New Year's Eve" anomalous event is clearly located across the Matochkin Shar from the test site.

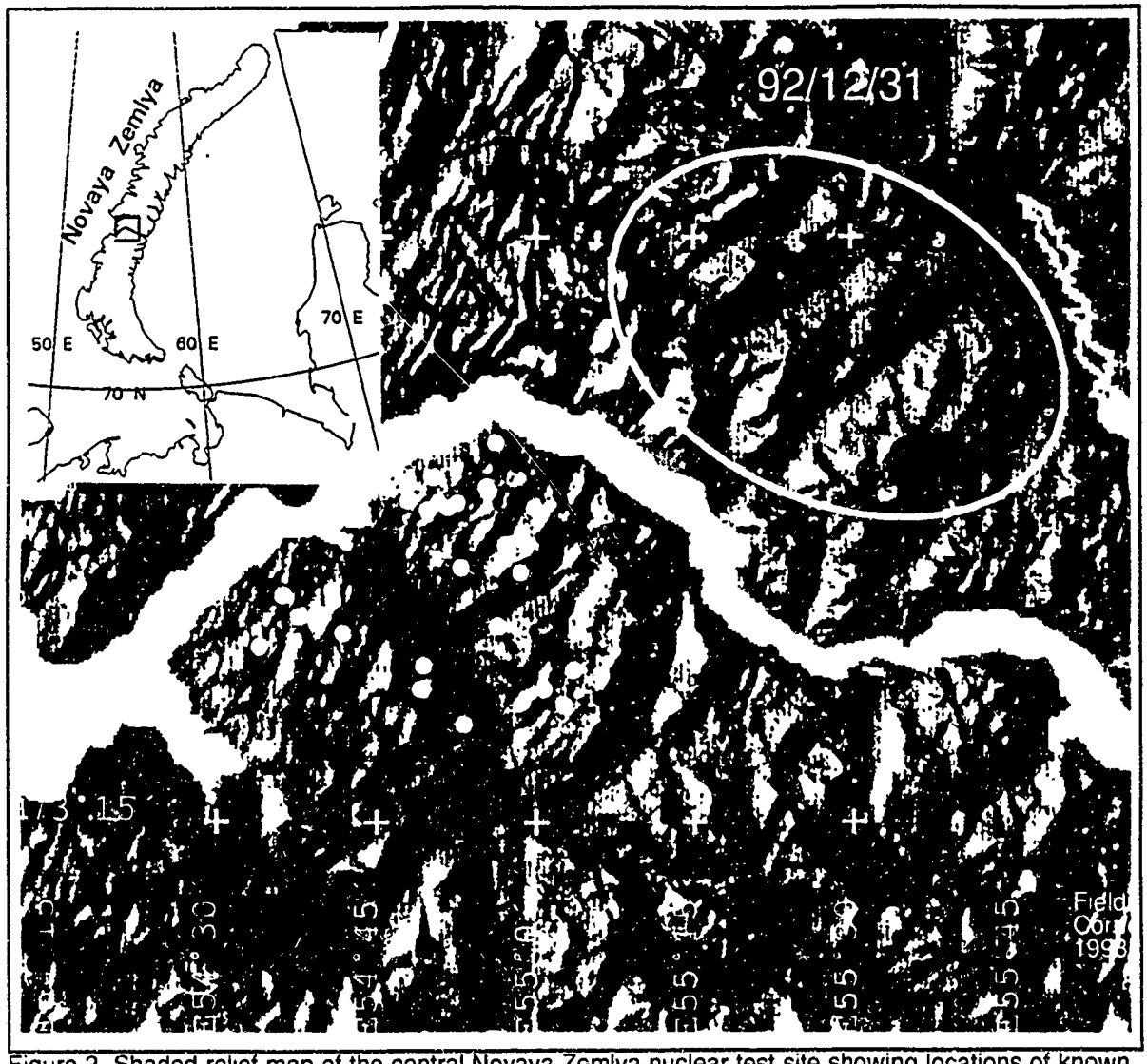

Figure 2. Shaded relief map of the central Novaya Zemlya nuclear test site showing locations of known tests and an enigmatic event on 92/12/31. Known nuclear test locations are shown as *small white circles*, and the error ellipse of the "New Year's Eve" event is shown as a *white outline*. The full resolution topography was shaded with a light from the west-northwest. *White crosses* mark 15 minute latitude and longitude tics. Water of ocean and Matochkin Shar is shown in *white*. Map is in an azimuthal equidistant projection centered on 73°N and 55°N. Inset map shows location *box* of image.

We began our digitization of lithospheric structure with a set of seismic structure maps of Eurasia. These include 1:15,000,000 maps of depth to Moho and to seismic (metamorphic) basement (Kunin and others, 1987). These maps provide first-order data on crustal structure for all of Eurasia at a moderate resolution, but the data may not be correct in detail for every area. To improve our datasets, we have begun digitizing more detailed maps of crustal structure that are available, beginning in Europe, where the most detail is published. Using the attributes capability of the Arc/Info GIS, we can record which contours are dashed (inferred or interpolated) and which are solid, or record other information about the data reliability from the maps such as the locations of the seismic refraction and reflection lines used. Arc/Info was used to edit the resulting databases and project the data from each map's projection into latitude-longitude coordinates. Some maps have "faults" or discontinuities in the Moho, and these are digitized as well. We then created regularly spaced grids of the crustal and sediment thickness values from each of these digitized maps, including the offsets of "faults".

A map of a new gridded dataset of depths to Moho for the Baltic area is shown in Figure 3. This map is the result of a collaboration with Dr. Vlad Ryaboy at CSS.

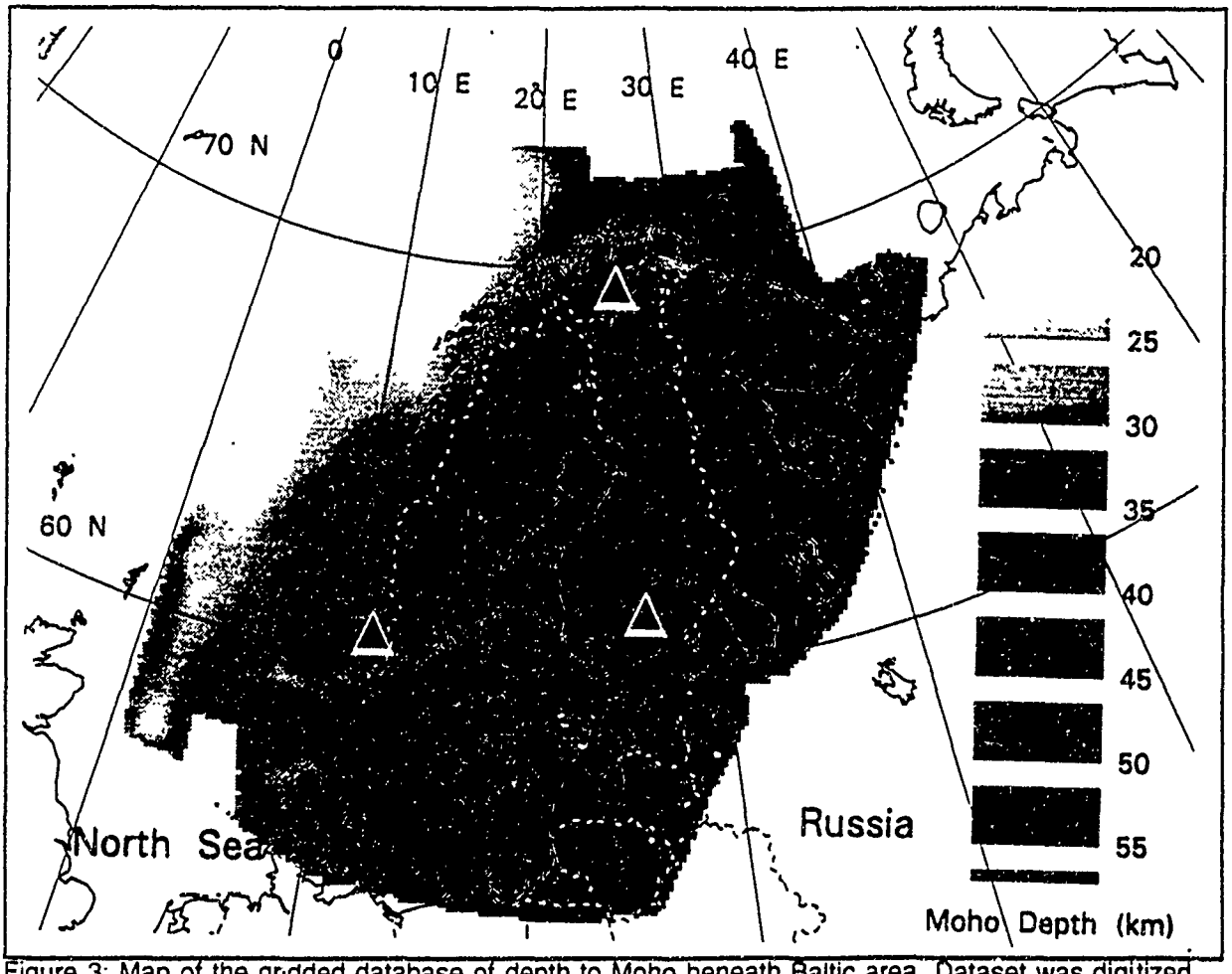

Figure 3: Map of the gridded database of depth to Moho beneath Baltic area. Dataset was digitized from a combination of maps (see text). *Gray scale* shows depth in km. This gridded dataset, along with similar datasets of depth of sedimentary section can be used for two- and three-dimensional modeling of crustal phase propagation and P_n travel time delays. *Solid black lines* mark coastlines and major lakes. *Dashed lines* mark country boundaries. Locations of NORESS, ARCESS, and FINESA arrays are marked by *black triangles with white borders*. Map projection is Lambert Conformal Conic.

We digitized two previously published Moho maps of area around the Baltic (Kinck and others, 1992; Sharov, 1991) and then plotted them at the same scale and map projection. Vlad then used these two maps and other info (Ryaboy, 1990; BABEL, 1993) to produce a new combined map that we digitized and converted into a gridded database. These gridded data can then be used to calculate grids of source-specific station corrections for P_n travel times using an empirical equation relating travel-time delays to the depth to Moho beneath the source (at each point of the grid) and the receiver (each of the three arrays: NORESS, ARCESS, and FINESA) as described by Suteau-Henson and others (1993, this volume). The locations of the arrays are marked. These kinds of travel-time corrections may greatly improve the locations of regional events. This and all of our completed crustal structure datasets are available over the network from our raster server and via ftp.

Another map of depth to Moho has been recently published as part of the European GeoTraverse (EGT). We have completed the digitization of this map which runs from the Arctic Ocean across central Europe to Tunisia, shown in Figure 4 below. The map includes several "faults" or discontinuities in the Moho, in the Alps and Apennines of Italy, where the Moho changes depth by up to 20 km over distances of a few dozen km horizontally, marked on the map. Several of these faults can be also seen in the cross-section of Figure 5 below. We are now digitizing the locations of the seismic refraction and reflection lines that were interpreted to make this EGT map, as recorded on the back of the map. The gridded version of this dataset has a point spacing of about 10 km.

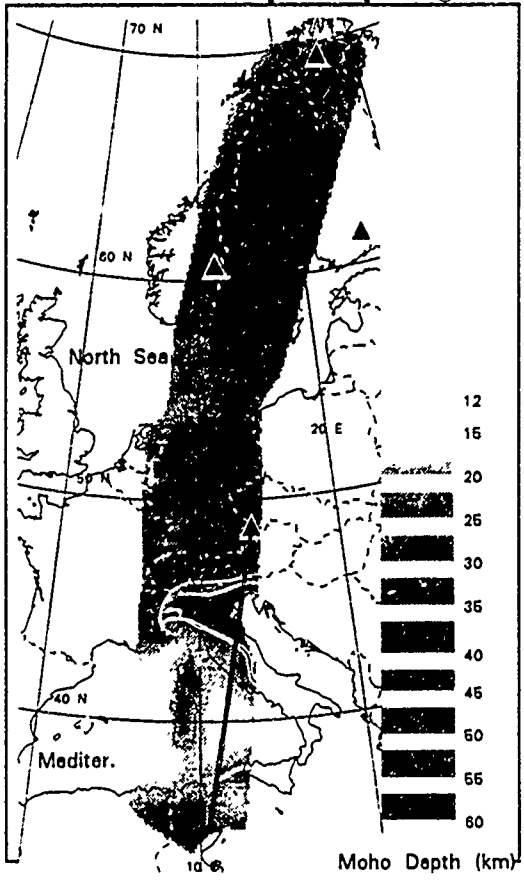

Figure 4: Map of depth to Moho from European Geotraverse. *Gray scale* shows depth in km. This gridded dataset, along with similar datasets of depth of sedimentary section can be used for two- and three-dimensional modeling of crustal phase (L_g) propagation and P_n travel time delays. *Solid black lines* mark coastlines and major lakes. *Dashed lines* mark country boundaries. *White lines* mark "faults" in Moho. Locations of NORESS, ARCESS, GERESS, and FINESA are marked by *black triangles with white borders*. *Thick black line* shows location of profile of Figure 5. Map projection is Lambert Conformal Conic.

These gridded datasets can be used to extract the crustal structure profile along a given propagation path. An example is shown in Figure 5, which shows the depth to Moho profile from the GERESS array towards the south. This type of profile of crustal structure can be compared by an analyst or an automatic program with the crustal seismic phases received along the propagation path to better understand and predict the path effects. The Xgbm (v. 1.1) program can connect to our raster database server over the network, extract the depths of the Moho and seismic basement along a great circle, and then use this type of profile as the basis for

ray tracing of seismic phases and gaussian beam approximation of the seismic waveforms (Davis and Henson, 1992; 1993).

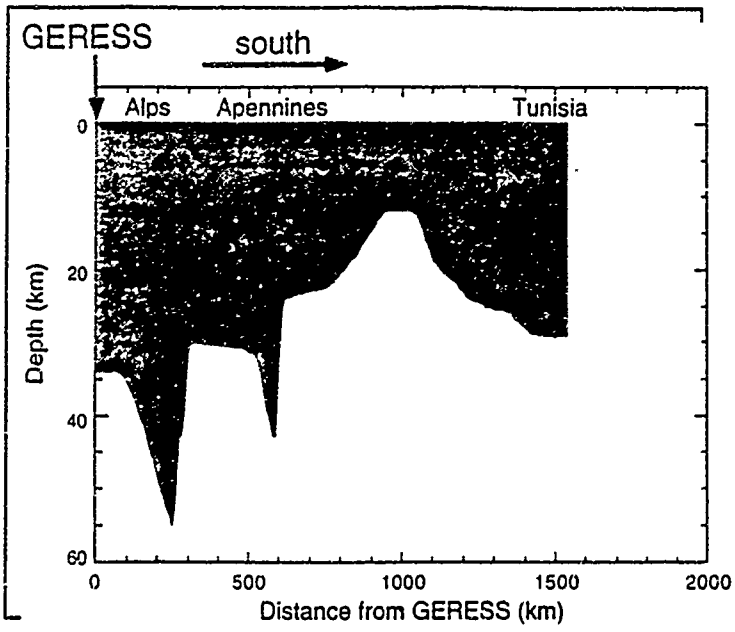

Figure 5: Profiles of Moho database along great circle path from GERESS towards the south. Note the extreme variations in crustal thickness that will affect the propagation of crustal phases, such as L_g. No L_g is observed for events more than 500 km from the GERESS array in this direction (Harjes and others, 1992). Location of profile shown on Figure 4.

Harjes and others (1992) have described a lack of significant L_g energy at the GERESS array from distances greater than 500 km for propagation paths in most directions, and this effect is especially strong for events to the south and southwest. They also observe a corresponding increase in S_n energy starting at about an epicentral distance of 350 km in the same direction. The extreme variations in depth to Moho shown in Figure 5 beneath the Alps and Apennines at distances of 300–700 km from GERESS are likely to be the cause of these major disruptions of regional phase propagation. The deep Moho root of the Alps may also explain an azimuthal bias or secondary arrivals and other anomalies of events in the eastern Mediterranean received at GERESS (Jenkins and others, 1992; Harjes and others, 1992).

We are expanding the scope of our information system to include data on the Middle East and North Africa. Under the auspices of several other ongoing projects at Cornell we have collected a very large literature collection, satellite imagery and some detailed datasets, especially in Syria and Morocco. In Syria, data include DSS and industry seismic reflection profiles, drill hole analyses, magnetic and gravity measurements, and possibly the data from a 20 station digital seismograph network to be installed soon with the help of Cornell scientists. For Morocco, data include seismic reflection profiles with drill hole tie points, gravity measurements, and many digital records from a network of about 30 seismograph stations that we helped to establish. For both Syria and Morocco, we have complete coverage of digital Landsat Multispectral Scanner scenes, complete sets of geologic maps, and all available DTED. In the near future, we will be making new databases from the Middle East and North Africa available via the Internet.

CONCLUSIONS AND RECOMMENDATIONS

We are happy to report that numerous CSS, ARPA and Air Force researchers are already using our databases in their ongoing studies. We have supplied datasets and maps made from our datasets to CSS, SAIC, ENSCO, Phillips Lab, SUNY Binghamton, Univ. of Conn., Univ. of Wisconsin, Harvard, and ARPA scientists in the last year or so.

Geophysical and geological datasets can provide important anciilary information on the propagation of seismic phases through the continental lithosphere. In turn, this bears on the detection, discrimination, and yield estimation of nuclear explosions. The rapidly changing geopolitical situations in Eurasia, North Africa, and the Middle East make it imperative that databases are extended to areas outside the former Soviet test sites. The types of datasets that we are compiling can be used to compare well studied propagation paths, such as within Europe, with paths to events in other locations that have not been studied in great detail to enhance the monitoring of nonproliferation treaties.

These datasets of digital geological and geophysical information can now be incorporated into modules of the IMS at the CSS and will be extremely useful for the interpretations of seismic data. We will continue to make our databases available via Internet to ARPA and AFOSR researchers. We have proposed some modifications to the protocol of the raster server to make some data types more accessible, especially high-resolution satellite imagery and lithospheric structure along great circle paths. The direct connection of Cornell to the NSFnet (T3 backbone) makes communication between Cornell and the Internet especially rapid. As described above, we are making the processed topography data available, beginning with the reduced resolution mosaics that will be most useful for seismic researchers.

REFERENCES

Davis, J. P., and I. H. Henson, 1992, An X-windows graphics tool to compute synthetic seismograms for 2-D models using Gaussian beams, in Lewkowicz, J. F., and McPhetres, J. M., (eds.), *Proceedings of the 14th Annual DARPA/PL Seismic Research Symposium, Phillips Lab., Hanscom AFB, MA., PL-TR-92-2210*, p. 92–98, ADA256711.

Davis, J. P., and I. H. Henson, 1993, User's guide to Xgbm: an X-windows system to compute Gaussian beam synthetic seismograms, v. 1.1 , *TGAL-93-02 (draft)*, 52 p.

BABEL working group, 1993, Integrated seismic studies of the Baltic shield using data in the Gulf of Bothnia region, *Geoph. Jour. International*, v. 112, no. 3. p. 305–324.

Harjes, H. P., N. Gestermann, M. Jost, J. Schweitzer, and J. Wüster, 1992, Advanced waveform research methods for GERESS recordings, *Scientific Report No. 2, Phillips Laboratory, Hanscom AFB, MA, PL-TR-92-2142*, 148 pp, ADA253686.

Jenkins, R. D., W. C. Nagy, T. J. Sereno, H. J. Swanger, and D. D. Wahl, 1992, Regional attenuation and travel-time characteristics at GERESS (abstract), *EOS Transactions AGU*, v. 73, no. 43, Fall meeting supplement, p. 374–375.

Kinck, J. J., E. S. Husebye, and F. R. Larsson, 1992, The Moho depth distribution in Fennoscandia and the regional tectonic evolution from Archean to Permian times (manuscript available at CSS)

Kunin, N. and others, 1987, Map of depth to Moho and Map of depth to seismic basement, Institute of Physics of the Earth, Moscow, 1:15,000,000 scale

Ryaboy, V., 1990, Upper mantle structure along a profile from Oslo (NORESS) to Helsinki to Leningrad, based on explosion seismology,*BSSA*, v. 80, no. 6, p. 2194–2213.

Sharov, N. V., 1991, Lithosphere of the Baltic Shield according to seismic data, *Proceedings of the Second Workshop on Investigation of the Lithosphere in the Fennoscandian Shield by Seismological Methods, Institute of Seismology, University of Helsinki, Report S-25*, p. 87–95.

Suteau-Henson, A., Ryaboy, V., Israelsson, H., and Carter, J., 1993, Station evaluation and accurate event locations for global monitoring, *this volume.*

APPLICATIONS OF A ROBUST STATISTICAL FRAMEWORK FOR SEISMIC EVENT IDENTIFICATION

Mark D. Fisk
Mission Research Corporation

and

Henry L. Gray and Gary D. McCartor
Southern Methodist University

Contract No. F19628-C-90-0135

OBJECTIVE

This work is directed at providing robust statistical methods to perform seismic event identification, to assess error rates associated with event classification, and to address statistical issues regarding transportability of discriminants. We have developed statistical methods to perform event identification under a wide range of conditions of training set availability and to treat the statistical distributions of discriminants rigorously. Along with other application, we show how one of these methods, an outlier test, can be used to detect peculiar events in data sets lacking ground-truth. We have also implemented a number of preliminary tests and data transformations to be performed on training sets to ensure that the appropriate assumptions of the event identification tests hold. The combination of these techniques provides a robust statistical framework to identify seismic events and estimate classification probabilities rigorously under extremely general or restricted conditions. We have applied these methods to seismic event identification using feature data extracted by ISEIS.

RESEARCH ACCOMPLISHED

Event Identification Methods. Among the crucial statistical issues associated with seismic event identification are the availability of useful training sets and the complicated statistics of discriminants. Data sets for new regions of interest may be extremely limited. Path differences often prohibit direct application of training sets to classification in new regions. Ground-truth data sets are being established, but progress is relatively slow. In addition, discriminants rarely have normal distributions, and the distribution type and covariance structure typically differ from one event type to the next (e.g., Baumgardt, 1992). Some very useful discriminants are in fact discrete rather than continuous. Combinations of these issues have limited useful application of many statistical classification methods in the past. It is vital, however, for monitoring applications that these issues are all addressed with statistical rigor so that classification accuracy can be optimized and so that estimated error rates have precise meaning; improper treatment of discriminant distributions can lead to misclassifications and biased estimates of error rates.

To address these issues, MRC and SMU (Baek et al., 1992, 1993) developed statistical methods for classification and outlier detection. The methods, based on the generalized likelihood ratio (GLR) and the bootstrap technique, have considerable flexibility to rigorously treat a mixture of continuous (e.g., amplitude and spectral ratios, spectral and cepstral variances, etc.) and discrete (e.g., presence of cepstral peaks, seismicity, deep/shallow, offshore/onshore, etc.) features, normal or non-normal statistics, equal or

unequal covariance matrices, and different distribution functions for different event types. (Detailed technical discussions of the methods are presented by Gray et al., 1993).

The GLR outlier test is particularly useful for situations with training data limited to one class. Here a hypothesis test is used to determine whether an event belongs to the same population as the training data or not. For example, when monitoring a new region there may only be a handful of earthquakes or mining blasts. In fact, we may not even know what the event type is for a particular set. The GLR outlier test can still be applied to flag peculiar events that are not "business as usual." A related application of the outlier test is to test training sets which lack ground-truth for possible contamination. In this way, peculiar events can be flagged for further expert analysis or corroboration with bulletins, etc. Thus, the GLR outlier test allows monitoring to be performed under conditions for which minimal information is available.

For situations were more training information is available, the GLR classification method provides an improved procedure to optimize classification accuracy. In this case, training data for all available classes are used and the event in question is allocated into one of two or more classes. In addition to proper treatment of the discriminant distributions, the Bootstrap GLR method allows the overall cost of misclassification to be minimized or, alternatively, the false alarm rate associated with misclassifying a particular type of event (e.g., nuclear explosions) to be controlled. The latter is a particularly important aspect since for most monitoring applications we want to limit the number of undetected nuclear explosions to a very small number. Applications of both tests are discussed below.

Preliminary training set analyses. Since the statistics of most discriminants are quite complicated and the validity of classification results depend on their proper treatment, we apply several tests to training sets to determine whether necessary assumptions hold. Although the Bootstrap GLR methods do not require that features are normally distributed, implementation of the tests simplify greatly if this assumption is made. In most cases, however, discriminants do not obey normal statistics. To remedy this situation we first apply two hypothesis tests to determine whether the data are normal. The Wilk-Shapiro test is powerful for detecting skewed distributions and the Anderson-Darling test is powerful for detecting long-tailed distributions. If the data are rejected by either test at fixed significance level, then the features are transformed using Box-Cox transformations. Special cases of Box-Cox transformations are the square root and the logarithm. In general, the procedure automatically finds a power-law transformation that maximizes the normal likelihood function of the transformed data. Once transformed, the data sets are tested again for normality. Although these transformations do not ensure normality, we have found that ~90% of the features of the data sets investigated are accepted as normal after applying the transformations, even though only ~10% of the original features were normal.

Robust application of the GLR classification tests also depend on whether covariance matrices of the features are equal for the various event types. If sample sizes are small or covariance matrices are not significantly different, using a classification method based on a pooled estimate of a single covariance matrix is more robust. If the covariance matrices are significantly different, estimating separate covariance matrices and basing the classification test on this information has greater power. Thus, we have implemented hypothesis tests (F-test and Standard Error test) to determine whether covariance matrices are equal. Based on results, the appropriate GLR classification procedure is applied.

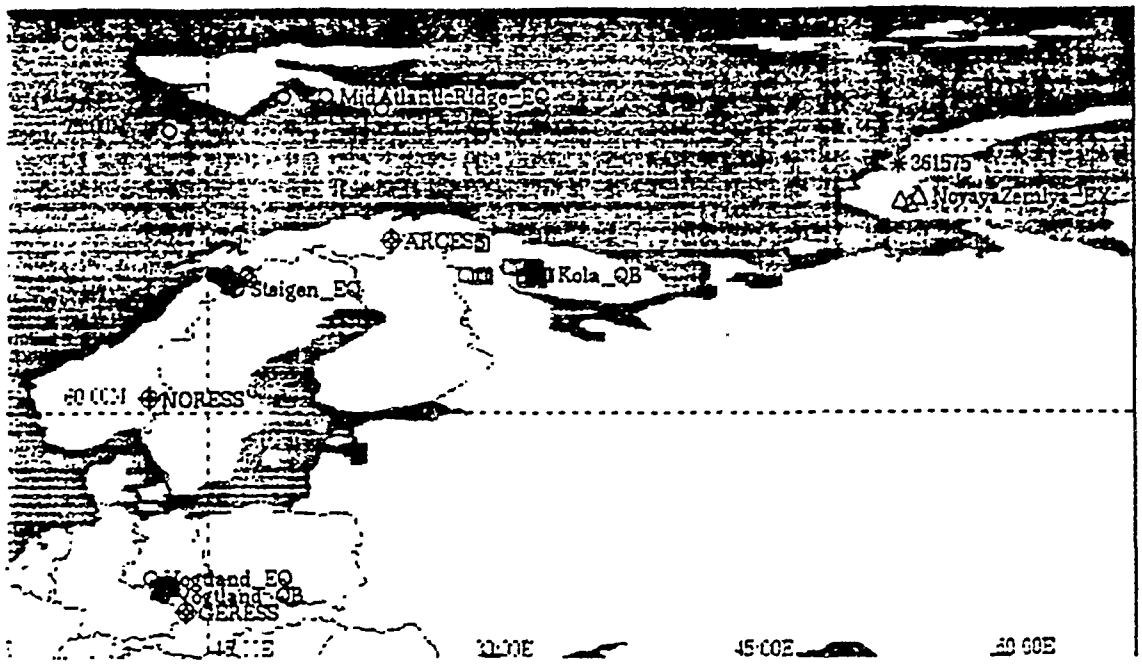

Figure 1. Locations of seismic events and station for data sets used in event identification analysis.

Another practical statistical issue that arises is that of missing data values. Often particular phases are undetected or interference with other events may prevent them from being used. It is nevertheless useful to include such events with partial information in the training sets, rather than discarding them altogether. One approach is mean replacement which simply replaces a missing value of a particular feature with the mean computed for that feature from the remaining events. This is a simple procedure but it does not utilize available information regarding feature correlations. An approach that does so is called the EM (Estimation-Maximization) algorithm (Dempster et al., 1977), which estimates the sufficient statistics of the missing values by regression analysis, based on maximum likelihood estimates (MLEs) from available data, and then updates the MLEs using the available data and the estimates of the missing values. The procedure is iterated until the MLEs converge to within a specified tolerance.

In many cases, the number of available discriminants can be large (see below) and it is not clear from the outset which are the best to use in every situation. Thus, we have implemented and applied statistical procedures to select the optimal subset of discriminants based on training data. Features are first ranked based on error rates estimated using training data and associated with GLR classification for each univariate case. A stepforward selection procedure (Seber, 1988) is then used on the best univariate features to determine which set provides the best multivariate discrimination. The stepforward procedure starts with the best univariate feature and adds successive features as long as there is a continued reduction in the overall error rate estimate.

Data Sets. Training sets used for applications here are based on ISEIS feature data provided by Baumgardt (1993). Data sets consist of 10 earthquakes (EQs) and 13 quarry blasts (QBs) recorded at GERESS which occurred in the Vogtland region in Germany; 53 Kola Peninsula QBs and 25 EQs which occurred in the Steigen region of Norway, recorded at ARCESS; 5 EQs recorded at ARCESS which occurred in the direction of the Mid-Atlantic Ridge; 3 nuclear explosions (EXs) and 1 unknown event at Novaya Zemlya recorded at ARCESS. Locations of the events and seismic arrays are shown in Figure 1.

ISEIS feature data include amplitude ratios, Pg/Lg, Pg/Sn, Pn/Lg, Pn/Pg, Pn/Sn, Rg/Lg, Rg/Sn, and Sn/Lg of either maximum or rms amplitude in 9 frequency bands, spectral ratios of maximum and rms amplitudes of Lg, Pg, Pn, Rg and Sn in 5 different combinations of frequency bands, and the variance, skewness and kurtosis of detrended spectra and cepstra computed by MERSY. Not all features were available for all events and the total number was reduced from 204 to at most 5 for applications described below.

We have performed event identification analysis, including discrete features such as presence of cepstral peaks, using DataSet #1 established by Sereno (1991). We have also performed script-matching including day-of-week as a discrete feature to associate mining blasts with particular mines. The GLR tests appear to perform reasonably well, based on the data and simulation for a mixture of continuous and discrete features.

Monitoring applications and error rate estimates. In the first part of this analysis, we assumed that we have only a few EQs to start with in a particular region. We then treated the QBs as new observed events and used the GLR outlier test to determine whether we can monitor the region for peculiar events. Each EQ was also tested as a new event using the leave-one-out procedure. The significance level was set at 0.05. Using Pn/Sn(max; 8-16 Hz), Pn/Lg(max; 8-16 Hz) and Lg(rms; 2-5 Hz)/Lg(rms; 5-8 Hz) were used as discriminants, we found that all 13 QBs were detected as outliers while, appropriately, none of the EQs treated as new events were. Using the Steigen EQs, 51 of 53 (96.2%) Kola QBs were detected as outliers and 21 of 24 (87.5%) EQs were correctly identified.

In the second part of this analysis, we assessed how error rates are affected when training data are available for all relevant event types. In this case, the GLR classification test was trained on both EQ and QB sets with each event tested using the leave-one-out procedure. As for the outlier test, all of the Vogtland events were correctly classified. For the Kola/Steigen case, 52 of 53 (98.1%) of the Kola QBs and 23 of 24 (95.8%) of the Steigen EQs were correctly classified.

Contaminated training set study. The purpose of this study was to assess whether the GLR outlier test can be used to detect contaminating events in a training set and to assess what impact the contaminated data set can have on error rates. To carry out this study, we randomly selected 2 Vogtland QBs and inserted them in the Vogtland EQ set. We then ran the GLR outlier test on each event in the EQ set using the leave-one-out procedure and the same discriminants as above. If an outlier is detected, it is removed from the set and the remainder are re-tested. In this case, both QBs were detected on the first pass. If the QBs are not removed from the EQ training set, 2 other QBs of the remaining 11 are undetected when subsequently tested. This analysis was also repeated by randomly selecting 2 Kola QBs and inserting them in the Steigen EQ set. Only one of the QBs was detected on the first pass, but once removed, the other one was also detected. If the 2 Kola QBs are not removed from the Steigen EQ training set, 7 other QBs of the remaining 51 are undetected when subsequently tested.

Event identification results for event 361575 at Novaya Zemlya. The GLR outlier and classification tests were applied to an event recorded at ARCESS which occurred at Novaya Zemlya (NZ) on 31 December 1992. (We will refer to this event by its ORID=361575.) Discriminants used here consist of Pn/Sn(max) ratios in five frequency bands, 4-6, 5-7, 6-8, 8-10, and 8-16 Hz recorded by ARA0. Data for four events at NZ were provided, three of which are known nuclear explosions (EXs) and the fourth is the event in question (Figure 1). For comparison, we also used the Kola and Steigen data sets, as well as the 5 EQs which occurred in the direction of the Mid-Atlantic Ridge. The same features, obtained from seismograms recorded by ARA0, were used. Figure 2 shows a scatter plot of the amplitude ratios in the 5 frequency bands for all event types.

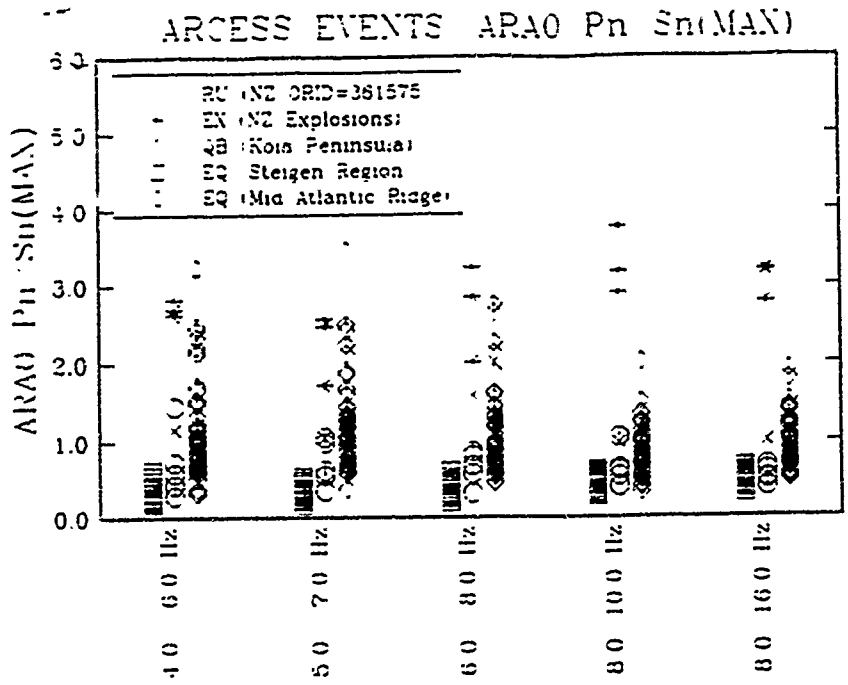

Figure 2. Plot of Pn/Sn(max) in 5 frequency bands for events recorded by ARA0.

Event 361575 was tested as an outlier of each of the 4 data sets. Results are represented graphically in Figure 3 for the 4 tests. The distributions shown are smoothed histograms of the likelihood ratio (LR) obtained by bootstrapping the corresponding training set. The vertical lines shown correspond to critical values of the tests for various significance levels given in the lowest legend. The LR for 361575 is denoted by the triangle marker. The training set and discriminants are listed in the upper legends. Figure 3 shows that event 361575 is rejected as a belonging to the same populations as NZ EXs or Steigen EQs at the 0.025 significance level. It is also rejected as belonging to the same population as Mid-Atlantic Ridge EQs at the 0.05 significance level. It is not rejected as belonging to the Kola QB population unless the significance level is set at 0.345 or greater. Thus, it is not considered an outlier of the Kola QB population.

GLR classification tests were also applied to event 361575. It was first tested as belonging to NZ EXs versus the alternative that it belongs to Kola QBs. It was then tested as belonging to the combined Steigen/Mid-Atlantic Ridge EQ population versus belonging to Kola QBs. Last, it was tested as a NZ EX versus an EQ. Figure 4 shows the results of the first 2 tests. The distributions shown are smoothed histrograms of the LR, bootstrapped from the training data, where the H_0 distribution corresponds to LRs if the new event is from the first population and the H_1 distribution corresponds to LRs if the new event is from the second population. The thick vertical lines are values of the LR which minimize the overall misclassification rate. The other lines correspond to various significance levels of rejecting the null hypothesis (H_0). Figure 4 shows that 361575 is rejected as a NZ EX and as an EQ, both at the 0.01 significance level. Classification based on minimizing overall error rates also allocate 361575 to the QB population.

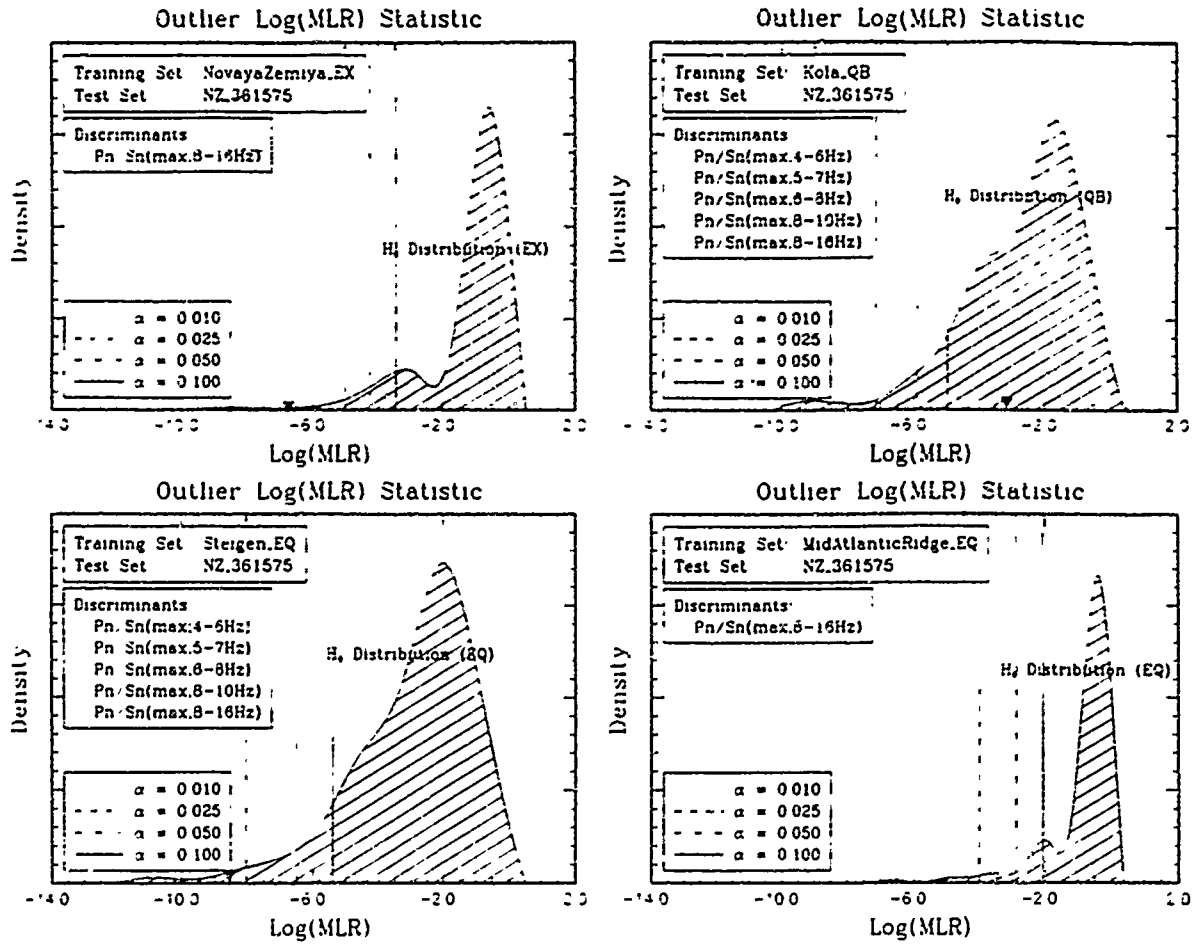

Figure 3. GLR outlier test results for Novaya Zemlya event 361575.

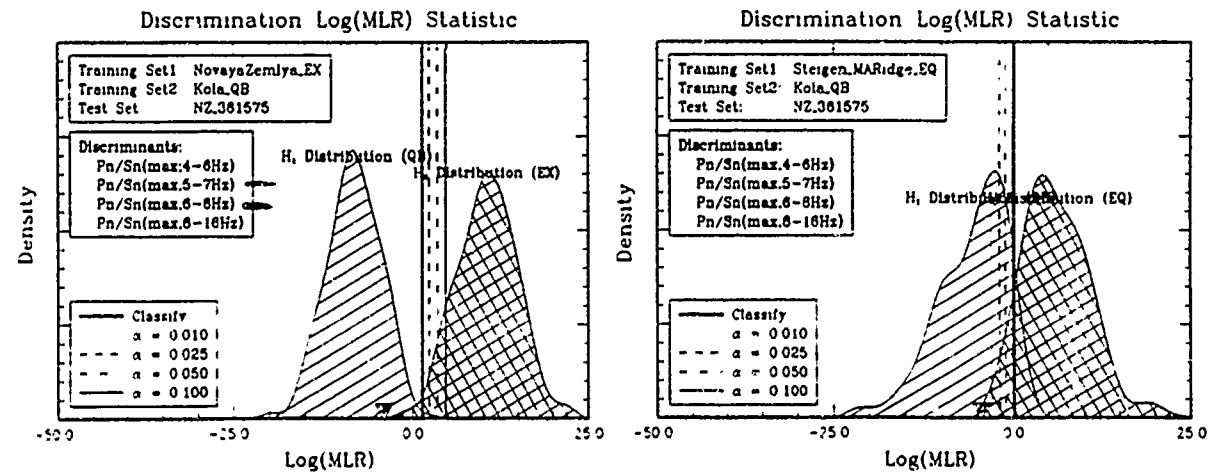

Figure 4. GLR classification results for Novaya Zemlya event 361575.

Although our quantitative measures differ, our qualitative results are the same as those of Baumgardt (1993), who also concluded, based on a neural net approach and a similar set of discriminants, that 361575 looks most like a Kola QB. These results should be tempered by the caveat that there may be significant path differences to ARCESS from the Kola Peninsula, the Steigen region and Novaya Zemlya which warrant investigation. Note, however, that our outlier test based on the 3 NZ EXs is not subject to this caveat. Thus, until path differences can be investigated suitably, this test may provide the only reliable statistical evidence that event 361575 was not a nuclear test. Even so, a larger nuclear explosion training set for NZ events is desired to strengthen our conclusions.

CONCLUSIONS AND RECOMMENDATIONS

Applications of the GLR outlier and classification tests demonstrate that they provide useful event identification procedures under a wide range of conditions. Not only do they treat the statistics correctly, but they also allow monitoring to be performed in new regions where training data are limited and lacking ground-truth. Fisk et al. (1993) provide a more complete description of these results, applications to other data sets, and applications of preliminary training set analyses. Work is being performed currently to implement all of the methods described above, as well as novel graphical displays, in a software package with a X-Window graphical user interface.

REFERENCES

Baek, J., H. L. Gray, and W. A. Woodward (1992). A Generalized Likelihood Ratio Test in Outlier Detection or Script Matching, submitted to *J. Am. Stat. Assoc.*, Southern Methodist University.

Baek, J., H. L. Gray, W. A. Woodward and M.D. Fisk (1993). A Bootstrap Generalized Likelihood Ratio Test in Discriminant Analysis, submitted to *J. Am. Stat. Assoc.*, Southern Methodist University.

Baumgardt, D.R. (1992). Investigation of Seismic Discriminants in Eurasia, SAS-TR-92-81, ENSCO, Inc.

Baumgardt, D.R. (1993). Private Communication.

Dempster, A.P., N.M. Laird and D.B. Rubin (1977). Maximum Likelihood Estimation from Incomplete Data via the EM Algorithm, *J. Royal Stat. Soc.*, **39**, 1-38.

Fisk, M.D., G.L. Gray and G.D. McCartor (1993). Applications of Generalized Likelihood Ratio Tests to Seismic Event Identification, MRC-R-1444, to appear as a Phillips Laboratory Techical Report, Mission Research Corp.

Gray, H.L., W. A. Woodward, G.D. McCartor and M.D. Fisk (1993). A Bootstrap Generalized Likelihood Ratio Test in Discriminant Analysis, to appear in *Proceedings of the Fifteenth Annual Seismic Research Symposium*, Phillips Laboratory, Hanscom AFB, MA.

Seber, G.A.F. (1984). Multivariate Observations, John Wiley, New York.

Sereno, T.J., and G.B. Patnaik (1991). Data to Test and Evaluate the Performance of Neural Network Architectures for Seismic Signal Discrimination, PL-TR-92-2110(I), Phillips Laboratory, Hanscom AFB, MA, ADA254413.

An Investigation of the Practical Limits of Accuracy for Relative Seismic Event Locations

Cliff Frohlich[1] and Katharine Kadinsky-Cade[2]

[1]Institute for Geophysics
University of Texas at Austin
8701 North Mopac
Austin, Texas 78759
cliff@utig.ig.utexas.edu

[2]Earth Sciences Division
Geophysics Directorate
Phillips Laboratory, Hanscom AFB
Massachusetts 01731
kadinsky@doc.plh.af.mil

Contract No. F19628-91-K-0026

Objectives:

The usual process of locating a cluster of seismic events is hierarchical, i. e., one begins with available low-quality data and simple location methods, then, one applies increasingly sophisticated methods to better-quality data as it becomes available. Our primary objective is to develop practical and flexible location software which is appropriate for the entire location process. This software must:

- Be usable with either local network or teleseismic phase arrival data;
- Determine locations using P and S phases as well as more "exotic" phases such as ScP or PKP;
- Permit a variety of schemes for weighting residual quality, and permit the user to choose either single-event or joint locations;
- Provide quantitative information assisting the user to evaluate location quality.

As a secondary objective we shall evaluate the attainable accuracy of relative seismic event locations in several practical situations. For this, we shall utilize the program we have developed and apply several different location methods to a variety of phase arrival data sets, each representing a different common location problem.

Research Accomplished:

1. Practical Software for Seismic Event Location

As a practical product of this research, we have developed a flexible Fortran program for seismic event relocation. This program, called **TexFlex**, has several special features which make it useful for routine research applications:

- The program calculates travel time residuals using either user-supplied flat-earth velocity models, using teleseismic look-up tables like the Jeffreys-Bullen (1970) tables, or using the IASPEI91 teleseismic software described by Kennett (1991) and Kennett and Engdahl (1991). If desired, the user can choose to use different travel time models for calculating residuals at different stations.
- The program performs either single-event locations or joint hypocenter (JHD) relocations using the method of Frohlich (1979).
- For JHD relocation, the input file structure allows the user to group station correction variables so that several stations or station/phase combinations are assigned the same station correction variable. Thus, if desired one can assign the same correction to all stations in the same tectonic regime, or to two nearby stations with different names. The user can choose to assign either the same or different station correction variable to different phases arriving at the same station.

• The program allows the user to select from a variety of weighting schemes. The least-squares residual weights may depend on user-assigned phase quality, on residual absolute value, or on the azimuthal distribution of observing stations.

• As described in the following section, the program can calculate the volume of the smallest convex polyhedron enclosing groups of hypocenters, if the user so chooses.

• The input file structure requires a minimum of editing as the user chooses different relocation options, or relocates different groups of seismic events with different combinations of stations. There are numerous output files, some in identical formats as the input files, and others including a broad variety of tablular and statistical information to help the user evaluate the relocation process.

A preliminary version of the **TexFlex** program is now available for distribution. For more information, please contact the first author by email.

2. The Utility of the "Volume" of a Cluster of Seismic Events

In situations where all members of a group of seismic events seem to originate from nearly the same focus, it is reasonable that the "volume" of a particular cluster is a measure of relative location accuracy. We have developed a straightforward algorithm for determining the volume of the smallest convex polyhedron which encloses a set of points. This volume is unique, and independent of the coordinate system used to describe the points. For seismic events the set of points can be their hypocenters, and the algorithm thus finds the smallest enclosing volume. Output from this algorithm can easily be used to plot maps and cross sections of the bounding polyhedron (e. g., Figures 1 to 3).

The algorithm finds the triangular faces of the bounding polyhedron one-by-one, starting with the lowermost faces and working upward. The routine considers triples of hypocenters to define planes, and knows that such a triple defines a polyhedron face of all hypocenters lie on one side of the plane. The search for polyhdedron faces gains efficiency because the program searches triples of hypocenters going from deepest to shallowest hypocenters, and does not need to search hypocenters deeper than the "bounding polygon" formed by the edges of the faces found so far. We have successfully used this algorithm to determine volumes for data sets having more than 4000 points.

While **TexFlex** uses the polyhedron volume as a measure of location accuracy, it is useful for other reasons as well. For example, Kostrov (1974) noted that the strain ε released by earthquakes occuring within a volume V is related to their seismic moment tensors M_i by:

$$\varepsilon = \Sigma M_i/(2\mu V)$$

where μ is the rigidity. Thus, our algorithm permits us to determine the strain release associated with the moment tensors reported for groups of earthquakes.

The bounding polyhedron also is an essential tool if one wishes to evaluate how edge effects influence statistical tests. The basic approach is to compare results when the tests are applied to both real and simulated sets of data. If there are N points, of which M form the bounding polyhedron, the procedure is to:

• Determine which M points form the bounding polyhedron for the real data,

• Include these M points in the simulated data set;

• Use some appropriate random procedure to add N-M more points to the simulated data set, taking care that these points lie within the interior of the bounding polyhedron.

This procedure assures that the real and simulated data sets have precisely the same boundary. Thus, the boundary will not be the source of any differences between applications of the statistical test to the real and simulated data.

3. Application to Phase Arrivals in Three Geographic Regions

We are presently investigating seismic events in three different geographic regions, and comparing locations obtained from a variety of data types. The event types, geographic regions, and data types are:

• Nuclear explosions from Mururoa in French Polynesia located using teleseismic data obtained from cross-correlation of digital seismograms, and using phases reported by the International Seismological Centre (ISC).

• Earthquakes from the intermediate-focus "nest" occurring near Bucaramanga, Colombia (Schneider et al., 1987), located using data obtained from reading selected microfiche seismograms at Columbia University, using data obtained from cross-correlation of digital seismograms, and using phases reported by the ISC.

• Microearthquakes occurring in a region of intense shallow activity west of Efate, Vanuatu, southwest Pacific (Chatelain et al., 1986), located using data recorded by a regional land station network, and using data recorded by a temporary network of ocean bottom seismograph stations (Frohlich et al., 1990).

Relocations of earthquakes occurirng in a localized nest near Bucaramanga, Colombia (Figure 1), illustrate typical results of our investigations. For 26 events, our relocations were more strongly clustered than those reported by the ISC, regardless of whether we relocated using phases reported by the ISC or teleseismic phases we personally reread (Figure 3 and Table 1). These results suggest that the nest has dimensions smaller than 10-20 km. In constrast, Schneider et al. (1987) used phases read from a temporary local network and determined nest dimensions of 2-4 km.

Conclusions:

The new scheme we have developed for associating a unique volume with a group of hypocenters may have a variety of different applications in seismology. Its most straightforward use is when all hypocenters in a group apparently originate from nearly the same source region, and thus the volume is a powerful measure of the relative location error.

The relocation program we have developed, **TexFlex**, uses methods developed prior to this study for determining travel times, for weighting phase arrival times, and for finding improved locations by least squares. However, the program is unusually flexible, and thus is especially useful when a research project will require relocations for a broad variety of seismic events, using phases from both nearby and very distant stations, and reporting data of variable quality.

Our investigations confirm that the strategy for obtaining the most accurate locations for seismic events depends strongly on the type of data available. To locate teleseismic events when data are numerous but of poor or unknown quality, the optimum strategy is to select a phase weighting scheme where the weights depend both on the size of the residual and on the azimuthal distribution of stations. However, when there exist

exceptionally high-quality data at a few stations, the best approach often is to determine a reliable set of station corrections and obtain final locations using single-event methods. Locations obtained using regional network data are almost never reliable unless the network provides a good azimuthal distribution of stations and unless the data include a sufficient number of both P and S phases.

References:

Chatelain, J.-L, B. L. Isacks, R. K. Cardwell, R. Prevot and M. Bevis. Patterns of seismicity associated with asperities in the central New Hebrides island arc, *J. Geophys. Res., 91*, 12497-12519, 1986.

Frohlich, C. An efficient method for joint hypocenter determination for large groups of earthquakes, *Comput. Geosci., 5*, 387-389, 1979.

Frohlich, C, R. Louat and Y Nakamura. Earthquake activity in the southern Vanuatu arc recorded by the Texas digital OBS, *Mar. Geophys. Res., 12*, 253-267, 1990.

Jeffreys, H. and K. E. Bullen. *Seismological Tables*, Grey Milne Trust, London, 50 p., 1970.

Kennett, B. L. N. (editor). *IASPEI 1991 Seismological Tables*, Australian National University, 167 p., 1991.

Kennett, B. L. N. and E. R. Engdahl. Travel times for global earthquake location and phase identification, *Geophys. J. Int., 105*, 429-465, 1991.

Kostrov, V. V. Seismic moment and energy of earthquakes, and seismic flow of rock, *Izv. Acad. Sci. USSR Phys. Solid Earth*, Engl. Transl. *1*, 23-44, 1974.

Schneider, J. F., W. D. Pennington and R. P. Meyer. Microseismicity and focal mechanisms of the intermediate-depth Bucaramanga Nest, Colombia, *J. Geophys. Res., 92*, 13913-13926, 1987.

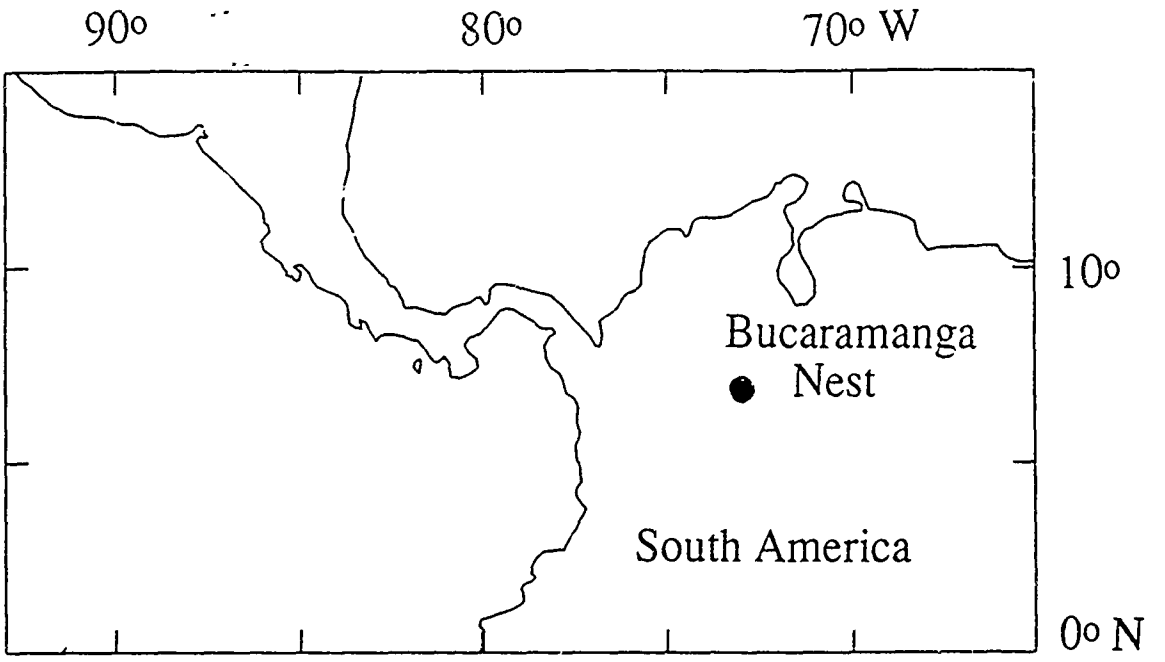

Figure 1. Location map for the earthquake nest near Bucaramanga, Colombia.

Table 1. Volumes and surface areas of minimum-volume convex polyhedrons enclosing four sets of hypocentral locations for the Bucaramanga nest.

Data Set	Volume (km^3)	Surface Area (km^2)
ISC locations[a]	2085	1026
ISC phases: relocations[b]	1635	911
Phases reread by authors[c]	1299	690
Schneider et al. (1987)[d]	11	34

[a]These are hypocentral locations reported in the ISC Bulletin for 26 selected events.

[b]These are relocations of the same 26 events, determined using phase arrival data reported in the ISC Bulletin at 28 selected stations.

[c]These are relocationsof the same 26 events, determined using phase arrival data personally reread by the authors at 18 selected stations.

[d]These are locations reported by Schneider et al. (1987) for 27 events occurring in June and July, 1979, located by a temporary local network.

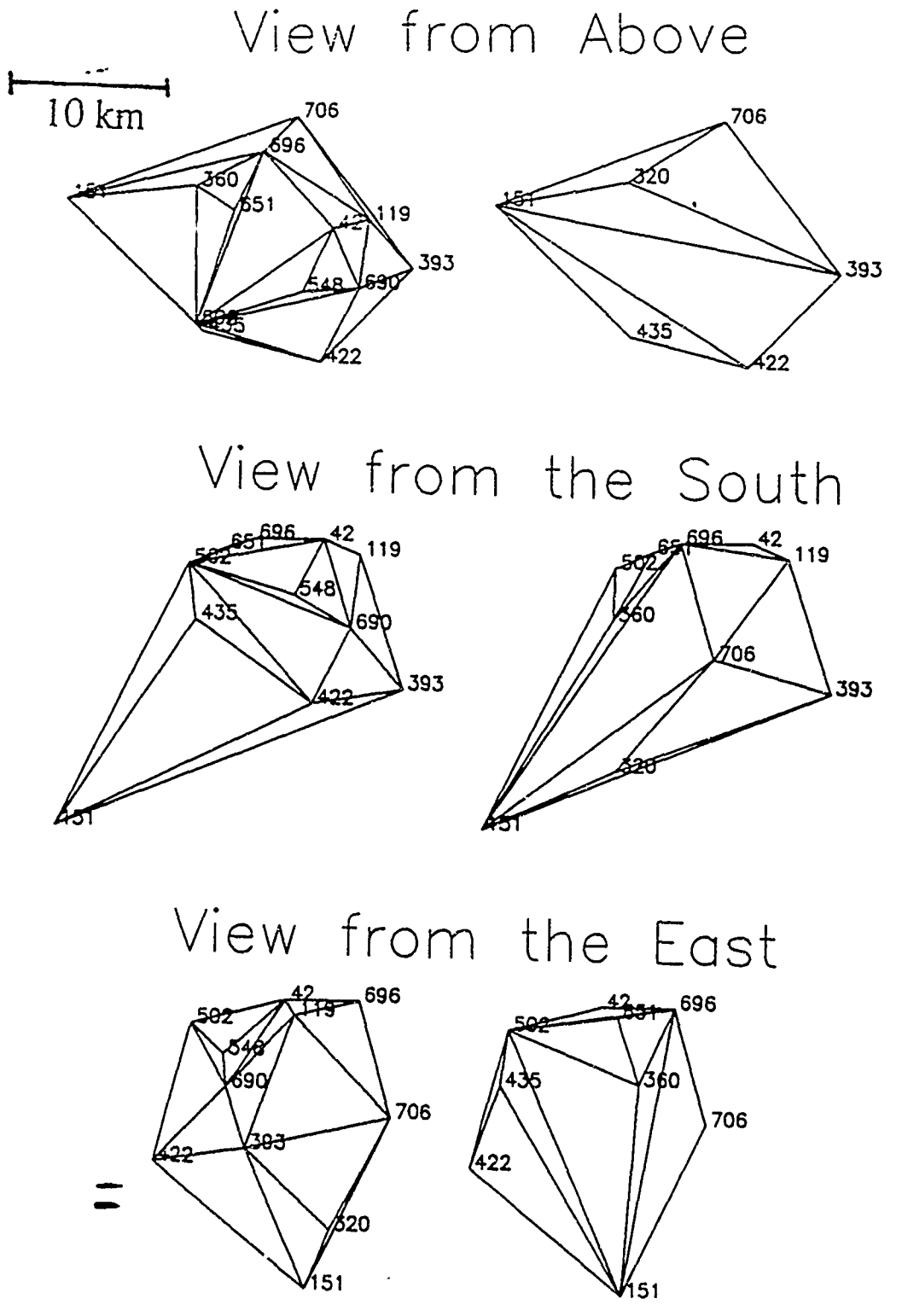

Figure 2. Six views of the faces forming the bounding polyhedron enclosing 26 hypocenters in the Bucaramanga nest, located using phase arrival times read by the authors from microfiche seismograms. At left are views of upper surface (view from above) or front surface (views from the east or south). At right are views of lower surface (view from above) or back surface (views from the east or south). Numbers to the right of each vertex are event identification numbers.

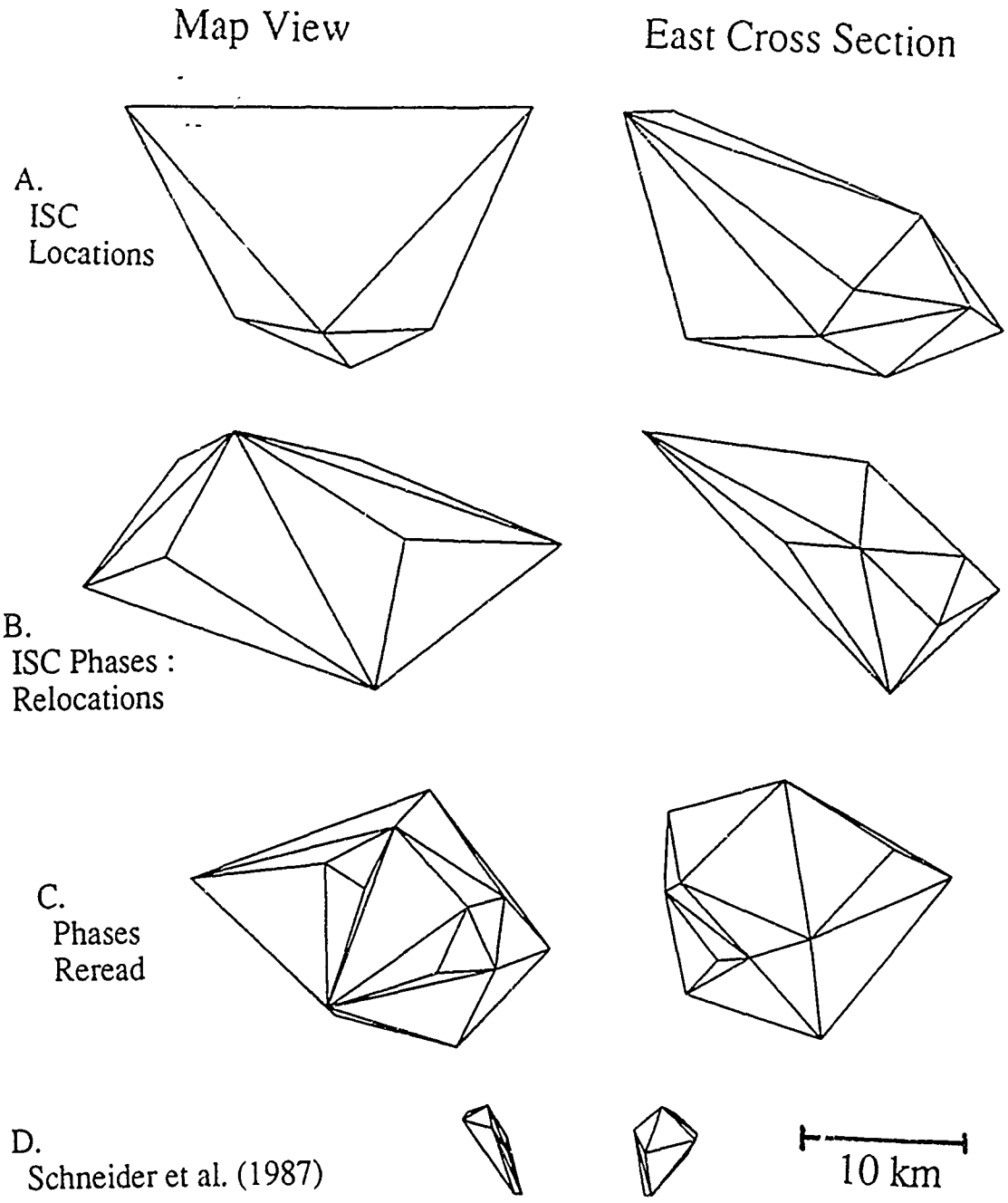

Figure 3. Bounding polyhedrons for four sets of hypocentral locations in the Bucaramanga nest. At left are map views of the upper surfaces of polyhedrons. At right are cross sections as viewed from east, and front surfaces of polyhedrons. However, so that north and south correspond to the map views, these cross sections are rotated 90°, so that the upward vertical is to the left and downward vertical is to the right. A) Polyhedron for 26 hypocenters occurring from 1965 to 1986, locations as reported by the ISC; B) Polyhedron for same 26 hypocenters, relocated with a weighted least-squares JHD method using phase arrivals reported by the ISC at 28 selected stations; C) Polyhedron for same 26 hypocenters, relocated with a weighted least-squares JHD method using data personally read by the authors at 18 selected stations; D) Polyhdedron for 27 hypocenters with locations reported by Schneider et al. (1987), determined from a temporary local network.

CSS Ground-Truth Database: Update and Case Study

Lori Grant, Floriana Ryall, and John Coyne
Center For Seismic Studies
1300 North 17th Street
Arlington, VA 22209

Contract No. F29601-92-C-0005

Objective

The current concept for the U.N. Conference on Disarmament, Group of Scientific Experts "Technical Test 3" includes three levels of data collection. An "Alpha" network of sensitive three-component and array stations provides the basic detection capability of the system. Data from the Alpha network are telemetered continuously to an International Data Center (IDC) where they are processed automatically for detection and location of seismic events. Post-detection analysis is enhanced by data from open seismic stations of a "Beta" network. Disk loops at these stations will be queried automatically by the IDC, after initial event detection by the Alpha system, to obtain supplementary waveform data needed to accurately locate the events and determine their magnitude.

The GSE concept also provides for alphanumeric data from local and regional networks, called "Gamma" networks. Gamma information obtained through the IDC will potentially augment the CSS Ground-Truth Database. These data can be used for a number of purposes, including the calibration of seismic characteristics of the regions containing the Gamma networks. By such calibration, the capability of the Alpha and Beta components of the system to accurately locate events can be improved over time.

The objective of this paper is to provide a case study simulating how Gamma (or ground-truth) information can be used to improve the performance of the GSE system. The particular case analyzed consists of a number of mine "tremors" (earthquake-like events induced by mining activity) in the Upper Silesian Coal Basin in Poland. The events analyzed were initially mislocated because of phase misidentification by the Intelligent Monitoring System (IMS, Bache *et al*, 1990), and provide an illustration of the problems that will be encountered in a future global monitoring system. The coal basin has several features that would be of concern if such events occurred in or near a country identified as a potential nuclear proliferator:

- The mine tremors in the Upper Silesian Coal Basin are sizeable, with ML≈1.5-3.5, which includes the magnitude range expected for a fully or partly decoupled 1 kiloton nuclear explosion.

- Mine tremors are of general interest to nuclear monitoring research because in some areas they can be generated in a planned way (triggered by small blasts), and as a result might be used to help conceal simultaneously detonated decoupled nuclear shots.

- The Upper Silesian Coal Basin is close to the border between Poland and the Czech Republic. As a result, events are erroneously located in a wrong country if seismic phases are incorrectly interpreted by the IMS. Under a Comprehensive Test Ban Treaty (CTBT) monitoring regime, this could lead to "false alarms" where suspicious events are mistakenly located in a country in which they had not, in fact, occurred.

Research Accomplished

Upper Silesian Coal Basin (The followint two paragraphs are derived from letters from Dr. P. Wiejacz and Dr. S.J. Gibowicz of the Polish Academy of Sciences)

In the Upper Silesian Coal Basin there are approximately 50 underground mines within a 40 km radius of the city of Katowice. Exploitation of the coal is made by the longwall mining method in which a pilot tunnel of a few hundred meters length is first drilled and several long-walls, each of about a hundred meters length, are extended to the sides. Generally, the excavated space is not backfilled, except when it is in the vicinity of an important mining installation. The mining is carried out at many levels, reaching 1200 m underground at one mine

Strong seismic events often occur when the working face crosses a remnant in a layer above, such as a dike. Some mines use blasts for construction of the pilot tunnels, but the charges are not large enough to be registered at regional distances. Preventive blasts are also sometimes used. If a gap in seismicity is observed, a preventive blast may be ordered for the purpose of off-setting a strong event. All events of energy above 10^5 joules are well-located horizontally by underground seismic networks operated by the mines. The horizontal location errors may be different at different mines, but in most cases do not exceed ± 20 meters. Depth determination is poorly constrained as the seismic instruments are generally all located at the same level as the mining operation. Usually it is assumed that the events take place at the mining level.

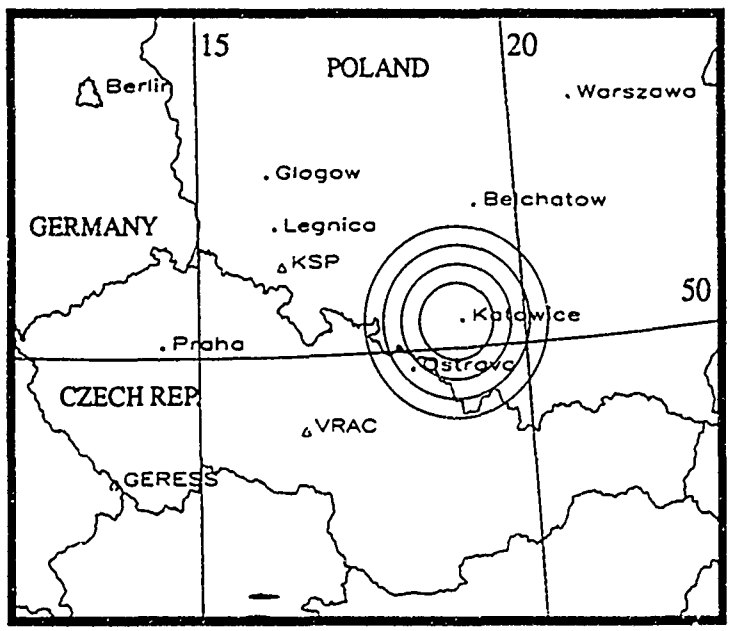

Figure 1: Geographic location of Upper Silesian Coal Basin. Frequent mining-induced tremors in Poland take place in two regions: the Lubin Copper Basin between the cities of Legnica and Glogow; and the Upper Silesian Coal Basin centered around the city of Katowice. Radii of the rings centered on the Upper Silesia area are 40 - 100 km. Mining-induced events also occur on the Czech side of the border near the town of Ostrava (P. Firbas, personal communication). A third area of potentially large mining-induced events is near the city of Belchatow, but no large tremors have occurred in that area in the last three years.

Use of Gamma Network for Regional Calibration

In early 1993 S. J. Gibowicz provided a list of well-located mining induced tremors from the Upper Silesian Coal Basin for the first six months of 1991. Figure 2 shows the location of these 275 events. While there appears to be distinct spatial distribution and groupings of the events, individual mines are not identified by name in the list. The events were accurately located by underground seismic networks operated by the mines for the purpose of monitoring their own events. These networks constitute the simulated "Gamma" network.

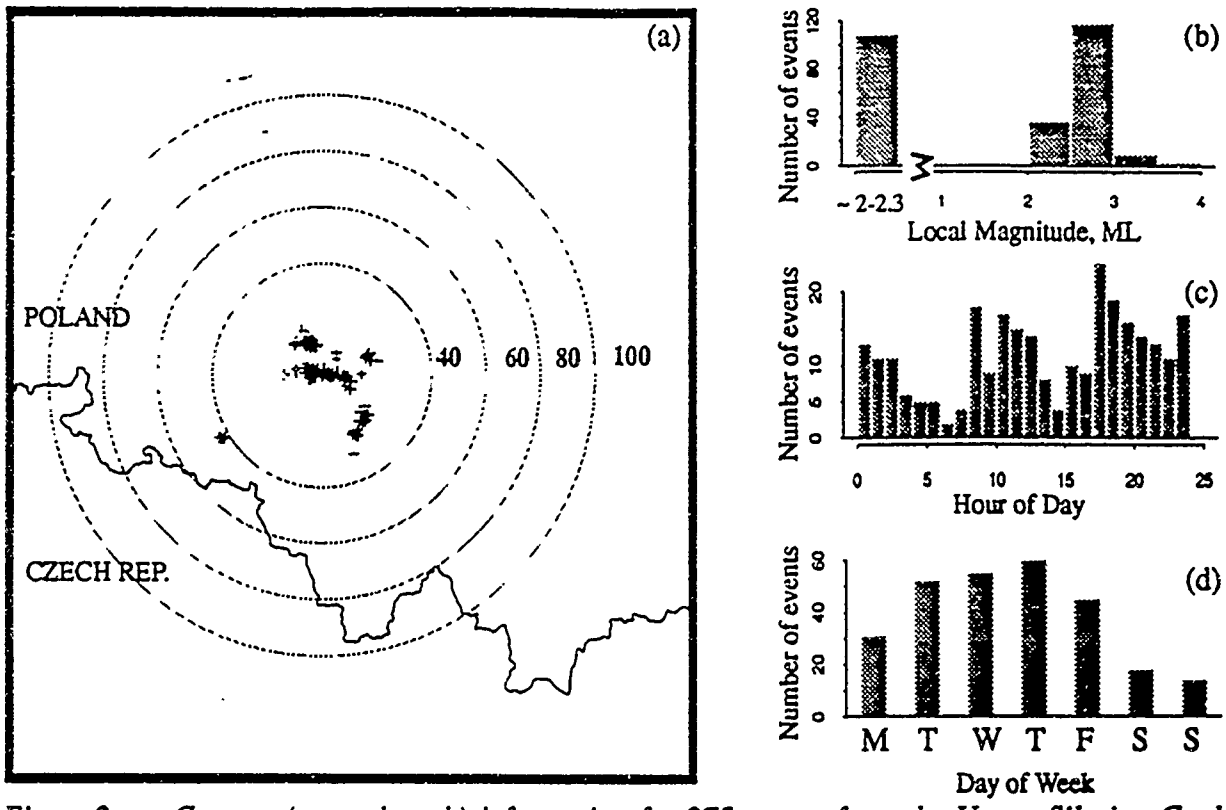

Figure 2: Gamma (ground-truth) information for 275 events from the Upper Silesian Coal Basin. (a) Event locations based on mining seismic networks. Rings have radii of 40-100 km, centered on the average latitude and average longitude of the 275 events. (b) magnitude distribution, ML, calculated by Gibowicz. Bar on left represents events with no calculated Ml, but are estimated between 2.0 and 2.3. (c) Diurnal event distribution. Some events are triggered by small blasts, usually detonated during shift changes. (d) Day-of-week distribution.

Re-analysis of Alpha with knowledge from Gamma

A total of 31 events resulted from a search for events common to both the Gamma and Alpha bulletin. The majority of the Alpha locations fall 40-100 km short of the corresponding Gamma locations. The first detected phase at GERESS, 3.7 degrees from the events, was consistently interpreted as Pn in the Alpha bulletin.

After carefully re-analyzing these events, it was determined that the first detected phase at GERESS is not Pn. The Pn phase, due to its emergent quality and small amplitude, was not detected at GERESS for any of these events. The first detected phase was Pg. This observation was confirmed by the velocity calculated by the automatic signal processing routine (SIGPRO) as being between 6.1 and 6.9 km/s, and by the improvement in location when the correct phase identification is used in calculating the location. Figure 3 shows the locations of these events before and after re-analysis compared to the locations provided by the Gamma network. The average location error in the Alpha bulletin of 50 km was reduced to 19 km. Although other changes were made during re-analysis, such as re-timing the Lg phase or adding the Pn phase where visible, the primary factor in improving the locations was the correct identification of the initial P phase detected at GERESS.

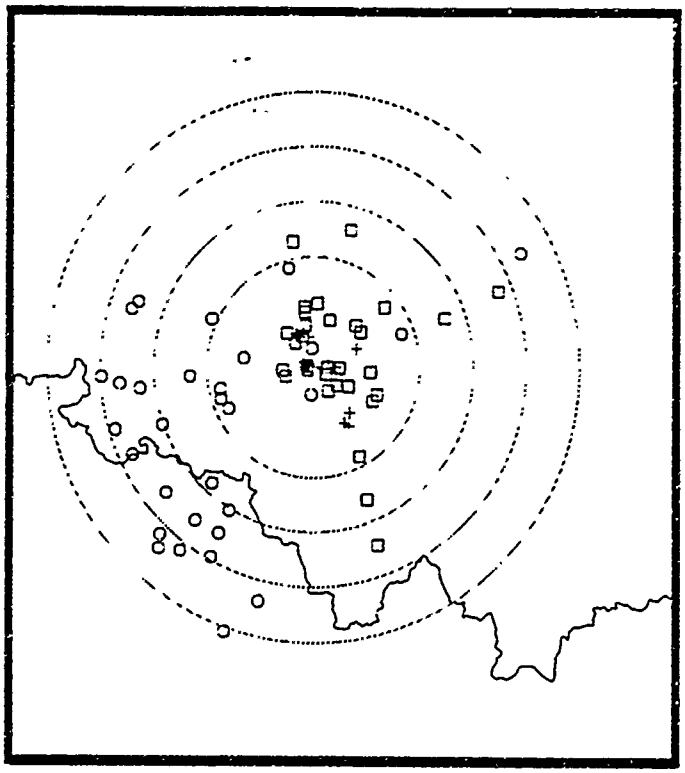

Figure 3: Results of careful re-analysis of 31 events from the Alpha bulletin with matching Gamma information. Rings have radii of 40-100 km The average distance between Alpha locations (circles) and Gamma locations (crosses) is 50 km. The locations after re-analysis (squares) have an average distance error of 19 km. Eleven epicenters moved from the Czech Republic into Poland. Location scatter in the NW-SE direction is due to azimuth error. Location spread in the NE-SW direction is due to scatter in time picks. The event farthest to the east was located by NORESS and ARCESS without GERESS contribution. For all other events, which were recorded at GERESS, the primary factor in improving location was to correct the identification of the first detected P phase.

Since Pg is the first detected arrival at distances where Pn is assumed to be first, the phase was consistently misidentified as Pn both by the Expert System Association and Location program (ESAL) and the many analysts involved in processing the data. Other authors have documented similar distance errors due to misidentification of the first detected P phase at NORESS when the Pn phase is undetected (Vogfjord and Langston , 1990; Baumgardt and Ziegler, 1988).

Calibration of Alpha station

Of the 31 re-analyzed Alpha events described in the previous section, 14 simply had the wrong phase identification for the first arrival with no other compounding errors. This group of 14 events was used as a "control" group to characterize this error and to quantify the effect of this one error on location. The characteristics of the 14 "control" events are: velocity of 6.53 ± 0.41 km/s for the phase labeled "Pn"; azimuth 66.2 ± 4.2 degrees for the phase labeled "Pn" (true station-to-event azimuth averages 65.6 degrees); and Alpha magnitude range, ML, between 2.3 and 2.7 (the corresponding Gamma ML range is 2.6 - 3.0).

The effect of correcting only the phase name of the first arrival was tested on the "control" group. Pn was renamed Pg and the events relocated. Figure 4 shows the locations before and after this test. The relative locations are the same, but all events moved 49 km away from GERESS in the direction of the estimated station-to-event azimuth. The new locations were calculated exactly as in the Alpha bulletin except for the phase names. Thus, any errors in azimuth and Lg - Pg time still are apparent in the location scatter.

Based on the characteristics of the "control" events, a larger set of events was selected in order to estimate the number of events in the Alpha bulletin from this area which may be subject to the same phase misidentification as described above. A total of 96 events fit the criteria derived

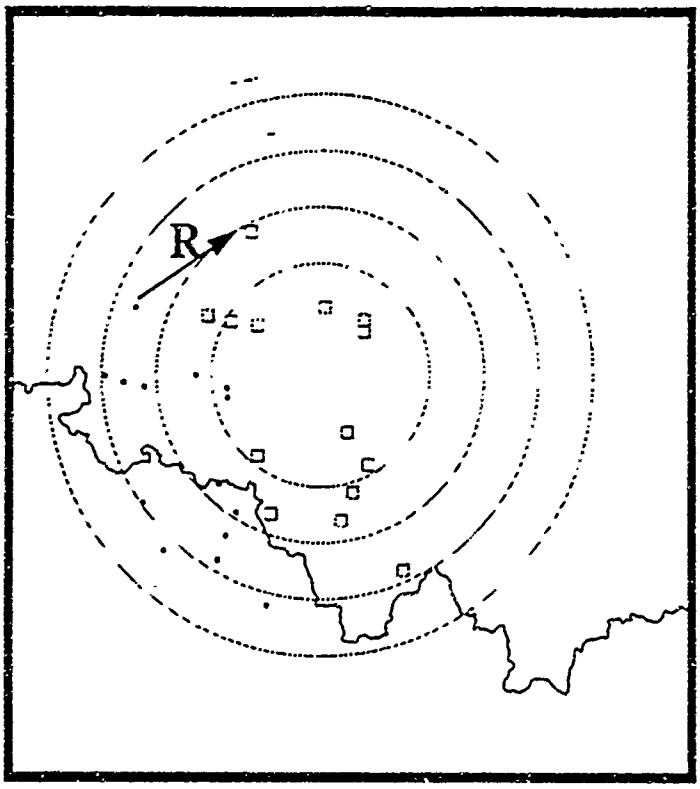

Figure 4: Relocation of "control" group. The control group is the subset of 14 events from the 31 re-analyzed events which had the simplest phase identification errors: Pg misidentified as Pn. Small squares are original locations in Alpha bulletin. Large squares are locations after reinterpreting Pn as Pg. The average relocation vector, R, has magnitude 49 km and direction 70 degrees. Events have the same relative location before and after the relocation test but are shifted away from GERESS in the directions of the station to event azimuth. New locations were calculated exactly as in the Alpha bulletin except for the phase names. Scatter in locations due to azimuth and Lg-Pg time remains. This test quantifies the effect of the one error common to all events in the set of 31.

from the "control" events. The relocation test on this larger group of events was not as simple as the "control" group because almost half of the events had compound phase identification errors in addition to the simple case where Pg was misidentified as Pn. Events were sorted by their characteristic problems into the 5 groups shown in Table 1.

Table 1: Phase Identification Corrections for Re-location Test

Group, based on Alpha phase identification	Members	phase id corrections
Pn, Pg, Lg - analyzed correctly	3	no changes
Pn, Lg	57	Pn -> Pg
Pn, Pg, Lg - P's picked late	4	Pn -> Pg, Pg -> Px
Rg	20	Pn -> Pg, Rg -> Sx
Sn	12	Pn -> Pg, Sn -> Sx

Figure 5 shows the locations before and after the relocation test. As expected, the main effect was to shift events away from GERESS. The number of events inside the smallest ring (40 km radius) increased from 16 to 57. All other events are considered outliers and have various explanations for their locations. Events that are farther from GERESS generally have an Lg time that is picked late. Events north and south of the 40 km ring generally have azimuth errors. The closer events have an Lg-Pg time that is smaller than the 57 events inside the ring. These closer events may in fact be located in the Czech Republic near the Ostrava mining region or other mine or quarry sites. In the case that they do belong in one of these other regions, their location is also improved significantly by the correct phase identification of the first arrival at GERESS.

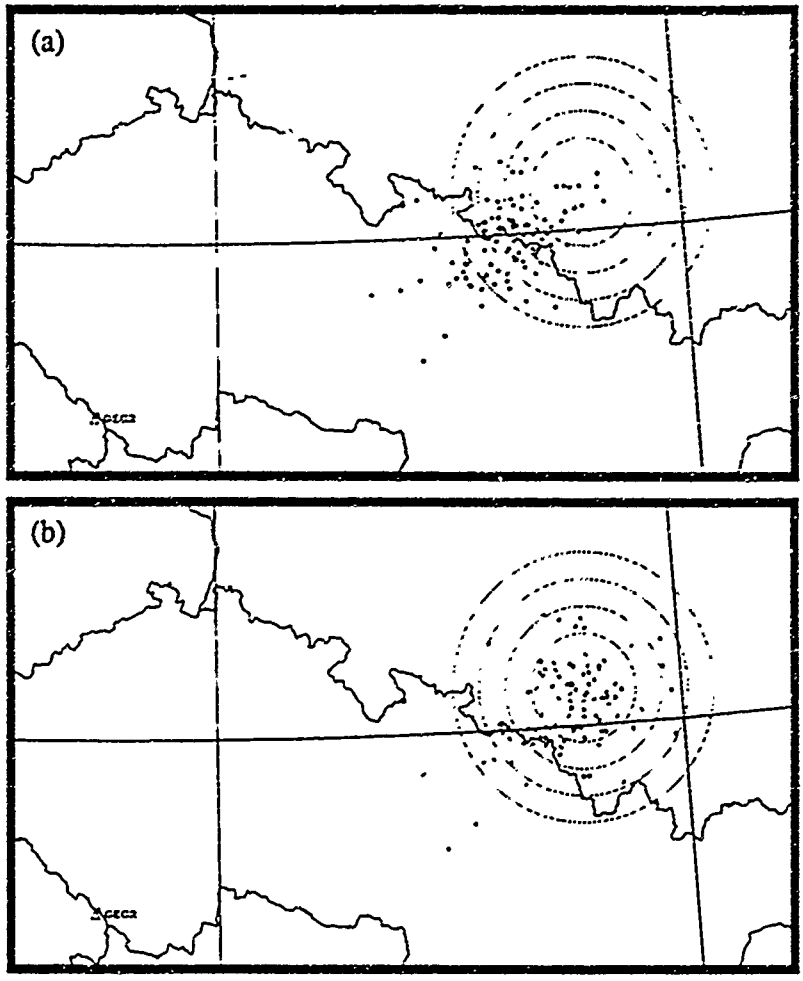

Figure 5: Relocation test on 96 events selected from Alpha bulletin based on characteristics of the 14 "control" events in Figure 4. (a) Locations from Alpha bulletin. (b) Locations after making the phase identification corrections in Table 1 while keeping all other location parameters constant. The main effect on locations is to shift the events away from GERESS. The number of events inside the smallest ring (40 km radius) increased from 16 to 57. Events outside of the 40 km ring are considered outliers. Additional phase identification errors for events associated with this area have been documented, such as the identification of Rg and Sn phases which are, in general, not observed at GERESS from the Upper Silesian mining area.

Conclusions and Recommendations

The use of knowledge from Gamma networks in an effort to improve automatic locations produced by Alpha networks has been outlined in this simulated case study. The seismic events are mining-induced tremors from an underground coal mine at a distance of about 3.7 degress N-NE from GERESS. Local magnitudes, ML, are estimated to be between 2.0 and 3.8. Careful re-analysis of 31 events with the aid of Gamma information confirmed that the first detected arrival at GERESS for these events is the Pg phase. The FK-velocity of this phase is between 6.1 and 6.9 km/s. However, since Pg is the first detected arrival at distances where Pn is usually assumed to be first, the phase was consistently misidentified as Pn both by the Expert System Association and Location program (ESAL) and the many analysts involved in processing the data. Based on a relocation test of 14 "control" events, the mislocation due to this error alone is about 50 km. This misidentification of phase type can now be avoided since we have confirmed that the FK-velocity for this phase at GERESS is consistent for Pg and is a dependable indicator of phase type. Therefore, we are able to recommend a modification to the rules of ESAL allowing the first detected phase to be properly identified as Pg, based on automatically calculated phase parameters.

As the load on the automatic system increases, it becomes critical to reduce the analyst's interactions with repeatable events such as the mine tremors used in this study. The process of building enough confidence in an automatic system to rely completely on its location can be quickened by utilizing Gamma information for assessing and improving location accuracy of the Alpha network. In this study, we have shown how Gamma information serves as a guide to which phase parameters, automatically calculated, are reliable and robust. Once the locations and phase identifications are correct in an automatic sense, they can be further refined by other methods.

Correct phase identification and location impacts performance of automatic event identification programs. These programs often compute spectral content in a small window centered on a particular phase. If correct phase identification and timing do not result from the location procedures, then the event identification stages of the monitoring program will suffer from false information, or at the least, will be slowed down. This case study has resulted in the following recommendations:

• **Use slowness estimates for the P-phase identification.** Alow the *expert system to override the rule that the first P-phase for events beyond the cross-over distance is Pn* for events detected at GERESS when: (1) the first arrival azimuth is between 62 ^{o} and 70.4 ^{o} and (2) the first arrival velocity is between 6.2 and 6.9 km/s. We anticipate that this rule applies to other clusters in the vicinity and will verify this assumption through additional studies.

• **Use the best-recorded phases.** GERESS recordings of events from the Upper Silesian Coal Basin show that the most reliable and dependably-picked phase is Pg and that Pn is not necessary for location. Similarly, Gibowicz (1987) used events from the Lubin Copper Basin to evaluate the NORESS array and found that the Sn phase was the best recorded secondary phase because of Lg blockage by the Tornquist-Teisseyre tectonic zone. In that case, the automatic system had misidentified Sn as Lg for a location error of up to 340 km. This has since been corrected.

• **Continue use of Gamma information to improve automatic locations.** Studies such as the one outlined here, using Gamma information, should be an ongoing part of the IDC and will prove especially valuable in new, uncalibrated areas where sensitive regional arrays are installed.

Acknowledgments

Dr. P. Wiejacz and Dr. S. J. Gibowicz provided the ground-truth information for this study. Dr. P. Firbas provided information on the mining activity in the Czech Republic. This study benefited from guidance and comment by Dr. A. Ryall.

References

Bache, T. C., S. R. Bratt, J. Wang, R. M. Fung, C. Kobryn, and J. M. Given (1990). The Intelligent Monitoring System, *Bull. Seism. Soc. Am.* **80**, 1833-1851.

Gibowicz, S. J. (1987). NORESS capability for detection and location of mining tremors in the Lubin area in Poland. in, NORSAR Scientific Report No. 2-86/87.

Vogfjord, K. S. and C. A. Langston (1990). Analysis of regional events recorded at NORESS, *Bull. Seism. Soc. Am.* **80**, 2016-2031.

Baumgardt, D. R. and K. A. Ziegler (1988). Spectral evidence for source multiplicity in explosions: application to regional discrimination of earthquakes and explosions. *Bull. Seism. Soc. Am.* **78**, 1773-1795.

A BOOTSTRAP GENERALIZED LIKELIHOOD RATIO TEST IN DISCRIMINANT ANALYSIS

H. L. Gray, W. A. Woodward, and G.D. McCartor
Southern Methodist University
Department of Statistical Science
Dallas, TX 75275

and

M.D. Fisk
Mission Research Corporation
Santa Barbara, California

CONTRACT NO. F29601-91-K-DB25

OBJECTIVE

One of the primary problems associated with monitoring worldwide nuclear proliferation is the problem of distinguishing seismically between small earthquakes and explosions. Usual methods of classification are based on minimizing a loss function which in its most straightforward application results in the minimization of the sum of the misclassification errors. However, in the current application, the error of classifying an explosion as an earthquake is far more serious than the reverse, i.e. an earthquake as an explosion. Therefore it is absolutely necessary to fix the error of the former. The objective of this research is to develop a classification rule for which one of the misclassification probabilities can be controlled, and that can also be applied to any mixture of continuous and discrete variables for which the likelihood function is defined.

RESEARCH ACCOMPLISHED

The typical setting in classification analysis involves the classification of a vector observation, $\underline{x}$, as belonging to the multivariate population π_1 or π_2, given training samples $\underline{x}_1^{(1)}, \underline{x}_2^{(1)}, \ldots, \underline{x}_{n_1}^{(1)}$ and $\underline{x}_1^{(2)}, \underline{x}_2^{(2)}, \ldots, \underline{x}_{n_2}^{(2)}$ from π_1 and π_2 respectively. For purposes of this discussion we assume that π_1 is the population of explosions and π_2 is the population of earthquakes. Many of the standard classification procedures such as Anderson's W (see Anderson, 1984) are based on the further assumptions that the populations are multivariate normal and that these multivariate normal populations have covariance matrices that are equal to each other. These classification techniques are not appropriate for the problem of discriminating between earthquakes and explosions for several reasons. First, as mentioned in the objectives section of this report, in the problem of interest here, one of the probabilities of misclassification

is extremely important, and straightforward application of the classification procedure does not provide the ability to control a particular misclassification error. Second, the classification of earthquakes and explosions involves important discrete variables such as day of the week and binary variables such as a characterization of the region as seismic or non-seismic. For these reasons it is necessary to develop new techniques for classifying in this setting.

Actually, although the statistical problem here has the characteristics of a classification problem, it is technically a hypothesis testing problem because of our desire to fix a particular misclassification error. Let

$$P(2|1) = \text{probability of classifying } x \in \pi_2 \text{ when in fact } x \in \pi_1 .$$

Then $P(2|1)$ is the misclassification error of primary interest, i.e. the error of classifying an explosion as an earthquake. (Ultimately, of course, our concern is misclassifying a nuclear explosion. In that event $\pi_1 =$ nuclear explosions and $\pi_2 =$ conventional explosions.) Since $P(2|1)$ is our primary concern, we fix $P(2|1) = \alpha$, where α is preassigned, by testing the following hypotheses at the $100(1-\alpha)\%$ significance level:

$$H_0: x, x_1^{(1)}, x_2^{(1)}, \ldots, x_{n_1}^{(1)} \in \pi_1;\ x_1^{(2)}, x_2^{(2)}, \ldots, x_{n_2}^{(2)} \in \pi_2$$

vs

$$H_1: x_1^{(1)}, x_2^{(1)}, \ldots, x_{n_1}^{(1)} \in \pi_1;\ x, x_1^{(2)}, x_2^{(2)}, \ldots, x_{n_2}^{(2)} \in \pi_2 .$$

When π_1 and π_2 are normal populations with equal covariance matrices, Anderson (1984) and John (1960, 1963) have considered a similar hypothesis testing approach, and using results by Kanazawa (1979), it is possible to obtain asymptotic critical values for this test that control $P(2|1)$. Additionally, Anderson (1973) has given asymptotic results that also provide asymptotic critical values for Anderson's W. However, the need exists for a classification procedure that controls the misclassification probability but at the same time is applicable in more general settings including the case in which the covariance matrices are unequal and the case in which some of the variables are discrete. Krzanowski (1980, 1982) considered a mixture of continuous and discrete variables, but his results do not provide for the control of $P(2|1)$.

Baek, Gray, and Woodward (1993) have extended the procedure to provide a classification procedure which controls this misclassification probability in a more general setting. Specifically, they use a bootstrap of the generalized likelihood ratio in such a way that it is not necessary to assume normality or even continuous component variables. Thus, data can be a mixture of continuous and discrete observations. For $i = 1, 2$, let $f_i(x \mid \theta^{(i)})$ denote the probability or probability density function evaluated at x, if x comes from population π_i, where $\theta^{(i)}$ is the set of unknown parameters. The components of X may be all discrete, all continuous, or mixture of discrete and continuous variables. The generalized likelihood ratio is given by

$$LR = \frac{f_1(x \mid \hat{\theta}_0^{(1)}) \prod_{i=1}^{n_1} f_1(x_i^{(1)} \mid \hat{\theta}_0^{(1)}) \prod_{i=1}^{n_2} f_2(x_i^{(2)} \mid \hat{\theta}_0^{(2)})}{f_2(x \mid \hat{\theta}_1^{(2)}) \prod_{i=1}^{n_1} f_1(x_i^{(1)} \mid \hat{\theta}_1^{(1)}) \prod_{i=1}^{n_2} f_2(x_i^{(2)} \mid \hat{\theta}_1^{(2)})} \qquad (1)$$

where $\hat{\theta}_0^{(i)}$ is the Maximum Likelihood Estimate (MLE) of $\theta^{(i)}$ under H_0 and $\hat{\theta}_1^{(i)}$ is the MLE of $\theta^{(i)}$ under H_1, $i = 1,2$. Now let $\lambda = \log(LR)$. It intuitively follows that small values of λ provide evidence against H_0, and thus the generalized likelihood ratio test is to reject H_0 if $\lambda \leq \lambda_\alpha$, where λ_α is chosen to provide a size α test.

Let $P(\lambda \leq \lambda_\alpha \mid H_0)$ denote the size of the Type I error, and $P(\lambda > \lambda_\alpha \mid H_1)$ denote the size of the Type II error for a constant λ_α. Then $P(\lambda \leq \lambda_\alpha \mid H_0)$ is the probability of misclassification $P(2|1)$, and $P(\lambda > \lambda_\alpha \mid H_1)$ is the probability of misclassification $P(1|2)$. Therefore we can construct a classification rule which can control one of the probabilities of misclassification by fixing the size of the test if we know the distribution of λ. In most cases it is difficult to obtain the exact distribution of the test statistic λ. The distribution, however, can be approximated by employing the bootstrap method (Efron 1979, 1982).

Since the form of the probability density function is assumed known, the bootstrap samples can be obtained from the estimated density functions. This is called the parametric bootstrap (Efron 1979), and we employ it in this study. The likelihood ratio statistic for the test of the null hypothesis H_0 versus the alternative H_1 can be parametrically bootstrapped as follows. Bootstrap samples $x_1^{*(1)}, x_2^{*(1)}, \ldots, x_{n_1}^{*(1)}, x_{n_1+1}^{*(1)}$ and $x_1^{*(2)}, x_2^{*(2)}, \ldots, x_{n_2}^{*(2)}$ are generated randomly from densities $f_1(x|\hat{\theta}_0^{(1)})$ and $f_2(x|\hat{\theta}_0^{(2)})$, respectively where $\hat{\theta}_0^{(1)}$ and $\hat{\theta}_0^{(2)}$ are the MLE's described previously obtained from the original training samples. A "bootstrap" value for λ, to be denoted λ^*, is computed for the bootstrap samples using (1). This process is repeated independently B times, and the replicated values of λ^*, $\{\lambda_j^*\}_{j=1}^B$, evaluated from the successive bootstrap samples, can be used to assess the true null distribution of λ. In particular, the αth empirical quantile of $\{\lambda_j^*\}_{j=1}^B$, denoted by λ_α^*, will essentially approach λ_α, the true critical value for the test of size α, for large n_1 and n_2 as B tends to infinity. Thus we use λ_α^* as a critical value for the test of size α. Therefore, we allocate the observation x to π_2 if $\lambda \leq \lambda_\alpha^*$, and to π_1, otherwise where λ is the log-likelihood ratio calculated from the actual data.

Baek, Gray, and Woodward (1993) used a simulation study to investigate this bootstrapping procedure. This procedure was applied in three situations: (1) the distributions within each population are multivariate normal and the associated covariance matrices are equal, (2) the distributions are multivariate normal with unequal covariance matrices, and (3) the multivariate distributions involve a mixture of binary and normal component variables. In the simulations the bootstrap procedure was examined to determine how close simulated estimates of P(2|1) were to the theoretical misclassification probability. In all cases the simulation-based estimates were close to the true value of P(2|1). Simulations were also run to estimate the power of the test, i.e. to estimate P(2|2), the probability of classifying an observation as being from π_2 when in fact it belongs to π_2. As mentioned previously, classification procedures are available in the literature that fix the misclassification error in case (1). The bootstrap technique was compared with these known results in this case and gave similar results in terms of power. In cases (2) and (3) there are no competing techniques with which to compare our results. Our simulations indicated, however, that the bootstrap procedure also performs well in these cases. Details concerning these simulations will be shown at the poster session.

CONCLUSIONS AND RECOMMENDATIONS

We recommend that the bootstrap classification procedure be used for seismic-based classification of events. This procedure is recommended because it allows the ability to control one of the misclassification probabilities. it is general enough to apply to multivariate distributions which are a mixture of continuous and discrete variables. and simulations show that it performs well.

REFERENCES

Anderson, T.W. (1973), "An Asymptotic Expansion of the Distribution of the Standardized Classification Statistic *W*," *Annals of Statistics*, 1, 964-972.

Anderson, T. W. (1984), "An Introduction to Multivariate Statistical Analysis" 2nd Ed., John Wiley & Sons, New York.

Baek, J., Gray, H.L., and Woodward, W. A. (1993), "A Bootstrap Generalized Ratio Test in Discriminant Analysis," Department of Statistical Science Technical Report, Southern Methodist University.

Efron, B., (1979), "Bootstrap Methods: Another Look at the Jackknife," *Annals of Statistics*, 7, 1-26.

Efron, B., (1982), "The Jackknife, the Bootstrap and Other Resampling Plans," *SIAM*, Philadelphia.

John, S., (1960), "On Some Classification Problems, " *Sankhyá*, Series A 22, 301-308.

John, S., (1963), "On Classification by the Statistics R and Z," *Annals of the Institute of Statistical Mathematics*, 14, 237-246.

Kanazawa, M., (1979), "The Asymptotic Cut-off Point and Comparison of Error Probabilities in Covariate Discriminant Analysis," *Journal of the Japan Statistical Society*, 9, 7-17.

Krzanowski, W. J., (1980), "Mixtures of Continuous and Categorical Variables in Discriminant Analysis," *Biometrics*, 36, 493-499.

Krzanowski, W. J., (1982), "Mixtures of Continuous and Categorical Variables in Discriminant Analysis: A Hypothesis-Testing Approach," *Biometrics*, 38, 991-1002.

Resolution of Velocity Structure determined by Velocity Spectrum Stacking of Receiver Functions

H. Gurrola, J. B. Minster

Institute of Geophysics and Planetary Physics, University of California at San Diego, La Jolla, CA, 92093

Contract No: AF F29601-91-k-db13

OBJECTIVES

The primary objective of our research is to determine the velocity structure beneath three-component seismic stations. Emphasis is given to the interpretation of depths and average velocity structure to the upper mantle discontinuities. We have employed the velocity spectrum stacking (VSS) technique derived from reflection seismology to the interpretation of receiver functions. Using this technique, we image the upper mantle discontinuities by stacking receiver functions from different ray parameters after applying a moveout correction. The velocity spectrum is a contour map of stacked amplitudes on the receiver functions as a function of depth and velocity. The depth-velocity pair which produces the most coherent arrival on the VSS is presumed to indicate the correct velocity structure to the given discontinuity. This depth estimate can be biased as a result of: noise in the original receiver functions; bias in the distribution of receiver functions as a function of ray parameter; smearing as a result of the trade-off between depth and velocity in computing the moveout correction; the fact that different combinations of Vp and Vs result in similar moveout curves which can produce significant secondary peaks, "ghosts"; etc. To determine the confidence of a given depth-velocity estimate we employ a bootstrap technique in which we compute thousands of VSS by resampling the data — each time picking the combination of parameters that produces the largest peak. Our process of computing the VSS has been described previously (Gurrola et al. 1993, Gurrola, et al., 1992), as a result the emphasis of this report is to describe the manner in which we employ the bootstrap to determine the velocity structure beneath a seismographic station.

Research Accomplished

The velocity spectrum stack

The functional dependence of arrival times on ray parameter p, relative to a reference phase with ray parameter p_0 is called the "moveout" (Sheriff 1982). The "normal moveout correction" (NMO) then refers to the time adjustment necessary to correct the arrival time to what would have been observed for a vertically incident ray, irrespective of amplitude, assuming a given velocity structure. Figure 1 shows synthetic receiver functions computed for plane P waves with ray parameters from 0.04 to 0.08 s km^{-1}, traveling through PREM. Each was low pass filtered with a corner frequency of 0.3 Hz, comparable to typical observations. The dashed lines are true NMO curves for the P-to-S converted phase (Ps) from the respective upper mantle discontinuity produced by raytracing through PREM. The P2p1s and P1p2s are phases composed of reverberations ending in an s leg (the number preceding the small p and s indicate the number of P and S legs respectively). The solid lines are the moveout curves computed by replacing PREM with a layer over a half space that would result in a vertical travel time equivalent to PREM.

The typical "velocity spectrum stack", used in near surface reflection studies is a contour map of amplitudes across constant velocity stacks (produced by stacking the observed records after NMO assuming a uniform velocity) in the velocity-time plane. As illustrated in Figure 1, for depths greater than 400 km, moveout corrections computed in this manner are not accurate. For

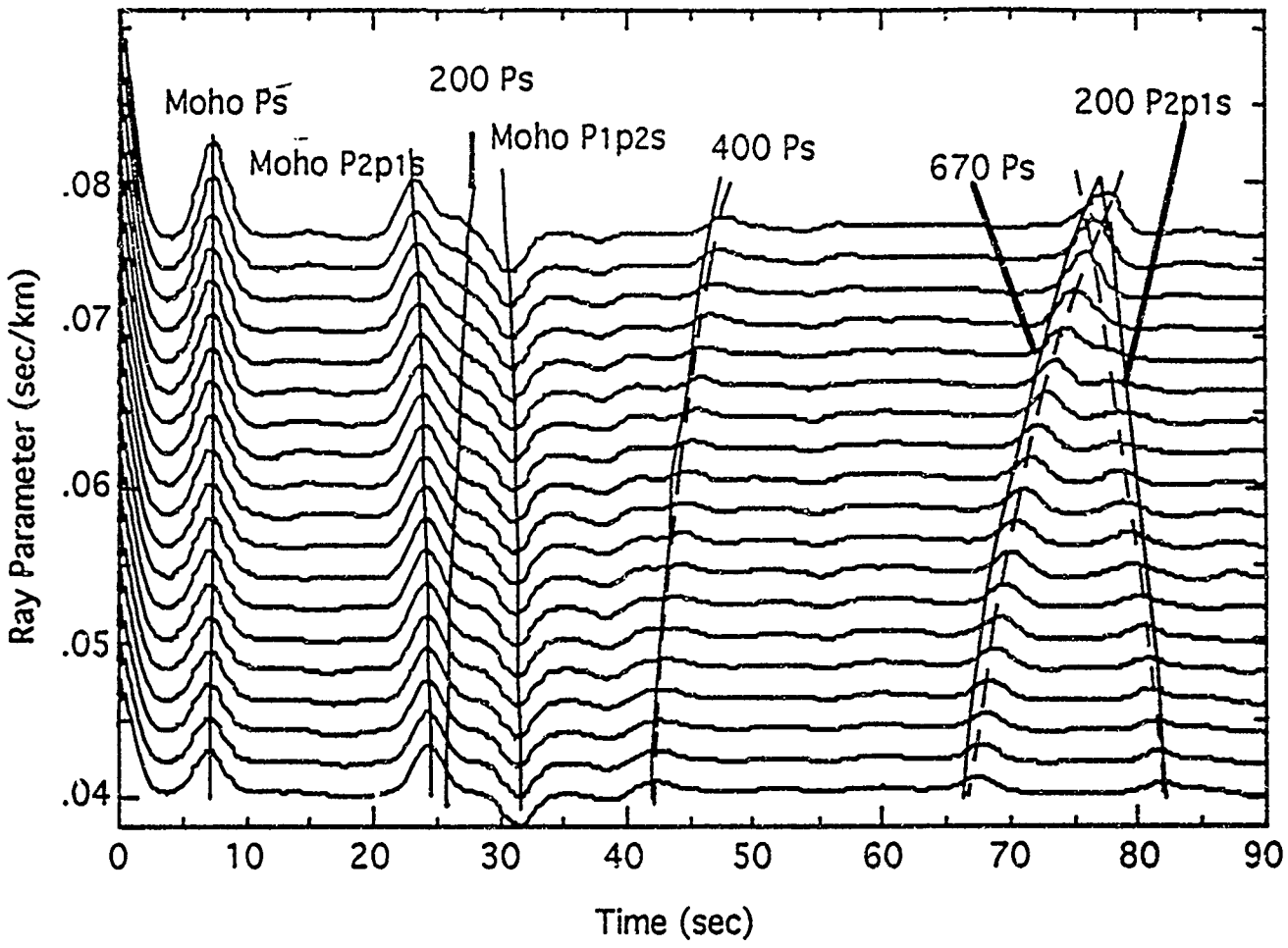

Figure 1. A representative display of the 80 low pass filtered (corner frequency of 0.3 Hz) PREM synthetic receiver functions. The moveout curve associated with Moho and upper mantle discontinuities are labeled. The dashed lines are the true moveout curves produced by raytracing through PREM. The solid lines are the moveout curves computed by replacing PREM with a layer over a that would result in a vertical travel time equivalent to that of PREM.

upper mantle depths we therefore, compute, by raytracing from the source to the receiver, the difference in the arrival time of the P-wave and the arrival times of the would be converted S-wave from all possible depths. In this manner, we compile NMO corrections as a function of depth which upon stacking enables us to transform the receiver functions to "reference velocity model stacks" (RVMS) with amplitudes as functions of depth rather than time. By multiplying all velocities of the reference model above z_1 by a constant α, we define a one-parameter family of models close to the reference model. A VSS is then constructed by contouring RVMS produced for a range of values of a close to 1. The axes of the VSS are depth versus "fraction of reference model" α; therefore, to any phase identified on the VSS, we attach a velocity described as a certain fraction or percentage above or below the reference model. This also overcomes errors that would be introduced as a result of the assumption of a planar wave front typically used in receiver function studies.

We show on Figure 2 Ps VSS for the PREM synthetics depicted in Figure 1. The left frame was computed using the actual PREM P and S velocities; the one to the right uses P-velocities from PREM and a constant value of $R_v = Vp/Vs = 1.825$. The fact that these plots are virtually

identical justifies *a posteriori* the use of a constant value for R_v instead of a depth-dependent one. The peaks on these two VSS occur for $\alpha \approx 1.0$ and at the expected 670 km depth.

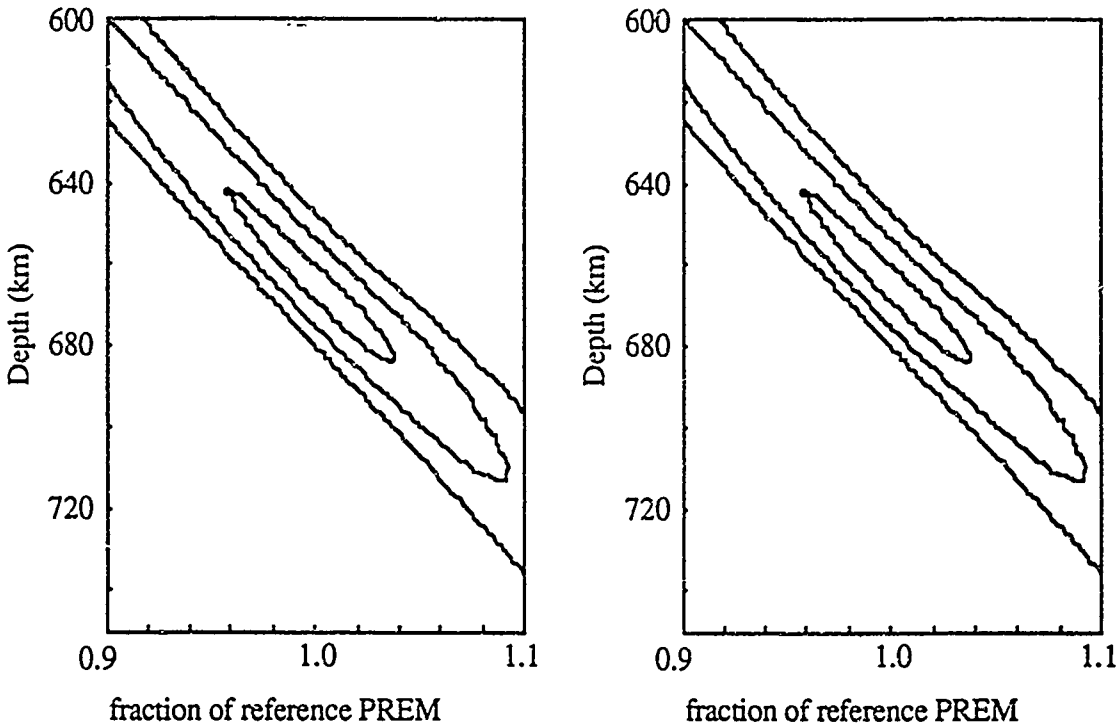

Figure 2. The VSS produced from the PREM synthetics depicted in Figure 1. The VSSc to the left was computed using PREM P and S velocities as the reference model. The one on the right was computed using PREM P velocities and $Rv = 1.825$.

Application of Bootstrap

In Figure 2, we observe that the expected Ps phase from the 670 km discontinuity is rather spread out. This is not only dependent upon the width of the Ps conversion on the receiver functions, but is elongated toward the low velocity—shallow depth corner of the VSS as a result of the trade-off between depth and velocity to produce similar moveout curves. The presumption underlying the VSS technique, however, is that the largest value on the peak will occur when the moveout curve for the correct velocity-depth pair connects the centers of the Ps converted phases on all the receiver functions. Noise effects and incomplete data sets notwithstanding, we are interested only in the velocity-depth pair associated with the largest value. For the VSS generated from PREM synthetics (Figure 2) the apex occurs at the expected 670 km depth at 1.0 times the PREM velocities. This is not a very conclusive test of the technique considering that the VSS was computed from noise free synthetic receiver functions distributed evenly over the entire teleseismic range of ray parameters. To determine more accurately the certainty of velocity and depth estimates based on VSS, we have performed a series of tests using an adaptation of the bootstrap method (e.g. Elfron, 1989). Our purpose is to assess the variability of the peak position with (1) data coverage, particularly sampling over the teleseismic ray parameter range, (2) noise levels, and (3) interference with possible, but not necessarily identified phases.

We added 4 to 8 percent white noise to each of the synthetics represented by Figure 1, then computed 1600 different VSS resampling (with replacement) the 80 synthetics. The velocity—depth pair was determined for the highest peak on each of these 1600 VSS. Figure 3 (VSS_b) depicts the regions on the VSS in which 80, 99 and 100 percent of these velocity depth pairs were

located. The frames on the left were computed using PREM synthetics depicted in Figure 1 — the synthetics used in computing the frames on the right were derived from a modified PREM model which excluded the 220-km discontinuity. In the frame to the left, we found that all 1600 of the bootstrap velocity—depth pairs fell within 10 km of the expected 670 km depth. Comparing this with the frame on the right, in which all the depth estimate were within 5 km of the expected 670 km depth, we conclude that much of the error is due to mis-stacking between the Ps from the 670 km discontinuity and the P2p1s from the 220 km discontinuity. In both of these examples, however, the 80 percent of the bootstrap depth estimates fall within 2 km of the expected 670 km depth.

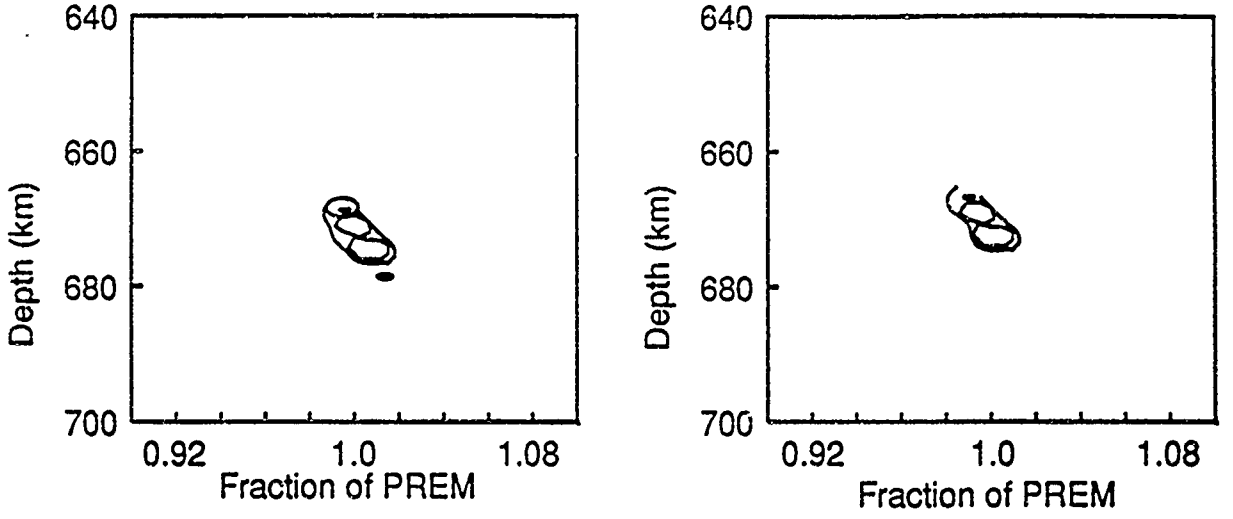

Figure 3, the VSS_b on the left depicts the bootstrap results of depth—velocity pairs for VSS computed from PREM synthetics with 4 to 8 percent white noise added. The VSS_b on the right was computed from a modified PREM without a 220 km discontinuity. Contour levels are 80,99 and 100 percent of the 1600 velocity depth pairs.

UPPER MANTLE DISCONTINUITIES AT OBN

Receiver functions for the IRIS/IDA station at OBN were computed using data collected in 1989-92. The station is equipped with a broadband three-component system with response nominally flat with respect to velocity from approximately 3 mHz to 5 Hz. We used teleseismic P and PP phases which, due to the uneven distribution of source regions during the three year period covered by the data, primarily sample the northeast and southeast quadrants. We included the PP phases to improve the azimuthal distribution of the data. In a limited data set, the inclusion of PP arrivals are useful in VSS studies because they improve ray parameter sampling. The broadband OBN receiver functions are dominated by reverberations within a shallow surface layer, and in order to identify phases from deeper layers, we have attenuated the contribution of the near surface structure by low-pass filtering these data using a phaseless Gaussian filter with a half power width of 0.6 Hz. We also applied a high-pass filter to the seismograms in order to counter the effects of occasional nonlinear noise problems at frequencies below 20 mHz.

Ps phases from the 400 and 670 km discontinuities are observed in Vss produced from OBN data (Gurrola et. al, 1992, Gurrola et. al, 1993). The purpose of this paper, however, is to describe the bootstrap technique we employed to determine the depth to the discontinuities, therefore we will confine our discussion to the 670 km discontinuity.

As demonstrated with the examples above, the amplitude of the peak on the VSS is dependent on three variables: P velocity, V_P/V_S ratio or Rv, and depth. The VSS is simply a slice through this space. A vertical slice through this space perpendicular to the VSS would be a contour map of

stacked receiver function amplitudes vs depth vs *Rv* (R_vSS) and could be used to determine the V_P/V_S ratio which best stacks the receiver functions. With real data we do not know what region of this space the correct combination of these three parameters lie. The VSS method would, therefore be most powerful if one of these parameters were provided independently by an other method. For example, the average V_P/V_S ratio for PREM to the 670 km depth is about 1.83. The VSS of the left in Figure 4 depicts the velocity (fraction of PREM)—depth pairs for which the largest peak was produced in 20000 realizations (resamplings) of the available data. From this figure we determine that with a value of Rv equal to that of PREM about 90 percent of the depth estimates fall between 640 and 670 km and about half of them fall between the 660 and 670 km. The inferred velocity is between 1.0 to 1.5 times that of PREM. These results are well within global depth estimates of the 670 km discontinuity by Shearer and Masters (1992) and velocity estimates determined by tomography Masters (personal comm.). Figure 4 also depicts the depth vs. *Rv* estimates from 20000 realizations determined from *Rv*SS computed by adhering strictly to PREM P-velocities. Almost 90 percent of the depth estimates were greater than 690 km. This is beyond the depth found anywhere in the world by Shearer and Masters (1992); as a result we believe that the higher velocities of 1.3 to 1.4 times PREM found on the VSS are probably closer to the truth.

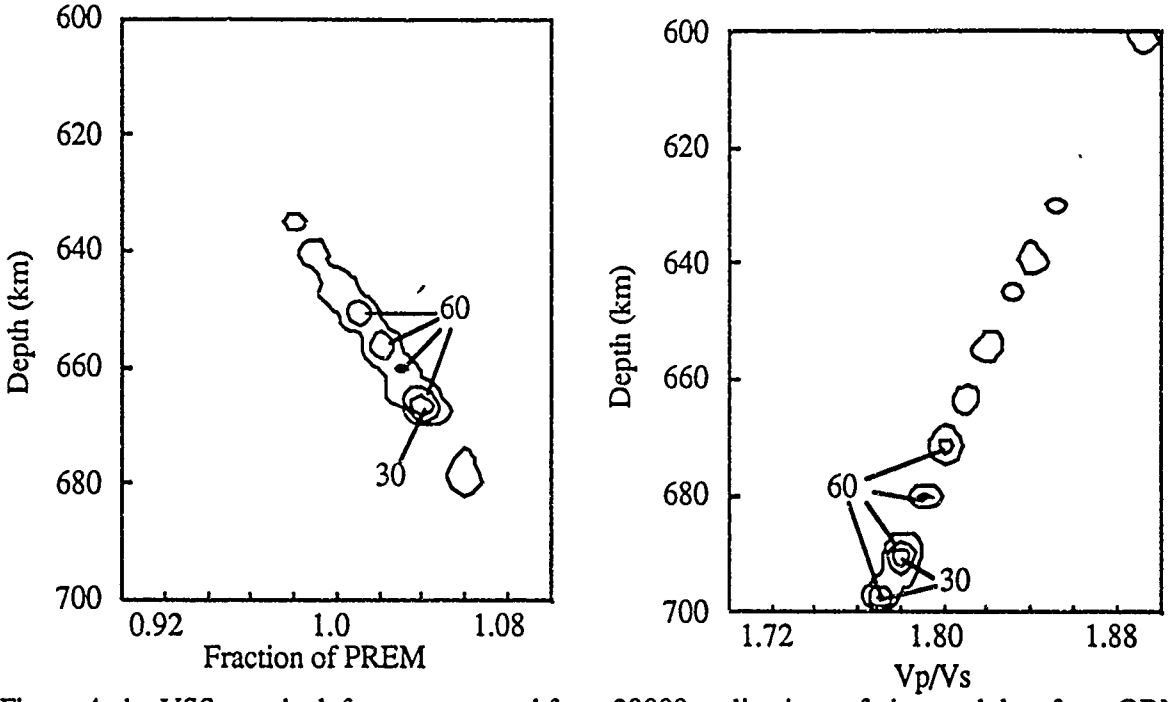

Figure 4, the VSS_b on the left was computed from 20000 realizations of observed data from OBN with Rv=1.83. The $RvSS_b$ on the right was computed from OBN receiver functions using PREM P velocities.

To determine if it would be possible to determine all three parameters (depth, Rv, and fraction of PREM), we computed 20000 sets of VSS for every value of *Rv* from 1.7 to 1.9. In each realizations, we searched for the combination of parameters which produces the largest amplitude on the stacked receiver functions. Nearly half of the data resulted in a depth estimate of about 663 km, with *Rv* = 1.85, and a velocity of 1.07 times that of PREM (Figure 5). Smaller peaks were found — the strongest of which was discussed above in the description of the RvSS depicted in Figure 4. From a similar set of VSS computed from synthetic receiver functions (Figure 1) we determined that these side peaks are expected and result from mis-stacking of unevenly distributed data. Figure 5 depicts 3 slices through the major peak of the velocity—*Rv*—depth picks from the

above 20000 sets of VSS: the velocity—depth estimates are compiled on the upper left VSS_b; the Rv—depth estimates are depicted on the upper right $RvSS_b$; the lower left panel is a compilation of the Rv—velocity estimates at a constant depth of about 663 km. On each of the panels in Figure 5, the confidence levels are based exclusively on the estimates (depth, *Rv* and/or velocity) that fell on that particular plane and are therefore conditional estimates. The depth estimate from the constant VSS_b for this value of *Rv* is not as well constrained as that found on the VSS_b computed with *Rv*=1.83. There are 2 major peaks on the $RvSS_b$ depicted in Figure 5. We believe that the shallow peak at about 625 km is an artifact of misstacking because it indicates a depth much shallower than found by Shearer and Masters (1992). The peak centered at the 663 km depth on the other hand is fairly sharp and agrees well with the depth of the major peak on the VSS_b. The values of Rv and velocity determined from the constant depth plane (lower right on Figure 5) are: Rv between 1.8 and 1.86; velocity between 1.0 and 1.8 times PREM.

CONCLUSIONS AND RECOMMENDATIONS

Through the use of velocity spectrum stacks we can stack receiver functions calculated from data with different ray parameters, and by doing so infer velocity structure beneath the seismographic station. This technique can be used to distinguish between a Ps phase and a P2p1s reverberation based on differences in the shapes of their respective moveout curves. The method looks most promising for the interpretation of upper mantle structure. The shape of the moveout curve for a particular phase is dependent on the depth of the interface from which it originates and the velocity structure above the interface. In order to compute moveout for the curved ray path of Ps phases for upper mantle discontinuities, we trace rays through a reference model and infer a fractional difference between the reference model and the structure necessary to satisfy the data. It should be clear from the examples above that the depth of an interface from which the phase of interest originated is poorly constrained by the VSS method unless assumptions are made about the velocity structure or R_v. For OBN, we assumed that the PREM model P-velocities are reasonably close to the truth and inferred the value of *Rv*, depth and a fractional multiplier for the PREM velocities. In doing so, we arrived at depth estimates for the 670 km discontinuity beneath OBN to be between 640 and 665 km at the 90 percent confidence level. The strongest peaks comprising more than a 40 percent of the estimates indicate that the discontinuity is between 660 to 665 km depth. Most of the estimates require a V_P/V_S ratio of between 1.8 to 1.86 and a velocity model of between 1.0 and 1.07 times PREM. Again about 40 percent of the depth estimates indicate a V_P/V_S ratio between 1.83 and 1.85 and a velocity between 1.04 to 1.07 times PREM.

We will continue to study the pattern of misstacking of the data in an effort to determine if the source of the bias can be determined and thereby removed. We are applying this technique to many other seismographic stations around the world (IRIS/IDA stations, RSTN stations, Grafenberg stations, etc.) and will present results from many of these stations at the conference. We will also include results for velocity structure determined by stacking the Ps phase from the 400 km discontinuity. This method will be most useful if used in coordination with other methods such as tomography or surface wave dispersion that are less sensitive to discrete velocity discontinuities.

REFERENCES

Dziewonski, A.M. and D.L. Anderson 1981, Preliminary reference Earth model, *Physi. Earth and Planet. Int.*, **25**, 297-356.

Efron, B., and R. Tibshitani, Bootstrap methods for standard errors, confidence intervals, and other measures of statistical accuracy, Stat. Sci, 1, 54-77, 1986.

Gurrola, H., J. B. Minster, and T. Owens,1993, The Use of Velocity Spectrum for Stacking Receiver Functions with Application to the IRIS/IDA Station at Obninsk, Russia, submitted to *Geophys. Jour. Int.*

Gurrola, H, J.B. Minster, and T. Owens, 1992, Depths to upper mantle discontinuities beneath broad band seismic stations by velocity spectrum stacks of receiver functions, 14th annual DARPA/GL Seismic Research Symposium, Geophysical Laboratory Hanscom AFB, Mass, PL-TR-92-2210, ADA256711.

Owens, T.J., G. Zandt, S.R. Taylor, 1984, Seismic evidence for an ancient rift beneath the Cumberland plateau, Tennessee: a detailed analysis of broadband teleseismic P waveforms, *J. geophys. Res.*, 89, 7783-7795.
Shearer, P.M., and T.G. Masters, Global seismic record sections — Data and synthetics, Eos Trans. AGU, 71, 1465,1990.
Sheriff, R.E., 1982, Encyclopedic Dictionary of Exploration Geophysics, *Society of Exploration Geophysicists*, Tulsa, Ok.
Yilmaz, O., 1987, Seismic Data Processing. *Society of Exploration Geophysicists, Investigations in Geophysics* Volume 2.

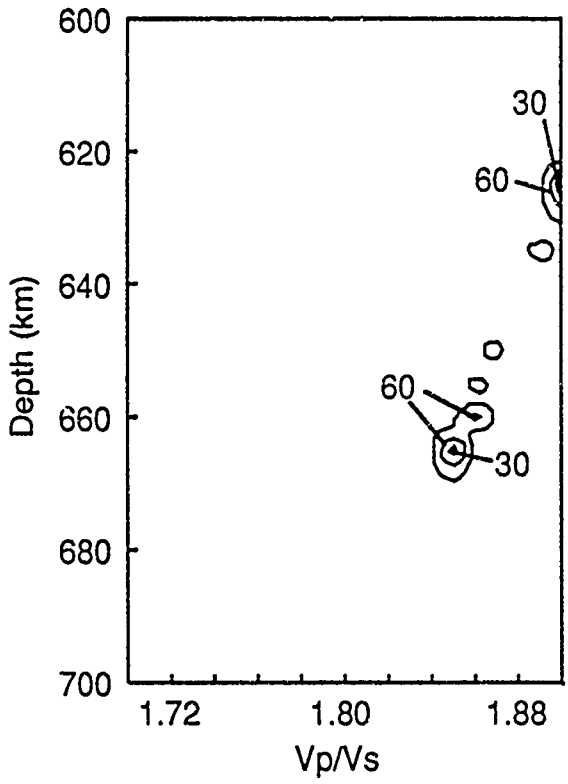

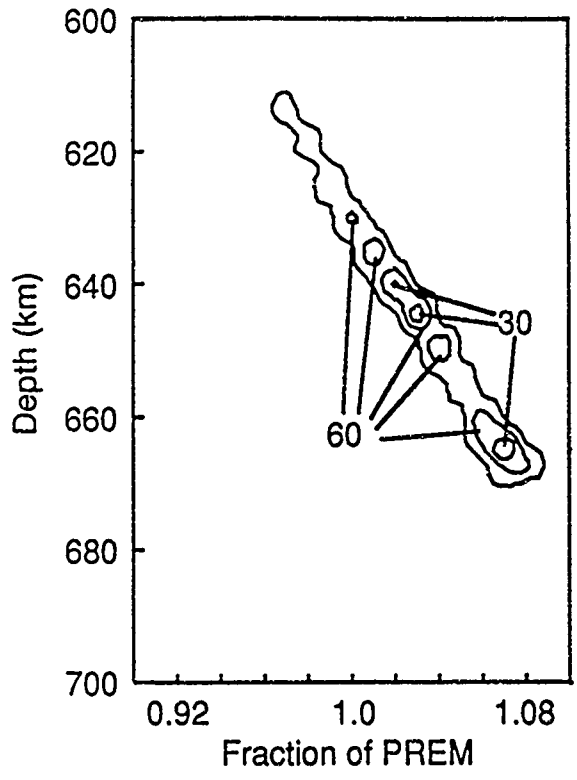

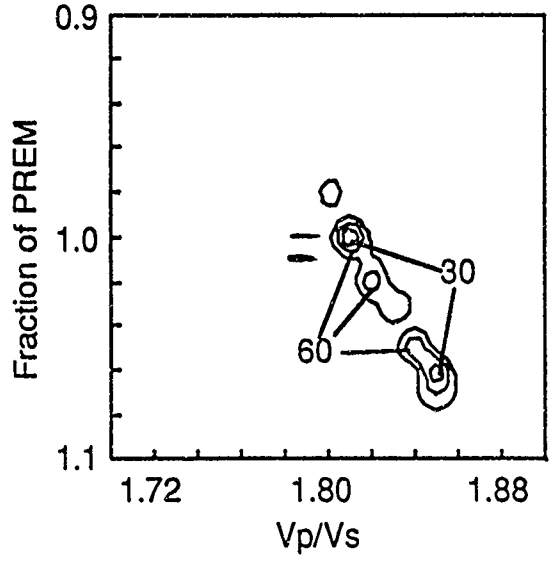

Figure 5, The upper left VSSb was computed using Rv=1.85, The RvSSb on the upper right was computed using 1.07 times PREM P velocities. The panel on the lower left was computed for a constant depth of 663 km and depicts velocity Rv pairs derived from this assumption. All three panels depict the result of 20000 realizations of the data.

Characteristics of Frequency Dependent Polarizations for Local Events Recorded on Surface and Borehole Instruments

J. A. Hanson, J. B. Minster, and F. L. Vernon
Institute of Geophysics and Planetary Physics
University of California, San Diego, La Jolla, CA 92093

Contract Number: MDA972-91-C-0005

OBJECTIVE

High frequency body waves measured at surface stations, such as those from small local events, often display non-rectilinear particle motion even for the initial arrival. This deviation from linear motion arises from two causes: the steep velocity gradient at the surface and scattering due to lateral velocity heterogeneities. The strongest frequency dependent characteristics of polarizations are in general due to local receiver structure, thus they provide valuable information of the site response. Using a simple 1-D model we are able to account for much of the complexity in the polarizations of the initial *P*-arrival recorded at Piñon Flat Observatory, California.

Small, local events have peak energy at high frequencies (> 10Hz), but at these frequencies the waveform characteristics are dominated by the local site response. Since the strongest gradients in velocity are often shallow, less than 60 meters, borehole sensors provide the possibility of better observing source and path effects of small events. Frequency dependent polarization analysis of the *P*-arrival at 2 borehole sensors shows a strong correlation with ray parameter estimated from event locations. The dependence on ray parameter can be observed at frequencies up to 30 Hz indicating the borehole sensors contain valuable information of event and along path parameters.

RESEARCH ACCOMPLISHED

Experiment

The Small Aperture Array 1 (SAA1) experiment was conducted in the spring of 1990 at Piñon Flat Observatory (PFO) in the desert north-east of San Diego to study wavefield coherency for local and regional events. PFO was chosen for its geologically simple, hard rock structure, relatively level topography, and its proximity to two major fault zones (Owens et al. 1991)(Figure 1). The array consisted of 60, 3-component, L-22 velocity sensors with a flat response between 2 and 100 Hz. These are well suited to record local events which typically have peak energy between 10 and 30 Hz. We selected 119 events out of the 268 local earthquakes recorded during the experiment. From these events, 73 have been located by regional networks (Scott, 1992) and are shown in Figure 1. The ray-parameters estimated from locations range from 0.11 to 0.17 s/km, with clusters around 0.14 and 0.16 s/km.

Polarization Analysis

We are interested in the near surface seismic structure which has a strong frequency dependent effect on the wavefield, and thus we want a robust estimate of the frequency dependence of the polarizations. Here the polarizations were determined in the frequency domain using a multi-taper algorithm (Thomson 1982) to estimate the spectral density matrix (Park et. al., 1987, Laske and Masters, 1992) which is then diagonalized (Samson 1983) and is referred to as multi-taper polarization analysis (MTPA). Eigenvalue decomposition of the spectral density matrix defines a coordinate system such that the amplitude of a single linearly polarized phase appears in only one eigenvalue corresponding to an eigenvector which points in the direction of particle

motion. In our case the spectral density matrix contains the complex spectra for each instrument component so that at each frequency each component has an amplitude and phase, and thus allows elliptical particle motion to be considered as a single polarization direction.

To describe fully the particle motion ellipse in 3-space four quantities are needed: the azimuth, incidence, ellipticity, and tilt. Here we are primarily concerned with the initial *P*-arrival and a 1-D model so only the two quantities, incidence and tilt, are of interest. The incidence angle is defined as the angle that the major axis of the particle motion ellipse makes with the vertical. The term incidence angle is somewhat of a misnomer since the major axis of this ellipse need not be coincident with the direction of propagation which is certainly the case for *S*-waves, and as it turns out, for *P*-waves which interact with the upper most, low velocity, surface layers.

Modeling Technique

We used a generalized reflection and transmission coefficient method to calculate the complete response of a stack of surface layers to a plane wave incident from below (Shearer and Orcutt, 1987). Varying the frequency of the plane *P*-waves for a given ray parameter allows us to calculate the frequency dependent polarization directly, or a time domain synthetic can be produced and used as input to the MTPA. Apparent incidence angles can be calculated at any depth desired.

Results

Apparent incidence angles were calculated for the surface stations using a 0.5 second window surrounding the *P*-wave arrival. The variations of the polarization across the array are large enough that some sort of averaging is needed to obtain results that are representative of the 1-D response. In order to observe the general properties of the polarizations without having to assume anything about the underlying statistical distribution of the measurements, histograms were made of the incidence angle estimates. Figure 2a shows the evolution of these histograms with frequency between 0 and 45 Hz. The incidence is shallow at low frequencies, 50-60°, and passes through a dramatic transition at 10-12 Hz above which it is widely scattered around 0°.

We calculated the apparent incidence angle using a simplified version of the velocity model obtained by Fletcher et al., (1990), from borehole logging data (Figure 2b)and a simple two layer attenuation model from Aster and Shearer (1991). The polarizations were calculated using the generalized reflection/transmission coefficient method described above and are shown in Figure 2c for a variety of surface layer thicknesses. The transition occurs at approximately the frequency which corresponds to a layer thickness equal to a quarter wavelength of the *P*-wave, in other words the fundamental "organ pipe" mode. Increasing the layer thickness decreases the transition frequency and vice versa. A "best" model was found for our data, and the polarization estimates for this model are shown in Figure 2d for a variety of ray parameters. The variation in ray parameter is only significant at low frequency so that the large amount of scatter in the data at high frequencies is probably due to local scattering.

Histograms of the incidence angle for the two borehole sensors are shown in Figure 3. They differ dramatically from the surface instruments results which is a consequence of being in a more homogeneous region and of the reflection from the free surface. The apparent incidence angles were calculated for the 150 and 300 meter boreholes using a simple velocity model (see Figure 3). The borehole polarizations are not sensitive to the uppermost surface layer velocity structure; instead the average values of the model above the sensor determine the frequency at which the first transition occurs. The first two transitions at low frequencies are seen in the model and data and correspond to the standing wave nodes due to the zero traction boundary condition at the free surface. This occurs at 1 and 3 quarters wavelength below the surface, and thus the transition of the 150 meter borehole is approximately twice the frequency of the 300 meter borehole.

The fairly stable incidence between the 2 transitions is modeled well, but the models do a poor job of matching the data above 20 Hz.

Figure 4 shows examples of the variation in measured apparent incidence angle with ray parameter for both data and models. The amount the incidence changes with ray parameter is strongly frequency dependent, and it can be shown that there are specific frequencies which are optimal for observing this variation. It is interesting to note that if there were no reflected wave then we would expect the incidence to range from about 35 to 65 degrees, significantly less than the variation seen at 11 Hz.

CONCLUSIONS AND RECOMMENDATIONS

The polarization of the initial *P*-wave arrival shows dramatic variation in frequency for both the surface and borehole instruments. The variation at the surface is primarily due to the low velocity weathered granite upon which the instruments sit. The apparent incidence at low frequencies agrees with expectations of a simple half space model, and at 10 Hz passes through a transition to where the incidence is scattered about vertical. These general features can be explained by a simple 1-D velocity/attenuation model, but it is clear that above 10 Hz local scattering from 3-D structure is having a predominant effect. Thus interpreting polarization data for deeper structure is tenuous at best. The borehole polarizations are affected by the surface reflection and can be modeled quite well with a simple 1-D model. Unlike the surface polarizations, the borehole polarizations show significant correlation with ray parameter even at high frequencies indicating that the waveforms contain information about the source. With the use of an inversion scheme (e.g. genetic algorithms) an optimal model to fit the data could be found and then used to predict the effect of the free surface reflection on the *S*-arrival to aid in future high-frequency source studies.

References

Aster, R. C. and P. M. Shearer (1991). High-Frequency Borehole Seismograms Recorded in the San Jacinto Fault Zone, Southern California. Part 2. Attenuation and Site Effects, *Bull. Seism. Soc. Am.* **81**, 1081-1100.

Fletcher, J. B., T. Fumal, H. Liu, and L. C. Carroll (1990) Near-Surface Velocities and Attenuation at Two Boreholes Near Anza, California, from Logging Data, *Bull. Seism. Soc. Am.* **80**, 807-831.

Laske G. and G. Masters (1992) The Multiple Taper Polarization Analysis for Surface Waves, *Sonderforschungsbereich* **108**, 1335-1360.

Owens, T. J., P. N. Anderson, and D. E. McNamara (1991) Data Report for the 1990 Pinyon Flat High Frequency Array Experiment. An IRIS Eurasian Seismic Studies Program Passive Source Experiment, *IRIS/PASSCAL Data Report* **#91-002**, 14pp.

Park, J., F. L. Vernon, and R. Lindberg (1987) Frequency Dependent Polarization Analysis of High-Frequency Seismograms, *J. Geophys. Res.* **92**, 12664-12674.

Samson, J. C. (1983) The Spectral Matrix, Eigenvalues, and Principal Components in the Analysis of Multichannel Geophysical Data, *Ann. Geophys.* **1**, 115-119.

Scott, J. (1992) Microearthquake Studies in the Anza Seismic Gap, *Ph.D. dissertation*, UCSD, Scripps Institution of Oceanography, La Jolla, California.

Shearer, P. M. and J. A. Orcutt (1987). Surface and Near-Surface effects on Seismic Waves - Theory and Borehole Seismometer Results, *Bull. Seism. Soc. Am.* **77**, 1168-1196.

Thomson, D. J. (1982) Spectrum Estimation and Harmonic Analysis, *IEEE Proc.* **70**, 1055-1096.

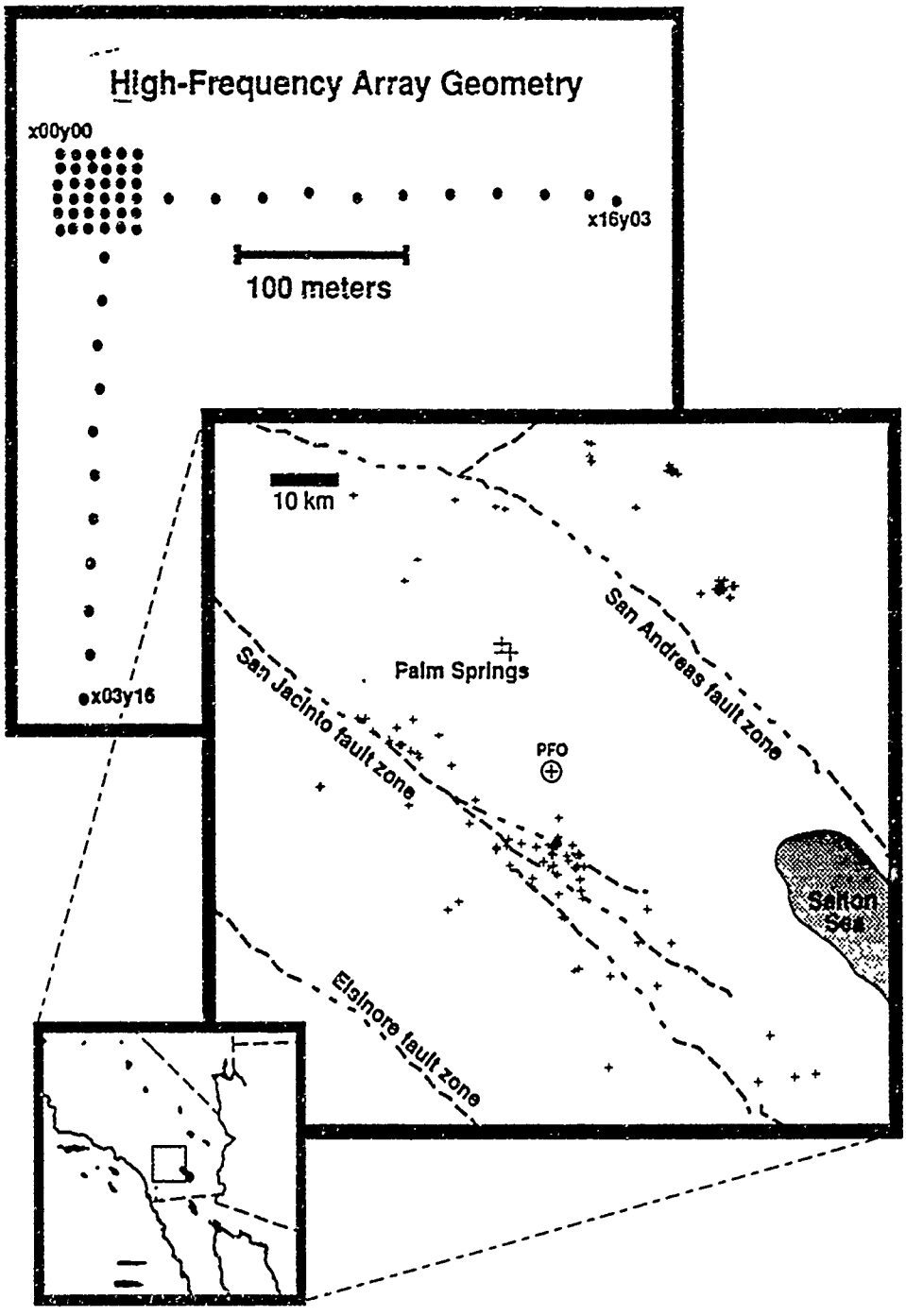

Figure 1. Small Aperture Array I Experiment at Piñon Flat Observatory, California. The top figure shows the layout of the array; the 2 boreholes (at 150 and 300 meter depths) lie within the small grid of instruments. The located events are shown in the middle map. In addition we use 46 events recorded during the experiment that were not located by the regional network. There is a 3-D velocity model available for the area around the San Jacinto fault zone, but it does not include the area to the north-east of PFO.

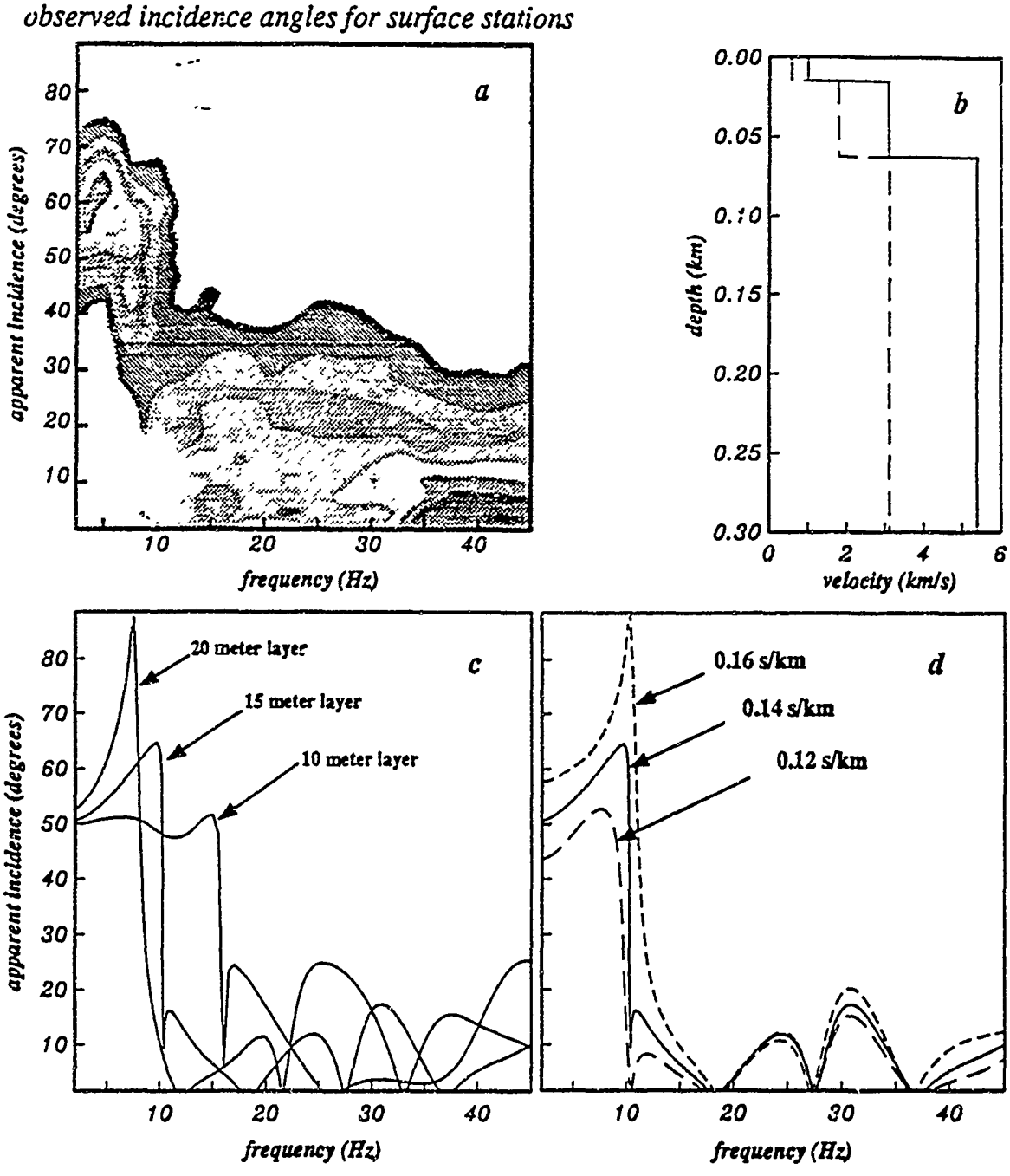

Figure 2. Apparent Incidence Angle at Surface. (a) This shows the results for all surface stations and all events; at each frequency there are 5677 incidence angle estimates. The main feature is the transition from shallow incidence below 10 Hz to a largly scattered, near vertical incidence at high frequencies. (b) P (solid) and S (dash) velocity models used in making synthetics shown in the next two figures. (c) Decreasing the thickness of the top layer in the velocity model pushes the transition to higher frequencies. (d) The apparent incidence angle was calculated for our "best" model at variety of ray parameters. The variation with ray parameter is only significant below 10 Hz.

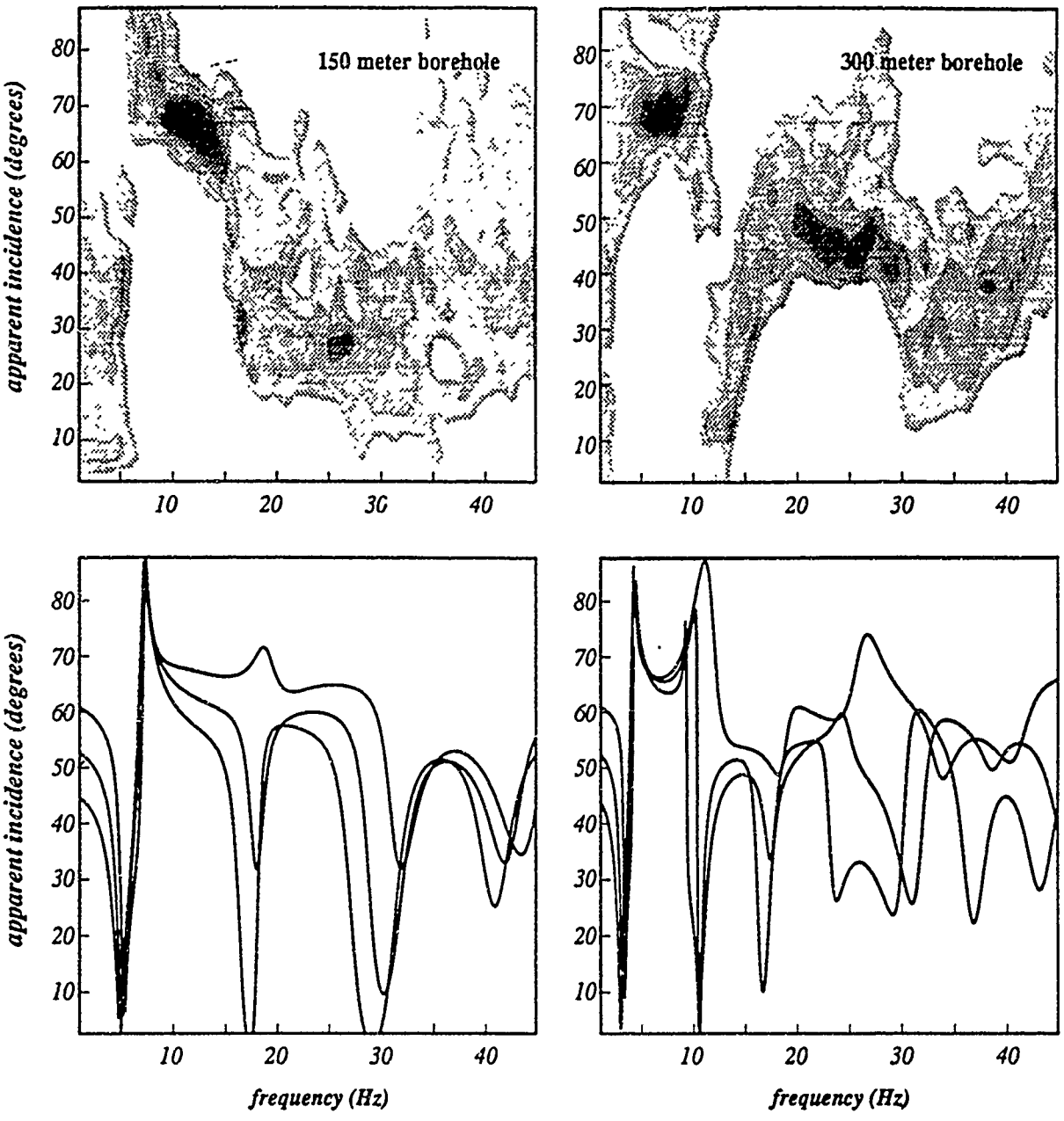

Figure 3. Apparent Incidence Angle for Borehole Sensors. The top two figures show the evolution of the binned data with frequency. The estimates from the 119 events were binned in 5 degree intervals, and the resulting histograms contoured in the shade plot. The bottom figures are the theoretical curves for 3 different ray parameters: 0.12, 0.14, 0.16 sec/km from bottom to top. The first 2 transitions for both boreholes are modeled well using a simple 3 layered model, but at higher frequencies the model does not perform as well. This may be due to to greater variability of incidence angle with ray parameter (all ray parameters have been stacked together) and the resolution not being sufficient to detect the more oscillatory nature at high frequencies.

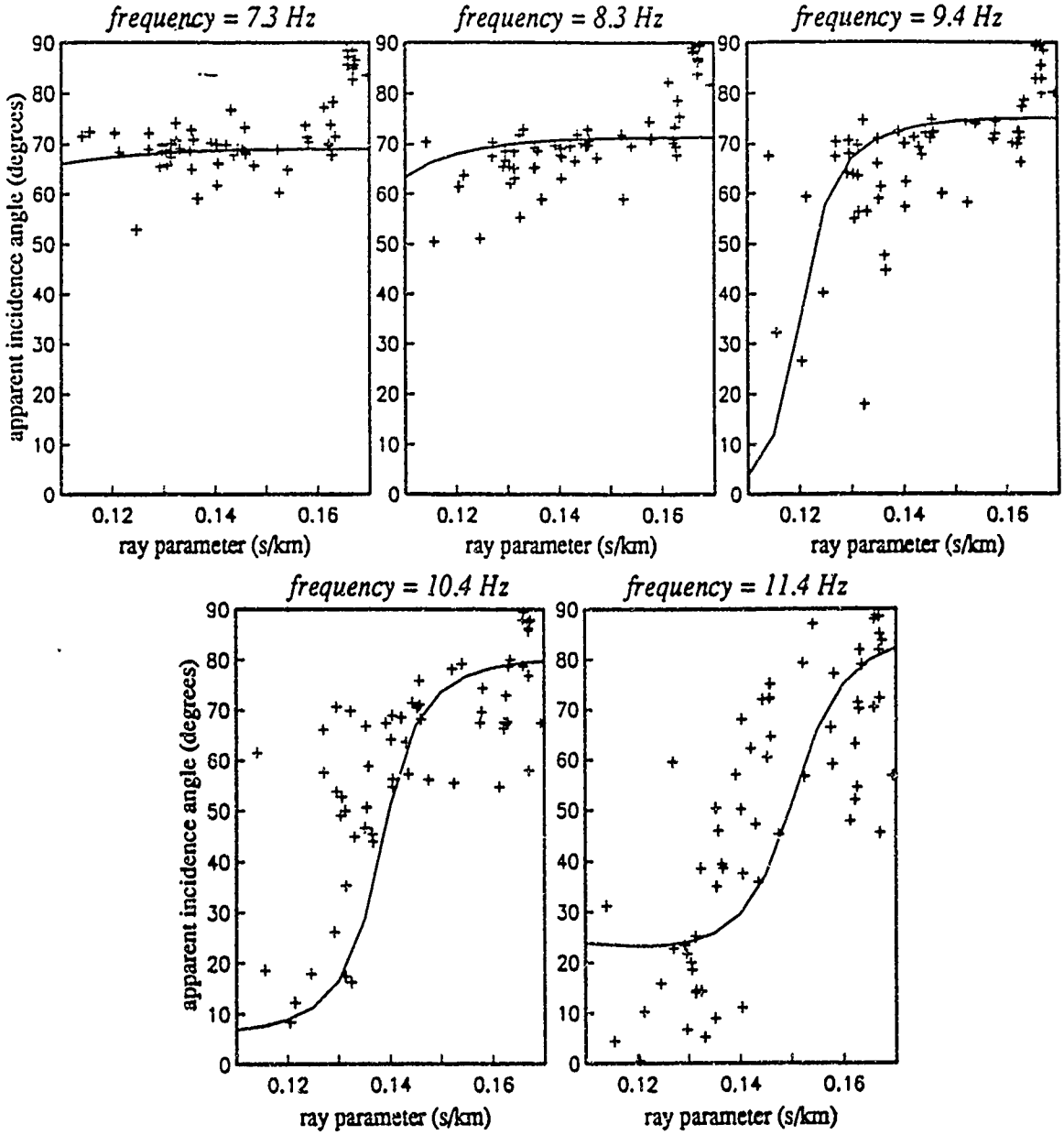

Figure 4. Apparent Incidence Angle vs. Ray Parameter for 300 meter Borehole at a Sequence of Frequencies. The +'s are estimates for each event. The apparent incidence angles were estimated using the MTPA and the ray parameters are from locations using a local 3-D velocity model. The curves are the theoretical values calculated from the simple velocity model shown in Figure 2b. The amount of variation in apparent incidence angle with ray parameter for both data and model is greater at certain frequencies (10.4 or 11.4 Hz) than would be expected in a whole space. The events with ray parameter ~0.17 s/km, which do not fit the model well and are seemingly inconsistent with the other data, are located across the Coachella Valley from PFO where we do not have a 3-D velocity model to locate events.

GERESS - A Key Station in a Future Global Monitoring Network

Harjes, H.-P., M. L. Jost, and J. Schweitzer

Institute of Geophysics, Ruhr-University Bochum, Germany

Grant AFOSR-90-0189

Objective

The German Experimental Seismic System (GERESS) is a cooperative research program of Southern Methodist University Dallas (USA) and Ruhr-University Bochum (Germany). GERESS contributes to the IMS (operated at the Kjeller data center, Norway) together with the Fennoscandian regional arrays (NORESS, ARCESS, FINESA), the two new arrays near Apatity and on Svalbard. It was suggested to include GERESS as an α-station in the recent GSE-concept. The objective of research activities carried out at the data center in Bochum aimed at calibration concepts of an α-station using GERESS as an example. In this respect, the α-network of about 50 globally distributed stations is regarded as a teleseismic monitoring system. The calibration includes characterization of the noise, evaluation of the detection capability (signal to noise ratio improvement by beamforming), an estimate of station sensitivity, the station residuals w.r.t. travel-time and magnitude, and the determination of mislocation vectors.

Research accomplished

a) GERESS Noise Characteristics

Previous to the installation of GERESS, the area was carefully monitored with respect to noise characteristics (e.g., Harjes, 1990). It was found that noise at GERESS is significantly different from that at the Fennoscandian arrays: at NORESS, low frequent noise (around 1 Hz) shows an order of magnitude higher peak spectral displacement values than at GERESS (10 nm^2/Hz versus 0.7 nm^2/Hz, respectively). At high frequencies (around 10 Hz), the noise values at GERESS are significantly higher than at NORESS (2.5 10^{-4} nm^2/Hz versus 0.6 10^{-4} nm^2/Hz). Harjes (1990) also concluded that the noise at GERESS lacks the noise correlation minimum, generally observed at the Scandinavian arrays. This finding implies a different noise structure in Central Europe.

b) GERESS P-Wave Detectability

The SNR improvement by beamforming at GERESS was assessed for P-phases of strong local, regional, and teleseismic events at various frequencies and for different array subgeometries (Jost, 1992). The mean values for 5 of the 11 GERESS subarray-configurations (AB, ABC, ABCD, CD, and D) indicate that the full array has the highest SNR gain from 1 - 6 Hz and configuration ABC (inner 3 rings) from 6 - 10 Hz. The mean values for GERESS and NORESS (Kvaerna, 1989) for the full array (ABCD), which is based on 25 channels at NORESS (14.0 db) and 22 channels at GERESS (13.4 db), show higher P-wave detectability for GERESS in the frequency range 1 - 3 Hz. The differences between NORESS and GERESS can be explained by the noise characteristics at both arrays.

c) GERESS Teleseismic Detection Capabilities

GERESS data are continuously transmitted from the array HUB in Bavaria to Bochum via a 64 kbit line. At Bochum, an on-line processing system based on RONAPP (Mykkeltveit and Bungum, 1984; Fyen, 1987) is operated to monitor data quality, initiate maintenance activities, and produce an automatic event bulletin. All teleseismic phase detections, interactively reviewed by an analyst, are sent to the US National Earthquake Information Center (NEIC) in Golden, Co.
The GERESS contribution to global seismic data analysis has been evaluated taking the NEIC bulletin (Earthquake Data Reports, EDR) as reference (Schweitzer, 1993). Fig. 1 shows all events (20° - 180°, with reported body wave magnitude) for which NEIC associated a phase detected by GERESS from Oct. 18, 1991 to Feb. 28, 1993. In this teleseismic distance range, GERESS detected 44.6 % of the corresponding NEIC events.
The GERESS contribution can be compared with long-established high-sensitive arrays like Yellowknife (YKA) or three-component stations on the same geological setting as GERESS like KHC. On average, YKA reported 59.3 % and KHC 26.2 % of NEIC- events in the corresponding teleseismic window. The detectability with respect to epicentral distance (Fig. 2) shows a decrease for GERESS between 60° and 70° around the North Pacific subduction zones. This observation is due to the large number of small events (mb < 4.5) that are detected by local and regional stations reporting to NEIC. Beyond the core shadow, GERESS detected 85 % of all NEIC events (PKP phases between 135° and 155°). GERESS shows a larger percentage of detected PKP onsets than YKA which reflects the low network detection capability for small events (mb < 4.5) in the south-west Pacific. It also demonstrates that sensitive seismic stations in epicentral distances around the PKP caustic can significantly improve the detection capability for remote areas where nearby stations do not exist or would be difficult to operate.
The seasonal pattern (Fig. 3) shows significant differences in detection probability of GERESS and KHC on one side and YKA on the other. YKA shows a decrease of about 25 % during summer, when the Great Slave Lake is open. For the observed 1 1/2 years, YKA is somewhat less sensitive than GERESS during late summer and early fall. There appears very little seasonal variation at GERESS or KHC.
On the other hand, the detection capability of GERESS with respect to time of day shows a decrease during daylight hours as a result of man made noise and mining activities. A comparison with KHC reveals that this daily variation is not a local effect at GERESS but a common feature for seismic stations in Central Europe. At daylight hours, a decrease of the detection probability of about 8 % for GERESS and about 5 % for KHC can be observed.

d) Travel Time and Amplitude Residuals of GERESS

To determine a mean travel time residual for GERESS, only large and well constrained events were used (mb > 5.0 (NEIC), more than 19 defining P phases). In addition, onsets with an absolute value of the travel time residual larger than 3.0 sec were rejected. The mean travel time residual based on 1520 GERESS phases is -0.66 sec with a standard deviation of +/- 0.68 sec. Fig. 4 shows the mean travel time residuals of proposed α-stations or stations in their neighborhood. Residuals are plotted with respect to the percentage of observed EDR events. The comparison is based on the contribution of seismic stations from Apr. 1990 to Jun. 10, 1993. The percentage of observed events gives a rough idea of the sensitivity of the stations. It is obvious that all highly sensitive arrays have negative travel time residuals and that single stations show a similar trend: the more sensitive the station, the more negative is its travel time bias. This observation is confirmed by Grand (1990), who showed that the travel time residuals of different stations in the ISC bulletins correlate with the amplification of the stations. This result suggests that the source times of larger events can systematically be biased to later times due to a large number of

less sensitive stations which observed these events.

For the estimation of the magnitude residual of GERESS, the same events used above resulted in 945 mb values. The mean mb residual at GERESS is -0.60 with a standard deviation of 0.35. This relatively large magnitude residual results from several effects that all act to decease measured amplitudes: First, GERESS has its best SNR gain for P onsets in the frequency range between 1.0 Hz and 3.0 Hz (Jost, 1992). Therefore, this narrow frequency band is often used to measure amplitudes. (Note that many of these onsets would not be visible on a WWSSN short-period instrument at the GERESS site.) This narrow-band filtering increases the SNR but decreases the mean amplitudes. Second, some signal loss can occur due to beamforming. Finally, at GERESS, we generally do not observe any site amplification due to the missing sedimentary cover. All these effects tend to decrease the amplitudes observed at GERESS. Fig. 5 shows mb residuals of different stations plotted with respect to the mean reported period T to compute log A/T (which is thought to compensate for different instrumentation and observing periods). All stations that measure amplitudes generally at mean periods less than 1.0 sec show a negative mb residual. This indicates that the compensation for period in the magnitude formula is not sufficient. For arrays, signal loss after beamforming may cause still smaller amplitudes.

e) GERESS Mislocation Vectors

Although the small aperture (4 km) GERESS array has only limited resolution for measuring slowness and back-azimuth (BAZ) of teleseismic onsets, the differences to theoretical values have been determined. Locations of NEIC were employed to calculate epicentral distance and theoretical BAZ; the IASP91 travel time tables (Kennett and Engdahl, 1991) were employed to calculate the theoretical slowness of the first arrival (P, Pdiff, PKP) using theoretical epicentral distance and reported depth (NEIC). All slowness and BAZ values of first arrivals with a travel time residual $| t_{obs} - t_{theo} | > 3.0$ sec and with a slowness mislocation vector of more than 4.0 sec/deg were omitted. With the first arrivals analyzed during the GSETT-2 period (Schweitzer, 1992) and the onsets reported between Oct. 18, 1991 and Jun. 10, 1993, a total of 3910 slowness and BAZ values were available.

Fig. 6 shows the observed mislocation vectors in slowness space, which has been divided into cells (1 sec/deg by 10 deg in the outer regions and 1 sec/deg by 20 - 30 deg in the central part). Mislocation vectors displayed are averages for each cell in the slowness space and contain at least 5 observations. The theoretical value is indicated by a circle. The mean slowness residual of all observations is -0.42 sec/deg with a standard deviation of 1.17 sec/deg. The mean BAZ residual is 5.3 deg with a standard deviation of 23.7 deg. Fig. 6 shows that BAZ residuals show a common trend: they change from positive residuals between 350 deg to 30 deg and from 90 deg to 170 deg to negative residuals from 40 deg to 80 deg and from 180 deg to 340 deg. The observed slowness values are systematically too small with respect to IASP91 It remains to be analyzed, whether this observation is due to the Earth's structure, the local geology, the topography at the array site, the array configuration, or just the algorithm of the implemented fk-analysis. Most of the mislocation vectors of GERESS in Fig. 6 are small with respect to their standard deviation. Therefore it may not be useful, to correct the observed slowness and BAZ values with above mislocation vectors. Until a more complete set of mislocation vectors becomes available, mean standard deviations (1.17 sec/deg and 23.7 deg) can be used to weight the GERESS slowness and BAZ values in location algorithms (e.g., IMS).

Conclusions and Recommendations

For calibrating an α-station, various investigations are recommended: the characterization of the noise, the estimation of the station sensitivity as a function of frequency (including signal to noise ratio improvement by beamforming for arrays), and the determination of station residuals (w.r.t. travel-time, slowness vector, and magnitude).

For the GERESS array, studies of this kind have been performed. The noise and detectability studies have been presented previously.

The GERESS contribution to global seismic data analysis has been evaluated taking the NEIC bulletin as reference. In the teleseismic distance range (20° - 180°), GERESS detected 44.6 % of the corresponding NEIC events. As expected, the detection capability of GERESS changes with epicentral distance; for events in the Earth's core shadow GERESS observed only 10 % to 20 % of all corresponding EDR events. In contrast, for PKP arrivals GERESS observed about 85 % of all EDR events due to the caustic. The daily variation (about 8 %) of the detection capability for GERESS could be associated to an increase of cultural and industrial noise during working hours. Seasonal effects of the detection capability for GERESS could not be identified.

Due to the small aperture, GERESS has only a limited resolution in measuring slowness and back-azimuth of teleseismic onsets. However, systematic mislocation vectors were found for GERESS.

GERESS shows a pronounced negative travel time residual (-0.66 sec) similar to highly sensitive arrays (e.g., YKA, HFS, NB2); GERESS also exhibits a negative mb residual (-0.60) which correlates to the general trend of other small aperture arrays.

Literature

Fyen, J. (1987). Improvements and modifications, Semiannual Technical Summary, 1 October 1986-31 March 1987, NORSAR Sci. Rep. No. 2-86/87, Kjeller, Norway.

Grand, S. P. (1990). A possible station bias in travel time measurements reported to ISC, *Geophy. Res. Let.* **17**, 17-20.

Harjes, H.-P. (1990). Design and siting of a new regional array in Central Europe, *Bull. Seism. Soc. Am.* **80**, 1801-1817.

Jost, M. (1992): GERESS P-wave detectability. In: Advanced waveform research methods for GERESS recordings. DARPA Annual Report No. AFOSR-90-0189, Scientific Report No. 2, PL-TR-92-2142, 13-24, ADA253686.

Kennett, B. L. N. and E. R. Engdahl (1991): Travel times for global earthquake location and phase identification. *Geoph. J. Int.* **105**, 429 - 466.

Kvaerna, T. (1989). On exploitation of small-aperture NORESS type arrays for enhanced P-wave detectability, *Bull. Seism. Soc. Am.* **79**, 888-900.

Mykkeltveit, S. and H. Bungum (1984). Processing of regional seismic events using data from small- aperture arrays, *Bull. Seism. Soc. Am.* **74**, 2313-2333.

Schweitzer, J. (1992): The GERESS contribution to the GSETT-2 experiment 1991. In: Advanced waveform research methods for GERESS recordings. DARPA Annual Report No. AFOSR-90-0189, Scientific Report No. 2, PL-TR-92-2142, 25 - 49, ADA253686.

Schweitzer, J. (1993): Teleseismic detection and location capabilities of the GERESS array. In: Advanced waveform research methods for GERESS recordings. DARPA Annual Report No. AFOSR-90-0189, Scientific Report No. 3, 33 - 50.

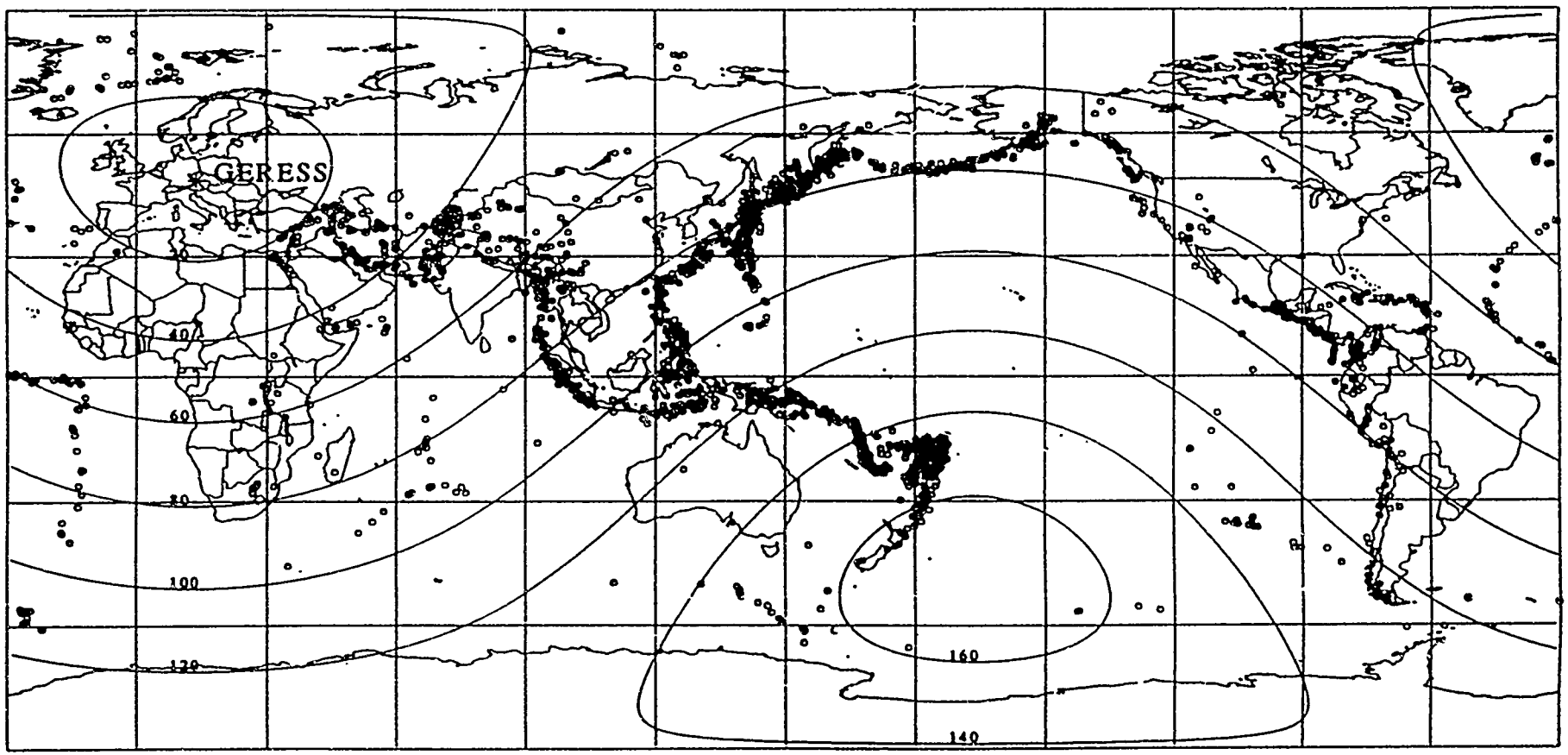

Fig. 1: All events (Δ> 20 deg) for which NEIC associated a GERESS onset (Oct. 18, 1991 - Feb. 11, 1993).

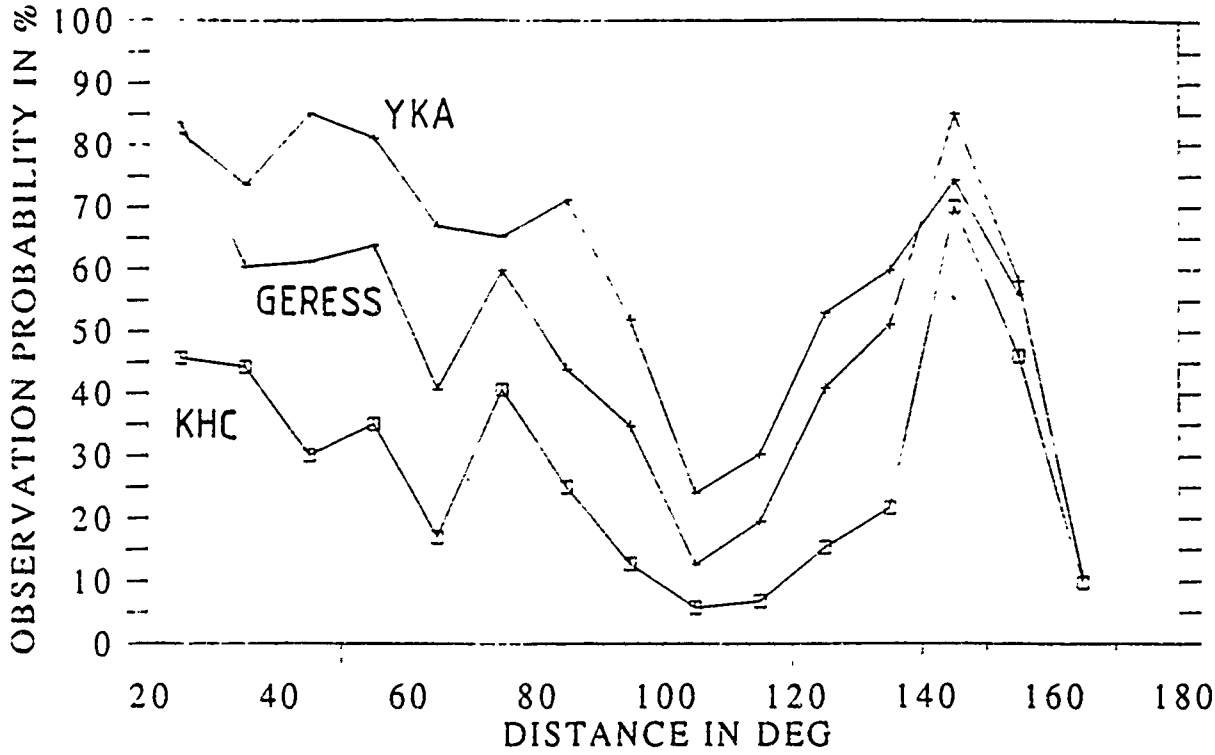

Fig. 2: The probability to observe an EDR event at GERESS (crosses), at YKA (triangles), and at KHC (circles) with respect to epicentral distance (Oct. 18, 1991 - Feb. 11, 1993).

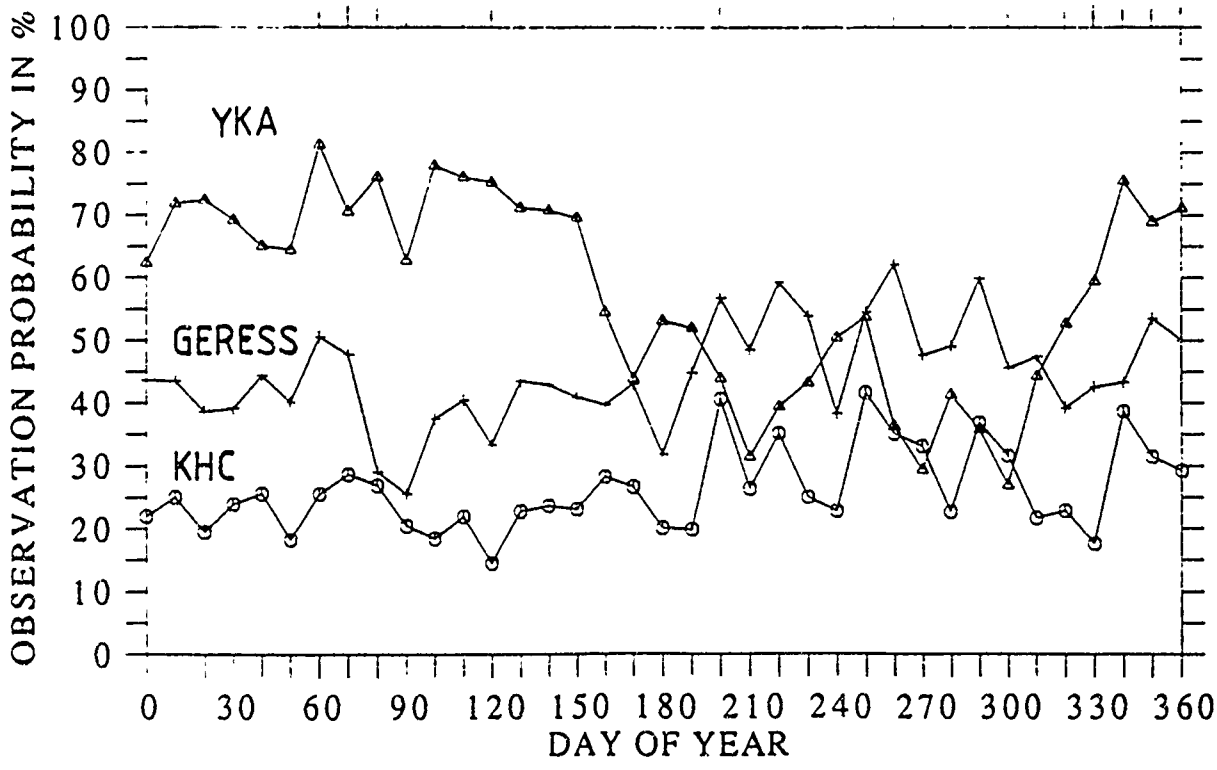

Fig. 3: The probability to observe an EDR event ($\Delta > 20$ deg) at GERESS (crosses), at YKA (triangles), and at KHC (circles) with respect to day of year (Oct. 18, 1991 - Feb. 11, 1993).

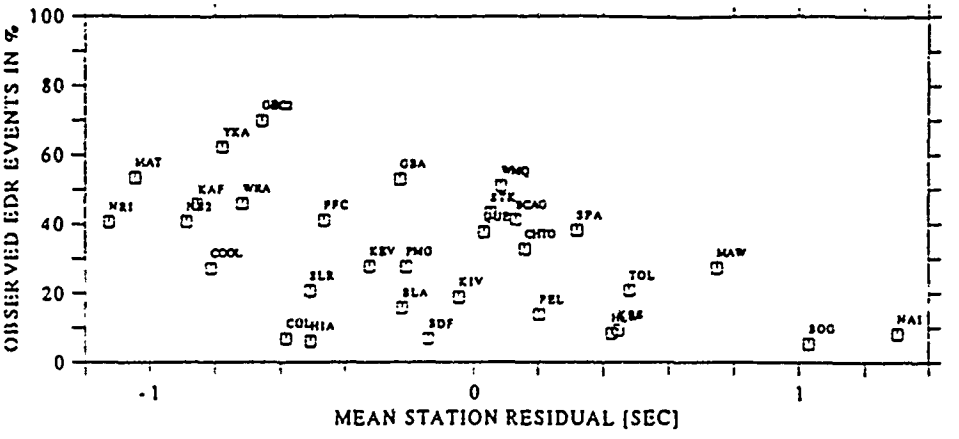

Fig. 4: Percentage of NEIC events (Apr. 1990 -Jun. 10, 1993) observed at various seismic stations versus mean travel time residual.

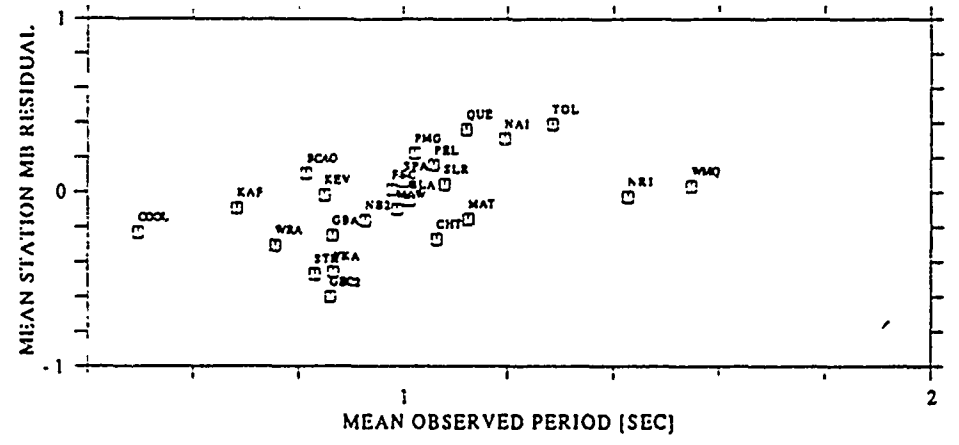

Fig. 5: Mean m_b residuals of various stations with respect to the average observed periods (events of Apr. 1990 - Jun. 10, 1993).

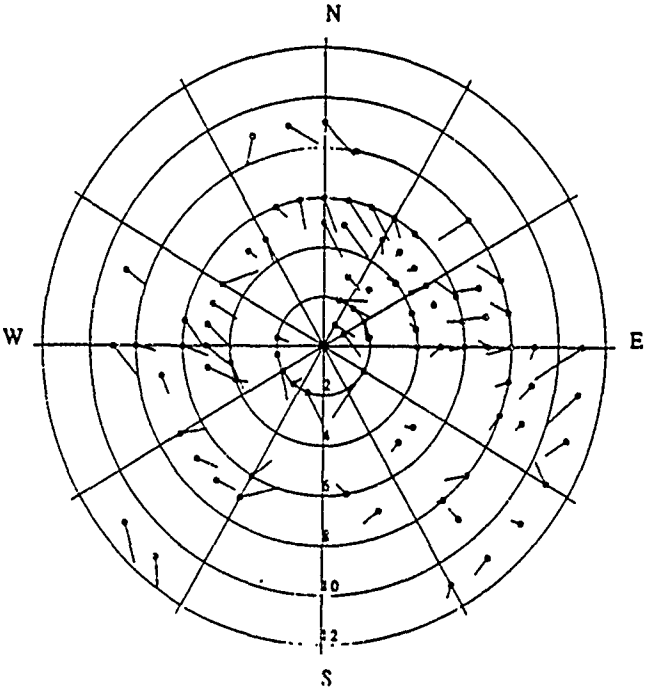

Fig. 6: GERESS average mislocation vectors with at least 5 observations (symbol is for the theoretical value; Apr. 22 - Jun. 2, 1991 and Oct. 18, 1991 - Jun. 10, 1993)

Resolution of prominent crustal scatterers using a small aperture array

Michael A. H. Hedlin, J. Bernard Minster and John A. Orcutt
Institute of Geophysics and Planetary Physics
Scripps Institution of Oceanography, University of California at San Diego

Contract No. F19628-93-K-0021

1. Objective

Recently, we have assessed the degree to which large topographic features, illuminated by teleseisms, contribute identifiable seismic phases to coda recorded by nearby seismometers. We have developed a technique that images local scatterers in 2-D in much the same way that subsurface interfaces are imaged in 1-D by standard reflection seismic profiling. Local scatterers are resolved by migrating the array records after suppressing the direct (teleseismic) energy. Our imaging technique (Hedlin *etal*, 1991) has been applied to NORESS array recordings of teleseisms to image the local crust for prominent scatterers. Two scatterers have been located near this array (Hedlin, 1991).

Currently, we are developing processing techniques that can be used to increase image resolution and stability. Our efforts have concentrated on deconvolution, stacking and image focusing.

2. Research Accomplished

2.a Review of the imaging technique

The underlying premise of our technique is that incident seismic waves impinging on a scatterer generate coda waves which can be detected by nearby seismometers. Given an array recording of the scattered waves enough information exists to locate and image the secondary source. We assume that the array elements are distributed in 2-D (x-y) and record in time (t). It is easily shown that the spherical wavefronts produced by a point source in a homogeneous medium appear in x-y-t space as hyperboloids about the time axis (t). To achieve the greatest enhancement of seismic motions caused by this source (at the expense of motions caused by secondary sources at other locations), and thus to achieve the best image of the source itself, we sum the motions recorded by the sensors after applying the appropriate hyperbolic time shifts. We image the local scatterers by systematically scanning for secondary sources at discrete locations throughout the area of interest. This imaging approach is a simple extension of the hyperbola summation migration method (Yilmaz, 1987) used in seismic reflection.

Since a delay-and-sum operation is involved, this method is akin to standard beamforming techniques and bears some resemblance to *f*-k analysis. This technique is distinguished, however, by its cognizance of not only the wavenumber but the onset time of a seismic arrival. As a result, the technique can be used to infer the likely geographic location of the secondary source. This method differs from previous attempts to locate large near-receiver scatterers since it is capable of accommodating simultaneously many primary events from different azimuths to give a balanced, redundant, illumination of local scatterers while suppressing the influence of near-source scatterers.

Since it is not known when, in absolute time, excitation of the scatterer occurs, it is necessary to use elementary ray theory to estimate what time delay, τ, should exist between the arrival of the primary energy and the scattered phases. Considering a single event-scatterer pair, the time offset, τ, between the arrivals of energy propagating directly from the source (at vector slowness p_i) and via the scatterer (vector slowness p_s) at a vector distance R_{as} from the array is given by:

$$\tau = R_{as} \cdot (p_i - p_s) \qquad 1)$$

In practice, there are a number of complicating factors that must be taken into account prior to constructing images of faint, local sources using synthetics or data:

• To examine local scattered phases it is necessary to first suppress the primary energy. The method we have adopted to accomplish this, introduced by Gupta *etal* (1990), is known as beam correction and simply involves the coherent subtraction of the primary source beam from all the individual channels to yield residual seismograms.

• Because we are dealing with dispersed energy, we have concluded that the trade-off between image resolution and stability can best be mitigated by not migrating coherent records but converting the results to envelopes prior to integration in a method akin to incoherent beamforming (Ringdal *et al*, 1975). To further enhance image stability we integrate the envelopes in time prior to migration.

2.b Image resolution

The resolution of the imaging technique can be assessed by imaging synthetic scatterers. Using wavenumber integration (Apsel and Luco, 1983) we consider a localized omnidirectional scatterer (delta function in space) illuminated by an impulsive incident wave (delta function in time). Considering our analysis of data in the next section we have located our synthetic receivers as actual receivers are deployed in the NORESS array. In the preliminary analysis of synthetic seismograms, computed individually for each of the sensors in the array, we have placed a secondary R_g source at the free surface 35 km to the southwest of the array.

The radial resolution of this source (Figure 1) is limited somewhat by the dispersion of the R_g packet, but to a greater extent by the time-averaging (in this case 5 seconds). The azimuthal resolution is very poor primarily because the coherence of the surface waves, computed with only a small degree of numerical noise, is very high, because we are employing envelopes of the beams and because of the small aperture of the array. Energy is aliased away from the actual location of the scatterer to locations which share the same delay time. By manipulation of equation 1, it can be shown that scatterers which share a common delay time τ lie on a curve described by:

$$R_{as} = \tau / [|p_s| - |p_i| \cos(\theta)] \qquad 2)$$

where θ is the angle between the back azimuth to the primary source and the back azimuth to the scatterer. When p_s is greater than p_i (*e.g.* P to R_g scattering) this describes an ellipse with one focus at the center of the array, major axis pointing to the primary source and eccentricity equal to p_i / p_s. In this synthetic calculation the primary source was located directly beneath the array ($p_i = 0$) and thus the curves of constant τ have degenerated into circles centered on the array.

2.c Resolution enhancement

2.c.i Deconvolution

The imaging technique described above assumes that the scatterers are excited only once by an impulsive teleseism - an assumption clearly at odds with reality. A fundamental ambiguity exists when trying to locate sources of scattered energy using protracted teleseisms. One apparent source may be inferred to exist at a greater distance from the array than another either because it is truly located farther from the array or due to excitation by a tardy primary arrival. To demonstrate the impact ignoring this complication we display an image computed from a NORESS recording of an earthquake (day 134, 1985, 10.7° S, 41.3° E) in Figure 2. Two sources appear near the array (to the east and southwest). Considering the findings of Gupta *etal* (1990) and Bannister *etal* (1990) it seems likely that these sources are due to topographic features located 10 km to the east and 35 km to the southwest of the array. The ellipses displayed in the figure were calculated for sources at these locations. An additional, relatively distant, apparent source inferred to exist in the third quadrant is not predicted by either ellipse. Is this distant source real or simply due to late excitation of the closer scatterer?

We attempt to answer this question by adopting a simple model for the array records. In this model, the individual sensor recording, $d(t)$, is expressed as the convolution of the site impulse response, $m(t)$, and the sequence of arrivals from the primary source, $b(t)$, *i.e.*:

$$d(t) = m(t) * b(t) \qquad 3)$$

We define the site impulse response, $m(t)$, to be the wavefield that would be recorded by that sensor in the event of impulsive excitation of the local scatterers by a plane wave with the wavevector appropriate for the teleseismic source. We estimate $b(t)$ by beamforming the array records for the primary source.

To synthesize the interaction between a scatterer located 35 km to the southwest of the array and the earthquake teleseism we have convolved the beam of this event with the synthetics displayed in Figure 1. This image (Figure 3) implies the existence of a false source roughly 70 km to the southwest of the array. We know that this energy originated only 35 km from the array but is due to an energy burst that arrived roughly 10 seconds after the primary onset. The similarity of the third quadrants of Figures 2 and 3 is unmistakable - the distant source in Figure 2 is clearly false.

Given the convolutional model we can suppress the influence of tardy arrivals by deconvolving an estimate of the teleseismic wavefield from the individual array records. We have treated this deconvolution as an inverse problem (see Hedlin, 1991 for details). In Figure 4 we present the results of this processing applied to the data in Figure 3. By comparing Figures 1, 3 and 4 we see that the false source has largely been removed, and that the true source has been placed in the proper location (closer to the array) and accurately imaged.

2.c.ii Stacking

Imaging local scatterers with only a single primary event has several drawbacks. It leaves the image susceptible to near source effects and incomplete beam correction. The analysis of single primary events forces a trade-off between azimuthal and radial resolution. Azimuthal smearing along elliptical curves can be suppressed by increasing time-averaging, but this causes degradation of radial resolution. Image quality (resolution and stability) in the current analysis can be increased by simultaneously considering a number of primary events. In effect we are increasing the fold of coverage (Yilmaz, 1987) to achieve superior images.

To demonstrate the power of stacking we begin the analysis by considering a single hypothetical scatterer located 35 km from NORESS at a back azimuth of 225°. We know that if this source is illuminated by teleseismic energy propagating at a non-infinite phase velocity then energy will be aliased from this source along elliptical curves that depend on the back azimuth to the primary event and slowness of the teleseismic energy. Specifically, the ellipse has one focus at the array, the major axis points toward the primary source and the eccentricity is proportional to $|p_i|$. We can thus increase azimuthal resolution of the point source by stacking images obtained using a broadly distributed set of teleseismic events since much of the aliased energy should sum incoherently. Intuitively, it seems clear that the greatest gain in image quality will be achieved using a suite of primary events that are evenly dispersed azimuthally. Such an event suite will yield the most "balanced" illumination of the local crust and the greatest suppression of primary energy not removed by beam correction. Let's assume our hypothetical scatterer has been illuminated by 30 teleseisms all arriving at a phase velocity of 15 kms^{-1}. To achieve the most balanced illumination of the scatterer, that is possible given 30 primary events, each event is located at a multiple of 12° from due north to 348°. Since the location of the scatterer and the incident, and scattered, slowness vectors ($|p_i|$ and $|p_s|$ respectively) are known we can use Equations 1 and 2 to predict where energy will be spatially aliased when the scatterer is illuminated using each of these primary events. The aliasing caused by these 30 events is described by the set of 30 ellipses displayed in Figure 5. This figure gives some indication of the enhancement of azimuthal resolution we can hope to attain via the stacking of a uniformly distributed suite of teleseismic events. The more broadly spaced the ellipses are, the greater the suppression of amplitudes (originating at the secondary source) should be, since the energy is being more spatially dispersed. Conversely, the more closely the curves are grouped, the greater the enhancement should be. All 30 curves converge at the location of the scatterer and thus maximum enhancement of amplitudes will occur at this point. This figure illustrates that energy aliased to distant azimuths (greater than 45° from the secondary source) should be well dispersed. All ellipses emanate from the secondary source location to the northwest and southeast, so we might expect local distortion of the image of the point source. Specifically, it should become elongate to the northwest and southeast, and, if time averaging is used, somewhat blurred radially. Finally, since each ellipse comes tangent to either the inner, or outer, bound, the ellipses are somewhat concentrated at the edges of the bounding curves.

To take this analysis one step further we place an omnidirectional scatterer at this location and illuminate it by the 30 synthetic teleseisms, which we constrain to be impulsive in time. The scattered wave synthetics were generated using wavenumber integration. If we compute images using all 30 teleseisms and then stack we arrive at the image displayed in Figure 6. As predicted by Figure 5 the distant aliasing is reduced by a significant degree (beyond 45° the maximum amplitude in Figure 1 is roughly -10 dB, in Figure 6 it is reduced to -25 dB). At close azimuths the image is distorted to be elongate to the northwest and southeast and slightly wider radially - conditions predicted by Figure 5. As expected, energy tends to concentrate at the edges of the bounding curve. Despite the minor drawbacks, the synthetics reveal that image quality should be dramatically enhanced by stacking. The advantage provided by stacking should increase in the presence of seismic noise. A stack of events should suffer less from the effect of additive noise that is temporally uncorrelated over the time scales that separate the primary events. Furthermore, using a broadly distributed suite of primary events should lead to the greatest possible suppression of primary energy which remains after beam correction.

2.c.iii Focusing

When stacking it is important to ensure that the correct velocity (p_S) is used. Given a well distributed set of teleseisms, use of an inaccurate velocity will lead to the loss of spatial resolution through defocusing. To demonstrate this we re-examine the synthetics presented in Figure 6. In Figure 7 we look at the source in the third quadrant by employing three scattered wave slownesses. In this example the resolution gain achieved by using the correct slowness is subtle (*e.g.* note the -15 dB contour). The effect is particularly subtle in this example because while the teleseisms are well distributed azimuthally, they all had phase velocities of 15 km/s. A more dissimilar group of teleseisms would lead to more dramatic focusing

3. Conclusions and Recommendations

We have migrated small aperture array recordings of teleseisms to resolve nearby synthesized and real scatterers in much the same way that subsurface sources are resolved by migrating 1-D reflection profiles. We have found that processing techniques common in reflection profiling (deconvolution and stacking) are useful in enhancing the resolution of the secondary sources. We have used image focusing to optimize the resolution gain made possible by stacking. We are currently assessing the resolution gain that can be realized by combining the array processing just described and three component analysis.

4. References

Apsel, R.J. and Luco, J.E., On the Green's functions for a layered half-space, part II. *Bull. Seismol. Soc. Am.*, 73, 931-951, 1983.

Bannister, S.C., Husebye, E.S. and Ruud, B.O., Teleseismic P coda analyzed by three-component and array techniques: Deterministic location of topographic P-to-Rg scattering near the NORESS array. *Bull. Seismol. Soc. Am.*, 80B, 1969-1986, 1990.

Gupta, I.N., Lynnes, C.S., McElfresh, T.W. and Wagner, R.A., F-k analysis of NRESS array and single station data to identify sources of near-receiver and near-source scattering, *Bull. Seismol. Soc. Am.*, 80B, 2227-2241, 1990.

Hedlin, M.A.H., Analysis of seismic coda to identify regional sources and image strong crustal scatterers, PhD thesis - University of California at San Diego, 1991.

Hedlin, M.A.H., Minster, J.B. and Orcutt, Beam-stack imaging using a small aperture array, *Geophysical Research Letters*, 18, 1771-1774, 1991.

Ringdal, F., Husebye, kE.S. and Dahle, A., P-wave envelope representation in event detection using array data. *Exploitation of Seismograph Networks, K.G. Beauchamp, Editor, Noordoff-Leiden*, 1975.

Yilmaz, O., *Seismic data processing*. Society of Exploration Geophysicists, investigations in geophysics, 2, 1987.

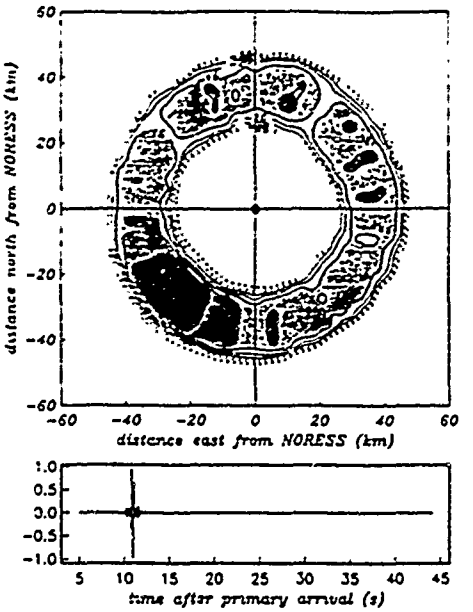

Figure 1 Image of a synthetic point source located 35 km from the array at a back azimuth of 225°. Wavenumber integration was used to generate synthetic seismograms individually for each of the 25 vertical component sensors in the NORESS array (illustrated is the synthetic computed for the center station). In this, and all subsequent images, contour values indicate amplitudes in dB relative to the largest value in the image and cylindrical propagation of scattered wavefronts was assumed.

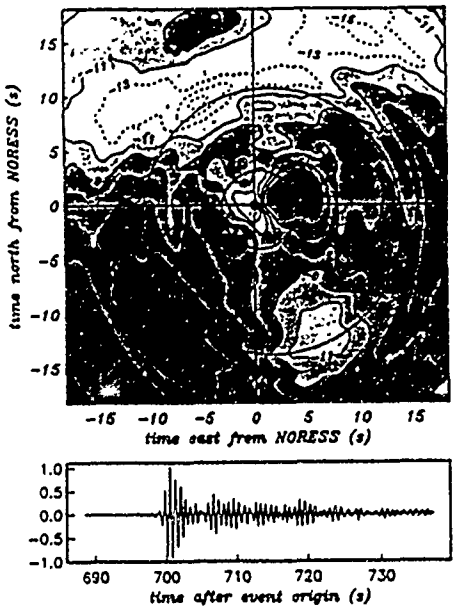

Figure 2 Image of the scattering field in the vicinity of the NORESS array obtained using recordings of a single earthquake (day 134, 1985; 10.7° S, 41.3° E). The beam computed for the earthquake is pictured in the lower half of the figure. Overlain on the image are ellipses representing the curves of constant delay time appropriate for scatterers illuminated by this event).

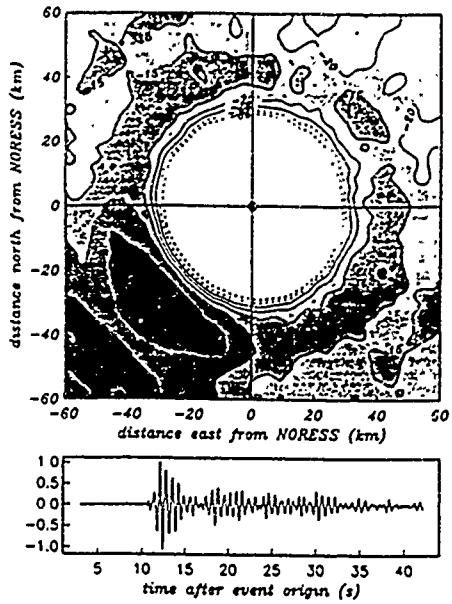

Figure 3 Displayed is the image computed using time series that have resulted from the convolution of the synthetics displayed in Figure 1 and the recorded teleseism displayed in Figure 2. Illustrated in the lower figure is the a0 synthetic/recorded seismogram. This figure is included to illustrate what degradation of radial resolution we expect when local point scatterers are excited by a relatively protracted teleseism.

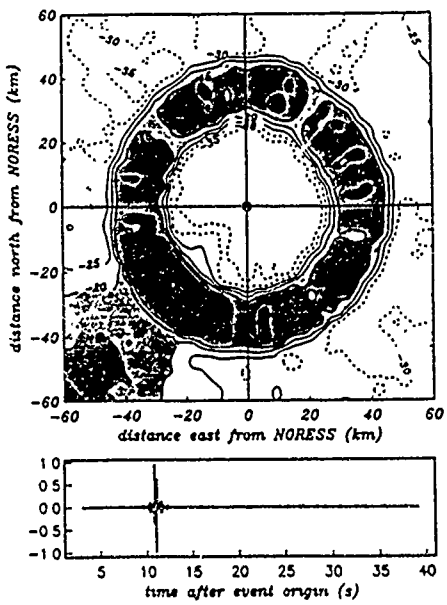

Figure 4 The result of the deconvolution of the teleseism displayed in Figure 2 from the seismograms represented by the trace in Figure 3. Perfect deconvolution would result in this image being identical to that displayed in Figure 1. Displayed in the lower figure is the deconvolved channel a0.

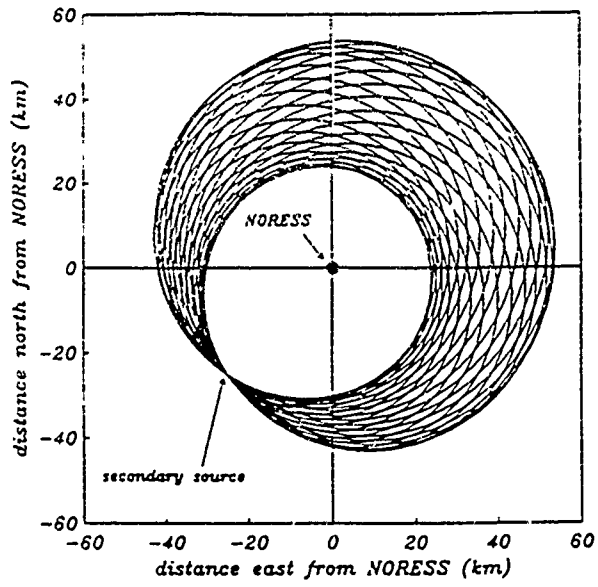

Figure 5 A suite of 30 ellipses computed using equation 1. A single point scatterer has been located 35 km from NORESS at a back azimuth of 225°. This scatterer is illuminated by 30 teleseismic events regularly spaced in back-azimuth. All teleseismic arrivals have a phase velocity of 15 km/s.

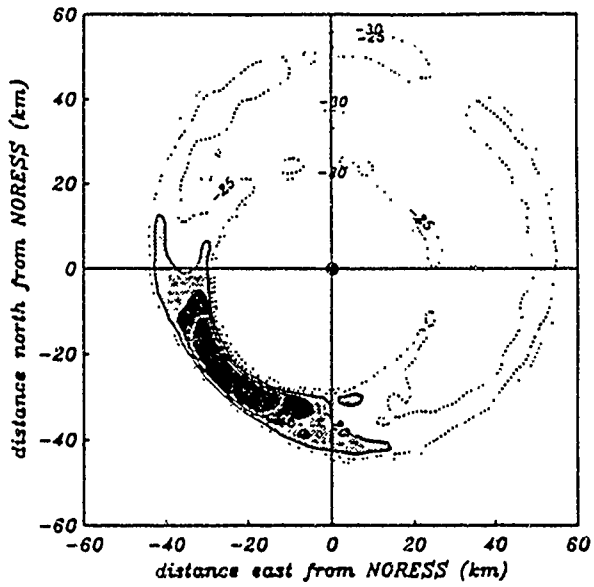

Figure 6 Image of a synthetic point source located 35 km from NORESS at a back azimuth of 225°. The secondary source is illuminated by 30 impulsive teleseisms arriving from all quadrants at 15 km/s.

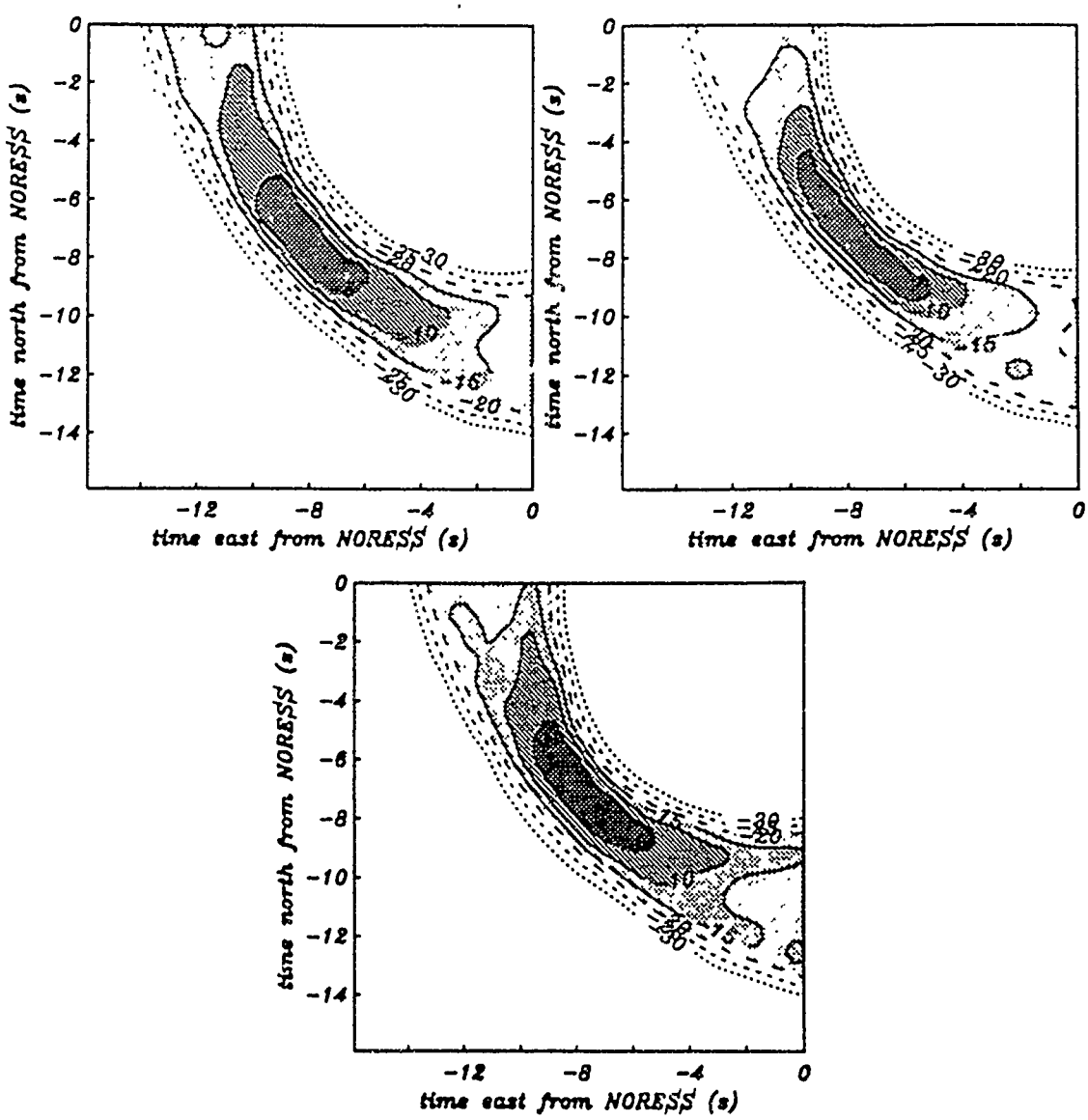

Figure 7 Image of the synthetic point source considered in Figures 5 and 6 calculated assuming a scattered wave slowness of .36 s/km. (top left) Image of the same source calculated using a scattered wave slowness of .30 s/km. (top right) Image computed using a scattered wave slowness of .27 s/km (bottom). The synthetics were produced using .30 s/km

Source Estimation, Energy Levels, and a New Discriminant

D. V. Helmberger, L. S. Zhao and B. Woods
California Institute of Technology
Contract No. F49620-92-J-0470

OBJECTIVE

Teleseismic observations of explosions tend to be richer in short-period energy than are earthquakes and, thus, the effectiveness of the m_b:M_S discriminant. At regional distances the same basic separation occurs for smaller events in terms of M_L:M_O (Woods et al., 1993) and m_b:M_O (Patton and Walter, 1993). While these studies demonstrate the basic differences in excitation they suffer in practical application because of the detailed information required in the retrieval of M_O. The objective of this report is to relax this condition and develop effective and efficient means of distinguishing small explosions from earthquakes.

RESEARCH ACCOMPLISHED

Introduction

Recent advances in broadband instrumentations coupled with new analytical techniques allows the estimations of source excitation from regional seismograms down to relatively low magnitude. To pursue this approach requires the determination of regional crustal models and path calibrations from moderate sized earthquakes or master events; in short, where earthquakes are plentiful and discrimination is difficult. Recent broadband studies of earthquakes and explosions observed on the TERRAscope array in Southern California, figure 1, demonstrate that regional recording of explosions contain considerably higher frequencies than do earthquakes, Woods, et al. (1993).

In this report we will first demonstrate that regional seismograms from earthquakes can be used to estimate their fault parameters, moment and depths applying a procedure developed in Zhao and Helmberger (1993). Next we examine the energy content of the various phases, define M_B (broadband moment) and M_E (energy strength) and introduce a new method of discrimination. In this method all events are processed as earthquakes, and explosions are distinguished by their stronger energy levels relative to their long period amplitudes.

Estimation of Earthquake Parameters

The approach followed here (Zhao and Helmberger, 1993) uses a direct grid search and does not require stable partial derivative of waveforms. This method matches complete broadband observed seismograms against synthetics over discrete phases so that timing shift between particular arrivals are allowed. This feature desensitizes the crustal model used in generating the synthetics. We demonstrate this conclusion by generating fault parameters for a number of regional events using two strongly contrasting crustal models, namely the standard SC model and a basin and range model, PB by Priestley and Brune (1978), displayed in figure 2.

As mentioned earlier we have a stor[illegible] Green's functions computed on a range interval of 5 kms for the SC model (Dreger, 1992) which are used routinely to obtain fault parameters. The fits obtained are displayed in figure 3. Note that in the automated mode the code does not always match the Rayleigh and Love waves in the most sensible fashion, see for example, the Love wave fit at ISA and the Raleigh wave fit at PFO (figure 3a). Thus, some care is needed in adjusting the model and/or some hands on adjustment if only a few stations are used. The PB model does a better job since this path is mostly basin-and-range, see figure 3b. Note that the

time shifting between P_{nl} (first 20 secs of record) and the Rayleigh wave is particularly needed in the SC case. The fits of the P_{nl} and SH phases over the TERRAscope array (figure 3b) is rather amazing and suggests that the over-all crust is not as complex as found in the earlier study of New England data, see Zhao and Helmberger (1991).

We conclude from this example that the cut and paste method allows reasonable source estimation and that the SC model is sufficient for studies of earthquakes and explosions throughout the region. This feature proves useful when addressing the discrimination issue later, since we can use the same model for the entire region.

Estimation of Seismic Energy

With the advent of broadband instrumentation we can make some useful estimates of the energy levels of sources as discussed by Kanamori et al. (1993). This is especially attractive at local and regional distances before the strong attenuation of the upper-mantle has stripped away the higher frequencies. However, we must be able to correct for the strong propagational effects produced by the crust before obtaining accurate estimates. This can be achieved empirically as suggested in the above paper. The approach developed here is more theoretically based on Green's functions even though the appropriateness of such high frequency corrections is questionable.

We proceed by making some useful definitions in terms of a source time history needed in making a broadband moment estimate. This is essential because of the importance of characterizing the source description at all periods . We define the broadband time history, assumed to be a triangle, such that the energy in the short-period (WASP) divided by the long-period window (LPZ) is equalized between the observations and synthetics over the P_{nl} phase. The broadband moment is than defined as the best fitting synthetic to the observed data assuming this time history with the orientation parameters determined by the long-period fit. Because the Green's functions are generally shorter period then the data we obtain smaller M_B moments as discussed earlier.

We define the energy, M_E, in the same fashion as M_B in that we simply define M_E to be the ratio of the total integrated broadband energy (3 components) divided by the corresponding integrated Green's functions. If the synthetics fit the observed data exactly we would obtain M_E equal to M_B or a ratio (M_E/M_B) OF 1. The plot of (M_E/M_B) for the three largest events in the region is displayed in figure 4. Most of the points fall between 1.5 and .5 except for the open star point near Δ = 428 (GSC, Arizona). An examination of this station, figure 9, indicates that the SH-component is causing the difficulty in that the synthetic is anomolously small. This is caused by fitting the data with the average mechanism over all stations. Allowing the GSC station to choose its own mechanism drops this point into the population.

This plot shows no obvious distance dependence which suggests that our path corrections are adequate. However, there is a slight base-line shift with the PB model yielding higher values. This feature is caused by the soft surface layer for this model that produces stronger Green's functions for a given moment. Thus, M_B is smaller for this structure and causes this slight shift. One might expect certain stations (soft sites) to have high (M_E/M_B) ratios. This is probably true but such stations (SBC, San Barbara) are not normally included in source studies, see Helmberger et al. (1993).

The discriminants introduced earlier were based primarily on the short-period richness of explosions relative to earthquakes. Woods et al. (1993) exploited this observational feature in their M_L:M_O plots. Another difference between earthquakes and explosions, as displayed in figures 6, is in the obvious complexity of the explosion records, especially at the shorter periods. Thus, if we compare the explosion data against the synthetics we see a strong difference in the

number of arrivals which translates into a large difference in energy. The precise origin of these arrivals is not known but near-in studies at NTS suggests that they are scattered Rayleigh waves, see Stead and Helmberger (1988), and others. The scattering is apparently complicated because of the shallow 3D geology with basins and ridges. TERRAscope observations of NTS events display this complexity quite well as given in figure 6. The most stable portion of these records appears to be in the fundamental Rayleigh wave. Thus, we emphasize this feature in estimating the long-period strengths of explosions. We find that synthetics Rayleigh waves remain quite simple if the source depths are confined to be greater than about 5 km. For example, synthetics for explosion sources at a depth of 1 km are distinctly discordant for the two models discussed earlier, see figure 2, while they proved quite similar for deeper earthquake sources. Moreover, our source estimation code has no difficulty with matching the Rayleigh waves with this depth restriction.

In this match of synthetics to observations we have used the (WASP/WALP) ratio to fit the time history because of the noise in LPZ. A source time function triangle (0.1, 0.1) is obtained. While the short period details are not well explained, the over-all estimate of long-period are reasonable. We obtain a moment of 1.1×10^{22} dyne-cm and a source orientation of (220, 30, 115). The source depth search preferred the depth of 5 km which is the shallowest depth allowed. Woods et al. (1993) obtained a $M_O = 3 \times 10^{21}$ dyne-cm for this event or about 4 times smaller. This difference is expected because of the relative strengths of Rayleigh wave Green's functions. But the absolute value of M_O does not matter if we compute the (M_E/M_B) ratio which is in this case (2.3).

The explosion data of figure 6 should be contrasted with a natural earthquake in the same region (Yucca Mtn) shown in the lower panels. Again the (WASP/WALP) ratio was used in fixing the time history, (.1,.1). The over-all fits of the various pass-bands for this small event is quite good and indicates that modeling earthquakes is relatively easy compared to modeling explosions. This match is reflected in its relatively low (M_E/M_B) ratio of (1.6).

The parameters for these two events along with a small population of events occurring at NTS and southern California are displayed in figure 5. Most of the earthquakes have ratios near 1 while the explosions are larger, especially for the smaller magnitudes. Note that the data has been analyzed by individual stations so that estimated source parameters vary but the (M_E/M_B) ratios appear to behave quite well. The basic reason is that changes in the faulting parameters introduces the multiplication of the moment by radiation patterns which tends to compensate one another, that is weak radiation factors lead to enlarged moments and etc.

There is a tendency for these ratios to drop with magnitude or M_O for both populations. This feature is not understood except that the smaller the event the shorter the time history and therefore, more scatterings. The explosion populations drops faster, perhaps, indicating a source depth effect with events below the water table producing a more stable wavefield.

CONCLUSIONS AND RECOMMENDATIONS

This study demonstrates that broadband regional seismograms contain an immense amount of information about crustal structures and source characteristics. By allowing some simple time shifts to 1D synthetics we can recover much of the fundamental information about the latter without modeling all the propagational detail. Furthermore, broadband modeling allows a useful definition of broadband moment, M_B where the time history is adjusted such that the short period to long period ratio of synthetics is equalized to that in the observed P_{nl} wavetrain. M_B's tend to be smaller than M_O since they are influenced more by the largest asperity of any particular event. Accumulated energy from these Green's functions can be used to correct for path effects and estimate the energy strength, M_e. This measure appears to be independent of distance and proves effective in the recovery of short period information that can not be modeled

easily in the time-domain. We find that shallow events such as explosions tend to have extra scattered phases, probably produced by converted surface waves, and distinguished from deeper earthquakes by their (M_E/M_B) ratio. Thus, we introduced a new method of discrimination based on the use of a single broadband station. The method does require a regional model that can be developed by studying local earthquakes and, therefore, limited to tectonic regions, for example see Zhao and Helmberger (1993). In the Southwestern U.S., plots show that explosions and earthquake separate into clear populations, at least in this pilot study of 30 events. We now recommend that this technique be tested for a larger event sample, in particular for known shallow earthquakes as well as for populations in other regions.

References

Dreger, D. S., and D. V. Helmberger, Determination of source parameters at regional distances with three-component sparse network data, *J. Geophys. Res*, **98**, 8107-8125, 1993a.

Helmberger, D. V., Dreger, D., R. Stead, and H. Kanamori, Impact of broadband seismology on strong motion attenuation, *Bull. Seism. Soc. Am.*, **83**, 830-850, 1993.

Patton, H. J. and W. R. Walter (1993), Regional moment: magnitude relations for earthquakes and explosions, *Geophys. Res. Letters* (in press).

Priestley and Brune, Surface Waves and the Structure of the Great Basin of Nevada and Western Utah, *J. Geophys. Res.* **83**, 2265-2272, 1978.

Stead, R. J. and D. Helmberger, Numerical-analytical interfacing in two Dimensions with applications to modeling NTS Seismograms, *PAGEOPH*, **128**, 157-193, 1988.

Woods B., S. Kedar and D. Helmberger (1993), M:M as a regional seismic discriminant, *Bull. Seism. Soc. Am.*, (in press).

Zhao, L. S., and D. V. Helmberger, Broadband modeling along a shield path, Harvard recording of the Saguenay earthquake, *Geophys. J. Int.*, 301-312, 1991.

Zhao, L. S. and D. Helmberger (1993), Source estimation from broadband regional seismograms, *Bull. Seism. Soc. Am.*, (in press).

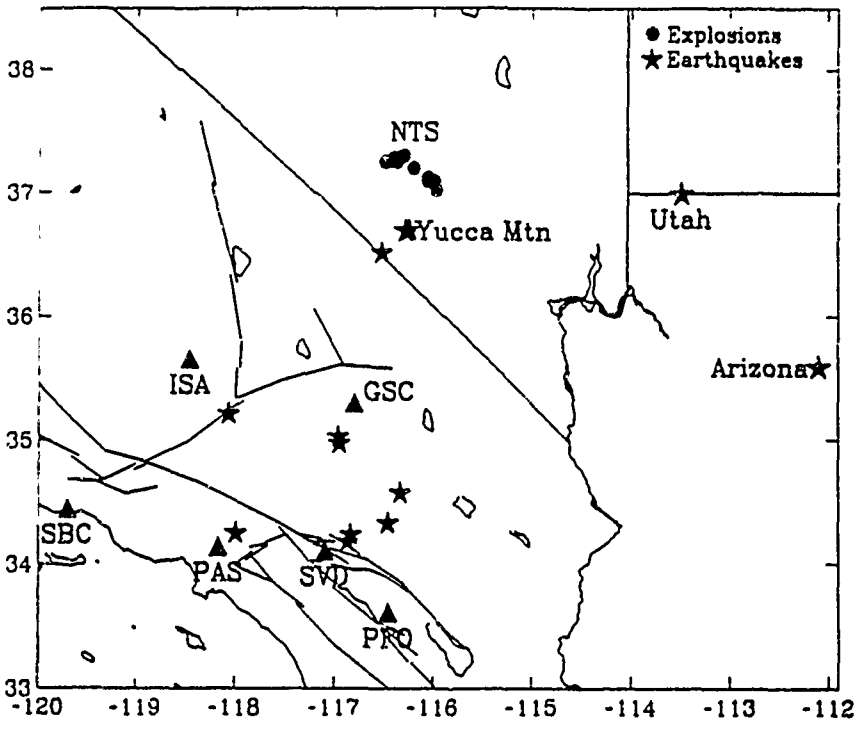

Figure 1. Map of Southwestern U.S. with locations of a number of regional earthquakes and NTS explosions.

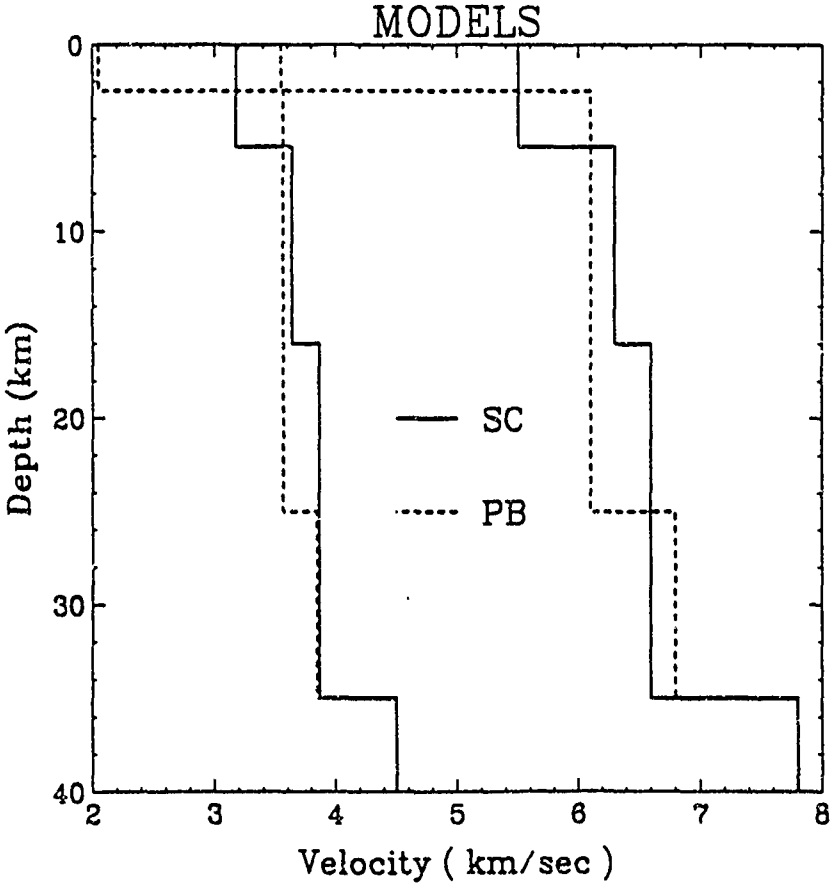

Figure 2. Crustal models of the region. SC (Dreger and Helmberger), PB (Priestley and Brune).

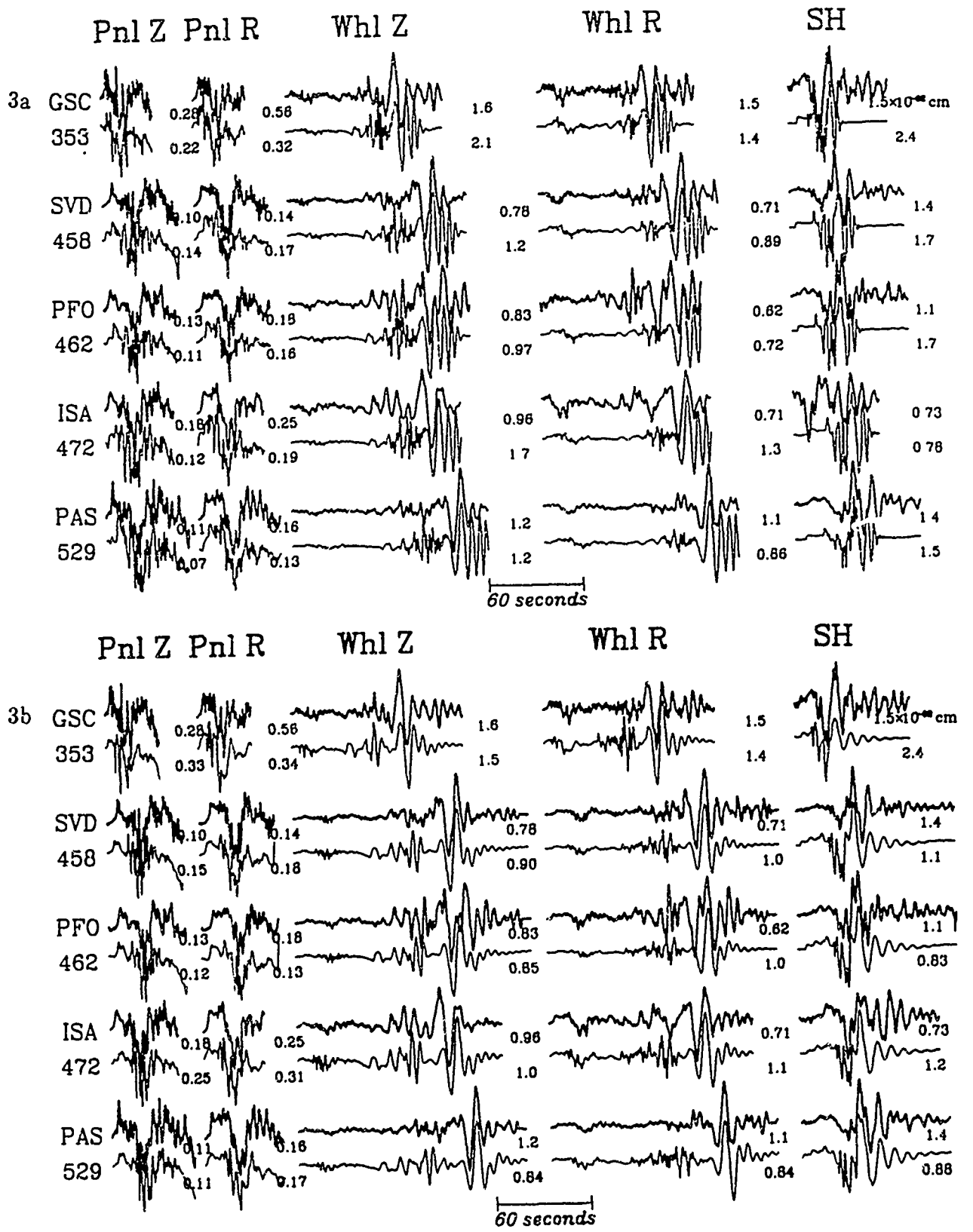

Figure 3. Comparison of broadband observations with synthetics, 3a (SC model), 3b (PB model). The former yields source parameters (345 (strike), 30 (dip), 245 (rake)), M_0=1.4X10^{24} dyne-cm, and a time history of (0.5, 0.5). The latter yields similar results, (180, 50, 250) and a moment of M_0=1.6X10^{24} dyne-cm. These results compare well with other long period regional inversions (Ritsema and Lay, 1993).

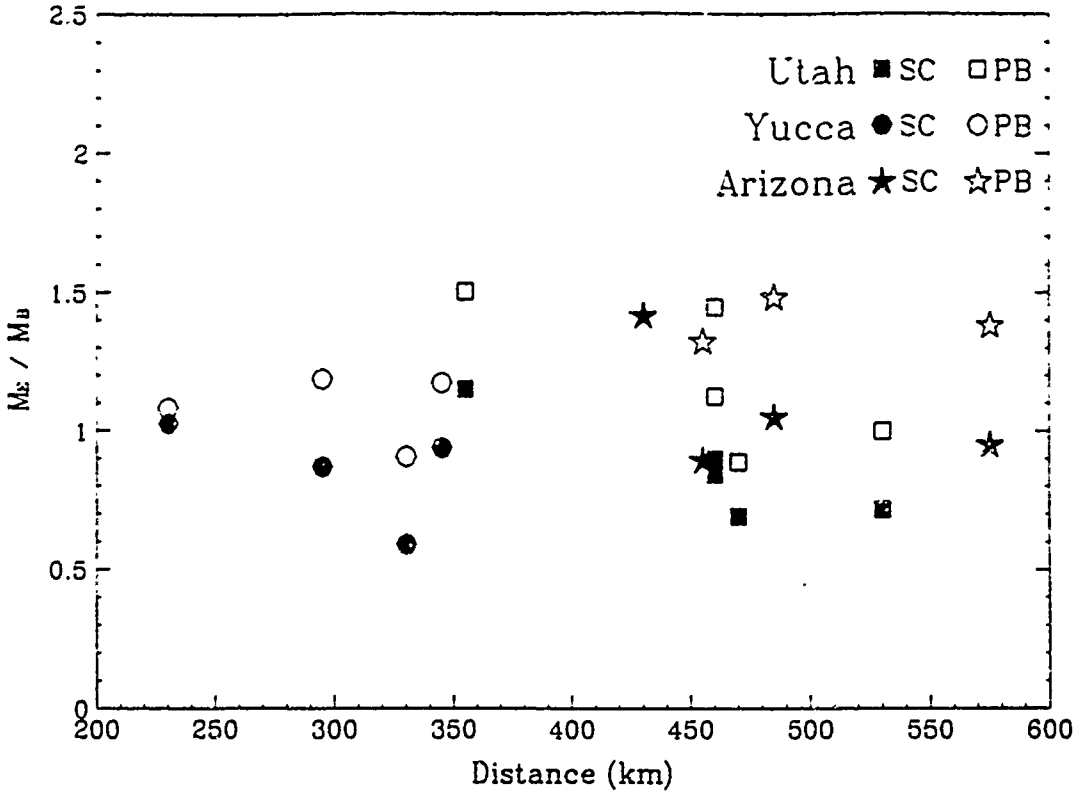

Figure 4. Plot of (M_E/M_B) ratios as a function of distance.

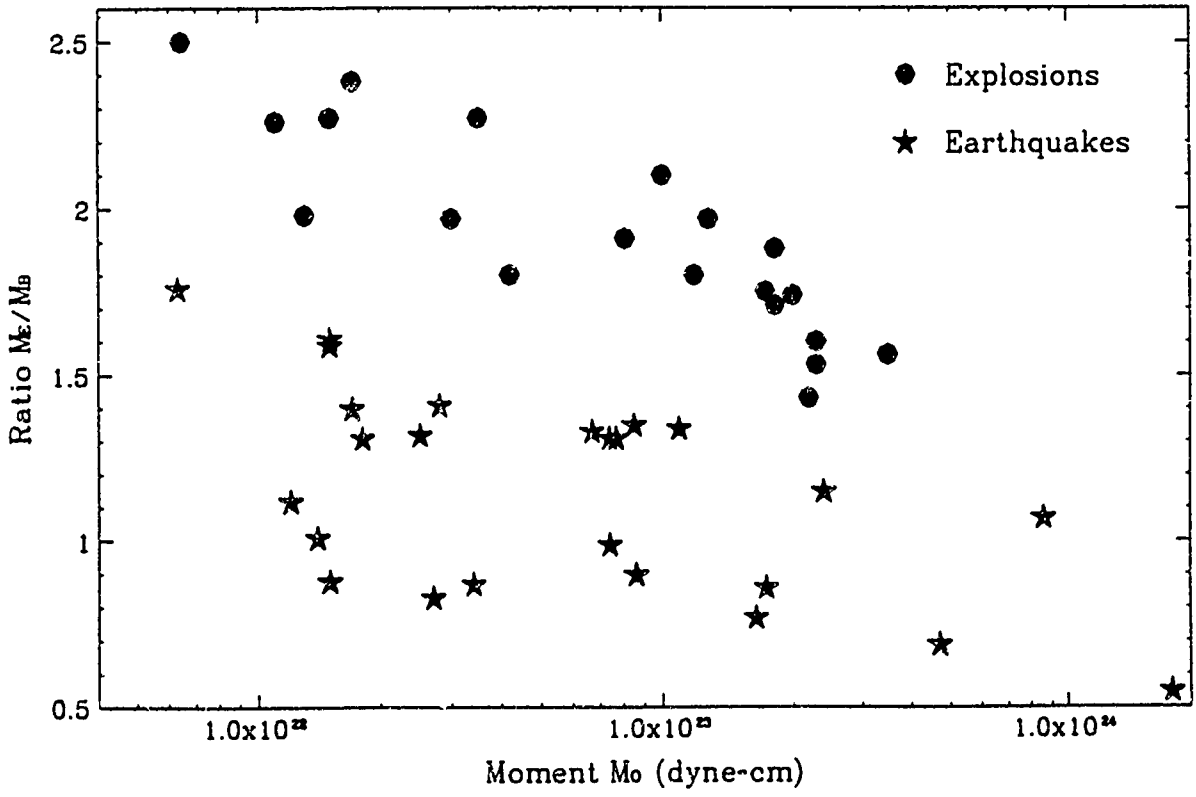

Figure 5. Plot of (M_E/M_B) ratios vs. M_0 for a population of NTS explosions and earthquakes.

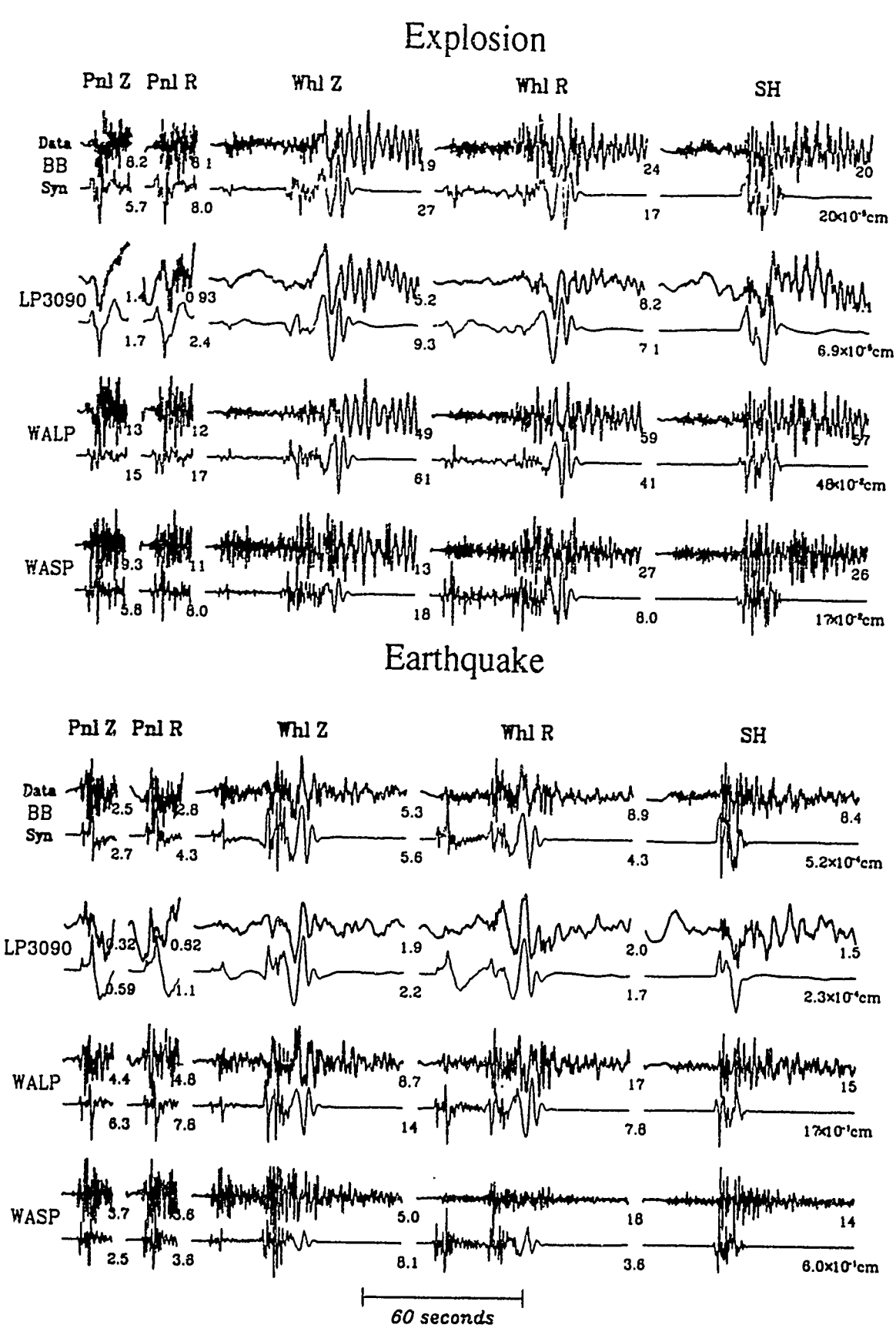

Figure 6. Comparison of the synthetic fits for two small events along similar paths displaying the complexity of explosions (6a) as compared to natural earthquakes (6b).

THE GEOTOOL SEISMIC ANALYSIS SYSTEM

Ivan Henson
Teledyne Geotech Alexandria Laboratory,
314 Montgomery Street, Alexandria, VA 22314-1581

John Coyne
Science Applications International Corporation
Center for Seismic Studies
1300 N. 17th St., Suite 1450, Arlington, VA 22209-3871

Contract No. F19628-93-C-0094

1. OBJECTIVE

The objective of this project is to continue the development of the seismic analysis system **geotool**, an X Window System-based graphics tool for displaying waveforms and performing basic analysis operations. The development of this system began in response to a need for an X Window program to display waveforms in a free format, with a highly interactive user interface suitable for research applications. **geotool** was introduced to the research community early in its development, and user needs have been the primary guide for its design. The general design philosophy is to incorporate functionality to meet specific user needs in a manner which minimizes restrictions imposed on the program as a whole. Maintaining program flexibility is a high priority. No unnecessary restrictions are imposed on how a user can combine program options, so that in addition to satisfying specific user needs, the system will also have the potential to meet many unanticipated research needs.

The program has several general functional requirements. It must be able to interpret all CSS 3.0 database tables. These can be read directly from disk files, or optionally obtained from an ORACLE database. The user interface should be as intuitive as possible, eliminating the need to study lengthy operation manuals. The data display-delay-time (the time the program requires to read and plot waveforms on the screen) must be minimized. The program must offer a set of convenient graphical tools enabling a complete visual examination of the data. A basic set of data analysis functions must be included, and the procedure for integrating new analysis functions should be as simple as possible. The program must be capable of functioning in two different environments: it must be able to interface with other software at the Center for Seismic Studies, and it must also be a standalone system easily ported to other environments. In its basic configuration, the current system requires only an X Window server. No IPC or database software is needed. Executables are currently available for SUN3, SUN4 and SGI machines.

This report is basically an introduction to **geotool**, including an overview of the system's current functionality with illustrations of its graphical tools and analysis functions and some example applications.

2. GRAPHICAL TOOLS

geotool has an unconventional, if not innovative waveform display format. There is only one set of axes for all waveforms displayed (Figure 1). The x-axis represents relative, not absolute time. The y-axis can represent a sort index, distance, back azimuth, not the usual amplitude. This format was chosen to allow an object oriented interaction with the waveforms. With mouse movements, individual waveforms can be "grabbed" and repositioned anywhere within the display window. Similarly, a waveform's amplitude scale can be changed by grabbing the curve and stretching it either away from or toward the mean amplitude. This "free" display format is very convenient for comparing waveforms by overlaying them and adjusting their amplitude scale, and it also allows waveforms to be positioned over travel time curves, a program option discussed below. As shown in Figure 1, the conventional axes coordinate values, absolute time and amplitude for each waveform, are displayed for the data values nearest a vertical line cursor which can be dragged across the window. Time windows can be specified using a set of vertical line cursors, as illustrated in Figures 5 and 6.

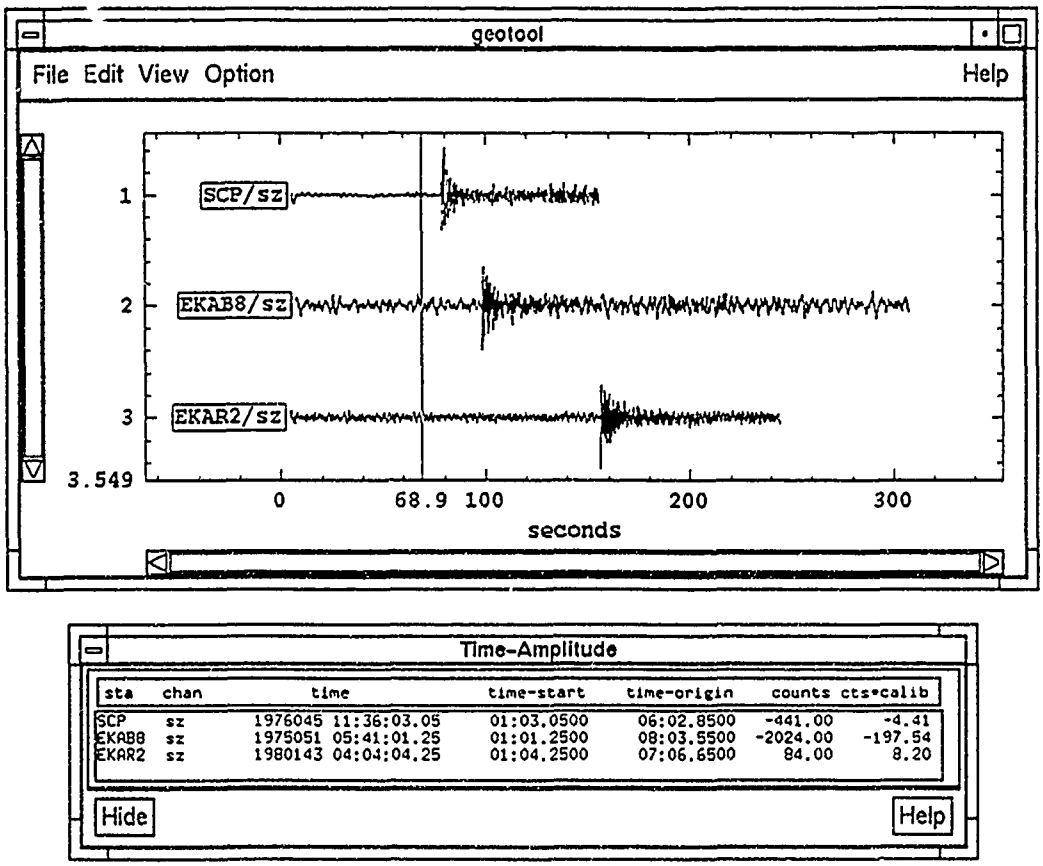

Figure 1. The main display window with three waveforms from three different events. The x-axis represents relative time and the y-axis, in this case, simply represents input order. The window beneath the waveforms displays absolute time and amplitude values for the nearest data point of each selected waveform as the vertical line cursor is dragged horizontally across the window.

The waveforms can be automatically positioned vertically by sorting with one of several different sorting criteria, such as station name, distance or azimuth, and they can be automatically positioned horizontally according to absolute time, time minus origin time, reduced time, slownesses, and predicted or measured arrival times.

The visible limits of the waveform display window can be changed with a simple zoom-in and zoom-out feature, and a separate magnify window allows small details to be examined while leaving the larger picture visible (Figure 2.). Scroll bars in both the main and magnify windows facilitate viewing. For example, a hundred waveforms can be input into the main window and scrolled one by one through the magnify window. Waveforms can be moved against a background of travel time curves to assist in phase identification. The program can display curves for JB travel times, IASPEI travel times and regional phase travel times computed from two-layer-crust models. When origin times are available, predicted phase arrival times can be displayed as tags below individual waveforms, as shown in Figure 3. Measured arrivals can also be displayed as tags above waveforms. Waveforms can be aligned on predicted and measured arrival times. **geotool** has a set of tools for picking arrivals and measuring amplitudes and periods. It is particularly efficient at making such measurements when data from one station for many events at the same source region are examined together.

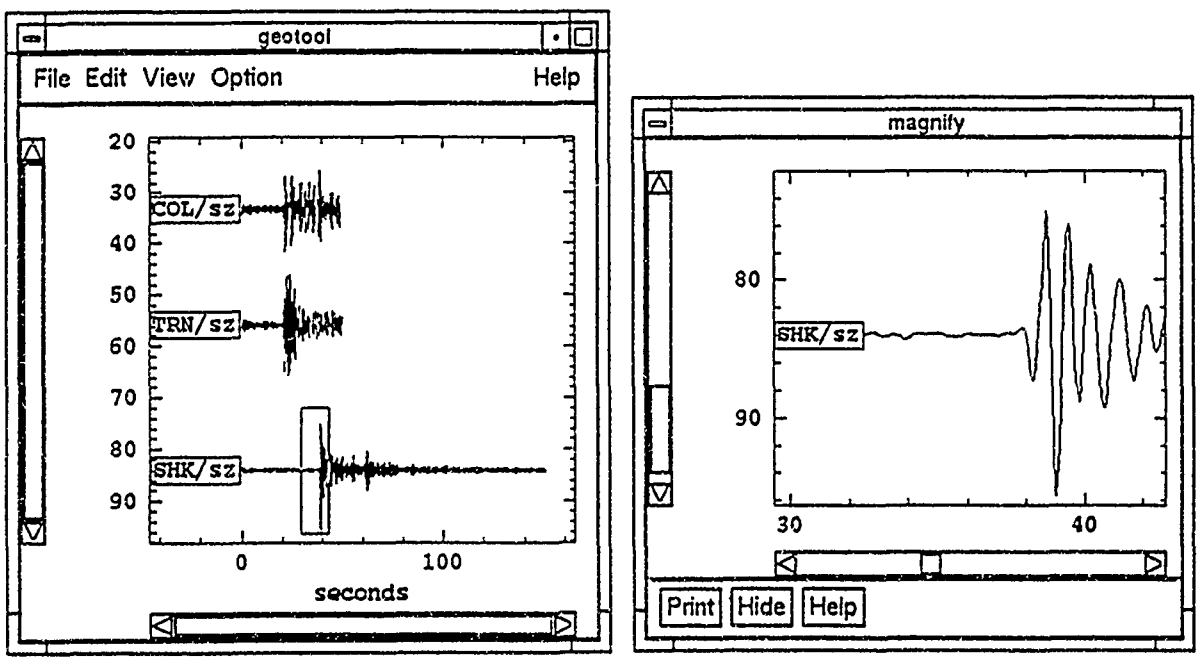

Figure 2. Left: The main display window of **geotool** displaying distance-sorted records. Right: The magnify window showing an enlargement of a small segment of the SHK/sz record which is enclosed by a rectangle in the main window. The two windows are completely coordinated and all program options are available and displayed in both windows.

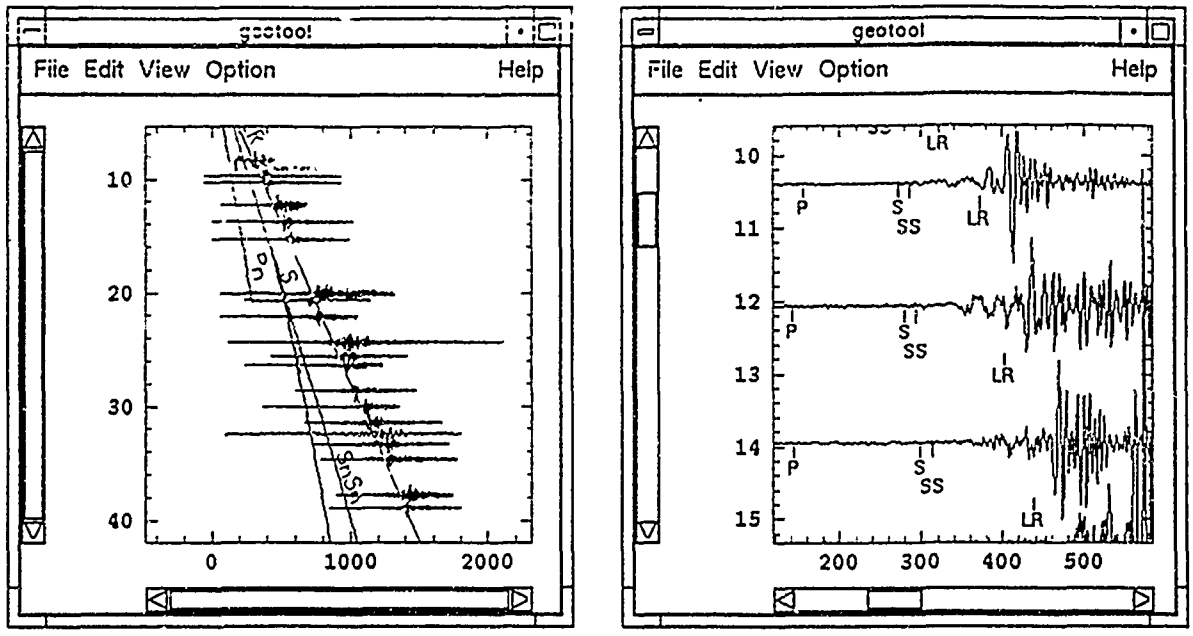

Figure 3. Left: waveforms can be freely moved against a background of selected travel time curves to assist phase identification. Right: When origin information is available, the predicted arrival times for selected phases can be flagged with labels beneath each waveform.

Nearly all of geotool's graphical windows can be regenerated into a PostScript file. Current output options include page orientation, positioning and font selection. A color option is supported in the main window.

geotool provides a map window on which stations, sources and travel paths can be displayed. The map supports three projections and coordinate system rotation. Operations between the main window and the map can be linked, for example, repositioning a source on the map can reposition waveforms based on the new source location.

3. ANALYSIS FUNCTIONS

geotool's analysis functions include beamforming, IIR filtering, particle motion, polarization analysis (Figure 4.), Fourier analysis (Figure 5.), cross correlation, deconvolution/convolution of instrument responses, f-k analysis (Figure 6.), a spectrogram and component rotation. These operations can be applied to whole waveforms or segments by designating a data window between two vertical line cursors.

A goal of the current project is to isolate these analysis functions from the graphics part of the program in a manner which will allow the easy integration of additional or replacement analysis functions. For example, it will be possible to substitute another f-k algorithm for the one supplied with geotool.

4. IPC FUNCTIONS

geotool can be receive requests through interprocess communication and it can also initiate communication with supporting programs. The CSS program CenterView, which performs database queries, can be used in combination with geotool to gather and display waveforms. The CSS program Xgbm, which generates Gaussian beam synthetic seismograms can also communicate with geotool. It can query geotool for some parameters needed in the computation, such as station location, start and end times, and phases to be included, and it can request geotool to automatically display the synthetic waveforms beside the corresponding recorded waveforms.

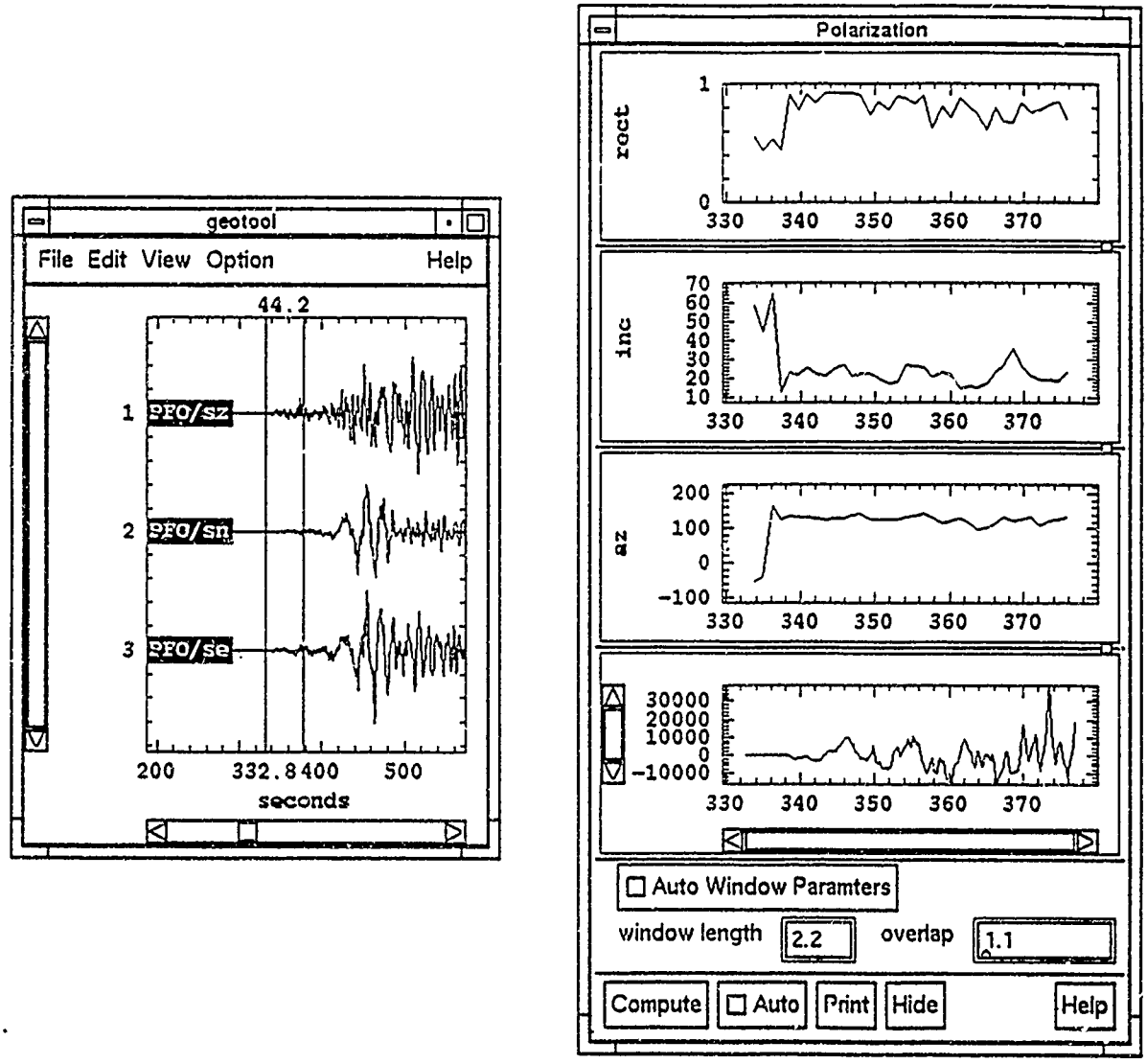

Figure 4. Left: The main display window of geotool displaying 3-component data for which a time window has been selected. Right: Polarization indicators rectilinearity, incidence and azimuth computed for the data window. geotool also contains a polarization filter option which creates a polarized trace, based on the rectilinearity, incidence, azimuth and aperture settings.

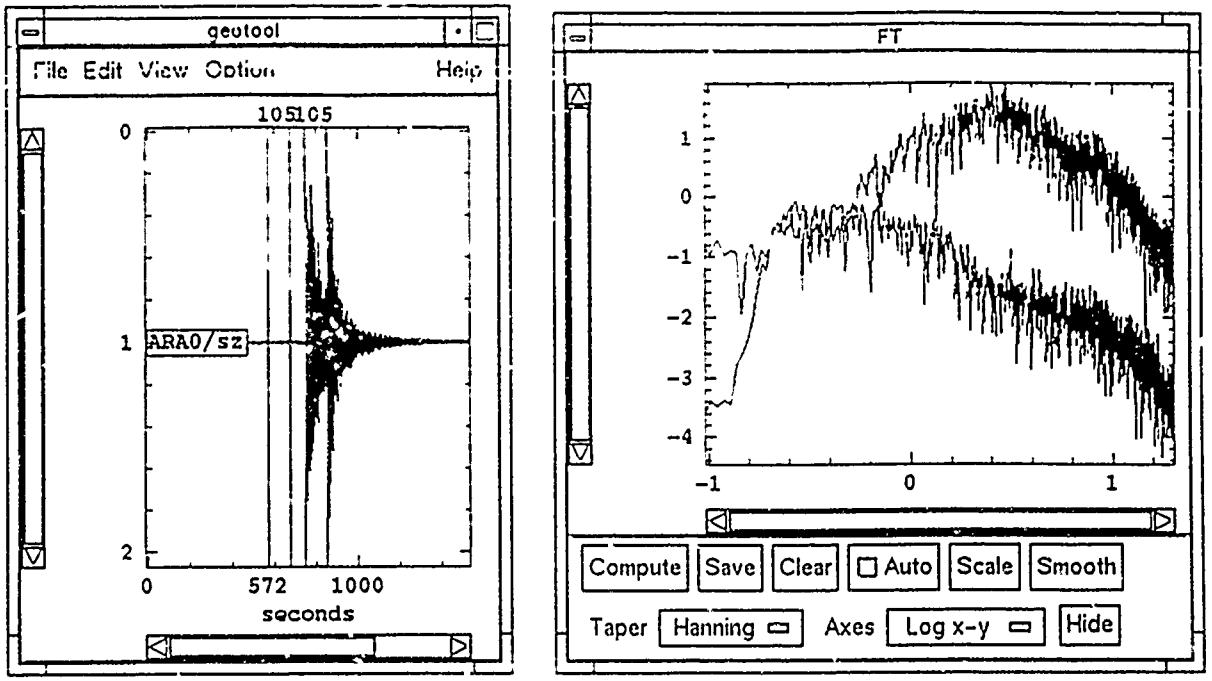

Figure 5. Left: The main display window of geotool displaying a waveform for which a noise window and a signal window (both 105 seconds wide) have been selected using two sets of vertical line cursors. Right: The amplitude spectra for the noise and signal windows in log/log space.

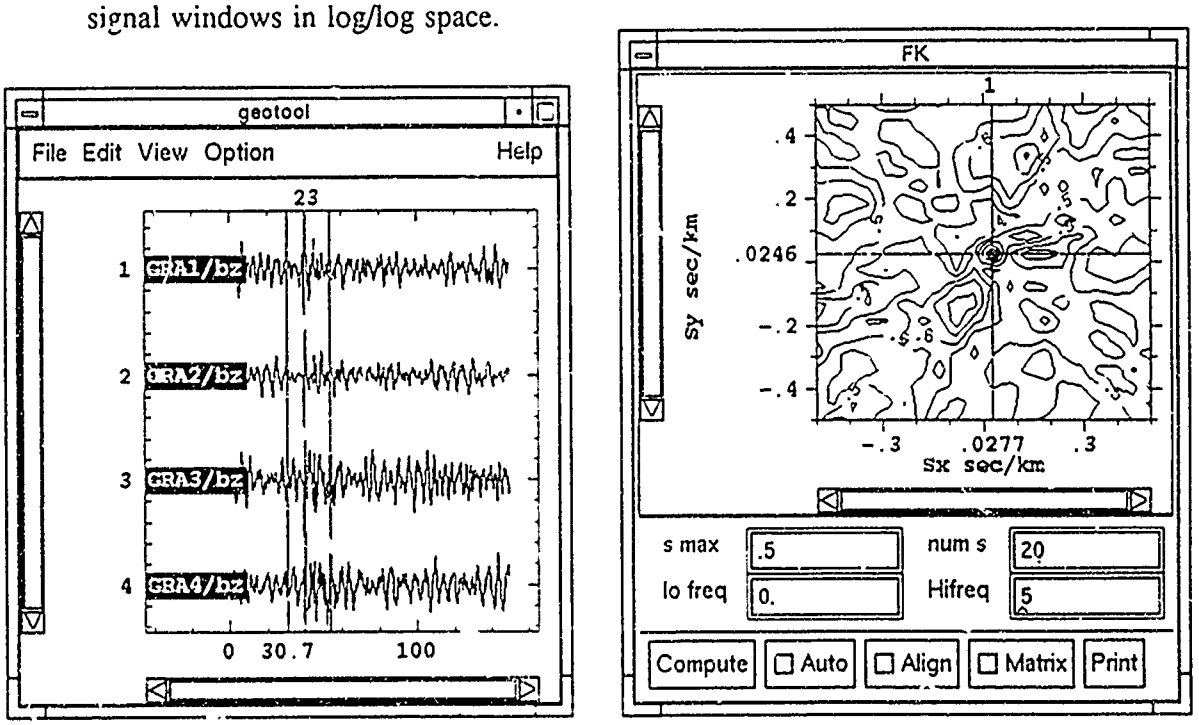

Figure 6. Left: The main display window of geotool displaying array data for which a time window has been selected. Right: A contour plot of slowness/slowness. Waveforms can be aligned and beamed for any Sx/Sy values by simply positioning the crosshair on the slowness contour plot.

5. CONCLUSIONS

geotool has proven to be a useful data display and analysis system. A number of researchers at institutions in addition to CSS have received copies of the program and have applied it to their own projects. It has proven to be an efficient tool for making measurements interactively on large data sets. Under the new contract which is just now underway, we intend to make the program even more useful to researchers on diverse projects by enabling the integration of user-defined analysis functions. Researchers will thus be able to integrate their own software smoothly with geotool's display and measurement capabilities. In this manner, it should become a standard piece of software which all researchers in the ARPA seismic research program can use, and we intend to make it generally available throughout the seismological community. For more information about the program and its current availability, please contact the authors at the addresses give above, or electronically at ihenson@beno.CSS.GOV or coyne@beno.CSS.GOV.

6. REFERENCES

Anderson, J., W.E. Farrell, K. Garcia, J. Given, and H. Swanger (1990), Center for Seismic Studies Version 3 Database: Schema Reference Manual, *Sci. Applic. Internat. Tech. Rep.*, **C90-01**, 61pp.

Corley, D. (1992), CenterView Version 1 Tutorial, Technical Report C92-01, Center for Seismic Studies, Arlington, VA, 32pp.

Davis, J. P. and I. H. Henson (1993), Development of an X-Windows tool to compute Gaussian beam synthetic seismograms, *TGAL-93-03*, Phillips Laboratory, Hanscom AFB, MA, 16pp.

Jeffreys, H. and K.E. Bullen (1940), Seismological Tables, British Association for the Advancement of Science, Burlington House, London.

Jurkevics, Andy (1988), Polarization Analysis of Three-Component Array Data, *Bull. Seis. Soc. Amer.* **78**, 1125-1743.

Kennett, B.L.N. (1991), IASPEI 1991 Seismological Tables, Australian National University, Canberra.

TITLE: Design, Evaluation and Construction of Two Nine Element Experimental Arrays TEXESS and LUXESS

AUTHOR(S)& AFFILIATION
Eugene Herrin, Paul Golden
Southern Methodist University
Department of Geological Sciences
Dallas, TX 75275

CONTRACT NO.: F19628-93-C-0057

OBJECTIVE

The objective of our program is to develop new seismic array technology for use in a global data exchange program conducted under the auspices of the United Nations Conference on Disarmament (UN/CD). Current UN/CD plans call for a full scale data exchange experiment to begin in early 1995. The plans include a network of up to 50 'Alpha' array stations sending continuous data to an International Data Center (IDC). In addition, there could be as many as 150 'Beta' stations which can send data to the IDC on request, to refine the locations of events determined from the Alpha network.

SMU participation in the program involves the construction of two experimental seismic arrays, one in Egypt approximately 100 km east of the city of Luxor, to be named the Luxor Experimental Seismic Station (LUXESS) and one at the existing Lajitas (LTX) station, designated the Texas Experimental Seismic Station (TEXESS). Both these arrays will then perform as Alpha stations in the global network.

Modern seismic data acquisition equipment, implementation of the Global Positioning System (GPS) and the advancement of Radio Frequency (RF) digital modem technology has allowed us to minimize the construction requirements of a traditional, NORESS or GERESS type array. We have already begun the construction of the prototype experimental array at the LTX site. The array consists of eight vertical seismometer sites and one three component site, configured as one central location and two 'rings'. The central location has a three component system, the inner 'ring' contains three vertical systems with a radius of approximately 0.5 km and the outer 'ring' contains five vertical systems at a radius of approximately 2.0 km.

In addition to providing the array systems we are developing new data processing techniques required for arrays with smaller numbers of elements. The most promising technique is based on a cross correlation method and is similar to that described by Bernard Massinon in his description of a proposed array in France, which he presented at the GERESS symposium in Bavaria. Preliminary results indicate that cross-correlation methods applied to data from a sparse array will yield substantially better estimates of azimuth for regional events than current estimates utilizing a 25 element array.

RESEARCH ACCOMPLISHMENTS

The following pages reflect research accomplishments to date.

SUMMARY

- GERESS array geometry is a copy of NORESS, ARCESS, utilizing a central hub that sends power to each site and sends data on buried fiber optic cables.
- GERESS is technologically advanced over previous arrays with greater sensitivity and wider dynamic range.
- GERESS design began in 1987 and was implemented in 1990.
- The GSE - Alpha design began in 1991 and is being implemented in 1993.
- Innovations in emplacement techniques have led to less costly installations in shallow boreholes instead of vaults.
- Simpler installations and modular equipment allow the host-country to install and maintain an array.
- Advancements in component design have led to smaller, lighter weight modules that require less power.
- Use of the Global Positioning Satellite (GPS) system enables each array element to time-tag to within 20 microsecs.
- Radio modems eliminate the need for buried fiber optic cable.
  *Full Duplex error correcting protocol insures a bit error rate of less than 1 in 10 million.
- Lower power consumption allows on-site power to be provided using solar or thermoelectric generators.
- Elimination of trenching and underground cabling and the use of boreholes rather than vaults reduces costs by about a factor of ten.
- Advanced communication equipment eliminated a complicated array data controller that required considerable power.
- New data processing techniques allow arrays with fewer elements to perform as well as existing arrays
- New array hardware is powerful enough to support data compression. Algorithms which can significantly reduce communication costs are under development.
- Research and development is required to adapt the new array design to a variety of terrains and climates and provide for data authentication.

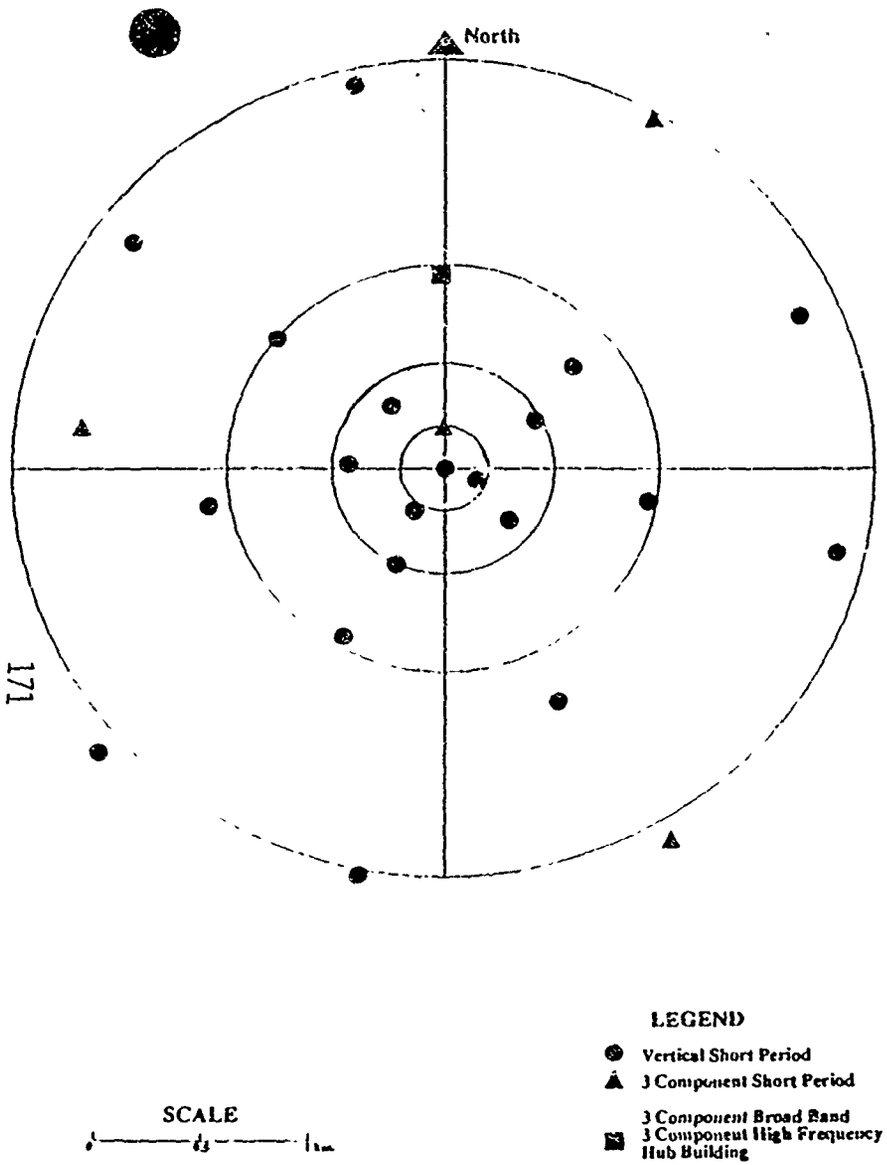

The GERESS array geometry and design was a copy of previous successful arrays in Scandinavia, NORESS and ARCESS. The installation is similar, utilizing a central hub that sends power to each underground vault on cables buried in conduit. Timing signals and intra-array communications are carried on buried fiber optic cables.

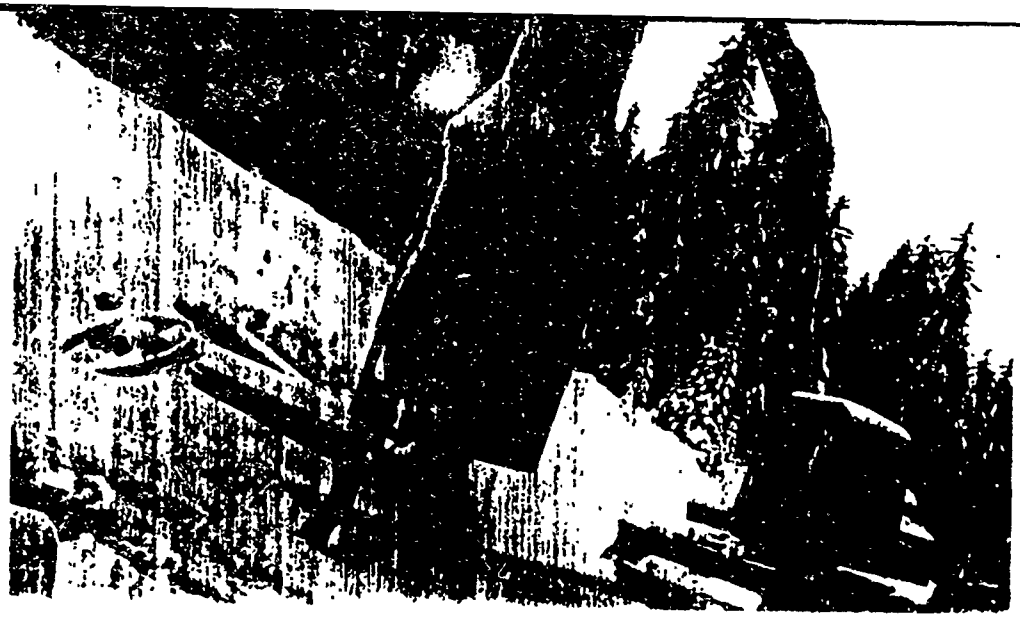

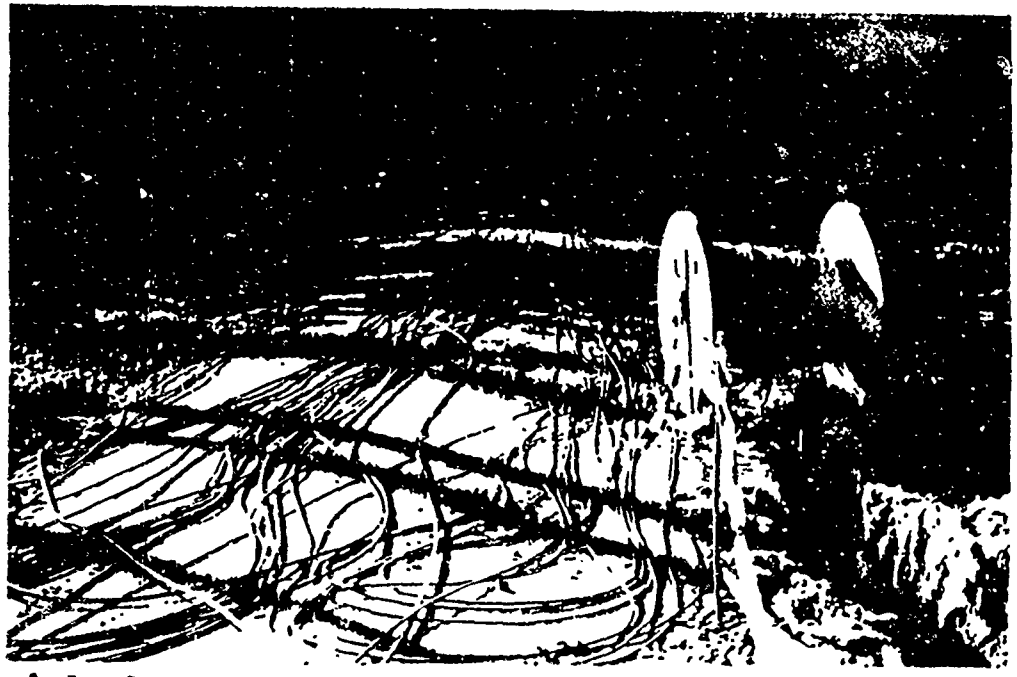

Pre-fabricated vaults and cabling material alone cost almost $800,000 for the GERESS arrray. That amount represents the total cost of a new GSE-Alpha 9 element array.

Table 6: Types and Volumes of Data in the Global System

ATTRIBUTES	ALPHA	BETA	GAMMA
DATA	60 STATIONS 40 Arrays/20 station	250 STATIONS 10 Arrays/240 station	UNKNOWN AT THIS TIME
TRANSMISSION	Near Real-time	Within one hour	As available
	Full Network Daily	125 Accesses daily	Varies with NDC
DAILY VOLUMES	165 MB/Array 30 MB/3cpt station 7000 MB/Network	165MB/Array 30 MB/3cpt station 450 MB on average	Varies with NDC
DATA ACCESS	Sent to IDC	Automatic by IDC	Sent by NDC to IDC
DATA ARCHIVE	Full Period Bulletin 7 GB/Network Day	Segments Bulletin .5 GB/Day	Segments Bulletins Other information
COMMUNICATION BANDWIDTH	15.4 kbps/Array 5.1 kbps/3cpt station	15.4 kbps/Array 5.1 kbps/3cpt station	Varies with request
PROCESSING	Near Real-time	Daily as Needed	Installed in database

The table above comes from report GSE/US/84 submitted by the US Delegation to the United Nations Conference on Disarmament Group of Scientifc Experts calling for the establishment or upgrading of 50 seismic arrays for the next GSE Technical Test , which is scheduled to begin in early 1995.

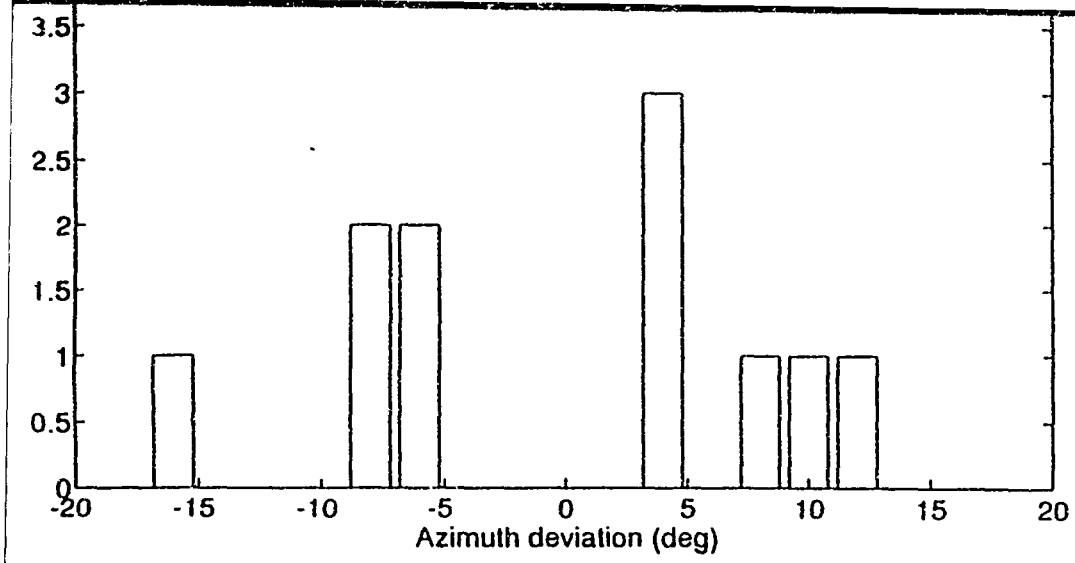

17h

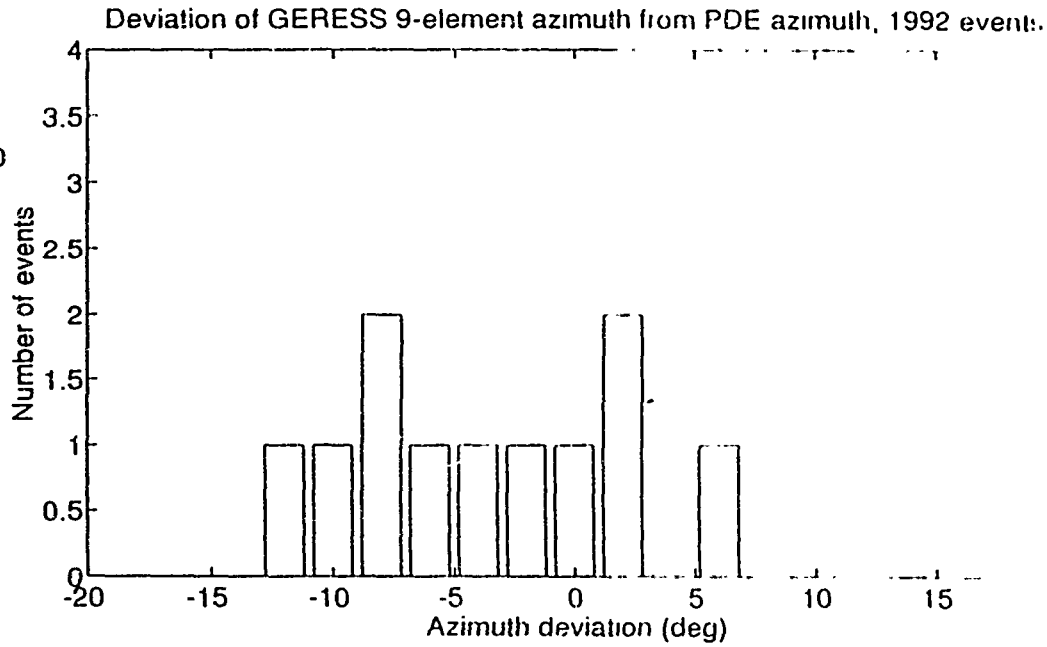

New data processing techniques allow arrays with fewer elements to perform some functions as well as existing arrays. The plots above show variations of azimuth between GERESS locations and PDE reported locations. New processing techniques applied to only 9 elements of the GERESS array show smaller deviations between new locations and PDE locations. The modular design of the elements allows more sites to be added as needed to improve the array response and signal-to-noise ratios at noisy sites.

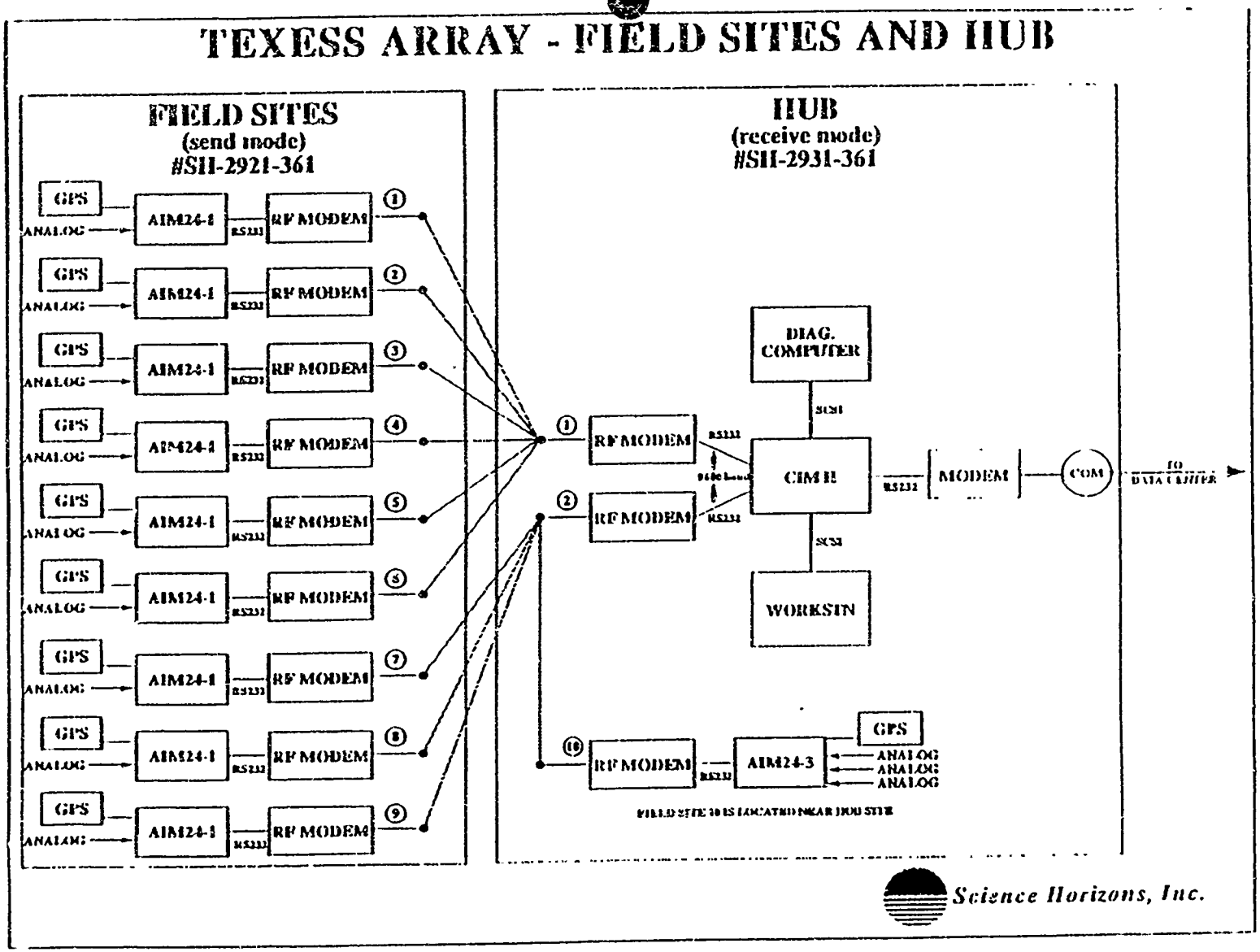

This schematic diagram shows the design of the prototype GSE-Alpha array being built in southwest Texas designated TEXESS, the Texas Experimental Seismic Station. TEXESS is a 9 element array utilizing the latest technology and incorporating new concepts in design and installation procedures.

Topics for Research and Development

Multipurpose Arrays

Array geometries and signal processing techniques should be developed that will perform adequately with events at both regional and teleseismic distances.

Communications

Communication costs for a real-time network of arrays would be very high using current technology. Data compression techniques, designed specifically for seismic data, are expected to greatly decrease these costs.

Data Authentication

Secure data authentication techniques need to be developed which will insure the integrity of the seismic data.

Array Calibration

Experience in processing data from GERESS has shown that calibrations and static corrections must be applied to the data. Techniques to accomplish these calibrations must be developed and will need to be implemented on an array-by-array basis.

Power Requirements

The prototype array currently under construction uses solar cells to power the individual elements. Alternative power sources must be developed and tested for use in regions where solar power is not a feasible option.

Intra-array Communications

In some areas, the terrain may be such that a Radio Area Network is impractical. Alternative, cost-effective methods for communication among elements of the array must be developed and tested.

AUTOMATED ANALYSIS OF REGIONAL WAVE PROPAGATION

R. B. Herrmann
Department of Earth and Atmospheric Sciences
Saint Louis University
rbh@slustl.slu.edu
TEL: 314/658-3131 FAX: 314/658-3117

AFOSR Contract No. F49620-93-1-0276

OBJECTIVE

The objective of the research effort is to develop a robust technique for inverting regional waveforms for earth structure/seismic source parameters. The portion of the program for determining earth structure will be based on modal summation and variational techniques. The program will then be used to perform the following tasks:

1) Using broadband regional seismic data in the distance range of 0 - 300 km, determine the limits of simple 1-D plane layered earth models in matching observed data.

2) Apply the program to broadband data sets from Iran to the Arabian shield to better define curstal structure and capability of source discrimination in the regional distance range out ot 10°.

RESEARCH ACCOMPLISHED

Initial efforts have combined forward modeling techniques with systematic search over the source parameter space. The reason for this initial approach is to build up experience in the difficulties inherent in modeling broadband data. Considerable work has already been done in a series of papers by Helmberger and others at the Seismology Laboratory of CALTECH. Their papers have emphasized the value of matching the P and S wavefields and the sensitivity of the surface wave to shallow structure. Hence, to determine source parameters, they place more confidence on the body waves that sample the lower crust than on the surface waves.

On the other hand, given only a single recording of an event, it may not be prudent to reject the surface wave, a significant portion of the wavefield, for source determination, especially when the surface wave may have the greatest S/N ratio. In some cases, the surface wave may be less sensitive to model assumptions than the body-waves. An example of this is for events in a subduction zone recorded inland. In this case, the validity of using 1-D wave propagation models for rays leaving the source downward may undergo significant plate interaction prior to propa gating in a normal 1-D crust, while rays propagating upward, which would include significant parts of the surface wave, could be described by a 1-D upper crustal model.

USE OF FORWARD MODELING FOR SOURCE STUDIES

INTRODUCTION

The purpose of this exercise is to use *Computer Programs in Seismology* to analyze data from the broadband station at UNAM. The illustration used the Very Broad Band data of the earthquake of March 31, 1993. The *Servicio Sismologico Nacional* location was 17.19°N, 101.01°W with a depth ~10 km and an origin time of $10^{hr}18^{mn}15.69^{sec}$. UNAM is 305.6 km from the event, along an azimuth of 39°, with an approximate back azimuth of 219°. The first sample of the digital file is 18.11 seconds after the origin time. The P-wave first motion at UNAM is a compression. The takeoff angle computed using the location program is 51°.

DATA MODELING

Initial Model

The data were extracted from the UNAM format, and processed. Group velocities were determined using multiple filter analysis, and these were used to define the first initial model, called Model 1 in Table 1.

Table 1
Earth Models

H (km)	V_P (km/s)	V_S (km/s)	ρ (gm/cm^3)	Q_P	Q_S
Model 1					
5	5.18	3.047	2.54	300	150
10	6.23	3.60	2.77	300	150
10	6.48	3.74	2.85	300	150
10	6.63	3.83	2.88	300	150
--	8.00	4.70	3.31	800	400
Model 2					
5	4.987	2.933	2.497	400	200
10	6.202	3.581	2.761	400	200
10	6.484	3.742	2.845	400	200
5	6.649	3.842	2.889	400	200
10	6.653	3.844	2.890	400	200
--	8.001	4.700	3.310	400	200

Green's functions were computed using both modal superposition and wavenumber integration. Figure 1 presents a comparison of the observed and synthetic data in the 0.05 Hz, 0.10 Hz and the 0.50 Hz lowpass bands (a second order lowpass Butterworth filter is used). A focal mechanism with angles of dip of 85°, a rake of 85°, a strike of 285° and a depth of 15km are used.

In these figures, in each set of three traces, (a) is the filtered observed data, (b) is the filtered wavenumber integration synthetic, and (c) is the filtered modal summation synthetic. It is obvious that the modal summation agrees with the wavenumber integration results for arrivals following S, or more precisely for arrivals with phase velocities less than 4.7 km/s.

The comparison between the observed and synthetic vertical component time histories is quite good. The low frequency components of the radial component agree well at low frequencies, but the synthetics do not have the large

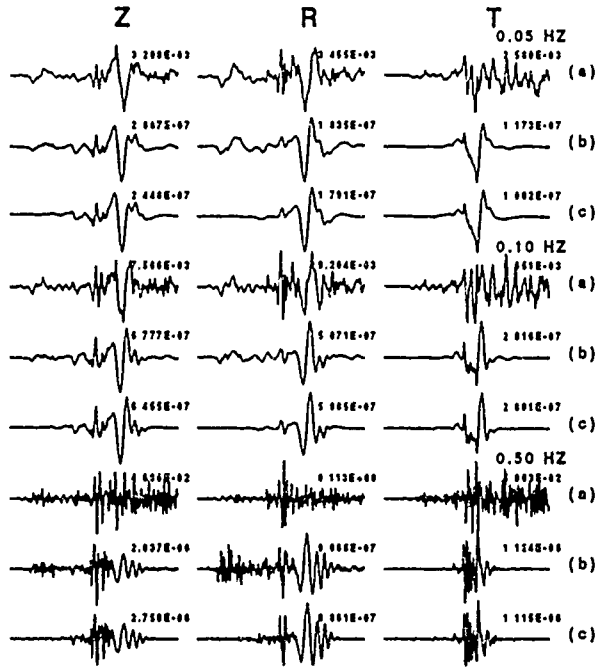

Fig. 1. Comparison of observed (a), wavenumber integration (b) and modal superposition synthetics (c) for lowpass corner frequencies of 0.05, 0.10 and 0.50 Hz. The source depth is 15 km. All time histories start 38 seconds after the origin time and continue to 140.2 seconds after the origin time.

S-arrival as is observed. The observed transverse component is more complicated than predicted.

Since the units given in the velocity model for the synthetics were km, km/s and gm/cm^3, the filtered synthetic ground velocities are in cm/s for a seismic moment of 1.0×10^{20} dyne-cm. By using just the ratio of peak amplitudes on the vertical and radial components of the observed to wavenumber integration synthetics, we obtain the seismic moment estimates listed in Table 2. The interesting thing about this comparison is the consistency of the Z estimate in different frequency bands and the significant variation of the R component estimate at high frequency. This again reflects the large observed S-wave arrival on the R component, which is not described by this simple, plane layered model.

The comparison also shows little sensitivity in the waveforms to source depth, but also that the P-wave wave is well modeled. This may be because the P-wave and its coda are due to waves propagating in the upper crust, while the problematic S-wave pulse depends on deeper crustal structure or to interesting S-wave paths along the descending slab at the source.

Due to the location of the seismograph station with respect to the source, there is little sensitivity to small changes in dip and rake angles in the synthetics. This lack of sensitivity may be due to the lack of a good SH

Table 2
Seismic Moment Estimates

Depth (km)	Filter Band (Hz)	Estimate (10^{24} dyne-cm) Z	R
15	0.05	1.20	1.88
	0.10	1.16	1.82
	0.20	1.47	4.85
	0.50	1.65	12.4
25	0.05	1.71	2.82
	0.10	1.92	3.23
	0.20	1.61	10.2
	0.50	1.96	17.8

arrival from the source for this mechanism, e.g., unfortunately UNAM is at an SH node for this event.

Revised Model and Depth Sensitivity

The initial model used surface wave data in the 10 - 35 second period range. Study of the dispersion in the xspmft(II) display, showed what looked like fundamental mode Rayleigh wave dispersion in the 5 - 10 second period range. In addition, the model was changed to permit a depth to the Moho of 40 km instead of 35 km. If the short period dispersion was really to be fit, the top layer could be split into two layers, and the damping reduced. The model so obtained is given as Model 2 in Table 1. Figure 2 shows the fit of Model 2 predicted group velocities to the observed. The model does not do well at long periods, where the observed value of about 3.45 km/s may be too large. At very short periods, the presence of a shallow 2 km thick low velocity layer is required. Because of the upper period limit of the observed data is less than 30 sec, the lower crust of the model is not well resolved.

The purpose of this model was to study the effect of depth on the synthetic seismograms. Figure 3 presents a comparison of the observed and synthetic seismograms for different source depths after lowpass filtering the data at 0.05 Hz. In each figure, the top trace is the observed signal, and the others are for sources with focal depth increasing from 5 to 35 km. The mechanism is fixed in these figures.

There are several notable features in this figure. First the observed high frequency shear-wave pulse on the radial component is not well modeled. The particle motion seems to indicate an SV arrival steeply incident at the free surface, thus giving a large horizontal motion. Since this arrival dominates the high frequency pass band, it is important to determine if this arrival is seem for other earthquakes. Possible explanations are either the need for a much more refined lower crust model than is used in Model 2, or perhaps the need to consider 2-D wave propagation from a source in the descending slab, with a complicated ray path for the shear wave leaving the source in a downward direction.

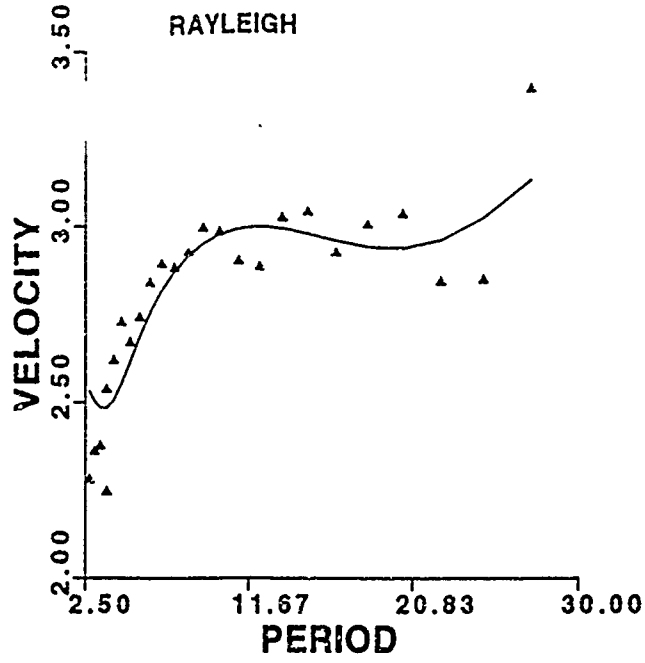

Fig. 2. Observed (curve) and predicted (symbols) Rayleigh fundamental mode group velocities for Model 2.

Another feature is the sensitivity of the width of the fundamental mode Rayleigh wave pulse to depth. As depth increases, this pulse decreases in amplitude and increases in width, both of which follow directly from eigenfunction theory. There is a subtle indication that the P-wave code on the R component is sensitive to depth, since the peaks shift to later time with depth.

Focal Mechanism Sensitivity

The focal mechanism for this event was determined one the basis of an initial estimate from P-wave first motion data, and from a search of waveform using a simple shell script. Determining a precise focal mechanism was hampered by the fact that there is no strong SH arrival in the long period band of the observed data. This necessary constraint places significant reliance on the Rayleigh-wave and P-wave arrivals on the Z and R components, neither of which were very sensitive to changes in strike, dip and rake of ±15° about the solution used above. The strike is certainly not 315°, since the SH motion has a polarity opposite to that observed.

The display script requires a Tektronix window (easily obtained from xterm(1) by using the Control-Center_Mouse_Button to invoke a menu). To use this script, it is assumed that Green's functions have been computed. Here they are File91.*depth*, which were computed using hspec91(VI). If only the shear wave and surface waves are to be modeled, then modal summation

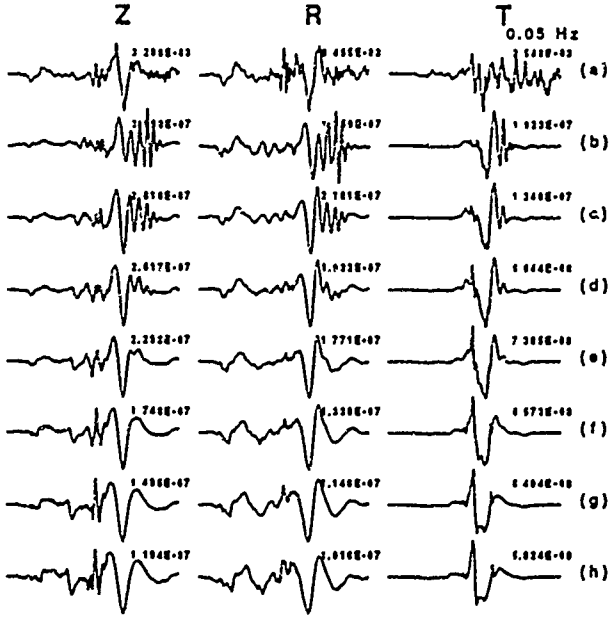

Fig. 3. Sensitivity test of waveforms to changes in source depth for the earthquake of March 31, 1993. A two-pole lowpass Butterworth filter with corner at 0.05 Hz is used. A total of 102.2 seconds of time history are displayed, starting 38.0 seconds after the origin time. All time histories are filtered ground velocities with units of cm/s. A focal mechanism with dip=25°, rake=85° and strike=285° is used. The UNAM station is at an azimuth of 39° from the source at a distan ce of 305.6 km. The back azimuth for rotation into R and T components is assumed to be 219°. (a) observed trace, (b) source depth = 5 km, (c) 10 km, (d) 15 km, (e) 20 km, (f) 25 km, (g) 30 km, and (h) 35 km.

can be used. an example of this script is also shown. What makes this script interesting is the use of the program fmplot(VIII) to display the current focal mechanism and the S-wave polarization on the focal sphere, Certainly the display window can be further used to simultaneously display the fits to another data set or to indicate the goodness of fir to P-wave first motion data.

Script MM91 - uses wavenumber integration Green's functions

```
#!/bin/sh
rm plot*

for FH in 05
do
for DEPTH in 15
do
        for DIP in  25
        do
                for RAKE in 35
                do
                        for STK in 285
```

```
                                do
cltek
echo DIP $DIP RAKE $RAKE STRIKE $STK > /dev/null
cat File91.${DEPTH} | mech91 -M0 15000 -R -D ${DIP} -S ${STK} -L ${RAKE} -A 39 -B 219 | \
        bfilt3 -fh 0.${FH} -n 2 > junk
plot3 -ts 38 -te 130 -f1 fileobs3ZRT.0.${FH} -f2 junk > /dev/null
rm junk

fmplot -dip ${DIP} -slip ${RAKE} -stk ${STK} -X0 9.0 -Y0 3.0 -R 1.0 -FMFILL > /dev/null
mv FMPLOT FMPLOTP
fmplot -dip ${DIP} -slip ${RAKE} -stk ${STK} -X0 9.0 -Y0 5.5 -R 1.0 -pol > /dev/null
mv FMPLOT FMPLOTPOL

cat plot* FMPLOTP FMPLOTPOL | plot_4014 -N S0.8
rm FMPLOTP FMPLOTPOL
rm plot*
sleep 10
                                done
                        done
                done
        done
done
done
```

and

Script MM - usee surface-wave Green's functions

```
#!/bin/sh
rm plot*
for FH in 05
do
for DEPTH in 15 25
do
        for DIP in   25
        do
                for RAKE in 85
                do
                        for STK in  285
                        do
cltek
echo DIP $DIP RAKE $RAKE STRIKE $STK > /dev/null
cat wig91.${DEPTH} | mech91 -M0 15000 -R -D ${DIP} -S ${STK} -L ${RAKE} -A 39 -B 219 | \
        bfilt3 -fh 0.${FH} -n 2 > junk
plot3 -ts 38 -te 130 -f1 fileobs3ZRT.0.${FH} -f2 junk > /dev/null
rm junk

fmplot -dip ${DIP} -slip ${RAKE} -stk ${STK} -X0 9.0 -Y0 3.0 -R 1.0 -FMFILL > /dev/null
mv FMPLOT FMPLOTP
fmplot -dip ${DIP} -slip ${RAKE} -stk ${STK} -X0 9.0 -Y0 5.5 -R 1.0 -pol > /dev/null
mv FMPLOT FMPLOTPOL

cat plot* FMPLOTP FMPLOTPOL | plot_4014 -N -S0.8
rm FMPLOTP FMPLOTPOL
rm plot*
sleep 10
                                done
                        done
                done
        done
done
done
```

These scripts are used as follows: to change the presentation, just add more entries to the *for* loop entries, e.g.,

for STK in 270 285 300 315

The surface wave Green's functions have been computed using the program wig91(III). In each case the file *fileobs3ZRT.0.XX* contains the corresponding filtered observed data. The command cltek(I) erases the Tektronix screen.

Figures 4 and 5 show what would be seen on the screen by using these scripts. This emphasizes the ability to place a lot of information on the screen to assist the analyst.

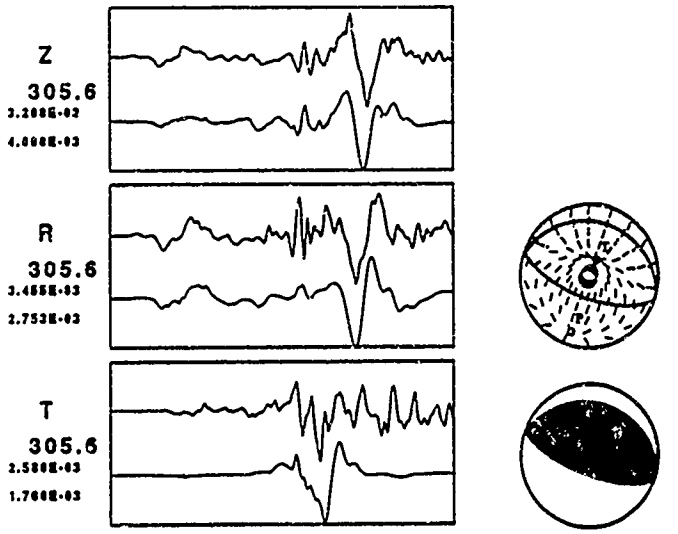

Fig. 4. Demonstration of the script MM91.

DISCUSSION AND RECOMMENDATIONS

This example illustrates that models can be derived to describe the low frequency portion of the P-wave and surface-wave fields, but also that the same models are not adequate for describing the high frequency S-wave arrivals. This may be due to the simple 1-D models used, but may also be due to wave propagation in a 2-D model with dipping interfaces. Until the waveform inversion program is completed, we cannot distinguish between these two possibilities. It is anticipated that the waveform modeling, even using 1-D models, will provide very strong constraints on crustal structure, and hence indirectly on the use of regional waveforms for source discrimination.

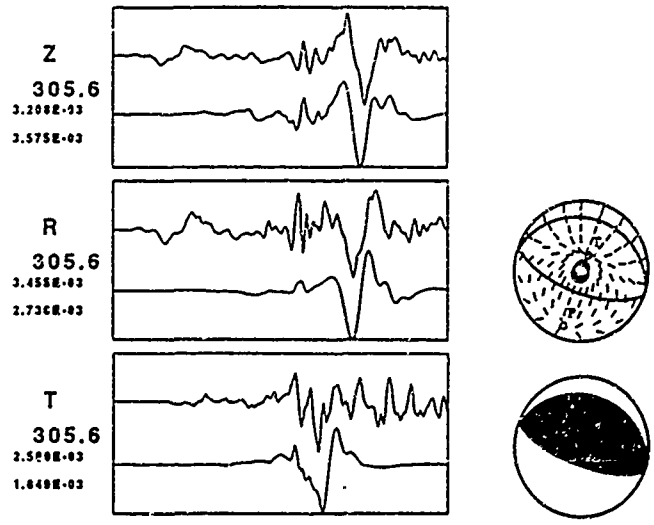

AZ = 39.00 BAZ = 180.00 MOM = 15000.00 TAU = 0.200
DT = 0.2000 DIP = 25.00 SLIP = 35.00 STR = 285.00
TMIN = 37.91 TMAX = 129.91 DIST = 305.60 DEPTH = 15.00

Fig. 5. Demonstration of the script MM.

STATISTICAL ANALYSIS OF SOVIET NUCLEAR EXPLOSIONS

R.-S. Jih*, R. A. Wagner*, and R. H. Shumway**
*Teledyne Geotech Alexandria Laboratory, Alexandria, Virginia
**Univ. of California, Davis

Contract Number: F29601-91-C-DB23

Project Objective

The primary objective of this study is to develop and apply improved statistical methodologies for relating seismic magnitudes to explosion yields, treating both magnitudes and yields as uncertain variables and incorporating the censored information into the yield estimation procedure. Parallel to the extensive statistical analysis of teleseismic phases and the regional phase L_g, forward modeling experiments are also utilized to improve the fundamental understanding of how energy from explosions and other sources is partitioned into various seismic wave types due to different geological models.

Research Accomplished

1. Expansion of Explosion m_b Database: Our database of station m_b values based on the short-period vertical-component (SPZ) recordings of body waves has been expanded from 112 to 252 events from a variety of regions including the NTS (U.S.), French Sahara, Azgir (U.S.S.R.), Orenburg (U.S.S.R.), Urals (U.S.S.R.), Murzhik (E. Kazakh, U.S.S.R.), Degelen Mountain (E. Kazakh, U.S.S.R.), Balapan (E. Kazakh, U.S.S.R.), Novaya Zemlya (U.S.S.R.), Tuamoto Islands (France), Rajasthan (India), and Lop Nor (Sinjiang, China). This database, which is currently dominated by WWSSN [World Wide Standard Seismograph Network] recordings, consists of 744 usable "a" (*i.e.*, zero-crossing to first peak), "b" (*i.e.*, first peak to first trough), and "max" (*i.e.*, max peak-to-trough or trough-to-peak in the first 5 seconds) event phases. Along with other utility software developed/updated under this project (*e.g.*, Jih, 1993b), this data set is being installed at CSS (Jih *et al.*, 1993).

2. Methodological Improvement in m_b Determination: The standard procedure used in estimating the source size of underground nuclear explosions using m_b measurements has been to separate the station terms from the network-averaged source terms. The station terms thus derived actually reflect the combination of the path effect and the station effect, when only those events in a close proximity are utilized. If worldwide explosions are used in the inversion, then the path effect tends to be averaged out at each station. In either case, the effect due to the propagation path alone would not be obvious. In this study, we decompose the station magnitudes with the following joint model:

$$E(i) + S(j) + F(k,j) + \varepsilon(i,j) = \log_{10}[A(i,j)/T(i,j)] + B(\Delta(i,j)) \; . \qquad [1]$$

The right-hand side of [1] is the conventional raw station m_b of the i-th event observed at the j-th station where A, T, and B(Δ) are the displacement amplitude, the dominant period, and the distance-correction term, respectively. On the left-hand side, S represents the station correction, and F(k,j) is the path correction at the j-th station for explosions from the k-th source region. The resulting new event magnitude (*viz.*, E(i) in [1]) is hereby called $m_{2.9}$ to avoid confusion with the m_3 defined in Marshall *et al.* (1979) that corrects for the source-region attenuation and station terms solely based on published P_n velocity. Short-period *P*-wave amplitudes of 252 worldwide underground nuclear explosions, including 30 blasts from northern Novaya Zemlya and 114 from Semipalatinsk, recorded at 132 seismic stations have been used in one single inversion. Table 1 gives a partial listing of the resulting station and path terms for nine major test sites in Eurasia. Applying these path and station corrections to any individual explosions would yield a reduction in the fluctuational variation of station magnitudes with a factor ranging from 1.2 to 3. Most Novaya Zemlya events have a typical reduction factor of 2 (Jih and Wagner,

1992ab; Jih *et al.*, 1993).

The inferred path terms for Novaya Zemlya and Semipalatinsk explosions have been compared against the travel-time residuals to characterize the propagation paths (Jih and Wagner, 1992ab). Our results indicate that paths from the northern test site in Novaya Zemlya to stations in North America have systematically faster arrivals and smaller amplitudes, suggesting a profound defocusing effect on the first arrivals, whereas stations in Ireland, Scotland, Spain, Bangladesh, northern India, Pakistan, Korea, and Kenya report slow arrivals and large amplitudes, suggesting a focusing effect. Amplitudes for paths to Greenland, Iceland, Alaska, Turkey, Germany, Luzon, Zimbabwe, Italy, Pueto Rico, Ethiopia, and Hawaii, however, seem to be controlled by the anelastic attenuation with slow rays also associated with small amplitudes, and fast rays associated with large amplitudes. Our empirical path corrections for Semipalatinsk explosions are in good agreement with those independently derived by Marshall *et al.* (1992) based on the digital data recorded at 4 U.K.-designed arrays (Jih *et al.*, 1993).

Table 1. Partial Listing of Receiver and Path Terms for Eurasian Nuclear Test Sites

Station Term [S]		Path Terms [F]								
Code	Rcv[1]	Azgir	Orn	Mzk	Deg	BTZ	BNE	BSW	NNZ	PRC[2]
AAE	-.306	.178	.424	-.452	-.281	-.530	-.419	-.351	.360	____
AAM	.207	.244	.097	-.357	-.231	-.051	.124	.272	.160	____
AKU	-.022	-.271	____	-.013	.144	.277	.051	.147	-.111	-.407
ANP	-.163	____	____	-.299	.139	-.266	____	-.252	-.134	.074
AQU	-.117	-.359	.160	-.115	-.047	-.124	-.180	-.115	.619	.249
ATU	.170	-.612	.264	-.201	-.322	.015	.011	.020	.064	.440
BAG	-.020	.228	.233	-.248	-.173	-.149	-.076	-.178	.211	-.642
BEC	-.091	-.111	____	-.340	-.123	.288	-.175	.200	-.202	____
BKS	.077	.083	-.065	.113	-.009	-.081	-.106	.006	-.173	____
BLA	-.022	-.138	-.447	-.390	-.182	-.239	-.191	-.115	.216	____

1) the station bias which needs to be corrected (in addition to the path effect).
2) BSW = SW subsite, Balapan, BNE = NE subsite, Balapan, BTZ = transition zone, Balapan, Deg = Degelen Mountain, Mzk = Murzhik, NNZ = northern island, Novaya Zemlya; Azg = Azgir, Orn = Orenburg; PRC = Lop Nor.

3. m_b-L_g Bias at Various Test Sites: We followed the zoning of Ringdal *et al.* (1992) in partitioning Balapan test site into three regions: southwest (SW), transition zone (TZ), and northeast (NE). The $m_b(P_{max})-L_g$ bias of 0.07 m.u. between SW and NE we derived (*cf.* Table 2) is significantly smaller than that of previous studies. Regressing the *RMS* L_g furnished by Israelson (1992) and our $\overline{m}_{2.9}$ on the yields published by Bocharov *et al.* (1989) (and Vergino, 1989) show that NE explosions have positive L_g residuals and negative m_b residuals; whereas SW explosions show the opposite trend. A three-dimensional geological model of the Balapan test site by Leith and Unger (1989) shows a distinct difference between the NE and SW portions of the test site, with the granites closer to the surface and the alluvium thinner in the southwest. The thicker alluvium layer in NE region could increase the waveform complexity and reduce the magnitudes measured with P_{max}. The first motion should be least affected by this factor, however. We suggest that the m_b-L_g bias between SW and NE Balapan can be tentatively decomposed into several parts:

[I] Difference in *pP* between SW and NE,
[II] Difference in m_b coupling, *i.e.*, m_b (SW) > m_b (NE),
[III] Difference in L_g coupling, *i.e.*, L_g (NE) > L_g (SW),
[IV] Effects due to the station-station correlation structure,
[V] Effects due to the uneven geographical clustering of stations, as well as any path effect which is not fully accounted for through the network averaging.

Based on our $\overline{m}_{2.9}$, [I] is about 0.03-0.06 m.u. (*cf.* Table 3), whereas [II] and [III] could be about 0.01-

0.02 m.u. each. The bias of 0.07 m.u. for $m_b(P_{max})$ (Table 2) is essentially the sum of [I] through [III]. However, when m_b based on the first motion is used (Table 2), the $m_b - L_g$ bias between NE and SW regions is not that significant. For ISC data, we estimate that [V] is about 0.02 m.u. when the event $\overline{m}_{2.2}$ values derived by the conventional LSMF are used. If $\overline{m}_{2.9}$ were used instead, this term is eliminated, and hence a smaller $m_b - L_g$ bias can be obtained, as it should. Our current m_b determination procedure as described in [1] may not eliminate [IV] completely. However, the residual contribution of the inter-station correlation alone is believed to be relatively insignificant for WWSSN (as compared to ISC) after the (site-dependent) path terms are removed.

Table 2. $\overline{m}_{2.9}$ vs. *RMS* L_g (NORSAR)[1] at Various Sites

Site	$m_b(P_a)-m_b(L_g)$, #[2]	$m_b(P_b)-m_b(L_g)$, #	$m_b(P_{max})-m_b(L_g)$, #
BSW	-0.473±0.008 42	-0.207±0.008 42	0.013±0.009 42
BNE	-0.499±0.028 15	-0.259±0.024 16	-0.056±0.015 16
BTZ	-0.521±0.030 8	-0.229±0.016 8	-0.025±0.013 8
Deg	-0.469±0.046 5	-0.194±0.042 5	0.024±0.034 5
Mzk	-0.532±0.073 3	-0.232±0.044 3	-0.019±0.032 3
KTS	-0.486±0.009 73	-0.221±0.008 74	-0.007±0.007 74
NNZ	-0.527±0.019 15	-0.305±0.022 15	-0.128±0.023 15

1) from Ringdal and Fyen (1991) and Ringdal *et al.* (1992). 2) #: number of events.

Table 3. $m_b(P_{max})$ and $m_b(P_b)$ vs. $m_b(P_a)$ (with $\overline{m}_{2.9}$ only)

Test Site	$m_b(P_b)-m_b(P_a)$	$m_b(P_{max})-m_b(P_a)$	#
BSW	0.271±0.006	0.491±0.008	48
BNE	0.235±0.023	0.431±0.031	19
BTZ	0.302±0.017	0.513±0.029	10
Deg	0.287±0.012	0.513±0.014	21
Mzk	0.298±0.017	0.528±0.019	13
KTS	0.274±0.006	0.491±0.008	111
NNZ	0.218±0.010	0.392±0.010	30
Orn	0.168±0.010	0.426±0.021	8
Azg	0.410±0.049	0.686±0.058	10
PRC	0.162±0.043	0.406±0.063	13

4. Yield Estimates of Semipalatinsk Explosions: We have recomputed the yield estimates of Semipalatinsk explosions based on the path-corrected m_b values (Jih *et al.*, 1993). First motion (*viz.*, P_a) of the initial short-period *P* waves appears to be a very favorable source measure for explosions fired in hard rock sites underlain by a stable mantle such as Semipalatinsk (*cf.* Table 4). For example, based on $m_b(P_a)$ alone and without any extra cratering-to-contained correction, the Balapan explosion of Jan 15, 1965, is estimated to have a yield of 119 kt. The $m_b(P_a)$-based yield estimate for the JVE event of Sep 14, 1988, is 112 kt. Between 100 and 150 kt, the m_b bias between Eastern Kazakh and NTS using our $m_b(P_{max})$ values is 0.35 m.u. (Table 5). It is interesting to note that three out of the five "historical events" (for which the yields were exchanged in 1988) have a yield of 153 kt, based on our $m_b(P_a)$ (Table 4). The remaining two historical events and the JVE all have a yield very close to 112 kt, based on the first motion. The 15 common events in Israelson's (1992) *RMS* L_g data set and our $\overline{m}_{2.9}$ data set for which the Soviet-published yields are available show very weak correlation between the *RMS* L_g and $\overline{m}_{2.9}$ residuals. Hence the combination of these two methods for better yield estimate is justifiable.

Table 4. Yield Estimates of Semipalatinsk Explosions

Event		Epicenter		Yield Estimate			Yield
Date	Site	Lon	Lat	P_a	P_b	P_{max}	Announced
650115B	BTZ	79.009	49.935	119	99	84	100-150
651121D	Deg	78.064	49.819	25	24	23	29
660213D	Deg	78.121	49.809	221	192	187	125
660320D	Deg	78.024	49.762	92	89	92	100
660507D	Deg	78.105	49.743	2	1	1	4
661019D	Deg	78.021	49.747	45	40	35	20-150
661218M	Mzk	77.747	49.925	91	77	80	20-150
670226D	Deg	78.082	49.746	99	87	92	20-150
670916M	Mzk	77.728	49.937	11	10	11	<20
670922M	Mzk	77.691	49.960	7	8	9	10
671122M	Mzk	77.637	49.942		1	1	<20
680619B	BNE	78.986	49.980	12	13	14	<20
680929D	Deg	78.122	49.812	53	52	50	60
690531M	Mzk	77.694	49.950	6	9	9	<20
690723D	Deg	78.130	49.816	12	13	12	16
690911D	Deg	77.997	49.776	2	2	2	<20
691130B	BTZ	78.956	49.924	87	111	99	125
691228M	Mzk	77.714	49.937	62	61	59	46
700721M	Mzk	77.673	49.952	12	14	14	<20
701104M	Mzk	77.762	49.989	24	18	18	<20
710322D	Deg	78.109	49.798	39	38	34	20-150
710425D	Deg	78.034	49.769	97	89	86	90
710606M	Mzk	77.660	49.975	20	23	22	16
710619M	Mzk	77.641	49.969	20	20	20	<20
710630B	BTZ	78.981	49.946	4	6	6	<20
711009M	Mzk	77.641	49.978	16	13	12	12
711021M	Mzk	77.597	49.974	20	23	23	23
711230D	Deg	78.037	49.760	35	40	37	20-150
720210B	BNE	78.878	50.024	18	16	16	16
720328D	Deg	78.076	49.733	6	7	7	6
720816D	Deg	78.059	49.765	6	6	6	8
720826M	Mzk	77.717	49.982	12	14	13	<20
720902M	Mzk	77.641	49.959	2	2	2	2
721102B	BSW	78.817	49.927	162	175	188	165
721210B	BNE	79.011	50.036		129	127	140
721210D	Deg	78.058	49.819	34	38	38	20-150
790804B	BSW	78.887	49.903	153	150	159	HE
791028B	BNE	78.994	49.976	116	98	106	HE
791223B	BSW	78.753	49.933	152	150	172	HE
811018B	BSW	78.846	49.928	113	109	112	HE
840526B	BNE	79.004	49.968	153	153	131	HE
880914B	BSW	78.823	49.878	112	112	133	JVE

HE: historical events discussed at U.S.-U.S.S.R. negotiation during '87-'88.

JVE: Joint Verification Experiment.

Table 5. Expected m_b Bias Relative to NTS

	$\overline{m}_{2.2}$				$\overline{m}_{2.9}$			
Phase/Site	10kt	50kt	100kt	150kt	10kt	50kt	100kt	150kt
$m_b(P_{max})$ (KTS)	0.47	0.44	0.42	0.41	0.40	0.37	0.35	0.35
$m_b(P_b)$ (KTS)	0.50	0.47	0.46	0.45	0.43	0.41	0.40	0.40
$m_b(P_a)$ (KTS)	0.37	0.37	0.38	0.38	0.27	0.29	0.30	0.31

1) KTS = all 5 subsites in Eastern Kazakh combined.
2) $m_{2.2} = m_b$ with station terms corrected (Jih and Wagner, 1991). $m_{2.9} = m_b$ with station and path terms corrected (Jih and Wagner, 1992a, 1992b).
3) P_a = the first motion (0-to-peak); P_b = 'b' phase, first peak-to-first trough; P_{max} = the peak-to-peak amplitude within the first 5 seconds (Jih and Shumway, 1989).

5. Simultaneous Inversion of Event $m_b(L_g)$ and Path Attenuation: An iterative procedure is developed to invert for the path γ and the event $m_b(L_g)$ values simultaneously without using any *a priori* path γ information (Jih, 1992). This joint inversion scheme can be applied to data from multiple test sites as well. With this iterative method, it is rather easy to incorporate the appropriate constraint into the inversion. The iterative scheme is less sensitive to rounding errors, and hence it is numerically more accurate than those direct methods based on matrix factorization or Gaussian elimination. When the number of equations becomes large, the iterative method is often the only practical means to tackle the problem. The necessity of incorporating an extra constraint is also reviewed in Jih (1992). This joint inversion scheme is a natural extension to crustal phases of the one we used in the m_b analyses.

The joint inversion scheme has been applied to Nuttli's (1986, 1987) Semipalatinsk $m_b(L_g)$ data set recovered by ARPA/NMRO. The results indicate that the majority of Q_0 values Nuttli used in his pioneering L_g study are very good except for the path from Eastern Kazakh to COP (Copenhagen, Denmark). Assuming Nuttli's station L_g were all measured at 1 Hz, then an 8% increase in Nuttli's postulated coefficient of anelastic attenuation, Q_0, for this particular path would seem to be necessary in order to bring the station recordings at COP in alignment with other stations (Jih, 1992).

6. Theoretical Study of Ripple-fired Explosions: Ripple-fired explosions are commonly used to fragment rocks during quarry and open-pit mining. The periodicity inherent in the ripple firing could produce a seismic reinforcement at the frequency of the delay between shots or rows. Such spectral modulation can be easily modeled by the convolution of a single explosion with a comb function of variable spacing and amplitude. There are, however, other wave excitation characteristics of ripple-fired explosions which are not predicted by such spectral or waveform superposition approaches. Numerical modeling techniques such as the linear finite-difference method can provide insights into the waveform characteristics of the ripple-fired explosions by using various flexible combinations of the experimental set-up. In the simplest case of a linearly distributed ripple-fired explosion, a very clear R_g is excited in the forward direction of the ripple firing. This result supports the standard industrial practice of detonating ripple shots in a direction away from the buildings to reduce potential damage caused by ground vibration. An immediate implication of this exercise on the discrimination problem is that the lack of R_g is not necessarily indicative of deep sources. Furthermore, although path effects such as anelastic attenuation and the scattering by shallow heterogeneity and topography in the upper crust can reduce R_g significantly, the reported lack of R_g in many seismograms from known quarry blasts could also be due, in part, to an intrinsic source effect (such as the shooting pattern) rather than path effects alone (Jih, 1993ab).

Conclusions

Under this contract, we have developed several new methodologies in the determination of source size, propagation effect, and yield estimation; and we have applied these techniques to a huge data set collected over the past decade, resulting in many interesting observations. Along with other software tools developed under this project, the explosion m_b data set is being installed at CSS.

The simultaneously-inferred path and station corrections are related to known geological/geophysical features. Applying these path and station corrections to the raw station magnitudes of any individual explosion yields a systematic reduction in the fluctuational variation of station magnitudes across the whole network with a reduction factor ranging from 1.2 to 3 for all Soviet events in our data set. Most Novaya Zemlya events exhibit a variation reduction factor of 2. With these path-corrected/station-corrected $m_b(P_{max})$, the $m_b(P_{max})-m_b(L_g)$ [NORSAR] bias between the southwest and northeast subregions of the Soviet's Balapan test site is assessed as 0.07 magnitude unit [m.u.], which is significantly smaller than that of previous studies. This bias can be further reduced somewhat when the m_b based on the first motion is used. The better locations of Balapan events (which are based on the satellite imagery) as recently released by Thurber and Quin (1993) also contributed to a more accurate grouping of Balapan events and hence a better determination of the path effects, source size, as well as the regional m_b -L_g bias. First motion of the initial short-period P waves also appears to be a very favorable source measure for explosions fired in hard rock sites underlain by a stable mantle such as Semipalatinsk. For example, based on $m_b(P_a)$ alone and without any extra cratering-to-contained correction, the Balapan explosion of Jan 15, 1965, is estimated to have a yield of 120 kt. The $m_b(P_a)$-based yield estimate for the JVE event of Sep 14, 1988, is 112 kt. Between 100 and 150 kt, the m_b bias between Eastern Kazakh and NTS using our $m_b(P_{max})$ values is 0.35 m.u. (Jih *et al.*, 1993).

Recommendations

The focus of seismic monitoring research has shifted from issues related to TTBT monitoring to those related to CTBT and NPT monitoring. The location and discrimination of small events now receive much more attention than does the yield estimation. One of the critical issues in event identification is to isolate the propagation effects before many discriminants can be tested. However, the effects of propagation and source a. . often indistinguishable, and in many cases unless one is known the other cannot be uniquely determined (Johnson, 1981). Our improved m_b inversion scheme tackles this problem in a systematic manner, which can certainly be applied to regional phases as well (as suggested by the preliminary test with Nuttli's L_g data set). A better determination of the size of man-made seismic sources (*e.g.*, quarry blasts) with confidence for events at and below 1 kt with improved statistical methodologies will benefit the understanding of the source and path effects, which in turn will improve the identification of small events as well.

References

Bocharov, V. S., S. A. Zelentsoz, and V. Mikhailov (1989). Characteristics of 96 underground nuclear explosions at the Semipalatinsk test site, *Atomic Energy*, **67**, 210-214

Bonham, S., W. J. Dempsey, J. Rachlin (1980). Geologic environment of the Semipalatinsk area, U.S.S.R. *(Preliminary Report)*, U.S. Geological Survey, Reston, VA 22092.

Israelson, H. (1992). L_g as a yield estimator in Eurasia, *PL-TR-92-2117(I), Final Report*, Phillips Laboratory, Hanscom Air Force Base, MA, ADA256692.

Jih, R.-S. (1992). Simultaneous inversion of explosion size and path attenuation coefficient with crustal phases. *TGAL-92-11, Semi-annual Technical Report #2*, Teledyne Geotech, Alexandria, VA.

Jih, R.-S. (1993a). Directional excitation of R_g due to ripple-fired explosions: 2-dimensional finite-difference calculations, *DoE/LANL Numerical Modeling for Underground Nuclear Test Monitoring Symposium*, March 23-25, Durango, CO.

Jih, R.-S. (1993b). User's manual of FD2: a software package for modeling seismological problems with 2-dimensional linear finite-difference method, *Special Topical Report TGAL-93-06*, Teledyne Geotech, Alexandria, VA.

Jih, R.-S. and C. S. Lynnes (1993). Studies of regional phase propagation in Eurasia. *PL-TR-93-2003*

(=TGAL-93-01), Final Report, Phillips Laboratory, Hanscom Air Force Base, MA, ADA262801.

Jih, R.-S. and R. A. Wagner (1991). Recent methodological developments in magnitude determination and yield estimation with applications to Semipalatinsk explosions, *PL-TR-91-2212(I) (=TGAL-91-05), Final Report,* Phillips Laboratory, Hanscom Air Force Base, MA **(ADA244503).**

Jih, R.-S. and R. A. Wagner (1992a). Path-corrected body-wave magnitudes and yield estimates of Novaya Zemlya explosions, *PL-TR-92-2042 (=TGAL-91-09), Scientific Report #1,* Phillips Laboratory, Hanscom Air Force Base, MA **(ADA251240).**

Jih, R.-S. and R. A. Wagner (1992b). Path-corrected body-wave magnitudes and yield estimates of Semipalatinsk explosions, *TGAL-92-05, Semi-annual Technical Report #1,* Teledyne Geotech, Alexandria, VA.

Jih, R.-S., R. A. Wagner, and R. H. Shumway (1993). Statistical study of Soviet nuclear explosions: data, results, and software tools, *TGAL-93-05, Final Report,* Teledyne Geotech, Alexandria, VA.

Jih, R.-S. and R. H. Shumway (1989). Iterative network magnitude estimation and uncertainty assessment with noisy and clipped data, *Bull. Seism. Soc. Am.*, **79**, 1122-1141.

Johnson, L. R. (1981) Near-source effects on *P* waves, in *"A technical assessment of seismic yield estimation", Report DARPA-NMR-81-01, Appendix,* DARPA, Arlington, VA.

Leith, W. and J. Unger (1989). Three-dimensional geological modeling of the Shagan River nuclear test site, paper presented at *DARPA/AFTAC Annual Seismic Research Review,* Patrick AFB, FL.

Marshall, P. D., D. L. Springer, and H. C. Rodean (1979). Magnitude corrections for attenuation in the upper mantle, *Geophys. J. R. astr. Soc.*, **57**, 609-638.

Marshall, P. D., D. Porter, and P. Peachell (1992). Analysis of seismograms from nuclear explosions of known yield at Degelen Mountain and Konystan in East Kazakhstan, USSR, *UK/AWE Report O-2/92,* HMSO, London, UK.

Marshall, P. D., T. C. Bache, and R. C. Lilwall, R. C. (1984). Body wave magnitudes and locations of Soviet underground explosions at the Semipalatinsk Test Site, *UK/AWE Report O-16/84,* HMSO, London, UK.

Nuttli, O. W. (1986). L_g magnitudes of selected East Kazakhstan underground explosions, *Bull. Seism. Soc. Am.*, **76**, 1241-1251.

Nuttli, O. W. (1987). L_g magnitudes of Degelen, East Kazakhstan, underground explosions, *Bull. Seism. Soc. Am.*, **77**, 679-681.

Ringdal, F., P. D. Marshall, and R. Alewine (1992). Seismic yield determination of Soviet underground nuclear explosions at the Shagan River Test Site, *Geophys. J. Int.*, **109**, 65-77.

Thurber, C. H. and H. R. Quin (1993). Seismic event location at regional and teleseismic distances, *PL-TR-92-2304, Final Report,* Phillips Laboratory, Hanscom Air Force Base, MA

Vergino, E. S. (1989). Soviet test yields, *EOS, Trans. A.G.U.*, Nov 28, 1989.

LOCATION AND PHASE ASSOCIATION FOR SEISMIC EVENTS AT REGIONAL AND TELESEISMIC DISTANCES

B.L.N. Kennett
Research School of Earth Sciences
Australian National University, Canberra ACT 0200, Australia

Grant: MDA972-91-J-1021

OBJECTIVES

The objective of this research is to develop flexible and efficient procedures for the location of seismic events which can incorporate a wide range of information from stations at both regional and teleseismic distances. The techniques must be able to handle arrival time, slowness and azimuth information from arrays or single stations. Many different phases from each record should be used so that multiple propagation paths from source to receiver can be used to compensate for a limited number of stations. In addition to the assignment of a location it is important to understand the likely errors in the hypocentral estimates and the way in which these might be modified as the magnitude of the event is changed.

The efficient use of later phase information on a seismogram depends on recognition of the character of the arrival and effective assignment of a phase identifier. For discrimination purposes it is important to constrain the depth of the event and this may well depend on the recognition of converted phases such as SP or SKP, using vector measures of the wavefield.

RESEARCH ACCOMPLISHED

In the context of monitoring seismic events using a moderately sparse network of seismic arrays or sensitive single stations, one cannot rely on the use of large numbers of P observations to force the accuracy of a hypocentral estimate. Techniques are therefore required which can use a wide range of seismic phase information (arrival times, slowness or azimuths) in a single coherent location procedure.

The construction of the four vector describing a seismic hypocentre (latitude, longitude, depth and time) from such a set of observations can be cast as a non-linear optimisation problem. The conventional approach is to use an iterative procedure such as Geiger's method in which local linearisation is used about the current location estimate. Such methods require the construction of the partial derivatives of the phase data with respect to the four hypocentral parameters and need to be carefully handled to compensate for the rather different dependence on the space and time variables.

An alternative approach which can be used with fast methods of constructing travel time information is to use a direct non-linear procedure and thereby avoid the need of constructing derivative information. Such methods have the advantage that they can be used with any convenient measure of the misfit between observed and calculated quantities (arrival times, slowness, azimuth). Indeed it is appropriate to use robust statistical measures such as an L1 norm to minimise the influence of any low quality information from a restricted network.

We have investigated a number of different procedures of this type, which are based on different strategies for minimising the misfit functional. A very stable and generally effective procedure is the direct grid search method of Kennett (1992) in which the smallest misfit encountered in a search over a four-dimensional net is chosen as the centre for finer scale search. This strategy is safe provided that the original search area samples a broad zone around the actual hypocentre. An alternative approach that showed initial promise was the application of Genetic Algorithm procedures (Kennett & Sambridge 1992). When the network geometry is reasonable such an approach with a search over all four variables gives good results, but does not exploit the low computational cost of modifying the origin time alone. Modifications of the Genetic Algorithm procedure to exploit the separation of spatial and temporal components, or else to separate latitude/longitude from depth/time improve computational efficiency.

However we have found that an even more effective approach is to use a Simulated Annealing algorithm, a computational procedure based on analogies with the freezing of crystals. In the simulated annealing approach the general trend of the system is towards minimising the misfit but along the way the misfit can be allowed to temporarily increase. This feature of the algorithm allows it to avoid local minima in misfit and to home in on the best fitting estimate of the hypocentre. Such local minima can be quite significant when only a limited number of observations are available.

The calculation times for the non-linear procedures are reasonable on a workstation and do not need more than a general indication of the location as a starting point. Even for an initial search area as large as 20 degrees in latitude and longitude, 600 km in depth and 120 seconds in time, it is possible to get 10 km constraints on the location in a most a two-stage location process.

Simulations of broad-band theoretical seismograms have been used to investigate the relative observability of different seismic phases which might help to constrain the depth of an event when depth phases cannot be recognised. Phases with conversion e.g. SP and SKP are very useful in improving resolution in depth but their observability is strongly dependent on the disposition of the receiver station relative to the radiation pattern.

Even when the best hypocentral estimate has been found we still need to know what is its reliability. The internal consistency of location estimates may not be as helpful as often supposed. For example an event at the Iran/Iraq border located with just P observations was placed at 50 km depth, the inclusion of pP observations changed the depth to 27 km - well outside the previously estimated confidence regions. Interestingly the inclusion of a range of other phases (with pP excluded) gave a depth of 28 km, so that it can be possible to compensate for the absence of depth phases.

In some areas there can be significant effects of earthquake magnitude on the supposed location of an event. As an illustration we consider a event in Indonesia, near Sumbawa, for which paths to Australian stations are fast compared to paths in other directions. For a small magnitude event the majority of the stations reporting are in Australia and so the hypocentre gets dragged in that direction, as the magnitude increase the distribution of seismic stations improves and the estimated location for an event in the same place will move. This behaviour is illustrated in figures 1 and 2 by taking the set of readings for a magnitude 5.5 event and then truncating the readings to those available for nearby events of magnitude 4.9 and 4.4.

The relative locations for each of the three simulated events is shown in figure 2 in 4 planes. The reference location is the large magnitude event (filled hexagon) with the intermediate event shown by a filled triangle and the low magnitude event with an open diamond. The hypocentre of the intermediate magnitude event differs only slightly from the hypocentre of the large magnitude event. However, the low magnitude event hypocentre has been pulled towards the Australian stations a distance of 8-9 km, has increased depth by 12 km and decreased origin time by 0.7 s. The fast paths to Australia are being compensated by moving the event towards the Australian stations and
increasing the depth of focus. These both have the effect of decreasing the calculated travel-time. The influence of the station distribution on the residuals is illustrated in figure 3. For the low magnitude event
the residuals are either positive, or very small and negative. This is consistent with the event being pulled towards these stations. The two stations with negative residuals are to the south-east of the earthquake, partly away from the south-westerly mislocation of the epicentre. For the intermediate and large magnitude locations the residuals all become more negative, indicating that the influence of the Australian stations is being downweighted.

Even with a dense network a substantial shift occurs with magnitude and such errors are even more likely with a sparser global array.

CONCLUSIONS AND RECOMMENDATIONS

The effective non-linear location methods for multiphase information are likely to be of greatest value in the analyst review stage for suspect events coupled to an automated procedure.

Once a location has been estimated it should be possible to estimate theoretical seismograms for each of the reporting stations (for variable source mechanisms) for comparison with observed waveform data. This can already be done by a lookup procedure in an atlas of seismograms for 5 degree epicentral distance intervals and a limited range of depths, and has revealed the strong variability in some significant later phases with source mechanism.

REFERENCES

Kennett B.L.N. (1992), Locating oceanic earthquakes - the influence of regional models and location criteria, *Geophys., J. Int.*, **108**, 848-854

Kennett B.L.N. & Sambridge M. (1992) Earthquake location - genetic algorithms for teleseisms, *Phys. Earth Planet. Int,*, **75**, 103-110

Figure 1
Station distribution for the three Flores events. Stations marked by an open diamond recorded arrivals during the low magnitude event. Additional stations that recorded arrivals for the medium (filled triangles) and large (filled hexagons) are also shown.

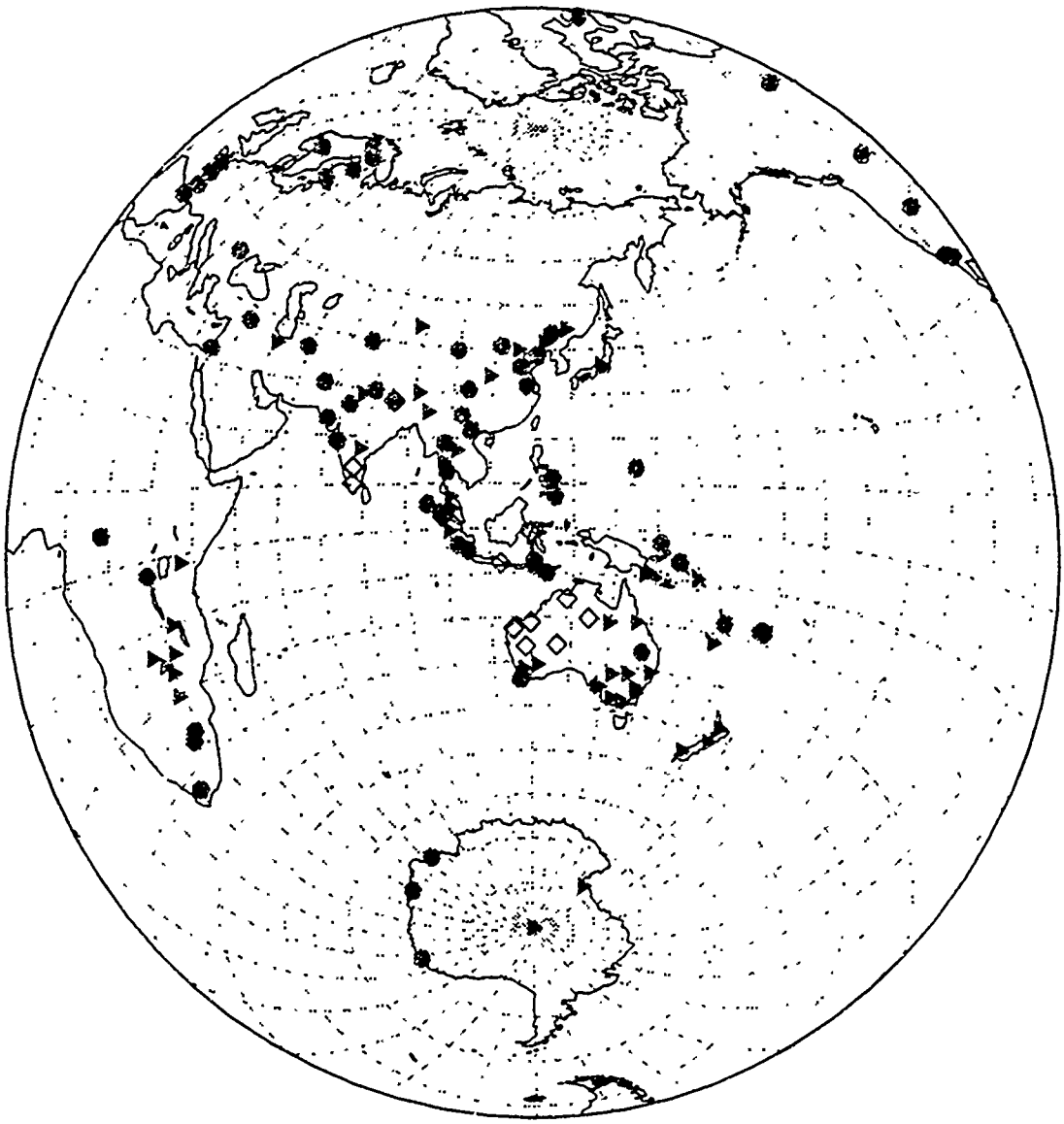

Figure 2
Relative locations for the large (filled hexagon), intermediate (filled triangle) and low (open diamond) magnitude Flores events. The low magnitude event has been dragged south-west towards the Australian stations.

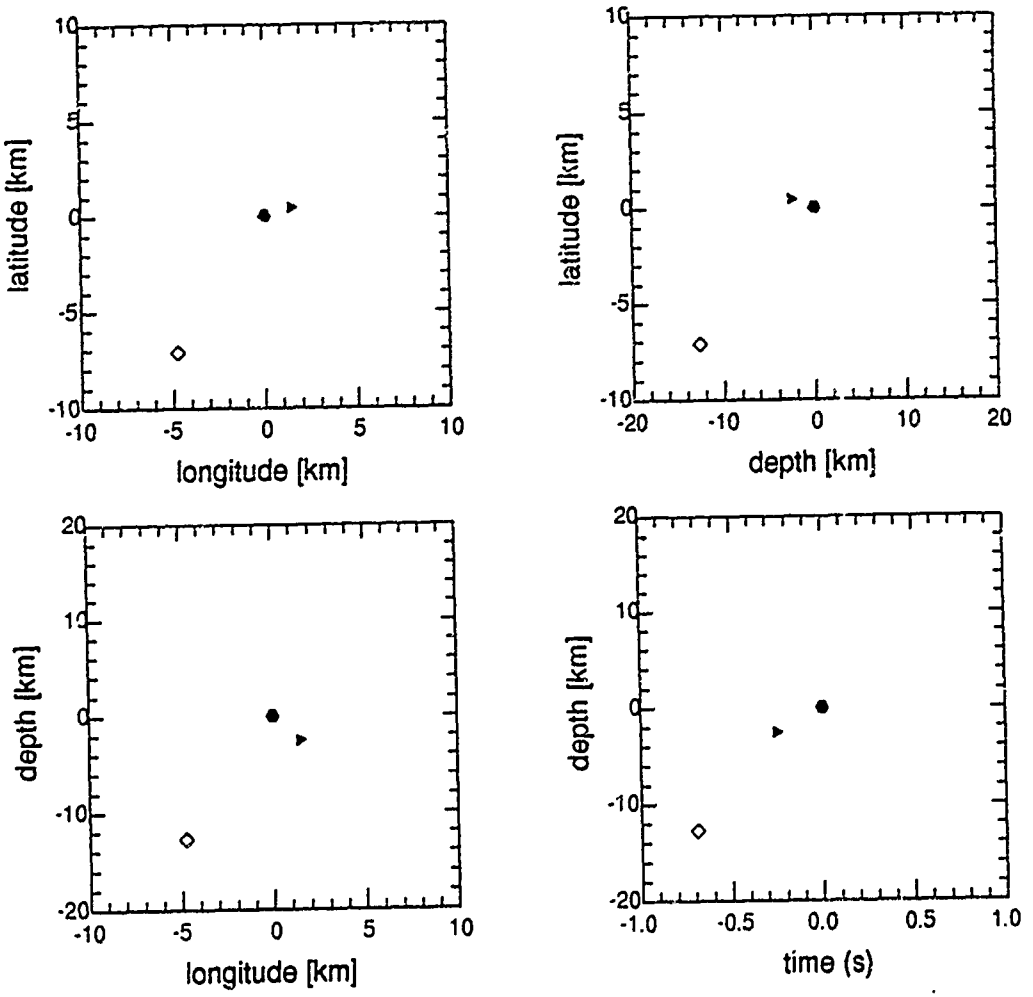

Figure 3
Residuals at Australian stations that recorded all three events. For the low magnitude event the residuals are either positive, or very small and negative. For the intermediate and large magnitude locations the residuals all become more negative, indicative of the fact that the event is dragged away from Australia.

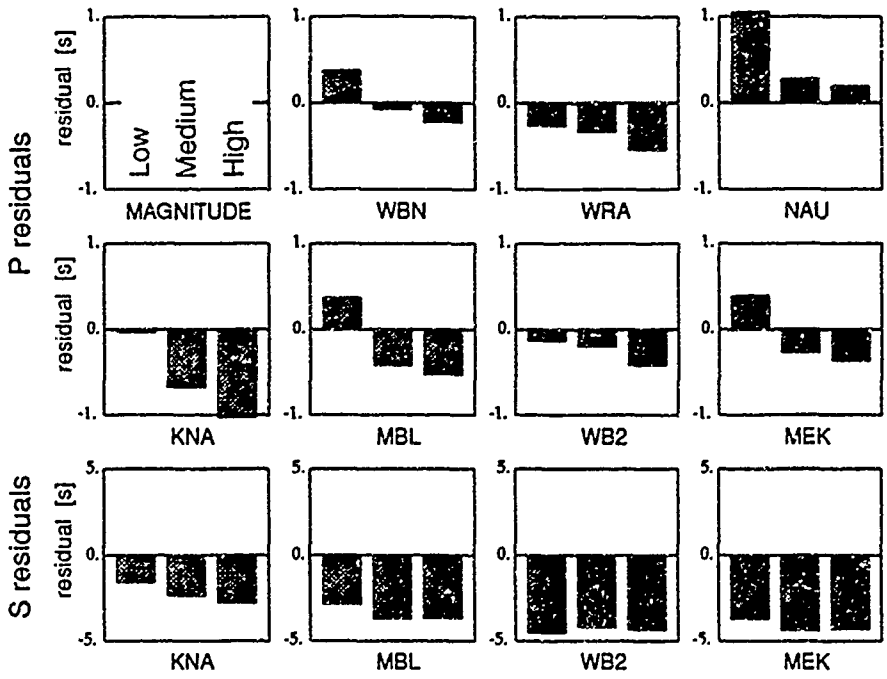

SEISMOLOGICAL STUDIES USING BOROVOYE DATA

Won-Young Kim and Paul G. Richards*
Lamont-Doherty Earth Observatory, Palisades, NY 10964
(* also, Dept. of Geological Sciences, Columbia University)

F49620-92-J-0497

OBJECTIVES

It has been shown that the seismographic station Borovoye (BRVK) in Kazakhstan provides high-quality digital data due to its low noise environment and careful operation over many years. In light of availability of this unique data, our objective has been to evaluate nuclear explosions in Central Asia (former Soviet and Chinese), for which we have obtained new collection of *Lg* signals, and to analyze regional as well as teleseismic waveform data recorded at BRVK for determining geophysical properties in the crust and upper mantle under Central Asia.

RESEARCH ACCOMPLISHED

We have carried out three projects:

- an evaluation of digital *Lg* signals recorded in Borovoye, Kazakhstan at a regional distance from Chinese underground nuclear explosions in the Lop Nor test site;
- an analysis of instrument responses for BRVK seismographs using available information on amplitude responses as well as digital calibration test pulses;
- a study of regional and teleseismic signals recorded at BRVK for crust and upper mantle structure in Central Asia.

RMS Lg Measurements of Chinese Underground Explosions at Lop Nor

RMS *Lg* measurements using digital seismograms recorded at the Borovoye Geophysical Observatory, Kazakhstan (station BRVK) from Chinese underground nuclear explosions in the Lop Nor test site ($\Delta \approx 1880$ km) show fairly good correlation with ISC $m_b(P)$. Regression of five RMS *Lg* measurements using BRVK data yields a standard deviation of only 0.045 magnitude units.

In this study, we used vertical component digital seismograms from five Lop Nor underground explosions (magnitude 4.7 - 6.2) recorded on short-period seismographs at BRVK. Epicentral distances ranges from 1879 to 1894 km with a mean distance of 1884 km (Table 1). Four explosions records on SKM-3 high-gain channel of STsR-SS seismograph and an explosion record on KSVM low-gain channel of STsR-TSG seismograph are used for RMS *Lg* measurements. Characteristics of the STsR-SS and -TSG seismographs are given in Table 2.

The SS-SKM-3 channels use Kirnos short-period seismometers and record 3-component high-gain and vertical component low-gain channels. The high-gain channels have been operating with a nominal gain of about 2000 count/μ and have nearly flat response to ground displacement in the frequency band 0.8 - 3.3 Hz (3 db level). This high-gain vertical channel provides good regional signals with frequencies up to about 3-4 Hz for most of the underground explosions from the Lop Nor test site (Fig. 1). The KSVM channel of the TSG seismograph has similar characteristics as SS-SKM-3 channels, but has only low- and high-gain vertical components.

To measure the RMS *Lg*, we followed a procedure similar to Hansen et al. (1990), except that we used a gaussian window instead of the usual box-car window. Noise in the signal is corrected as suggested in Ringdal & Hokland (1987) by taking RMS values of the trace (50 sec window) preceding the first arrival *P*-wave. *Lg* signal-to-noise ratios were about 2.5 to 92.

Table 1. Lop Nor Underground Explosions(*)

Origin time		Latitude	Longitude	ISC Magnitude				$\log_{10}$(RMS *Lg*)	S/N
Year Mon Day	(h: m: sec)	(°N)	(°E)	(m_b)	#	(M_S)	#	(nanometer)	
1983 OCT 06	09:59:58.0	41.53	88.72	5.5	73	4.2	2	1.3907	13.7
1984 OCT 03	05:59:57.9	41.54	88.67	5.4	81	-		1.1956	10.8
1984 DEC 19	06:00:02.8	41.62	88.22	4.7	11	4.2	1	0.6236	2.5
1987 JUN 05	04:59:58.5	41.55	88.72	6.2	145	4.7	5	2.1385	92.3
1990 AUG 16	04:59:57.7	41.52	88.75	6.2	138	4.4	17	2.1008	67.4

(*) Origin time, location and magnitudes are from ISC bulletin; S/N=signal-to-noise ratio.

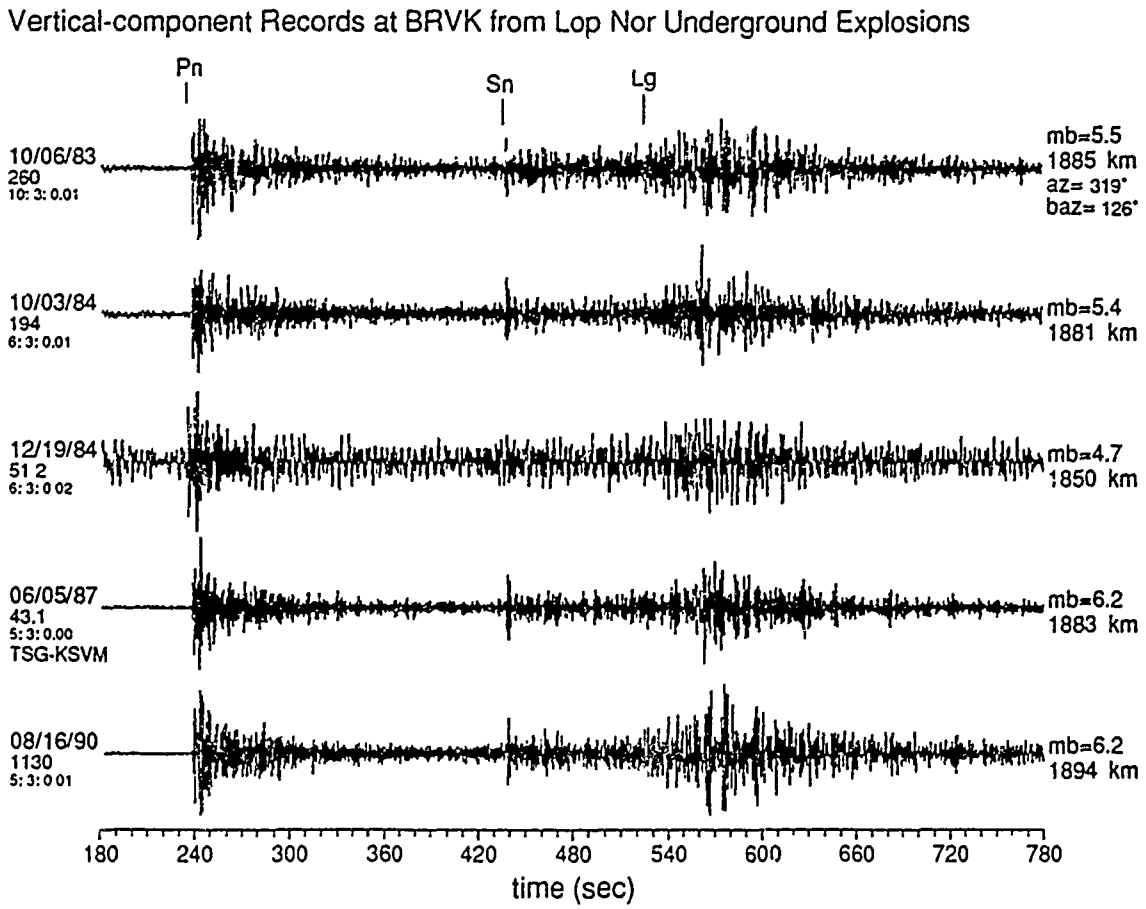

Fig. 1. Vertical component records (SS-SKM-3) recorded at BRVK from Lop Nor explosions.

We used a gaussian with width σ_{ref} = 45 s at a reference distance, Δ_{ref} = 1000 km. This gaussian window ($\pm\sigma$) covers the *Lg* phase in group velocity range 3.66 to 3.0 km/s when centered at the group velocity around 3.3 km/s. The gaussian is truncated at 2.58σ (99 % of unit area). The width of the gaussian can be conveniently scaled as a function of distance, $\sigma = \sigma_{ref} * \Delta/\Delta_{ref}$, allowing the RMS *Lg* measurements at many stations at different epicentral distance ranges to be combined to obtain a network $m_b(Lg)$ based on the RMS *Lg* measurements. The successive gaussian windows were shifted by 0.2 σ relative to the previous window to sample the *Lg* waves smoothly. The *Lg* signals are not corrected for the geometrical spreading and anelastic attenuation along the path because all explosions are at nearly the same location.

Fig. 2 shows the $\log_{10}$ of RMS *Lg* measurements in nanometer of ground displacement plotted against ISC $m_b(P)$. Regression of ISC $m_b(P)$ against $\log_{10}$ (RMS *Lg*) for five explosions in the magnitude range 4.7 - 6.2 yields a slope of 0.98 and a standard deviation of only 0.045 magnitude units. It appears that BRVK data is useful to measure source strength of Lop Nor explosions for explosions with magnitude down to about $m_b(P) \approx 4.5$. Examination of all available GSN digital seismograms for 13 known underground explosions during 1976-1992 at Lop Nor indicates that BRVK provides unique regional data for RMS *Lg* studies.

The RMS measurements of *P* waves are also obtained following a similar procedure used for *Lg* signals to examine the stability of the method for the *P* signals. Regression of ISC $m_b(P)$ against $\log_{10}$ (RMS *P*) values at BRVK for six explosions in the magnitude range 4.7 - 6.2 yields a slope of 1.03 and a standard deviation of 0.065 m. u. Though this result is preliminary in nature, it indicates that RMS *P* wave signals may provide an alternative tool for measuring the strength of the seismic source when the records have only *P*-wave portion of triggered data.

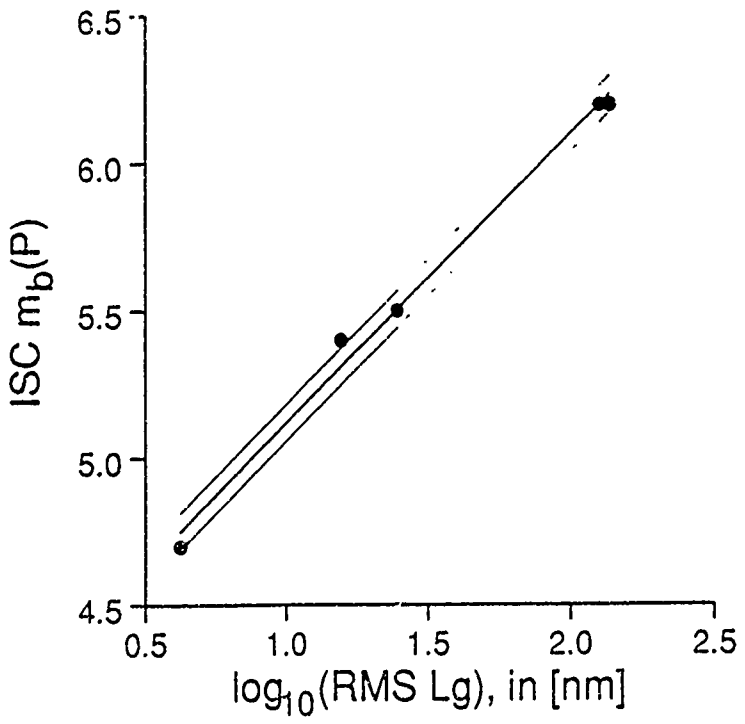

Fig. 2 Comparison of $\log_{10}$ of RMS *Lg* (in nm) at BRVK with ISC $m_b(P)$. Solid line is a fitted slope of 0.98 and an orthogonal rms misfit of 0.045 m. u. Dotted lines correspond to ±2 S.D.

As a first step in conducting detailed analysis of BRVK digital waveform data for crust and upper mantle structure in Central Asia, nominal instrument responses for STsR-SS (10 channels) and STsR-TSG (24 channels) seismographs used at the BRVK station are obtained by using available information on amplitude responses as well as characteristics of the seismometers and recording devices. Table 2 lists basic instrument parameters of the SS and TSG seismographs.

For the STsR-SS seismograph (Table 2), amplitude responses of the short-period SKM-3 and the long-period SKD are determined using the amplitude-frequency response curve given in Adushkin & An (1990) and crude information provided by the Borovoye Observatory in response to our inquiries made in the spring of 1991 (see Fig. 3 of Richards et al., 1992).

For STsR-TSG seismograph, theoretical transfer functions of all the long- and short-period channels are obtained using; 1) seismometer free period and damping, digital sensitivity (in count/μ) given in Adushkin & An (1990); 2) notes made at Borovoye by Paul Richards and Göran Ekström during August, 1991 on calibration tables of TSG seismograph (Richards & Ekström, 1991); 3) digital recording of calibration pulses of all 24 channels of the TSG seismograph. These calibration pulses are generated by feeding a Heaviside step calibration pulse with duration of 8 msec into the damping coils.

According to the linear system theory, these seismographs can be represented by a linear combination of the 1st and 2nd order high- and low-pass filters which are characterized by their cutoff frequencies (ω_c) and damping factors (ξ) (e.g., Graupe, 1972; Farrell & Berger, 1979).

We parameterized the impulse responses of all channels of the TSG system in terms of cutoff frequencies and damping factors of a set of linear 1st and 2nd order filters. The shape of the

Table 2. **Characteristics of STsR Seismographs at Borovoye Seismic Station(*).**

Seismograph	Seismometer	Data channel	T_s(a) (s)	D_s(b)	S_m(c) (unit/μ)	f_m(d) (Hz)	dt(e) (msec)	Channel(f) number
STsR-SS	SKM-3	High-gain	2.0	0.5	2000	0.8-3.3	24	7,8,9
		Low-gain (Z)†			200		32	1
					20		96	6
	SKD	High-gain	25.0	0.5	5.0	0.05-0.4	192	2,3,4
		Low-gain			0.5		192	1,5,10
STsR-TSG	KS		1.5	0.7	4500	1.0-3.3	26	7,8,9
	DS		20.0	0.5	50	0.05-0.2	312	19,20,21
	KSM	High-gain	1.5	0.35	100000	0.7-5.0	26	10,11,12
		Low-gain			1000		26	3,4,5
	DSM	High-gain	28.0	0.5	1000	0.04-0.1	312	22,23,24
		Low-gain			10		312	15,16,17
	KSVM	High-gain (Z)	1.5	0.35	4600	0.8-2.5	26	2
		Low-gain (Z)			50		26	1

(*) STsR system from Feb 1973 to present, (a) T_s=Seismometer natural period in second, (b) D_s=Seismometer damping constant, (c) S_m=Nominal gain in count/μ, (d) f_m=passband (90 % of peak), (e) dt=Sampling interval in millisecond, (e) Channel identifier, † Only vertical component.

calibration pulses are inverted for these parameters in the time domain using the standard damped least-squares method. Kernel functions in the inversion are impulse responses of the 1st or 2nd order filters with perturbation -- cutoff frequency ($\omega_c+\delta\omega_c$) and damping factor, ($\xi + \delta\xi$). The transfer functions of each channel obtained from the inversion are represented with complex poles and zeros in the complex s ($=i\omega$) plane. Poles and zeroes are very convenient for further analysis of observed records, for convolution or deconvolution of their instrument responses.

A comparison between the actual calibration pulses and corresponding theoretical calibration pulses, which are calculated with the transfer function obtained from the inversion, are shown in Fig.3. Excellent agreement between the two pulses indicates that the parameters obtained are quite good. The results of this analysis suggest that seismometer natural period and damping constant of some channels show significant departure from the nominal settings. For example, the calibration pulses of 3-component long-period DS channels indicate that seismometer natural periods vary by as much as about 10 % among vertical and horizontal components, while the seismometer damping constants vary up to 16 % from the nominal setting given in Adushkin & An (1990).

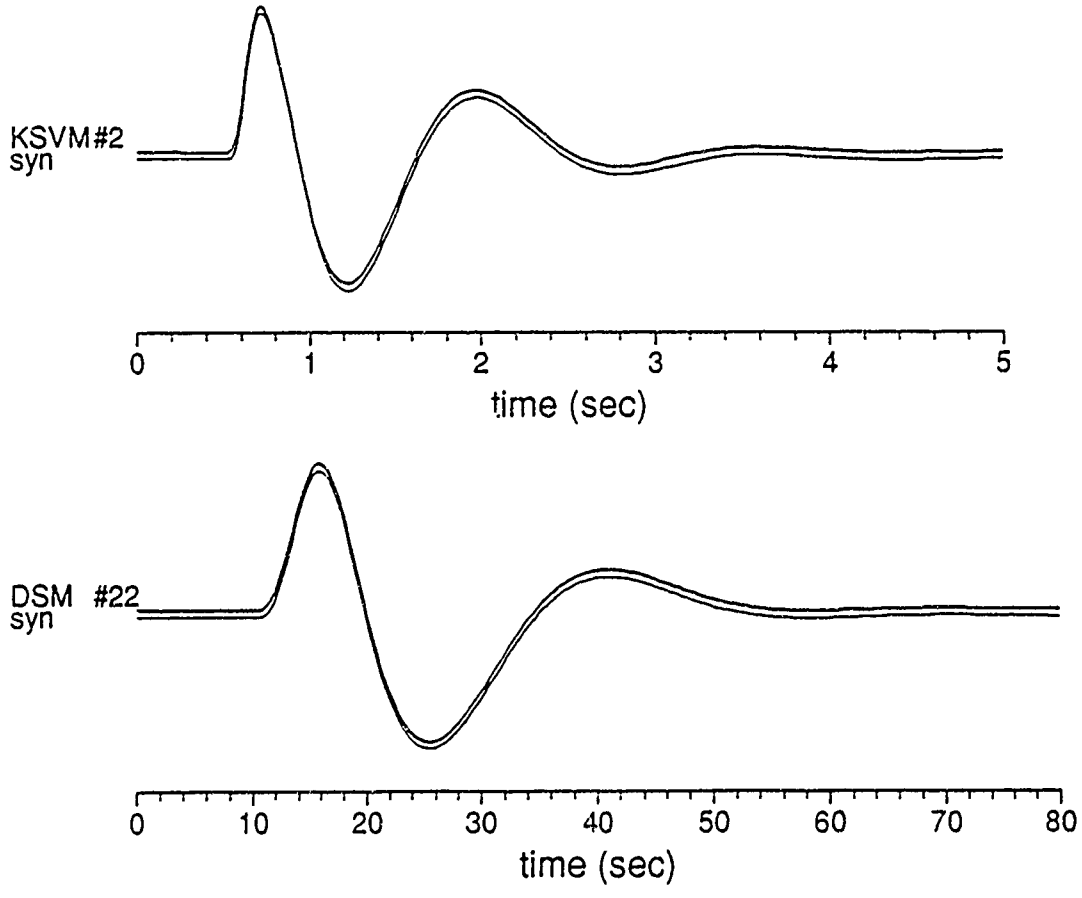

Fig. 3. Comparisons between actual calibration pulse and synthetic pulse (*thin trace*) calculated with theoretical transfer function obtained. (*upper*) TSG-KSVM channel, (*lower*) DSM channel.

Following the evaluation of instrument responses of various seismographs at BRVK station, we have begun to analyze teleseismic signals recorded at BRVK to determine seismic velocities in the crust and upper mantle, particularly the nature of seismic discontinuities in the upper mantle (e.g., Garnero et al., 1992). A comparison between the observed and synthetic vertical- and radial-component records from a deep focus earthquake that occurred in Southern Honshu, Japan is shown in Fig. 4. Some relatively simple *P*-wave records from this and other deep focus teleseismic earthquakes are used to assess the reliability of instrument responses obtained in this study.

Observed vertical- and EW-component (≈ radial) traces are modelled with a point shear dislocation source imbedded in a standard Earth model (PREM). Direct *P*, free surface reflected rays, *pP* and *sP*, as well as core-mantle boundary reflected ray, *PcP*, are generated with WKBJ seismogram method (Chapman, 1978). These primary rays are convolved with a simple triangular source time function (1 s), an attenuation operator with attenuation time, $t^* = 0.5$ sec and TSG-DS seismograph responses as following a standard practice. Double couple point source mechanisms given in the Harvard CMT catalog are used for the source radiation pattern.

The overall fit of relative amplitudes and durations between the observed and the synthetic phases are fairly good suggesting that the source parameters as well as the instrument response used for the modeling are reasonably good. Focal depts of this event is determined in this study by matching the arrival times of *PcP* and surface reflections *pP* and *sP*. We are carrying out this work to identify other phases on the observed records, for instance, *P* to *S* converted phases at the discontinuities in the upper mantle (see phases marked $P_{400}S$ and $P_{600}S$ in Fig. 4; see also, Petersen et al., 1993) as well as at the Moho by calculating synthetic seismograms.

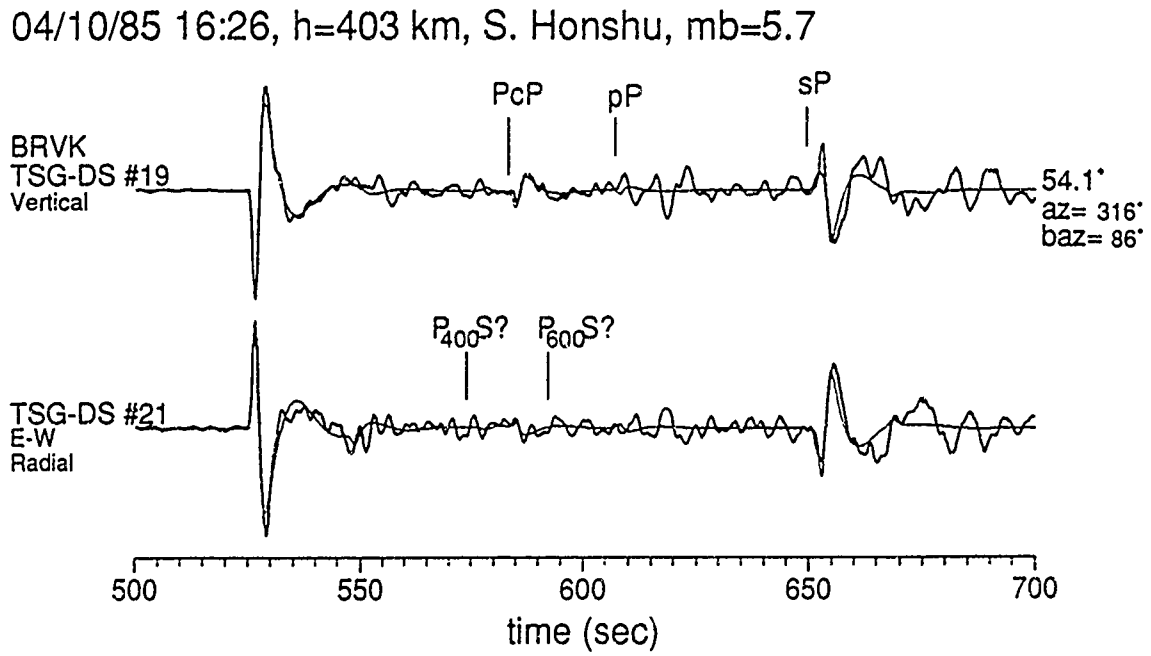

Fig. 4. Comparison of observed vertical and radial components from deep focus earthquake and corresponding synthetics. Arrivals marked as $P_{400}S$ and $P_{600}S$ are presumed *P* to *S* converted phases at 400 and 600 km discontinuities in the upper mantle beneath station.

CONCLUSIONS AND RECOMMENDATIONS

The regional seismic data now becoming available for Central Asia, digitally recorded at Borovoye, Kazakhstan, appear to be useful to measure source strength of Lop Nor explosions for explosions with magnitude down to about $m_b(P) \approx 4.5$.

Instrument calibration (gains) of various seismographs at Borovoye station appear to be stable over many years. Stability of *Lg* amplitudes for explosions at the Lop Nor test site over several years suggests reasonable instrument calibration. However, some of the 3-component channels suggest significant departure of seismometer constants from their nominal setting, and care must be taken to interpret results (phase information) using such records.

The broadband nature of BRVK digital records provides an opportunity to examine seismic velocities and discontinuities in the upper mantle beneath Central Asia.

In these three conclusions, the common theme is new opportunities to work with high-quality regional signals for Central Asia recorded at BRVK. We recommend a concerted effort by academic institutions to ensure timely salvage of these valuable seismic data.

References

Adushkin, V. V. and V. A. An, Seismic observations and monitoring of underground nuclear explosions at Borovoye Geophysical Observatory, *Izvestiya Akademii Nauk SSSR*: Fizika Zemli, 47-59, **No. 12**, 1990.

Chapman, C. H., A new method for computing synthetic seismograms, *Geophys. J. R. astr. Soc.*, **54**, 481-518, 1978.

Farrell, W. E. and J. Berger, Seismic system calibration: 1. Parametric model, *Bull. Seism. Soc. Am.*, **69**, 251-270, 1979.

Garnero, E. J., D. V. Helmberger and L. J. Burdick, Preliminary observations from the use of US-Soviet Joint Seismic Program data to model upper mantle triplications beneath Asia, *Geophys. J. Int.*, **113**, 252-259, 1992.

Graupe, D., *Identification of Systems*, van Nostrand Reinhold Co., 276pp, 1972.

Hansen, R. A., F. Ringdal and P. G. Richards, The stability of RMS Lg measurements and their potential for accurate estimation of the yields of Soviet underground nuclear explosions, *Bull. Seism. Soc. Am.*, **80**, 2106-2126, 1990.

Petersen, N., L. Vinnik, G. Kosarev, R. Kind, S. Oreshin and K. Stammler, Sharpness of the mantle discontinuities, *Geophys. Res. Lett.*, **20**, 859-862, 1993.

Richards, P. G. & G. Ekström , Report of a visit to the Borovoye Geophysical Observatory (seismic station BRV) in Kazakhstan, Technical Report No. 1 for DARPA/NMO, 18 September 1991.

Richards, P. G., W. Y. Kim and G. Ekström, The Borovoye Geophysical Observatory, Kazakhstan, *EOS*, **73**, 201-206, 1992.

Ringdal, F. and B. Kr. Hokland, Magnitudes of large Semipalatinsk explosions using P coda and Lg measurements at NORSAR, in Semiannual Technical Summary, NORSAR Sci. Rept. 1-87/88, NTNF/NORSAR, Kjeller, Norway, 1987.

CONSTRAINTS FROM SURFACE WAVE INVERSION FOR UPPER MANTLE SHEAR STRUCTURE OF THE BASIN AND RANGE

Karl Koch, Brian W. Stump
Southern Methodist University, Dallas

Contract No: F19628-91-K-0016

OBJECTIVE

Full wave modeling of seismograms at far-regional distances including body and surface waves with application to source contributions in regional seismograms

RESEARCH ACCOMPLISHED

INTRODUCTION

This study focuses on the constraint of the upper mantle shear velocity structure for propagation paths in the western United States along the great circle path between Lajitas (LTX) and the Nevada Test Site (NTS) for events located on the coast of Northern California and off the coast of southern Oregon at distances as great as 2500 km. In a previous study (Koch & Stump, 1992) we have investigated mantle S waves in the Basin and Range which provide strong constraints on the upper mantle transition zone under NTS. To some extent these data also placed bounds on the associated upper mantle discontinuities. However, the mantle S waves left some ambiguities in the shallower shear velocity structure. These uncertainties are addressed by inverting the dispersion relations from the observed surfaces waves. The previous data set (Koch & Stump, 1992) has been supplemented by the earthquakes of the spring 1992 Petrolia sequence. This data set is unique in that it provides multiple samples of identical propagations paths, so that we are able to average various dispersion estimates to improve their reliability for both Love and Rayleigh waves. This paper will first discuss the results from a multiple filter analysis, which gives initial group velocity dispersion curves. These dispersion curves are then used in a phase-matched filtering procedure to retrieve phase velocity information used in the surface wave inversion.

DISPERSION ANALYSIS

Data at LTX are recorded with three component short period instruments (S-13) and three component broadband instruments (BB-13). For the current study we used the broadband data recorded in acceleration from 300 sec to 5 Hz. For some of the events the broadband instruments were not operative or some of the components included data glitches, in particular for the Petrolia data. For these events we used the short-period data and produced simulated broadband records according to the procedures developed by Seidl (1980). The data were then analyzed with the multiple filtering analysis technique (Dziewonski et al., 1969; Herrmann, 1988).

The group velocity dispersion curves for all Love wave data are shown in Fig.1a. These group velocity dispersion curves are quite similar from event to event. The scatter of the data is of the order of 0.1 km/sec in the applicable frequency band between period of 10 and 80-100 sec, where the signal to noise ratio is about a factor of 5-10. For the longer periods the dispersion curves show considerably more scatter due to the reduced signal to noise ratios for the smaller events which are mostly at the smaller range. While the dispersion curves are well reproduced for all events, we observe a clustering of dispersion curves for on-shore and off-shore events close to periods of about 40-50 sec where the two sets intersect at two different points. The two sets of

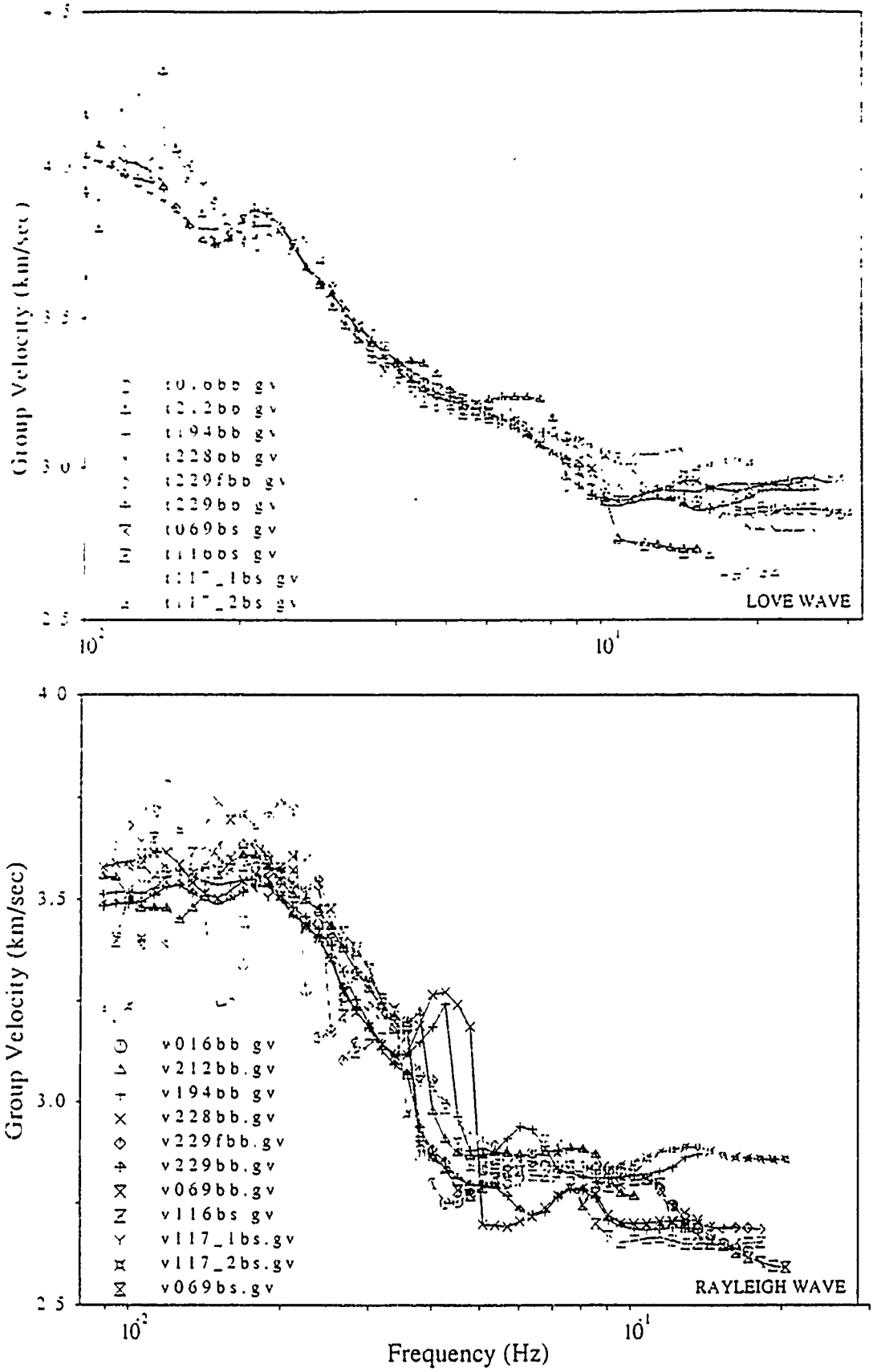

Fig.1 : Group velocity dispersion curves from multiple filter analysis for (a) Love waves and (b) Rayleigh waves (on vertical component). Dispersion curves from on-shore events are indicated by the solid line, while off-shore events are shown with shaded lines

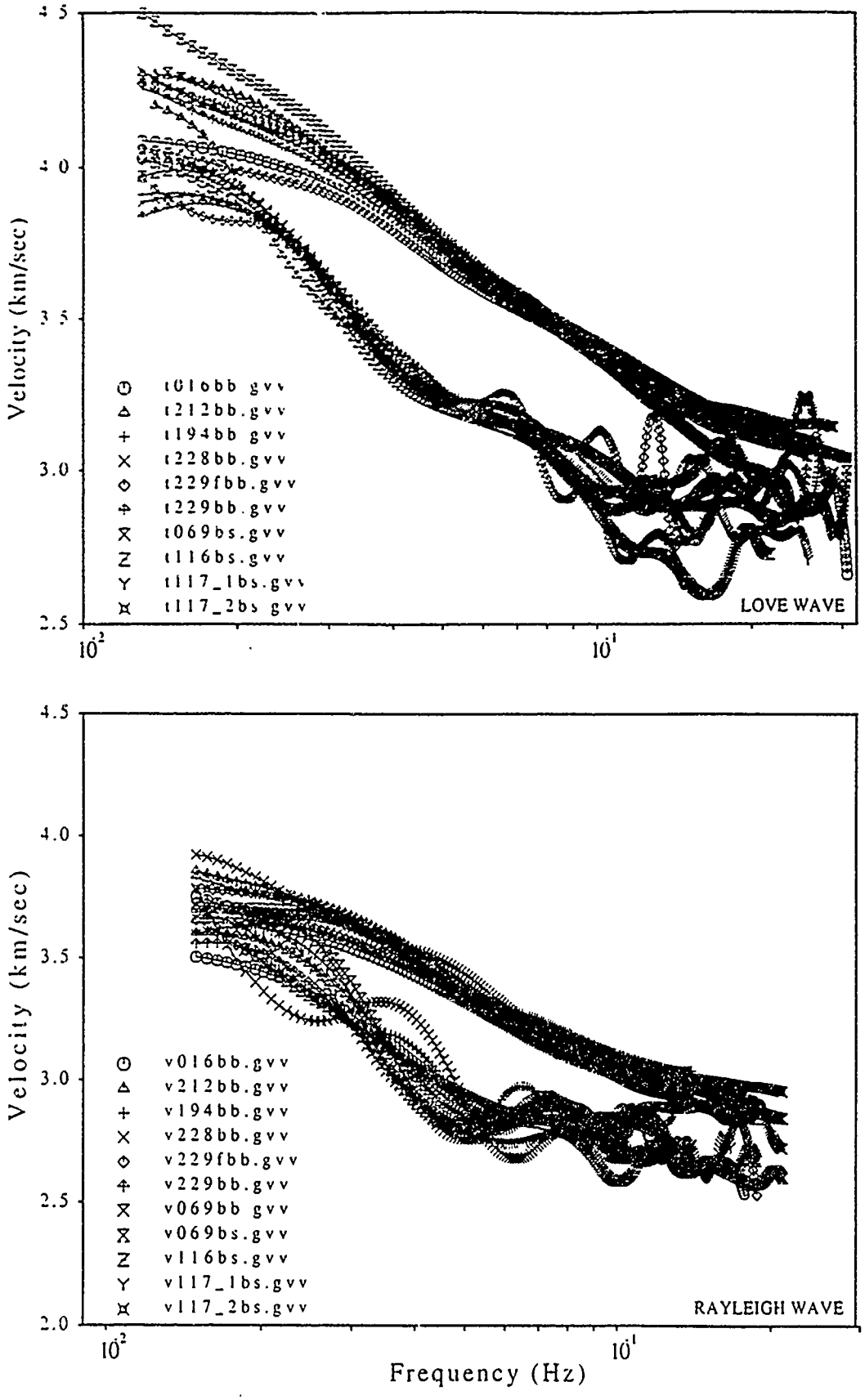

Fig.2 : Group velocity and phase velocity dispersion curves from phase matched filtering for (a) Love waves and (b) Rayleigh waves (on vertical component). See also Fig.1.

curves also display a local minimum in the group velocity curve at those periods. This observation is the result of interference between the mantle S body wave and the surface waves in the multiple filter analysis. The difference in the interference pattern between the on-shore and off-shore data is the result of the different arrival times. The S arrival is also manifested in the contour plots by a group velocity branch near 4.5 km/sec, with no apparent dispersion, especially prominent at periods below 10 sec. We were able to eliminate this pattern in the case of the impulsive mantle S arrival by windowing the surface waves. However, we could not apply this procedure to all events, as it was not possible for the on-shore events without truncating the longest period surface wave energy.

The Rayleigh wave dispersion curves shown in Fig.1b, display increased scatter throughout the period range of interest. This effect appears to be related to a reduced signal to noise ratio. Dispersion curves appear to be useful between 70 and 10 sec, with very poorly determined dispersion near 20-30 sec due to spectral holes. Separation of the data according to the source region or source mechanism (both strike-slip and normal faulting events are used) suggests slightly smaller scatter for the normal faulting events, indicating stronger Rayleigh wave excitation for these earthquakes. Analysis was conducted on both vertical and radial seismograms. While the vertical component data were useful for retrieving Rayleigh wave dispersion, radial component data gave poor results. It is suspected that multipathed Love-waves are interfering with the Rayleigh waves and therefore lead to results not useful for interpretation in this case.

The initial group velocity curves were used to design a phase-matched filter (Herrin & Goforth, 1977; Herrmann, 1988) for retrieving improved group velocity estimates. This procedure should eliminate multipathing as well as higher mode surface waves (Herrin & Goforth, 1977) and possibly the interference of the mantle S wave arrivals. The resulting group velocity curves for all events are shown in Fig.2a (for Love waves) and Fig.2b (for Rayleigh waves from vertical component). For the Love waves, the mantle S wave interference pattern is no longer observed, indicating that the phase-matched filtering procedure was successful in eliminating this phase. Again, there is little scatter for the group velocities over a fairly large period range, with scatter increasing for the longest periods and smaller events. The phase velocity dispersion is well constrained in the considered period range. The results for the Rayleigh wave data on the other hand show a fair amount of scatter which is expected from the reduced signal to noise ratio as found in the multiple filter analysis. However, the larger scatter at intermediate periods is reduced, indicating that the phase-matched filter results are less susceptible to noise.

RESULTS FROM SURFACE WAVE INVERSION

The dispersion results were then used to invert for the shear wave structure in the western United States. In order to estimate confidence limits for the velocity model, we inverted different data sets including single event group velocities, average group velocities from multiple filter analysis for both Love and Rayleigh waves, and combined group and phase velocity data, averaged for all events. We selected the largest event in the data set, with presumably the best single event dispersion estimate, as a first example. The results for this event are shown in Fig.3. The starting model for the inversion is shown as a thin solid line and was but one of the models capable of explaining the mantle S wave observations. Also shown in this and following figures (as a dotted line) is the model obtained by Priestley & Brune (1978) by surface wave analysis of observations on great circle paths in the Basin and Range. The model from the surface wave inversion is shown as solid line with the error bar indicating the uncertainty from the residuals after 5 iterations (Additional iterations proved not to increase the overall fit but rather introduced trade-off effects). This resulting model is similar to the model of Priestley & Brune (1978) to depths of about 250 km, which represents the depth resolution limit for our dispersion data as deduced from the resolving kernels. The most significant difference between the two models is the thin mantle lid in the new results, which might not be resolved by Priestley & Brune's data.

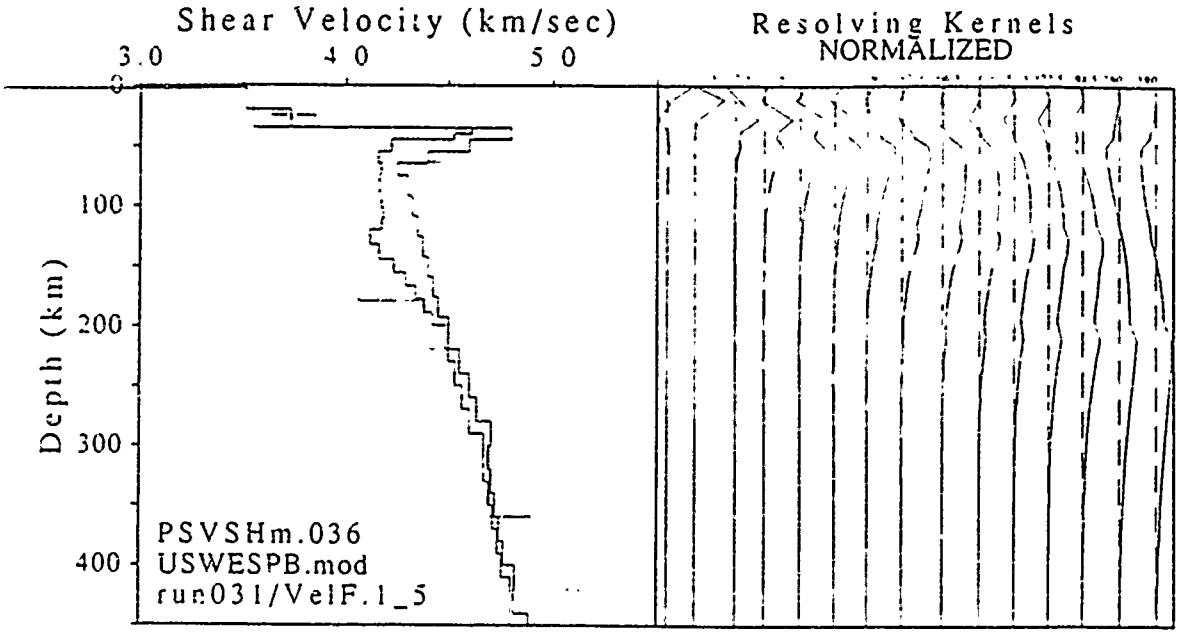

Fig.3 : Inversion for event 1991_194 (Jul 13, 1991) using only Love wave dispersion curves (group and phase velocity). Starting model (thin solid line) includes a thin mantle lid. Inverted model is diagrammed with thick solid line with error bar. The model of Priestley & Brune (1978) is shown as a dotted line for comparison. On the right side normalized resolving kernel are shown.

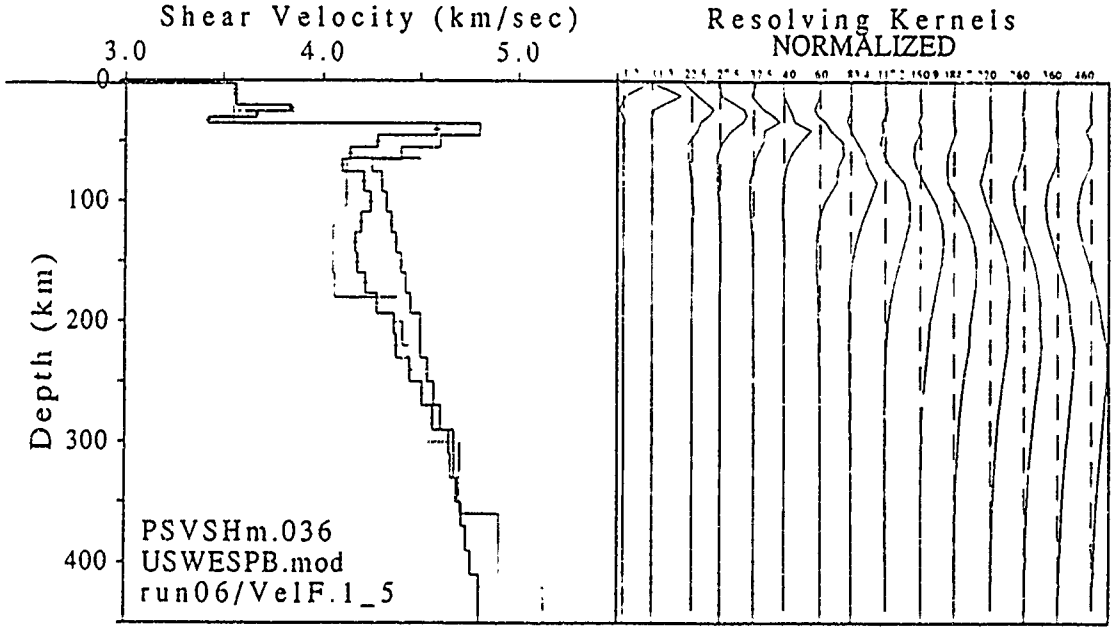

Fig 4 : Inversion for all Love wave and Rayleigh wave dispersion (group and phase velocity). See also Fig.3 above for line type description.

In Fig.4 we show the velocity model determined from the averaged group and phase velocity dispersion curves using the same starting model. The inversion model is very similar to the results given in Fig.3, indicating consistency between the two data sets. Although the previous model shows a relatively uniform velocity distribution in the low-velocity zone, the results of Fig.4 argue for an intermediate increase in this zone. In order to verify the reliability of the inversion results, we also used a different starting model, which was considered the preferred model from the mantle S wave analysis (Koch & Stump, 1992), as it placed the less constraints on the adopted attenuation model. The results of this inversion (Fig.5) suggests that the results reported here are nearly independent of the starting model. These models provide additional support for structure within the Basin and Range low velocity zone.

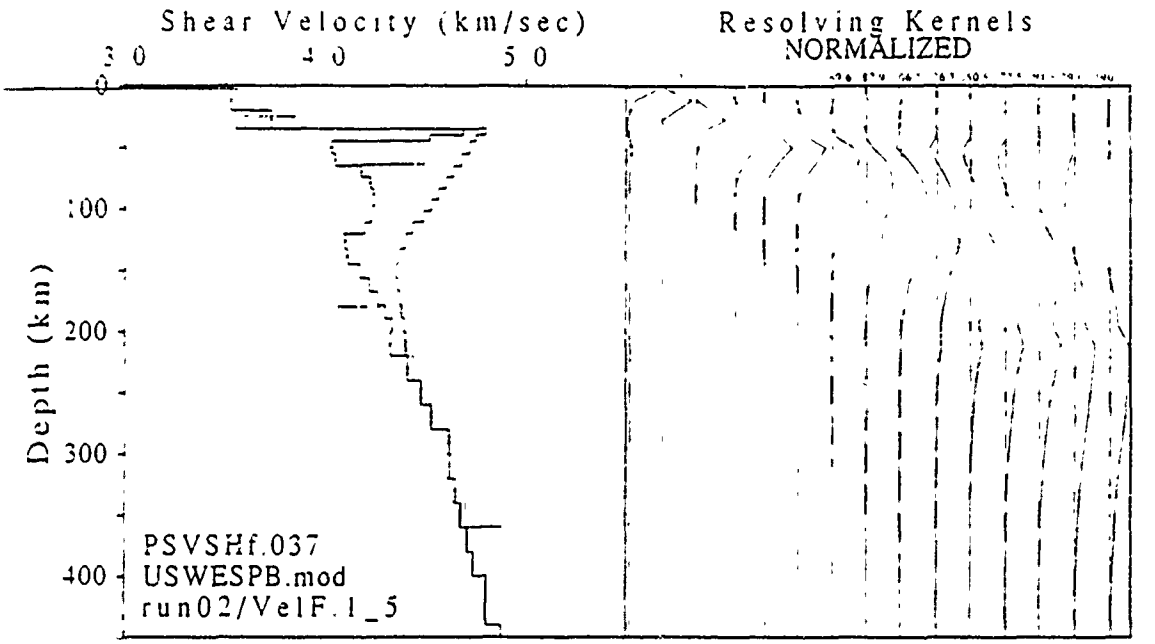

Fig.5 : Same as Fig.4 for a different starting model. The main features of the inverted shear velocity structure are preserved, i.e. thin mantle lid, large low-velocity zone and an indication of two low-velocity layers within the LVZ.

CONCLUSIONS AND RECOMMENDATIONS

Surface waves have been used to constrain the shallow part of the upper mantle shear wave structure in the western United States for paths along the great circle between LTX and NTS. These results complement the analysis of mantle S waves for the same propagation path and support our ultimate goal of modeling complete far-regional seismograms. The results indicate a low-velocity layer between depths of about 80 to at least 200 km, which is similar to the model of Priestley & Brune (1978). However, the results also indicate a consistent pattern of a very thin mantle lid and a larger amount of velocity variation throughout the low velocity layer, possibly identifying a subdivision into two low-velocity layers to be scrutinized for their statistical significance.

This work have been directed at developing a full wave model for the Basin and Range built by using P, S and surface waves. The refined upper mantle models will be used to quantify the effects of different source contributions with synthetic seismograms. The models will be more appropriate than previous models in examining the significance of various regional discriminants. This analysis of broadband regional signal from earthquakes and explosions suggests a methodology for approaching regional observations in a new area ultimately leading to a quantification of discrimination tools.

REFERENCES

Dziewonski,A.M, S.Bloch & M.Landisman (1969): A technique for the analysis of transient seismic signals, Bull.Seism.Soc.Am., 59, 429-444

Herrin, E.T. & T.T.Goforth (1977). Phase-matched filters: application to the study of Rayleigh waves, Bull.Seism.Soc.Am., 67, 1259-1275

Herrmann, R.B. (1987): Computer programs in seismology, Vols. II-IV, St.Louis University

Koch, K. & B.Stump (1992): Far-regional seismogram analysis for the western United States and the role of short-period mantle S waves, in: Proc. 14th Annual PL/DARPA Seismic Research Symp, Tucson, AZ, PL-TR-92-2210, 252-259, ADA256711.

Priestley & Brune (1978): Surface waves and the structure of the Great Basin of Nevada and western Utah, J.Geophys.Res., 83, 2265-2272

Seidl,D. (1980): The simulation problem for broad-band seismograms, J.Geophys.,48, 84-93

Pulse reflection from locally layered random media

Werner K... [*] George P... [†] Benjamin S. White [‡]

1 Objectives

We have studied extensively the reflection of acoustic waves by randomly layered media [1]. Here we present briefly recent work [2] that extends our theory to locally layered random media. This is one of three objectives in our work. The second is the extension of [1] to elastic waves in randomly layered media, especially the study of mode conversion, which has been completed [3] for obliquely incident time-harmonic and pulsed plane waves. The third is the use of the theory to study inverse problems as we did in [1]. We do not have any new results on inverse problems at present, beyond what is in [1].

The general framework of our analysis of reflection of waves from a locally layered random half space is based on three basic assumptions:

- The incident pulse is short (around 150 meters, for example) compared to propagation distances (several kilometers) so geometrical acoustics methods can be used at this level.
- The incident pulse is long compared to the typical thickness of the random layers (which is of the order of meters) so that the effects of random scattering can be described in a general way that does not depend on the details of the random layering. The fluctuations in sound speed from layer to layer are not small.
- The random layeres are not plane. They are either small perturbations of plane layers or large but slowly varying (on the macroscopic scale of kilometers) perturbations. In both cases the purely layered theory changes in an essential way.

Let $\mathbf{u}(t,x,y,z)$ and $p(t,x,y,z)$ be the acoustic velocity and pressure satisfying the equations of continuity of momentum and mass

$$\rho \mathbf{u}_t + \nabla p = \epsilon^{1/2} f(\frac{t}{\epsilon})\delta(x)\delta(y)\delta(z-z_s)\mathbf{e}\,, \tag{1}$$

$$\frac{1}{K} p_t + \nabla \cdot \mathbf{u} = 0. \tag{2}$$

Here ρ is the material density, K is the bulk modulus, f is the pulse shape function, $\mathbf{e} = (e_1, e_2, e_3)$ is the source directivity vector and $(0,0,z_s)$ is the source location. We assume that z_s is positive and that the random medium in the half space $z < 0$. The parameter ϵ is the ratio of a characteristic pulse width to observation times and it is assumed small, as noted above. The factor $\epsilon^{1/2}$ in front

[*] Department of Mathematics, Virginia Polytechnic Institute and State University, Blacksburg, VA 24061.

[†] Department of Mathematics, Stanford University, Stanford CA 94305, email papanic@math.stanford.edu. Contract number F49620-92-J-0098.

[‡] Exxon Research and Engineering Company, Route 22 East, Annandale, NJ 08801.

of the source term normalizes the total energy released by the source so that it does not depend on ϵ.

The density and bulk modulus have the following form

$$\rho(x,y,z) = \begin{cases} \rho_0 & \text{for } z > 0 \\ \rho_1 & -L < z < 0 \\ \rho_2 & z < -L \end{cases} \tag{3}$$

and

$$K^{-1}(x,y,z) = \begin{cases} K_0^{-1} & \text{for } z > 0 \\ K_1^{-1}(x,y,z)(1+\nu(\frac{\phi(x,y,z)}{\epsilon^2})) & -L < z < 0 \\ K_2^{-1} & z < -L \end{cases} \tag{4}$$

Thus, the randomly layered medium occupies the slab $-L < z < 0$ and the acoustic medium is homogeneous in the source region $z > 0$ and below the slab in $z < -L$. In [1], [2] and here we assume that ρ is equal to a constant ρ_1 in the random slab in order to simplify the presentation. The analysis can be extended to the general case in a routine manner as for example in [4]. The inverse bulk modulus, the compressibility, has the form (4) with $K_1^{-1}(x,y,z)$ the mean or average compressibility and ν the fluctuation. When the mean K_1^{-1} is a function of z only and the fluctuations have the form $\nu = \nu(\frac{z}{\epsilon^2})$ then the random medium is layered. Here ν is a stationary random function with mean zero and finite, decaying correlations. The scaling of the fluctuations is as was described above, the random layering varies on a scale much shorter than the pulse width. In the general case (4) we have a locally layered random medium because the average compressibility K_1^{-1} is a function of (x,y,z) while the fluctuations ν are constant on the surfaces $\phi(x,y,z) = \text{const}$ and remain functions of a single variable. This is what we call a **locally layered random medium**. It is shown in detail in [2] that we can actually let

$$\phi(x,y,z) = z \tag{5}$$

in (4) without loss of generality because the apparently more general case reduces to this one after a change of variables.

We are interested, therefore, in solving equations (1) and (2), assuming that p and u are zero initially and that p and the normal component of u are continuous across the interfaces $z = 0$ and $z = -L$. We are interested in calculating statistical properties of the solution when ϵ is small. We are particularly interested in the two-point correlation function for the pressure on the surface $z = 0$

$$\langle p(t_1,x_1,y_1,0)p(t_2,x_2,y_2,0)\rangle. \tag{6}$$

Here the angular brackets denote ensemble or statistical average.

2 Results

To describe the analytical results we must first go through a series of transformations that do not involve the random fluctuations. We deal with the random fluctuations after the equations have been suitably transformed.

Since the coefficients in (1) and (2) do not depend on time we can use Fourier transforms. Let

$$\hat{p} = \int_{-\infty}^{\infty} e^{\frac{i\omega t}{\epsilon}} p \, dt \,, \quad \hat{\mathrm{u}} = \int_{-\infty}^{\infty} e^{\frac{i\omega t}{\epsilon}} \mathrm{u} \, dt \tag{7}$$

[illegible]

$$\frac{\partial}{\partial t}\mathbf{u} - \nabla \cdot [\text{illegible}] \quad \text{i.e.} \quad \frac{\partial}{\partial t}p - \nabla \cdot \mathbf{u} = [\text{illegible}]$$

[illegible]

$$[\text{illegible}] = \int_{-\infty}^{\infty} [\text{illegible}]\, e^{-i\omega t}\, dt$$

[illegible] Fourier transform [illegible] shape function F assumed to be zero for $t < 0$ and [illegible]

$$= [\text{illegible}].$$

[illegible] $\mathbf{u} = (u, v, w)$ [illegible] then in the region $-L < z < 0$ the above equations become

$$\frac{\partial \hat{p}}{\partial z} = \frac{i\omega\rho_1}{\epsilon}\hat{u}, \quad \frac{\partial \hat{u}}{\partial z} = \frac{i\omega}{\epsilon K_1}\hat{u} - \nu\frac{\epsilon}{\epsilon^2}\hat{p} - \frac{\partial}{\partial x}\frac{\epsilon}{i\omega\rho_1}\frac{\partial \hat{p}}{\partial x} - \frac{\partial}{\partial y}\frac{\epsilon}{i\omega\rho_1}\frac{\partial \hat{p}}{\partial y}. \tag{9}$$

When the coefficients in (9) depend only on z, which is the case of a plane-layered random medium, then we can continue the analysis of (9) by taking Fourier transforms in the horizontal variables (x, y). We cannot do this for a locally layered medium, however. Instead, we use a special geometrical acoustics representation of $\hat{p}$ and $\hat{u}$ which is

$$\hat{p} = \frac{1}{(2\pi\epsilon)^2}\int\int_{-\infty}^{\infty}\left[Ae^{\frac{i\omega S^-}{\epsilon}} - Be^{\frac{i\omega S^-}{\epsilon}}\right]d\kappa \tag{10}$$

$$\hat{u} = \frac{1}{(2\pi\epsilon)^2}\int\int_{-\infty}^{\infty}\left[\zeta_- Ae^{\frac{i\omega S^-}{\epsilon}} + \zeta_- Be^{\frac{i\omega S^-}{\epsilon}}\right]d\kappa \tag{11}$$

where

$$\zeta_\pm = \frac{\rho_1}{S_z^\pm} \tag{12}$$

and $S^\pm = S^\pm(x, y, z; \kappa)$ are solutions of the deterministic eikonal equation

$$(\nabla S^\pm)^2 = \frac{1}{c_1^2}, \text{ with } c_1(x, y, z) = \sqrt{\frac{1}{\rho_1}K_1(x, y, z)}. \tag{13}$$

in $z < 0$ with the boundary condition

$$S^\pm(x, y, 0; \kappa) = \pm\kappa \cdot \mathbf{x}, \quad \mathbf{x} = (x, y), \quad \kappa = (\kappa_1, \kappa_2). \tag{14}$$

Here κ is the horizontal slowness vector at $z = 0$ and we assume that the eikonal equation (13) has a smooth solution in the random medium $-L < z < 0$. In (10,11) A and B are the up and down going **local** wave amplitudes and they depend on the depth z, the horizontal slowness κ, the frequency ω and the horizontal coordinates $\mathbf{x}$.

When the layering is plane then $c_1 = c_1(z)$ and it is easy to see that

$$S^\pm(\mathbf{x}, z; \kappa) = \pm\kappa \cdot \mathbf{x} \pm \int_0^z \frac{1}{c_1(s)}\sqrt{1 - c_1^2(s)\kappa^2}\,ds \tag{15}$$

in $z < 0$ and (10,11) are essentially equations (2.29) of [1], after taking account of the inverse Fourier transform in time and the different normalization of A and B here[1].

[1] The amplitudes A and B correspond to $\zeta_+^{1/2}A$ and $\zeta_-^{1/2}B$ in [1], respectively. Note also that in the plane layer case $\zeta_+ = \zeta_-$.

Since the equations (9) are linear it is sufficient that the integrands in (10) satisfy them for each horizontal slowness κ. After a straightforward but lengthy calculation we find that the up and down going local wave amplitudes A and B satisfy the following stochastic transport equations, up to terms that are negligible in the asymptotic analysis for small ϵ:

$$\frac{\zeta_- + \zeta_-}{\zeta_+\zeta_-}\frac{\partial A}{\partial z} - \alpha^- \frac{\partial A}{\partial x} - \beta^- \frac{\partial A}{\partial y} - \gamma^- A = \frac{i\omega n}{\epsilon} A - B\epsilon^{\frac{-2i\omega\tau}{\epsilon}} - \text{negl. terms} \tag{16}$$

$$\frac{\zeta_+ + \zeta_-}{\zeta_+\zeta_-}\frac{\partial B}{\partial z} - \alpha^- \frac{\partial B}{\partial x} - \beta^- \frac{\partial B}{\partial y} - \gamma^- B = \frac{-i\omega n}{\epsilon} B - A\epsilon^{\frac{2i\omega\tau}{\epsilon}} - \text{negl. terms} \tag{17}$$

where

$$\alpha^\pm = \frac{2}{\rho_1} S_x^\pm \,, \quad \beta^\pm = \frac{2}{\rho_1} S_y^\pm \,. \tag{18}$$

$$\gamma^\pm = \frac{\partial}{\partial x}\left(\frac{1}{\rho_1} S_x^\pm\right) + \frac{\partial}{\partial y}\left(\frac{1}{\rho_1} S_y^\pm\right) + \frac{\partial}{\partial z}\left(\frac{1}{\rho_1} S_z^\pm\right) . \tag{19}$$

$$\tau = \frac{1}{2}(S^+ + S^-) \,, \quad n = K_1^{-1}(x,y,z)\nu\left(\frac{z}{\epsilon^2}\right) \tag{20}$$

In the plane layer case we see from (15) and (12) that

$$S_z^\pm = \frac{1}{c_1}\sqrt{1 - c_1^2\kappa^2} \,, \quad \zeta_\pm = \zeta = \frac{c_1\rho_1}{\sqrt{1 - c_1^2\kappa^2}} \tag{21}$$

Thus,

$$\frac{\zeta_+\zeta_-}{\zeta_+ + \zeta_-} = \frac{1}{2}\zeta \,, \quad \gamma^\pm = \frac{d}{dz}\left(\frac{1}{\zeta}\right) \tag{22}$$

and $\alpha^\pm = \beta^\pm = 0$ so that equations (16,17) reduce to

$$\frac{dA}{dz} = \frac{i\omega}{2\epsilon}\zeta K_1^{-1}\nu\left[A - B\epsilon^{-2i\omega\tau/\epsilon}\right] - \frac{1}{2}\zeta\frac{d}{dz}\left(\frac{1}{\zeta}\right)A + \text{negl. terms} \tag{23}$$

$$\frac{dB}{dz} = \frac{-i\omega}{2\epsilon}\zeta K_1^{-1}\nu\left[B - A\epsilon^{2i\omega\tau/\epsilon}\right] - \frac{1}{2}\zeta\frac{d}{dz}\left(\frac{1}{\zeta}\right)B + \text{negl. terms} \tag{24}$$

Noting as above that A and B correspond to $\zeta_+^{1/2}A$ and $\zeta_-^{1/2}B$ in [1], that $\zeta_+ = \zeta_- = \zeta$ in the plane layer case and that the local sound speed $c_1 = \sqrt{K_1/\rho_1}$, equations (23,24) coincide with equations (2.27a-b) of [1]. The order one, rapdly oscillating terms

$$\frac{1}{2\zeta_1}\frac{d\zeta_1}{dz}e^{-2i\omega\tau/\epsilon}B \,, \quad \frac{1}{2\zeta_1}\frac{d\zeta_1}{dz}e^{2i\omega\tau/\epsilon}A$$

that appear in (2.27a-b) of [1] do not appear in (23,24). They are the negligible terms in these equations. The terms neglected in the more general equations (16,17) are of this type and higher order in ϵ. We note that in the plane layer case the variable τ defined by (20) coincides, in view of (15), with the oblique travel time $\tau(z,\kappa)$ of [1] (eqn. (2.24) in [1]).

When the random fluctuations $n = 0$ in the general transport equations (16,17) we note that they decouple into the usual transport equations of geometrical acoustics for the local wave amplitudes A and B.

So far the randomness of the medium has played no role. We have simply reduced the original problem to the analysis of the transport equations (16,17), which are complicated stochastic equations containing, however, the simplifications that come from the geometrical acoustics approximation in the locally layered medium. In particular, when $S^\pm$ satisfy the eikonal equation (13) then the $O(\frac{1}{\epsilon})$ random terms on the right side of the transport equations (16,17) have zero mean.

2.1 Brief review of results for layered random media

[illegible] matched case, where the acoustic properties on the two sides of the interface $z = 0$ are the same.

The first step in the analysis of the transport equations (23,24), which are ordinary differential equations with random coefficients, is to introduce the reflection coefficient $\Gamma(z) = \Gamma(z, \omega, \kappa)$ by

$$\Gamma(z) = \frac{A(z)}{B(z)} \tag{25}$$

and get the Riccati equation that it satisfies:

$$\frac{d\Gamma}{dz} = \frac{-i\omega n}{\epsilon}\left\{e^{-2i\omega\tau} - 2\Gamma - e^{2i\omega\tau}\Gamma^2\right\} - \text{negl. terms} \tag{26}$$

for $-L < z < 0$ with Γ given at $z = -L$, for example $\Gamma = 0$ if the media are matched at the interface $z = -L$. It is easy to see, in the matched case, that the reflected pressure at the surface $z = 0$ due the incident pulse emanating from $(0, 0, z_s)$ is given by

$$p_{\text{refl}}(t, \mathbf{x}, 0) = \frac{-1}{2(2\pi)^{3/2}}\int\int\int \hat{f}(\omega)\omega^2 e^{-i(\kappa\cdot\mathbf{x} + c_0^{-1}(1-c_0^2\kappa^2)^{1/2}z_s - \omega t)}\cdot\Gamma(0, \omega, \kappa)d\omega d\kappa \tag{27}$$

where $c_0 = \sqrt{K_0/\rho_0}$ is the sound speed in the medium above the randomly layered slab.

The two-point correlation function for the reflected pressure at the surface is given by

$$I(t, \mathbf{x}, \tilde{t}, \tilde{\mathbf{x}}) = \lim_{\epsilon\to 0}\langle p_{\text{refl}}\left(t + \frac{\epsilon\tilde{t}}{2}, \mathbf{x} + \frac{\epsilon\tilde{\mathbf{x}}}{2}, 0\right) p_{\text{refl}}\left(t - \frac{\epsilon\tilde{t}}{2}, \mathbf{x} - \frac{\epsilon\tilde{\mathbf{x}}}{2}, 0\right)\rangle. \tag{28}$$

Note that the offsets in time t and horizontal coordinate $\mathbf{x}$ are of order ϵ. It is easy to see that for larger offsets the relected pressures are statistically independent. The correlation time and length are comparable to the pulse width, which is of order ϵ in our scaling. Inserting the integral (27) into (28) we get the following expression for the intensity where for simplicity we set the spatial offset $\tilde{\mathbf{x}}$ equal to zero.

$$I(t, \mathbf{x}, \tilde{t}, 0) = \frac{1}{2\pi}\int |\hat{f}(\omega)|^2\omega^2 e^{-i\omega\tilde{t}}\Lambda(t, \mathbf{x}, \omega)d\omega \tag{29}$$

Here Λ is the local power spectral density of the reflected pressure signal and it is given by

$$\Lambda(t, \mathbf{x}, \omega) = \frac{1}{4(2\pi)^2}\int\int d\kappa W^1(0, t, \mathbf{x}, \kappa, \omega) \tag{30}$$

where

$$W^N(z, t, \mathbf{x}, \kappa, \omega) = \lim_{\epsilon\to 0}\int\int dh d\lambda\langle\Gamma^N(z, \omega + \frac{\epsilon h}{2}, \kappa + \frac{\epsilon\lambda}{2})\bar{\Gamma}^N(z, \omega - \frac{\epsilon h}{2}, \kappa - \frac{\epsilon\lambda}{2})\rangle \tag{31}$$

with $N \geq 0$ an integer.

The main result of our theory presented in [1] is the derivation of a system of transport equations for the moments of the reflection coefficient W^N. This comes from the asymptotic analysis of the stochastic equation (26) and has the form

$$\begin{aligned}\frac{\partial W^N}{\partial z} &- 2N\left\{\frac{1}{c_1(1-c_1^2\kappa^2)^{1/2}}\frac{\partial W^N}{\partial t} + \frac{c_1\kappa}{(1-c_1^2\kappa^2)^{1/2}}\cdot\nabla W^N\right\} \\ &- 2\frac{\omega^2\alpha N^2}{c_1^2(1-c_1^2\kappa^2)}\{W^{N+1} - 2W^N + W^{N-1}\} = 0\end{aligned} \tag{32}$$

where $N \geq 0$, $z < 0$, t, ω are in R^1 and x is in R^2. Equations (32) are to be solved in $-L < z < 0$ with the initial condition

$$W^N|_{z=-L} = \delta_{N0}\delta(t)\delta(\mathbf{x}) \tag{33}$$

The parameter α depends on the fluctuations ν and is given by

$$\alpha = \frac{1}{4}\int_0^\infty \langle \nu(s)\nu(0)\rangle ds \tag{34}$$

We recall that we have assumed the medium to be matched at both interfaces $z = 0$ and $z = -L$. Note that the system of transport equations (32) is an initial value problem with z, the depth coordinate, playing the role of time while real time and the horizontal coordinates behave like space variables. This is because of the invariant imbedding that is brought in by the reflection coefficient Γ and the Riccati equation (26) it satisfies. It is the use of invariant imbedding that allows us to analyze waves in randomly layered media in such detail.

Given the mean sound speed $c_1(z)$ in $-L \leq z \leq 0$ the transport equations (32) with initial condition (33) are well defined and can be solved numerically with relative ease, as was done in [1]. In the special case when the mean sound speed c_1 is constant the transport equations can be solved analytically. It is useful in this case to include in the formula for the local power spectral density the effect of dissipation in the medium when modelled by the term σu on the left side of the momentum equation (1). We assume that the medium is matched, as noted above, that the source is located at the interface so that $z_s = 0$ and that the directivity vector $\mathbf{e} = (0, 0, 1)$ is vertical. With $r = |\mathbf{x}|$ we then have

$$\Lambda(t, r, \omega) = \frac{e^{-\sigma_1 t/\rho_1}}{4(2\pi)^2 c_1 (c_1 t)^2} \frac{\frac{\alpha\omega^2}{c_1^2(1-(r/c_1 t)^2)^{1/2}}}{\left[1 + \frac{\alpha\omega^2}{c_1^2(1-(r/c_1 t)^2)^{1/2}} c_1 t\right]^2} \tag{35}$$

This result (and the more general ones in [1]) is quite interesting because it shows explicitly the effect of multiple scattering on reflected signals: the slowly decaying coda of the signal because of the multiple scattering as well as the exponential attenuation due to real dissipative effects. Aki has long been interested in the quantitative analysis of codas [5] as are Richards and Menke [6] whose work stimulated our own efforts in this area.

2.2 Nearly plane locally layered random media

We assume in this case that the mean compressibility given by (4) has in the region $-L < z < 0$ the form

$$K_1^{-1}(x, y, z) = K_{11}^{-1}(z) + \epsilon K_{12}^{-1}(x, y, z) \tag{36}$$

so we are dealing with a small perturbation of a plane layer medium. We solve the eikonal equation (13) by expanding $S^\pm$ in the form $S^\pm = S_0^\pm(z; \kappa) + \epsilon S_1^\pm(x, y, z; \kappa) + \cdots$ where $S_0^\pm$ are the plane layer S functions, given by (15) with $c_1(z)$ replaced by $c_{11}(z) = \sqrt{\rho_1^{-1} K_{11}(z)}$, and $S_1^\pm$ are solutions of

$$\kappa \cdot \nabla_H S_1^\pm + \frac{1}{c_{11}}\sqrt{1 - c_{11}^2\kappa^2}\frac{\partial S_1^\pm}{\partial z} = \frac{1}{c_{12}^2}\ , \text{with}\ \ c_{12}(x, y, z) = \sqrt{\rho_1^{-1} K_{12}(x, y, z)} \tag{37}$$

Here $\nabla_H = (\frac{\partial}{\partial x}, \frac{\partial}{\partial y})$ and (37) can be solved readily by horizontal Fourier transforms. The stochastic transport equations (16,17) reduce to the plane layer transport equations (23,24) with c_1 replaced with c_{11}. The only difference comes in the travel time τ in these equations. The $O(\epsilon)$ correction to τ, given by (20) with $S^\pm$ expanded as above, is important and introduces dependence on the

[illegible] coordinates $x = (x, y, z)$ [illegible] ordinary differential equations with [illegible] coefficients [illegible] the plane layer case obtained in the previous section called [illegible] and [illegible] analogous to the W equations (32) except that A [illegible] and now [illegible] which is proportional to H with the coefficient depending on the medium [illegible] through κ_1^{-1}. The W equations have now a term with x dependent coefficients and [illegible]

2.3 General locally layered random media

In the general case where the mean compressibility κ_1^{-1} depends in a nontrivial way on the coordinates (x, y, z) we have to solve the full eikonal equations (13) and the stochastic transport equations (16.17) do not simplify to ordinary differential equations, so we cannot use global reflection coeffients (25) as in the plane layer case. We introduce the **local** reflection coefficients $\Gamma(z, x, y, x', y'; \omega, \kappa)$ by

$$A(x, y, z; \omega, \kappa) = \int\int \Gamma(z, x, y, x', y'; \omega, \kappa) B(x', y', z; \omega, \kappa) dx' dy' \qquad (38)$$

and using (16.17) we get a **distributed** Riccati equation, analogous to (26).

$$\Gamma_z + D_-\Gamma - \Gamma D'_- - \gamma_-\Gamma - \Gamma\gamma'_- - \frac{i\omega}{\epsilon}(n\Gamma - \Gamma n') + \frac{i\omega}{\epsilon} n\delta(x - x')e^{-2i\omega z/\epsilon} = 0 \qquad (39)$$

up to negligible terms as ϵ tends to zero. Here we have used the notation $D_\pm = \alpha^x\partial_x + \beta^x\partial_y$, prime denotes action or evaluation on the variables (x', y') and we have put the primed operators on the right to emphasize that they act on the second set of horizontal variables in $\Gamma(z, x, y, x', y'; \omega, \kappa)$. The key observation regarding (39) is that it is a **linear**, stochastic Riccati equation, in contrast to the plane layer case (26) where the term Γ^2 is quite important. This means that (39) can be analyzed in considerable detail [2] despite the fact that it is a stochastic **partial** differential equation.

3 Conclusions and recommendations

Our results have a simple physical interpretation. In the plane layer or nearly plane layer case we get very strong reflection from multiple scattering, and slowly decaying wave codas as can be seen from (35). In the locally layered case multiple scattering is distributed along the layers and is hence weaker. The increased complexity of the problem, which makes analysis look hopeless at first, has in it the important simplification of leading to a **linear** Riccati equation (39). Details are in [2].

4 References

[1] M. Asch, W. Kohler, G. Papanicolaou, M. Postel and B. White, Frequency content of randomly scattered signals, SIAM Review, 33, 1991, 519-625

[2] W. Kohler, G. Papanicolaou and B. White, Pulse reflection from locally layered random media, SIAM J. Appl. Math, submitted 1993

[3] W. Kohler, G. Papanicolaou and B. White, Mode conversion and localization for elastic waves in randomly layered media, SIAM J. Appl. Math, submitted 1993.

[4] R. Burridge, G. Papanicolaou, P. Sheng and B. White, Probing a random medium with a pulse, SIAM J. Appl. Math, 49, 1989, 582-607

[5] K. Aki and B. Chouet, Origin of coda waves: Source, attenuation and scattering effects, J. Geophysical Res., 80, 1975, 3322-3342.

[6] P. Richards and W. Menke, The apparent attenuation of a scattering medium, Bull. Seismol. Soc. Amer., 73, 1983, 1005-1021.

CONTINUOUS SEISMIC THRESHOLD MONITORING

Tormod Kværna and Frode Ringdal
NORSAR, P.O. Box 51, N-2007 Kjeller, Norway

Contract No. F08650-93-C-0002

Objective:

The project objective is to develop and implement a prototype seismic analysis system based on the continuous seismic threshold monitoring method (Ringdal and Kværna, 1989, 1992). Using data from any type of seismic stations (single-component, three-component or arrays), the method provides, at a given confidence level, a continuous assessment of the upper magnitude limit of possible seismic events that might have occurred in a predefined target area. The prototype system will be capable of conducting continuous processing of real-time data from the six regional arrays in northern Europe, and it will focus on monitoring northern Europe and western Russia, including Novaya Zemlya. The system will be adaptable to extension to other areas of special interest and to inclusion of data from other seismic stations, both on-line and off-line.

Research accomplished:

The NORSAR staff has during the last four-five years conducted extensive research on the development and application of the Continuous Seismic Threshold Monitoring method (CSTM), and two different approaches have been developed:

Site-specific threshold monitoring:

By 'focusing' a seismic network on a specific target site, continuous threshold monitoring of that site is achieved. We optimize the monitoring capability by tuning the frequency filters and array beams to known characteristics from previously recorded events at the site. We define the *threshold trace* for the network as the continuous time trace of computed upper magnitude limits of seismic events in the target area at a 90 per cent confidence level.

For example, we have conducted several monitoring experiments of the northern Novaya Zemlya nuclear test site, using data from the Fennoscandian regional array network (NORESS, ARCESS, FINESA). As illustrated in Fig. 1, these three arrays are all within regional distances from the test site. Fig. 2 shows results of the monitoring of October 24, 1990, which was the day of the most recent nuclear explosion at the northern Novaya Zemlya test site. The upper three traces of the figure represent the *threshold traces* obtained from the three individual arrays, whereas the bottom trace illustrates the combined network threshold. Typically, the individual array traces have a number of significant peaks for each 24 hr period, due to interfering events (local or teleseismic). On the network trace, the number and sizes of these peaks are greatly reduced, because an interfering event will usually not provide matching signals at all stations. On the one-day figure, we have included comments in the figure caption explaining the presence of the most significant peaks on the network trace. The previously mentioned nuclear explosion (m_b = 5.7) on Novaya Zemlya naturally stands out on the plot. While the peak value of the network trace does not represent the actual magnitude of the event, it is in fact close (5.64).

As a general comment to Fig. 2, we note that such plots enable the analyst to obtain an instant assessment of the actual threshold level of the monitoring network. The peaks on the network traces may be quickly correlated with a detection bulletin, in order to decide whether they originate from interfering events or from events in the target region. At NORSAR, such detection information is currently provided by the Intelligent Monitoring System (IMS) (Bache *et al.* 1993).

After 1 October 1992 a moratorium on nuclear testing has been in effect for the US, UK, Russia and France. On this background, we have applied the CSTM technique to the northern Novaya Zemlya test site for a full six-month period (1 October - 31 March 1993), using the NORESS, ARCESS and FINESA regional arrays. Starting 1 December 1992, we have compiled daily statistics of all peaks on the network threshold trace exceeding $m_b = 2.75$, and associated these peaks to regional or teleseismic events whenever possible. In addition, we have analyzed smaller peaks (below $m_b = 2.75$) that can possibly be associated with Novaya Zemlya epicenters.

Fig. 3 shows a histogram of the number of peaks exceeding given magnitude thresholds. During the entire four-month period, there were only 40 peaks exceeding $m_b = 3.0$. Each of these peaks could be unambiguously associated with either a regional or teleseismic event. Consequently, at the specified confidence level, we can state that no seismic event of $m_b > 3.0$ occurred at the test site during this four-month period.

At 09:29 GMT on 31 December 1992, a peak in the network threshold trace, see Fig. 4, occurred that corresponded to an event located slightly to the north of the Novaya Zemlya test site. This event was located by the IMS, and has been extensively studied by various research groups (e.g., Carter et al, 1993). The event magnitude was by Carter et al (1993) estimated at local magnitude 2.5. The corresponding upper magnitude limit estimated by the CSTM method was 2.6, see Fig. 4. In fact, the event magnitude (2.5) was below our target threshold, but the peak was still easily identified on the threshold trace.

Regional threshold monitoring:

This involves conducting site-specific monitoring of a dense grid of geographical aiming points (Fig. 5) and requires the development of generic phase attenuation relationships for covering an extended geographical region. Using data from the Fennoscandian regional array network, we have demonstrated that the network thresholds in Fennoscandia and adjacent regions show strong regional dependence (Ringdal and Kværna, 1992). As shown in Fig. 6, the thresholds are below $m_b = 0.5$ close to each array (<300 km distance) and range from $m_b = 2.0$ to 2.5 in parts of the Norwegian Sea and Barents Sea. The thresholds also vary significantly under different background noise conditions, and an increase of about 1.0 m_b units is typically observed during a large teleseismic earthquake (Ringdal and Kværna, 1992). The regional threshold maps are in some ways similar to the standard network capability maps traditionally used in seismic monitoring studies (Networth, Snap/D, etc.). Thus, Fig. 6 could be seen as a capability map. However there are some fundamental differences.

- Standard capability maps use, as a basis, statistical models of signal and noise characteristics; in particular a signal variance and a noise variance is assumed to compensate for statistical fluctuations. In contrast, the regional CSTM maps give 'snapshots' of the capability as actually observed at a given point in time.
- With standard maps, no allowance is made for unusual conditions, such as, for example, the occurrence of a large earthquake or an aftershock sequence which may cause the network capability to deteriorate for hours. With the CSTM approach, the actual variation in detection capability is immediately apparent.

- Standard capability maps require assumptions, e.g. with regard to 'SNR threshold required for detection' and 'minimum number of stations required to locate'. The CSTM maps require no such assumptions since they are not tied to 'detecting and locating' seismic events, but rather describe the observed 'seismic field' at any point in time.

Such regional threshold maps have advantages over standard network capability maps in being more accurate during time intervals when interfering seismic events occur. They can also more easily reflect special conditions such as particularly favorable source-station propagation paths, and have the advantage of not being tied to specific event detection criteria.

Conclusions and recommendations:

The Continuous Seismic Threshold Monitoring has been demonstrated to provide a simple and very effective tool in day-to-day monitoring of a site of particular interest, and thereby offers a valuable supplement to the Intelligent Monitoring System (IMS) in nuclear test ban monitoring.

The future work will concentrate on developing and implementing a computer system that facilitates CSTM analysis, both site-specific and regional using map displays.The system will be closely integrated with the IMS, and the peaks on the threshold traces will we analyzed with an automatic event explanation facility based on the IMS bulletin. In cases when the CSTM results suggest that further off-line analysis should be invoked, the Analyst Review Station of the IMS will be used. Concerning regional threshold displays, we will emphasize the development of an 'animation/ scrolling' display showing how the threshold situation fluctuates with time.

References:

Bache, T., S.R. Bratt, H.J. Swanger, G.W. Beall and F.K. Dashiell (1993): Knowledge-based interpretation of seismic data in the Intelligent Monitoring System, Bull. Seism. Soc. Am., in press.

Carter, J., H. Israelsson and V. Ryaboy (1993): Location of the December 31, 1992 Novaya Zemlya Event, Center for Seismic Studies, 12 Apr 93.

Ringdal, F. and T. Kværna (1989): A multi-channel processing approach to real time network detection, phase association and threshold monitoring, Bull. Seism. Soc. Am., 79,1927-1940.

Ringdal, F. and T. Kværna (1992): Continuous seismic threshold monitoring, Geophys. J. Int., 111, 505-514.

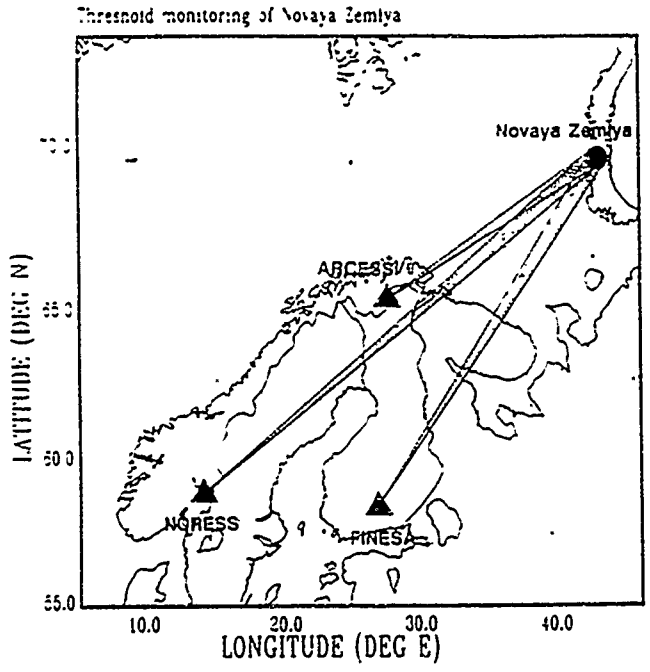

Fig. 1. Location of the target area (the northern Novaya Zemlya test site) for the threshold monitoring experiment. The locations of the three arrays NORESS (Δ = 2280 km), ARCESS (Δ = 1100 km) and FINESA (Δ = 1780 km) are indicated.

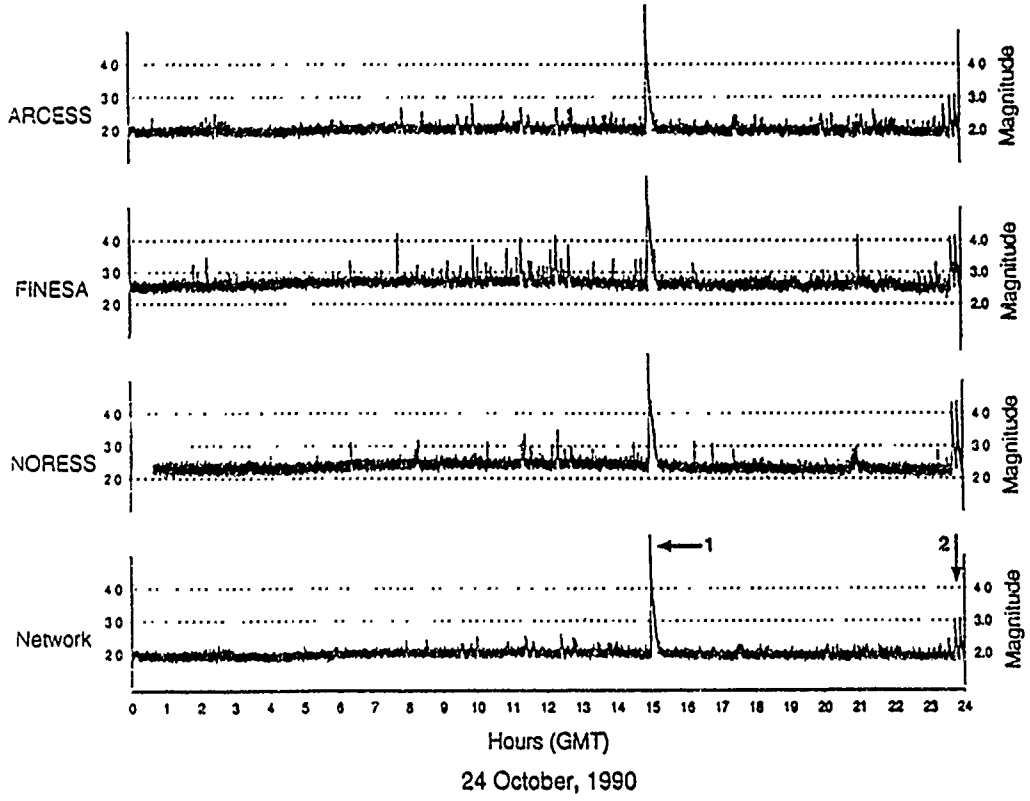

Fig. 2. Threshold monitoring of the Novaya Zemlya test site for day 297 (1990 October 24). The top three traces represent thresholds (upper 90 per cent magnitude limits) obtained from each of the three arrays (ARCESS, FINESA, NORESS), whereas the bottom trace shows the combined network thresholds. NOTES: (1) an underground nuclear explosion (m_b = 5.7) at Novaya Zemlya at 14:58:00 GMT. The peak of the network trace is 5.64. (2) Two teleseismic earthquakes from N. Xinjang province, China (m_b = 5.2 and 5.4). The P-wave and coda from each of these earthquakes cause the network threshold to increase to about m_b = 3.0 for the target region.

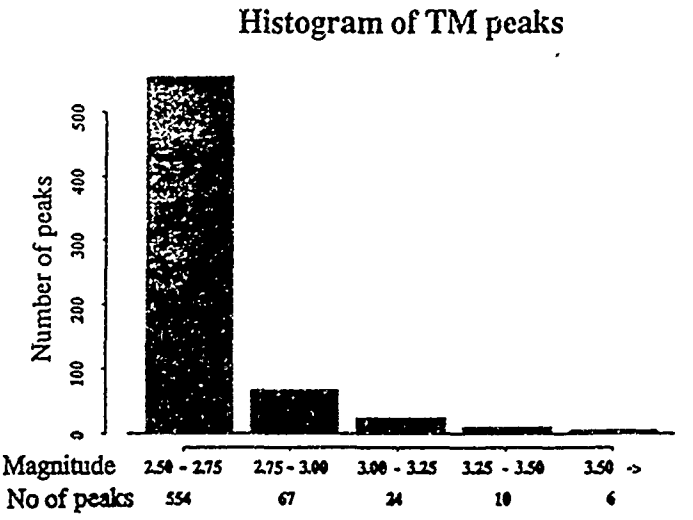

Fig. 3. Histogram showing the distribution of peaks on the network threshold trace for the four-month monitoring experiment.

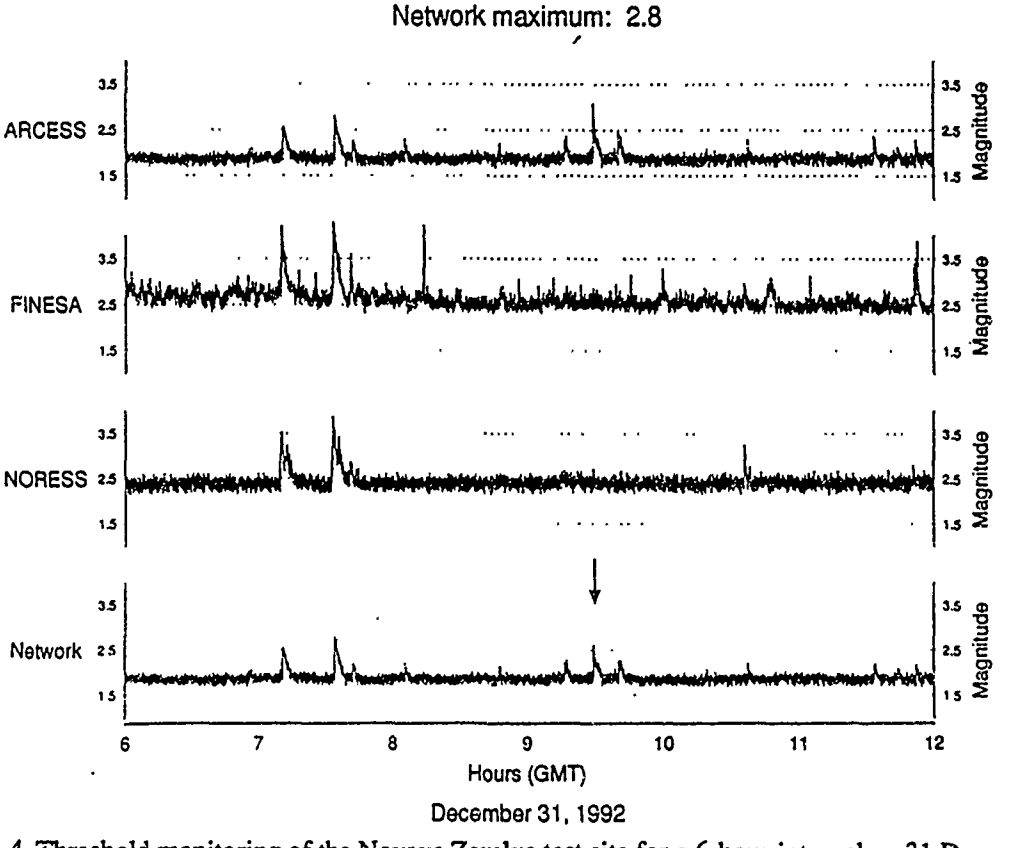

Fig. 4. Threshold monitoring of the Novaya Zemlya test site for a 6-hour interval on 31 December 1992. The threshold traces are similar to those of Fig. 2. The peak in the network threshold trace corresponding to the Novaya Zemlya event at 09:29 GMT ($M_L = 2.5$) is indicated by the arrow.

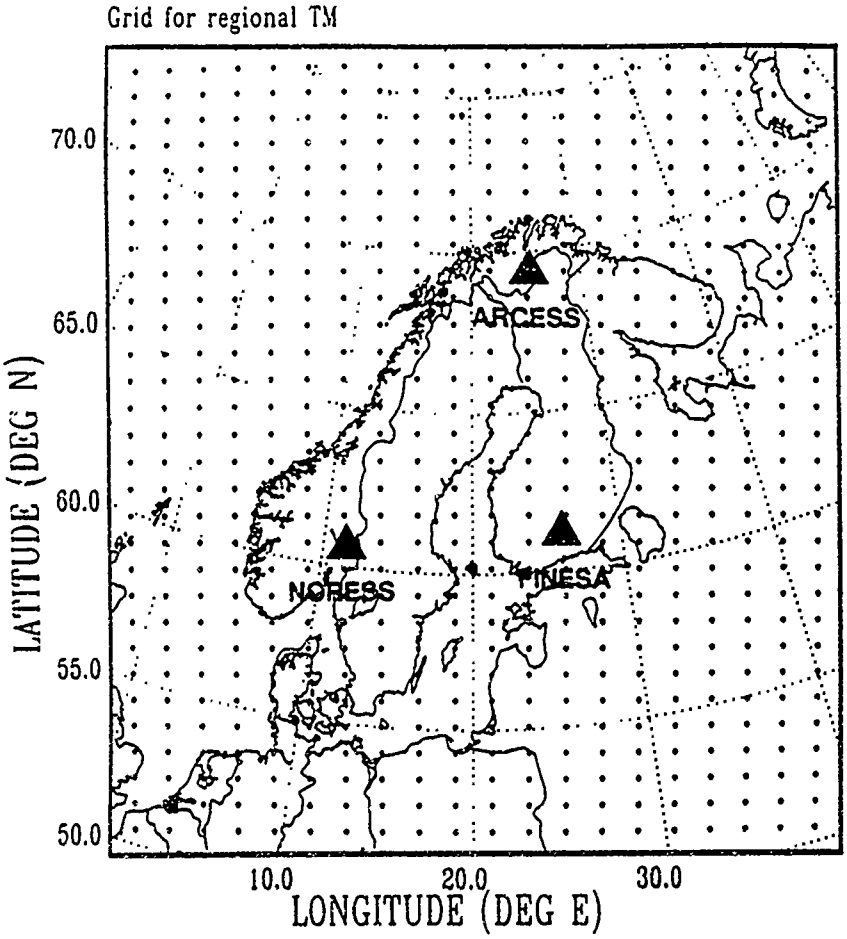

Fig. 5. Beam grid used for calculating regional thresholds with the array network NORESS, ARCESS and FINESA. The location of the three arrays is shown on the map.

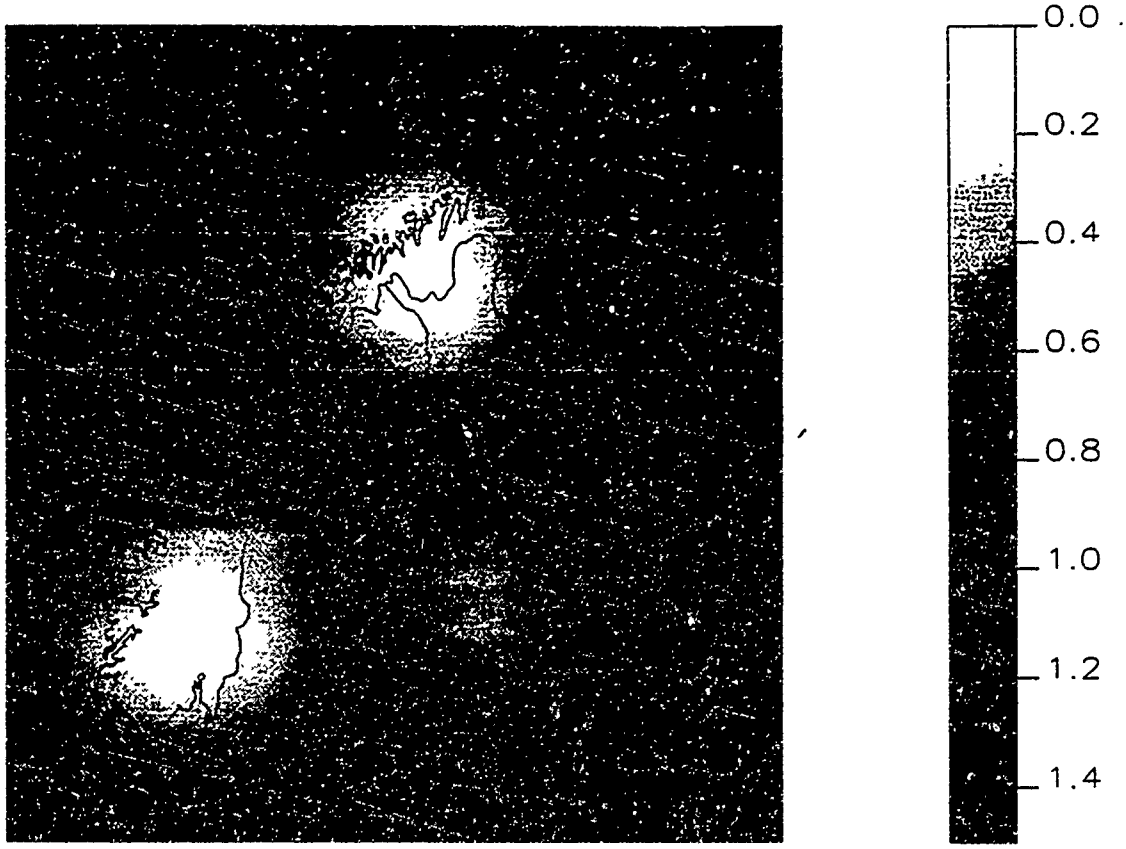

Fig. 6. Example of regional threshold display of network threshold levels at a typical time period with no seismic activity. The thresholds are below $m_b = 0.5$ close to each array (< 300 km) and exceed 2.0 in parts of the Norwegian Sea and Barents Sea.

AN INTERNATIONAL DATA EXCHANGE SYSTEM OF OPEN STATIONS USING TWO STANDARD INTERNET TOOLS: GOPHER PLUS AND NFS REMOTE MOUNT

James Edward Lawson Jr.

Oklahoma Geological Survey Observatory

Contract: F91628-92-K-0028

OBJECTIVES

Using existing software and existing networks, design a communications infrastructure that will meet all or most of the requirements of "Technical Concepts for an International Data Exchange System, United States Delegation GSE/US/84, February 1993".

RESEARCH ACCOMPLISHED

The Tulsa GSE Open Station continuously records 19 seismic and magnetic data channels at 60, 40, 10, or one sample(s) per second, with a total of 484 samples per second. One day's data is 170 MB, slightly over the amount specified for an array in GSE/US/84.

For testing data transfer, we assume that every alpha and beta station has a data machine (computer, host), and a communications machine. At Tulsa these were a Sparc 1+ (64 MB RAM, 5.5 GB disk), and an SLC (16 MB RAM, one GB disk). Other machines on the LAN were not involved. The data communications machine at a station runs gopher plus, and probably handles mail and a real time data display as well.

For six months SMU and Tulsa have remote mounted each other's disk waveform files, about two GB in each case, with Sun NFS (Network File System). NFS is an easy, transparent method of working with files from another site. NFS files must be mounted directly from the data machine. Although you can export a soft link, you can't export a file system which is itself remote. The waveform file tree may be exported in a read only mode to only machines listed in the exports file.

NFS is transparent, but any data (or directories) which are actually used at a remote site must be physically transmitted. Any data actually used by the IDC should be copied there, to avoid retransmission in processes such as beamforming, which would repeatedly use the same samples. Data not actually processed would not be copied and archived at the IDC. The only complete archiving would be at the alpha station, unless the station was considered unreliable as a archive of its own data.

Figure 1 shows the remote mount configuration. In many locations, the lack of internet connections (internet is present on all seven continents) would be a problem. However, existing internet providers could probably extend to these sites cheaper than dedicated links could be established. Low bandwidth on some internet connections could be addressed by equipment and line upgrades.

During the day, when internet use was fairly high, we are able to copy a four hour, 40 samples per second, SMU waveform file from the NFS mount to a local file at 8.4xRT (8.4 times real time, meaning, in this case, four hours divided by 8.4). That speed is adequate for alpha station transfers. However, examining a detailed traceroute indicated most of the delay was in the slow leased line from Leonard (site of the Tulsa Open Station) to a node in the city of Tulsa. If this one line was upgraded to T1, the copy speed would be 31xRT. At least 20xRT could be expected for any station with a T1 connect, during daytime heavy traffic. Nighttime speeds could exceed 60xRT. Routes crossing from day to night would be more complicated.

We make the assumption that the IDC may possibly be established at the CSS. Paths from the CSS to far places (we have looked in particular at South Africa, Western Australia, Slovokia, Singapore) will probably approach one-half the SMU to Tulsa Open Station speeds. Paths to South America will be

significantly slower without upgrades to the long slow land lines within the continent.

Without giving specific numbers, I strongly recommend that the CSS itself upgrade from T1/DS1 to T3/DS3.

The Russian Federation is the largest nearly blank area in the internet world. Even there, I believe that existing European and Russian net providers can extend the internet faster and cheaper than dedicated links can be added.

Beta station data is intended to be transmitted only in segments as needed. For efficiency, I suggest that this data not be transmitted through NDCs to the IDC, but instead be pulled directly from the stations by the IDC with the internet gopher plus. Gopher plus is an internet wide information system. It is not related to the IRIS DMC gopher.

Gopher plus presents a file tree as a hierarchy of menus (figure 2). When a file is selected, it is automaticly transmitted in the correct mode (binary or ascii). A gopher plus server can be run secure, with only listed hosts allowed to pull files. Gopher plus can also be run on the communications machine at each site. It could be used for transmission between any combination of alpha and beta stations, NDCs, and the IDC.

Gopher plus speed is adequate. We can pull hour channel files from the Tulsa Open Station to the CSS (their Xgopher client) 9xRT during the day. Assuming a T1 upgrade to our leased line, we could go 32xRT (40 sample per second channels). Upgrading the CSS to T3/DS3, and switching from their Xgopher client to a curses version of gopher plus client, would give additional small increases. The T3/DS3 upgrade at CSS will only become important when several alpha stations are NFS mounted there.

Gopher plus is nearly in the public domain. The original developers at the University of Minnesota state that any gopher plus server which makes data available without charge over the internet is considered licensed. Gopher plus servers and clients are available for Unix, VMS, PCs, Macs, and other platforms. A server and client may be obtained by ftp from Minnesota, or several other sites. Client and server can be built and operating in two to 16 hours depending on the experience of the systems programmer with gopher plus and with her/his communications platform. The IDC could use internet to install the package on a communications machine at another site, if the site would allow the IDC systems person a temporary root password.

The use of gopher plus by the IDC, NDCs, and stations to pull files from a station assumes no station participation except running a gopher plus server on the communications machine. The waveform files are remote mounted from the data machine into the gopher data area on the communications machine. The gopher plus server will optionally log the date, time, host name, and directory or file read in every transaction. A secure mode gopher will log the same data for every refused connection.

At the Tulsa Open Station, we run both a secure gopher plus server and an open gopher plus server. The open gopher has all our waveforms and help files, as well as a few text files (Oklahoma earthquake catalog, nuclear explosion catalog, etc). Gopher plus will represent a mail spool as a directory of files. We use this capability to keep about the last thirty days of GERESS bulletins on gopher. We also NFS mount SMUs files in the gopher data area. Gopher is a viable method to distribute remote files, but it is slow and inefficient to bring NFS data in to send out by gopher on the same physical channel.

If gopher plus waveform files are pulled without resegmenting or other action at a beta or alpha station, the files have to be in manageable divisions. At the Tulsa Open Station, the files are logically divided into channel hours (refer to fig 2) by the Geotech GSE software. Although this software uses an Oracle RDBMS on the data machine, Oracle is not involved in NFS mounts or gopher plus transfers. The hourly waveform files are a convenient size for gopher plus. In CSS3.0 format an ascii file called dot wfdisc is required to use the waveform or dot w (filename.w) files. The dot wfdisc files are in station days, and must be edited to remove all lines except the line(s) for the .w file(s) on hand. This is not difficult to do with simple editors (eg Unix vi), but it is a function which could be scripted. Gopher plus also uses the .w extensions as a clue to transfer in a binary mode (disk to disk, no display; some older gopher clients will insist on displaying screenfulls of nonsense as a binary transfer occurs). Gopher plus also strips the .w filename extension. Dot w may be easily restored in the "Save in file:" box (last menu in figure 2), but this could also be scripted. The gopher plus standard allows for user definition of new data objects. Perhaps a seismic waveform gopher object should be designed.

Gopher plus is so friendly and rapid that we use a gopher client to examine on-site files, more easily

than we can use Unix commands like ls, pwd, and cd. It would be difficult to custom design a seismic data transfer system better than the existing gopher plus.

CONCLUSIONS

NFS, gopher, and internet should be used to establish the system outlined in GSE/US/84 (with changes discussed above, particularly not physically routing all data through NDCs. Even considering some new internet connections and upgrades, such a network could be established quickly and cheaply.

After the network was operating, a few alpha station NFS links might be replaced by dedicated circuits. I am convinced that gopher plus is nearly ideal for beta station transfers, and that there would be no reason to connect beta stations by dedicated link.

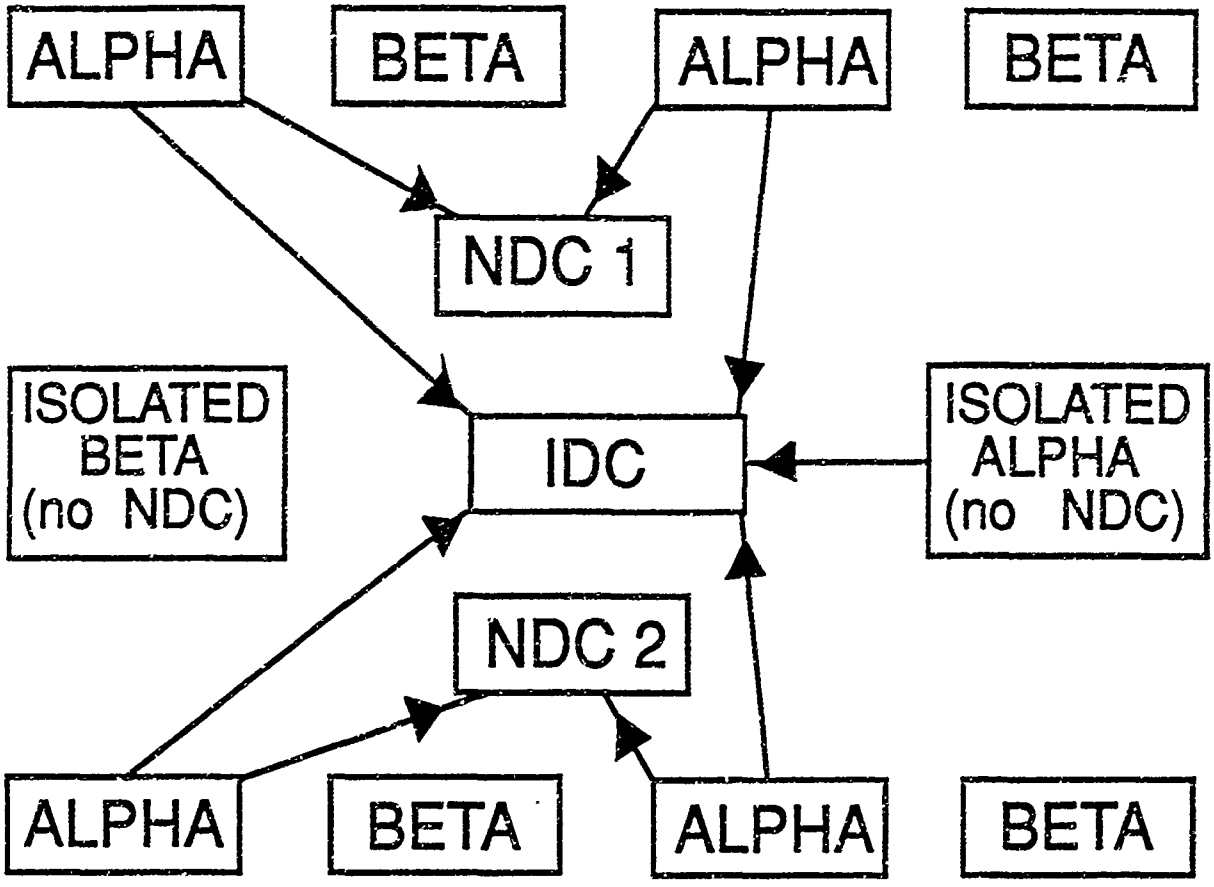

Figure 1. - International data exchange system based on NFS and Gopher plus. The solid lines indicate NFS remote mounts. Each Alpha station's waveforms are remote mounted at the IDC and at their NDC. The NDC files are not mounted at the IDC. All 13 entities shown are on Internet, and have Gopher plus clients and servers. Gopher plus will be used for any of the 13 to pull files from any of the other 13 entities. This gives 78 possible bidirectional Gopher paths which are not shown. In Gopher terms the entire system is within Gopherspace (also called Gopher meta-burrow or Gopher web). All, some, or none of the Gopher plus servers can be open - a part of the worldwide Gopherspace. Others can be secure - hidden from all but the Gopher clients in their access list.

```
                    Internet Gopher+ Information Client v1.2beta3

                    Root gopher server: wealaka.okgeosurvey1.gov

-->  1.  waveforms, last 9 days continuous waveforms + selected events/
     2.  Oklahoma Earthquake Catalog/
     3.  Oklahoma Geological Survey waveform, cal, station, and misc info/
     4.  OKGEOSURVEY Postscript Seismograms/
     5.  Catalog of known nuclear explosions *UNDER CONSTRUCTION*/
     6.  waveforms from other sites/
     7.  connect to seismic sites outside Oklahoma/
     8.  Nuclear testing treaties and related documents/
     9.  Seismic bulletins and info (not waveforms) from sites outside OK/
     10. ONENET Oklahoma State Regents Higher Education net info/
     11. Other gopher sites and veronica sites/
     12. K12/
```

```
                    Internet Gopher+ Information Client v1.2beta3

                    waveforms, last 9 days continuous waveforms + selected events

     1.  *READ*NOW* to select Logbook or dearchive.
     2.  *READ*NOW* before selecting Logbook.
     3.  *READ*NOW* before selecting dearchive.
-->  4.  Logbook: Last approximately nine days continuous waveforms/
     5.  dearchive: Packages of waveforms from selected events/
```

```
                    Internet Gopher+ Information Client v1.2beta3

                    Logbook: Last approximately nine days continuous waveforms

     1.  93194/
     2.  93195/
     3.  93196/
     4.  93197/
     5.  93198/
     6.  93199/
     7.  93200/
     8.  93201/
-->  9.  93202/
     10. 93203/
     11. 93204/
     12. 93205/
     13. 93206/
     14. 93207/
     15. 93208/
     16. 93209/
     17. 93210/
     18. 93211/
     19. 93212/
     20. 93213/
     21. 93214/
     22. 93215/
     23. NOTICE-empty-directories-with-future-dates-may-appear.
```

Figure 2. a. Top level gopher+ menu displayed on initial connection.
b. Second level gopher+ menu.
c. Third level menu; date menu.

```
                Internet Gopher+ Information Client v1.2beta3

                                    93202

     1.  LNO/
     2.  RLO/
     3.  SIO/
-->  4.  TUL/
     5.  VVO/
```

```
                Internet Gopher+ Information Client v1.2beta3

                                    TUL

    30. TUL.bn.93202.080000 <Bin>
    31. TUL.bn.93202.090000 <Bin>
    32. TUL.bn.93202.100000 <Bin>
    33. TUL.bn.93202.110000 <Bin>
    34. TUL.bn.93202.120000 <Bin>
    35. TUL.bn.93202.130000 <Bin>
    36. TUL.bn.93202.140000 <Bin>
    37. TUL.bn.93202.150000 <Bin>
    38. TUL.bz.93202.000000 <Bin>
    39. TUL.bz.93202.010000 <Bin>
+-------------------------------------------------------------------------------+
|                                                                               |
| Save in file:  TUL.bz.93202.150000                                            |
|                                                                               |
|                                        [Cancel ^G] [Accept - Enter]           |
|                                                                               |
+-------------------------------------------------------------------------------+
    47. TUL.bz.93202.090000 <Bin>
    48. TUL.bz.93202.100000 <Bin>
    49. TUL.bz.93202.110000 <Bin>
    50. TUL.bz.93202.120000 <Bin>
    51. TUL.bz.93202.130000 <Bin>
    52. TUL.bz.93202.140000 <Bin>
-->  53. TUL.bz.93202.150000 <Bin>
    54. TUL.magD.93202.000000 <Bin>
    55. TUL.magD.93202.010000 <Bin>
    56. TUL.magD.93202.020000 <Bin>
    57. TUL.magD.93202.030000 <Bin>
    58. TUL.magD.93202.040000 <Bin>

Press ? for Help, q to Quit, u to go up a menu                    Page: 2/10
```

Figure 2. c. Fourth level gopher+ menu; station menu.
d. Fifth level menu; file menu. A file has already been pulled. The dotted box allows the file name to be replaced or edited on the client.

Lg PROPAGATION IN EURASIA

Thorne Lay, Xiao-bi Xie, and Tianrun Zhang
University of California, Santa Cruz

Contract No. F29601-91-K-DB21
July 1, 1991-June 30, 1993

Objective:

This research effort was directed at improving our understanding of RMS-Lg yield-scaling for events in Eurasia. The motivation stems from the observed stability of RMS-Lg measurements as an indicator of relative source strength, even for very diverse paths and despite the presence of path-dependent yield-scaling slopes. In order to understand the variations in yield-scaling slope and the general energy partitioning in short-period regional phases we have conducted both numerical modeling and data analysis using digital seismograms from IRIS and CDSN stations and the JVE exchange seismogram data set collected from former Soviet analog stations for explosions at Semipalatinsk and Novaya Zemlya. The results of this research are presented in four papers that have been submitted for publication.

Research Accomplished:

We began this research with a numerical examination of different processes that excite Lg from underground explosions (Xie and Lay, 1993a). The objective of this work was to compare the relative efficiency of several excitation mechanisms that have been reported in the literature over the past few years. We achieved this by a uniform set of simulations, computed at near-in to regional distances using a finite-difference algorithm. This was a necessary step in the investigation of Lg scaling stability, as different excitation mechanisms may be associated with different scaling behavior. For example, variations in waveguide heterogeneity or attenuation on different paths, or variations in spall effects as a function of yield could result in frequency dependent yield-scaling behavior. We introduced a new procedure that greatly assists the interpretation of numerical regional distance synthetics, involving internal array analysis of the wavefield at depth (Figures 1, 2), and evaluation of the associated energy fluxes as a function of wave slowness and time.

For purely isotropic explosions in crustal structures with source P velocity higher than mantle S velocity, the S* non-geometric phase plays a leading role in Lg excitation. For lower source velocities, where the source P velocity is less than the mantle S velocity, the pS converted phase is the predominant source of Lg, as it becomes stronger than S*. Scattering heterogeneity can progressively convert P energy into S energy for all structures, leading to enriched Lg signals, but the most efficient way of generating Lg is through direct S wave generation at the explosion source, since a broader range of slownesses can be trapped in the waveguide. Spall and source asymmetry are the most likely processes that generate significant S wave energy near the source which can then contribute to the Lg signal.

The suites of synthetic seismograms computed in the Lg excitation study have been used to examine possible path effects that may explain the range of RMS Lg yield-scaling (Xie and Lay, 1993b). Clearly, what is required for this behavior is a sensitivity to the spectral structure of the Lg signals, allowing magnitude dependence of the RMS observations to appear for data with different bandwidth. While localized site factors for Lg may play some role, it is most likely that overall interaction of propagation and source effects is responsible for variable yield-scaling. Lg synthetics with Mueller-Murphy source functions display corner frequency shifts that lead to frequency-dependent yield-scaling coefficients. Variable attenuation and or elastic structure path effects can enhance or

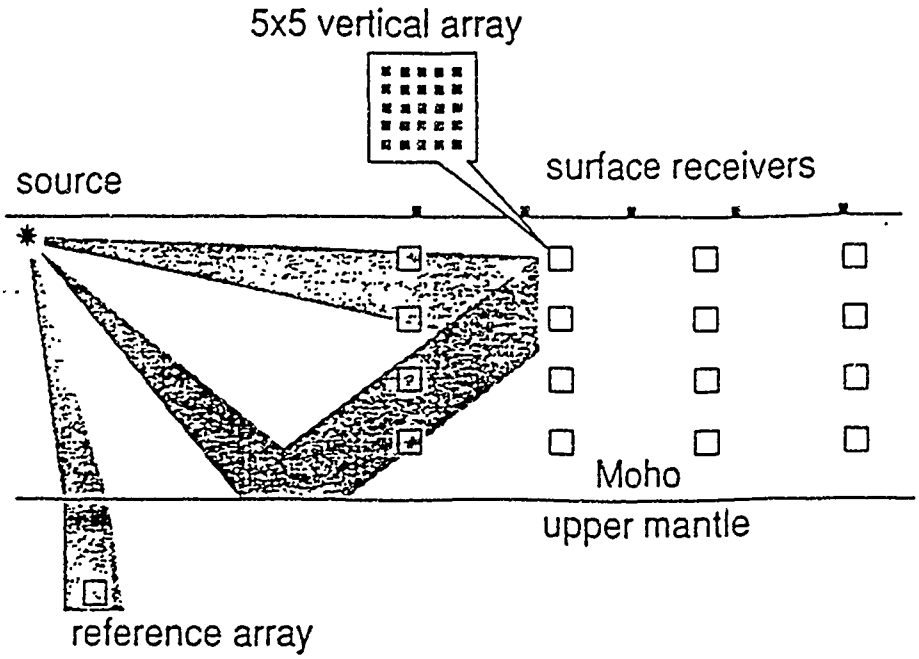

Figure 1. Cartoon showing the geometry of the finite-difference simulations. Several sets of receivers are placed on the free surface and inside the media for different purposes. The free surface receivers are used to record conventional synthetic profiles. Vertical receiver arrays, each of them composed of a 5 x 5 grid of receivers are used to monitor the energy flux inside the medium. An additional reference array is placed in the upper mantle with a source distance of 100 km and a take-off angle of 30 degrees.

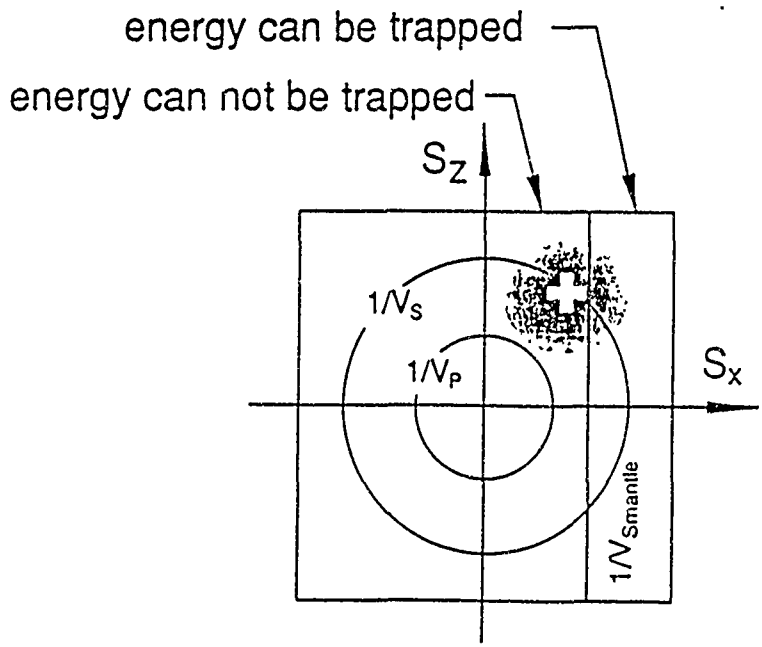

Figure 2. Example of the slowness domain display. The horizontal and vertical axes are horizontal and vertical slownesses; circles are P- and S-wave slownesses $1/V_p$ and $1/V_s$ near the receiver array, respectively; vertical line on the right side of the slowness domain is the horizontal slowness equivalent to the upper mantle S-wave velocity, $1/V_{Smantle}$.

suppress the frequency dependence. Elastic structure effects associated with differences in waveguide structure can produce mild frequency dependence, but attenuation has a stronger effect. Broadband Lg observations at larger distances tend to be more bandlimited by attenuation and thus have steeper yield-scaling slopes.

This interaction of source scaling and path attenuation is essentially the same effect as observed for m_b yield-scaling for high and low t* paths, with more strongly attenuated signals having higher m_b-yield slopes. Analysis of digital recordings of Semipalatinsk explosions at regional distances shows that more strongly attenuated Lg signals do exhibit the increase in scaling-slope, when broadband data are available. The behavior is further complicated by the instrument response characteristics, with short-period sensors yielding more variable RMS Lg yield-scaling. The path dependence can be suppressed by lowpass filtering of the signals, provided broadband data with adequate signal to noise are available. Extraction of frequency-dependent path terms by factor analysis can also objectively suppress path effects.

The Lg waveforms in the JVE exchange data set have fairly stable behavior, but the overall short-period regional waveforms do exhibit complex path and distance variations. We have performed an observational study of the behavior of Lg, Sn, and upper mantle distance P phases in relation with surface topographic properties along the corresponding paths (Zhang and Lay, 1993a). The basic objective was to seek any relationships between surface measurements and the overall waveguide characteristics that control the energy flux and frequency content of the regional phases used in small explosion discriminants and yield estimation. To our surprise, we have found that the Sn/Lg ratio (using RMS amplitude measures that encompass significant scattered wave energy) shows a strong correlation with simple path elevation properties for Semipalatinsk data (Figure 3). While this has not yet been quantitatively modeled, it appears that surface topography does indeed provide a means of characterizing the regional phase energy flux for at least some paths. It is likely that surface topography is correlated with both variable attenuation and scattering properties that partition the overall wavefield energy.

We have also conducted an analysis of the effects of propagation across continental margins on the partitioning of energy in the short-period regional wavefield (Zhang and Lay, 1993b). The data used were Eurasian recordings of nuclear tests at Novaya Zemlya, provided as part of the JVE data exchange. As shown in Figure 3, the Sn/Lg ratios for these events do not show the same sensitivity as the Semipalatinsk data to surface topography along the entire path. We examined empirically the effects of various underwater path segment characteristics on the regional signals (Figure 4), finding that maximum water depth along the path appears to be the most influential with regard to P/Lg and Sn/Lg energy partitioning. The under-water segment appears to overwhelm on-land propagation effects. This is likely to be the result of waveguide disruption associated with necking of the crust along the continental margin (Figure 5). The systematic relationship with maximum water depth again provides a means by which to reduce scatter in regional discriminant and yield estimation procedures, as well as a basis for numerical modeling to be conducted in the future.

Conclusions and Recommendations:

Lg wave propagation in Eurasia is influenced by path properties, but we have several new approaches to reducing the path influence. Variable yield-scaling for different paths appears to be largely a bandwidth controlled phenomenon. The intrinsic filtering characteristics of different paths and instrument responses interact with source spectrum scaling to cause the variable yield-scaling. Ensuring a uniform frequency content of the suite of signals by filtering is one means to reduce this problem, or one can explicitly correct for frequency dependent variations in the form of station terms. While Lg yield-scaling is relatively stable across Eurasia, there is complex partitioning of the overall short-period signal energy, which produces large variations in P/Lg and Sn/Lg amplitude ratios

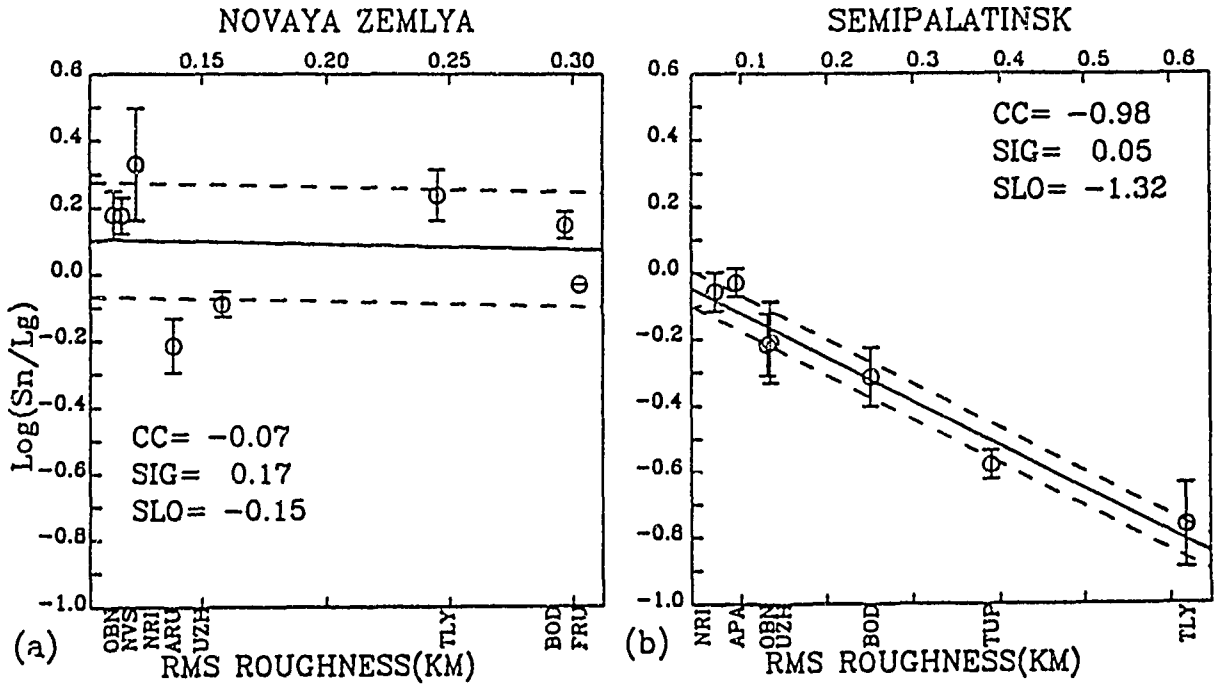

Fig. 3. Empirical relation between the RMS amplitude ratio of S_n/L_g versus along path topographic roughness (variance) for observations from the Semipalatinsk source region (right) and the Novaya Zemlya source region (left). The strong trend on the right was first reported by Zhang and Lay (1993), and indicates that irregularities in the waveguide structure influence the regional phase energy partitioning. The lack of a strong trend on the left indicates that additional factors, presumably associated with the underwater segments of the paths, dominate in the Novaya Zemlya data.

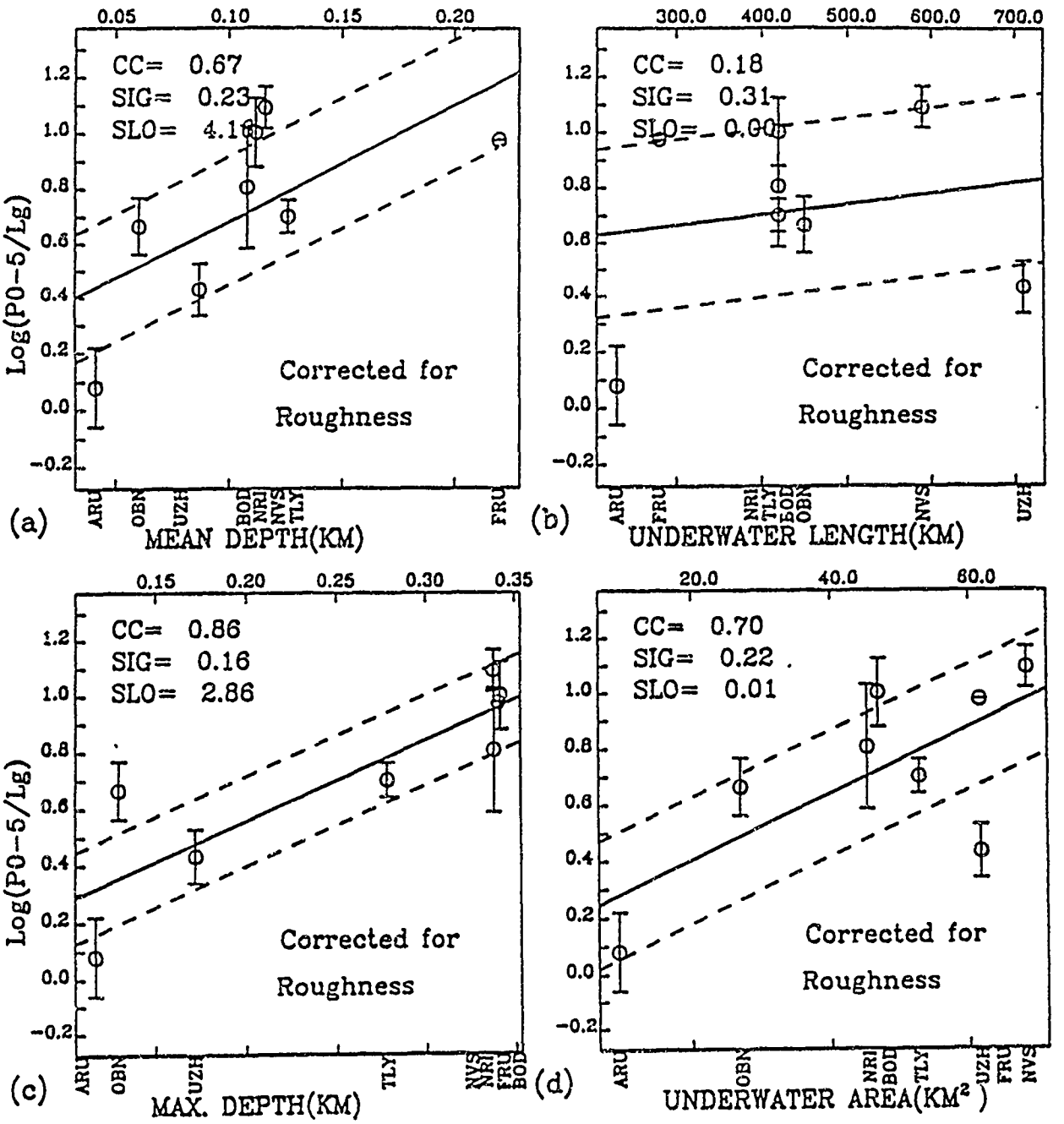

Fig. 4. Similar to Figure 12, but now the P/L_g ratios have been corrected for relative path roughness, using the continental path correlations found for Semipalatinsk data by Zhang and Lay (1993).

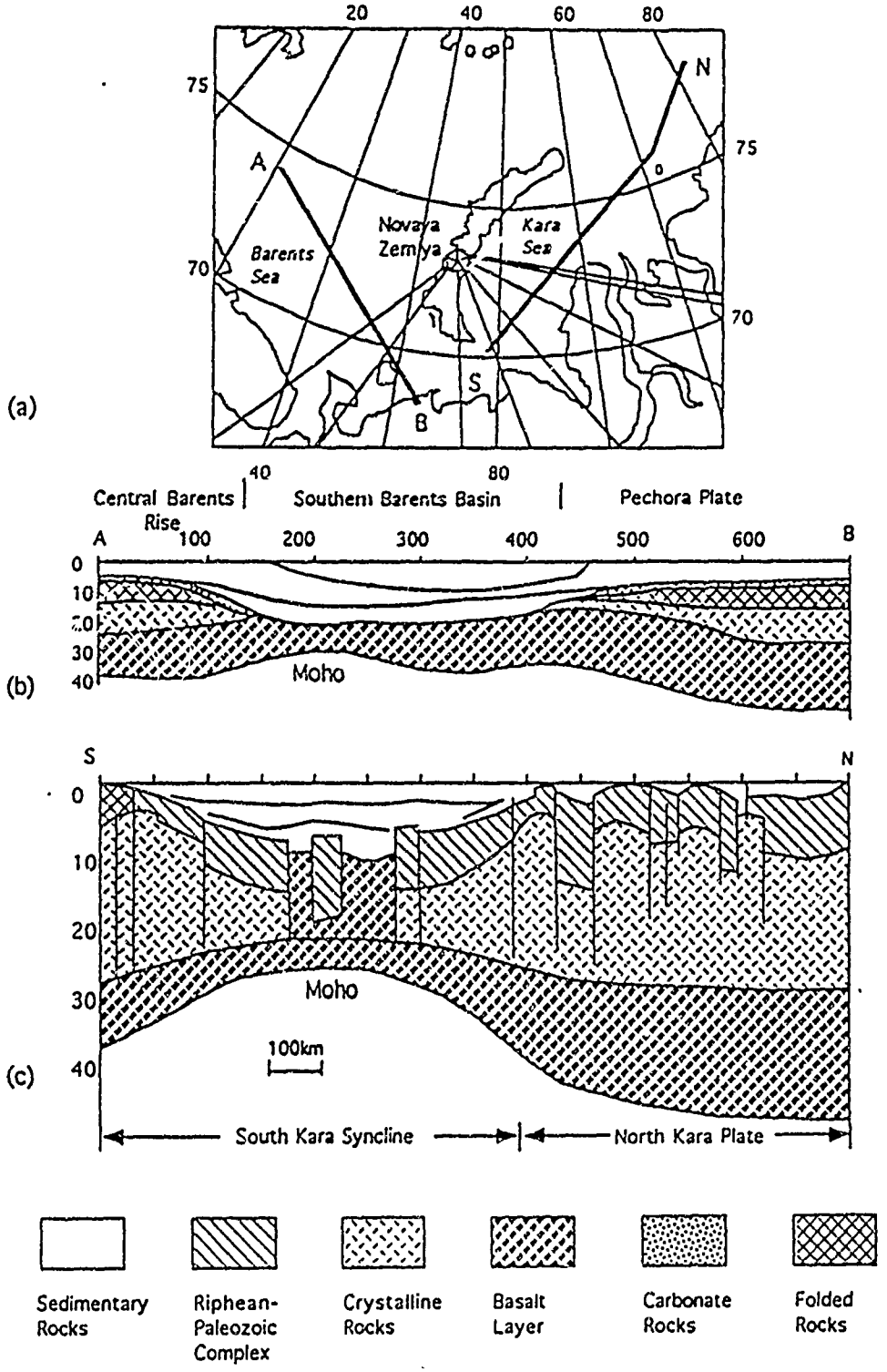

Fig. 5 (a) Map of the adjacent region of the islands of Novaya Zemlya, showing two lines of cross-section and eight paths. (b) NW-SE cross-section, labeled A-B in (a), across the southeastern part of the Barents Sea basin (after Gramberg, 1988). (c) NE-SW cross-section of the Kara Sea basin (after Bogolepov et al, 1990), labeled N-S in (a), across the North-Kara plate and South-Kara syncline.

for different paths. A preliminary study has shown that surface topography characteristics are strongly associated with Sn/Lg ratios, probably because topography reflects waveguide attenuation and scattering behavior. It may prove possible to reduce scatter in regional discriminants using surface topographic characteristics, if such relationships prove general. Similar influences on Sn/Lg ratios are found for bathymetric features, especially maximum water depth, for paths with underwater segments. Quantitative modeling of these observations may yield general procedures for significantly reducing path to path scatter in regional phase ratios used in discrimination procedures.

References

Xie, Xiao-bi., and Lay, T. (1993a). The excitation of explosion Lg: A finite-difference investigation, *Bull. Seism. Soc. Am.*, submitted.

Xie, Xiao-bi, and Lay, T. (1993b). Yield-scaling of RMS Lg Measurements, *Bull. Seism. Soc. Am.*, in preparation.

Zhang, T., and Lay, T. (1993a). Analysis of short-period regional phase path effects associated with topography in Eurasia, *Bull. Seism. Soc. Am.*, in revision.

Zhang, T., and Lay, T. (1993b). Effects of crustal structure under the Barents and Kara seas on short-period regional wave propagation for Novaya Zemlya explosions: Empirical Relations, *Bull. Seism. Soc. Am.*, submitted.

Analysis of 3D Complex Structure and Heterogeneity Effects on Formation and Propagation of Regional Phases in Eurasia

Thorne Lay and Ru-Shan Wu
University of California, Santa Cruz

Contract No. F49620-92-J-0461

Objective

This proposal is directed at development and application of a new three-dimensional wave propagation methodology in the context of improving our understanding of regional phase propagation and nuclear test monitoring in Eurasia. A new methodology, involving an Elastic Raleigh Integral-Elastic Born Scattering iterative formalism will be brought to bear on the problem of accurately synthesizing regional phases for three-dimensional earth models appropriate for the wide variety of Eurasian paths of interest. A large data set of Eurasian recordings for nuclear tests, moderate size earthquakes, and large quarry explosions is being analyzed under a parallel AFOSR-funded effort. The combined theoretical and observational effort should enhance our ability to extract quantitative information from regional phases, and to place regional discrimination and yield-estimation applications on a sound physical basis.

Research Accomplished:

I. Theory:

A breakthrough has been achieved in developing an elastic wave forward propagation theory (see Wu, 1993). Some substantial progress in programming this theory has also been made. The theory and method are the extension and combination of Wu's recent work on the Elastic-Wave Rayleigh Integral (ERI) (Wu, 1989a) and previous work on Elastic-Wave Born Scattering (EBS) (Wu and Aki 1985, Wu 1989b). The new theory extends the space-domain formulations of both ERI and EBS into wavenumber-domain formulations and combines these two into a unified procedure which can be implemented iteratively to propagate elastic waves. For different accuracy requirements, the theory offers two approximate methods. One is the more accurate formulation called "thin-slab" method, which uses the wide-angle approximation for both the scattering (interaction) and propagation processes and therefore can handle large-angle scattering problem, the other is the Elastic Complex-Screen (ECS) method, which uses the wide-angle approximation for propagation, but the small-angle approximation for scattering. The latter method (ECS) uses dual domain implementation (shuttling between the space and wavenumber domains by FFT) and is much faster than the thin-slab method. For a medium size 3D problem (128 x 128 grid in the transverse plane), the speed-up factor is more than 2 orders of magnitude.

1. Thin-slab formulas: The geometry of the formulation is schematically shown in the upper part of Fig. 1. Assume seismic waves propagate from left to right along the x-direction. The 3D heterogeneous medium is divided into thin slabs facing the propagation direction. The one-way wave propagation through the whole medium can be calculated by an iterative procedure which calculates the slab effects one by one. The total field at the right face of the thin-slab is calculated as the sum of the primary field and the scattered field from the heterogeneities within the thin-slab. the primary field is calculated by ERI, and the scattered field, by EBS. The formulation is valid for wide-angle scattering. However, the numerical operation involves matrix multiplications in the wavenumber domain. This formulation is computationally extensive, though it is still much faster than the elastic finite difference method.

2. Elastic Complex-screen method: When only small-angle scattering is considered, the scattering effect of a thin-slab can be approximately equated to that of passing through a screen. As shown in the lower part of Fig. 1, the thin-slabs are squeezed into screens. It is shown that the P-P and S-S common-mode scattering can be represented by pure phase-screens, but the P-S, S-P or S-S cross-coupling scattering must be represented by complex screens, which are not standard phase-screens. Therefore, the method is called complex-screen (or "generalized phase-screen") method.

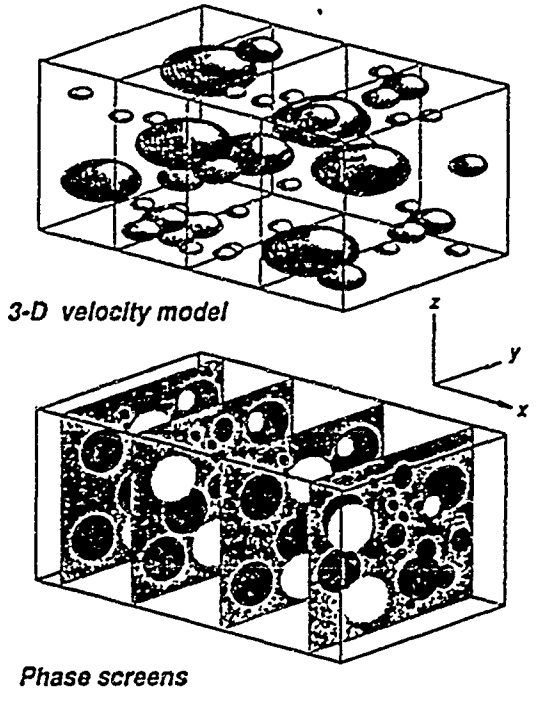

Figure 1. Schematic explanation of "thin slab" and "phase-screen" method.

II. Programming and Numerical tests:

1. 2D SH problem: In order to test the theory and study the properties of phase-screen method when applied to regional wave propagation, we first consider the simple SH problem. In this case, we need only to program the scalar phase-screen method. A 2D scalar phase-screen program has been written and tested for different cases. Here we give two examples of numerical simulation using our program with comparison to a 2D finite difference code. Fig. 2 shows the simulation for a model of multi-cylinders. A plane wave is incident from the bottom of the model propagating to the top. We see that for up to 30% velocity perturbations the results of our code are almost identical with the FD method except for the receivers near the edge which may be caused by boundary effects. For the case of 50% perturbation, the agreement of the early part of the waveform is still very good. The second example is given in Fig. 3 for the case of self-similar random medium. The agreement with the FD results is good for up to 10% velocity perturbations. These tests give us confidence in our method and programs.

2. 3D Elastic Complex-screen Method: At present we are developing the 3D ECS computer code. To test our algorithm for the complex screen method and to compare our method with the vector screen formulation of FM91 (Fisk and McCartor, 1991), we present in this paper two 3D numerical examples.

(1). The case of only P-velocity perturbation: The first example is the case in which only the Lame constant λ is perturbed. In this case, there should be no P-S conversion, as correctly predicted

a)

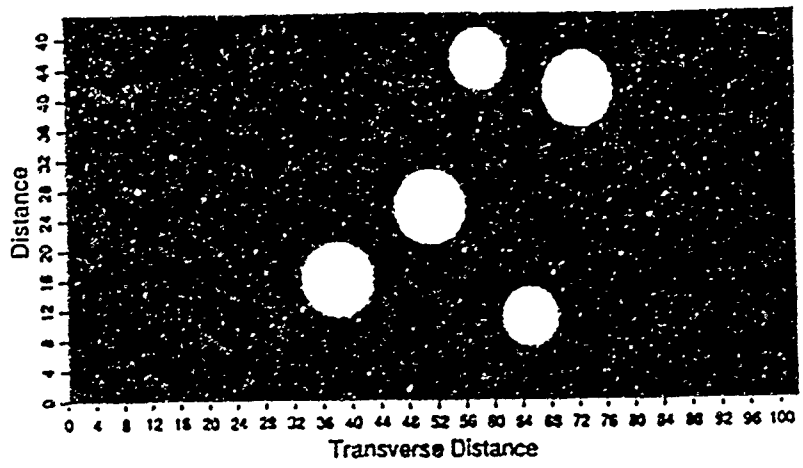

b)

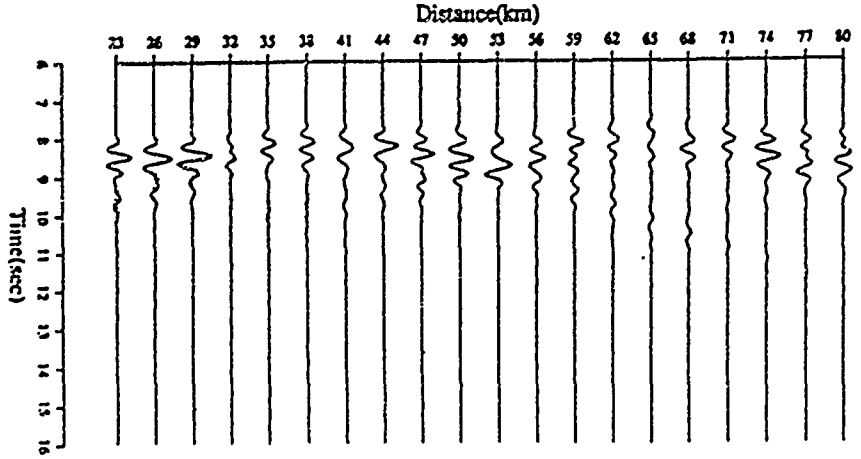

c)

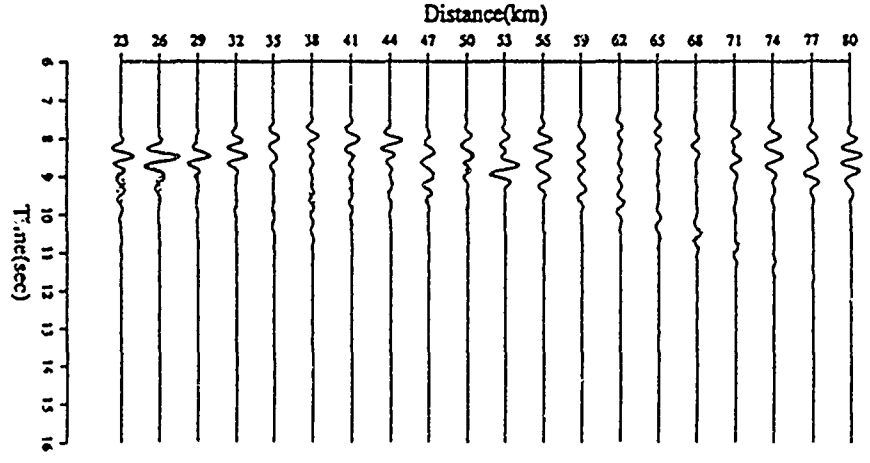

Fig. 2 Comparison of 2D phase screen method with FD method for a multi-cylinder model. a) The model, b) comparison for 30 % perturbation, c) Comparison for 50 % perturbation. —— phase screen ---- FD

a)

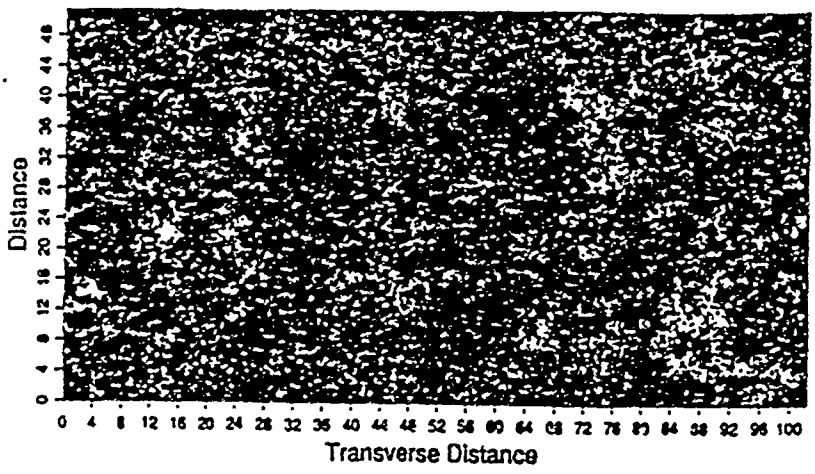

b)

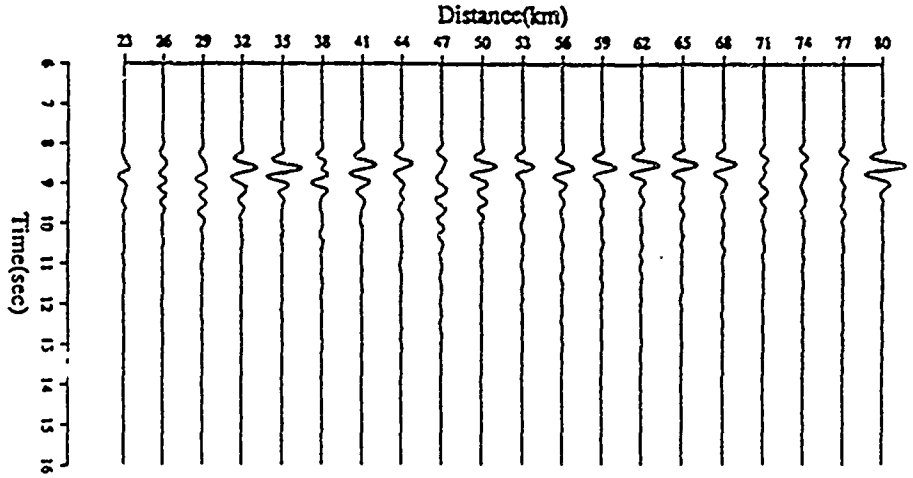

c)

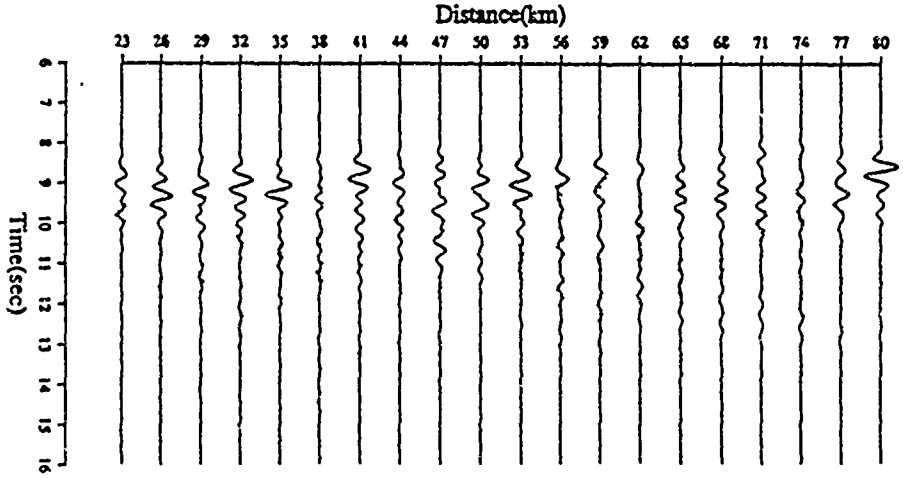

Fig.3 Comparison of 2D phase-screen method with FD method for a self-similar random media. a) The model , b) comparison for 5 % perturbation, c) Comparison for 10 % perturbation. —— phase screen ---- FD

by this theory and the scattering theory. However, from FM91, an erroneous P-S conversion would be generated. Our theory is supported by 3D finite difference calculations. The experimental geometry is shown in Fig. 4. The background medium has P wave velocity of 4.206 km/s, S wave velocity of 2.664 km/s and density of 2.14 g/cm^3. The model is a solid sphere with 10% P velocity perturbation (a fast sphere) and no S velocity or density perturbations. The radius of the sphere is 7 km. A plane P wave is incident on the sphere along the x-axis and the receiver line parallel with z-axis is located 8 km from the center of the sphere (see Fig. 4). There are 25 receivers on the receiver line with interval of 0.5 km. The source time function is of Kelly type with center frequency at 1.0 Hz. In Fig. 5 a comparison between the results of 3D FD (finite difference) and the ECS (Elastic Complex-Screen) method is shown. The 3D FD has model parameters of nx = 128, ny = 96, nz = 96, dx = dy = dz = 0.25 km, nt = 1500 and dt = 0.005 sec. The calculation is performed on the 128 node nCUBE computer at the Geophysical Center for Parallel Processing, part of the Earth Resources Laboratory of MIT by C.B. Peng. The CPU time for this example is about 29 min. Note that due to the symmetry of the problem, only one quarter of the model space is included in the FD calculation. For more general problems, no such saving of time can be achieved. The complex screen calculation is performed on the SUN SPARC station 2 computer at the Institute of Tectonics, University of California, Santa Cruz. For this example, we use a 64 x 64 grid for the y-z plane and variable step length in x-direction (0.5 km inside the sphere). The CPU time is less than 30 min on the SPARC station 2. In Fig. 5, the distortion of the incident P wave and the diffracted P waves from the top and bottom points of the sphere are seen clearly. There are no converted S waves, consistent with the scattering theory. It is seen also that the complex screen method agree well with the finite difference calculation.

(2). The case of only S-velocity perturbation: In this case, the major purpose is to check the P-S converted waves. Since for the FD method it is difficult to separate P and S waves, we compare our results with an exact solution for a solid sphere with 10% S-velocity perturbation. The experimental geometry is similar to Fig. 4, but with different parameters. The background medium has P wave velocity of 6.0 km/s, S wave velocity of 3.5 km/s and density of 2.7 g/cm^3. The radius of the sphere is 1 km. A plane P wave is incident on the sphere along the x-axis and the receiver line is parallel with the z-axis, located 2 km from the center of the sphere (see Fig. 4). There are 24 receivers on the receiver line with interval of 0.1 km. The central frequency of the source is $f_0 = 10.0Hz$. the exact solution is calculated using the eigenfunction expansion series (Korneev and Johnson 1993) by V. A. Korneev on a Sun-Solbourne computer at the Center for Computational Seismology, Lawrence Berkeley Laboratory, University of California, Berkeley. Both P and S scattered waves should be generated for a P wave incidence in this case. Here we compare only the P-S converted waves. In Fig. 6 the comparison of x- and z-components calculated by exact solution and by ECS is given. We see the two results are in very good agreement. The first S arrival is the P-S scattered wave produced by the right half of the spherical surface. The second and third arrivals are the P-S-S scattered waves produced by the left half of the spherical surface. We see that not only the direct P-S converted waves but also the converted P-S head waves can be modeled correctly by the complex screen method. In contrast, there will be no scattered waves at all from the formulation of FM91 in this special case.

Conclusions and Recommendations:

Wide-angle one-way elastic wave propagation in arbitrarily heterogeneous media is formulated using the elastic Rayleigh integral and elastic Born scattering theory in both space domain and wavenumber domain. The wavenumber domain formulation leads to a compact solution to the one-way propagation and scattering problems. It is shown that for wide-angle scattering the scattering effects of a thin slab cannot be equated to passage through a regular phase-screen, since the

interaction between the incident wave field and the slab is not local in both the space domain and the wavenumber domain. We call this more generally valid formulation the "thin-slab" formulation. After applying the small-angle approximation, the thin-slab effect degenerates to that of a elastic complex-screen. A dual-domain technique using FFT is developed for the implementation of the elastic complex screen method with much faster computation speed, by 2 to 3 orders of magnitude for a medium size 3D problems. We will continue our programming effort for the 3D elastic complex screen method. In the same time the 2D SH program will be further developed and adapted for regional wave propagation and applied to the simulation of Lg and Lg-coda generation in complex crustal structures. The results will be compared with the Eurasia data sets for nuclear explosions. We plan to solve the free surface and Moho boundary problems for the full elastic wave complex screen method in the continuation of the current project.

Fisk, M.D. and G.D. McCartor, 1991, The phase screen method for vector elastic waves, *J. Geophys. Res., 96,* 5985-6010.

Fisk, M.D., Charrette, E.E. and G.D. McCartor, 1992, A comparison of phase screen and finite difference calculations for elastic waves in random media, *J. Geophys. Res., 97,* 12409-12423.

Wu R.S., 1989a, Representation integrals for elastic wave propagation containing either the displacement term or the stress term alone, *Phys. Rev. Lett., 62,* 497–500.

Wu R.S., 1989b, The perturbation method in elastic wave scattering, "Seismic Wave Scattering and Attenuation" Part II, ed. by Wu and Aki, *Pure and Apllied Geophys., 131,* 605-638.

Wu, R.S. and K. Aki, 1985, Scattering characteristics of waves by an elastic heterogeneity, *Geophysics, 50,* 582-595.

Wu, R.S., 1993, Wide-angle elastic wave one-way propagation in heterogeneous media and an elastic wave complex-screen method, submitted to *J. Geophys. Res.*

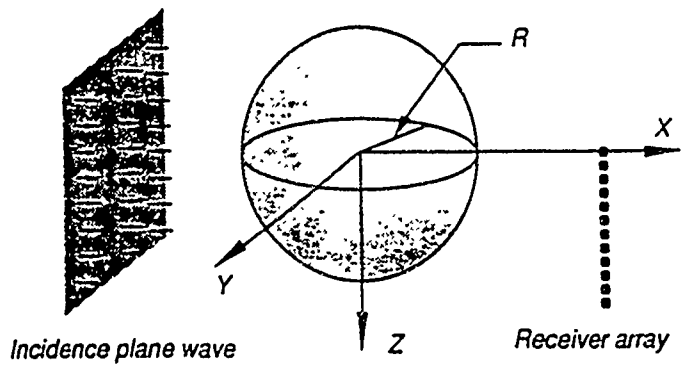

Fig. 4. The geometry of the 3D numerical experiments

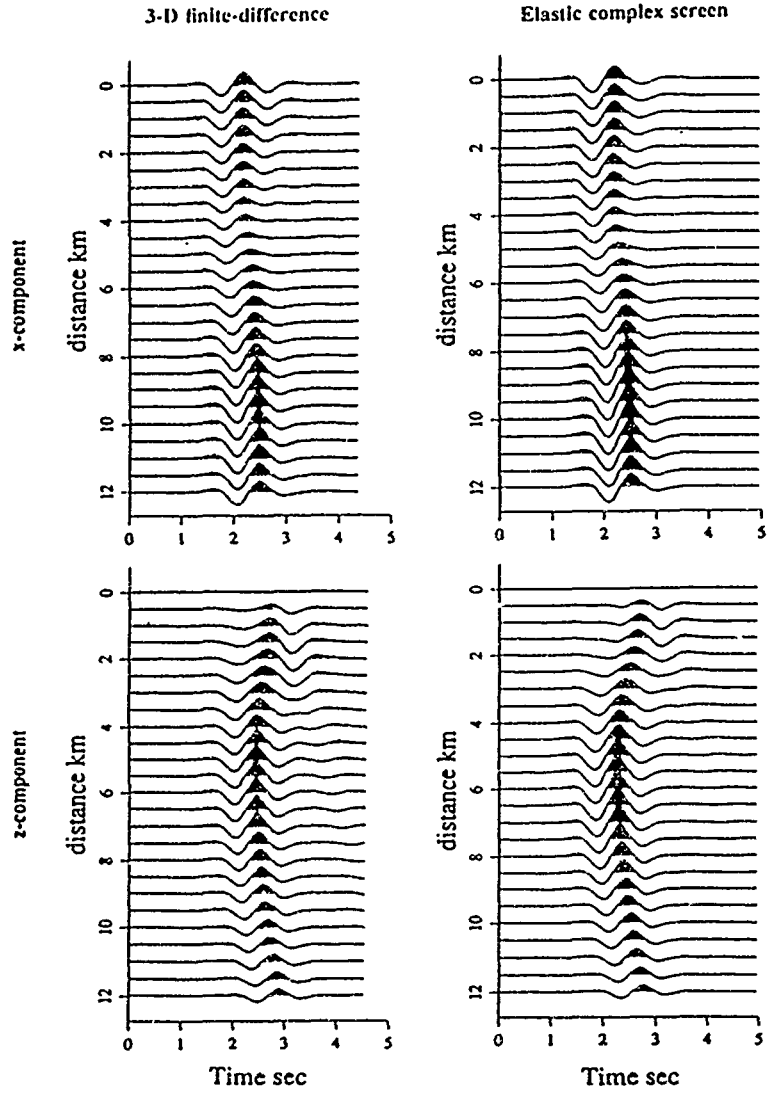

Fig. 5. Comparison of 3D ECS method and 3D finite difference for an elastic sphere with 10% P-velocity perturbation.

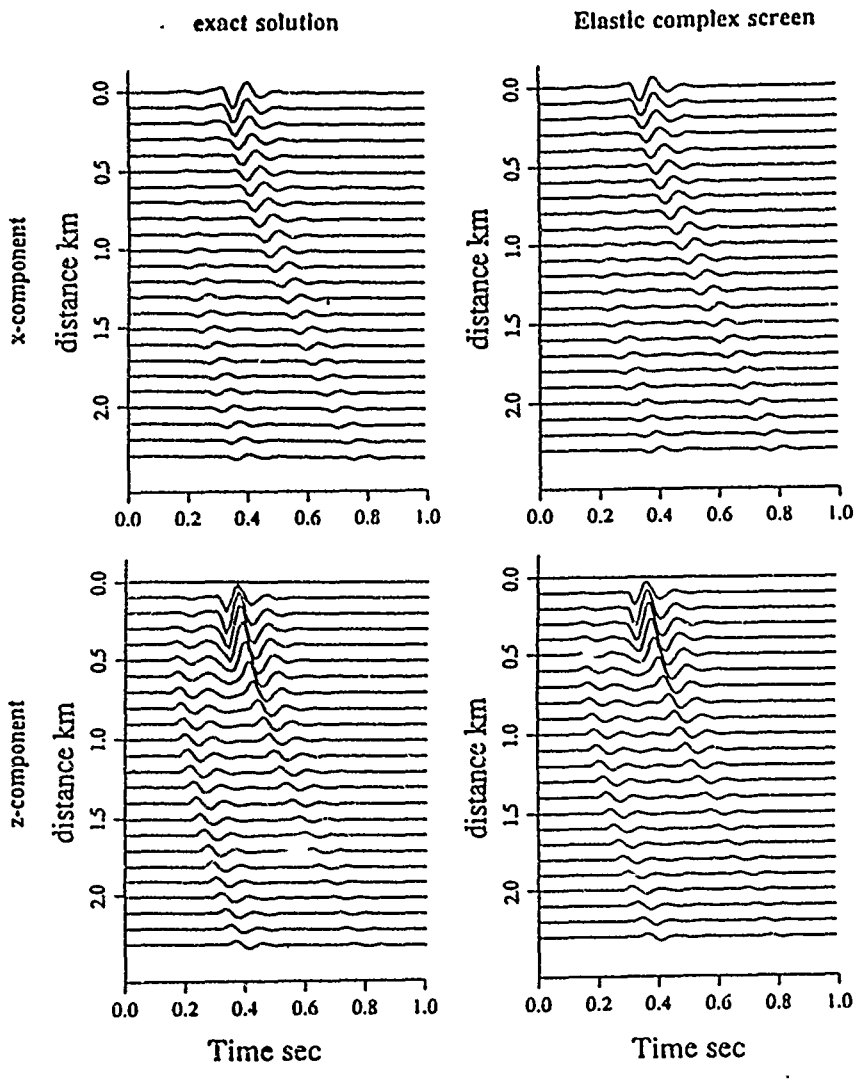

Fig. 6. Comparison of 3D ECS method and exact solutions for an elastic sphere with 10% S-velocity perturbation.

Automatic Global Seismic Event Association and Location Estimation using a Knowledge Based Approach to Generalized Beamforming

S. K. Leonard, ENSCO, Inc., 445 Pineda Ct. Melbourne, FL 32940

Contract No. F19628-91-C-0172

OBJECTIVE

The framework for a system for automatic global seismic event association using generalized beamforming (GBF) has been developed. The technique forms initial events by a non-combinatorial method, and allows the exploitation of all observed detection data (arrival time, azimuth, velocity, amplitude, period. etc.) but does not require any parameter except time. By design, beamforming enables us to ignore the data that are inconsistent with a region and to focus on only the small subset of the data that correlate with a potential epicentral region in terms of the observed information in the data, and what is known *a priori* about the potential epicentral region. Using GBF, the need to repeatedly access inconsistent data (the majority of the detection data) is eliminated. All possible combinations of consistent detections are necessarily associated to form a complete set of initial events to be evaluated systematically and automatically for their realness. In conjunction with applying the observed parameters for consistency, GBF provides a structure for applying knowledge gained from experts to automatically identify false or erroneous events.

Our objectives are to optimize the efficiency and accuracy of initial event formation using generalized beamforming, to exploit all available detection information, to define a framework for using knowledge obtained from expert seismic data analysts to process the initial events, and most importantly to test and evaluate the technical ability of the procedure. This may not entirely eliminate the need for human intervention, but will significantly reduce the time required by analysts.

RESEARCH ACCOMPLISHED

Our approach to the global automatic association problem is to apply the generalized beamforming technique to form initial events. In essence, we discretize the earth into a finite set of potential epicenters and procedurally "beamform" a network to each of these epicentral regions employing detection parameters such as azimuth and slowness in addition to arrival time. Initial events are examined for consistency among the detection set (*e.g.* variability of predominant period and magnitude), and individual detections within an event are evaluated for consistency with the epicentral region (*e.g.* "expectedness" of detection data from a station.) Inconsistent detections are eliminated from the initial events; most false events are subsequently disbanded due to sparseness of data. Remaining events are evaluated using *a priori* knowledge of seismic characteristics of the potential epicentral region and are rated in terms of quality or "realness" or are disbanded.

The fundamentals of the GBF process for regional event association are discussed by Ringdal and Kvaerna (1989), and the details of the GBF procedure for automatic global association are presented by Taylor and Leonard (1992). A brief review of the GBF process to

form initial events is provided here, but the reader is referred to the aforementioned works for details. The focus of this paper is to address the most recent research accomplished and to present examples of processing results.

The globe was subdivided into equally spaced grid points each corresponding to a potential epicenter. A circular epicentral region encompassing each potential epicenter is defined with a five degree radius. Each epicentral region overlaps with every adjacent region to ensure complete coverage of the earth as shown in Figure 1. Using GBF we systematically "beamform" a network to each of these predefined epicentral regions and process the beams independently.

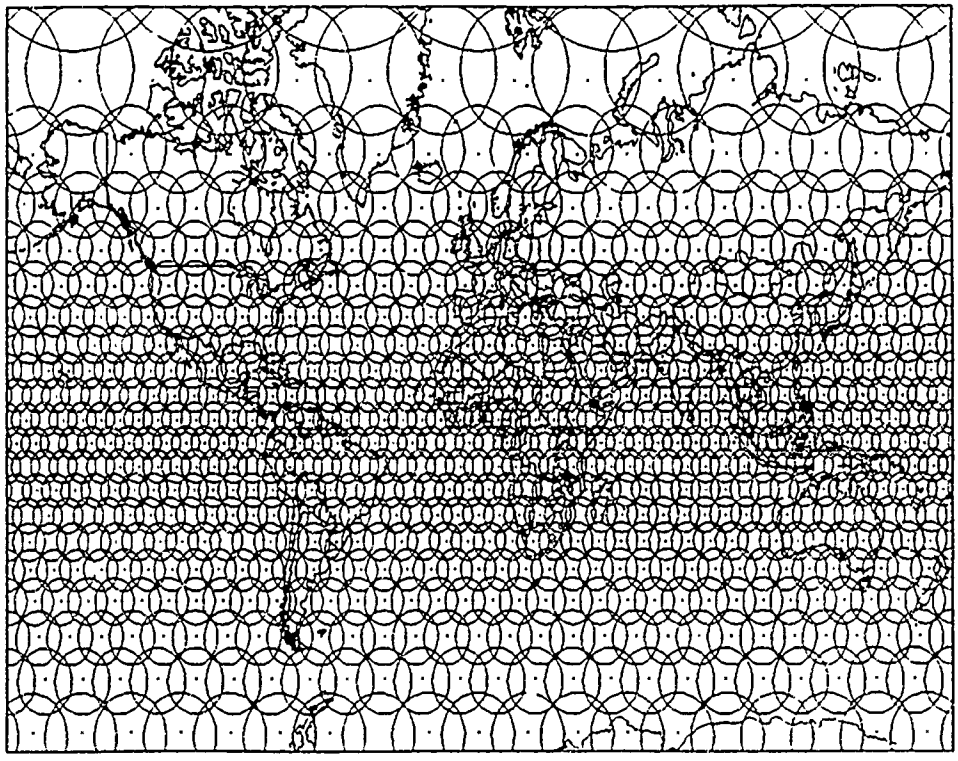

Figure 1. Subdivision of the globe into equally spaced potential epicentral regions.

A key factor for the computational efficiency of this processing scheme is that grid point locations are predetermined. Much of the station/grid point information required (such as, distance, azimuth, travel time, velocity, etc.) is computed before processing and stored in a database for each grid point to be accessed directly and quickly. Additionally, information that cannot be computed have been acquired from expert analysts and stored in "knowledge bases" for individual grid points. This information currently includes such data as the stations that are "expected" to detect an event from a given grid point region, and will include the historical seismicity of a region, typical depths of events in the region, significant geologic features (e.g., trenches, etc.) that are in the path between specific stations and a region, and any other knowledge about a region an analyst may have gained from experience.

A generalize beam is formed independently for each grid point. In terms of association, travel time remains the key discriminant between which detections can possibly be associated to

the same event. Accordingly, a superset of all detections that can form all possible events can be constructed based on arrival time. Figure 2 schematically illustrates how this time correlation, or generalized beamforming, is conducted for one grid point.

The large circle in Figure 2a defines the epicentral region whose center is the grid point shown by the asterisk. The triangle represents a station where a detection has occurred at time DetTime. If the observed detection at the station is caused by an event within this epicentral region, then the origin time of the event is bounded by

$$OTime_1 = DetTime - TT_1 + e_1,$$

and

$$OTime_2 = DetTime - TT_2 - e_2,$$

where e_1 and e_2 represent the variability in arrival time due to random errors, source effects and path effects. These two origin times define a window of time in which the event may have occurred. A similar time window applies to all detections, so we search for an origin time that is consistent for enough stations to define an event. In practice, azimuth and velocity can also be used as an effective association discriminant with generalized beamforming. The epicentral region described by the circle defines an acceptable azimuth and velocity range for stations detecting events from this region.

Figure 2b shows a set of these origin time windows computed from six sample detections and the associated generalized beam. The dashed line represents the event detection threshold. When the number of detections with overlapping origin times meets this threshold, an initial or preliminary event (PE) is declared.

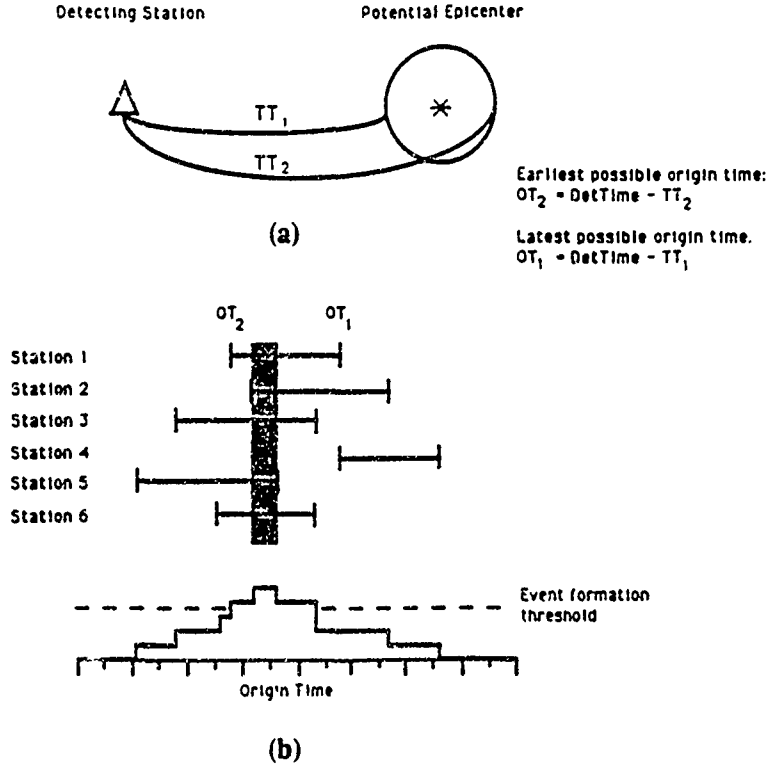

Figure 2. Formation of the generalized beam for a single potential epicentral region.

Figure 3 displays a typical generalized beam for a grid point region with a radius of five degrees. The beam is formed from three hours of actual detection data. The event detection threshold is set to 4, meaning that at least four detections must correlate in time, azimuth and velocity before a PE is declared. Notice that there are 24 preliminary events declared for these data. Because a PE may have an long time duration, we subdivide each PE into equal time intervals of less than five seconds. All combinations of detections within that time interval are formed to define the initial events that will receive further analysis.

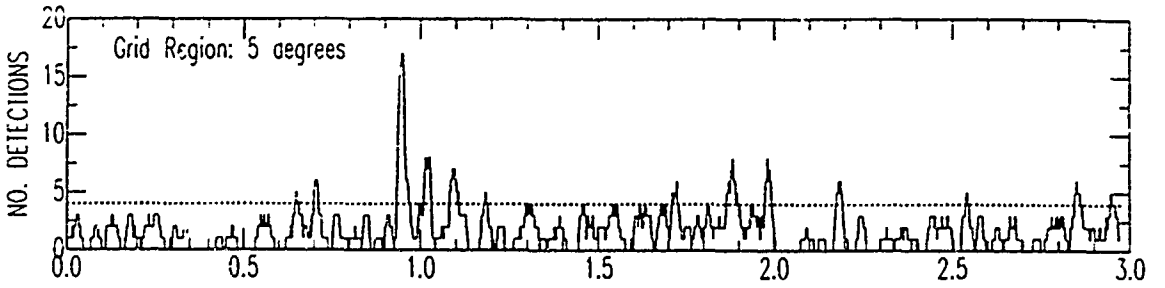

Figure 3. Generalized beam for a potential epicentral region of five degrees.

Automatic detectors frequently record multiple detections for an actual arrival. The result may be many instances of an event with slightly different combinations of detections. Resolving the conflicts for detections between events within a grid point region to identify real events and eliminate false events requires careful consideration. Implementing the evaluation process that a seismic data analyst uses to resolve these conflicts when manually associating events effectively resolves the conflicts automatically.

Many of the conflicts among events within a grid point are resolved by evaluating the consistency of the detections with respect to observed slowness, observed amplitude and the predominant period, then using the HYPO location algorithm iteratively, eliminating those detections that have inconsistent travel time residuals. If the number of detections in the event falls below the event detection threshold, the event is disbanded. Next an overall quality rating is assigned to each remaining initial event based on the following factors: 1) the number of detections defining the event, 2) the timing of detections from the same station, 3) the root mean square (rms) residual of the detection set, 4) the "competing" residuals from stations grouped by proximity, and 5) the relative "expectedness" rating of the combination of stations defining the event. The detections in the highest quality initial event are removed from the other conflicting initial events. The conflicting lower quality events are usually disbanded due to sparseness of data, or identified as having a low quality rating.

Every grid point region is processed independently. The result is a set of initial events located world-wide. Another type of conflict arises when events from separate (typically adjacent) grid point regions compete for detections. These between grid point conflicts must also be resolved. The problem here lies in determining to which event a detection is most strongly correlated. To resolve these conflicts, we remove the detection from each initial event that includes the detection and relocate the event. We normalize the effect of this detection by computing the ratio of the travel time residual of the detection in question to the standard deviation of the travel time residuals remaining in the event for each event. The event that has the lowest ratio "wins" the detection. This detection is then disassociated from the other events, thus

resolving the conflict. As detections are removed from events, many are disbanded due to sparseness of data. This processing may result in events with identical detection sets, as well as events with detection sets that are subsets of another event. The redundant and subset events are disbanded.

Association of later phases is the subsequent step in the process. From the origin time and location of the events formed with initial phases, we predict at what time a later phase should arrive, and from generalized beamforming, we know which detections are consistent with the region in which the event is located. Correlating this information, we search a small set of detections for one that meets the criteria of each feasible later phase for every station. Consistent later phases are then associated to the event.

The preceding steps yield the event bulletin produced in the current stage of the research, that will be discussed in later paragraphs. During the final stages of the processing, events must be evaluated to determine whether they represent real seismic events or whether they are just random correlations of data producing a false event. Evaluation factors and criteria that are applied to the conflict resolution problem may be applied here. The quality of fit of the data to the grid point information is the primary decision-making tool.

The final system output includes an appraisal of the results. The framework provided by generalized beamforming is a vehicle for storing and applying site-specific information. This final appraisal process can include such advice to the analyst as which additional stations are expected given the grid point location and magnitude, which detections are only marginally consistent with the event, whether events have historically occurred at the location, or any other phenomena based on historical observations. In addition, an overall determination of the quality, or confidence, in the event can be reported.

Discussion of Current Results.

Two data sets, each containing 22 hours of actual, automatically determined detection records provide the test data for this study. The data are from an active fifteen station global seismic network comprised of ten array sites and five single element stations. The detection records produced from the array sites are derived from the beamed digital waveform of the array elements. All data are short period and vertical component. Each detection record contains information such as the station identifier, arrival time, observed azimuth (for array sites) and uncertainty, observed velocity (for array sites) and uncertainty, observed distance (for array sites), amplitude, period, ground motion, and signal-to-noise ratio.

Both test data files are subsets of much larger data sets that include detection data for many additional stations. The supersets of data have been processed by a current method of "automatic" association. The existing association method entails processing the automatically detected data using a combinatorial technique to produce a preliminary seismicity bulletin. A seismic data analyst uses this bulletin as a starting point for manual analysis. Each event is scrutinized, the onset times are corrected, new detections are identified and erroneous detections eliminated. Real events formed automatically are refined, the events missed by the automatic process are manually associated and the erroneous events automatically formed are deleted by the analysts. Finally, additional phases are associated, and a final event bulletin is produced. These extensive and time-consuming analyses are performed manually, by analysts using detection data as well as graphical, raw waveform data. The manual analysis of the automatic results are a routine part of the current "automatic" seismic association process.

Because they have been reviewed and corrected by human seismic data analysts with the benefit of using the waveform data, the final event bulletins produced by the current procedure for these two data sets serve as fairly reliable baselines for testing the global GBF automatic associator. At least initially, we assume that the events presented by the analyst-reviewed bulletin are real and the set of events is complete, *i.e.* no real events remain unassociated. A comparison was made between the bulletin produced by current technology and reviewed by the analyst and the bulletin produced entirely automatically, without human intervention, by the GBF associator. For clarity, a distinction is made between the two bulletins: the ARB bulletin refers to the analyst reviewed baseline bulletin, and the GBF bulletin refers to the bulletin produced by using the generalized beamforming method.

The GBF associator is currently constrained to declare an event when four or more detections correlate to define the event. Fewer than four initial arrivals reduce the confidence in the validity of events, therefore these correlations are not considered. The system can be fine-tuned to declare events with a single station, as well as two and three station events.

For the purposes of this comparison, 64 grid point region each with a radius of five degrees are processed. The grid point regions were selected so that all of the events in both data sets are located (according to the ARB bulletin) within one or more of these grid point regions. In other words, because we assume that each grid point is a potential epicentral region, we are assured that the real events identified in the ARB bulletin are within these regions, and the system will be tested to determine if it automatically associates these events. In practice, all 763 grid points will be processed so the entire earth is represented; however, because we know the locations of the events, we can use this subset of grid point regions. Prior to processing, the grid point databases and the knowledge files have been created for each grid point.

Table 1 summarizes the results for the events associated with the first test dataset, by comparing the number of events formed according to the ARB bulletin with those formed completely automatically by the GBF associator. The left-most column identifies the bulletins produced by the two association processes. The second column tallies the total number of events formed by the respective processes. Column 3 indicates the number of events formed by the two

TABLE 1.

Data Set #1	Total events formed	Events >= 4 test data stations	Difference
ARB bulletin (+ analyst)	35	32	3
GBF bulletin (no analyst)	40	27	13

processes with four or more stations from the network providing the test data set, and the last column shows the differences in the results of the middle two columns. A discussion of these results follows.

All but three of the 35 events reported by the ARB bulletin are comprised of at least four stations that are represented in network producing our test data. However, some of the detections may have been manually generated by the analyst and will not be present in the automatically detected dataset and thus not available to the GBF automatic associator. Although there are four or more detections shown in the ARB bulletin, four detections may not be available to the automatic software and an event cannot be declared. This happened in five of the 32 cases. This accounts for the five event difference between the rows of the third column of Table 1. In this dataset there are 27 events that can possibly be formed automatically o match the ARB bulletin -

the results show that we have formed all of them entirely automatically. Three events reported in the ARB bulletin are built with fewer than four stations. These three are accounted for in the top row of the right-most column. Forty events were reported in the GBF bulletin. Twenty-seven of these match the 27 events with detections for four or more of the test stations reported in the ARB bulletin. Thirteen additional events were formed automatically that are not present in the ARB bulletin. Table 2 illustrates the results for the second test dataset. The explanation of the results shown in this table are identical to those for Table 1.

TABLE 2.

Data Set #2	Total events formed	Events >= 4 test data stations	Difference
ARB bulletin (+ analyst)	25	17	8
GBF bulletin (no analyst)	21	12	9

Upon initial inspection of these tables, the number of extra events for the GBF bulletin may seem to be cause for concern. A cursory manual examination has shown that these extra events are small regional events; or typically have four or five detections, are of questionable quality, and are most probably random correlations of detection data. The process of the automatic evaluation of such events is in progress.

The results of this knowledge based approach to automatic global seismic event association using the generalized beamforming methodology are encouraging. Even with the extreme limitations that are placed on the automatic system by the small number of stations in the network, the inaccuracies of detection onset times, the abundance of false detections, and the absence of many real detections, the process associated all possible four-station events from our test datasets without the need for human intervention. Further tuning will be required to minimize the number of extra events associated automatically.

With regard to later phase association, the processing results are equally as encouraging. Reliable later phases are automatically associated to the events formed. Further research is required to account for the characteristics and properties of later phases and includes an analysis of the validity of later phases associated in the ARB bulletin.

CONCLUSIONS AND RECOMMENDATIONS

The results indicate the processing framework of generalized beamforming can be effectively utilized as a means of performing global teleseismic automatic association. The approach successfully forms all possible initial events and provides an excellent vehicle for exploiting observed detection information and applying expert knowledge.

Future work will continue to expand upon the established procedures for properly automatically associating later phases to the events identified with defining phases. Evaluation of the events for the purpose of eliminating erroneously associated events and for generating an appraisal of the events will also be addressed.

The potential for expansion and improvement of the system is vast. As knowledge grows the system's performance will improve. Furthermore, the GBF framework lends itself well to parallel processing to significantly reduce the computational intensity of the association task.

REFERENCES

Taylor, D. W. A. and Leonard, S. K. (1992) Generalized Beamforming for Automatic Association, Proceedings of the 14th Annual PL/DARPA Seismic Research Symposium, 16-18 September 1992, PL-TR-92-2210, ADA256711

Ringdal, F. and T. Kvaerna (1989). A multi-channel processing approach to real time network detection, phase association, and threshold monitoring, *Bull. Seism. Soc. Am.* 79. 780-798.

Analysis of the SAA2 Experiment, Piñon Flat California

Sophie-Adélaïde Magnier, Frédéric Donzé,
Jeff Hanson, Bernard Minster and John Orcutt

Institute of Geophysics and Planetary Physics,
Scripps Institution of Oceanography,
University of California San Diego

Contract Number: Air Force F29601-91-K-DB13

1 Objectives

During the spring of 1991 a broadband array of twenty-eight three components sensors with apertures varying between 100 meters to 6 kilometers, was set up. This small aperture array henceforth referred to as SAA2, operated near Piñon Flat Observatory (center at 33.6065°, −116.4531° latitude, longitude) in Southern California. By making use of the different apertures and frequencies, characterization of scattering at different scale lengths is possible. This leads us to a better constrained three dimensional velocity model of the area.

During the experiment period local, regional and teleseismic events were recorded. The focus of the present work is on the local events (less than 100 km away). Polarization analyses on an earlier high frequency data set recorded in the same area (Hanson et al., 1993) have shown that some of the high frequency effects noted could be due to a thin superficial weathered layer of some tens of meters. We wish to show that other coherent features can be detected within both the P and S coda wavetrains which correspond to known features (Fuis et al. 1984).

2 Research accomplished

The experiment involved the deployment of 28 three component sensors, in five concentric rings. The sampling was performed at 100 samples per second and the frequency

bandwidth is between 0.0083 to 40 Hz (cut-off filter). Preliminary spectral analysis has shown that most of the coherent energy is concentrated below 15 Hz.

The local events are more or less clustered with 3 dominant regions of activity. A majority of these are located along the San Jacinto Fault zone with a cluster on Toro peak. This also coincides with the event locations of the 1990 small aperture array experiment (SAA1). These events are within 20 km of the recording array and exhibit high frequency characteristics. They are at depths ranging from 5 to 15 km. Most are within the trifurcation of the San Jacinto Fault zone.

Other events of interest to this study originate in two principal directions. The first is N300°E to N340°E and the second is N25°E to N45°E. The former are located on geological structures in continuation with those around Piñon Flat. The second series on the other hand is on the northern side of the San Andreas Fault zone and the propagation paths will thus reflect the characteristics of the Coachella Valley, which is made up of extensive marine and non-marine deposits (Calzia, 1988, Sharp 1979, Wright, 1946).

We shall consider here, the early P and S coda since the later coda is strongly affected by overlapping multiples and hence separation of different wavefronts is rendered difficult. All events have been located using either the Anza or Caltech network. Event magnitudes, locations, depths and origin time were provided by J. Scott, and where possible (Scott, 1992) a three dimensional velocity model was used in the determinations.

2.1 Method and data processing

We have noted that most of the data have frequencies below 15 Hz. Further analysis in various frequency bandwidths shows that energy packets may be optimally retrieved by filtering in the 4 to 6 Hz band. This removes the effects of the near surface weathered layer scattering and smoothes high frequency effects due to small-scale perturbations.

After filtering the data, separate wave packets are clearly identifiable. An attempt at associating these energetic arrivals to distinct reflectors is made. To do this the methodology developped by Hedlin et al., (1991) is applied in a particular case of the three dimensional approach. We consider that the velocity from the source to the reflector is identical to the reflecting velocity which means that we do not consider phase conversions. The method is based on the summation of probability ellipsoids whereby the three dimensional solution curve for the position of a reflector given a time delay of the reflected phase and a propagation velocity as well as the receiver position is an ellipsoid. One of the foci is positioned on the source while the second focus is at the center of the receiver array. The major axis of the ellipsoid is aligned along the azimuth as shown in Figure 1. In order to constrain the solution, additional information is provided by the three compoments.

All three components are used simultaneously so information may be separated between the vertical and the radial components. This can then provide incidence angles directly for a given wavefront by plotting the particle motion plots. It is done for both the P and S waves. By combining the incidence angle and the azimuth, the most probable

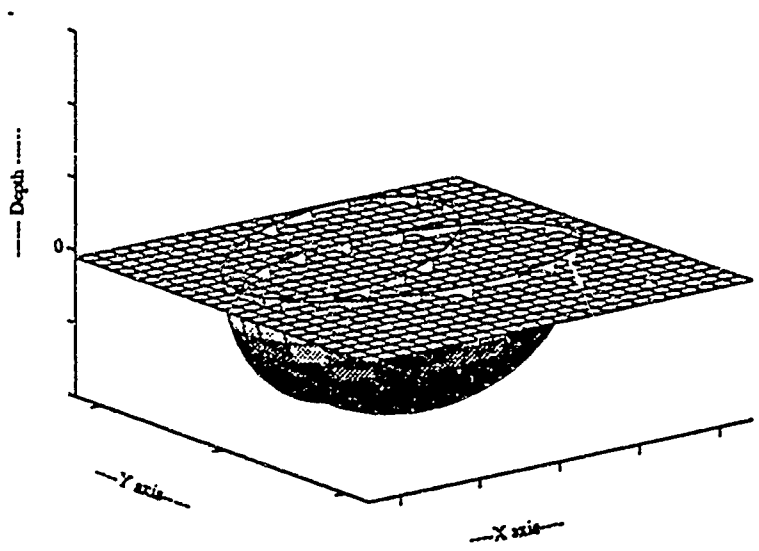

Figure 1: The probability ellipsoid given a delay travel time and an incident velocity and a reflecting velocity. Here they are identical suggesting that no conversion is occuring. The foci of the ellipsoid are one at the source and the other at the receiving array.

position on the ellipsoids is constrained. Numerous local events have been selected and phases picked. The ellipsoids are computed and summed. Let us state here that the processing depends on an adequate pick of both the P and S wavefronts. Although this is a relatively simple procedure for direct arrivals it is much less so for the coda wave packets which further emphasizes the absolute requirement of three-component processing.

Figure 2 shows such an example where for different events we have selected a strong secondary P arrival and have assumed that this arrival corresponds to the same reflector on all selected events. The horizontal projections of the ellipsoids are shown. The most probable location for a reflector is close to the array. Clearly this is biased since all ellipsoids have that point in common (given as the position 0 0). Nonetheless, the entire region surrounding the array has a high probability and not a single point which suggests that a strong velocity contrast does indeed exist at depth.

In order to verify the validity of the previous assumption, the data is then submitted to additional processing. In particular, a standard broadband *f-k* analysis is performed. Indications on the azimuth of arrival and incidence are thus obtained. This allows us to determine where the reflection took place, and how the ray paths have been affected by the substructure. The *f-k* analysis requires that the signal be recorded on a good number of sensors and time windows must be selected rather precisely to avoid a smearing of the information. We therefore chose to select the time windows on a stacked signal which

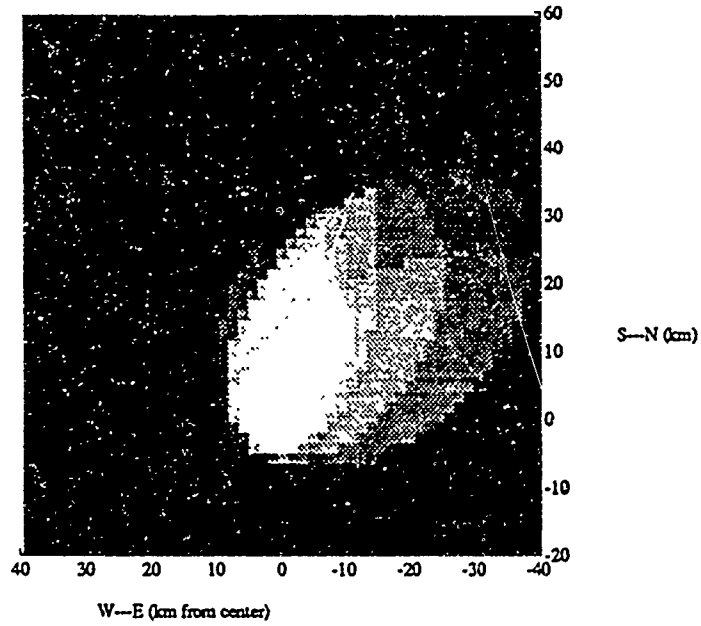

Figure 2: By plotting the probability ellipsoids of local events for selected secondary arrivals, it appears in this horizontal projection that the most probable location occurs close to the receiving array indicating a near scatterer.

gives a representation of the entire array response. The data are filtered in the 4-6 Hz frequency band and may be compared directly. Removal of the beam might have simplified the analysis but was not applied here.

Figure 3 is an example of such processing for an event located 83 kilometers from the array. The two *f-k* windows presented indicate that although the direct arrival has a N36°E backazimuth, the second wave packet is approximately N15°E and the raypath is clearly more vertically incident than the direct raypath. This would indicate that the reflection took place close to the array but not on the direct raypath.

This method is applied on the entire suit of events considered. The azimuth and incidence angles of the later phases may be compared to those of the direct arrivals. This helps in determining a plane or planes of reflections. In this region and with this analysis, evidence for dipping planes exists. This is seen when considering various source depths for similar backazimuths. According to the source depth and given a number of existing models for the region (Kanamori and Hadley, 1975, Vernon, 1989) then the only way to explain why the reflections vary in azimuth for events which have a common backazimuth is to include dipping planes. Images previously obtained with the ellipsoid summation techniques projected on vertical planes had already favored this hypothesis.

By using events at different azimuths, distances and depths we obtain a good sampling of the structures beneath the surface and we note that two separate reflectors seem to be responsible for the major part of the early coda. The first part of the coda reflects

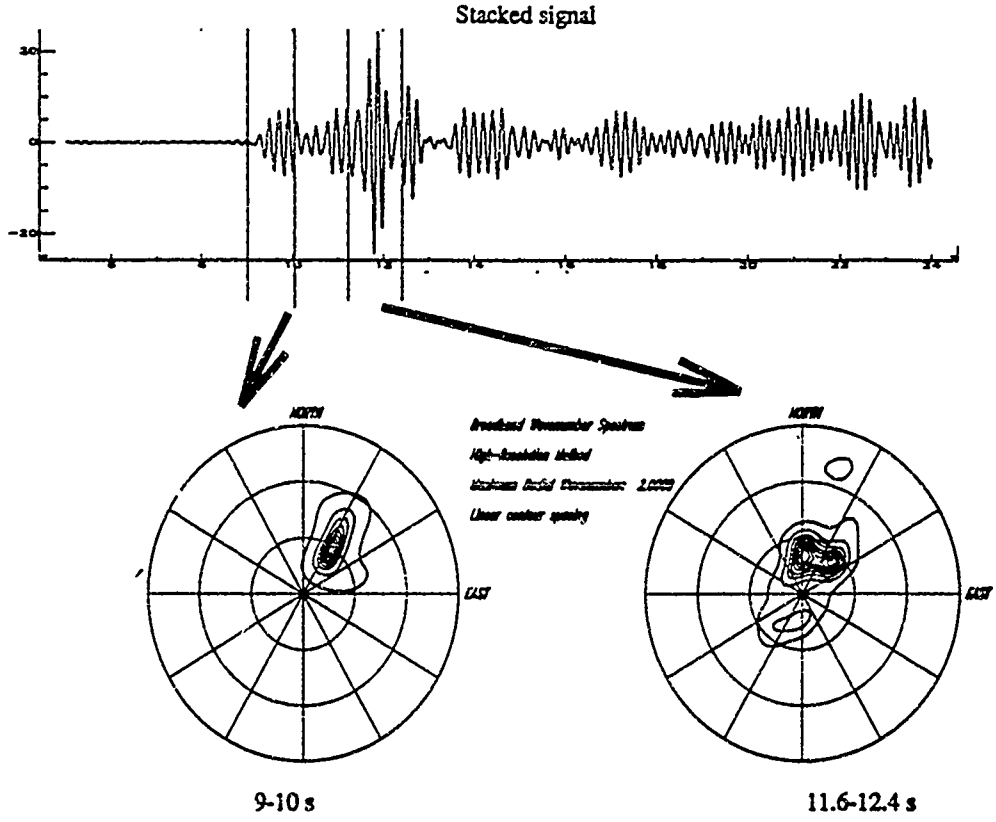

Figure 3: The top image is the stack trace resulting from beamforming the signal at the center of the array. The event is located 83 kilometers away at a backazimuth of N36°E and a depth of 6.37 km. The bottom two images are plots from $f-k$ analyses for two different time windows. It is clear that the later arrival has a more vertically incident raypath as well as a different azimuth indicating a near receiver reflection.

from an interface with a low angle dip. The later part of the coda is associated to a deeper reflector, at 15 km in depth. It is difficult to ascertain that this reflector dips although some evidence exists for a Northwest-Southeast strike. This corresponds well to noted paleo-boundaries.

The first shallow interface can be assimilated to a low angle contact between intrusive plutonic rocks and the metasedimentary basement. This contact may be intricately linked to the low angle thrust faults dating to mid to late Cretaceous bounding the Mylonitic belt to which Sharp (1979) and Erskine (1985) refer to.

The second interface is mentioned by other authors, (Kanamori and Hadley, 1975). They take into account a velocity transition that would occur between 10 to 20 km at depth. Vernon (1989) and Scott (1992) also mention the probable existence of this velocity contrast. Note that this contrast corresponds to the transition between the metasedimentary basement and the diabase-gabbro sub-basement (Fuis et al. 1984).

Although active faults in the region are nearly vertical (Sanders and Kanamori 1984), traces of paleo-faults on the other hand exhibit a slight dip as observed here.

3 Conclusions and recommendations

The data set under study provided us with a range of information. We chose to exploit the information found in the 4 to 6 Hz frequency bandwith which helped us in associating particular wave packets to known or putative structures. We can confirm the existing dip of paleo-thrust faults at depth as well as their importance. Finite difference modelling has been pursued in a two-dimensional approach and will be the topic of a paper in preparation (Magnier and Donzé 1993). A three dimensional model will be necessary to fully appreciate the importance of the paleo-faults and their impact on this area.

References

[1] Calzia, J. P., 1988, Mineral resources and resource potential map of the Pyramid Peak roadless area, riverside county, California, *USGS, Miscellaneous Field Studies*, MF-1999.

[2] Erskine, B. G., 1985, Mylonitic deformation and associated low-angle faulting in the Santa Rosa Mylonite zone, Southern California, *Ph.D Thesis, University of California, Berkeley.*

[3] Fuis, G. S., W. D., Mooney, J. H., Healy, G. A., McMechan and W. J., Lutter, 1984, A seismic refraction survey of the Imperial Valley region, California, *J. Geophys. Res*, 89, 1165-1189.

[4] Hanson, J. A., J. B. Minster and F.L. Vernon, 1993, Polarization characteristics of local events recorded on a small aperture array, *Submitted.*

[5] Hedlin, M. A., 1991, *Analysis of seismic coda to identify regional sources and image strong crustal scatterers*, Ph.D Thesis, University of California San Diego.

[6] Kanamori, H., and D., Hadley, 1975, Crustal structure and temporal velocity change in Southern California, *PAGEOPH*, **113**, 257-280.

[7] Magnier, S. A., and Donzé, F. V., 1993, A small aperture array, retrieving and modelling information, *In preparation.*

[8] Sanders, C. O. and H. Kanamori, 1984, A seismotectonic analysis of the Anza Seismic Gap, San Jacinto Fault Zone, Southern California, *J. Geophys. Res.*, **89**, 5873-5890.

[9] Scott, J., 1992, *Microearthquake Studies in the Anza seismic Gap*, Ph.D Thesis, University of California San Diego.

[10] Sharp, R. V., 1979, Some characteristics of the Eastern Peninsular Ranges Mylonite zone, *in: Evernden, J. F., Convener, Proceedings, Conference VIII, Analysis of actual fault zones in bedrock: United States Geological Survey Open File Report*, **79-1239**, 595p.

[11] Sylvester, A. G., and M., Bonkowski, 1979, Basement rocks of the Salton Trough region, in *Tectonics of the Juncture between the San Andreas Fault System and the Salton Trough, Southeastern California, Chapter 7*, Ed. J. C. Crowell and A. G. Sylvester, for the American Geological Society of America.

[12] Vernon, F. L. III., 1989, Analysis of data recorded on the ANZA seismic network, *Ph.D Thesis, University of California, San Diego.*

[13] Wright, L. B., 1946, Geology of Santa Rosa Mountain area, Riverside County, California, *California Journal of Mines and Geology*, 9-13.

Numerical Simulation of Quarry Blast Sources

K. L. Mclaughlin, T. G. Barker, J. L. Stevens, S. M. Day*

S-CUBED, Division of Maxwell Laboratories

POB 1620, La Jolla, CA 92038, 619-453-0060

***Department of Geological Sciences, San Diego State University**

Contract F29601-91-DB27

1.0 A physical model

The typical large quarry blast is designed to fracture and move large quantities of rock in a safe and economical manner. To accomplish this, explosives are placed at scaled burdens between 0.5 and 1 m per cube-root Kg of explosives (between 50 and 100 m/Kt$^{1/3}$) and detonated in many separate holes. Detonations are timed so as to allow the rock from one row of charges to move out of the way before the next row of charges are detonated. In this way, fracture from spallation is maximized. The blasting literature (Langefors and Kihlstrom, 1963) confirms that the spall momentum from charges detonated in this range of scaled burden is consistent with the spall momentum predicted by non-linear finite difference simulations of nuclear explosives in the same range of scaled depth of burial, 4 * 10^{10} Nt-sec per Kt explosive or 40 Nt-sec per Kg of explosive. (Barker et al., 1993)

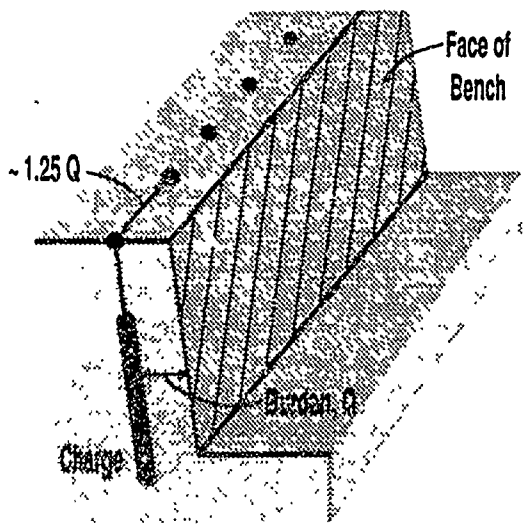

Figure 1.01 A typical quarry blast consists of multiple detonations of up to several tons each behind a quarry face. The charge size and burden for a given face height are specified in the literature to maximize rock fracture and yield a clean new face both economically and safely.

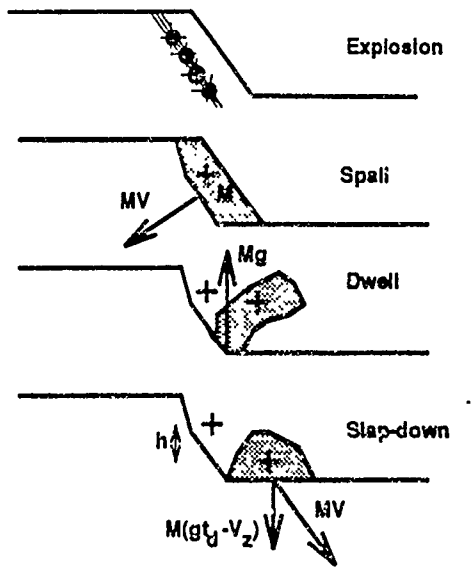

Figure 1.02 A physical model for the spall associated with a quarry blast. The explosions spall material from the face that then falls to the quarry floor. The spalled mas, M, may fall a net distance, h.

To describe the spall source for a quarry blast, we have adapted the spall model of Barker and Day (1990) to include the effects of horizontal throw and the net change in elevation of the spalled mass. Both of these effects are found to be significant contributions to the seismic source. The equivalent vertical spall force is given by

$$F_z = M[V_{z0}\delta(t) + (gt_d - V_{z0})\delta(t-t_d) - g(H(t)-H(t-t_d))] \quad \text{(EQ 1)}$$

and the horizontal force is given by

$$F_x = M\,V_{x0}[\delta(t) - \delta(t - t_d)], \quad \text{(EQ 2)}$$

where M is the spall mass, V_{z0} and V_{x0} are the initial vertical and horizontal spall velocities, g is the acceleration of gravity, and t_d is the spall dwell time,

$$t_d = [V_{z0} + (V_{x0}^2 + 2h\,g)^{1/2}] / g, \quad \text{(EQ 3)}$$

and h is the net change in elevation of the spall mass. The total spall momentum is $P = M\,(V_{z0}^2 + V_{x0}^2)^{1/2}$.

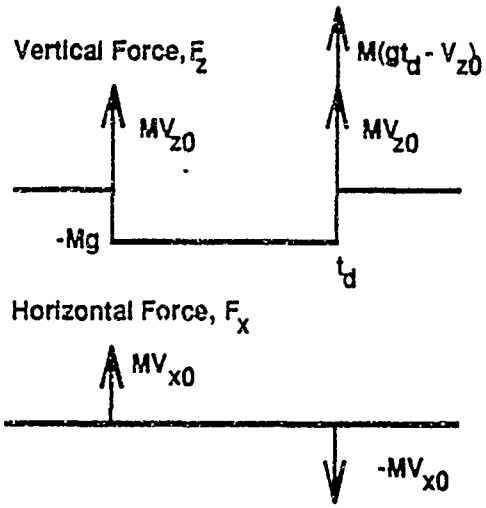

Figure 1.03 The dwell time is determined from the magnitude and direction of the takeoff velocity. If the spall mass falls a net distance, h, then there is a contribution from the gravitational potential. The vertical spall force still has no net D.C. value. The horizontal force is a dipole with no net D.C. value.

2.0 The hide in quarry blast scenario

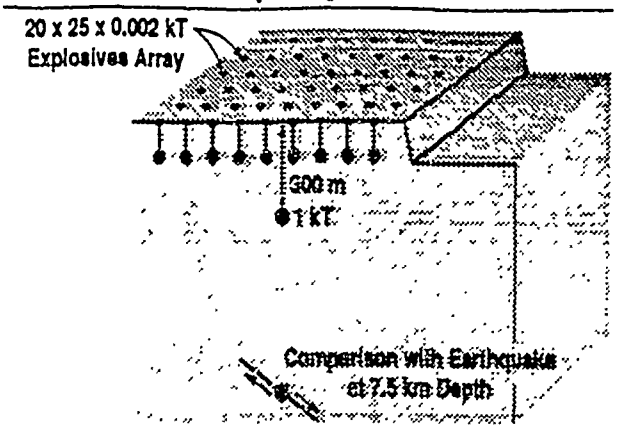

Figure 2.01 The hide in quarry blast scenario.

In the hide in quarry blast scenario, a large chemical shot designed to look like a quarry blast may be used to hide an overburied nuclear explosion. The nuclear explosion may be partially or fully decoupled. We have examined this

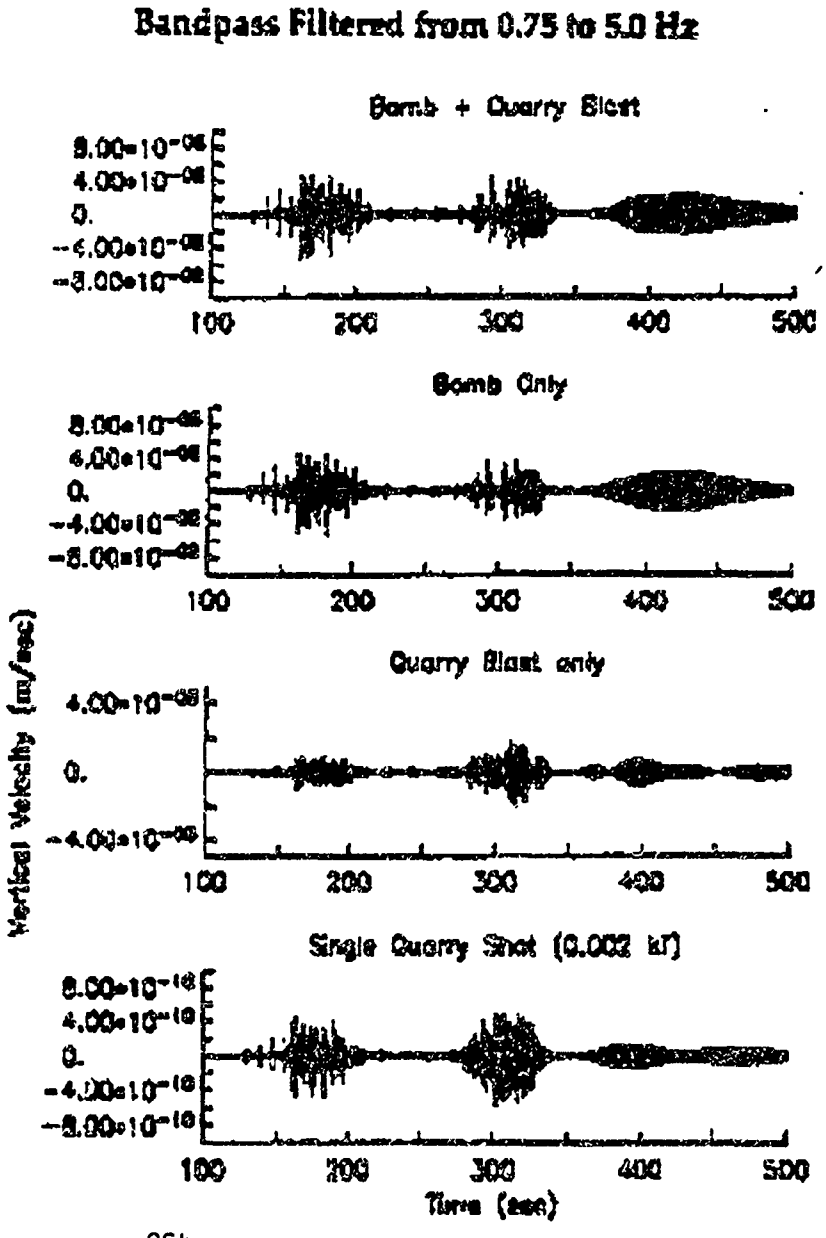

Figure 2.02 Vertical component synthetic seismograms (0.75-5 Hz) at 1000 km for the 1 Kt overburied bomb and the 1 Kt ripple fired quarry blast. The sum of the two is shown at the top. Note that the bomb dominates the ripple fired quarry blast. Note the different Pg/Lg ratio of the bomb and quarry blast. Note that the ripple fired quarry blast is not 500 times larger than the single 2 ton quarry blast shown at the bottom. This is because of the extended duration of the ripple fired quarry blast.

scenario under the assumption that the shots are fired row-by-row as well as simultaneously. In order to detonate 1 Kt of chemical explosive, 500 charges of 2 metric tons each would be fired. Regional synthetic seismograms were produced at a distance of 1000 km for a quarry blast of 20 by 25 2-ton charges and for an overburied nuclear explosion of 1 Kt at a depth of 300m. The quarry blasts were computed using the explosion plus spall model described in the previous section. Synthetics were examined for several cases, including pure vertical spall and spall with an initial angle of 45 degrees to the horizontal. Green's functions were computed from 0 - 5 Hz using a reflectivity code and convolved with the appropriate source time functions. The spall component of the quarry blast was found to be an important contribution to the quarry blast synthetic. Example synthetics are shown above for the 0.75-5 Hz bandwidth. Because the ripple fired quarry blast is detonated over an extended duration, the 500 2 ton blasts do not add up to an amplitude 500 times the amplitude of each individual 2 ton blast. In order to hide the explosion, the 500 separate charges must be detonated nearly simultaneously.

We conclude that in order to hide a nuclear explosion (bomb) with a seismic yield of 1 Kt, the 1 Kt of chemical explosives would have to be detonated nearly simultaneously. Even so, the overburied explosion may still be visible at high frequencies as anomalous high frequency energy in the quarry blast plus bomb seismogram.

3.0 The effects of the quarry face

3.1 A theoretical model

A theoretical model for the effects of the quarry face has been proposed (Barker et al. 1993). The essence of this model is that for a moment tensor source located behind a non-horizontal surface such as a quarry face, the horizontal couple perpendicular to the face is effectively reduced. Therefore an explosion source no longer looks isotropic when compared to an explosion in a half-space, Mxx < Myy = Mzz. In order to illustrate this effect, we have computed several simulations using 2D and 3D linear finite difference codes.This model is valid for wavelengths long compared to the height of the bench.

3.2 2D modeling

2D linear finite difference calculations have been performed using reciprocity to examine the radiation efficiency of a point explosive source in the vicinity of a quarry face. A plane P or Rayleigh wave is incident upon a

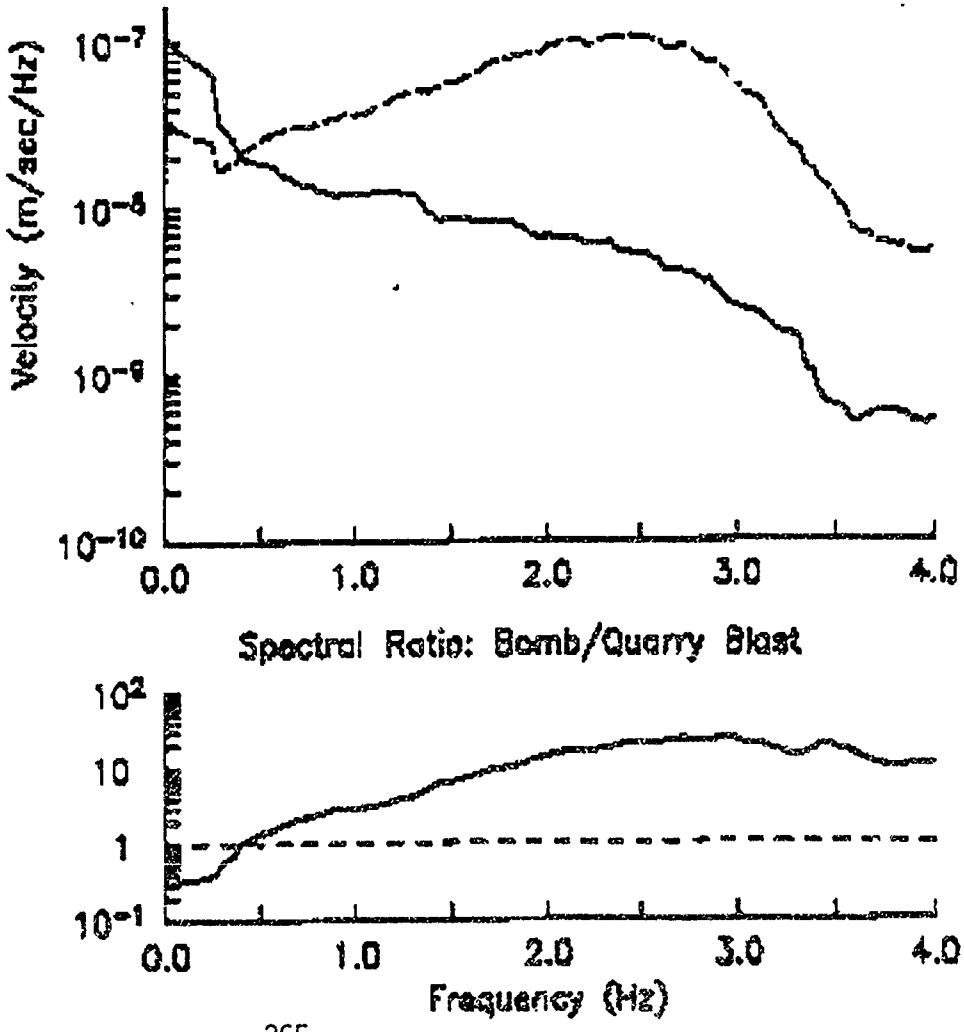

Figure 2.03 Predicted smooth Pg spectra (top) at a distance of 1000 km for the1 Kt bomb (dashed line) and 1 Kt ripple fired quarry blast (solid line). A spectral ratio is shown below to illustrate the enhanced high frequencies in the overburied bomb.

finite difference grid. The dilatation is then monitored on the finite difference grid. The dilatation for a model with free-surface topography (like a quarry) is then compared to dilatation in a half-space. Likewise displacements monitored in the grid are used to infer the radiation from point sources. The result is a map of the efficiency of radiation by sources in the finite difference model relative to sources in a half-space. The results are contoured in figure 3.2.1 for a plane P-waves arriving from the right.

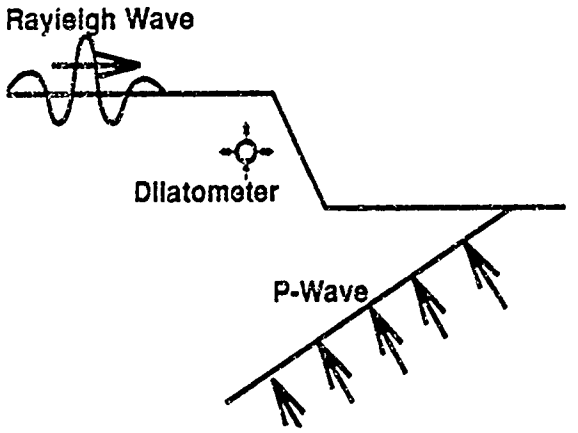

Figure 3.2.1 Reciprocity is used to infer the far-field radiation of P and Rayleigh waves by measuring dilatation and displacement at locations in the 2D grid from incident plane P and Rayleigh waves.

The results shown in Figure 3.2.2 have been found to be insensitive to the take-off angle of the P-wave. Similar results are found for Rayleigh waves arriving from either the right or the left. In all cases, the excitation from a point explosive source at a distance behind the bench less than 1/2 the height of the bench is reduced by nearly 50% relative to excitation in a half-space.

Simulations using incident SV waves show that SV radiation is enhanced by the presence of the bench for the explosive sources relative to sources in a half-space. The explosion behind the bench appears more deviatoric.

The 2D simulations lead to several predictions. First, an explosion behind a quarry face will show reduced excitation of P-waves and Rayleigh waves in directions perpendicular to the quarry face compared to an explosion in a half-space. Point forces applied to the quarry face and behind the quarry face will not be so affected. Half-space Green's functions may be used to model the explosion but the explosion source should be replaced with a non-isotropic source with Mxx about 50% of Myy = Mzz.

3.3 3D Modeling

A 3D finite difference calculation was performed that models a large quarry with vertical faces. A point explosive source was located directly behind the quarry face. Some results are shown in Figures 3.3.1 and 3.3.2 that indicate the P-wave amplitudes are reduced for azimuths

Figure 3.2.2 Excitation efficiency of a point source as a function of location behind a 45 degree quarry face. The moment tensor explosion source (top) is reduced by as much as 50% for locations behind the bench. At distances behind the bench greater than the bench height, the explosion source relative to the half-space is only reduced by 20% or less. A a location just below the toe of the quarry face, the explosion source is enhanced by a factor of 2 or more. The vertical point force source (bottom) is hardly affected by the presence of the quarry face. This analysis is valid for wavelengths much longer than the bench height.

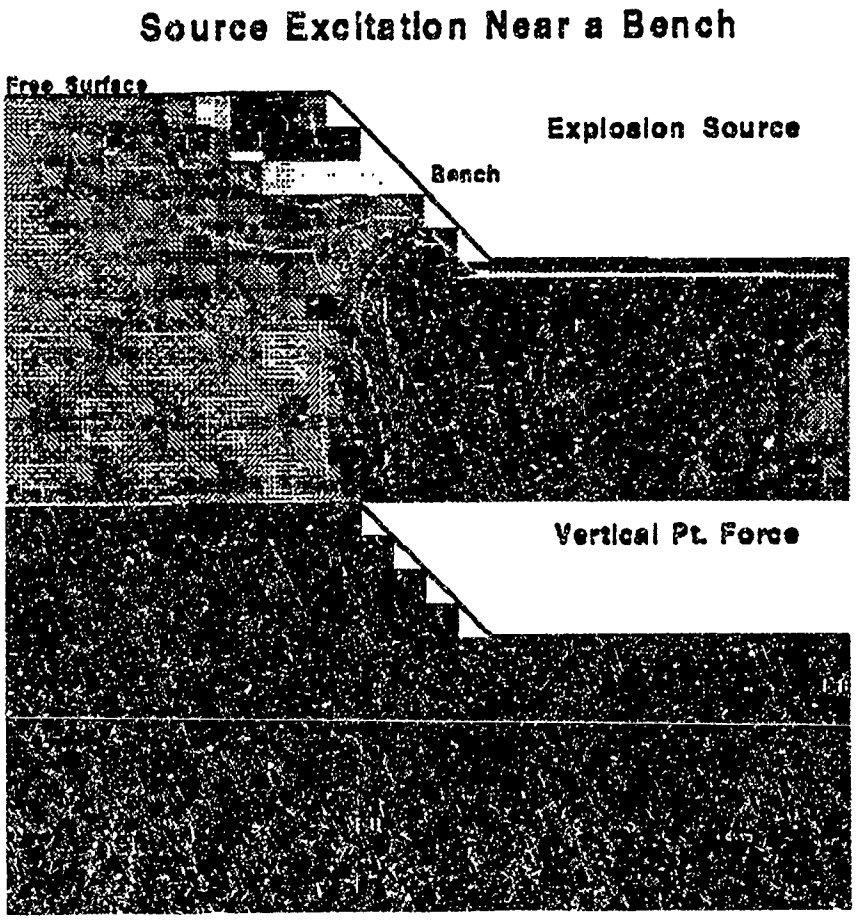

perpendicular to the quarry face. These results are consistent with the results of the 2D simulations.

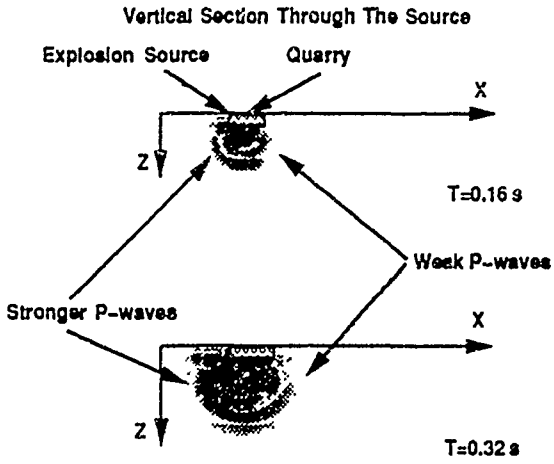

Figure 3.3.1 Vertical section from 3D finite difference simulation. The P-wave wavefront is clearly visible.

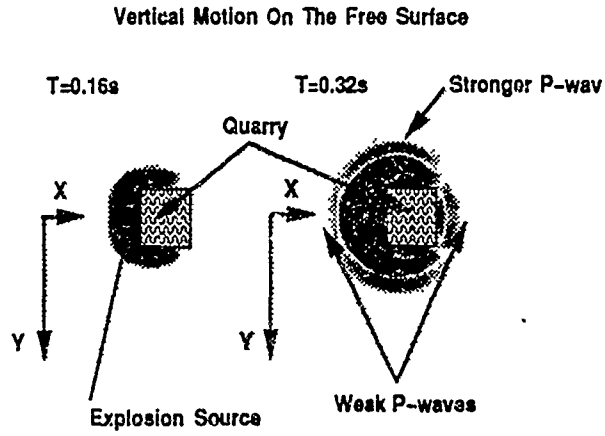

Figure 3.3.2 Vertical motion on the free surface of a 3D finite difference simulation showing the P-wave radiation from a point source behind the quarry face.

The 3D finite difference simulations show that the radiated P-wave is weakest in directions perpendicular to the quarry face, as if the Mxx component of the explosive source were reduced. P-waves radiated parallel to the quarry face are not significantly different from the half-space case (no quarry). The source also radiates SH wave.

4.0 Discrimination

An important problem in discrimination, is the identification of quarry blasts, earthquakes, normally buried nuclear explosions, and overburied or decoupled nuclear explosions. This problem is complicated by the fact that future events of interest will occur in areas where we have little or no prior experience in discriminating explosions and earthquakes. In particular, we expect that overburied and decoupled explosions will not have the characteristic spall signature of normally buried explosions. Even where we have experience with underground nuclear explosions and earthquakes, we have somewhat limited experience with overburied explosions. Most of our discrimination experience is based on normally buried explosions compared to earthquakes or on large quarry blasts compared to earthquakes. Therefore, numerical models of seismic sources may be useful in suggesting useful discriminants for new areas of interest provided they can be calibrated to regions for which we more extensive discrimination experience.

In Figure 4.01 we show comparisons of predicted Pg/Lg spectral ratios for four different M_L=4 seismic sources at 1000 km: a thrust earthquake, a ripple fired quarry blast, a normally buried explosion with spall, and an overburied explosion with no spall. The Lg/Pg ratio is scaled so that the ratio of the earthquake at 1 Hz is 10 and the Lg amplitude at 1 Hz is held nearly constant (M_L=4). The details of this figure depend on the crustal structures and particularly on the crustal Q's. However the qualitative prediction is that at frequencies above 2 Hz, we expect that the earthquake, will have enhanced Lg/Pg ratios relative to those at 1 Hz, the normally buried bomb with spall will have the lowest Lg/Pg ratios at 3 Hz relative to those at 1 Hz, and the quarry blast and overburied or decoupled bomb will be intermediate. These predictions are consistent with observations of Bennett, et al. (1989). In studies of spectral slopes, they found that the ratio of Lg-to-P fell off faster with increasing frequency for normally buried bombs than earthquakes or quarry blasts.

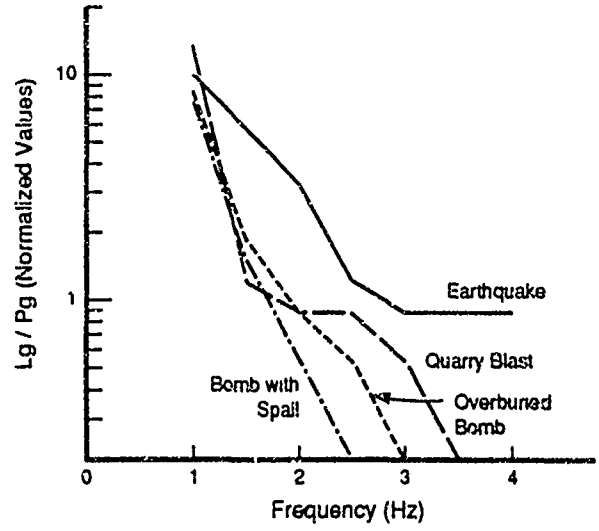

Figure 4.01 Lg/Pg spectral ratio at 1000 km for four sources. Spectra determined from smoothed envelopes of bandpass filtered seismograms.

In Figure 4.02 we show predicted Lg spectra for the same four sources. The spectra are all normalized to 1 at 1 Hz. The quarry blast falls off faster than the earthquake spectrum also consistent with observations of Bennett et. al. (1989). Again the details of this plot will depend on the particular crustal model chosen, but we expect that some of the qualitative results will apply to a wide range of structures. Because of the spall components of the quarry blast and the normally buried bomb we expect that they will show the greatest spectral decay with increasing frequency.

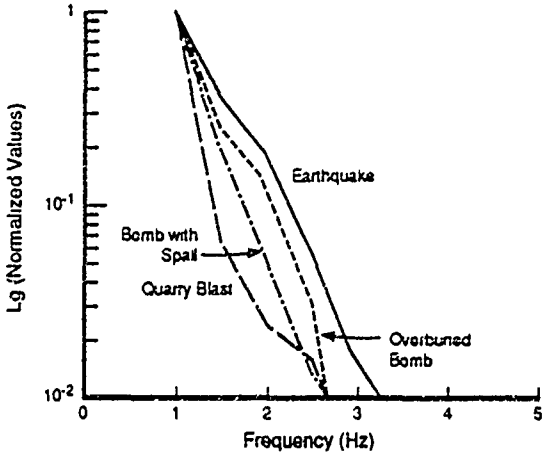

Figure 4.02 Normalized Lg spectra for four sources at 1000km. The earthquake is the most enriched in high frequency Lg.

5.0 Conclusions

We have proposed models for the "spall" contribution of the quarry blast and the effects of the quarry face on the explosive source. These models may have significant implications on our ability to identify and discriminate large quarry blasts from earthquakes, rock-bursts, and nuclear explosions. These models for radiation from the spall source and explosion source behind the non-horizontal free-surface could be tested in a properly designed experimental program. We summarize our specific conclusions below.

- Seismic radiation from the spall part of a typical quarry blast is comparable to the explosion part of the quarry blast source.
- The quarry blast source is a band-limited signal compared to the overburied bomb due to the spall signal and the duration of the distributed quarry blast.
- Pg spectral values rise in the 0.5-3 Hz band for the bomb but decay for the quarry blast source due to the spall contributions and duration of the quarry blast.
- Quarry blast spectra are scalloped primarily due to the duration of the source.
- The explosion will dominate a simultaneous bomb and ripple fired quarry blast if the explosion seismic yield of the bomb exceeds 10% of the total quarry yield.
- Near simultaneous detonation of the entire quarry blast is required to hide an overburied nuclear explosion.
- Seismic amplitudes are insensitive to the direction of the spall as long as there is minimal elevation change.
- A net elevation change comparable to the burden can significantly increase the seismic amplitudes from a quarry blast.
- 2D simulations predict that P and Rayleigh radiation from a point explosion behind the quarry face may be reduced by a factor 50% due to the free-surface face.
- 2D simulations predict that the reduction in seismic signals radiated by a point explosion behind the quarry face for P-waves radiated perpendicular to the face is independent of slowness.
- 2D simulations predict that seismic signals from the point force equivalents of spall are little affected by the free-surface face.
- 3D simulations predict that the effect of the free surface face i introduce an azimuthal radiation pattern and to radiate SH waves.
- Source models for earthquake, quarry blast with spall, overburied explosion, and normally buried explosion with spall predict that frequency dependent Lg and Lg/Pg rations may serve as useful discriminants.

The proposed spall model for seismic radiation from quarry blasts predicts enhanced SV radiation compared to the point explosion source alone. Furthermore, the directivity of spall from a non-horizontal face predicts that SH waves will be generated. Both of these effects make quarry blasts look like deviatoric sources. Because the dwell times for typical quarry blasts are near 1 sec, the typical quarry blast will have a peaked spectra and it is possible that this may lead to useful regional discriminants. Some elements of these models could be tested in properly designed field experiments.

6.0 References

Barker, T.G. and S. M. Day (1990). A simple physical model for spall from nuclear explosions based upon two-dimensional nonlinear numerical simulations, SSS-TR-90-11550

Barker, T.G., K. L. McLaughlin, J. L. Stevens (1993). Numerical simulation of quarry blast sources, SSS-TR-93-13859.

Bennett, T. J., B. W. Barker, K. L. McLaughlin, and J. R. Murphy (1989). Regional discrimination of quarry blasts, earthquakes, and underground nuclear explosions. GL-TR-89-0114, ADA223148.

Langefors, U., and B. Kihlstrom (1963). The Modern Techniques of Rock Blasting, John Wiley and Sons.

PARAMETRIC AND NONPARAMETRIC DISCRIMINATORS FOR REGIONAL EARTHQUAKES AND EXPLOSIONS

Allan D.R. McQuarrie
Robert H. Shumway

Division of Statistics
University of California
Davis, CA 95616

PHILLIPS LABORATORY
Contract F19628-91-K-0033

1. OBJECTIVES

Conventional methods for discriminating between earthquakes and explosions at regional distance have concentrated on extracting *specific features* from the waveforms of the P(usual P_g) and S (usual L_g) phases. The specific features considered generally are amplitude ratios, measures of waveform complexity or various kinds of spectral ratios, suggesting that the main characterization of the differences between earthquakes and explosions reduces to differences between the spectra or differences between the waveforms. Our objective here is to compare some of the classical discriminants in the literature with two methods based on *statistical optimality criteria*. We consider first an *optimal nonparametric discriminator*, derived under the assumption that the earthquake and explosion P and S phases are uncorrelated stationary Gaussian processes with unequal spectra. The likelihood criterion that obtains displays the optimal statistic as the result of comparing spectral matches between the observed series and the average earthquake spectrum against a comparable match with the explosion spectrum. A second *optimal parametric discriminator* models the P phase as a modulated autoregressive process, where the modulating function is consistent with models for earthquake and explosion waveforms found in the literature. The nonparametric method is obviously tuned to spectral differences whereas the parametric method is closely allied with notions relating to complexity and amplitude ratios.

Numerous investigators have pointed out that the logarithms of $P_g - L_g$ amplitude ratios tend to be lower for earthquakes than for explosions (see, for example Blandford, 1981, Bennett and Murphy, 1986, Taylor et al, 1989). This idea has been extended to include a consideration of spectral ratios involving the P and S groups. Bennett and Murphy (1986) note that for western U.S. events, earthquake L_g spectra contained more high frequencies, and that the ratio of the logarithms of low frequency (.5-1Hz) L_g to higher frequency L_g (2-4Hz) tend to be larger for explosions. Taylor et al (1989) also use this ratio over the frequency bands (1-2Hz) and (6-8Hz) and extended the consideration to the P_g phase. Dysart and Pulli (1990) have also considered various features extracted from the spectra and have developed neural networks as an alternative to simple linear combinations of features for discrimination. Finally, Kim et al (1992) note that for eastern U.S. events the ratios of P_g to L_g spectra are generally higher for explosions. Some early results using the three coefficients in an third-order autoregressive model for the coda as features are available in Tjøstheim (1974) and Bungum and Tjøstheim(1976).

The spectral methods discussed above generate *features* that can differ for earthquakes and explosions in certain specific data bases. Such features as P to S amplitude ratios or spectral ratios within phases or between phases can then be put into a vector and transformed (usually, logarithms are taken for a better approximation to normality) in order to apply one of the standard linear or quadratic discriminant analysis techniques. Examples are Shumway and Blandford (1974), Taylor et al (1989), Dysart and Pulli (1990) and Kim et al (1992). Two features at a time are often plotted in various combinations for earthquakes and explosions to show graphically the separation of the two populations (see the above references and also Bennett and Murphy, 1986).

Shumway and Blandford (1976) introduced an optimal method combining optimal linear and quadratic discriminant functions based on modeling the underlying short period teleseismic P waveforms as Gaussian processes differing in both the mean value signals and the spectral densities. For regional events, it is clear

that the notion of a fixed mean P or S waveform which differs for earthquakes and explosions is not a relevant comparison but that the notion that the earthquakes and explosions differ only in their spectra does make a lot of sense. This implies that the quadratic part of the optimal detector used by Shumway and Blandford (1976) (see also Shumway, 1982, 1988) will have the lowest misclassification rate of *any function* based on the spectra, including those given in the preceding paragraph. Such a detector has been applied several times in the literature to seismic discrimination, notably by Dargahi-Noubary and Laycock (1981), Shumway (1982,1988) and Alagon (1989). We develop and apply a modified version of such a detector to a P and S phases from population of regional Scandinavian earthquakes and explosions given in Blandford (1993). Since the model depends only on stationarity of the series and not on a specific parametric model for the spectrum, we refer to it as the *optimal nonparametric discriminator.*

Blandford (1993) discusses a notion of complexity as a discriminant and shows that it has potential for discrimination of the events in the Scandinavian database. The idea relates to the often quoted statement by analysts that complexity is a strong component of their visual procedure for discrimination. Blandford proposes a notion of complexity related to the observation that explosions generate usually an *impulsive signal* whereas earthquakes tend to generate a more *emergent signal.* We develop here an *optimal parametric discriminator* by assuming that the earthquake and explosion populations can be expressed as uniformly modulated autoregressive process, parameters of the modulating function characterize separately the emergent and impulsive properties of the signal. Our underlying model for complexity is taken directly from a suggestion of Dargahi-Noubary (1992) that is based on standard source theory.

2. RESEARCH ACCOMPLISHED

2.1 Data Compilation

For our test data, we use a subset of stations recording 8 earthquakes and 8 explosions in Scandinavia from the arrays NORESS, ARCESS and FINESS as described in Blandford (1993). According to Blandford, "The events were selected with consideration for having sufficient S/N at single elements so that all phases could be clearly seen on all component of a single instrument ". From Table 1 in Blandford, we took explosions three through ten and from Table 2, we used all eight earthquakes. All events chosen by Blandford were on or near land and were distributed uniformly over Scandinavia to minimize the possibility that discriminators might be keying on location or land-sea differences. Figure 1 shows portions of typical earthquakes and explosions (sampled at 20 Hz) along with the portions of the record that we visually determined as the P and S phases. We did not identify specific phases through velocity computations but simply chose fairly broad (25 second) windows that seemed to include the P and S phases.

2.2 Discriminators Based on Feature Extraction

For feature extraction, we consider a number of classical measures related to the spectrum. They are logarithms of (1) P and S amplitudes, (2) P and S mean square error, (3) combinations of P and S spectra (0-3Hz, 3-6Hz, 6-9Hz, 0-2Hz, 2-4Hz) and (4) autoregressive coefficients of the P and S phases for a third order model. The frequency ranges were not exactly comparable to those used in the literature (.5-1Hz, 2-4 Hz in Bennett and Murphy, 1986, 1-2Hz, 6-8Hz in Taylor et al, 1989, 5-25(5)Hz in Kim et al, 1992) but were chosen by visually inspecting the separate spectra and the average earthquake and explosion spectra shown in Figure 2. A further comment is that we have avoided taking ratios of spectra which tend to pre-assume that the best discriminator will be the simple difference ($\log \frac{P}{S} = \log P - \log S$). It is clear that taking logarithms improves the approximation to multivariate normality for these features but dividing may distort the variance and invalidate the equal covariance assumption that is helpful for linear discriminant analysis.

The best discriminators of this group were the classical and ordinary measures (1) and (2), (1) is plotted in Figure 3. A linear discriminant analysis with equal prior probabilities tended to confirm the ratio procedure. For example the optimal linear discriminant function for P and S amplitudes was

$$d = -20.59 \log P + 15.97 \log S + 14.32$$

Both (1) and (2) had perfect classification in the test sample and classified the first explosion as an earthquake in the holdout-one procedure. The best of the spectral group (3), also plotted in Figure 3, was the comparison

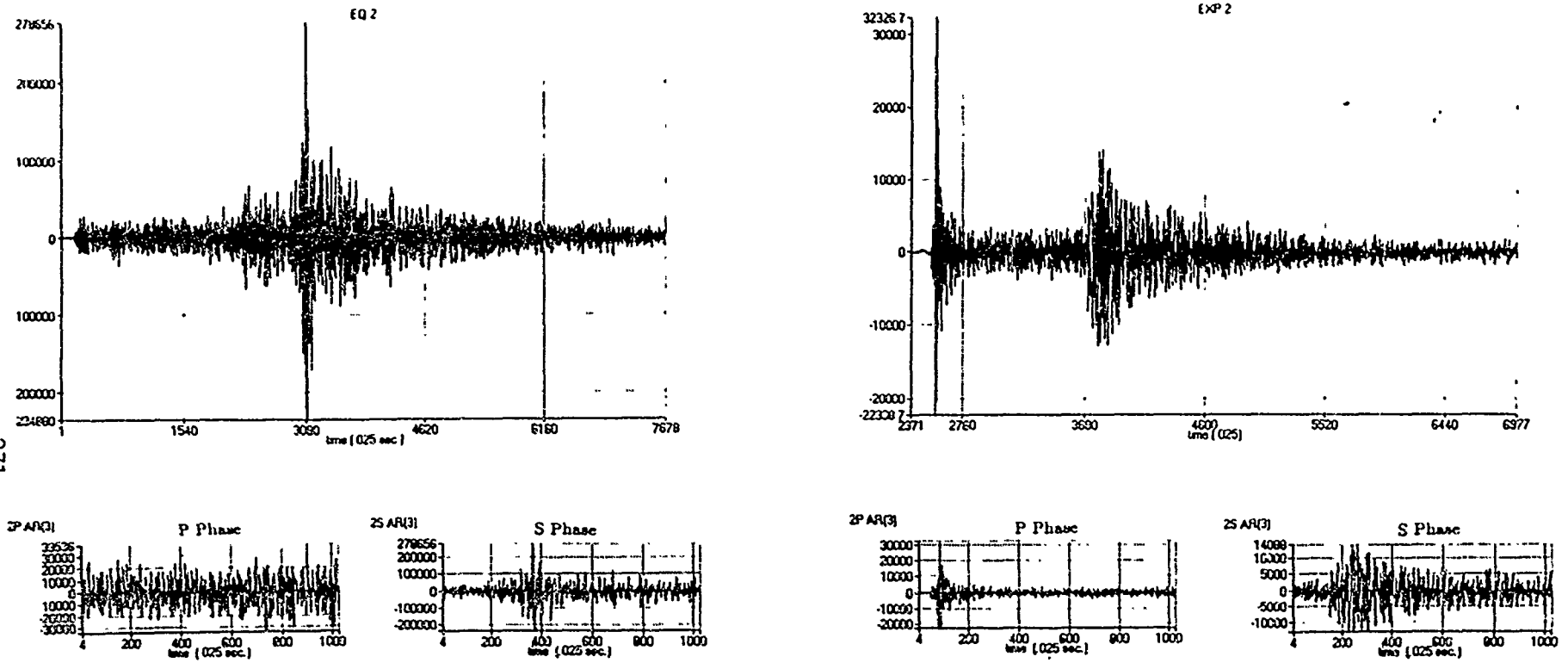

Figure 1: A well defined earthquake and explosion (Top Panel) and the extracted P and S components shown below. Note the emergent earthquake P and the impulsive explosion P and the relative amplitudes of the P and S components.

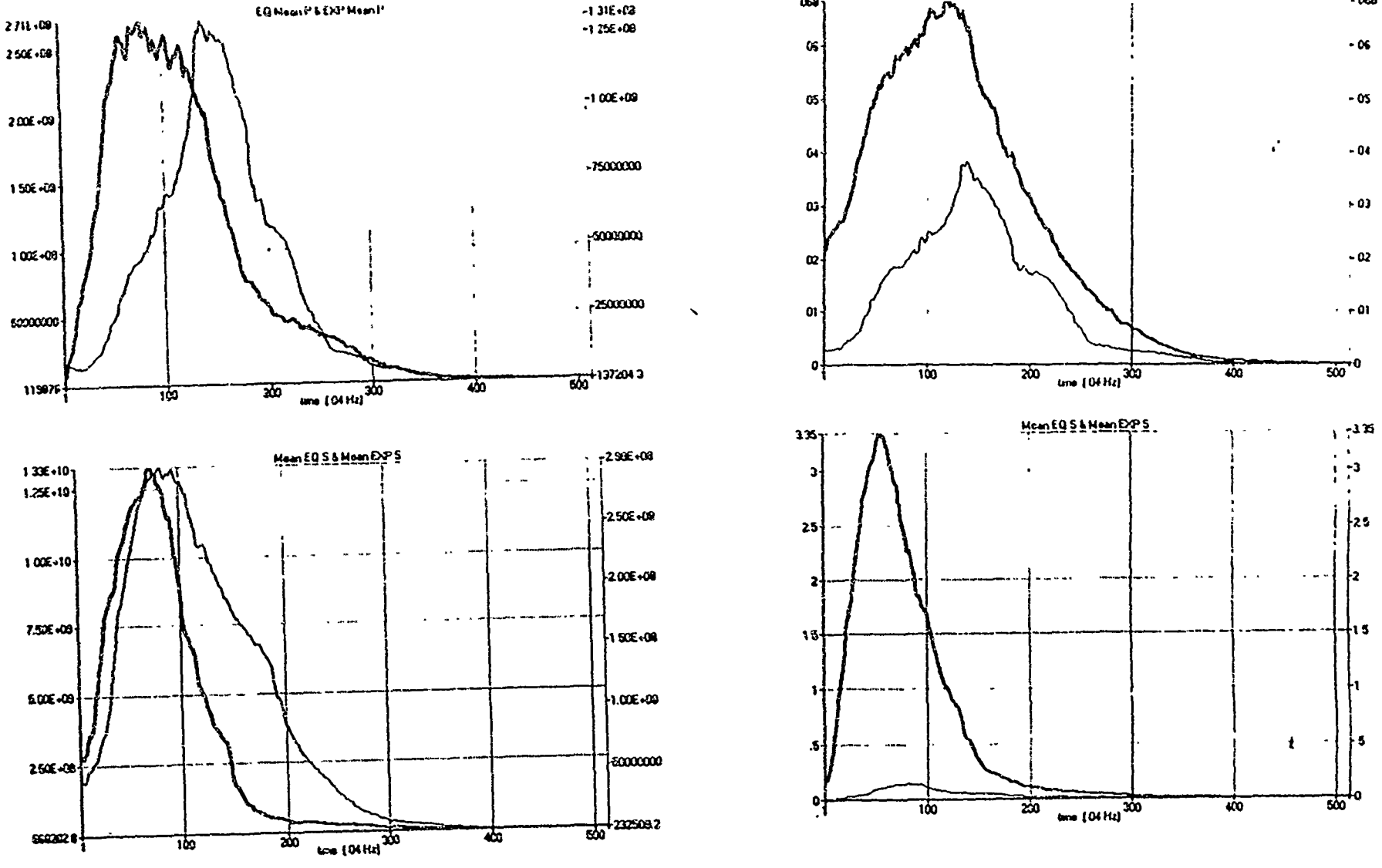

Figure 2: Average Earthquake and Explosion Spectra (0-20 Hz, 100 points=4 Hz). The darker line is for earthquakes and the lighter line is for explosions. The left side shows the spectra on two different scales (right and left ordinates). The right panel shows the spectra on the same scale. Note the higher frequencies (relatively) in the explosion P and the higher frequencies in the earthquake S.

of P(0-3Hz) to S(0-3Hz) which had the same performance as (1) and (2). The other techniques in (3) gave inferior performances and Method (4) had the worst performance with almost no discrimination capability. Because of the small samples involved, we only compared pairwise spectra under method (3).

2.3 Optimal Nonparametric and Parametric Discriminators

For our *optimal nonparametric* classification procedure consider the classical approach to discriminating between two stationary bivariate Gaussian processes (H_1 . Earthquakes and H_2 . Explosions) with unequal matrix covariance functions (spectra). An approximation (see, for example, Shumway, 1988)to the optimal test statistic is related to the match between the Fourier spectrum of the series of unknown origin and the spectrum of the earthquake or explosion process. Consider the matching function under $H_j, j = 1, 2$, say

$$d_j = -\sum_{k=0}^{T-1} \{f_j(\nu_k) + \frac{|X(k)|^2}{f_j(\nu_k)}\},$$

where we replace . by P or S depending on the phase to be considered, $X(k)$ is the discrete Fourier transform of the data x_t and $f_j(\nu_k)$ denotes the spectrum for phase . under hypothesis H_j. The optimal quadratic discriminator is then

$$Q = (d_{1P} - d_{2P}) + (d_{1S} - d_{2S})$$

where we accept H_1 (earthquake) if $Q > 0$ and H_2 (explosion) if $Q \leq 0$. Note that the P and S phases need to be uncorrelated processes for this detector to be optimal. We have computed cross spectra and coherence functions of the paired phases for every event and they are not significantly greater than zero.

In order to apply the discriminant function defined above, we need to have estimators for the earthquake and explosion spectra, say $f_1(\nu)$ and $f_2(\nu)$. These can be taken as predefined values if no training sample is available or as the averages of the earthquake and explosion spectra respectively if a training sample is available. We take the values here of the average earthquake and explosion spectra shown in Figure 2. The P and S components of the quadratic detector are plotted in Figure 4 and we see that both the test sample and the holdout procedures achieve perfect classification. Note that the performance of the holdout procedure emulates the performance that a discriminant function defined from a training sample would have on a new observation. One computes the average of the spectra holding out one observation at a time and then using the test statistic to classify the held out observation.

In order to define an *optimal parametric discriminator*, consider the model for the earthquake or explosion P phase specified as

$$y_t = a_t(\theta_1, \theta_2)x_t + v_t$$

where

$$x_t = \phi_1 x_{t-1} + \phi_2 x_{t-2} + w_t$$

with

$$a_t(\theta_1, \theta_2) = \theta_1 t e^{-\theta_2 t}$$

the modulating function of the underlying earthquake or explosion.

The modulating function, suggested by Dargahi-Noubary (1992), has a shape which depends on the parameters θ_1 and θ_2 Small values of θ_1 and θ_2 should be associated with earthquakes, large values of these two parameters would characterize explosions since these larger values will produce rather impulsive waveforms. The two errors have variances σ_v^2 and σ_w^2, for identifiability, it appears that σ_w^2 should be fixed at a constant value. Determining the optimal discriminant function would depend on developing a test of the hypothesis H_1 $\theta_1 = \theta_{11}, \theta_2 = \theta_{12}$ against H_2 $\theta_1 = \theta_{21}, \theta_2 = \theta_{22}$ We are using a hybrid of the EM and

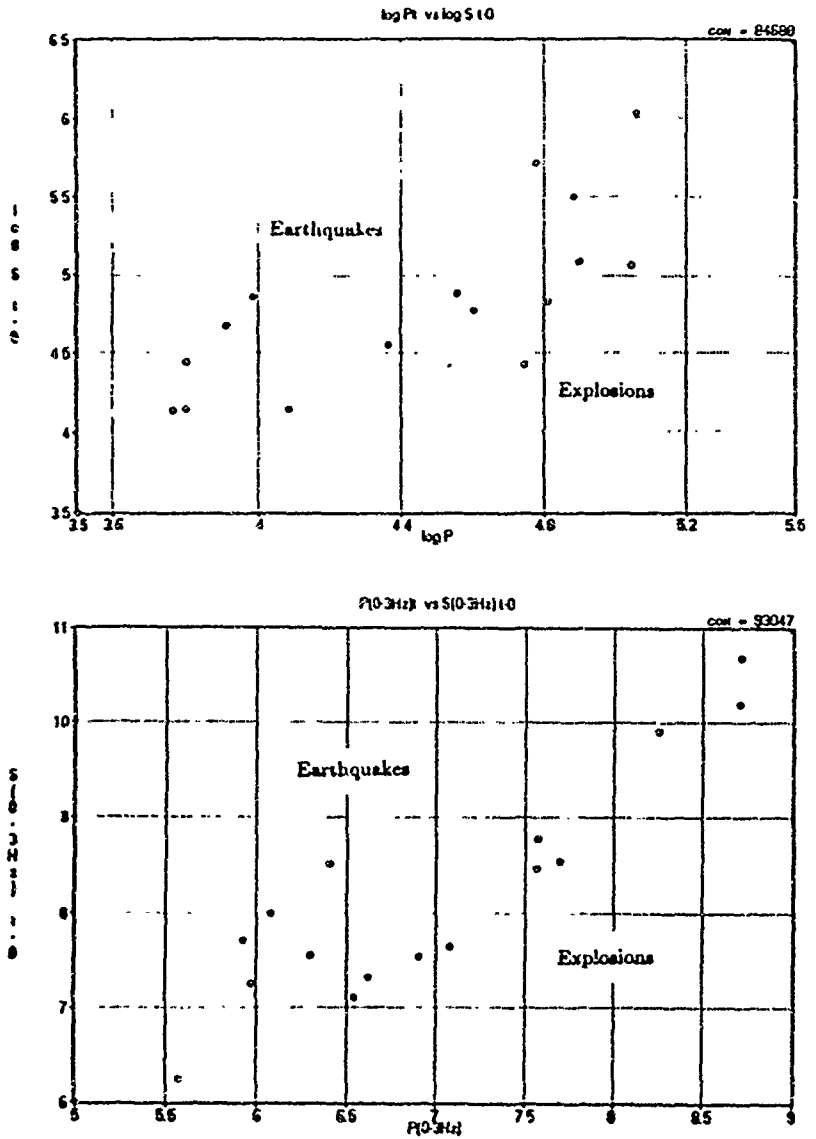

Figure 3: Scatter diagrams showing the separation between earthquakes (open circles) and explosions (solid circles) for log amplitudes of P and S (top panel) and log spectra from 0-3 Hz (bottom panel).

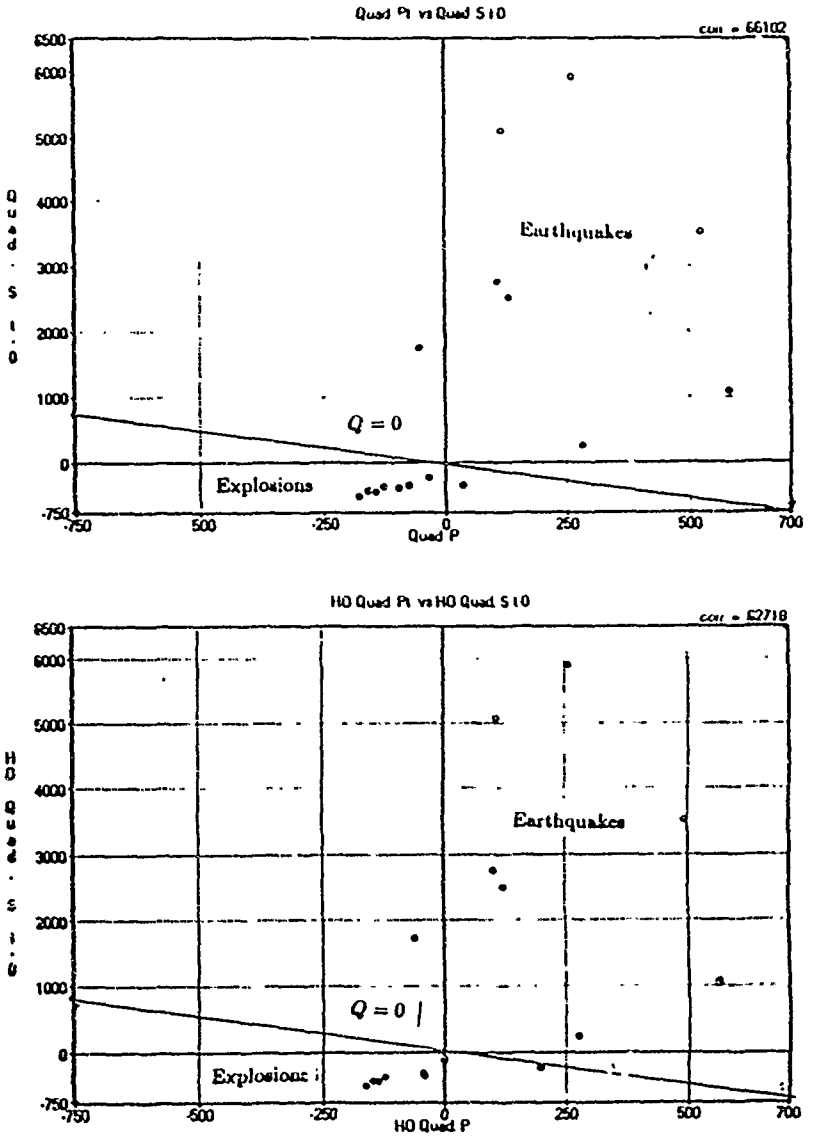

Figure 4: Separation achieved for earthquakes (open circles) and explosions (solid circles) using the optimal quadratic detector.The top panel gives the results using the learning sample whereas the bottom shows the holdout scores. The separation line $Q = 0$ is shown in both figures.

Newton-Raphson algorithms to estimate the parameters in the model by maximum likelihood. For values of the target θ's in the two hypotheses, we will use the overall values for these parameters estimated from the training sample. Then for each series, a likelihood test of the hypotheses would involve comparing the log likelihood evaluated at θ_{11}, θ_{12} with the log likelihood evaluated at θ_{21}, θ_{22}. Currently, we are developing the computational procedures for computing maximum likelihood estimators for the parameters of the model for a single process.

3. CONCLUSIONS AND RECOMMENDATIONS

We conclude that the optimal nonparametric procedures based on spectral differences discriminate significantly better than those based on extracting simple features of the process for the small population of Scandinavian earthquakes and explosions considered in this study. The advantage of the nonparametric procedure is its ability to tune against all differences present in the earthquake and explosion spectra and not to specific frequency bands or phases. Furthermore, for more realistic larger samples and more than one station used per event, the procedure can work even better. The application of the nonparametric procedure to larger data bases should provide the standard baseline statistic for comparison with more esoteric nonlinear methods such as classification trees or neural nets as applied to specific feature vectors.

The modeling of complexity using the waveform model proposed here may also add discrimination capability for the cases where the spectral matching function given by the nonparametric procedure is not enough. We will continue to develop the likelihood ratio properties of the waveform comparison test and apply it to the small test sample of Scandinavian events.

REFERENCES

Alagon, J. (1989). Spectral discrimination for two groups of time series. *J. Time Series Analysis*, **10**, 203-214.

Blandford, R.R. (1981). Seismic discrimination at regional distances. In *Identification of Seismic Sources-Earthquake or Underground Explosions*. Ed. by E.S. Husebye and S. Mykkeltveit, D. Reidel Publishing Co, 695-740.

Blandford, R.R. (1985). Regional detection, location, discrimination and yield determination. In *The VELA Program*, Ann Kerr, Ed. 787-816, Executive Graphic Services 85-080931, 787-816.

Blandford, R.R. (1993). Discrimination of earthquakes and explosions at regional distances using complexity. Presented at Air Force Technical Applications Review, Patrick AFB, Feb. 16-17, 1993.

Bennett, T.J. and J.R. Murphy (1986). Analysis of seismic discrimination capabilities using regional data from western U.S. events. *Bull. Seismolog. Soc. Amer.*, 76, 1069-1086.

Bungum, H. and Tjøstheim, D. (1976). Discrimination between Eurasian earthquakes and underground explosions using the M_b . M_s method and short period autoregressive parameters. *Geophys. J. Roy. Astonom. Soc.*, **45**, 371-392.

Dargahi-Noubary, G.R. and P.J. Laycock (1981). Spectral ratio discriminants and information theory. *J. Time Series Analysis*, **2**, 71-86.

Dargahi-Noubary, G.R. (1992). Models for seismic records, Why uniformly modulated ARMA?. *Soil Dynamics and Earthquake Engineering*, **11**, 381-384.

Dysart, P. and J.J. Pulli (1990). Regional seismic event classification at the NORESS array. Seismological measurements and the use of trained neural networks. *Bull. Seismolog. Soc. Am.* **80**, 1910-1933

Kim, W-Y, D.W. Simpson and P.G. Richards (1992). Discrimination of regional earthquakes and explosions in eastern U.S. using high-frequency data Lamont-Doherty Earth Observatory, Columbia University. Preprint.

Shumway, R.H (1982). Discriminant analysis for time series. In *Handbook of Statistics, Vol. 2, Pattern Recognition and Reduction of Dimensionality*, ed. P R. Krishnaiah. 1-43. Amsterdam. North Holland.

Shumway, R.H. (1988) *Applied Statistical Time Series Analysis*. Chapter 5. Englewood Cliffs. Prentice-Hall.

Shumway. R.H and R. Blandford (1974). An examination of some new and classical short period discriminants. *Seismic Data Analysis Center, Report No. TR-74-10*. P.O Box 334. Alexandria, VA.

Taylor. S.R.. M.R. Denny. E.S Vergino and R.E. Glaser (1989) Regional discrimination between NTS explosions and western U.S. earthquakes (1989). *Bull. Seismology. Soc. Amer.*, bf 79, 1142-1176.

Tjøstheim, D. (1975) Autoregressive representation of seismic P-wave signals with an application to the problem of short- period discriminants. *Geophys. J. R. Astro. Soc.*, 43. 269-291.

Lg Q, Lg Coda Q, and Yield Estimation in Eurasia

B.J. Mitchell, J.K. Xie, Y. Pan and J. Ni
Department of Earth and Atmospheric Sciences
Saint Louis University
St. Louis, MO 63103

Contract F29601-91-K-DB19

Objectives

There are two objectives of this research. First, we want to develop tomographic maps of Lg coda Q and its frequency dependence at 1 Hz which cover as much of Eurasia as possible and to relate these to tectonic and geologic features of the crust. Past research, such as Mitchell (1975, 1981) have shown that the degree of tectonic acitivity in a region is closely related to Q values there, but that other factors, such as the thickness of young sediments (Mitchell and Hwang, 1987) can also affect those values. A second object of this research is to develop a method to simultaneously determine Lg source spectra and path Q and to apply the method to events in Eurasia. The parameters to be determined are the corner frequencies and seismic moments for all sources and Lg Q_0 (Lg Q at 1 Hz) and its frequency dependence(η) along all paths between sources and recording stations.

Research Accomplished

We have applied the tomographic method of Xie and Mitchell (1990) to map the regional variation of Lg coda Q and its frequency dependence across most of Eurasia between about 20 and 80 degrees north latitude and between about 0 and 120 degrees east longitude (Figures 1 and 2). The region includes much of northern Europe, including the Barents shelf, almost all of eastern Europe, and all of northern and central Asia except for the northwestern portion of Siberia where data are lacking. Other regions where our maps are incomplete are the Iberian penninsula, the Arabian peninsula, southern portions of India, Pakistan and Iran, and a small region of sourtheastern Asia. The mapping was made using Lg coda written on 358 seismograms collected from various WWSSN, GSN, CDSN, IRIS, NORSAR, and ARCESS stations distributed throughout Eurasia. The maps of Figures 1 and 2 are similar to those presented earlier (Pan *et al.*, 1992), but incorporate additional data, especially in the region of Scandinavia and the Barents shelf.

Values of Q_0 and η for each event-station pair were obtained using the stacked spectral ratio (SSR) method of Xie and Nuttli (1988) where it is assumed that Lg coda Q can be expressed as $Q_C(f)=Q_0 f^{\eta}$. The SSR method yields values of Q_0 and η with smaller variances than those associated with earlier methods and reduces tradeoffs between Q_0 and η which have plagued some studies.

Our images of Q_0 and η show the following features:

1. A swath of high values 800-1100 extneding from the Barents shelf, across northern Scandinavia, the northern portions of eastern Europe and into central Asia. These high values correspond spatially with the the East European platform and the southwestern portion of the Siberian

Craton. Values throughout much of the Siberian Craton are substantially lower (500 or less) than than values throughout much of the East European platform and the southwestern portion of the Siverian Craton. These reduced values may be related to tectonic activity which occurred in that region in Mesozoic time.

2. The East European platform and Siberian craton are separated by the Central Asian Fold Belt which appears to be associated with lower Q values.

3. Very low values (200-300) occur through a belt in the southernmost portions of Eurasia stretching from Europe to southeastern Asia. These values are probably due to cracks and interstitial fluids produced by continuing tectonic activity those regions.

4. Frequency dependence values vary between about 0.0 and 1.0 with no clearcut relationship appearing to characterize those values with respect to the Q_0 values.

The procedure which we have developed for simultaneously determining source parameters and path Q and frequency dependence using Lg waves uses the formulation

$$A_i^{Lg}(f) = S(f,\theta_i)G(\Delta_i)\exp\left\{-\frac{\pi f \tau_i}{Q_i(f)}\right\}X_i(f)r_i(f) \qquad (1)$$

where f is frequency, $A_i^{Lg}(f)$ is the Lg displacement spectrum at the ith station, θ_i, Δ_i, τ_i, and $Q_i(f)$ are azimuth, distance, mean Lg travel time, and Lg quality factor from the source to the ith station. $S(f,\theta_i)$ is the source-to-Lg spectral radiation in the direction of θ_i, which we take as the Lg source spectrum. $G(\Delta_i)$ is the geometrical spreading factor and typically has the form

$$G(\Delta_i) = (\Delta_0\Delta_1)^{-1/2} \qquad (2)$$

where Δ_0 is a reference distance.

For earthquake sources, $S(f,\theta_i)$ can be represented by an omega-square model, and for explosive sources, by a simplified Mueller-Murphy model (Sereno *et al.*, 1988). If we assume that radiation patterns are radially symmetric then the equations which we invert can be applied to

$$S^{eq}(f) = \frac{M_0}{4\pi\rho v_s^3}\frac{1}{1+f^2/f_c^2} \qquad (3)$$

for earthquakes, and

$$S^{exp}(f) = \frac{M_0}{4\pi\rho v_s^3}\frac{1}{\left[1+(1-2\beta)f^2/f_c^2+\beta^2 f^4/f_c^4\right]^{1/2}} \qquad (4)$$

for explosions. In the above equations, M_0 is seismic moment, f_c is corner frequency, and β is a parameter which quantifies the overshoot effect in the Mueller-Murphy model. Synthetic Lg spectra calculated with inverted source parameters and path $Q_{Lg}(f)$ and for five stations which recorded the JVE event are compared with observed spectra in Figure 3. Details on the derivation of these equations and on the inversion process are given in Xie (1993).

The method was applied to Lg waves generated by three underground nuclear explosions in eastern Kazakhstan, the largest of which is a Joint Verification Experiment (JVE) event. Table 1 lists the location parameters of the events as well as the moments and corner frequencies determined for them. The values for the JVE event are in excellent agreement with previous estimates obtained using other methods and phases as well as with source scaling relationships developed for NTS explosions, and the values for the smaller events indicate that the yields are consistent with those predicted using ISC m_b values and an m_b-yield relationship.

The path-averaged apparent Q_0 values for the five paths of this study are shown in Figure 4 and the paths are superposed over the values of Lg coda Q at 1 Hz obtained by Xie and Mitchell(1991) in Figure 5. The Lg Q values of this study agree well with the Lg coda Q values determined earlier.

Conclusions and Recommendations

The pattern of Q_0 variations across Eurasia (Figure 1) shows clear relationships with many of the tectonic features of Eurasia. The highest values occur in the East European platform. The Siberian craton also exhibits high values, but not as high as those of the East European platform. Values in the latter region may have been caused by more recent (Mesozoic) tectonic activity there. Lower values, apparently associated with the Central Asian Fold Belt separate the two cratons. Very low values of Q_0 characterize regions where tectonic activity is still occurring throughout Eurasia. There are several ways in which this work can be extended to improve our knowledge of the attenuative properties of the Eurasian crust. These include obtaining tomographic images of attenuation of other regional phases, such as Sn, extension to higher frequencies, and integrated studies of Lg Q and Lg coda Q.

A new method of simultaneously determining event moments and corner frequencies along with anelastic parameters along paths of travel has been successfully developed and applied to three nuclear events in Kazakhstan. Results obtained for both source parameters and path Q values are consistent with values obtained using other methods. It will be important to apply this method to a large number of events and paths in Eurasia and other continents.

References

Mitchell, B.J., Regional Rayleigh wave attenuation in North America, *J. Geophys. Res.*, 35, 4904-4916, 1975.

Mitchell, B.J., Effect of low-Q sediments and crust Q on Lg attenuation in the United States, *Bull. Seism. Soc. Am.*, 77, 1197-1210, 1987.

Pan, Y., B.J. Mitchell, J. Xie, and J. Ni, Lg coda Q across northern Eurasia, in Proceeding of the 14th Annual PL/DARPA Seismic Research Symposium, 15-18 September 1992, edited by J.F. Lewkowicz and J.M. McPhetres, 311-317, 1992, PL-TR-92-2210, ADA256711.

Sereno, T.J., S.R. Bratt, and T.C. Bache, Simultaneous inversion of regional wave spectra for attenuation and seismic moment in Scandinavia, *J. Geophys. Res.*,, 93, 2019-2036, 1988.

Xie, J., Simultaneous inversion for source spectrum and path Q using Lg with application to three Semipalatinsk explosions, *Bull. Seism. Soc. Am.*, in press, 1993.

Xie, J., and O.W. Nuttli, Interpretation of high-frequency coda at large distances: stochastic modeling and method of inversion, *Geophys. J.*, 95, 579-595, 1988.

Xie, J., and B.J. Mitchell, Attenuation of multiphase surface waves in the Basin and Range province, part I: Lg and Lg coda, *Geophys. J. Int.*, 102, 121-137, 1990.

Xie, J., and B.J. Mitchell, Lg coda Q across Eurasia, in Yield and Discrimination Studies in Stable Continental Regions, Rpt. PL-TR-91-2286, Phillips Laboratory, Hanscom AFB, MA, 77-91, 1991, ADA251590.

able 1. Event and path parameters †

Event Date	Origin Time	m_b	Location	Seismic Moment (dyne.cm)	Corner Frequency	Average Q_0	Average η
ep. 14, 88*	3H59M57.6S	6.1	49.81°N, 78.80°E	$1.3 (\pm 0.1) \times 10^{23}$	0.56 ± 0.02 hz	657 ± 129	0.31 ± 0.02
ov. 12, 88	3H30M30.8S	5.4	50.05°N, 78.98°E	$2.6 (\pm 0.3) \times 10^{22}$	0.82 ± 0.02 hz	557 ± 94	0.48 ± 0.01
ov. 23, 88	3H57M06.8S	5.4	49.77°N, 78.06°E	$1.8 (\pm 0.2) \times 10^{22}$	0.70 ± 0.02 hz	621 ± 127	0.49 ± 0.02

The origin times, locations and magnitudes are from the ISC bulletin; the seismic moments, corner frequencies and ath-averaged Q_0 and η values are obtained in this study with β in equation (5) set to be 0.75 (Poisson media).

The Joint Verification Experiment (JVE) event.

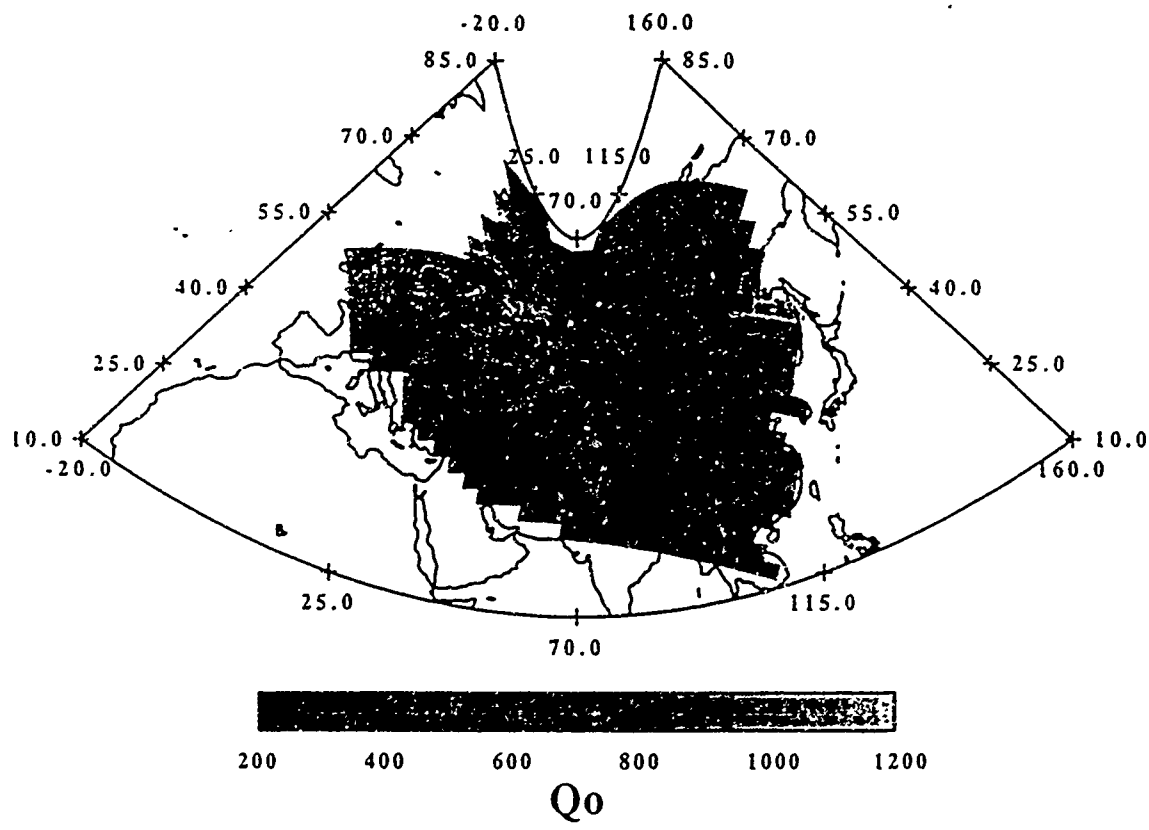

Figure 1. Map of Lg coda Q at 1 Hz derived from a tomographic inversion of recorded data in Eurasia.

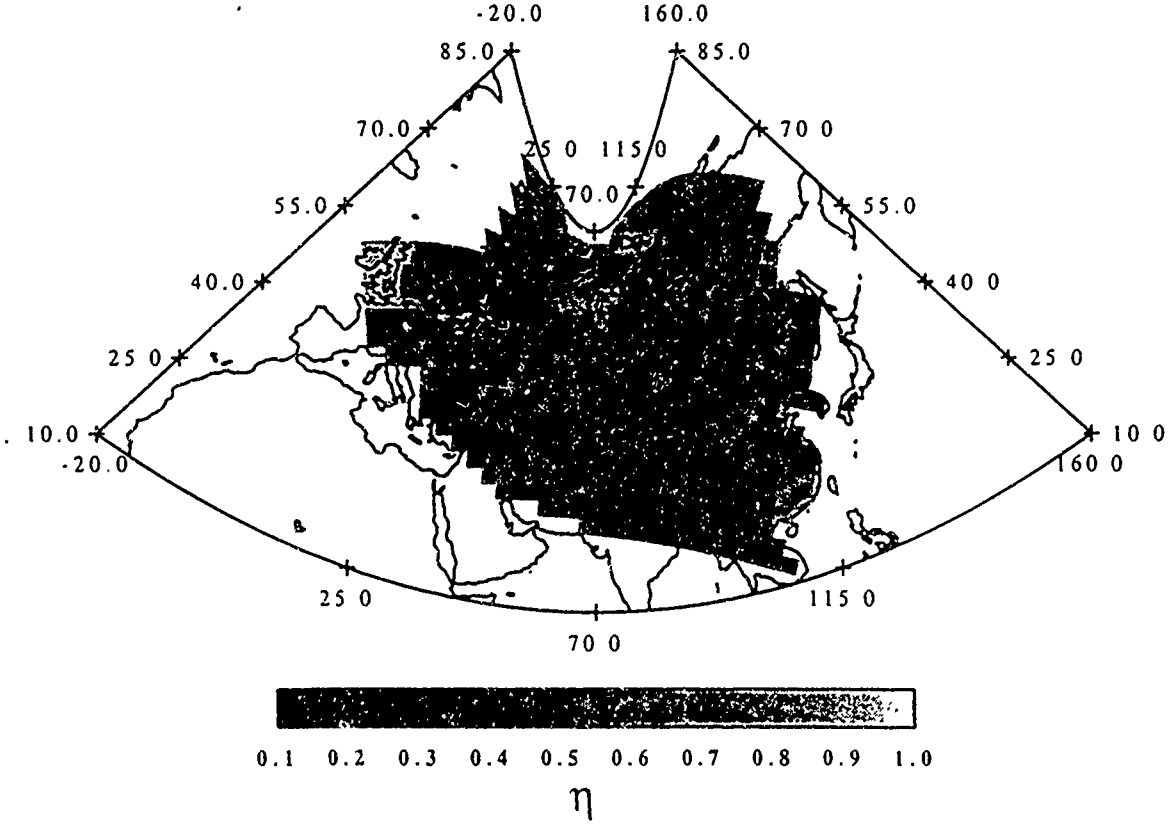

Figure 2. Map of the frequency dependence of Lg coda Q at 1 Hz derived from a tomographic inversion of recorded data in Eurasia.

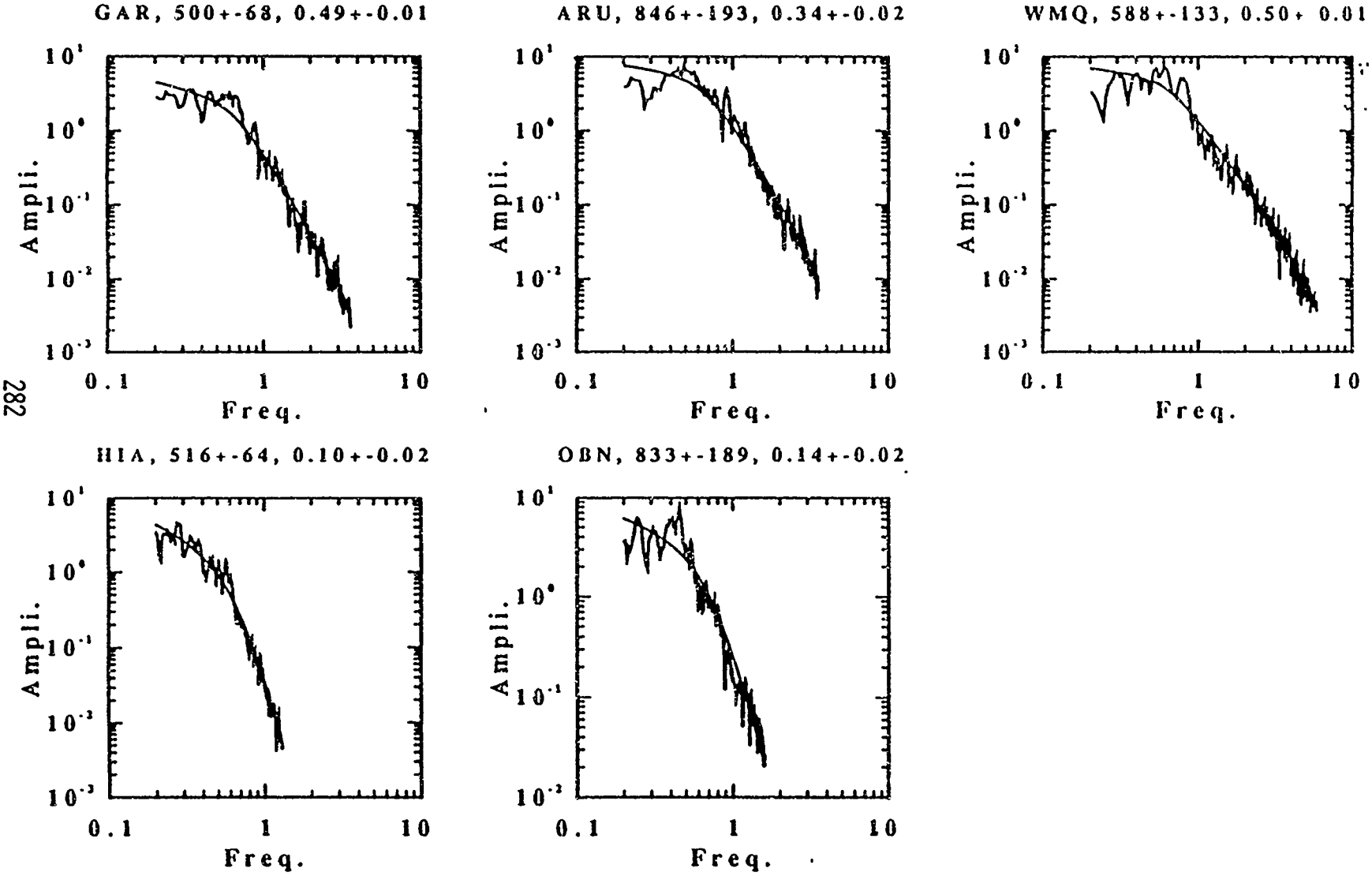

Figure 3. Synthetic Lg spectra for all five stations which recorded the JVE event plotted with observed the observed spectrum at each station. Amplitude is given in units of 10^{22} dyne-cm.

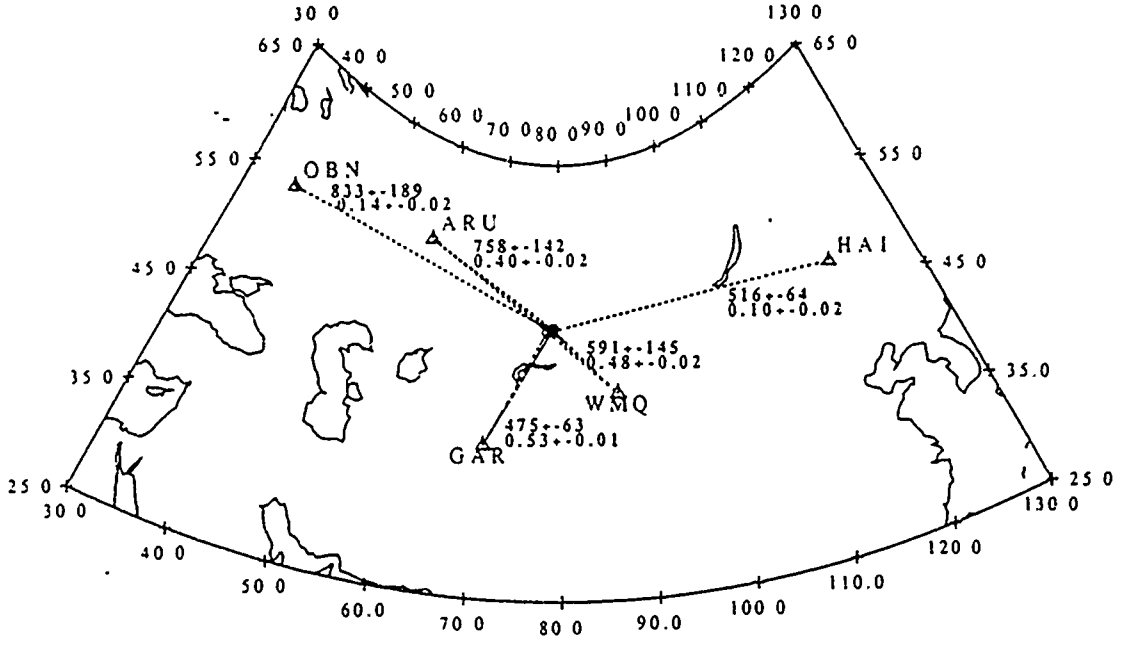

Figure 4. Great circle paths from the three nuclear explosions to five IRIS/CDSN stations. Numbers denote values of Q_o and η values for each path.

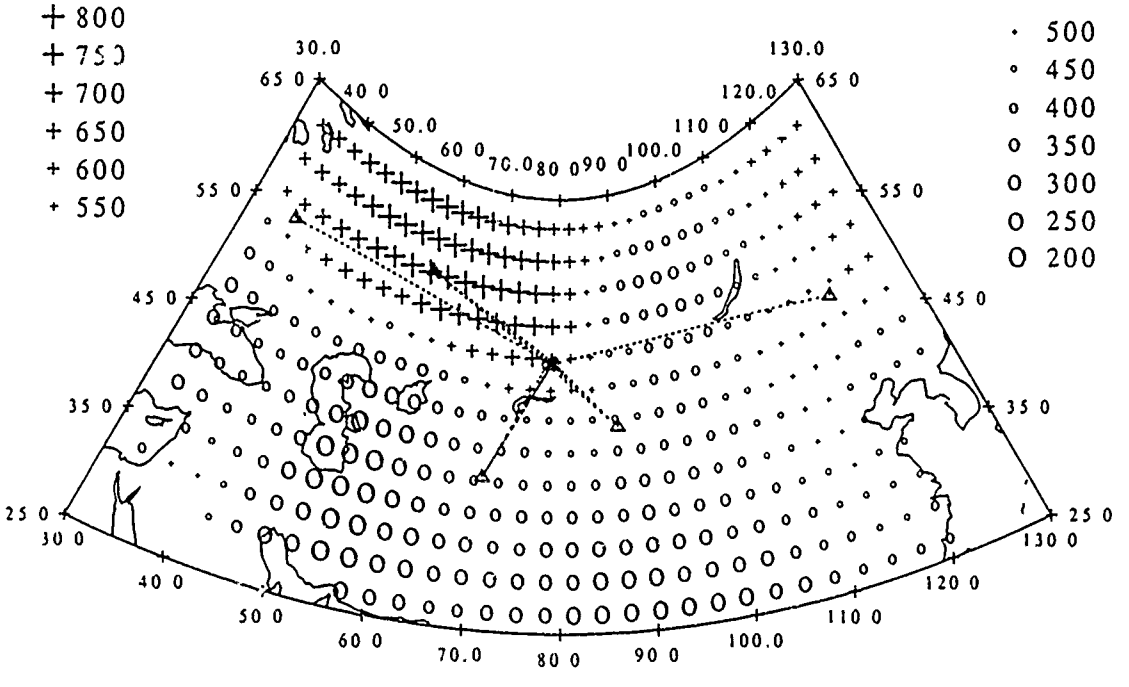

Figure 5. The great circle paths of Figure 4 superposed on the tomographically determined values of Q_o obtained by Xie and Mitchell (1991) for the region of the present study.

Application of Network-Averaged Teleseismic P Wave Spectra to Seismic Yield Estimation of Soviet PNE Explosions

J. R. Murphy, M. E. Marshall and B. W. Barker
S-CUBED
11800 Sunrise Valley Drive, Suite 1212
Reston, Virginia 22091
Contract No. F29601-92-C-DB01

Objective

The objective of the research being conducted under this contract is to derive a more generally applicable seismic yield estimation methodology for isolated explosions which are not located at well-calibrated, declared test sites. This is an issue of concern in that such isolated tests may be representative of the types of events which will need to be considered in a CTB or proliferation monitoring environment. Our selected analysis approach to this problem centers on model-based inversion processing of network-averaged, teleseismic P wave spectra which have been derived for a selected sample of Soviet PNE explosions, in order to obtain seismic yields and associated anelastic attenuation (i.e., t*) estimates for each explosion location.

Research Accomplished

In this phase of the investigation, an initial sample of 43 well-distributed Soviet PNE tests representing a wide range of m_b values extending from about 4.4 to 5.7, as well as a variety of tectonic regimes, has been selected for analysis. A comprehensive search of the GDSN database has been conducted to identify short-period signals recorded from these explosions and the resulting digital data have been collected, merged with the corresponding USAEDS and hand-digitized WWSSN data and assembled into a uniform database at the ARPA CSS. All of these data have been reviewed by an experienced analyst to verify arrival time estimates and to assess data quality and calibration accuracy. The resulting database includes at least 20 teleseismic stations for each event and large networks of more than 30 stations for 23 of the 43 selected explosions. In addition, information regarding the source characteristics of these explosions, as well as

tectonic and earth structure data relevant to the interpretation of the seismic data, have been collected from a variety of sources and used to construct classified and unclassified information files for each event. A map-based, graphical user interface has also been developed which permits the analyst to easily access the seismic data and to evaluate it in the context of other available information. This interface is illustrated in Figure 1 which shows the results of superimposing the 43 PNE event locations, as well as the historical ISC seismicity (1988-1990) and the country boundaries onto a color-coded surface topography map of the former Soviet Union and surrounding countries. Thus, in this example, the display provides the analyst with a quick graphical indication of which of the selected PNE events are located in tectonically active areas. Other functions provided within this module include the capability to display the seismic data and to interactively process it to obtain network-averaged, teleseismic P wave spectra corresponding to any selected event.

Once a final network-averaged P wave spectrum has been determined for an event, it can be inverted to obtain estimates of the required source and propagation path parameters using a semi-automatic algorithm which has been designed to facilitate this process. In applying this inversion procedure, the operator first selects a specific source model (e.g., Mueller/Murphy granite) from the menu and the system then automatically compares the observed spectrum with the theoretical P wave spectrum corresponding to the best-fitting yield and pP model parameters, under the assumption that the attenuation beneath the selected PNE site is the same as that beneath the Shagan River test site. At this point, the module provides the analyst with the option to interactively refine these automatically determined values of the yield, pP parameters and t* in order to resolve any remaining discrepancies in the fit to the observations. That is, it permits the analyst to assess possible variations in t* from the nominal Shagan River value and to generally explore a range of alternate solutions for the explosion under investigation. The final results of applying this yield estimation analysis procedure to the 43 selected PNE explosions are summarized in Table 1, where seismic yield and t* estimates are listed for each explosion. Of these 43 explosions, there is only one for which independent yield information has been reported by the Soviets at this time. This is the PNE test of 3/23/71, which is reported to have been a row cratering (i.e., canal excavation) experiment consisting of three, closely-spaced 15 kt devices fired simultaneously. From Table 1, our seismic yield estimate for that event is 35 kt, a value which is somewhat lower than the 45 kt total reported yield of this experiment. However, since these explosions produced a surface crater, it is not obvious how the seismic coupling for this event should relate to that from a single contained explosion of the same total yield. Consequently, at this time it is not possible to quantitatively assess the accuracy of our seismic yield estimates for these PNE explosions, and it

Table 1.
Summary of Seismic Yield and t* Estimation Results For Selected Soviet PNE Events

Date	Seismic Yield, kt	t*, sec
03-23-71	35	0.53
09-19-71	1.7	0.53
10-04-71	2.0	0.53
04-11-72	5.0	0.62
08-20-72	67	0.75
10-03-72	45	0.65
11-24-72A	3.0	0.53
11-24-72B	9.0	0.53
08-15-73	24	0.65
08-28-73	7.0	0.48
09-19-73	12	0.68
09-30-73	20	0.65
08-14-74	26	0.65
08-29-74	5.9	0.60
08-12-75	4.3	0.53
08-09-78	49	0.65
08-24-78	16	0.63
09-21-78	15	0.53
10-07-78	9.0	0.65
08-12-79	8.0	0.68
09-06-79	5.1	0.53
10-04-79	29	0.60
10-08-80	7.0	0.53
11-01-80	8.8	0.53
12-10-80	3.0	0.60
05-25-81	22	0.53
09-26-81A	4.0	0.53
09-26-81B	6.0	0.53
10-22-81	6.1	0.53
07-30-82	4.0	0.53
09-04-82	11	0.53
09-25-82	5.9	0.53
10-10-82	10	0.65
07-10-83A	8.0	0.53
07-10-83B	10	0.53
07-10-83C	6.0	0.53
07-21-84A	5.0	0.53
07-21-84B	6.0	0.53
07-21-84C	6.2	0.53
08-11-84	9.0	0.53
08-25-84	23	0.62
09-17-84	9.0	0.53
07-18-85	4.1	0.53

can only be stated that the model fits to the observed averaged spectra are generally well within the precision of the experimental data.

The overall geographical distribution of t* values inferred from the selected explosions is graphically displayed in Figure 2, where it can be seen that most of the stable continental interior locations are associated with t* values approximately equal to the value of 0.53 seconds which has been inferred for the Semipalatinsk test site. However, there are also some conspicuous geographical clusterings of higher t* values, some of which are consistent with currently available regional geophysical models and some of which are not. An example of the former category is the cluster of elevated t* values in the southern region bordering Iran and Afghanistan. With reference to Figure 1, it can be seen that this cluster coincides with a tectonically active region which might be expected to be characterized by a higher upper mantle attenuation. On the other hand, the presence of similar clusters of elevated t* values shown in the north central and far eastern regions of Figure 2 are harder to reconcile with what is known about the corresponding regional tectonic environments. The north central cluster does encompass part of the Ural Mountain chain which passes through this area, but we are unaware of any published studies which would suggest that enhanced upper mantle attenuation is associated with this structure. Similarly, while the far eastern cluster of elevated t* values shown in Figure 2 is not far removed from areas of active seismicity near the China border, available tectonic maps indicate that these explosions were detonated in a stable platform region which would not be expected to be associated with enhanced upper mantle attenuation. Nevertheless, the seismic data clearly indicate a significant difference in frequency content of these events relative to nearby events outside the cluster. More information will be required to determine whether the low frequency character of the teleseismic data recorded from these clustered events is actually associated with locally elevated t* values or whether systematic variation in source coupling might be contributing to this observed effect.

Since the yield estimates of Table 1 represent a fairly wide range of associated t* values, it would not be expected that they could all be reconciled with a single m_b/yield relation. This inference is confirmed in Figure 3 which show the m_b values as a function of the corresponding seismic yield estimates for those PNE events associated with inferred t* values of 0.53 sec (top) and for those PNE events with inferred t* values greater than 0.53 sec (bottom). It can be seen that the data for the former events tend to scatter about the reference Shagan River m_b/yield relation, consistent with inferred t* values near 0.53 sec, while the data for the latter events, which are associated with t* values greater than 0.53 sec, fall uniformly below the reference relation, consistent with our approximate model of m_b bias. Note that in both these figures there seems to be

some indication of an m_b/yield dependence for these PNE events which has a somewhat steeper slope than that of the Shagan River reference curve. This may just be an indication that the depths of burial of these PNE explosions vary with yield in a different manner than the Shagan River explosions, but more data will be required before any firm conclusions can be drawn.

Conclusions and Recommendations

Comprehensive samples of teleseismic P wave data recorded from 43 selected Soviet PNE tests have been collected and analyzed to obtain network-averaged P wave spectra corresponding to each explosion. These spectra have been inverted to obtain estimates of yield, pP parameters and t* using a model-based spectral analysis system which has been implemented specifically for this project. The graphical distribution of these derived t* values has been investigated in a preliminary fashion and it has been shown that, while there is some general correlation of these values with the locations of previously mapped tectonic regions, there also exist some anomalous regions of elevated apparent attenuation which will require further investigation. That is, it has been concluded that more information will be required to determine whether the low frequency character of the teleseismic data recorded from explosions in these anomalous regions is actually associated with locally elevated t* values, or whether systematic variations in source coupling might be contributing to this observed effect. Work is currently in progress to analyze P wave spectral data from a more complete set of these PNE events in order to better define the actual variations in t* and other yield estimation parameters as a function of location throughout the sampled regions of the former Soviet Union.

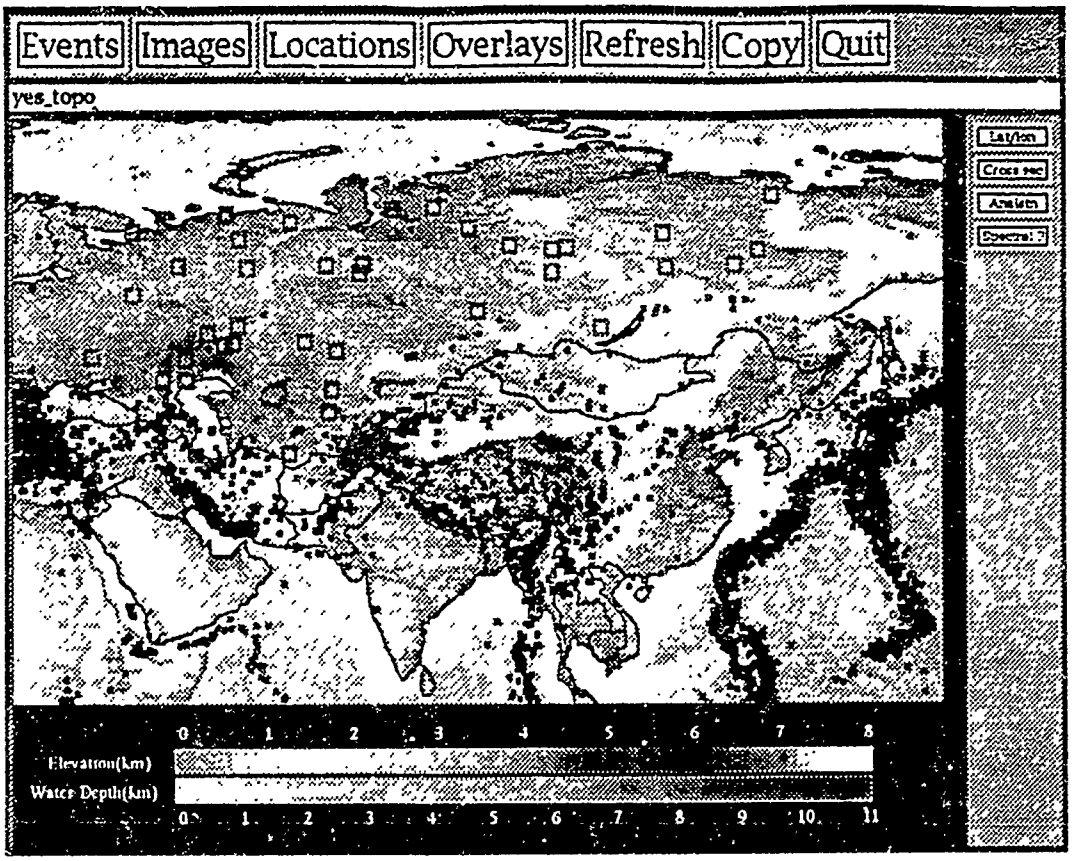

Figure 1. Selected PNE event locations (large squares) with respect to regional seismicity (small squares), shown as overlays to a color-coded topographic map of the former Soviet Union and surrounding countries.

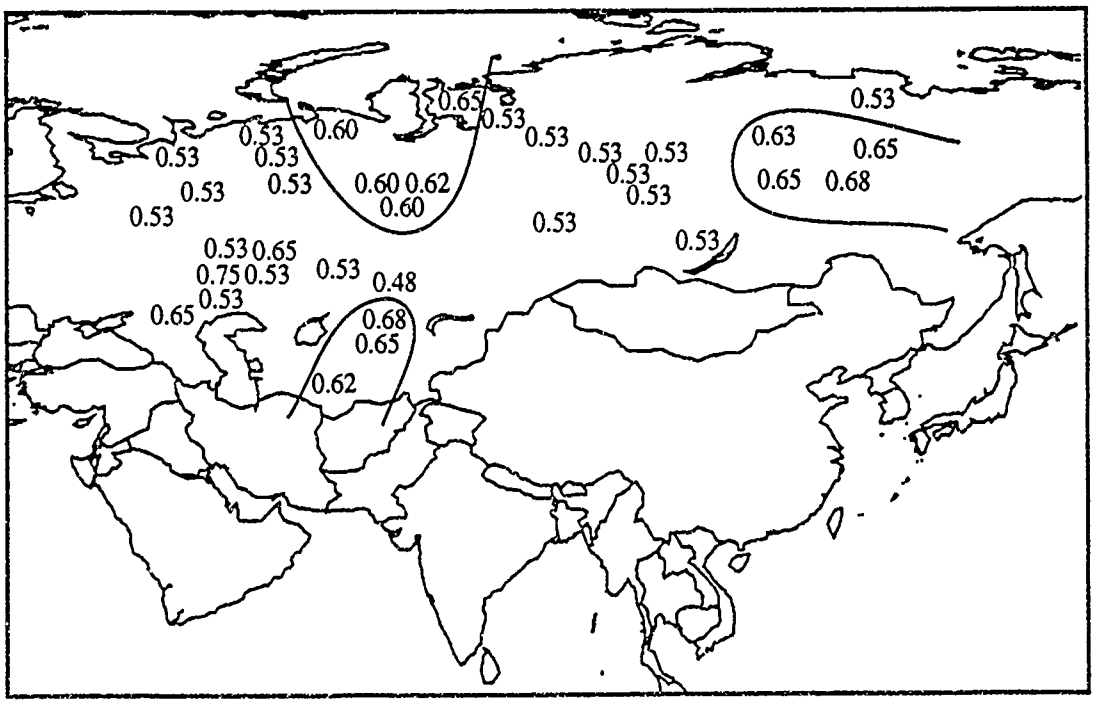

Figure 2. Map display of the geographical distribution of derived t* values for the 43 selected Soviet PNE tests.

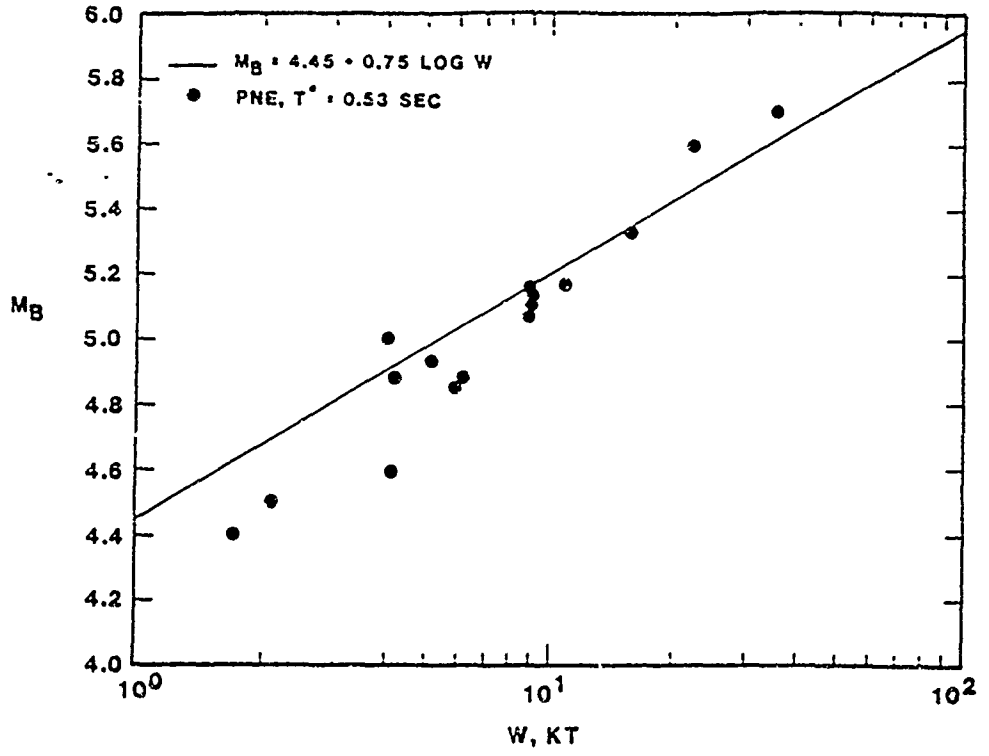

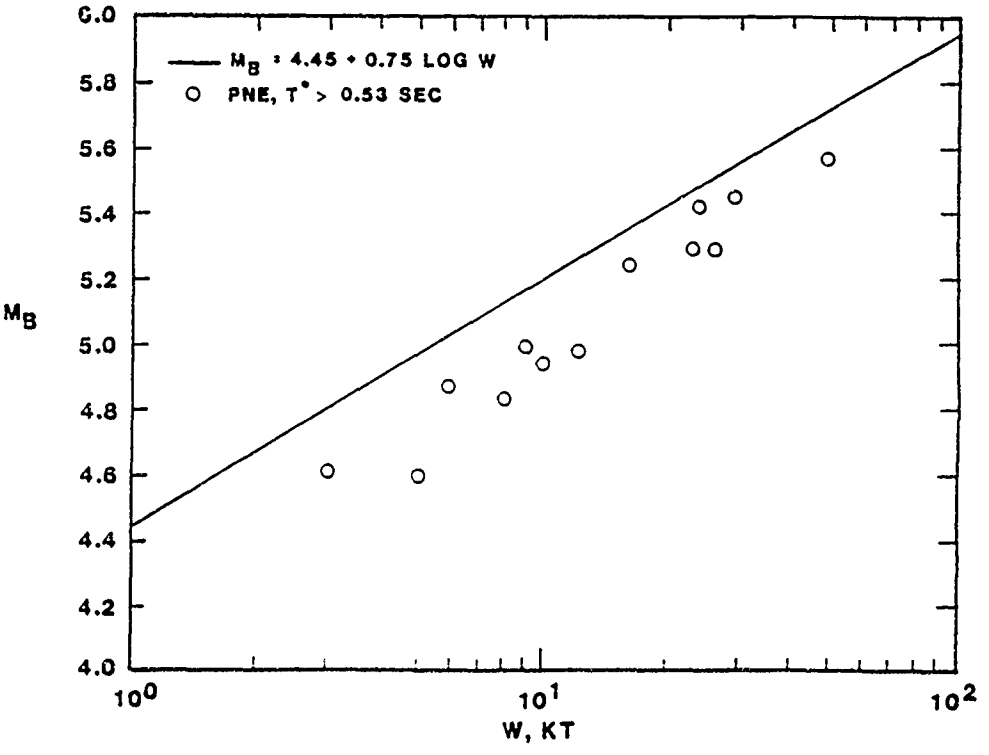

Figure 3. Comparisons of derived m_b/yield values for Soviet PNE tests associated with estimated t* values equal to (top) and greater than (bottom) the value of 0.53 sec associated with the nominal Semipalatinsk m_b/yield relation (solid line).

ARRAY RESEARCH AT NORSAR

Svein Mykkeltveit, Tormod Kværna, Jan Fyen and Frode Ringdal
NORSAR, P.O. Box 51, N-2007 Kjeller, Norway

and

Igor A. Kuzmin
Kola Regional Seismological Centre, Apatity, Russia

Contract No. F08650-93-C-0002

Objective

The basic objective of NORSAR's array program has been to provide high-quality data for use in seismological verification research, as well as to develop, test and implement methods to improve the detection, location and identification of low-magnitude events. In this work, techniques that may be useful in the further development of the Intelligent Monitoring System (IMS) are of particular interest.

This paper summarizes the status of development of the network of small-aperture arrays in northern Europe that provides seismic data to the IMS operated at NORSAR, and the focus is on the two new arrays on the Kola Peninsula of Russia and on the Arctic island of Spitsbergen. The paper also contains an assessment of the current performance of the IMS, based on results from thorough analysis of the automatic IMS results for a one-week evaluation period. Finally, we summarize work related to the development of a method for improved determination of phase arrival times, and the use of region-specific knowledge to provide event definitions of a quality that minimizes the need for subsequent analysis and review. The methodologies developed are well suited for implementation in the IMS.

Research accomplished

Status of network development

The network of regional arrays in northern Europe contributing data to NORSAR is shown in Fig. 1. The network currently comprises the NORESS and ARCESS arrays in Norway, the FINESA array in Finland, the GERESS array in Germany, as well as the two arrays established in the fall of 1992 near Apatity on the Kola Peninsula of Russia, and on the Arctic island of Spitsbergen. The NORESS, ARCESS and GERESS arrays are operating in stable modes and there are no current plans for modifications of these arrays. For the FINESA array, the University of Helsinki has started extensive field work in preparation for a significant upgrade of the field data acquisition system.

As part of an agreement on scientific cooperation between NORSAR and the Kola Science Centre of the Russian Academy of Sciences, a 1 km aperture array was installed in late September 1992 approximately 17 km to the west of the town of Apatity. The nine seismometer sites are on two concentric rings and one in the center. All instrument sites are equipped by a short period vertical seismometer of type Geotech S-500, and the site at the array center has in addition two horizontal seismometers of the same type. The data are transmitted from the seismometers to the central array site via buried cables, digitized at the central array site and then sent via radio to the Kola Regional

Seismological Centre (KRSC) in Apatity, where an array controller collects and timetags the data. The digitizers used are of types Nanometrics RD-3 and RD-6, both of which are 16-bit converters with gain ranging. In addition to this array, a three-component broadband seismometer was installed in the KRSC building in Apatity. The seismometer is of type Guralp CMG-3T, and these data are also digitized using a Nanometrics RD-3 digitizer. Timing throughout the system is based on reception of GPS signals. A computer system with Sun Sparcstations and peripherals installed at the KRSC allows its staff to perform on-line processing as well as interactive analysis of the data recorded by the Apatity installations. A dedicated 64 Kbps full duplex satellite link connects NORSAR and the KRSC. Using this link, data recorded at the Apatity installations are made available to the IMS at NORSAR. Conversely, all data recorded at NORSAR from the other arrays of the network can be retrieved by the KRSC personnel.

Our preliminary analysis indicates that the Apatity array represents an important extension to the seismic array network in northern Europe, both for regional and teleseismic event analysis. Its inclusion into IMS has served to improve the location precision of the large number of events in the Kola Peninsula and adjacent areas. While the noise level at the Apatity array at high frequencies is slightly higher than that of the other Fennoscandian arrays, its noise suppression capability matches that of ARCESS and NORESS (see Fig. 2). The noise suppression is of the order of $\sqrt{N}$ above 5 Hz, and better than this in the range 3-5 Hz. It thus appears that the spatial characteristics of the noise field at Apatity are similar to those found in other areas of Fennoscandia and the Baltic Shield.

A small-aperture array with a configuration very similar to that of the Apatity array was installed on the island of Spitsbergen in early November 1992. The array is sited on rocks of Cretaceous age, approximately 15 km east of Longyearbyen, which is the main settlement on Spitsbergen. Power at the Spitsbergen array is provided through the use of two windmills that deliver 12 V DC through a battery bank. The data are digitized using Nanometrics RD-6 units and then transmitted via radio to the array controller located in Longyearbyen. From Longyearbyen, the Spitsbergen array data are transmitted to NORSAR via a simplex 64 Kbps satellite link and thus provide another source of information for the IMS.

Preliminary analysis of data from the Spitsbergen array has revealed a large variation in signal and noise amplitudes across the sensors. Further investigations are needed in order to determine the reason for this variation, and it may prove necessary to redeploy one or more of the array sensors. Site B2 in this array exhibits a particularly favorable signal focusing for nearly all arrival azimuths. Initial studies of the noise characteristics show that the noise is quite stable over time, especially at high frequencies. Also, the noise amplitudes at high frequencies seem to be similar across the array, in contrast to the large variation seen at low frequencies.

An evaluation of the performance of IMS

Data from the network of six arrays described above are processed jointly by IMS. IMS is described in Bache (1993). One of the basic objectives of IMS is to provide automatic event definitions of a quality that significantly reduces the burden on the seismic analyst. Operational experience with IMS is thus taken into account to produce enhancements to the system that result in performance improvements. NORSAR has tried to assist in this process by undertaking evaluations of IMS performance following the release of new versions by SAIC, the system developer. A recent evaluation was conducted for the 7-day period 26 April - 2 May 1993 and focused on the performance of the ESAL (Expert System for Association and Location) element of IMS through detailed study and characterization of all events automatically declared by IMS.

Our main impression from this assessment is that the overall performance of IMS is now very satisfactory. About 80% of the events automatically declared by IMS were real events with IMS solutions that were rated acceptable in the sense that no or only minor changes had to be made during

the analyst review process. Also, the rules for automatic phase identification in ESAL now appear to work very well.

There is, however, still room for some improvements in IMS. About 20% of the events declared by IMS were false. For a number of these false events, it appears that parametric information (phase velocities, signal frequency content) was available to IMS that should have permitted ESAL to automatically reject them. Some events found in reference bulletins were missed by IMS, even though IMS had information that should make it possible for ESAL to form these events. Events missed by IMS represent a potentially more serious problem than that of the false events. Due to the large amounts of data processed by the IMS and the limited manpower resources available for interactive analysis of the automatic IMS results, it is unlikely that the analyst review process will pick up the events missed by ESAL. It is therefore necessary to have a close look at ESAL to rectify the problem of missing events. It should be noted though that all except one of the regional events missed by IMS during the test period were very small events detected on one array only.

Intelligent post-processing of seismic events

From experience with analyst review of events automatically defined by the IMS, we have realized that the quality of the automatic event locations can be significantly improved if the event intervals are reprocessed with signal processing parameters tuned to phases from events in the given region. The tuned processing parameters are obtained from off-line analysis of events located in the region of interest. The primary goal of such intelligent post-processing is to provide event definitions of a quality that minimizes the need for subsequent analysis and review.

The first step in this post-processing is to subdivide the area to be monitored in order to identify sites of interest. Clearly, calibration will be easiest and potential savings in manpower are largest for areas with high, recurring seismic activity. We have identified 8 mining sites in Fennoscandia/W. Russia/Estonia and noted that 65.6 per cent of the events of $M_L > 2.0$ in this region can be associated with one of these sites. This result is based on 1 1/2 years of data.

The second step is to refine the phase arrival time and azimuth estimates using frequency filters and processing parameters that are tuned to the initial event location provided by the IMS. We have studied, as a first example, a set of 58 events from the Khibiny Massif in the Kola peninsula. Very accurate locations of these events has been provided by the KRSC. Our refinement of phase arrival times for these events, as recorded in Apatity and at ARCESS, have given quite remarkable results. Using the autoregressive likelihood technique of Pisarenko et al (1987) we have been able to estimate onset times automatically to an accuracy (standard deviation) of about 0.05 s for P-phases and 0.15-0.20 s for S-phases, as seen from Table 1. These accuracies are as good as for analyst picks, and are considerably better than in the current SigPro analysis, used by IMS. This can be seen in Fig. 3.

The third step in the post-processing is a recomputation of the location estimate, using the refined arrival times and broad-band azimuths associated with a fixed frequency band (tied to the initial IMS location). Again using the set of 58 known Khibiny Massif events as a reference, we have investigated the accuracy of the LocSat location procedure (Bratt & Bache, 1988) using varying amounts of regional corrections, as exemplified by the following two scenarios.

Scenario 1) Using P arrivals, S arrivals and Rg azimuths at the Apatity array, without applying any regional corrections.

Scenario 2) Using P arrivals and S arrivals at both the Apatity array and the Apatity broadband three-component station, and Rg azimuths at the Apatity array, all with regional corrections. i.e., systematic biases removed.

Fig. 4 shows the location results for scenarios 1 and 2. In both scenarios, excellent location accuracy is achieved, with a median location error of 3.1 km for scenario 1 and 1.4 for scenario 2. This should be compared to the median error of 10.6 km for the automatic IMS processing for these events, and clearly demonstrated the usefulness of the refined arrival times and the regional corrections introduced.

After we have established the tuned processing parameters for events in this region, a natural next step will be to automatically activate such intelligent post-processing every time the IMS locates an event in the Khibiny region.

Conclusions and recommendations

In our view, the deployment of advanced small-aperture arrays and the associated development and implementation of automated and increasingly powerful data processing techniques (as exemplified by the IMS) represent major advances in seismic monitoring in recent years. Our assessment of IMS is that is has now advanced to a mature stage, but there is still room for some improvement in the event formation process. We have also demonstrated the potential of improved event definitions in IMS by refining the phase arrivals times and taking regional calibration data into account. Additional research along these lines and subsequent implementation into IMS of appropriate procedures is needed in order to fully exploit the potential of the array network data.

References

Bache, T.C., S.R. Bratt, H.J. Swanger, G.W. Beall and F.K. Dashiell (1993): Knowledge-based interpretation of seismic data in the Intelligent Monitoring System, *Bull. Seism. Soc. Am.*, in press.

Bratt, S.R. and T.C. Bache (1988): Locating events with a sparse network of regional arrays, *Bull. Seism. Soc. Am.*, 78, 780-798.

Pisarenko, V.F., A.F. Kushnir and I.V. Savin (1987): Statistical adaptive algorithms for estimation of onset moments of seismic phases, *Phys. Earth Planet. Int.*, 47, 4-10.

	σ_{manual}	$\sigma_{automatic}$
P, Apatity array	0.04 s	0.04 s
P, Apatity 3-comp.	0.06 s	0.05 s
Pn, ARCESS	0.06 s	0.05 s
S, Apatity array	0.19 s	0.19 s
S, Apatity 3-comp.	0.13 s	0.15 s

Table 1. Estimated standard deviations of manual and automatic (using the Pisarenko et al (1987) approach) P- and S-onsets at the Apatity array and the Apatity broadband 3-component station, and Pn-onsets at ARCESS.

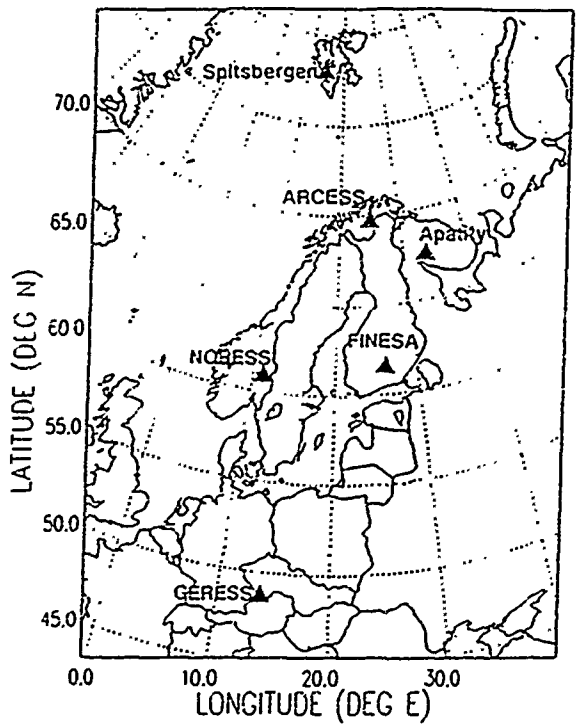

Fig. 1. The network of six regional arrays in northern Europe.

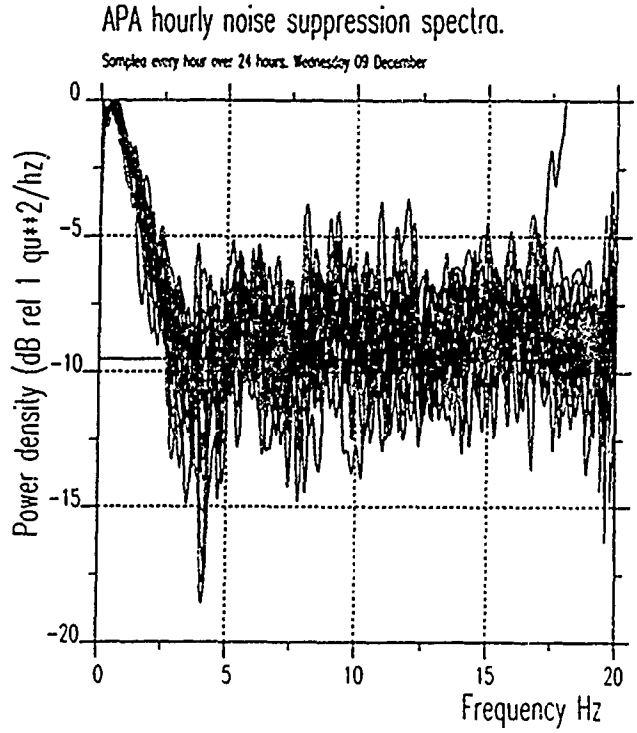

Fig. 2. Apatity array noise suppression by beamforming. To produce these curves, an infinite-velocity beam is formed and the spectrum for this beam is divided by the average of the single sensor spectra. The 24 curves result from one minute of data taken hourly between 00.00 and 23.00 GMT on day 344, 1992. The horizontal line at -9.5 dB represents $\sqrt{N}$ suppression for 9 sensors.

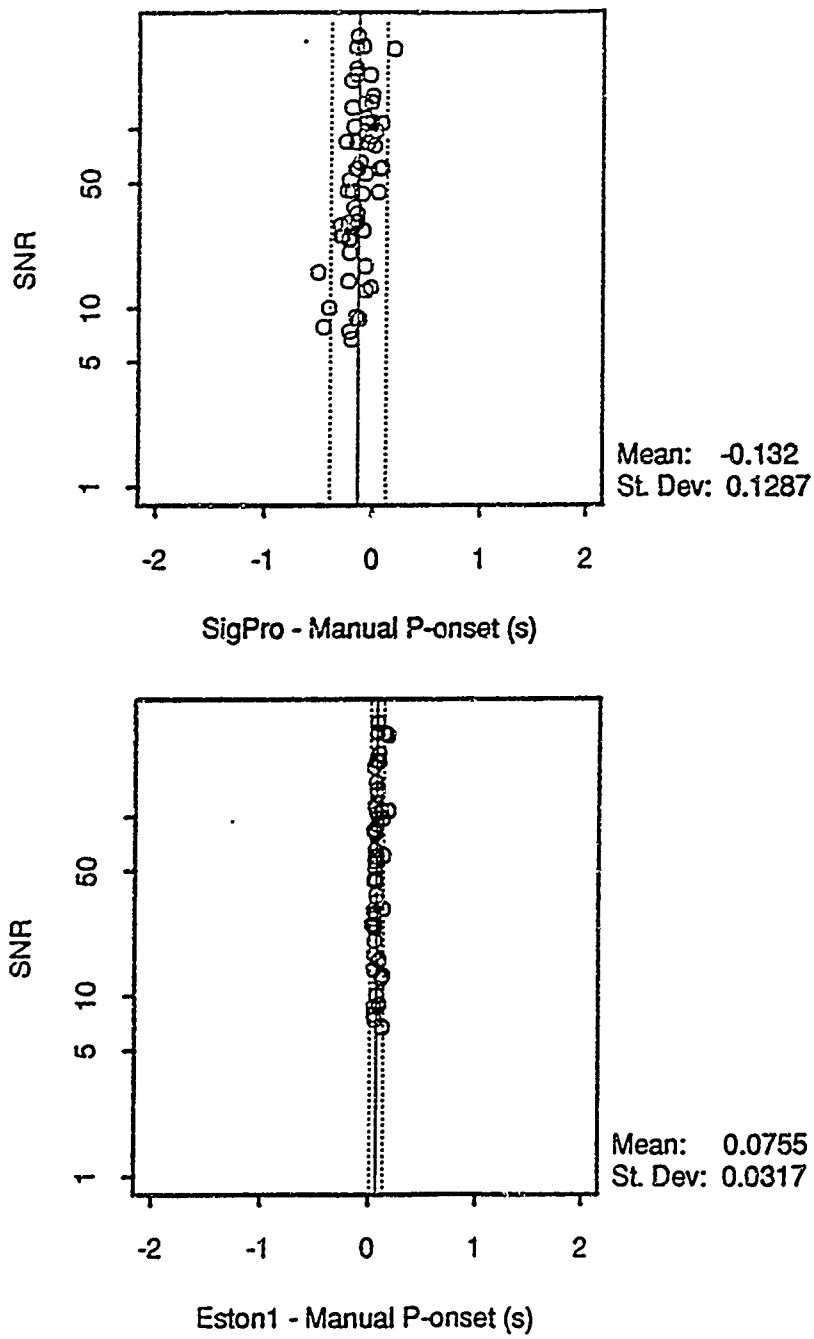

Fig. 3. The two plots show the time differences between automatic P-onsets and the manual pick at the ARCESS array as a function of SNR, for 58 Khibiny Massif events. The plot at the top shows the time differences between the automatic P-onsets used by the IMS (from SigPro) and the manual picks, whereas the bottom plot shows the time difference between the automatic P-onsets from the Pisarenko et al (1987) method (ESTON1) and the manual picks. The two vertical lines represent $\pm 2\sigma$.

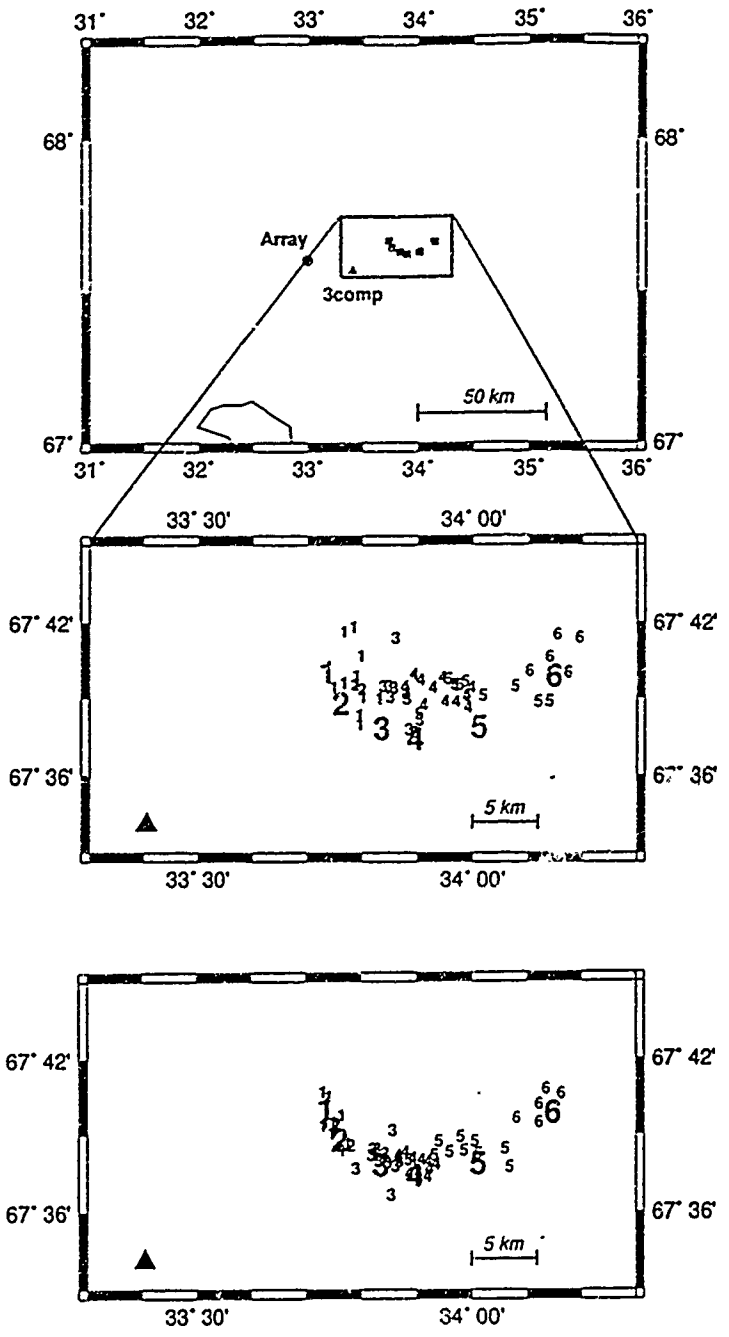

Fig. 4. The middle part of the figure shows the location of the six mining sites in the Khibiny Massif (large numbers 1-6) and the location of the 58 reference events (small numbers 1-6) located according to the assumptions for *Scenario 1* (see text). The lower part of the figure has the same meaning as the middle part, but now the reference events are located according to assumptions for *Scenario 2*. In the upper part of the figure, a larger reference area is shown, with the mines plotted as filled squares. The location of the Apatity array and the Apatity broadband 3-component station are also shown.

CENTRAL SIBERIAN UPPER MANTLE STRUCTURE and the STRUCTURE OF THE SOUTH CASPIAN BASIN

Keith Priestley, University of Cambridge, Cambridge, UK.

John J. Cipar, Phillips Laboratory, Hanscom AFB, MA, USA

CONTRACT NO. F49620-92-J-0475

OBJECTIVE: Analysis of Asian crust and upper mantle velocity structure

RESEARCH ACCOMPLISHMENTS:

The Yamal Peninsula -- Lake Baikal DSS profile: Seismograms from three nuclear explosions and thirty-four chemical explosions recorded along a 2400-km long deep seismic sounding profile extending across the Siberian Platform from the Yamal Peninsula to Lake Baikal (Fig. 1) are being analyzed to determine the upper mantle structure beneath this region. The northernmost nuclear shot (SP245) was located in the West Siberian rift, a deep sedimentary basin on the northwest edge of the Siberian Platform. The central nuclear shot (SP173) was located in the Tunguss Basin, approximately 700 km southeast of SP245. The southernmost nuclear shot (SP35) was located 250 km northwest of Lake Baikal. Each nuclear shot was recorded at about 200 sites each equipped with a "Taiga" seismic system (Chichinin *et al.*, 1969). The sensors have a natural frequency of 1.5 Hz, and the recording system has a usable bandwidth between 0.5 to 20 Hz. Chemical explosions (3000-5000 Kg each) were detonated at approximately 70 to 100 km intervals along the profile and the length of these reversed profiles are 250-300 km.

Crustal arrivals are prominent at short ranges, especially the Pg phase. The mantle refraction (P_n) is observed as a first arrival at epicentral distances of 150 to 200 km. It appears as a weak arrival in Figures 2 but is clearly seen in the digital data. The first arrival has a variable amplitude and arrival time at longer ranges. Since these can be correlated over several hundred kilometers, we believe they reflect variations in the lithospheric structure. Amplitude variations are complex. For example, in the distance range 1300 to 1500 km for SP245 (Fig. 2a), the high amplitude arrival that follows the first arrival at 1300 km progressively move forward, becoming the first arrival at 1500 km, a pattern characteristic of a reflection from a high-velocity layer. Other similar features in the data suggest complex layering within the upper mantle. Some of these observations may be due to lateral variations in structure. Arrivals from the mantle transition zone can be observed at longer ranges, particularly in the SP245 profile (Fig. 2a). The reflection/refraction from the 425-km discontinuity is a clear secondary arrival beginning about 1700 km, becoming the first arrival by 2200 km. There is a strong reflection from the 660-km discontinuity at 2100- to 2300-km range and 12-sec reduced time. Also notable is the considerable difference between the record section for SP245 (Fig. 2a) and SP35 (Fig. 2c) at comparable ranges (1700 to 2200 km). Whereas the SP245 data indicates strong arrivals from transition zone discontinuities, the SP35 data do not show such prominent arrivals. At this stage it is unclear whether this observation is the result of lateral variation in the mantle structure or some crustal feature that masks the arrivals.

The observations shown in Figure 2 constitute one of the most complete and detailed sets of regional seismic data available in the western literature. We have constructed a preliminary 1-D compressional velocity model to fit the major travel time and amplitude features of the data. The

dominant frequency of the P-wave is 2 Hz giving a resolution of 2-4 km. The starting model was KCA modified with a crustal section that more closely agrees with the close-in observations. Crustal thickness ranges from 47 km beneath the West Siberian rift to 42 km beneath the Siberian craton. However, our model assumes the same crust along the entire profile. Figure 3 compares the observed travel times with those calculated for the RIFT-245 model (Table 1). The mantle above the transition zone consists of material with P-wave velocities ranging from 8.25 km/s at the Moho to 8.53 km/s at 225 km. At 225-km depth, velocities increase abruptly to 8.63 km/s. Superimposed on this large scale structure are finer features, such as the strong gradient between 117- and 123-km depth, that produces the triplication at about 1000-km range. There is little evidence for a pronounced LVZ as is found in K8, although small velocity reversals are required to terminate several branches of the travel time curve. The worst fit (up to 1.5-sec discrepancy) is in the distance range 700- to 1000-km. Extensive modeling of the high-phase velocity segment A-A' (Fig. 3) indicates velocities near 8.58 km/s at 75-km depth. Since this branch is not observed on other record sections, we believe it may be a high-velocity body of limited lateral extent that cannot be modeled by the 1-D calculations. First and prominent second arrival times for SP245 are plotted in Figure 3. The transition zone is similar to other upper-mantle models. The upper discontinuity lying at 425-km depth is modeled as a sharp discontinuity with a velocity increase of 5.6%. The strong reflection from the lower discontinuity is best modeled as a 4.9% velocity increase over the depth range 656.5- to 659-km. The velocity gradient below the 425-km discontinuity is well constrained by a set of strong arrivals. Similar arrivals cannot be seen from the 660-km discontinuity, indicating a weak gradient below 660 km.

Seismic studies in the Caspian Sea region: The Caspian Sea region is geologically interesting because existing seismic data suggest that south Caspian Basin has an "oceanic" crust surrounded by regions of typical continental crust. If this is true, it is puzzling how a section of "oceanic" crust could maintain its integrity and remain unsubducted for long periods of time in a dominantly compressional environment. From a seismic discrimination/verification point of view, this region is important because there are a number of countries in the Middle East that have a possible nuclear capability. The Lg phase, proven to be an effective discrimination/yield estimation phase, does not propagate well across the Caspian Basin thus preventing or at least greatly reducing its use. During the summer 1993 we installed five broadband seismographs in the region surrounding the south Caspian Basin, two in Azerbaijan and three in Turkmenistan(Fig 4). A sixth instrument will be installed in September, 1993. Each seismograph consist of a Gurlap CMG-3T seismometer, a Refraction technology 72A-02 data logger and an Omega time code receiver. All stations are located at pre-existing short period seismograph sites There are two goals of this experiment: to better define the complex crust and upper mantle structure in this area; and to better understand regional seismic wave propagation from events in the Middle East

CONCLUSIONS AND RECOMMENDATIONS:

We have presented record sections from three nuclear explosions detonated in central Siberia. Forward modeling of the observed arrival times and amplitudes indicates an important change in the mantle at 225-km depth where the P-wave velocities increase from 8.53 to 8.63 km/s. The transition zone is similar to other models of the upper mantle. The reversed and overlapping coverage afforded by this data set will allow a detailed view of the central Siberian upper mantle. The purpose of this report is to show the potential of the data, compare it to prediction of existing Asian mantle models, and to provide a 1-D reference model for future 2-D interpretation. We plan to extend this analysis with the use of synthetic seismograms to better constrain the velocity gradients and attenuation, and with 2-D ray tracing to refine what is clearly laterally varying structure in the upper mantle. Five broad-band seismographs have been installed around the Caspian Sea and a sixth will be installed soon. Data from these instruments will allow determination of the velocity structure of the south Caspian basin and the characterization of

regional seismic wave propagation in the region.

REFERENCES:

Benz, H. M., J. D. Unger, W. S. Leith, W. D. Mooney, L. Solodilov, A. V. Egorkin, and V. Z. Ryaboy. Deep Seismic Sounding in Northern Eurasia, *EoS, 73,* 297-300, 1992.

Chichinin, I. S., G. V. Yegorov, A. V. Yemelianov, and A. J. Bochanov. Portable Telemonitored Seismic Equipment "Taiga", Methods of Seismic Research, Nauka, Moscow, 95-119, 1969.

Egorkin (Yegorkin), A. V., S. K. Ziuganov, and N. M. Chernyshev. The Upper Mantle of Siberia, *Proceeding of the 27th International Geological Congress, 8,* 29-56., 1984

Given, J. W. and D. V. Helmberger. Upper Mantle Structure of Northwestern Eurasia, *Jour. Geophys. Res., 85,* 7183-7194, 1980.

King, D. W. and G. Calcagnile. P-wave Velocities in the Upper Mantle Beneath Fennoscandia and Western Russia, *Geophys. Jour. R. Astr. Soc., 46,* 407-432, 1976.

Pavlenkova, N. I. and A. V. Yegorkin. Upper Mantle Heterogeneity in the Northern Part of Eurasia, *Phys. Earth Planet. Int., 33,* 180-193, 1983.

Yegorkin, A. V., V. Z. Ryaboy, L. P. Starobinets, and V. S. Druzhinin. Velocity Cross Sections of the Upper Mantle from DSS Data on Land, Izvestiya, *Earth Physics, 13,* 467-477, 1977.

Yegorkin, A. V. and N. I. Pavlenkova. Studies of Mantle Structure of U.S.S.R. Territory on Long-range Seismic Profiles, *Phys. Earth Planet. Int., 25,* 12-26, 1981.

Table 1. RIFT-245 Reference Model

Depth (km)	P-wave Velocity (km/s)	Depth (km)	P-wave Velocity (km/s)
0.0	3.5	225.0	8.53
11.0	5.1	225.0	8.63
11.0	6.35	325.0	8.64
19.8	6.35	350.0	8.68
19.8	6.5	375.0	8.69
24.8	6.9	400.0	8.70
24.8	7.0	425.0	8.90
43.9	7.5	425.0	9.40
44.0	8.25	520.0	9.65
75.0	8.27	550.0	9.88
108.0	8.3	656.5	10.15
117.0	8.28	659.0	10.65
123.0	8.5	800.0	10.98
145.0	8.55	900.0	11.15
195.0	8.50	1000.0	11.40

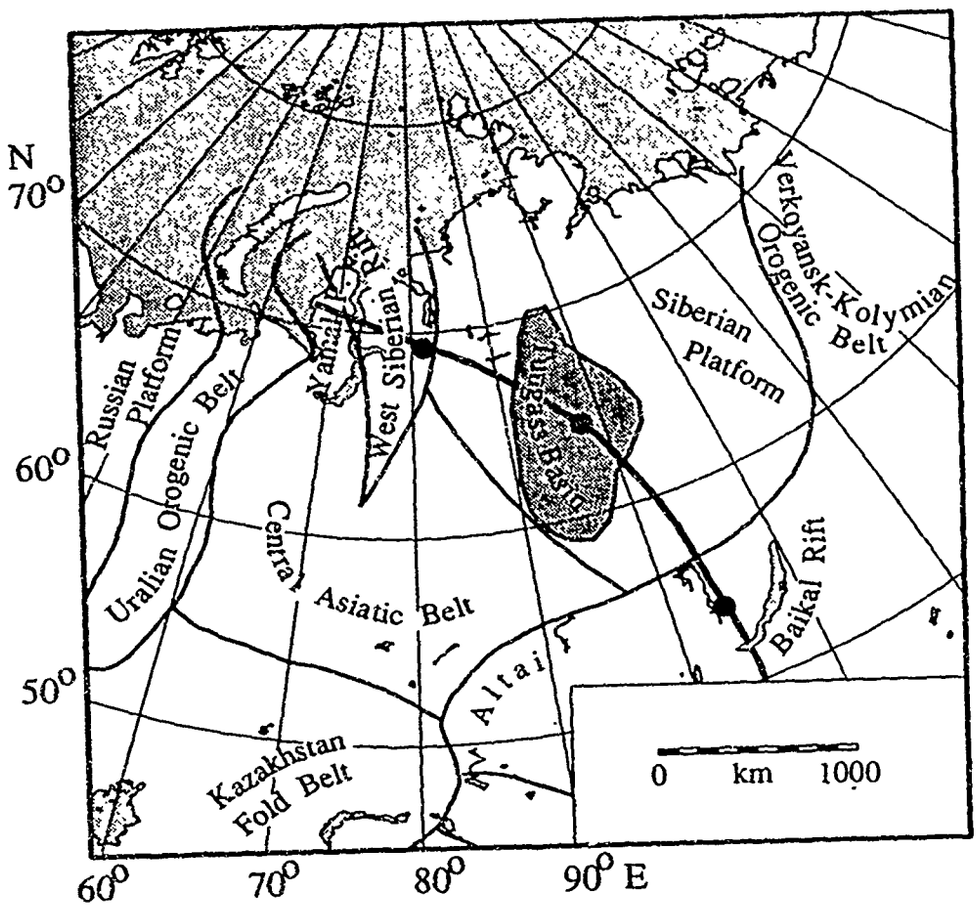

Figure 1. Simplified tectonic map of Central Asia. The "RIFT" profile is marked by the heavy solid line and the shot points are marked by the solid circles.

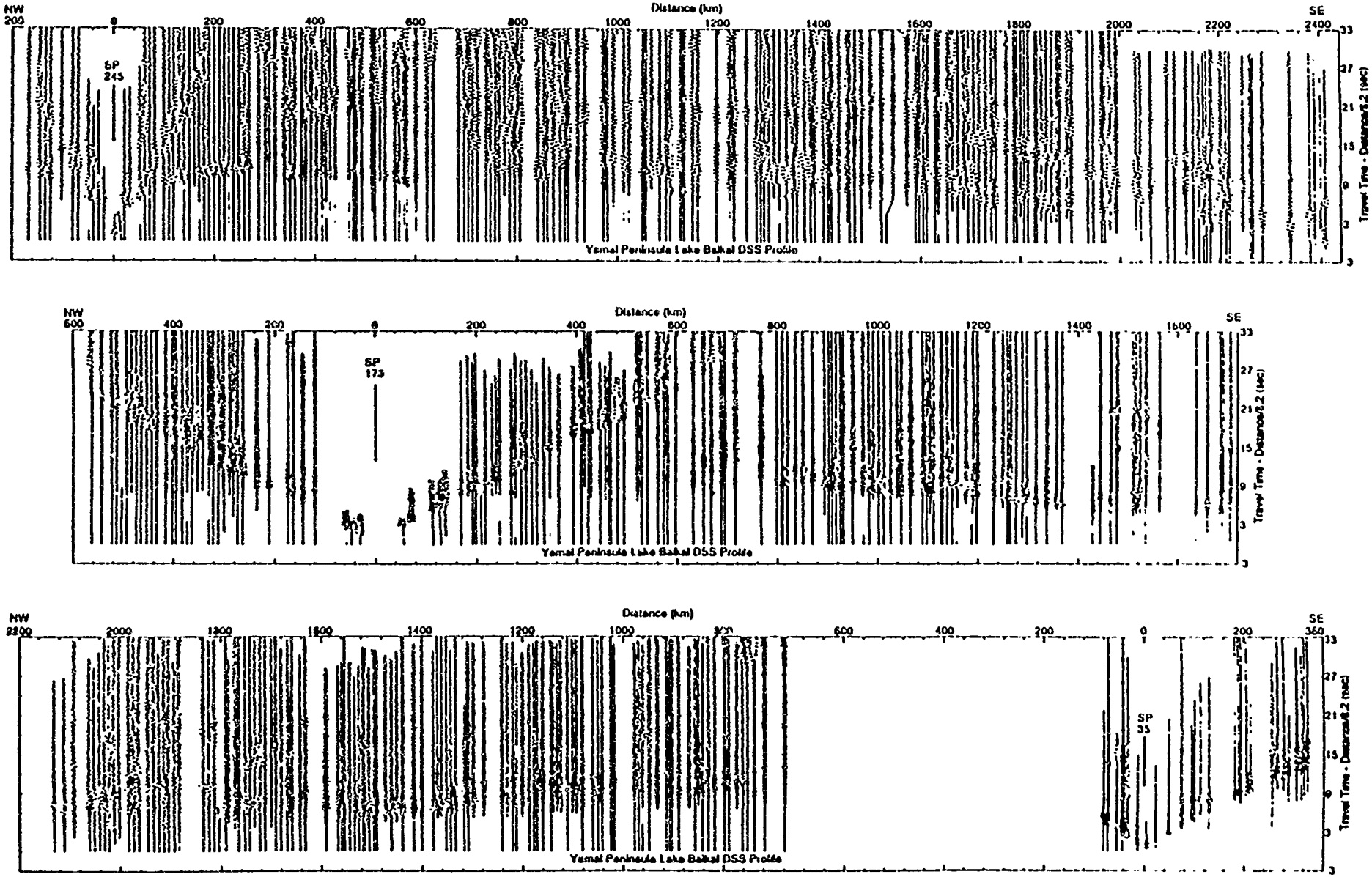

Figures 2. Record sections for the three nuclear explosions. The seismograms have been reduced by a velocity of 8.2 km/s, and the amplitudes have been trace normalized. The seismograms were recorded at two gain levels to increase the dynamic range and the original record sections were plotted using the high-gain channel for the first arrival and, if necessary, the low-gain channel for the remainder of the seismogram. An overlap of 1 to 3 seconds allowed both sections of the trace to be rescaled to the proper amplitude. (a) SP245, (b) SP173, (c) SP35.

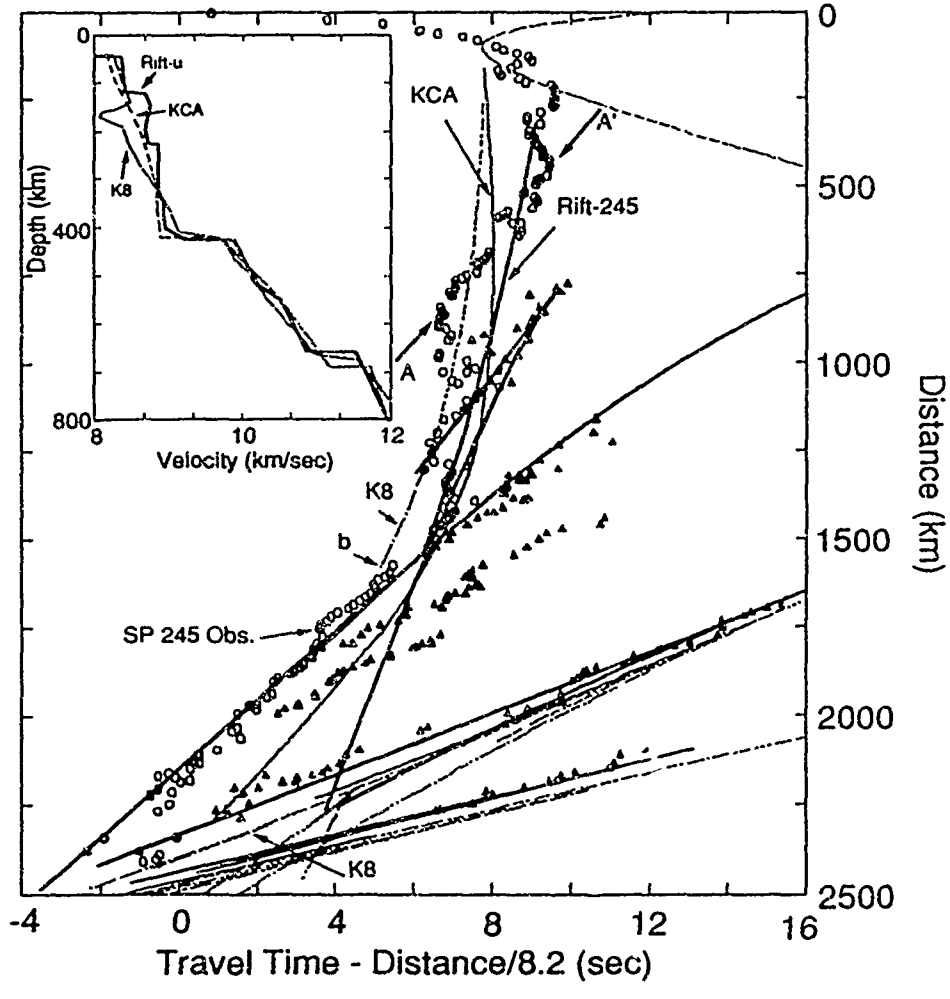

Figure 3. Comparison of the observed travel times from the SP245 shot point (open circles first arrivals; triangles secondary arrivals) with travel times predicted from models K8 (thin dotted line), KCA (thin solid line), and RIFT-245 (heavy solid line). The inset shows the P-wave velocity-depth functions for the models.

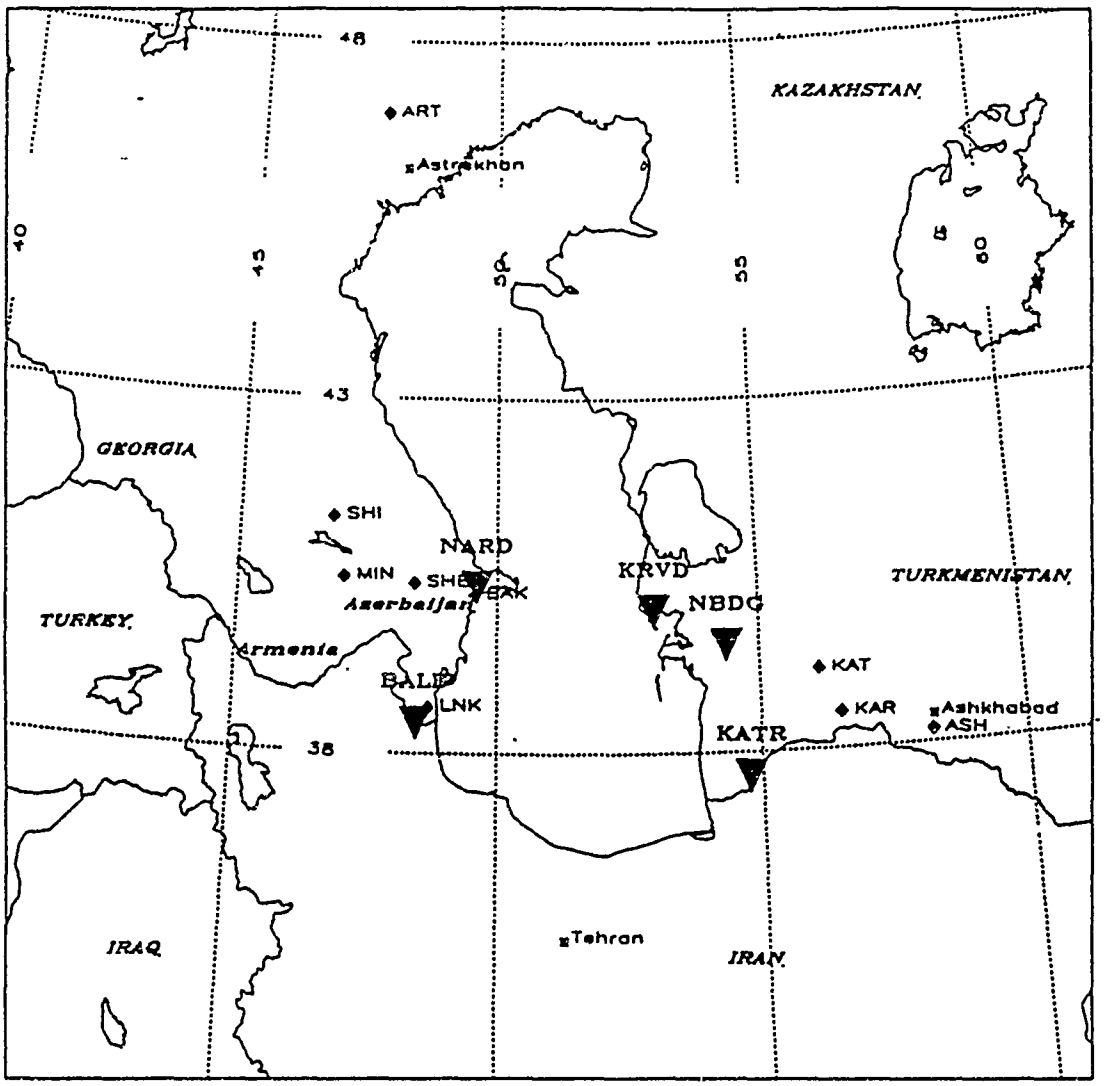

Figure 4. Station locations in the South Caspian basin region.

Regional Seismic Event Identification in Eurasia: A Hybrid Machine Learning Approach

Jay J. Pulli[1] and Paul S. Dysart[2]

[1] Radix Systems, Inc., 201 Perry Parkway, Gaithersburg, MD 20877
[2] Science Applications International Corp., 1710 Goodridge Dr., McLean, VA 22102

Contract No. F29610-91-C-DB10

Objectives

The objective of this research is to develop a methodology for regional seismic event identification in Eurasia. Our adopted methodology is termed a *hybrid machine learning* approach, because it combines observational seismology with classical pattern recognition, statistical analysis, and modern classifiers such as backpropagation neural networks. The goal of the effort is to apply this methodology to the automatic identification of seismic events recorded by the Intelligent Monitoring System (IMS). The methodology is adaptable, and the identification scheme can be retrained for new geographic areas or stations where source and propagation effects may differ.

Research Accomplished

Explanation of the Term *Hybrid Machine Learning*

Machine learning refers to the process by which computers form relationships between data and results without human programming. It is akin to forward mathematical modeling without the constraint of a model[1]. Machines can be trained to learn the relationships using either supervised or unsupervised learning. In supervised learning, the machine is given both the data and the results and then learns the relationship. In unsupervised learning, the machine is given only the data and then learns both the results and the relationships.

Because it is in general an unsolved problem, seismic event identification has always been a good candidate for machine learning experiments. But since seismic data spans such a large range of size and type (waveform, parameter, ancillary), the

[1] This is a slight exaggeration. In the case of a multilayered perceptron (neural network) the model consists of connections between a large number of nodes. The ouput of each node is the dot product of its inputs and the weights connecting it to the other nodes, which is then input to a nonlinear function, such as a sigmoid. The model is in effect a large nonlinear transfer function. The weights are determined through training (learning). A general reference for this field is Lippman (1987).

application of machine learning can sometimes lead to a machine that has learned irrelevant information or artifacts of the data unrelated to the problem being solved. Overfitting of the data is another problem; a large enough machine can fit any dataset with relationships that make no physical sense.

To mitigate these potential problems, we have adopted a hybrid approach which combines techniques of statistics and classical pattern recognition with machine learning. The goal is to minimize the number of input parameters, use only relevant parameters whose distributions provide the greatest class separability, and use the smallest possible machine (neural network) to learn the identification procedure.

Summary of Earlier Work

Our early work focused on the compilation of independently identified seismic events for training and testing. Most of the events were located in Scandinavia and recorded by the NORESS array; 102 events were included in the first analysis.

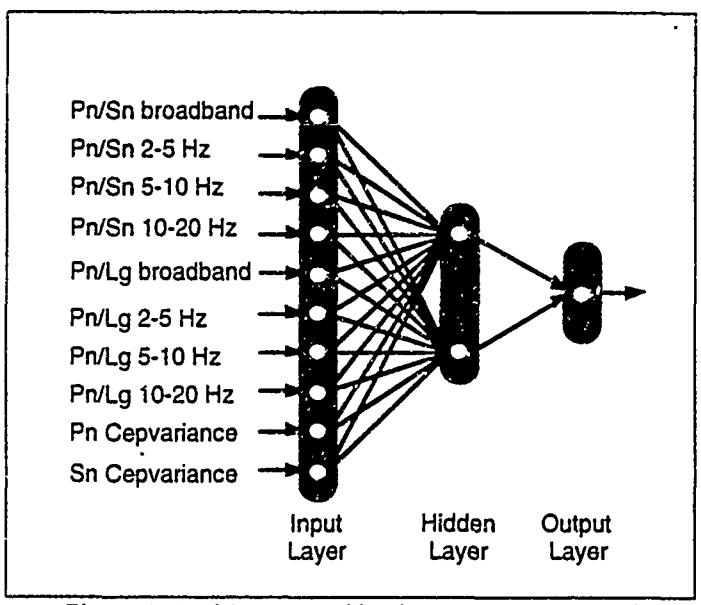

Figure 1. Architecture of backpropagation neural network used for event identification.

The Mahalanobis Distance[2] was used to rank the parameters; the most important parameters for event identification were found to be the *Pn/Lg* spectral ratio from 5-10 Hz, the *Pn/Sn* spectral ratio from 2-5 Hz, the mean cepstral variance, and the *Pn/Sn* wideband spectral ratio. Principal Components Analysis (Jackson, 1991) was used to estimate the dimensionality of the data and aid in neural network design. The chosen backpropagation neural network architecture is shown in *Figure 1.* A complete description of this effort is given in Pulli and Dysart (1992).

Analysis of the CSS Ground-Truth Database

The compilation of a ground-truth database is often the most difficult and time consuming part of any machine learning experiment. Fortunately, Grant *et al.* (1993) are currently compiling such a database, known as the CSS Ground-Truth Database. This database actually consists of three separate databases, called the Vogtland,

[2] Difference in class means divided by sum of class variances.

Steigen, and Lubin databases. Each database consists of parameters and waveforms for events with independently verified source types. As of this writing, we have examined two of the three databases.

Vogtland: The Vogtland database consists of 11 earthquakes and 16 quarry blasts located in northwest Bohemia, Czech Republic. All of the events were recorded by the GERESS array[3] *Figure 2* shows unfiltered seismograms for two of the events. Note the difference in the amplitude ratio of *P*-to-*Lg* for the sample explosion (Event 17) and earthquake (Event 9). This difference is consistent for all of the events in the database, making visual classification of source type very easy.

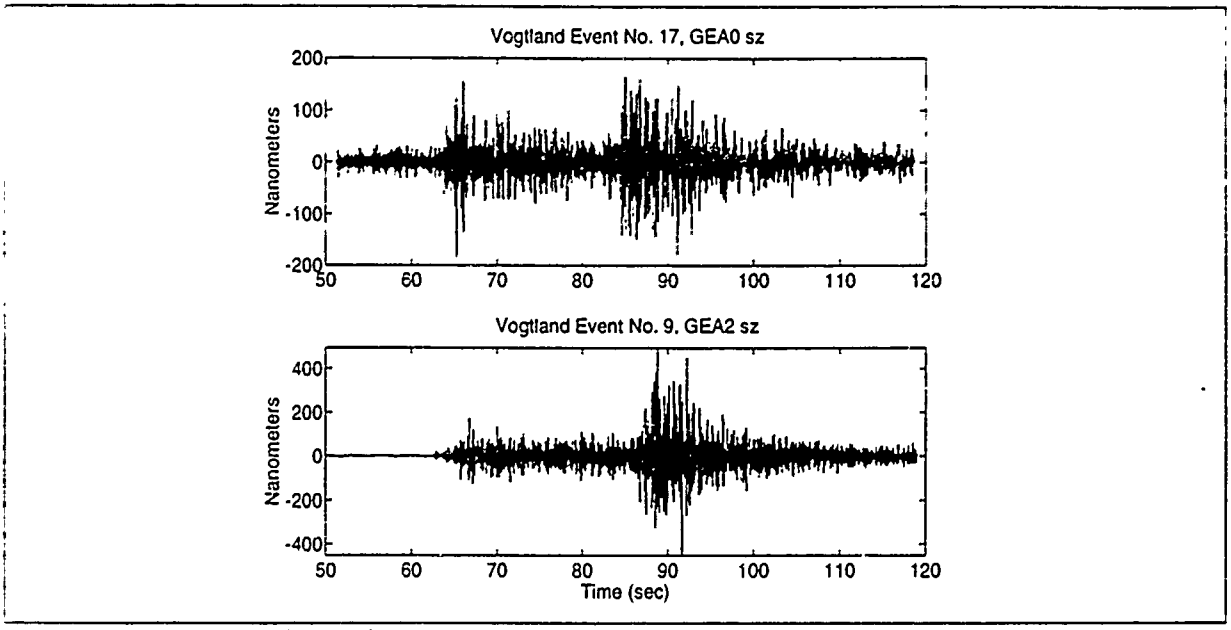

Figure 2. Examples of typical quarry explosion (Event 17) and earthquake (Event 9) from the GTDB Vogtland database. Note the difference in amplitude ratios of *P/Lg*. Data are unfiltered.

This observation is quantified on an event-by-event basis in *Figure 3*. The wideband *P/Lg* spectral ratios are close to unity for the explosions, while the values for earthquakes are closer to 0.5. As a test of identification capability for events in a new geographic area, spectral parameters extracted from these events were input to the trained neural network of *Figure 1*.[4] All of the events were correctly identified. An interesting observation is that the cepstral variance of P and Lg for the explosions is generally lower than is seen for explosions around NORESS. This is likely due to less

[3] Waveform data at GERESS often includes spikes and dropouts. These problems are usually undetectable on filtered waveform data, but must be eliminated from array-averaged spectral estimates used for classification experiments. Users are urged to review the raw data channel-by-channel before parameter extraction, the current authors can provide this information for all of the GTDB events to interested researchers.

[4] None of the Vogtland events were used to train the neural network.

use of ripple firing in the blasts. However, the network still correctly classified all of the events.

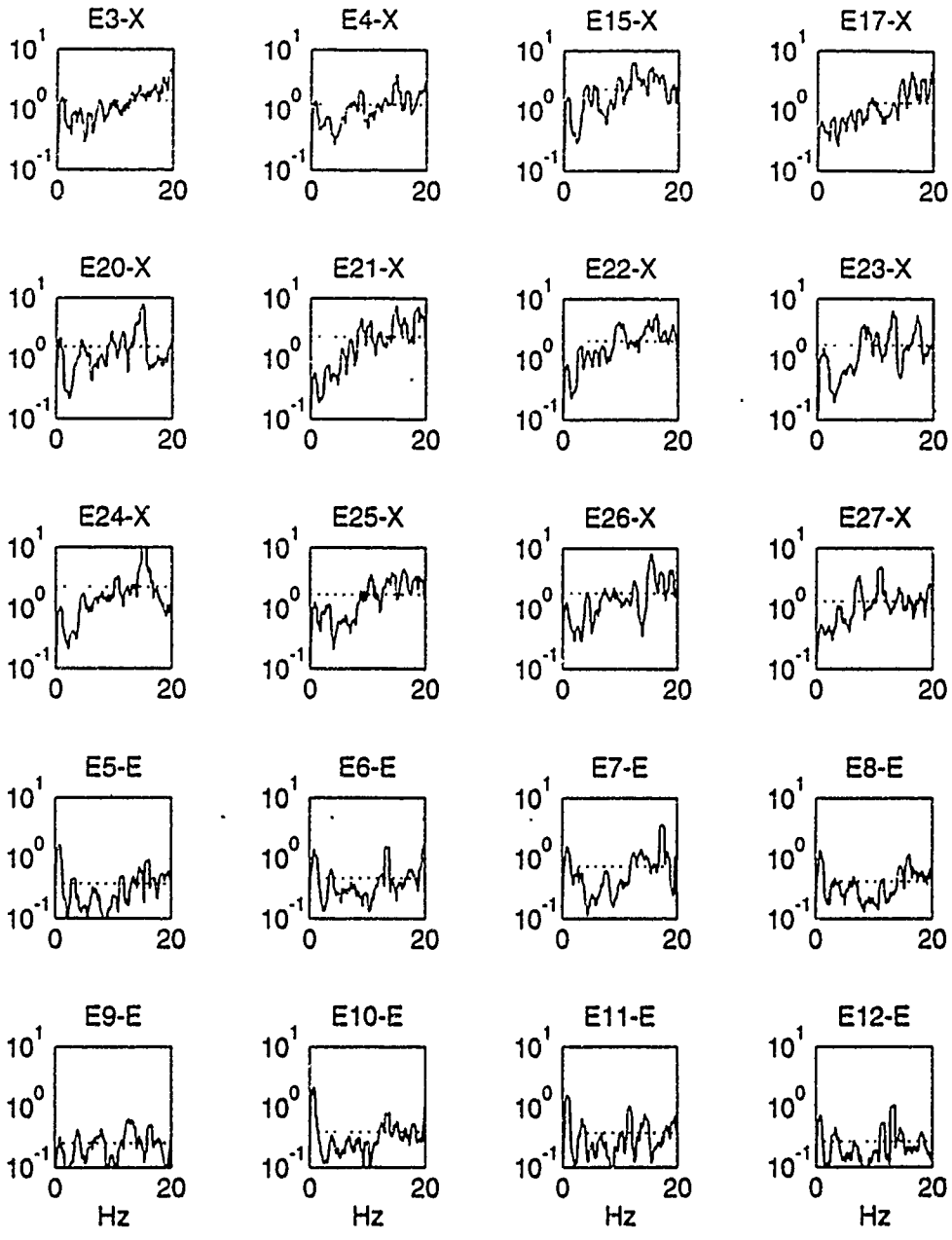

Figure 3. P/Lg spectral ratios for 12 explosions (X's) and 8 earthquakes (E's) in the GTDB Vogtland dataset. Dotted lines indicate average values across the band.

Lubin: The Lubin database consists of 31 *mining-induced tremors* in the Lubin Copper Basin of western Poland. This is an interesting dataset, because the seismograms and associated spectral features clearly fall into two classes, even though the event types are presumably all the same. *Figure 4* shows unfiltered seismograms for Events 67 and 68. Note that, as in the Vogtland dataset, there is a visible difference in the *P/Lg* amplitude ratios for the two events. The observation illustrated in *Figure 3* for Vogtland also holds for Lubin[5].

Spectral parameters extracted from these events were input to the neural network of *Figure 1*.[6]. Half of the events were identified as earthquakes, and half as explosions. Did the neural network fail this identification test?

Hasegawa *et al.* (1989) provide a review of mining-induced seismicity in Canada, and cite various mechanisms for the activity. These include rockbursts from the face of a quarry wall and tectonic movement on a pre-existing fault due to the removal of the overburden load. This may be what we are seeing in the Lubin dataset. It implies that two induced seismicity source types should be identified for machine learning experiments. We will retrain our neural network with these two classes of events and report on the results at the poster session.

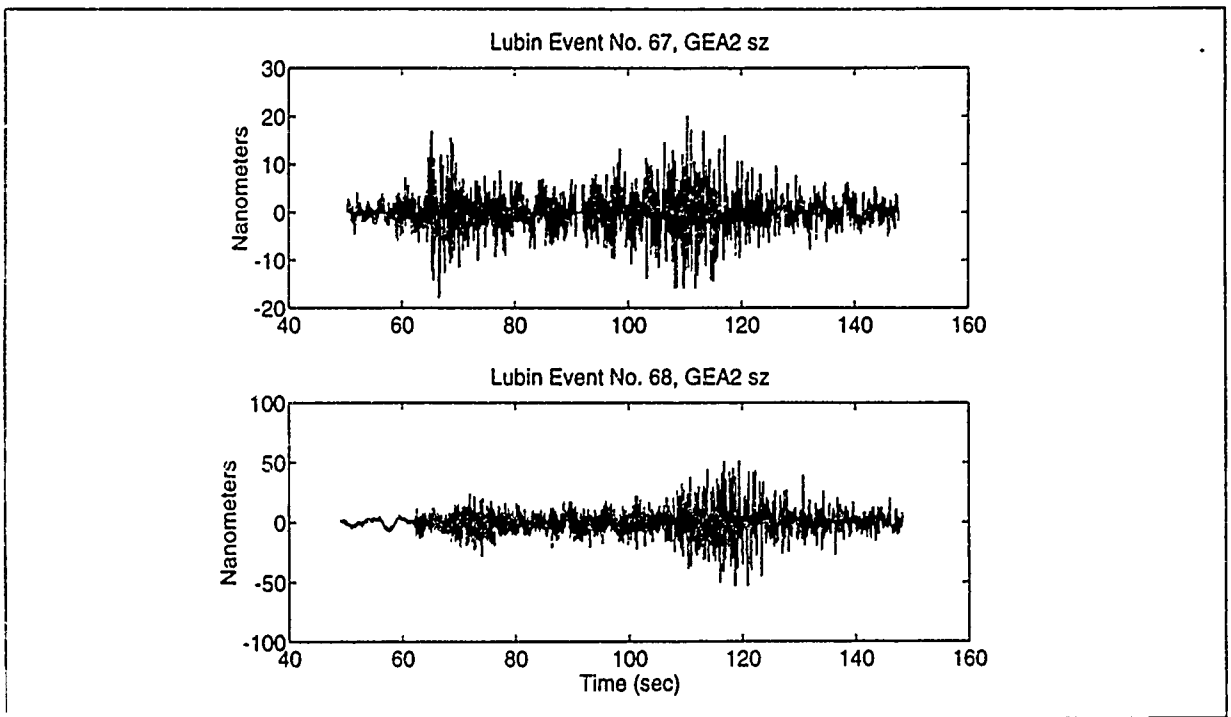

Figure 4. Unfiltered seismograms of Events 67 and 68 from the GTDB Lubin dataset. As in *Figure 2*, note the difference in amplitude ratios of *P/Lg*. Here, the events are both *mining-induced tremors*.

[5] See poster session at the meeting.

[6] Again, the Lubin events were not used to train the network.

The Dec. 31, 1992 Novaya Zemlya Event

At the request of Dr. Alan Ryall, an identification analysis was performed on the data for the Dec. 31, 1992 Novaya Zemlya event. Data from four regional arrays were available for examination: Apatity, ARCESS, Spitzbergen, and NORESS. Our identification was based on the ARCESS data, with the other array data proving to be of too low SNR for inclusion. Only *Pn* and *Sn* waves were visible at ARCESS (see *Figure 5*).

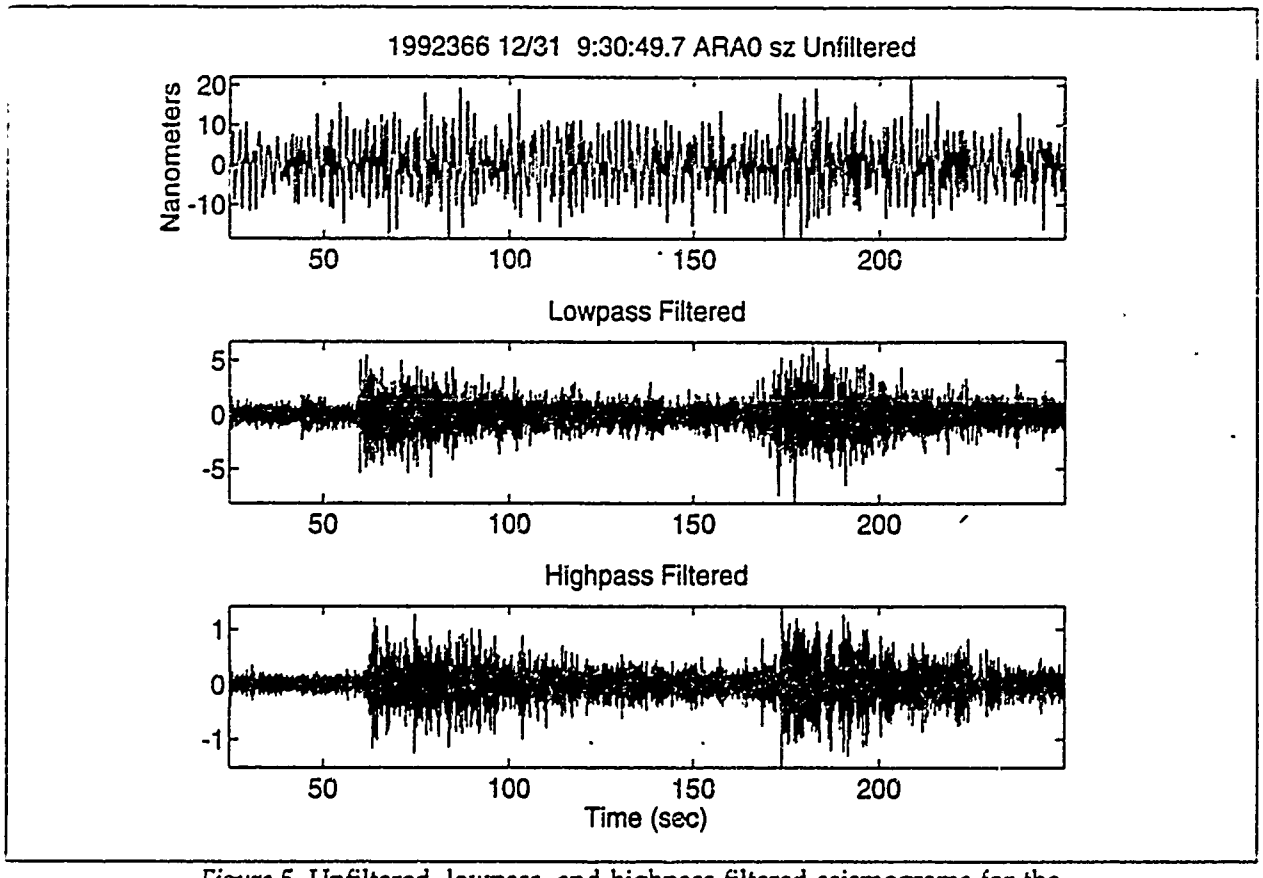

Figure 5. Unfiltered, lowpass, and highpass filtered seismograms for the Dec. 31, 1992 Novaya Zemlya event recorded at ARCESS.

Spectral parameters were determined using most array elements, with bad elements screened and deleted from the estimates. Values of the six spectral parameters are given in the following table.

Pn/Sn Broadband:	0.81
Pn/Sn 2-5 Hz:	0.76
Pn/Sn 5-10 Hz:	0.89
Pn/Sn 10-20 Hz:	0.75
Pn Cepstral Variance:	0.59
Sn Cepstral Variance:	0.61

These six parameters were fed into the trained neural network, with the resulting classification being a *chemical explosion*. But in a later conversation with Dr. Ryall, we were informed that the Russians have no record of chemical blasting in this area on the date in question. So, did the neural network produce an incorrect classification? Was this event actually an earthquake? Re-examination of individual spectral parameters still indicates that the data are closer to the explosion population than the earthquake population. However, given our recent experience with the Lubin dataset, it appears that this event may have been a mining-induced tremor.

Implementation as Part of the IMS

An effort is currently underway to include this identification capability as part of the IMS. The processing module is designed to run independently of the IMS, and only querries databases that the IMS produces. At the end of each day, a list of *origin-id's* is obtained, and the parameters (or waveforms) are obtained for these events. These are then input to the neural network, producing an event identification. Of course, ground-truth is not available for quantifying the network performance, but the results can be combined or compared with other event identifications provided by the IMS for a final event identification.

Conclusions and Recommendations

We have found backpropagation neural networks to be an effective tool for regional seismic event identification. Early reservations about overfitting the data and training on artifacts have been mitigated by the hybrid machine learning approach. We encourage the continued development of the Ground Truth Database as being essential for solving the general identification problem.

References

Crant, L., J. Coyne, and F. Ryall, CSS Ground-Truth Database: Version 1 Handbook, Scientific Report No. C93-05, Center for Seismic Studies.

Hasegawa, H.S., R.J. Wetmiller, and D.J. Gendzwill (1989), Induced seismicity in mines in Canada - an overview, *PAGEOPH, 129*, 423-453.

Jackson, J.E. (1991), *A User's Guide to Principal Components*, Wiley & Sons, Inc.

Lippman, R. (1987), An introduction to computing with neural nets, *IEEE ASSP Magazine*, April issue, 4-22.

Pulli, J. and P. Dysart (1992), Analysis and Testing of High-Frequency Regional Seismic Discriminants, Phillips Laboratory Report PL-TR-92-2125, 58 pp, ADA257763.

Two-Dimensional Signal Processing and Machine Learning for Regional Seismic Event Identification

Jay J. Pulli[1] and Paul S. Dysart[2]

[1] Radix Systems, Inc., 201 Perry Parkway, Gaithersburg, MD 20877
[2] Science Applications International Corp., 1710 Goodridge Dr., McLean, VA 22102

Contract No. F19628-93-C-0060

Objectives

The objective of this research effort is to develop and test a methodology for regional seismic event identification which combines 2-dimensional signal processing, image processing, and artificial neural networks. The methodology seeks to exploit the information content of an entire regional seismogram, and is particularly appropriate for small events, multiple events, and events with blocked, attenuated, or missing phases.

Research Accomplished

Background

The motivation for this research comes from our observation that the spectral features which distinguish quarry explosions from naturally occuring earthquakes can be seen throughout the entire seismogram. These features, which include the spectral complexity and spectral energy distribution (*P* vs *S*), are readily apparent in the time-frequency (TF) representation of the seismogram[1]. The TF distribution is particularly helpful in the analysis of events which have highly attenuated, blocked, or missing phases.

A number of investigators have pointed out the utility of the TF distribution for seismic analysis (Smith,1989; Hedlin et al., 1989). However, TF plots have not been widely used or accepted in the seismic community. There are a number of reasons for this situation: the difficulty of manipulating and operating on 2-D images vs 1-D time series or spectra; the lack of quantifiable measures of the features seen on TF plots; the lack of simple relations between TF images and the physics of the source

[1] The time-frequency distribution goes by many names. Examples include *spectrogram* and *sonogram*. We prefer the general term *time-frequency distribution*, because it includes many different types of distributions, such as Wigner-Ville, and special window functions such as the cone kernel. A spectrogram or sonogram implies a specific type of distribution.

and propagation effects, and the lack of a simple image discriminator which would allow automated processing of TF images.

During the course of our research on the application of artificial neural networks (ANN's) to seismic event identification, we have employed TF plots for the purposes of data review and phase timing. This use has led us to be able to perform simple visual classification of TF images which closely match the classification capability of our 1-D ANN-based processor. However, the TF image appears to excel in situations of low SNR, mixed events, or events with highly attenuated phases. Preliminary research has shown that we can exploit the information content of a TF distribution by first transforming the TF image into the wavenumber domain via a 2-D FFT, and then use a combination of image processing and simple backpropagation ANN's to extract 5 features which completely describe the spatio-temporal nature of the source. These 5 features can then be input to a separate ANN classifier to perform the final event identification. Our goal is to develop a processing module which impliments this scheme, and to test its performance with previously compiled databases of identified seismic events.

Signal Processing

To illustrate the specifics of the signal processing, we present the analysis of two small (m_b~2) seismic events recorded by the NORESS array. The first event is a quarry explosion at the Titania Mine in southwest Norway. The second event is a small earthquake along the southwest coast of Norway. Both events are approximately 500 km away from NORESS. Our discussion will demonstrate the utility of the combination of 2-D signal processing, image processing, and artificial neural networks to the identification of small seismic sources.

A key element of our methodology is the use of a parametric model to characterize the power spectrum of an arbitrary image. The model being used is a stochastic surface model originally developed by Goff and Jordan (1989) to characterize bathymetric surfaces. The model is parameterized in terms of 5 spectral features that completely describe the second order statistics of the image.

Step 1 involves the transformation of the original time series data (single station or array) into the time-frequency (TF) domain. There are numerous schemes for implimenting the TF transformation (Cohen, 1989), the simplest of which is to slide a tapered window down the time series and compute successive FFT's. The result can be displayed in a number of ways, but we prefer a 2-dimensional color-coded representation for simplicity. *Figure 1* shows the TF images of the two demonstration events[2].

---

[2] Publication restrictions do not allow the inclusion of color figures in this document. The black and white images convey much less information to the viewer. Please stop by the poster session, where all TF plots will be shown in color.

In *Step 2*, the TF image is transformed into the wavenumber domain using a 2-D FFT. The wavenumber representation of the demonstration events is shown in *Figure 2*. A variety of options exist at this stage, including the use of alternative 2-D images such as cepstra vs. time, *Lg/Pn* spectral ratios vs. time, binary images, and higher dimensional images.

In *Step 3*, an image processing algorithm developed using concepts from Johnson and Weichern (1992) is used to extract the angle, aspect ratio, and higher-order moments of the wavenumber image. The algorithm determines the covariance structure of the power spectrum by assuming it to represent a pseudo-probability density function. In addition to the covariance, from which the azimuth and aspect ratio are derived, the algorithm also computes several higher-order moments of the power spectrum that contain information about the remaining unestimated model parameters. The pattern recognition algorithm has been validated on a training set of synthetic power spectra which span the entire model parameter space (~4000 examples). The complete output of this validation exercise also provides the set of examples which are used to train an ANN to obtain the remainng model parameters.

In *Step 4*, an ANN is used to obtain the characteristic wavelengths and fractal dimension. The use of ANN's is subject to many of the constraints of classical error minimization techniques. The training set of exemplars derived from the synthetic power spectra are inavriant with respect to magnitude and azimuth. This has circumvented many of the potential difficulties due to image translation, rotation, and scaling. At the same time, the control inherent in the use of synthetic data has also been exploited to balance the number of exemplars with the number of ANN connections. Currently, the ANN obtains the three model parameters at an error level of less than 5%, although reductions in error could be attained by increasing the resolution of the training set.

In *Step 5*, a separate ANN is used to classify the unidentified events based on the predicted model parameters using both supervised and unsupervised learning. Model parameters are obtained quickly without iteration or starting values. The model parameters can be entered into a suprevised learning experiment given a large set of confidently identified events[3]. Alternatively, unsupervised learning may be employed to discover clusters potentially related to source type. In the case of the two examples presented here, the events are clearly separated by image azimuth and aspect ratio. For the Titania mine blast, the results indicate long wavelength lineations which extend across the TF image parallel to the time axis. In contrast, the coastal earthquake indicate largely isotropic features with a minor trend to lower frequencies with time. This feature may possibly be related to dispersion in the *Lg* wavetrain.

---

[3] For example, the CSS Ground-Truth Database, by Grant *et al.* (1993).

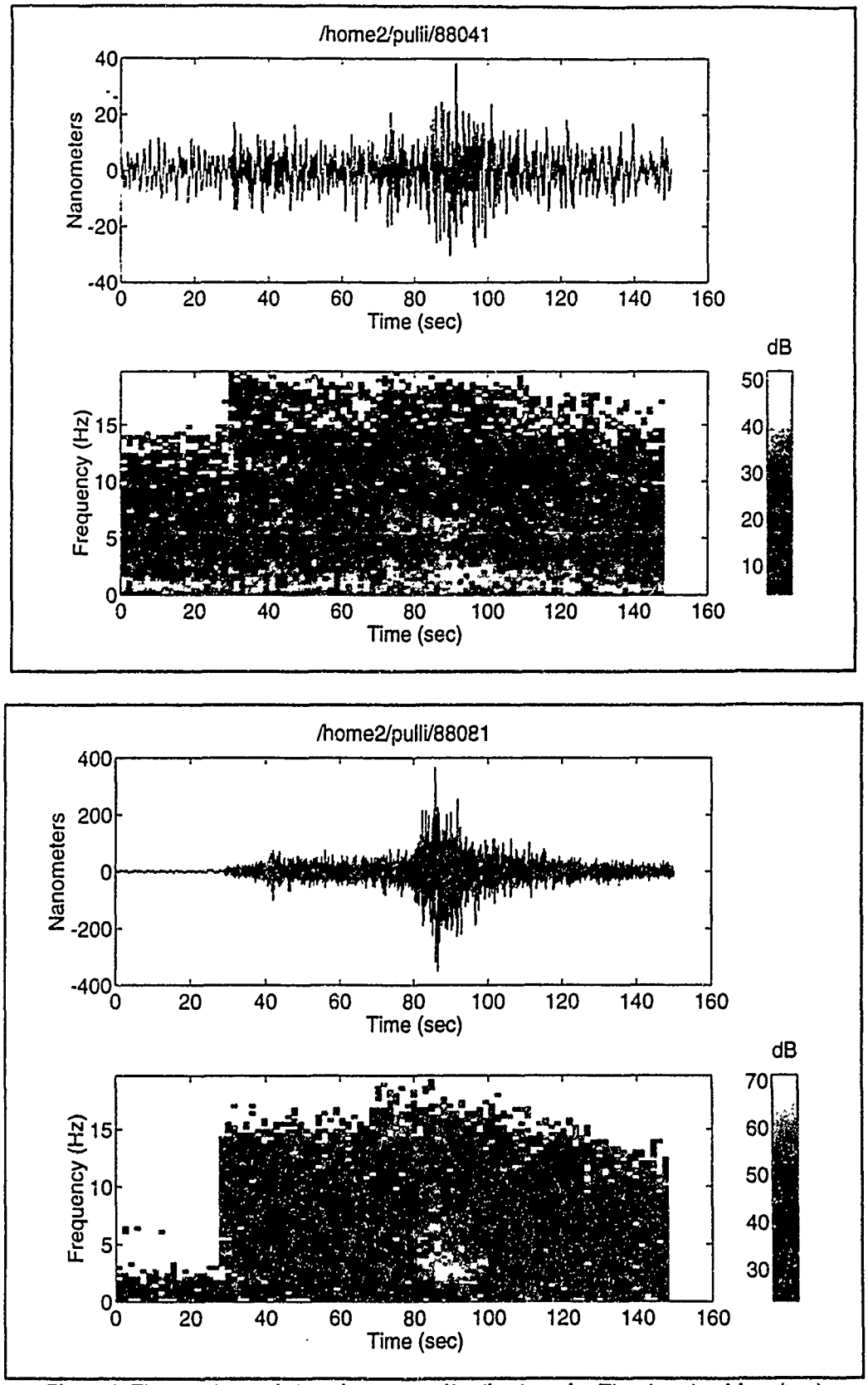

Figure 1. Time series and time-frequency distributions for Titania mine blast (top) and coastal Norway earthquake (bottom).

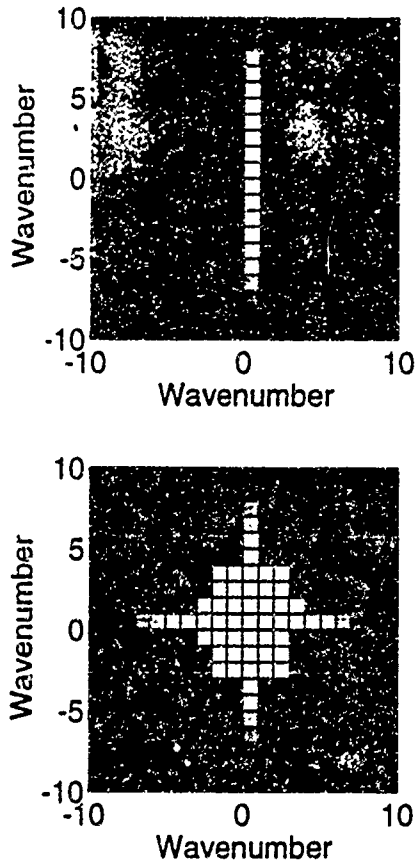

Figure 2. Wavenumber spectra of Titania mine blast (top) and coastal earthquake (bottom).

Conclusions and Recommendations

As of this writing, this research project is only 6 weeks old, so we do not yet have any conclusions to report. Our efforts to date have involved putting together the software to accomplish the research. By the time of the poster session, we plan to have applied this technique to the waveform data from the CSS Ground-Truth Database, being compiled by Grant *et al.* (1993).

References

Cohen, L. (1989), Time-frequency distributions - a review, *Proc. IEEE, 77*, 941-981.

Goff, J.A. and T.H. Jordan (1989), Stochastic modeling of seafloor morphology; inversion of sea beam data for second order statistics, *J. Geophys. Res., 93*, 13589-13608.

Grant, L. J. Coyne, and F. Ryall (1993), CSS Ground-Truth Database: Version 1 Handbook, Scientific Report No. C93-05, Center for Seismic Studies

Hedlin, M.A., J.B. Minster, and J.A. Orcutt (1989), The time-frequency characteristics of quarry blasts and calibration explosions recorded in Kazakhstan, USSR, *Geophys. J. Int.*, *99*, 109-121.

Johnson, R.A. and D.W. Weichern (1992), Applied Multivariate Statistical Analysis, Prentice Hall, N.J.

Smith, A.T. (1989), High-frequency seismic observations and models of chemical explosions: implications for the discrimination of ripple-fired mining blasts, *Bull. Seis. Soc. Amer.*, *79*, 1089-1110.

USING GROUPS OF SIMILAR EVENTS AT THE SCANDINAVIAN ARRAYS TO IDENTIFY AND TO RELOCATE EVENTS

F. Rivière-Barbier[1], D. Baumgardt[2] and W. Rodi[3]

[1] SAIC / Center For Seismic Studies, 1300 North 17th Street, Arlington, VA 22209
Contract # F29601-92-C-0005

[2] ENSCO, 5400 Port Royal Rd., Springfield VA 22151
Contract #F29601-92-C-0009

[3] MIT, Earth Resources lab., E34-458 42 Carleton St., Cambridge, MA 02139
Contract #F29601-91-K-DB15

OBJECTIVE

The number of events recorded each year at the Scandinavian arrays defeats the capabilities of a single analyst to review and improve the automatic location performed by the expert system IMS running at the Center for Seismic Studies. In order to build a tool that would automatically and reliably locate most of these events, thousands of them have been studied, reviewed and classified into 478 groups of similar events (Rivière-Barbier, 1993). From each group, a reference event was extracted as representing the other events. To complete the analysis of these events, an identification of the reference events was necessary that would establish the origin of each event in the same group. This data set was processed using different software and the results were compared to an independent source of identification: the Helsinki bulletin. The analysis of the results pointed out the influence of various factors in the event identification process. At the same time, the availability of such a large number of groups of similar events allowed us to test an event location algorithm based on differential times. The goal was to explore the capabilities of the algorithm using small events originating from the same area.

RESEARCH ACCOMPLISHED

Event identification

Description of the different identification methods

The EVID system was developed (Sereno and Wahl, 1993) using fuzzy-logic in order to combine regional discriminants applied to seismic signals (spectral variance, ripple-firing ...) with contextual discriminants (depth, seismicity level ...) to derive a composite identification. In a first step, the system separates earthquakes from explosions; then, a case-based approach is used to identify mining explosions.

The ISEIS system (Baumgardt *et al.*, 1991a,b) is a rule-based process taking into account several features of the seismic signals (*Pn/Sn* ratio, *Pn/Lg* ratio, *Sn* and *Lg* spectral ratios, ripple-firing ...). A process, using rules coded in the NASA expert systems shell, CLIPS, is used to identify events on the basis of individual discriminants extracted from the database, Finally, an overall event identification is made using a voting scheme. An important difference with the EVID system is that the ISEIS system does not include contextual discriminants in the identification process.

The event identification provided by the Helsinki Bulletin consists in determining an event location from the recordings of at least three stations and then comparing this with known mine locations. If the computed location is within 5 km of a mine and if the appearance of the seismic signal fulfills the known pattern from that mine, the mine location is reported in the bulletin (Tarvainen, 1993). Most of the events with magnitudes lower than 1.0 are not reported in this bulletin.

Application to the reference events

The reference events determined for each of the Scandinavian arrays have been processed through the event identification process described above. The results are summarized in Table 1.

Table 1: Summary of the event identification

Category	EVID	ISEIS	Helsinki bulletin	Helsinki bul. or similar events
Earthquakes	11	73	7	9[a]
Explosions	238	19	-	72[b]
Blasts	150[c]	147[d]	112	116
Undetermined	79	187	355[e]	281[e]
Total	478	427[f]	478	478

a. Includes events identified as "earthquakes" and events identified as "probably earthquakes".
b. Included reference events whose similar events were reported at different close mines in the Helsinki bulletin.
c. Events assigned to a particular mine.
d. Events with evidence of ripple-firing.
e. Events not reported in the Helsinki bulletin or reported with automatic locations.
f. Fifty-one events have not yet been processed by ISEIS.

EVID identified 81% of the reference events as being explosions; 39% of these explosions match a script for a particular mine (scripts are only available for the most active mines in Scandinavia). Among the 11 events identified as being earthquakes, two events confirmed the identification found in the Helsinki bulletin, and one event was located close to the Kiruna mine and showed an origin time similar to other events originating from this mine. No other sources of identification were available for the eight other events. Only 17% of the reference events were not automatically identified by EVID.

A review of the EVID results showed that 19 of the events were not identified because the script matching failed for a few parameters. If these parameters had not been inlcuded in the identification, EVID would have called these events "mine blasts". Several reasons account for poor results of the script matching process in these cases. The main reason is directly related to the quality of the automatic phase picks because the phase parameters used in EVID are computed at this stage of the data processing. The important scatter of the picks implies that the measurements being compared to the script are rarely the same, especially for phases coming after the first arrival. An example is shown on *Figure 1*. Values of five parameters have been plotted for 33 events (when data were available) originating from mine HV6 (61.4°N 34.3°E, Russia). The circled event was not identified by EVID because it did not match the script for those five of the

parameters. Another important parameter in the script match discriminant involves the origin time of the event being compared. It is split into an hour of the day and a day of the week. An example of mismatch due to the origin time is provided by an event originating from HV6 that occurred on January 5, 1991. The EVID process identified this event as an explosion with a moderate confidence as a result of the combination of the contextual discriminants and the regional discriminants. The fact that this event occurred on Saturday instead of on a week day (as shown in the script for the events coming from this mine) prevented EVID from calling it a mine blast from that mine. In this particular case, a waveform comparison would have allowed us to identify the event as a blast from mine HV6. *Figure 2* shows this particular event along with another from the same mine that occurred on a week day.

ISEIS provided an identification for 427 of the reference events which included 73 events identified as earthquakes, 19 events identified as generic explosions and 147 events identified as mine blasts. The reason for the large number of undetermined events is that these events were either too small for all phases (*Pn, Pg, Sn* and *Lg*) to be detected or they were local so only *Pg* phases were recorded. In addition, ISEIS is conservative in identifying events on the basis of *P/S* ratios alone, especially for explosions. It will tend to more likely identify the events as unknown than to misidentify an explosion. So, the number of "generic explosions" is low. Both generic explosions and mine blasts show large *Pn/Sn* and/or *Pn/Lg* ratios, but when spectral modulations (characterizing ripple-firing) are detected in a signal, the event is automatically identified as a mine blast because this feature has more weight than the other discriminants. In order for an event to be identified as an earthquake, at least one station should show a very low *P/S* ratio or two or more stations should show intermediate *P/S* ratios. So, many small earthquakes recorded by a single station may be unidentified. ISEIS identified many more earthquakes than either EVID or Helsinki and many less explosions. The reason is that, in absence of ripple fire, ISEIS must rely almost exclusively on high frequency regional *P/S* ratios (and the unreliable *Sn* and *Lg* spectral ratio). Recent studies by Baumgardt and Der (1993) have shown than mine blasts can produce strong shear waves, either due to spall or associated induced component. In addition, ISEIS does not use contextual discriminants, like regional seismicity or location, to identify explosions as does EVID. So, ISEIS may identify many blasts as earthquakes.

Event Location

We relocated a group of events on the basis of arrival time differences between events determined for regional phases (*Pn, Sn, Lg*) recorded at the Scandinavian arrays. For a given phase and a given array, the differential arrival time for a pair of events was obtained from the cross-correlation function between the waveform segments for the two events. The differential time is derived from the time lag corresponding to the cross-correlation function maximum. It is important in this technique that the waveform segments which are correlated include a similar portion of the seismogram around the phase of interest. The time windows for all phases were computed on the basis of the *Pn* arrival time since the expert system is able to pick *Pn* more consistently than the later phases. The differential times included in the relocation process were screened to exceed a threshold correlation coefficient (maximum of correlation function) and, in addition, the standard error assigned to a differential time measurement was inversely scaled by this coefficient. The most numerous and accurate data thus tend to come from the closest array to the events where signal-to-noise is generally highest.

Differential arrival time data were determined for two event clusters using all available

recordings at ARCESS, NORESS and FINESA. The cross-correlation computations were performed on the vertical component waveforms from sensors ARA0, NRA0 and FIA1. The first data set consists of 10 similar mining events originating from the Kovdor mine (Russia) according to the Helsinki bulletin identification (Uski et al., 1991). Their magnitudes range from 2.03 to 2.46 and their distances to the ARCESS, NORESS and FINESA arrays are 300 km, 1190 km, and 715 km respectively. The second data set consists of 35 earthquakes with magnitudes between 1.05 and 2.74 that occurred in the Steigen area (Norway) in 1991 and 1992. Most of the earthquakes were identified as being part of the same sequence (Atakan et al., 1992). They are located 480 km from ARCESS, 790 km from NORESS, and 880 km from FINESA. Of the 35 earthquakes, 16 produced arrival time data (absolute or differential) at only ARCESS and we thus show the relocations only for the remaining 19 events.

Event relocation

The arrival time data were inverted with M.I.T.'s multiple event location algorithm (Toksoz *et al*, 1993). This algorithm solves a nonlinear least squares criterion to simultaneously fit the hypocenters and origin times of all the events in a cluster to a combined set of absolute and differential arrival time data. The algorithm computes two confidence regions for each event: one on its absolute location and one on its location relative to the cluster centroid. The relative locations are generally more accurate than the absolute locations because of the information provided by the differential time measurements and because relative location estimates are less affected by errors in the travel-time model used in fitting the data. The first data set was inverted with the event depths fixed to the surface, and the second data set with variable depths but lower than 50 km.

The locations and error ellipses determined by the IMS are plotted for the first data set (Kovdor mine) on *Figure 3* (left). *Figure 3* (right) shows the new locations inferred on the basis of the differential times in addition to the IMS picks. Also shown is the 90% confidence ellipse on each location relative to the centroid of the group. The new relocation produces a much tighter cluster, slightly shifted toward the northwest with respect to the mine location. Eight of the ten events (excluding 4 and 8) are grouped within a few kilometers of each other. The error ellipses on the relative event locations have semi-axes of about 3 by 10 km, elongated in the east-west direction. While much smaller than the IMS error ellipses, they do not rule out the possibility that at least eight of the events have a common location. The error ellipse on the centroid location of the cluster (not shown), not accounting for travel-time modeling errors, is 5 by 13 km and also is oriented east-west. This implies that the relative locations of the events are determined much more accurately than their absolute locations.

Figure 4 shows three different sets of locations for the events from the Steigen area. The new locations are compared to IMS locations which are based on the same recordings and to the locations provided by K. Atakan (1993) which are based on several stations located close to the seismic area (19932). The locations provided by Atakan are circumscribed to a very small area while the IMS locations spread over 100 km^2. Our new locations are shifted closer to the "true" locations; part of them are aligned along a northeast-southwest trend parallel to and a few kilometers away from a possible fault shown by Atakan (*Figure 5*). Another group of these relocated events is located a few kilometers east of the "true" locations. The shift observed in the new locations can be due to errors in the travel time tables used as well as to the larger measurement errors in the absolute arrival times. Only 19 of the studied events had a defined error ellipse. The centroid of the 19-event cluster has an error ellipse of 8 by 2 km (semi-axes), not including the effects of

modeling errors. The relative error ellipses, shown in *Figure 6*, vary from 8 by 1.3 km to 69 by 6 km with the major axes in the southeast-northwest direction.

CONCLUSIONS AND RECOMMENDATIONS

The origin of most of the studied events could be determined using automatic processing. A "manual" review and a reinterpretation of the results will be necessary in order to get a better identification. When possible, the automatic results will be compared to the Helsinki bulletin identification. Our data set was dominated by small events (only 125 of the reference events had magnitudes above 2.0), and the two automatic systems presented in this paper show better performance for large events recorded at more than one array. The quality of the data processing preceding the identification is crucial since it determines the number of phases, their identification and the measurements made on these phases, all inputs to the identification process. The use of reference events waveform comparisons will allow the removal of most of the uncertainties related to the phase picking.

Our results show that the event relocation procedure using differential arrival times can reduce location errors considerably compared to the automated location procedure currently used in IMS. Relative location errors as small as one kilometer were achieved, which is useful in helping to identify events of unknown origin. We recommend that this approach be further improved and automated for use in automated event identification.

ACKNOWLEDGMENTS

The event identification processing using EVID and the interpretation of the results were performed by T.J. Sereno and D. D. Wahl from SAIC / San Diego.

REFERENCES

Atakan, K., C. D. Lindholm and J. Havskov (1993). Earthquake Swarm in Steigen, Northern Norway: An Unusual Example of Intraplate Seismicity. *Submitted to Terra Nova.*

Baumgardt, D. R. and Z. Der(1993). Investigation of Regional Seismic Discriminants Using Visualization and Statistical Analysis Methods in the Intelligent Seismic Event Identification System (ISEIS). in *Proc. of the 15th Annual ARPA/GL Seismic Research Symp.*, 8-10 September 1993, Vail, Colorado.

Rivière-Barbier, F. (1993). Constructing a Reference Event List for ARCESS. Special Technical Report C93.03. Center for Seismic Studies, Arlington, VA.

Sereno, T. J. and D. D. Wahl (1993). A Fuzzy-Logic Approach to the Regional Seismic Event Identification: Application to the Novaya Zemlya Event on 31 December 1992.

Tarvainen, M. (1993). *Personal Communication.* Institute of seismology, University of Helsinki, Helsinki, Finland.

Toksöz, M.N., Y. Li and W. Rodi (1993). Seismic Source Characterization With Empirical Green's Function and Relative Location Techniques, in *Proc. of the 15th Annual ARPA/GL Seismic Research Symp.*, 8-10 September 1993, Vail, Colorado.

Uski, M., E. Polkonen, M. Franssila, M. Raime (1990-1993). Seismic Events in Northern Europe. *Ed. H. Korhonen.* Institute of seismology, University of Helsinki, Helsinki, Finland.

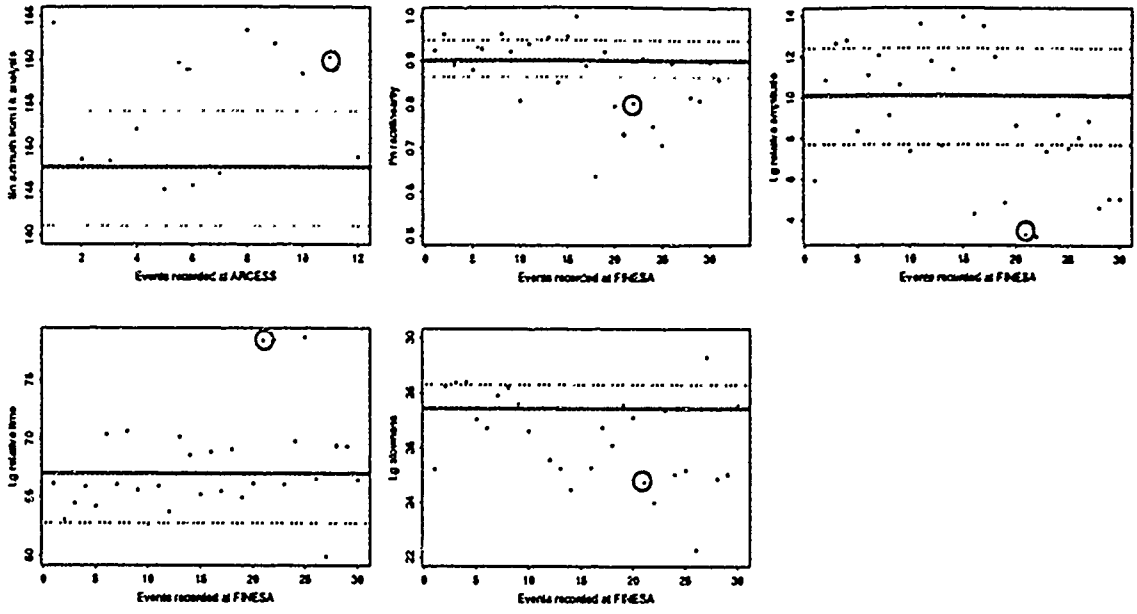

Figure 1: Five of the regional parameters used in the script matching are shown for a blast from HV6 that was not identified. The thick line represents the average value and the dashed lines, the standard deviation. Both values were derived from another data set. The *Lg* recorded at FINESA was not properly picked by the automatic system.

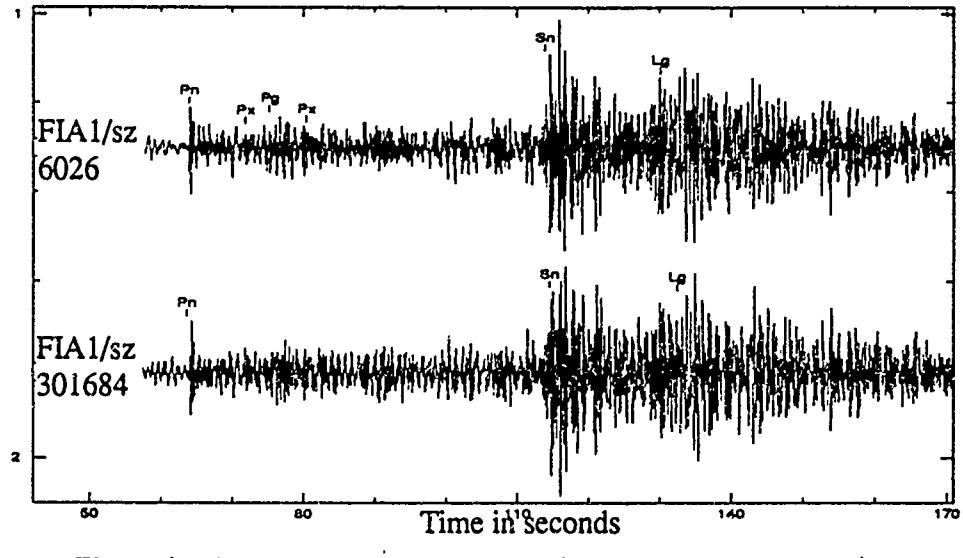

Figure 2: The top event was not identified as a blast by EVID because the script match failed on the parameter "day of the week". This event occurred on Saturday. It is compared to an event from the same mine (bottom) that occurred on Friday. Events from this mine occur almost always on between Monday and Friday.

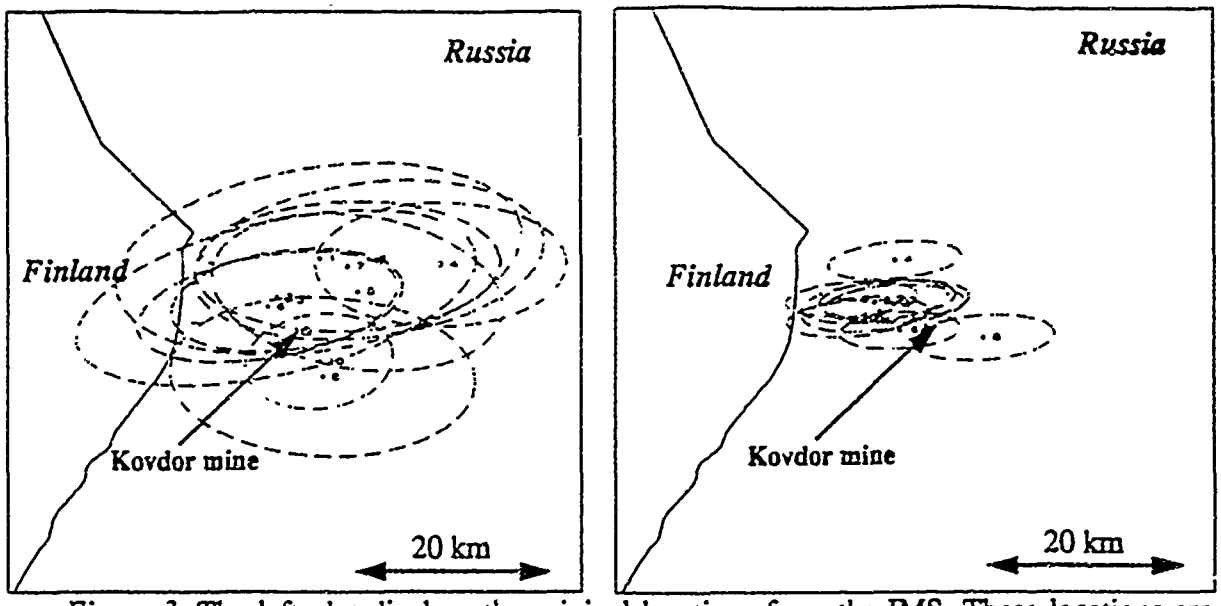

Figure 3: The left plot displays the original locations from the IMS. These locations are based on recordings from the 3 Scandinavian arrays (and from the Spitzberg station for the most recent events). The right plot shows the new relative locations also using data from the 3 arrays.

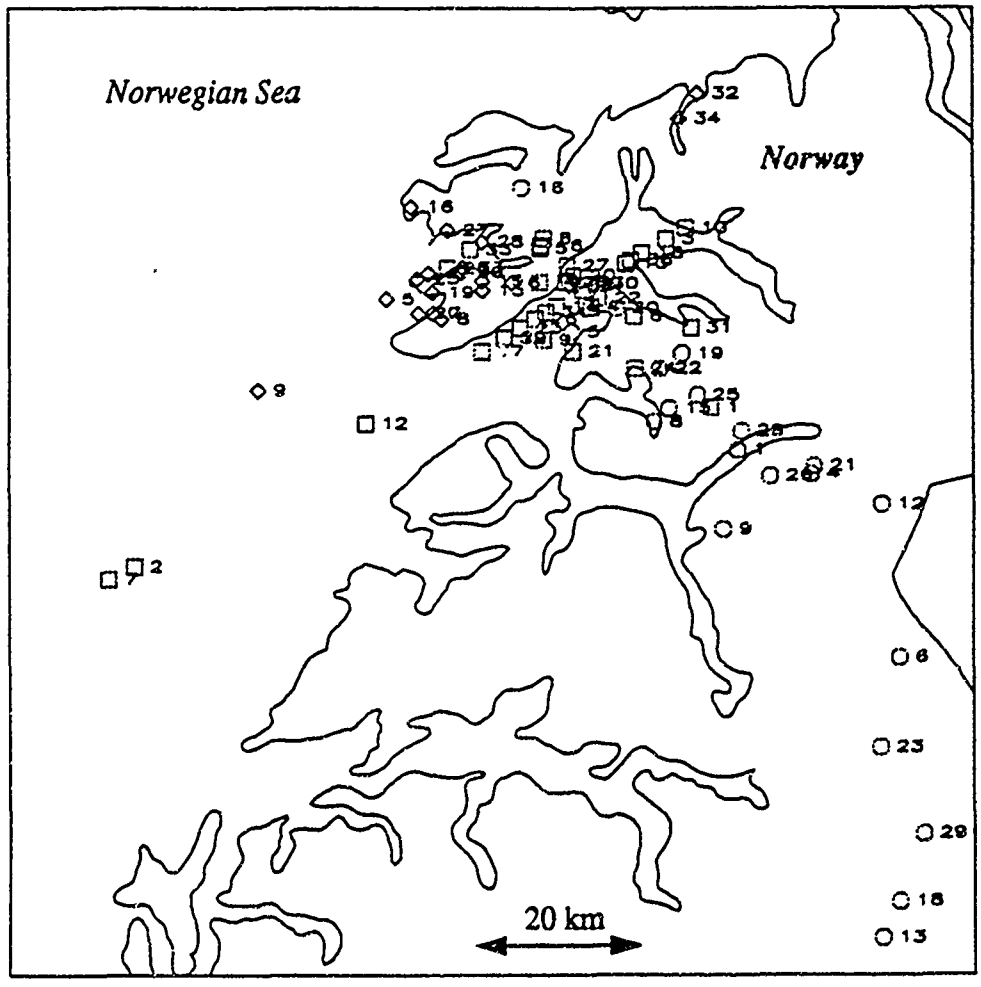

Figure 4: Comparison of the Steigen event locations from K. Atakan (lozenges), from the IMS (circles), and from inverting differential times (squares).

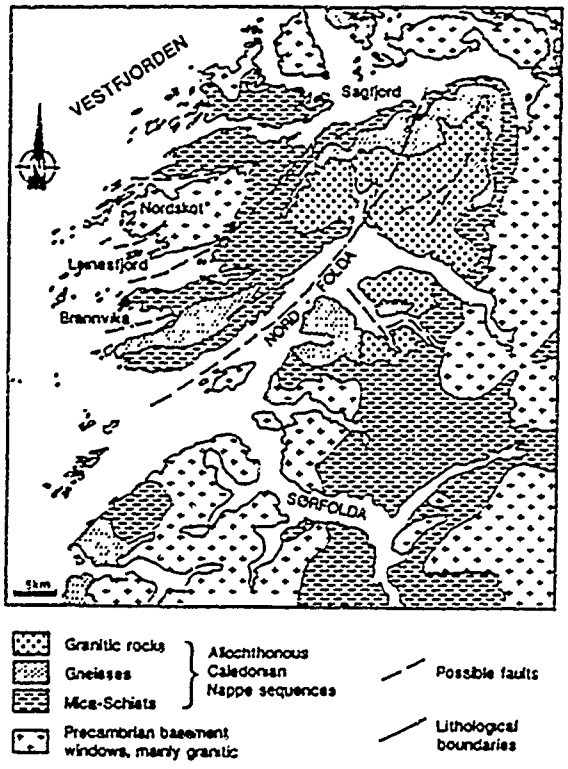

Figure 5: Detailed geological map of the Steigen area (Atakan, 1993).

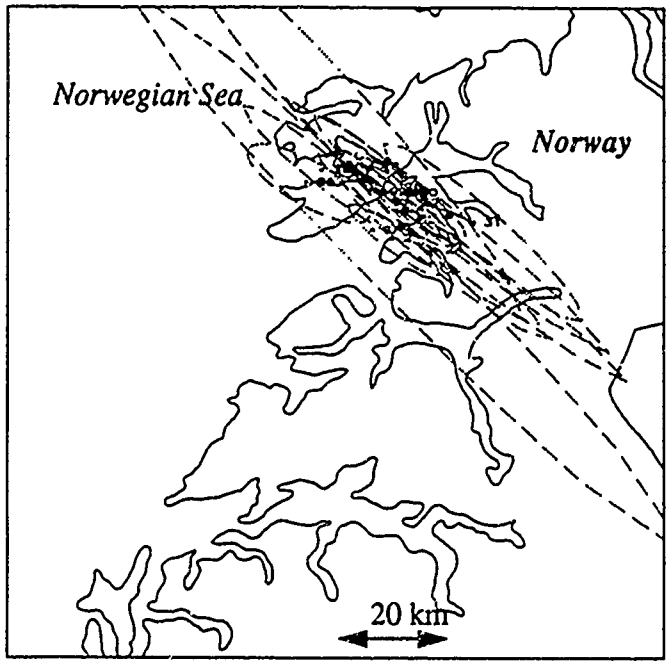

Figure 6: Locations based on differential times for 19 events of the Steigen sequence.

Modelling and analysis of seismic wave propagation in the lithosphere using 2D finite difference synthetics

B.O. Ruud[1], E.S. Husebye[2] and S.O. Hestholm[3]

[1] Faculty of Sciences, University of Oslo, Norway
[2] Institute of Solid Earth Physics, University of Bergen, Norway
[3] IBM Bergen Environmental Sciences and Solutions Centre, Bergen, Norway

Grant: AFOSR F49620-92-J-0510

Objective

The aim of this project is to foster a better understanding of seismic wave propagation in complex lithospheric media including surface topography through synthetic modelling and analysis of array data. Principal modelling tool is 2D finite difference (FD) synthetics; lithospheric representations range from a laterally homogeneous crust over a halfspace to inhomogeneous media including spatially anisotropic correlation functions with 2 to 4 per cent velocity perturbations and with von Kármán type of topography both at Moho and the free surface. Complementary array data analysis was tied to local events recordings from the NORESS and ARCESS arrays.

Research accomplished

In this section we first very briefly describe the research tools at hand, before presenting the outcome of various types of synthetic seismogram experiments.

2D FD synthetics: The FD schemes used here, have most recently been descriebed by Hestholm, et al (1993). The incorporation of 2D free surface topography is detailed by Hestholm and Ruud (1993) while its extension to 3D is presented by Hestholm (1993). Initially, we used rather simple compressional (P-wave) and rotational (S-wave) sources; we are now incorporating earthquake source representations.

Flexible lithosphere model representation: The basic lithospheric model have a crustal thickness of 35 km, and constant velocity gradients both above and below the Moho (Fig. 1). P- and S-velocities are related through the Poisson's ratio of 0.25, and model densities are calculated from the P-velocities via Birch's law. In our calculations of

synthetics, the above basic model has been perturbed in various ways including topography based on a 1D von Kármán realization. As a guide for judging the extent of scattering from various kinds of complex media, the synthetics from a simple laterally homogeneous model served as a reference (Fig. 2). Notice the lack of coda waves and the relative sharpnesses of P- and S-phase arrivals.

Interface and surface scattering: For convenience, geophysicists consider the Moho as an essensial smooth interface although it might well be irregular. This problem is not easily resolved by seismic means as the wave response of a corrugated Moho was found to be modest. On the other hand, the number of secondary P- and S-arrivals appear to be legio for a simple lithosperic model including topography (Fig. 3). Such irregularities effectively converts P-waves into Rayleigh (Rg) waves both in forward and backward modes and vice versa (Bannister et al, 1990; Ruud et al 1993). Indeed, the latter effect explain why Rg-waves seldom are observed in the NORESS and GERESS recordings at distances exceeding about 100 km; both arrays are situated in hilly areas.

Crust and upper mantle heterogeneities: A major drawback with the above interface scattering models are their inability to excite coda to levels comparable to real recordings. Our approach here was to generate synthetics for progressively more complex models essentially tied to introducing von Kármán type (order 0.3) of velocity perturbations in the crust and/or upper mantle. An example is given in Fig. 4 for a homogeneous crust but with 4 per cent RMS velocity perturbations in the upper mantle. Furthermore, spatial anisotropy is imposed on the heterogeneities by using horizontal correlation length four times that of the vertical. The displayed synthetics are interesting on two accounts; firstly sub-Moho layering or other types of heterogeneities appears to be a pre-requisite for observations of relatively strong Pn- and Sn-phases. Heterogeneities in the upper mantle apparently scatter the the Pn- and Sn-energy, consisting of head waves and diving waves propagating along and just below the Moho, up into the crust. Another feature is the prominent coda excitation. Semblance analysis of the synthetics implies that the P-source coda as shown in Fig. 4a) almost exclusively consists of P-to-S reflected wavelets from the sub-Moho heterogeneities. The relatively large amplitudes of these wavelets may indicate that our RMS velocity fluctuations of 4 per cent is too large. For example, Flatté and Wu (1988) using NORSAR teleseismic P-waves obtained a RMS velocity estimate of 2 per cent.

In Fig. 5 we display synthetics for a model where only the crust is inhomogeneous. In comparision to Fig. 2, the Pn-phase is essentially intact, while the conventional crustal phases have been strongly distorted. We take this 'smearing' to reflect the cumulative effect of wave propagation through an inhomogeneous medium. In Fig. 6 synthetics are shown for a model where both the crust and upper mantle are inhomogeneous. An equivalent snapshot presentation is given in Fig. 7. These synthetics are encouraging in the sense that their essential features are similar to those observed in real recordings. These are a relatively weak Pn followed by a stronger Pg/PmP and then a coda of long

duration with amplitudes similar to those of the Pn-phase. The first part of the coda is dominated by P-wavelets while P-to-S coverted waves become prominent at times coincident with the Sg/Lg arrival. Since P-to-S scattering is inefficient in the forward direction these wavelets would mostly arrive after the direct S-phase. The late coda appears to consists of diffusively scattered waves and is manifested in terms of low coda coherency.

Teleseismic coda excitation: The so-called complexity discriminant amounts essentially to a comparision of P-signal power to the P-coda power in two windows of 5 and 30 sec lengths (Tsvang et al, 1993). The workings of this discriminant is physically explained in terms of more efficient S- and Rg-excitation for earthquakes which in turn are converted into P-wavelets subsequently dominating the P-coda at the receiver end. We checked this hypothesis through examination of synthetics extracted at a depth of 100 km. To our surprise, at this depth the P-coda waves were mainly S-wavelets which would not contribute to the teleseismic P-coda. In other words, the relatively strong earthquake P-coda stem seemingly from source complexities as scattering and mode conversions appear to contribute only moderately.

Effect of spatial anisotropy: Most of the synthetics generated in our study (Hestholm et al, 1993) were tied to models with high aspects ratios which is intended to mimic a presumed dominance of horizontal layering in the lithosphere. The effect of spatial anisotropy was most clearly seen in the late coda. For example dominant horizontal correlation gave rise to relatively vertically travelling wavelets while dominant vertical correlation produced mainly horizontally travelling wavelets. However, we were unable to identify such coda feature in our analysis of NORESS and ARCESS event recordings. Probably, the crust is more heterogeneous than the upper mantle, thus scattered waves are mainly confined to the crust and will propagate almost horizontally even when the horizontal correlation is dominant.

Source depth effects: Since depth is a highly significant parameter in seismic event classification studies, we explored whether the seismic wavefield changes significantly with source depth. In Fig. 7 the synthetics are for S-sources at depths of 2 and 20 km respectively at a lapse time of 30 sec. Clearly, a shallow source is efficient in coda excitation because it generates more surface and body waves which propagate with low velocities in the upper part of the crust and subsequently can be scattered by surface topography. The upper snapshot gives an indication of the effectiveness of S-to-Rg conversions at the free surface (Rg waves confined to the upper 3 km of the crust). Likewise, the mentioned smearing of the P- and S-phases are relatively more prominent for shallow sources. In view of the above results it is not surprising that chemical explosion/earthquake source discrimination is feasible at local distances (Dysart and Pulli, 1990; Blandford, 1993). Of particular interest here is the potential of using coda waves as a discriminant as demonstrated by Hedlin et al (1990) and Su et al (1991).

Conclusions and recommendations

The major outcomes of our 2D FD experiments are that a basically simple crustal model (no layering) but with small scale velocity perturbation of 2 to 4 per cent suffice for generating realistic seismograms including coda excitations. Free surface topography influence wave propagation in several ways; most notably in efficient P-to-Rg and S-to-Rg scattering. Likewise the coda would be different for sources in the upper and lower crust respectively. Extensive propagation in an inhomogeneous lithosphere tends to 'smear' the once sharp P- and S-phases so clear secondary arrivals are difficult to indentify at epicenter distances beyond a few hundred kilometers. Strong Pn- and Sn-phases were obtained for models with sub-Moho heterogeneities with dominant horizontal correlation; an upper mantle velocity gradient and an irregular Moho interface proved relatively inefficient in this respect. Our overall conclusion is that the entire seismic record including the coda should be used for seismic source classification studies.

References

Bannister, S.C., Husebye, E.S. & Ruud, B.O., 1990. Teleseismic P-coda analyzed by three-component and array techniques - deterministic location of topographic P-to-Rg scattering near the NORESS array, Bull. Seism. Soc. Am., 80, 1969-1986.

Blandford, R.R., 1993. Discrimination of earthquakes and explosions at regional distances using complexity. Tech. Rep., AFTAC-TR-93-044, AFTAC Headquarters, Patrick AFB, Fl.

Dysart, P.S. & Pulli, J.J., 1990. Regional seismic event classification at the NORESS array: seismological measurements and the use of trained neural networks, Bull. Seism. Soc. Am., 80, 1910-1933.

Flatté, S.M. & Wu, R.S., 1988. Small-scale structure in the lithosphere and asthenosphere deduced from arrival time and amplitude fluctuations at NORSAR, J. Geophys. Res., 93, 6601-6614.

Hedlin, M.A.H., Minster, J.B. & Orcutt, J.A., 1990. An automatic means to discriminate between earthquakes and quarry blasts. Bull. Seism. Soc. Am. 80, 2143-2160.

Hestholm, S.O. 1993. 3D finite difference elastic wave modelling including surface topography. ERL/MIT Tech. Rep., Feb 1993, Cambridge, Ma.

Hestholm, S.O., Husebye, E.S. & Ruud, B.O., 1993. Visualizing seismic wave propagation in complex crust-upper mantle media using 2D finite difference synthetics.

Manuscript submitted for publication.

Hestholm, S.O. & Ruud, B.O., 1993. 2D finite difference elastic wave modeling including surface topography. Manuscript submitted for publication.

Ruud, B.O., Husebye, E.S. & Hestholm, S.O., 1993. Rg observations from four continents: inverse and forward modelling experiments. Geophys. J. Int., in press.

Su, F., Aki, K. & Biswas, N.N., 1991. Discriminating quarry blasts from earthquakes using coda waves. Bull. Seism. Soc. Am. 81, 162-178.

Tsvang, S.L., Pinsky, V.I. & Husebye, E.S., 1993. Enhanced seismic source discrimination using NORESS recordings from Eurasian events, Geophys. J. Int., 112, 1-14.

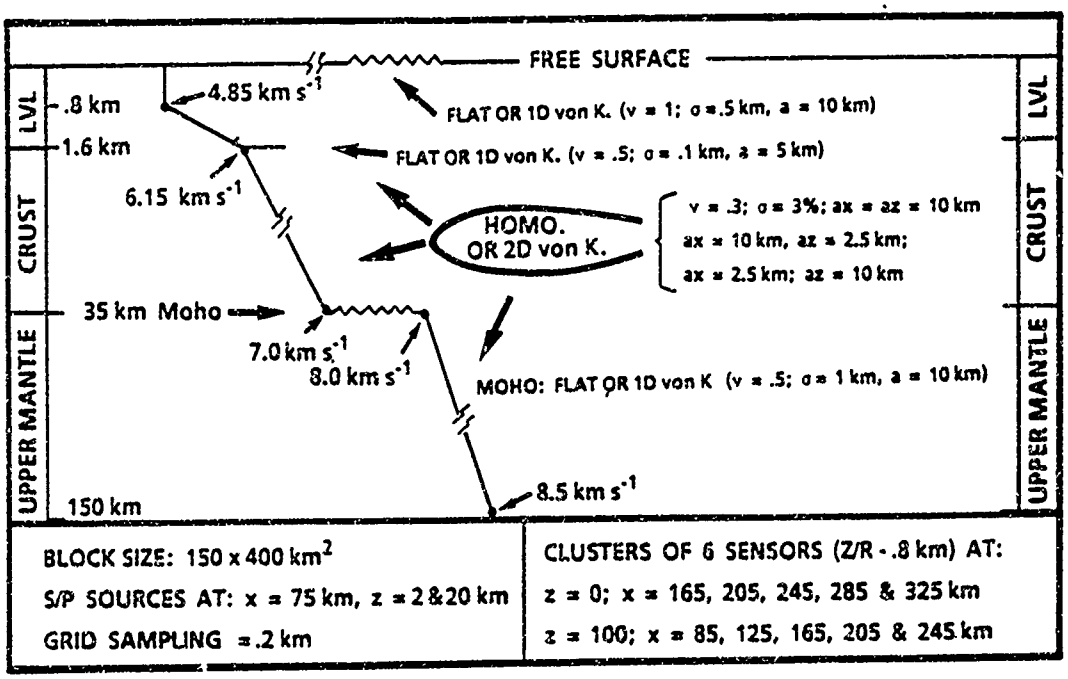

Fig. 1: The class of crust and upper mantle models used in our generation of 2D finite difference synthetic seismic records. Specific modal choices are detailed in the figure captions. The synthetic seismograms are calculated for 5 groups of 6 sensors each. Configuration details in the lower boxes. The minimum horizontal distances between the source and the closest sensor grouping (A0) are 90 km (surface) and 10 km (at 100 km depth).

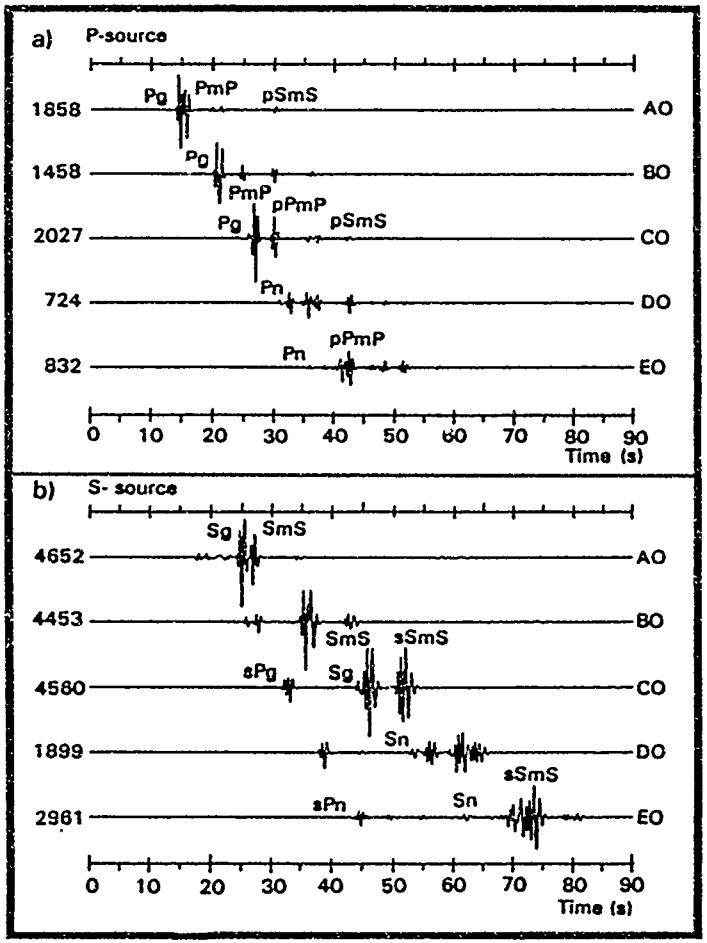

Fig. 2: The P- and S-source synthetic seismograms (Z) shown in a) and b), respectively, are for a homogeneous medium, that is, no velocity nor interface pertubations. Common features are a source depth of 20 km and that only the first trace from each of the free surface sensor clusters are shown. Adding figures a) and b) would give synthetics similar to those stemming from an earthquake source (except for radiation pattern). The synthetics in this figure are used as reference for comparing synthetics generated for various types of inhomogeneous media, shown in Figs. 3–7.

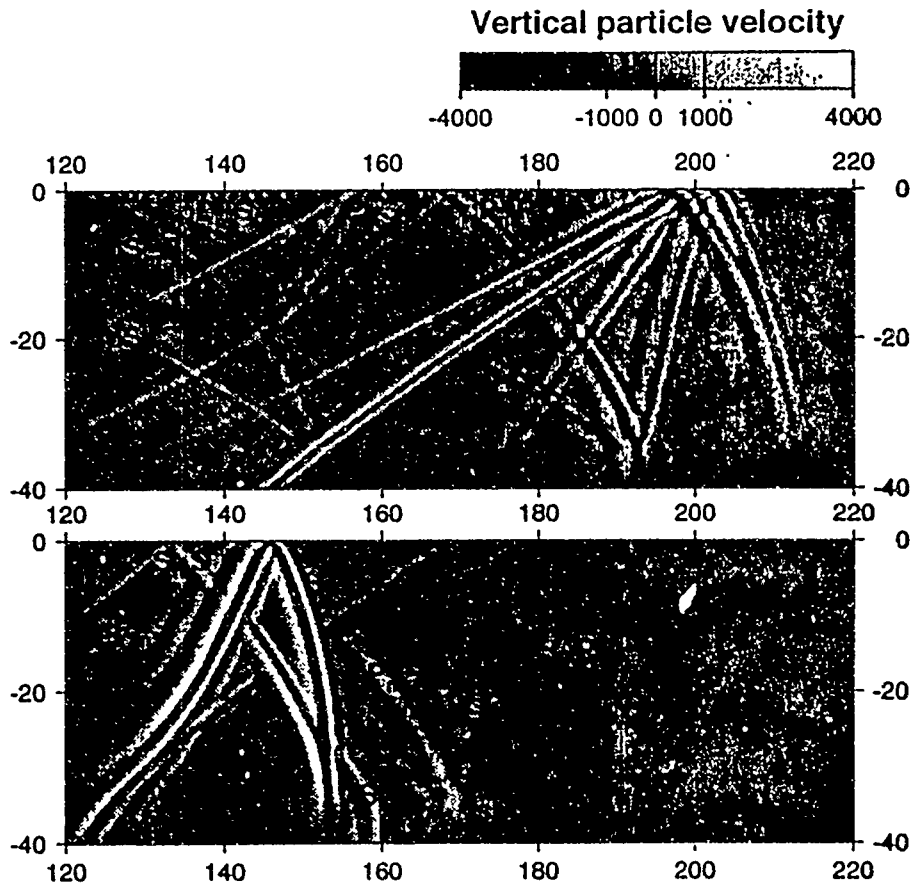

Fig. 3: Snapshot displays at a lapse time of 20 sec for P- and S-sources at 20 km depth and embedded in a homogeneous medium with free surface topography (von Kármán order of 1.0, correlation distance of 10 km and RMS fluctuations of 0.2 km). The synthetics are quite complex although only the major upgoing phases are labeled. The P-to-Rg conversions at the surface appears as a grey/white banding in the top crust of a). In b) P-to-S conversions can also be seen.

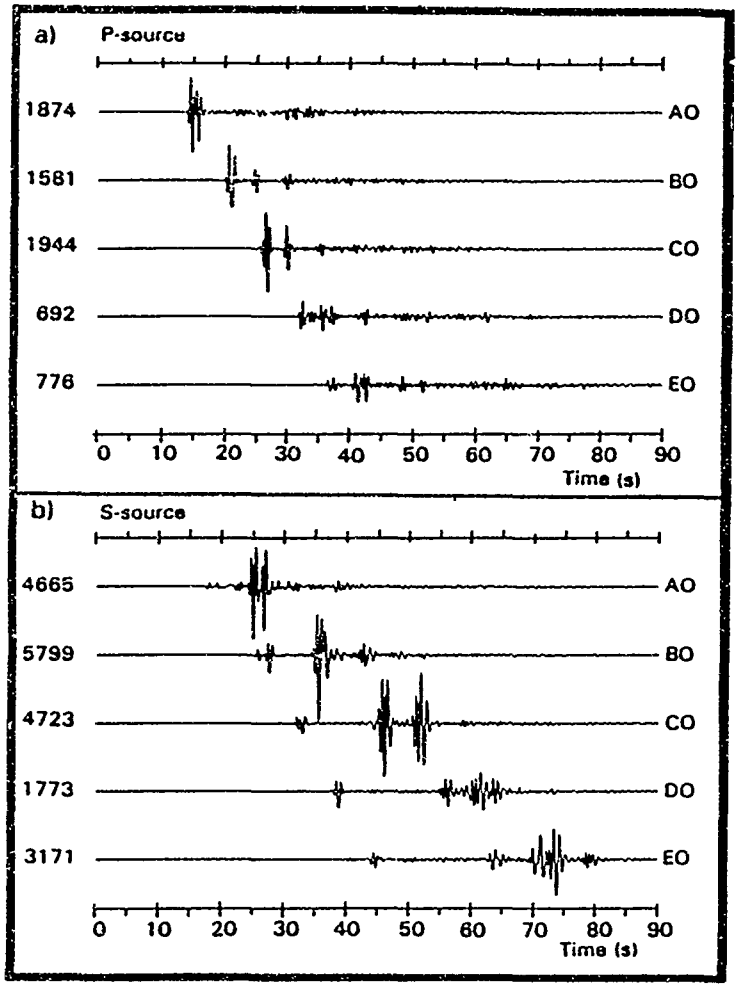

Fig. 4: P- and S-source synthetics in a) and b), respectively, for a homogeneous model except that the upper mantle part is inhomogeneous (source depth 20 km, von Kármán order of 0.3, correlation distances of 10 km (ax) and 2.5 km (az), and RMS velocity pertubations of 4 per cent. In comparison to Fig. 2 the crustal phases are little deformed, while the Pn and Sn phases on trace E0 are strong and appear to be delayed approx. 1 sec in time. The relatively strong coda reflects first order back-scattering contributions from sub-Moho inhomogeneities.

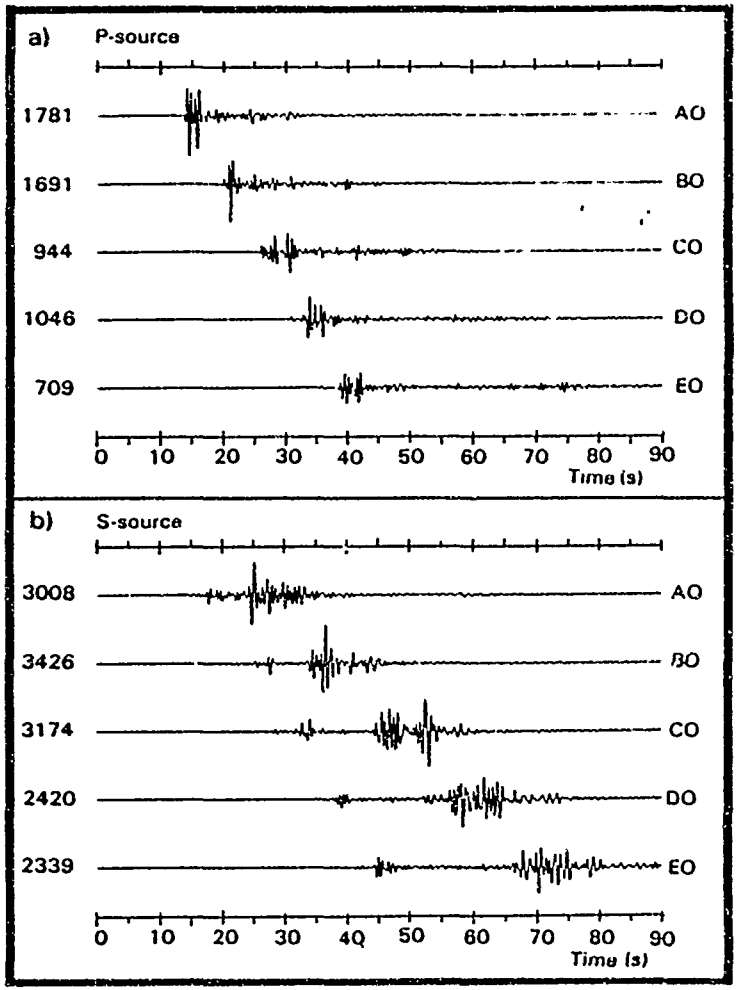

Fig. 5: P- and S-source synthetics in a) and b), respectively for a homogeneous model except that the crustal part is inhomogeneous (model parameters as in Fig. 4 caption). In comparison to Fig. 2, the crustal phases like Pg and Sg (Lg) are strongly deformed. The relatively high coda levels for the P-source imply that P-to-S scattering is efficient.

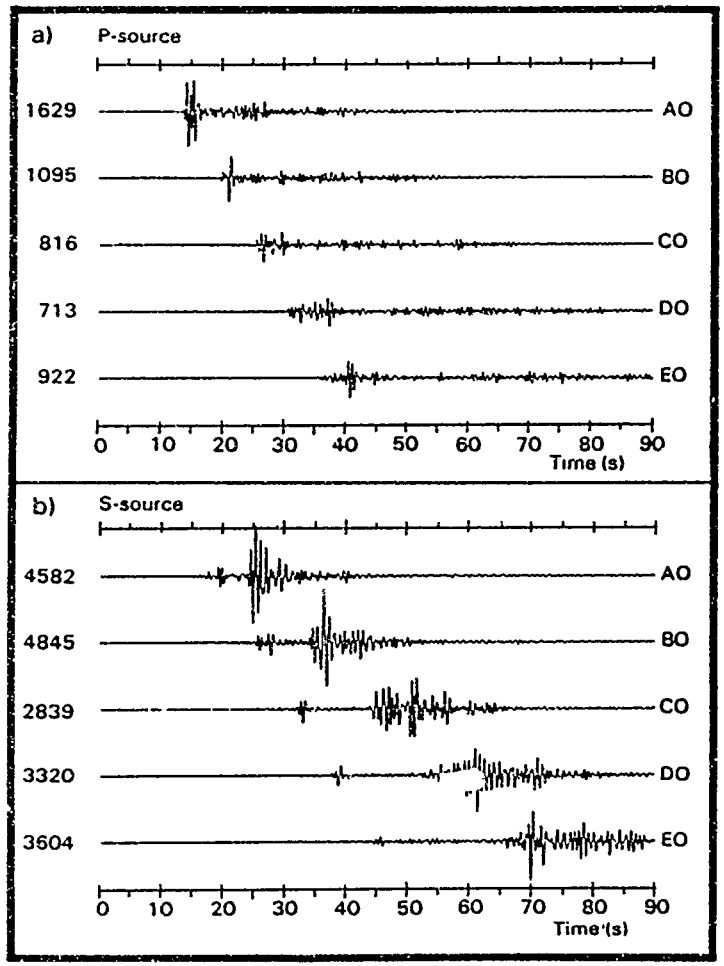

Fig. 6: P- and S-source synthetics in a) and b), respectively, for an inhomogeneous medium with a corrugated Moho but a flat free surface (Moho undulations: von Kármán of order 0.5, correlation distance 10 km and RMS fluctuations of 1 km; medium pertubations as in Fig. 4 caption except for RMS flutuations of 3 per cent). Compared to Fig. 5, all the major P- and S-phases are strongly distorted and besides a relatively strong coda emerges. Quantitatively, these synthetics including their coda waves are roughly similar to real event recordings.

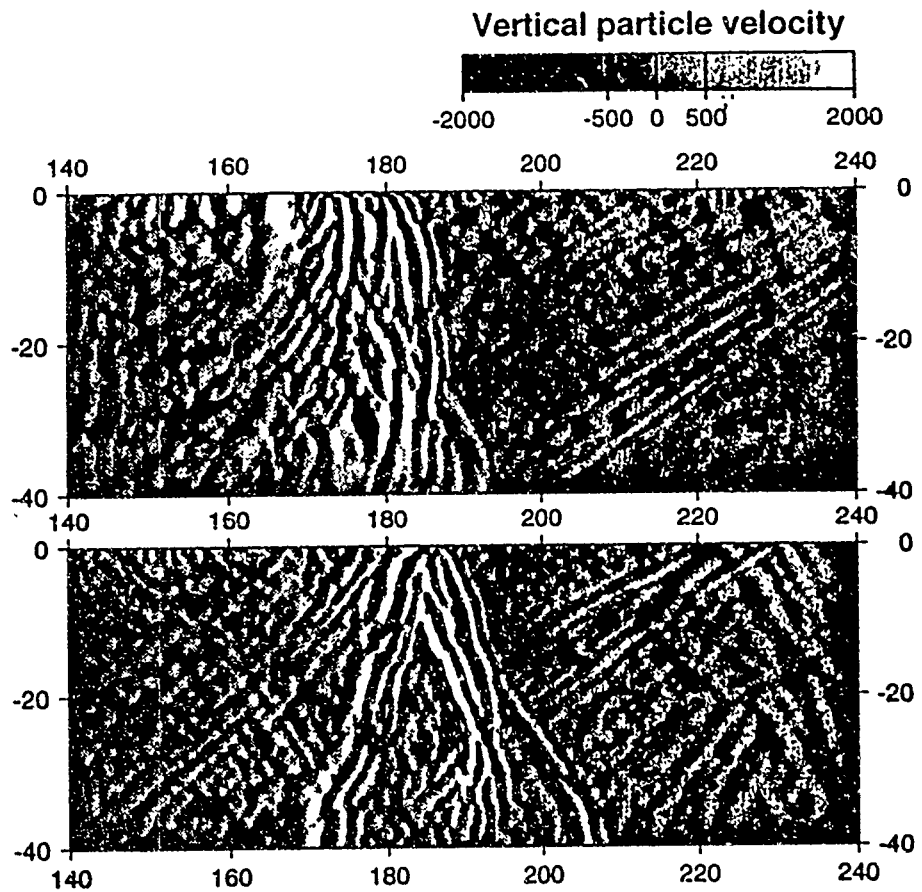

Fig. 7: Snapshot displays at a lapse time of 30 sec for S-sources at 2 and 20 km in a) and b), respectively (modelling parameters; free surface as in Fig. 3 caption while medium parameterization as given in Fig. 6). This figure is comparable to Fig. 3, except for a lapse time difference of 10 sec, roughly equivalent to a distance difference of 35 km for Sg/Lg. The increase in seismogram complexities for a medium with small scale velocity pertubations is rather dramatic.

Discrimination of Low-Yield Events Using Regional Seismograms: A Semi-Automated System

Chandan K. Saikia[1], Bradley B. Woods[2], L-S. Zhao[2] and Donald V. Helmberger[2]
[1]Woodward-Clyde Consultants, 566 El Dorado St, Pasadena, CA 91101
[2]Seismological Laboratory, CIT, Pasadena, CA 91125

Contract F29601-91-C-DB01

OBJECTIVES: Based on the analysis of regional seismograms observed on the TERRAscope network in southern California (Figure 1) from many earthquakes and NTS (Nevada Test Site) explosions, the M_L:M_o(M_L) and M_E/M_B vs M_o (where M_L is the local magnitude, M_E is the energy ratio set by the data and synthetics, M_B is the moment determined from broadband data, and M_o is the long-period moment) discriminants have proven their effectiveness in discriminating small events (Woods et al., 1992, Zhao and Helmberger, 1993a). The primary objective of this study is to test transportability of these two discriminants to a new testbed and develop some new ones, including the development of a semi-automated system which may be useful to identify the seismic sources.

RESEARCH ACCOMPLISHED: In addition to the above two discriminants, we have developed two energy-based regional discriminants using TERRAscope data and assembled an additional database comprising of broadband regional seismograms both from earthquakes and explosions recorded by a Streckeisen STS-1 force balance seismometer at WMQ station, located between the Junggar and Tarim Basin along the eastern Tien Shan of the Xinjiang Province, to test transportability of these discriminants. The STS-1 system has a flat amplitude response between 0.2 and 20s (Chen et al., 1990). The database consists primarily of seismograms from the Semipalatinsk explosions, located at about 950 km away from the station and from earthquakes occurring at a distance from 750 km to 1400 km from the station. We are currently updating this database to include the Chinese explosions and many broadband seismograms at the range of Lop Nor test site have been assembled. In the following, we briefly discuss the three discriminants.

Discriminant 1. Short-Period P(z):Long-Period Energy Discriminant:

This discriminant is based on the ratio of the short-period energy vertical P-wave train to long-period surface wave energy in all three components as a function of distance and is based on the observation that explosions tend to be richer in high frequency energy than earthquakes with comparable sized Rayleigh waves. For example, in Figure 2 we show broadband data recorded at Pasadena from the NTS (Nevada Test Site) event Kearsarge (August 17, 1988: 17h 00m) and the Skull mountain (Yucca) earthquake. Also shown are several seismograms simulated by convolving the response of Ewing and Press 30-90 (LP3090), Wood-Anderson short period (WASP) and Wood-Anderson Long Period (WALP) instruments. Clearly, while the LP3090 seismograms of both events have similar looking Rayleigh waves (marked by the arrows), the WASP seismograms, which are high-frequency seismograms, are markedly dissimilar. In addition, the explosion seismograms have strong P waves compared to the earthquake seismograms. This is a feature commonly observed in the seismograms of these two sources and is useful for developing regional discriminants.

The discriminant criterion is the ratio of short-period energy in the vertical component P-wave train to the long-period energy in the surface waves in all three components. Mathematically, we express this ratio as

$$\frac{\int_{t_1}^{t_2} V_{SPZ}^2(t)dt}{\sum_{k=0}^{3}\int_{t_3}^{t_4} V_{LP_k}^2(t)dt}$$

where (t_1,t_2) and (t_3,t_4) define the window timings of the short-period P i.e. for V_{SPZ} and long-period surface waves (V_{LP}) respectively. The long-period energy estimates are taken from all three components to avoid instability that may be caused by a possible node in the surface-wave radiation. A significant advantage of this discriminant is that it does not require the determination of any source parameters and does not require any assumptions about the source. To implement this discriminant, each broadband seismogram is convolved with the short-period Wood-Anderson and long-period Ewing and Press 3090 instrument responses to simulate the V_{SPZ} and V_{LP} functions.

Figure 3 shows this ratio versus distance for 106 earthquakes (crosses) from southwestern United States and 76 NTS explosions (circles). It includes earthquakes with M≥3.6 and explosions M≥4.0. Each point represents an individual station observation. It is evident that explosions tend to have larger short-period:long-period energy ratios than do the earthquakes. There is some overlap in the two populations at distances less than 450 km. The relatively low ratio explosions near 400 and 230 km are observations from large tectonic release events; that is their waveform displayed Love waves and anomalously large Rayleigh waves. The largest separation between the two populations is obtained at distances greater than 590 km.

Discriminant 2 M_E:M_B vs M_o

This discriminant is based on the source strength in energy, where M_E is the source strength required to match the energy in the synthetics computed using a flat-layered crustal model with the data. M_B is the moment determined from broadband modeling, while M_o in this case is a moment estimate from the long-period data. Mathematically speaking, M_E is expressed as

$$M_E = \sqrt{\frac{\sum_{i=0}^{3}\sum_{j=1}^{n} X_i^2(t_j)dt}{\sum_{i=0}^{3}\sum_{j=1}^{n} Y_i^2(t_j)dt}}$$

where X(t) and Y(t) are the recorded and simulated velocity time histories, respectively. Hence, M_E and M_o are nearly the same, provided the agreement is good.

To implement this discriminant, we need to have an appropriate crustal model so that the various phases observed on the recorded seismograms can be reasonably modeled. It also

requires estimation of M_o which involves processing of synthetic and observed waveforms and invoking techniques to determine the source parameters: dip, slip and strike of the causative faults. This involves an user to inspect the level of agreement between data and synthetics. Thus, unlike the SP:LP energy ratio, this discriminant can be applied in a semi-automatic manner to identify an event. We present an in-depth discussion of this semi-automated method in a later section.

In most cases, M_E for explosions is high because of the deficiency in the representation of the shallow structure. Figure 4 shows an illustration where various components of a set of three-component broadband seismograms from a small earthquake are displayed. For each set of seismograms (i.e., BB, LP3090, WALP, WASP), the data seismogram is plotted above the corresponding synthetic seismogram. In the first two columns, the P_{nl} waveforms of the vertical and radial components and in the last three columns, the whole seismograms for the vertical, radial and tangential components are shown. The synthetic seismograms are computed using the frequency-wavenumber integration code Filon_AS-O33 (Saikia, 1993) using the southern California crustal model (Figure 5, Dreger and Helmberger, 1991). The source mechanism and the seismic moment M_o of this event is obtained using the inversion technique of Dreger and Helmberger (1991). Figure 6 shows a similar comparison between data and synthetics for various components generated by an explosion, where the synthetics are obtained using a dominantly strike-slip mechanism determined by the inversion algorithm. While the agreement is remarkable for the earthquake seismograms, the surface waves are not well modeled in case of the explosion source. There may be several reasons for this mismatch. For instance, we treated this event as an earthquake and inverted for its mechanism, which primarily appeared to be a strike-slip source (this is likely to be the case because explosion waveforms match closely the waveforms generated by this double-couple mechanism) and secondly, a deeper source depth is estimated than the actual shallow depth of the explosion. Thus, the surface waves, which are strongly observed from a shallow source, are somewhat weak on the synthetics. Therefore, any estimate of energy in the synthetics will be smaller than the energy measured in the recorded seismogram if the source is an explosion in this computational scheme. Thus, M_E will become larger.

We used 20 NTS explosions and 25 southwestern earthquakes (Zhao and Helmberger, 1993a) and processed their M_E's and M_o's assuming each of these events as an earthquake. Figure 7 shows these preliminary results which clearly demonstrates that explosions are distinctly separable from the earthquakes.

Discriminant 3. Short-Period P to Short period S Energy Discriminant

This discriminant is based on the ratio of short-period P to short-period S energy and proved efficient in discriminating Semipalatinsk explosions (located about 950 km away) from earthquakes at similar distances, all recorded at broadband WMQ (Chinese digital network) station. Mathematically speaking, this discriminant can be expressed as

$$\left| \frac{\int_{t_1}^{t_2} V_P^2(t)dt}{\int_{t_3}^{t_4} V_S^2(t)dt} \right|_Z^{SP}$$

where this discriminant is based on only the short-period vertical component seismograms. We found this discriminant separates the explosions well from the earthquakes at large distances.

However, when applied to the regional seismograms at ELK, MNV, KNB, and LAC (stations of Lawrence Livermore National Laboratory, Figure 8) from NTS explosions and earthquakes from the California-Nevada border region, this discriminant still could separate the two populations, but the separation was small.

This discriminant was found very useful, especially in our attempt to characterize the source of the December 31, 1992 Novaya Zemlya event at the suggestion of Dr. Alan S. Ryall of DARPA/NRMO. The regional waveforms recorded on the high-frequency array SPAO (Spitzbergen), located at about 1140 km away were available, and these waveforms were extracted from the original seismograms in the frequency bandpass of 3 to 8 Hz. To characterize the source of this event, first we examined the short-period WWSSN film chips recorded at KBS station from many Novaya Zemlya events. Unfortunately, most of the events were not available on the film chips except for one event (October 21, 1967, 04h 59m 58.1s Latitude:73.4°N, Longitude:54.8°E, Mb=5.9). Even for this event, only the north-south component is recorded. Figure 9 shows a comparison between this event (NS component) and the vertical component of Spitzbergen array data of the December 31, 1992 event. Although the event magnitudes, the frequency bands and the components of the two waveforms are different, what is strikingly similar is the general characteristic of the P and S waveforms. This is what triggered us to explore a new discriminant (discriminant 3), useful to data recorded on the high-frequency array at such large distances and from events which have significantly low yields. Note that, other two discriminants (1 and 2) require broadband seismograms and are not useful in this case.

Figure 10 shows a set of vertical component seismograms for 5 explosions and 5 earth quakes recorded at WMQ stations. The upper diagram shows the broadband seismograms as recorded, the middle diagram shows the corresponding seismograms obtained by convolving each of the upper panel seismograms with a Wood-Anderson short-period instrument, and the lower panel shows the same Wood-Anderson seismograms in a bandpass of 3 to 8 Hz. These waveforms show one striking feature in the S-wave characteristics, especially in the band of 3 to 8 Hz. The explosion seismograms are highly deficient in S waves compared to the earthquake seismograms. Most likely, the explosion accompanied by high-frequency S waves, generated in the source region through phase conversion of P waves or sources not yet resolved, are almost completely attenuated within the crust at such large distances. It is expected that the energy ratio of P waves to S waves should have a higher value for the explosions than for the earthquakes. Based on this observation, we developed discriminant 3.

To construct the discriminant, we defined the P-wave window using a velocity window of 9 km/s for the start time and 4.8 km/s for the end time. The S-wave window was defined using a velocity window of 4.7 to 1.4 km/s. In addition to the digital waveforms at WMQ, we have obtained additional digital waveforms recorded on the LLNL network for many earthquakes to augment our previous LLNL data base consisting of only the explosion seismograms. We have processed these seismograms in the same way to estimate the short-period P wave to short-period S wave energy and constructed additional data points in the 200 to 550 km distance range.

Figure 11 shows how well this short-period P wave to S-wave energy ratios separate the explosions from the earthquakes (upper panel). Included in this figure are the NTS data (shown by solid squares), the WMQ explosion data (shown by solid circles) and the earthquake data (shown by open '+' symbol). The solid circles at 255 km were obtained from the Soviet JVE (September 14, 1988) explosion recorded at KKL (Kirklinsk) and BAY (Bayanual) stations.

December 31, Novaya Zemlya Event - Earthquake or Explosion:

Events of the December 31, 1992 Novaya Zemlya type are of primary concern because they fall into the category of typical events that would be concern in the CTBT or NPT environment in an area where a test can be conducted, and have magnitude of the order of M_L=2.5, appropriate for small nuclear tests. According to Alewine and Ryall (1993), various methods identified it as chemical blast (for example, event identification system, SAIC; neural net system, RADIX, intelligent seismic event identification system, ENSCO, S-Cubed researcher) and the bottom line is that the Russians reported no blasting on 12/31/93 in the area.

As discussed before, the regional signal from the Novaya Zemlya event could be seen at Spitzbergen array only after filtering the data using a bandpass filter with a low-cut of 3 Hz and a high cut of 8 Hz. These corners were selected by Dr. J. Carter of CSS (Center for Seismic Studies). To establish a compatibility of frequency content and instrument type, all the seismograms used in Figure 10 were convolved with a WASP instrument and a bandpass filter with a low-cut of 3 Hz and high-cut of 8 Hz. Similarly, the WASP instrument was convolved in to the Novaya Zemlya seismogram. The discriminant 3 was formed from these processed waveform and is shown Figure 11 (lower panel). The data point of the December 31, 1992 Novaya Zemlya event is marked by an open star. Clearly, this point aligns itself with the earthquake population, confirming the Russian's claim.

"DISCR" - SEMI-AUTOMATED SYSTEM

"DISCR" is a semi-automated model based event discrimination system and is in the process of being developed to identify an event using regional waveforms on a routine basis. It is based on the above three discriminants including the M_L:Mo discriminant (Woods et al., 1993; Woods and Harkrider, 1993). It has several modules in it. Figure 12 shows a flow-chart diagram of this system. In the following, we present a brief discussion of individual modules and discuss their relevance to the TERRAscope data.

Module 1. Given a set of regional seismograms, this module determines if the waveforms are suitable to retrieve the long-period information i.e., LP3090 response. This is done by visually inspecting the LP3090 versions of waveforms on the front-end computer monitor. If the waveforms are usable, it invokes constructing the discriminants. Of the four discriminants, two of them requires estimation of M_o and are constructed stepping module 2 through module 4.

Module 2. This uses the initial source depth and epicentral distance of the event (supplied by the user) and selects a set of Green's functions previously computed and stored on the system, processing is performed to prepare LP3090 response and perform a grid-search technique to determine the source parameters, including the seismic moment. Details of this procedure are discussed in Saikia and Burdick (1992) and Zhao and Helmberger (1993b).

Module 3. Using the M_o determined in module 2, M_L in module 1, this module constructs the M_L:Mo discriminant.

Module 4. Using the source parameters and M_o determined in module 2, this module computes M_E and M_B, and constructs the M_E:M_o discriminant.

Module 5. This module is designed to construct the energy ratio short-period P wave to short-

period S waves and does not require M_o. Each broadband waveform is convolved with a WASP response and with a bandpass filter with cut-off corners at 3 and 8 Hz, respectively.

Module 6. This produces four viewgraphs, each displaying the already identified discriminant data points obtained by modeling seismograms of known earthquakes and explosions. These four viewgraphs are the master view panels. When a new event is recorded, the four discriminants are formed and are allowed to flash on the corresponding master view panels, so that they can be identified.

RECOMMENDATIONS

In order to use **DISCR** successfully in a new testbed, the path effect should be calibrated and a set of discrimination data points should be established. We are now compiling additional data at WMQ from the Chinese test site and at KIV (Kislovask, a broadband station within CIS near Caspian Sea). Station KIV is located at regional distance from the southwestern Russia, a site of many low-magnitude possible explosions (ISC monthly bulletins). We plan to calibrate path and investigate the potential of the above mentioned discriminants on this database. As discussed in the text, discriminant 3 is useful when the high-frequency waveforms are only available. Therefore, we shall attempt to explore this discriminant using array waveforms contained in a recently released ground-truth database recorded at GERESS (Grant et al., 1993). This database consists of waveforms from earthquakes and mostly from many quarry blasts; thus providing an opportunity to test the discriminants on sources other than those of explosions.

REFERENCES

Alewine, R. and A. S. Ryall (1993). Verification of further limits of global testing, AGU Meeting at Baltimore, (Invited).

Chen, Y. T., Q. D. Mu, and G. W. Zhou (1990). Chuna digital seismographic network: current status and future direction, Workshop on: MedNet, the broadband seismic network for the Mediterranean, Edited by E. Boschi, D. Giardini and A. Morelli, IL CIGNO Galilei Edizioni Di Arte E Scienza, 114-120.

Dreger, D. S. and D. V. Helmberger (1991). Complex faulting deduced from broadband modeling of February 28, 1990 Upland earthquake (ML=5.2), Bull. Seis. Soc. Am., 81, 1129-1144.

Dreger, D. S. and D. V. Helmberger (1993). Determination of source parameters at regional distances with three-component sparse network data, J. Geophys. Res., 98, 8107-8125.

Grant, L., J. Coyne and F. Ryall (1993). CSS ground-truth database: version 1 handbook, Scientific Report No. C93-05, 58p.

Saikia, C. K. (1993). Modified frequency-wavenumber algorithm for regional seismograms using Filon's quadrature - Modeling of Lg waves in eastern North America, Geophysical J. International (Accepted).

Saikia, C. K. and L. J. Burdick (1991). Fine structure of Pnl from NTS explosions, J. Geophys. Res., 14,383-14,401.

Saikia, C. K. and L. J. Burdick (1992). Modeling crustal phases in the CIS and China, WCCP-R-92-01, Scientific Report #1, Prepared for Phillips Laboratory. Kirkland Air Force Base, New Mexico, 39p.

Woods, B. B., C. K. Saikia, and D. V. Helmberger (1992). An energy discriminant for regional seismic events, EOS, Am, Geophys. Un., Vol 73, 359p.

Woods, B. B. and D. G. Harkrider (1993). Determining surface wave magnitudes from regional NTS data, Geophys. J. International (Submitted).

Zhao, L. S. and D. V. Helmberger (1993a). Regional moments, energy levels and a new discriminant (In Preparation).

Zhao, L. S. and. D. V. Helmberger (1993b). Source estimation from broadband regional seismograms, Bull. Seis. Soc. Am., (In press).

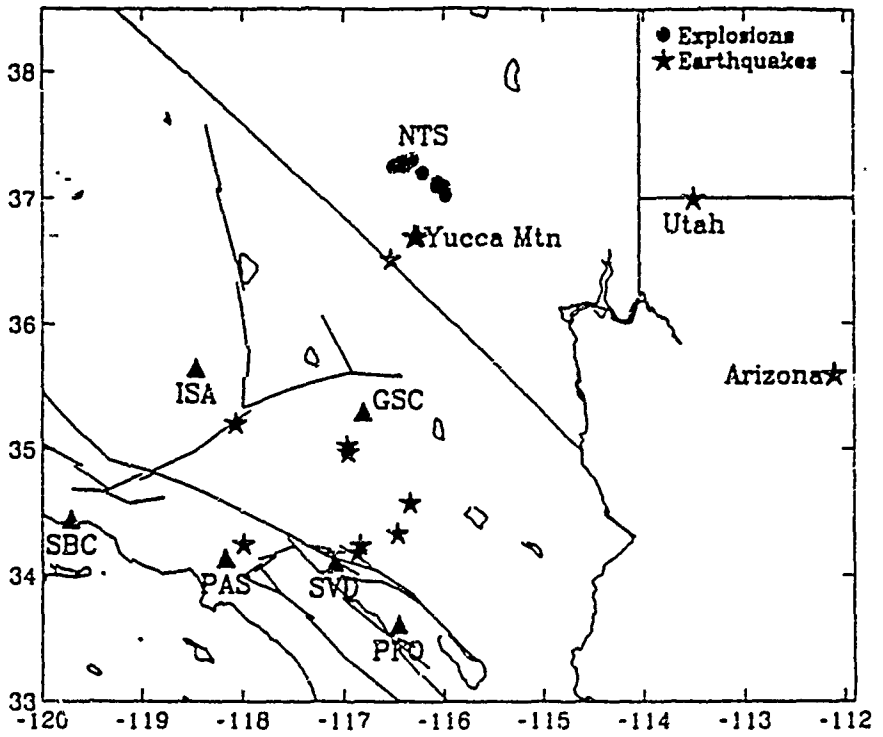

Figure 1. Map showing present TERRAscope stations and some regional events.

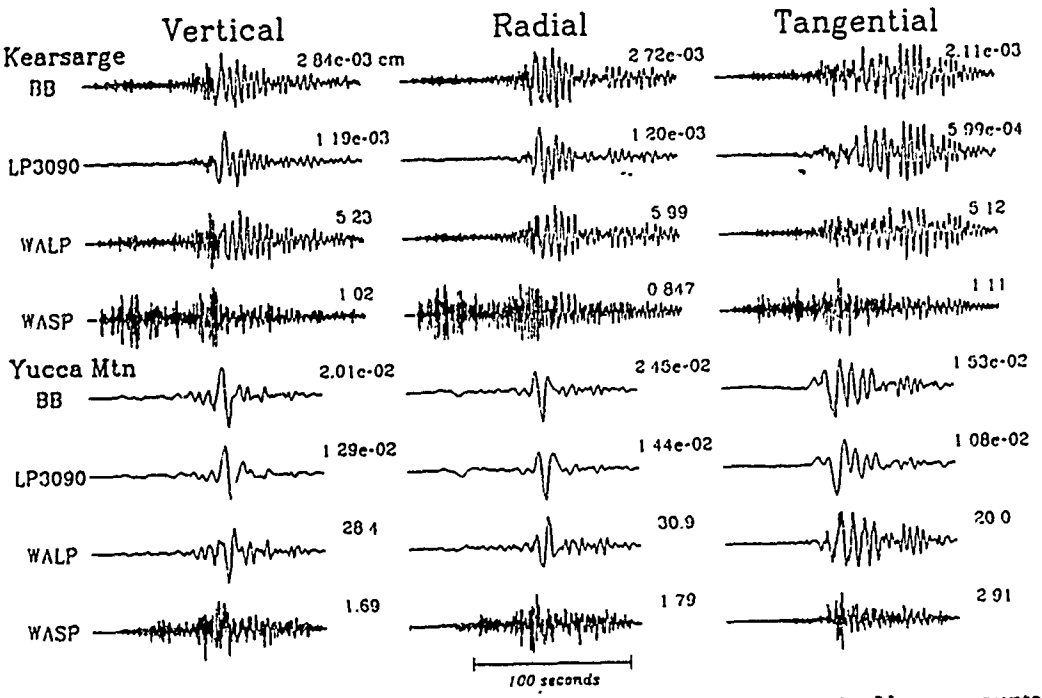

Figure 2. Comparison of broadband displacements of the NTS event Kearsarge with the Yucca mountain (Skull mountain) event as recorded at Pasadena (about 350 km). Note the high-frequency nature of the explosion as compared to the earthquake data.

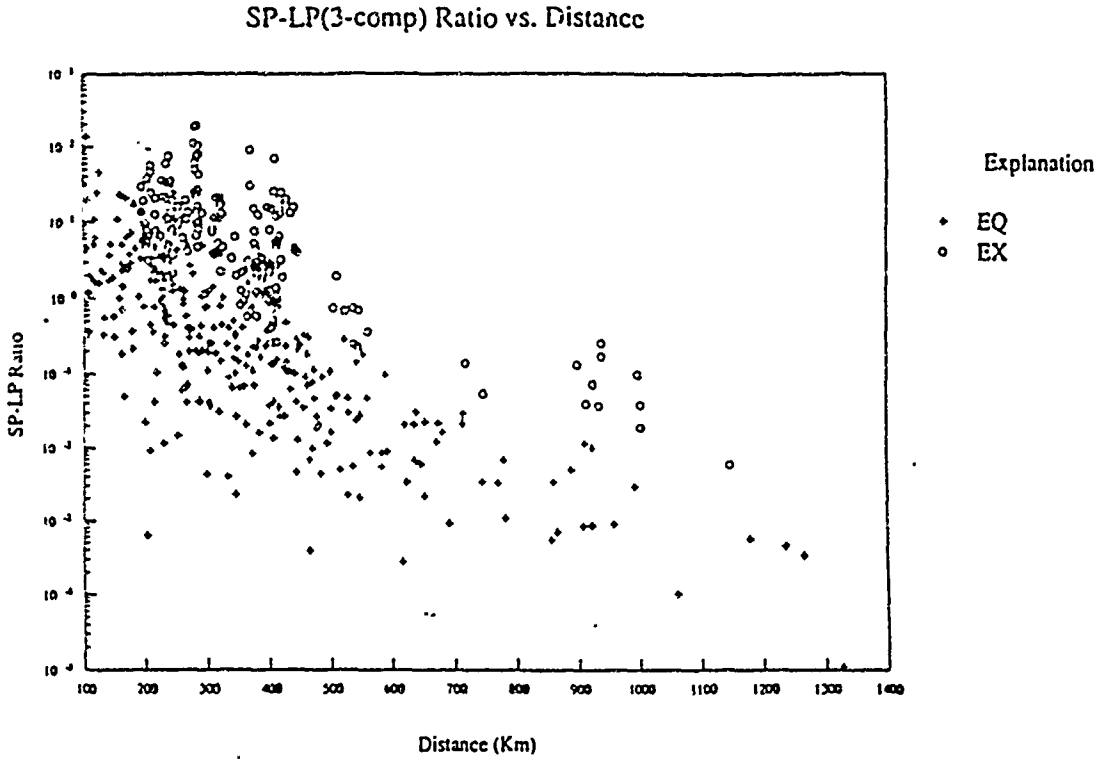

Figure 3. Plot of SP:LP energy ratio as M_0 discriminant (i.e., energy in the short-period band over the P_{nl} window divided by the total energy in all three long-period seismograms.

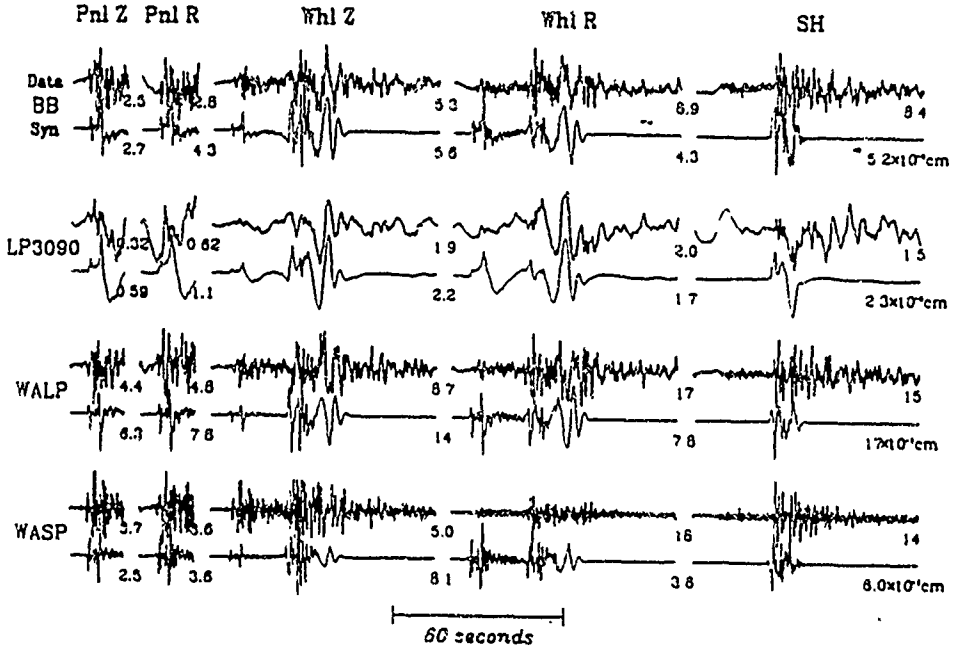

Figure 4. Comparison of data and synthetics for a small event. The time function is fixed by (WASP/WALP) energy ratio in the P_{nl} window (i.e., the synthetics are fit to the data ratio by varying the time history assumed to be a triangle) WASP: Wood-Anderson short period and WALP: Wood-Anderson long period.

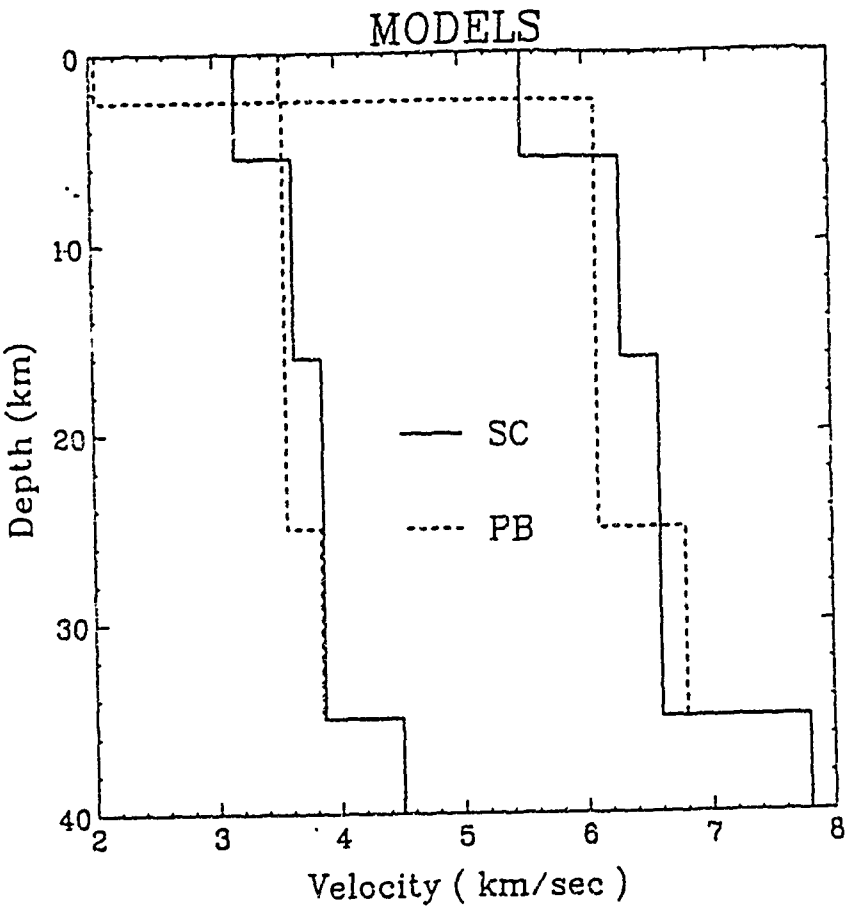

Figure 5. Crustal model for southern California.

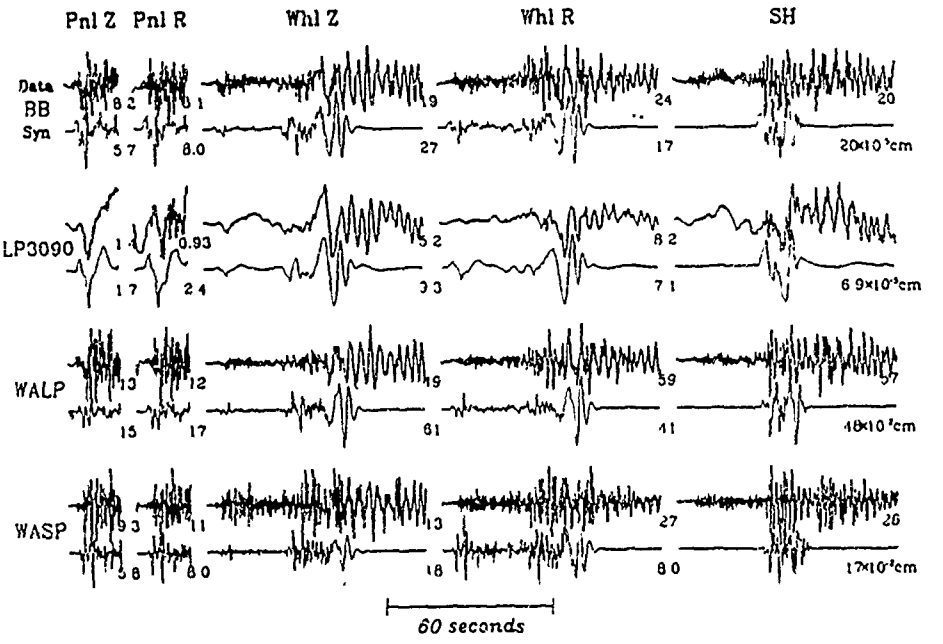

Figure 6. Comparison of data from a small explosion with synthetics (assumed to be a double couple). The synthetic for an explosion is essential the same as for a strike-slip earthquake at the same source depth.

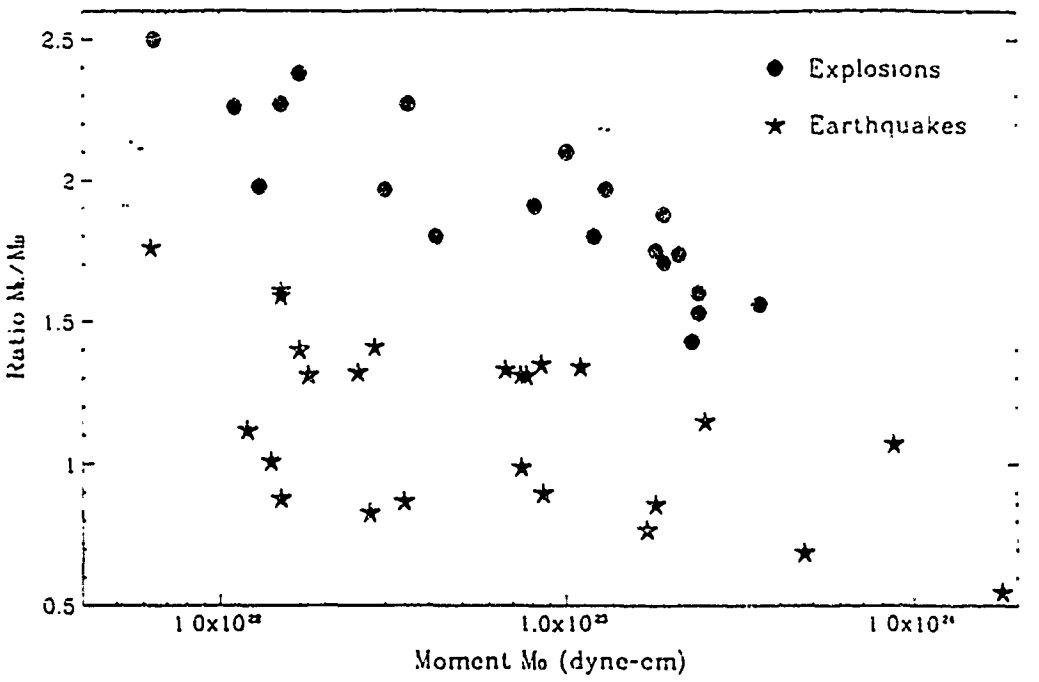

Figure 7. M_E/MB vs M_o discriminant. M_o is determined from WALP fit to data. M_B is determined from broadband record with time history chosen to match the WASP/WALP ratio. M_E is the energy strength determined by dividing the total energy contained in the observed data by the total predicted energy contained in the synthetics.

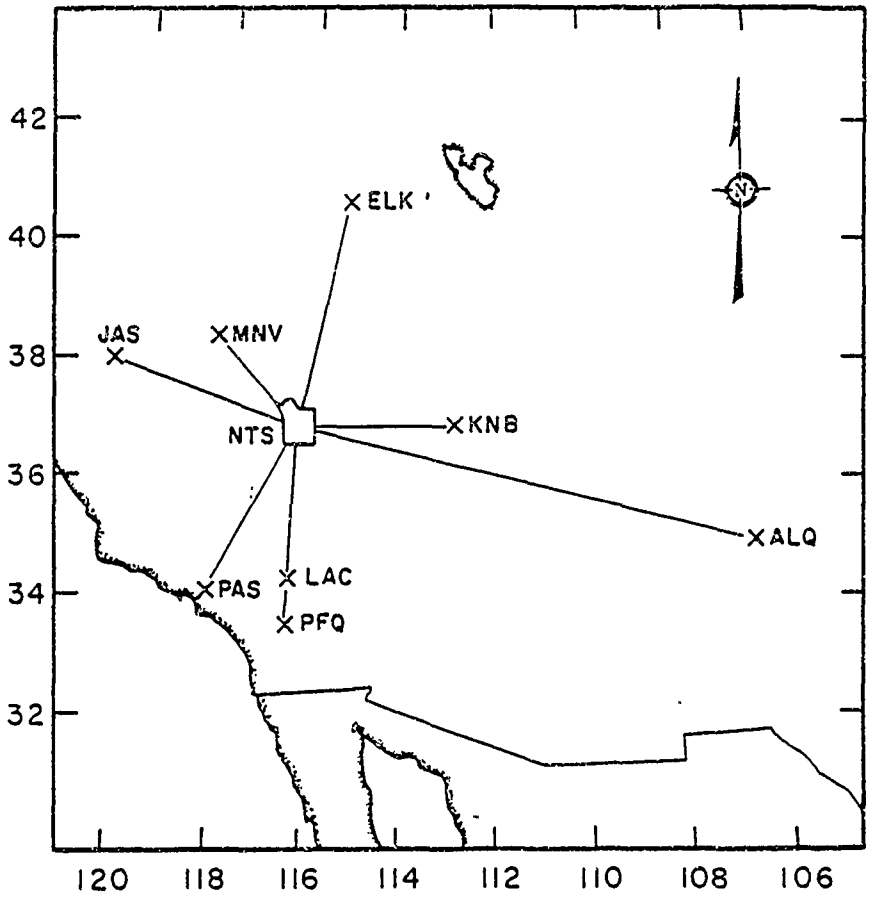

Figure 8. Network of Lawrence Livermore National Laboratory. Stations: ELK, LAC, KNB and MNV.

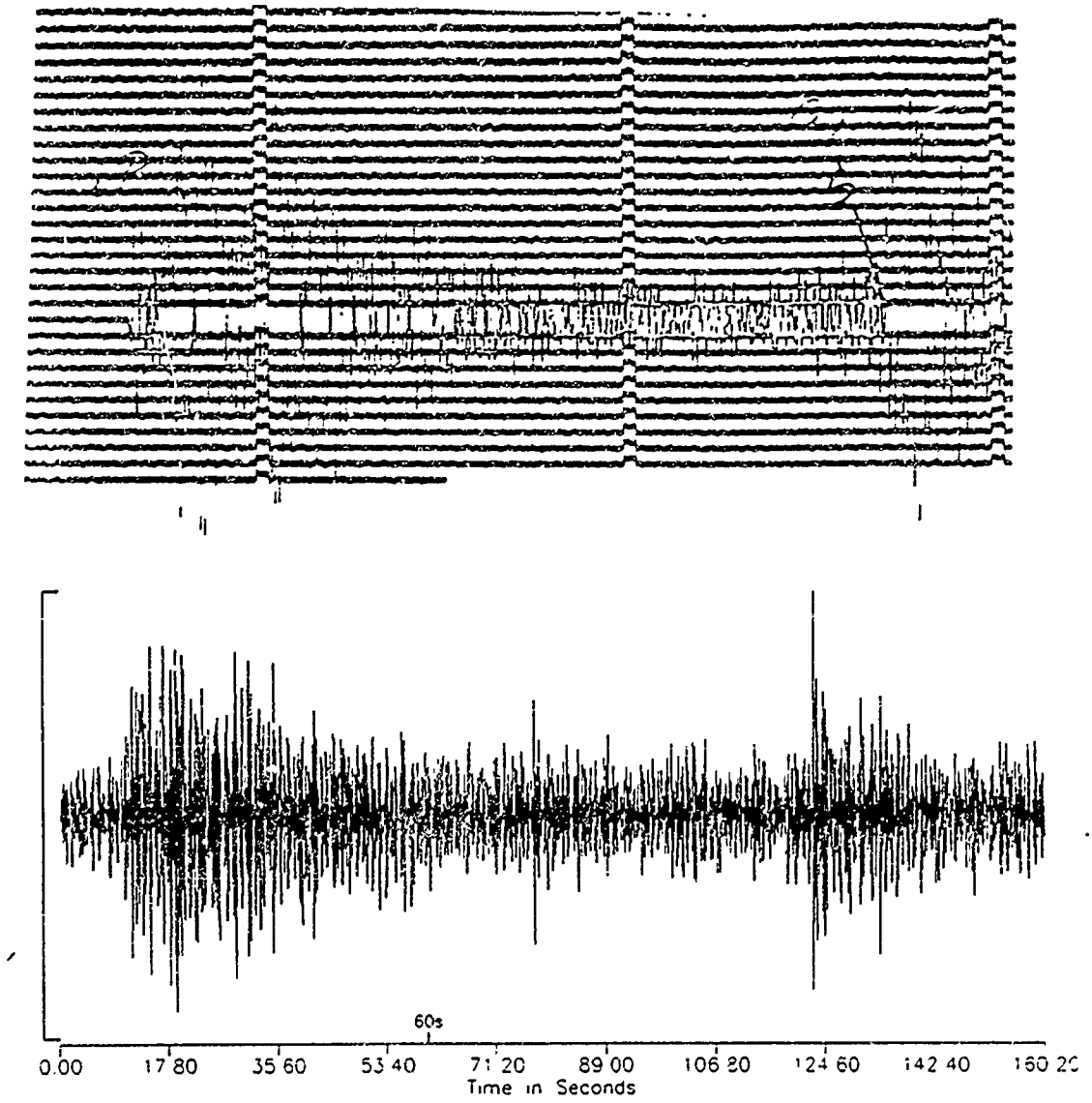

Figure 9. Comparison of the N-S short-period waveform characteristics recorded at KBS (WWSSN station) from a Novaya Zemlya explosion (upper seismogram) with the vertical component waveform recorded at Spitzbergen array from December 31, 1992 Novaya Zemlya event (lower seismogram). Note that the difference in the components and also in the frequency content as discussed in the text.

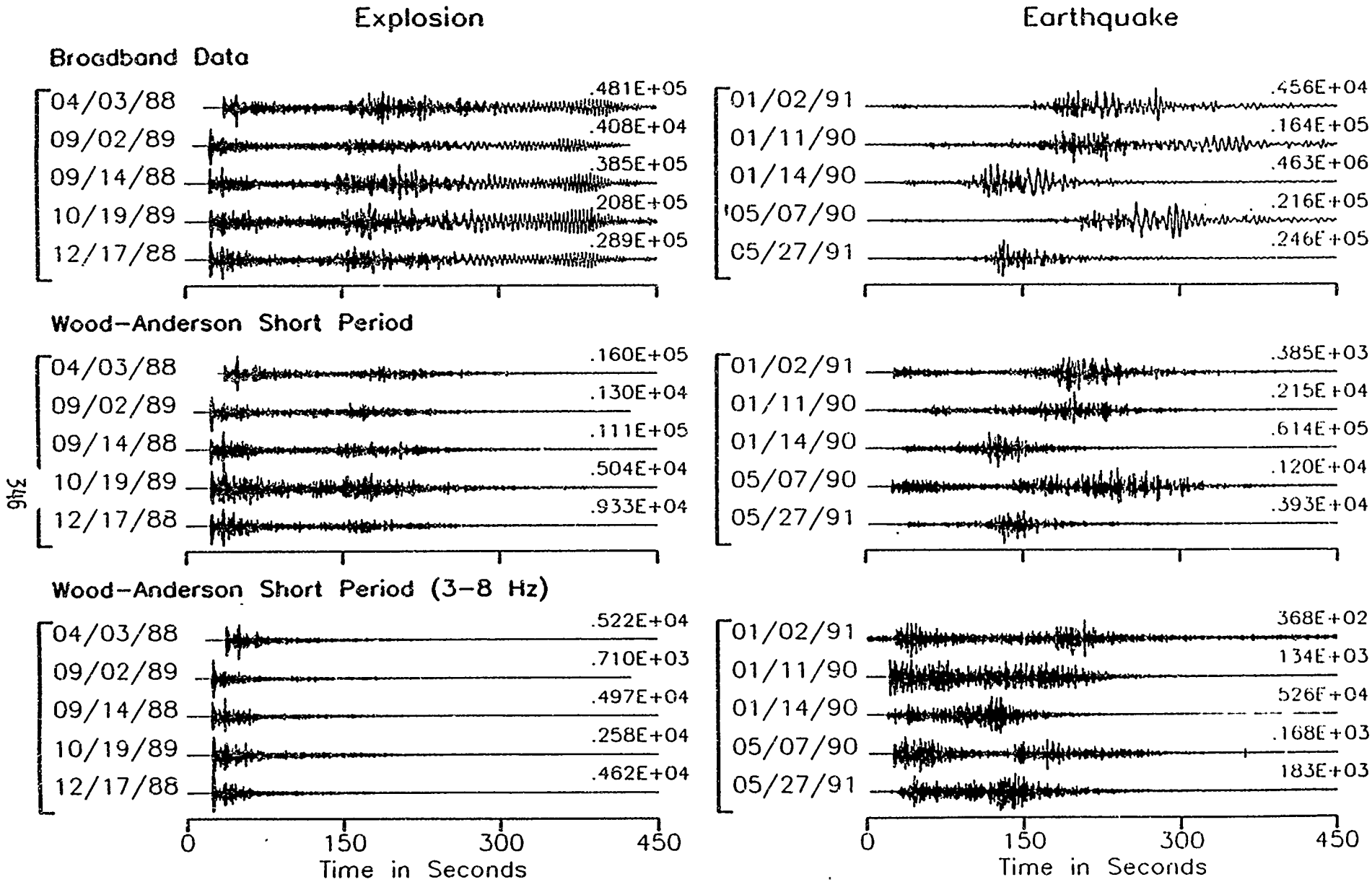

Figure 10. Vertical component seismograms from five Semipalatinsk explosions and five earthquakes at similar distances recorded at WMQ. The top panels are broadband waveforms. The middle panel shows the same waveforms after convolving with a Wood-Anderson short-period instrument. Those shown in the lower panel have an additional bandpass filter with corners at 3 and 8 Hz respectively.

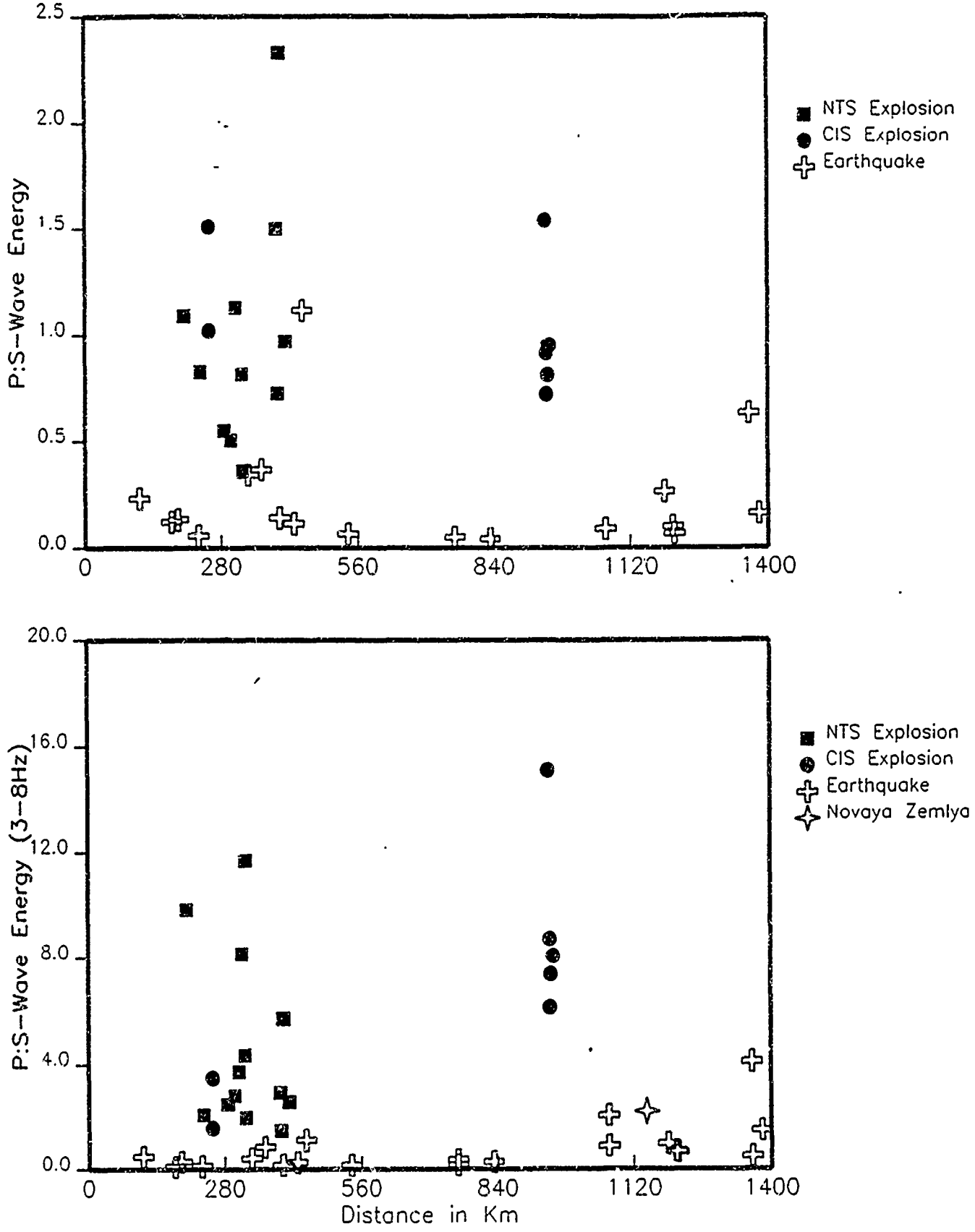

Figure 11. Short-period P to S-wave energy ratio discriminant. Upper panel: the discriminant was processed using the broadband data after convolving with a WASP response. Lower panel: the discriminant was processed from WASP response in the frequency band of 3 to 8 Hz.

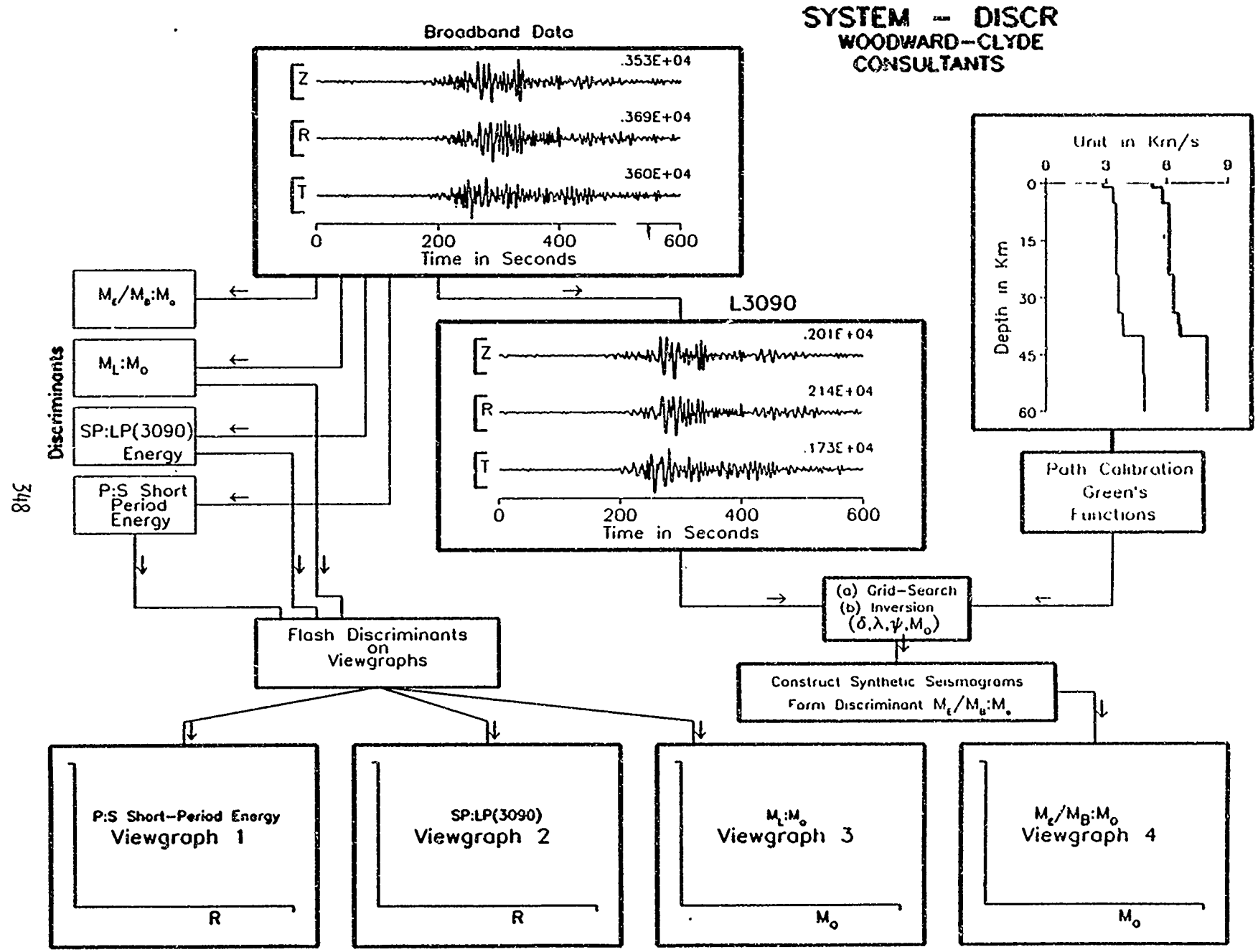

Figure 12. Flow-chart diagram for the semi-automated system - 'DISCR'.

INCORPORATING DAMAGE MECHANICS INTO EXPLOSION SOURCE MODELS

Charles G. Sammis
Department of Geological Sciences
University of Southern California
Los Angeles, CA 90089-0740

Contract # F49620-93-1-0284

OBJECTIVE

The overall objective of this line of research is to develop a damage mechanics for the compressive failure of rock which can be used as the constitutive relation in the numerical codes which simulate underground explosions. This work is motivated by the observation that elastic nonlinearities associated with the active fracturing of rock in the source region of underground explosions can effect the near-field seismic pulse shape. Toward this end, Ashby and Sammis (1989) modeled the growth and interaction of fractures which nucleate a preexisting cracks within the rock, and used the results to formulate a damage mechanics for the compressive failure of low-porosity crystalline rock (like granite). One immediate result of this work has been to emphasize the importance of scaling when applying rock mechanics laboratory results to field-scale underground explosions.

The objective of the work described below has been to develop an algorithm which may be used to incoprorate the damage mechanics into a spherically symmetric source model to study the effect of fracture on the seismic radiation.

RESEARCH ACCOMPLISHED

In the standard algorithms used to calculate the stress and strain paths in the source region of an underground explosion, the initial stresses are used in the equations of motion to find the displacements. These displacements are used to calculate the strains which are then used, with the elastic constants, to find the stress. The new stresses are then used in the equation of motion to find the displacements in the next time step, and so on. The incorporation of damage mechanics into this algorithm requires the introduction of a new variable, the damage. Damage is a measure of the fracture density in each material element of the model. In general damage is a tensor which reflects the distribution of fracture size and orientation at each location within the rock. However, for the simple spherically symmetric source shown schematically in Fig. 1, crack growth can be assumed to be radial and the damage written as

$$D = \frac{4}{3}\pi(\ell + \alpha a)^3 N_V \qquad (1)$$

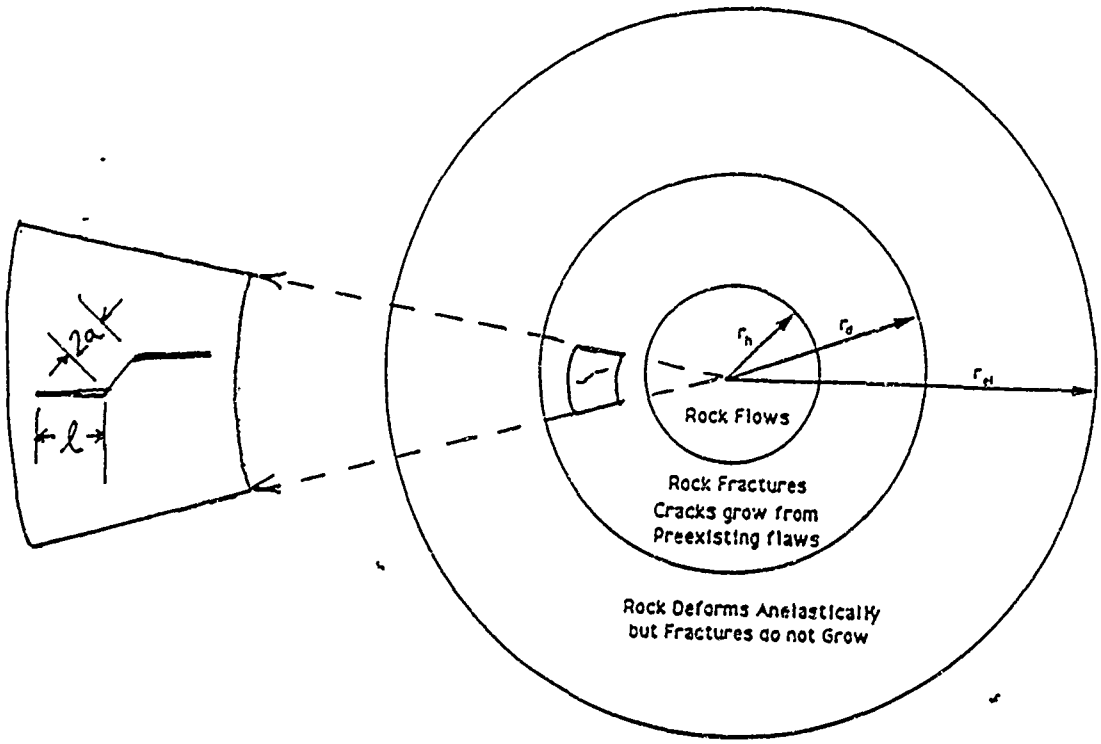

Figure 1. (Above) Schematic diagram of a spherically symmetric source region showing different regimes of deformation and the radial growth of fractures to a length ℓ nucleated at preexisting flaws of length 2a in the damage regime.

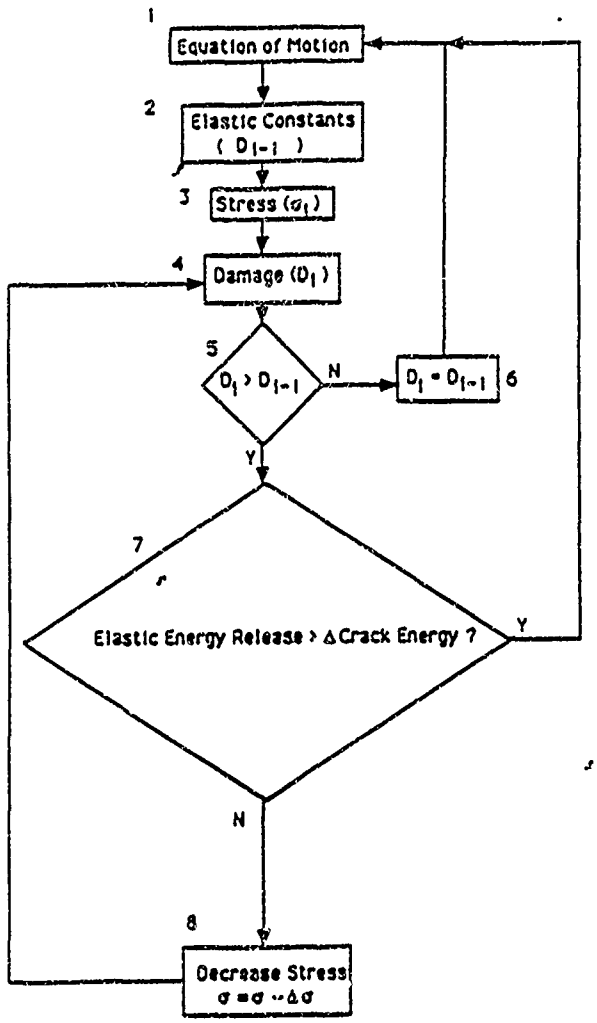

Figure 2. (Right) Flow diagram for a computer algorithm which can be used to include damage mechanics in the computer programs which simulate underground explosions.

where 2a is the length of the initial flaw which nucleates the fracture, ℓ is the length to which the fracture has grown(as illustrated in Fig. 1), N_v is the number of cracks per unit volume and α is a geometrical constant near 1.

The flow diagram for a computer algorithm which can be used to include damage in a spherical source is shown in Fig. 2. Each boxed procedure has been numbered and will now be discussed in turn.

Procedure 1: The Equations of Motion

Assume that we are beginning the i^{th} time step of the calculation. The stresses from the pervious time step, $\sigma_{\alpha\beta}^{i-1}$, are used to find the current displacements u_α^i , which, in turn, are used to compute the new strains, $\varepsilon_{\alpha\beta}^i$. This step is exactly as in the normal algorithm and is not affected by the incorporation of damage mechanics.

Procedures 2 & 3: The Elastic Constants and Stresses

The elastic constants are used to compute the new stresses $\sigma_{\alpha\beta}^i$ from the strains $\varepsilon_{\alpha\beta}^i$ found in Procedure 1 above. The most difficult issue to deal with in implementing the damage mechanics is that the elastic constants are not simply functions of the damage; they also depend on whether new damage is being done during the time step. Consider, for example, the stress-strain curve in Fig. 3.

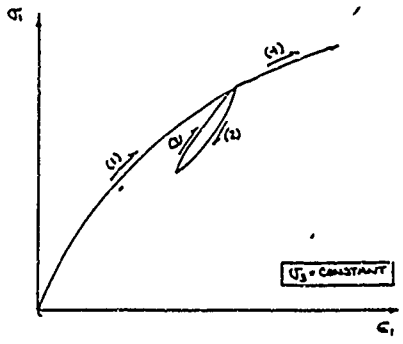

Figure 3 Schematic stress-strain curve showing lower elastic stiffness when fractures are growing than when they are not.

In this figure, the stress has been increased over the path labeled (1), decreased over path (2), and then increased again over paths (3) and (4). Note that the effective Young's modulus, $E = d\sigma_{11} / d\varepsilon_{11}$, is significantly lower over paths (1) and (4) where damage is increasing than it is over paths (2) and (3) where the stress is below that corresponding to the existing damage so that no new damage is being created. The hysteresis on the paths (2) and (3) is caused by frictional slip on the starter flaws (see Fig. 1), but the crack extension ℓ is constant over these paths.

For paths (2) and (3), where the cracks are not extending, the results of Budianski and O'Connell (1976) can be used to find the elastic constants as a function of the crack density. In their model the elastic moduli decrease as the crack density increases where the crack density is $\varepsilon = N_v \langle a^3 \rangle$, which may be expressed in terms of damage from eqn. (1) as $D = \frac{4}{3}\pi\varepsilon$. When the Young's modulus and Poison's ratio

predicted by the Budianski and O'Connell model are plotted as a function of the damage they are both roughly linear and may be closely approximated by

$$E = E_o(1 - 0.425D) \tag{2}$$

$$\nu = \nu_o - 0.10D \tag{3}$$

where E_o and ν_o are the moduli of the uncracked solid.

In Procedure 2 of the algorithm in Fig. 2, the isotropic elastic moduli are calculated using the damage from the previous time step D^{i-1} in equations (2) and (3). These moduli are then used, with the current strains, $\varepsilon^i_{\alpha\beta}$, found in Procedure 1, to calculate the new stresses $\sigma^i_{\alpha\beta}$.

Procedure 4: Calculating the Equilibrium Damage

The equilibrium damage D^i appropriate to the new stress state $\sigma^i_{\alpha\beta}$ is found using a table of equilibrium damage as a function of the dimensionless pressure p and maximum dimensionless shear stress, τ. which are defined in terms of the dimensionless stresses s_{ij} as

$$p = \tfrac{1}{3}(s_{11} + s_{22} + s_{33})$$

$$= \tfrac{1}{3}(s_{11} + 2s_{33}) \qquad \text{when } s_{22} = s_{33} \tag{4}$$

$$\tau = \tfrac{1}{2}(s_{11} - s_{33}) \tag{5}$$

where

$$s_{ij} = \frac{\sigma_{ij}\sqrt{\pi a}}{K_{ic}} \tag{6}$$

These tables are easily calculated using the analytic expressions in Ashby and Sammis (1990) for any given initial rock type and size spectrum of preexisting fractures.

Since Ashby and Sammis (1990) assume uniform deformation, the model is inadequate for the post-failure regime which is dominated by shear localization. As a first approximation, we assume that D remains fixed beyond failure at its peak value, and that τ falls to its frictional value, τ_f, given by

$$\tau_f = \left(\frac{\mu}{\sqrt{1+\mu^2} - \frac{\mu}{3}} \right) p \tag{7}$$

Finally, the shear stress can never rise above the yield stress, σ_y, which is given by

$$\sigma_y{}^2 = \tfrac{1}{2}\left[(\sigma_1 - \sigma_2)^2 + (\sigma_2 - \sigma_3)^2 + (\sigma_3 - \sigma_1)^2\right]$$

$$= (\sigma_1 - \sigma_3)^2 \qquad \text{when } \sigma_2 = \sigma_3 \tag{8}$$

The yield strength σ_y can be derived from the hardness, H, data since σ_y=H/3. At higher values of τ, strain is accommodated by plastic mechanisms which do not

involve crack damage. It is thus possible that, at very high values of p, the material could yield while the damage remains at Do.

Procedure 5: Has the damage increased during the i^{th} time step?

If the damage D^i appropriate to $\sigma^i_{\alpha\beta}$ found in the previous step is less than or equal to D^{i-1} in the preceding time step, then it was correct to use the Budianski and O'Connell (1976) elastic constants given by eqns. (2) and (3). As indicated in the flow chart the $\sigma^i_{\alpha\beta}$ just determined in the i^{th} time step can then be used in the equation of motion to begin the i+1 time step.

However, if $D^i > D^{i-1}$, then the damage has increased during the i^{th} time step and the effective elastic constant should be less than that given by equations (2) and (3). In the following procedure we develop an algorithm to find the appropriate stress and damage for the strain $\varepsilon^i_{\alpha\beta}$.

Procedure 6: If the Damage Has Not Increased During the i^{th} Time Step

If the equilibrium damage associated with the new stress state $\sigma^i_{\alpha\beta}$ is less than the current damage (from the previous time step) D^{i-1}, then the damage remains unchanged and we set $D^i=D^{i-1}$.

Procedure 7: Adjusting the Stress and Damage if the Damage Has Increased During the i^{th} Time Step

If the equilibrium damage associated with the new stress state $\sigma^i_{\alpha\beta}$ is greater than the current damage (i.e., if $D^i>D^{i-1}$) then we must recalculate the stress. As discussed above, this is because the elastic constants used to find $\sigma^i_{\alpha\beta}$ from $\varepsilon^i_{\alpha\beta}$ are too large. We do this by relaxing $\sigma^i_{\alpha\beta}$ until the elastic energy released during the i^{th} time step is equal to the increased crack energy associated with the associated damage.

For clarity, we begin our analysis with the special case of uniaxial compression. Consider an increment of strain $d\varepsilon_{11}$ which is caused by the stress σ_{11}. The work done per unit volume is then

$$\sigma_{11}d\varepsilon_{11} = \sigma_{11}d\varepsilon_{11}^{e} + dW_c \qquad (9)$$

The first term on the right is the work done over the elastic strain increment $d\varepsilon_{11}^{e}$; the second is the work done to extend the wing cracks. For $d\varepsilon_{11}^{e}$ we write

$$d\varepsilon_{11}^{e} = \frac{d\sigma_{11}}{E_o} \qquad (10)$$

The work required to extend the wing cracks from ℓ to $\ell + \delta\ell$ is

$$dW_c = 2N_v\left(2\int_A^{A+\delta A}\frac{[K_I(\sigma_{11},\ell)]^2}{E}dA\right)$$

$$= 4N_v\frac{K_{Ic}^2}{E}\delta A \qquad (11)$$

In this expression A is the area per crack at the beginning of the i^{th} time step while δA is the increase in this area during the i^{th} time step. E is the effective Young's modulus appropriate for D^{i-1} (eqn. 2). K_I can be replaced with K_{Ic} since the cracks grow at the critical stress intensity. We can express A and δA in terms of the damage as

$$A = \frac{\pi(\alpha a)^2}{D_o^{\frac{1}{3}}}\left[D^{i-1}\right]^{\frac{1}{3}} \qquad (12)$$

$$\delta A = \frac{\pi(\alpha a)^2}{D_o^{\frac{1}{3}}}\left\{\left[D^i\right]^{\frac{1}{3}} - \left[D^{i-1}\right]^{\frac{1}{3}}\right\} \qquad (13)$$

for N_V we write

$$N_v = \frac{3}{4\pi}\left(\frac{1}{\alpha a}\right)^3 D_o \qquad (14)$$

Hence the crack energy becomes

$$dWc = \frac{3D_o^{\frac{1}{3}}}{\alpha a}\frac{K_{Ic}^2}{E}\left\{\left[D^i\right]^{\frac{1}{3}} - \left[D^{i-1}\right]^{\frac{1}{3}}\right\} \qquad (15)$$

With these substitutions, equation (9) may be written

$$\sigma_{11}^i d\varepsilon_{11}^i \geq \frac{\sigma_{11}^i\left[\sigma_{11}^i - \sigma_{11}^{i-1}\right]}{E_o} + \frac{3D_o^{\frac{1}{3}}}{\alpha a}\frac{K_{Ic}^2}{E}\left\{\left[D^i\right]^{\frac{1}{3}} - \left[D^{i-1}\right]^{\frac{1}{3}}\right\} \qquad (16)$$

As indicated in the flow diagram, σ_{11}^i is incrementally reduced, a new D^i calculated, and equation (16) reevaluated until it is satisfied. The relaxed σ_{11}^i is then used in procedure 1 to begin the i+1 time step.

Now consider the case of interest: triaxial compression in which $\sigma_{11} > \sigma_{22} = \sigma_{33}$. In this case equation (9) becomes

$$\sigma_{11}d\varepsilon_{11} + 2\sigma_{33}d\varepsilon_{33} = \sigma_{11}d\varepsilon_{11}^e + 2\sigma_{33}d\varepsilon_{33}^e + dW_c \qquad (17)$$

Writing $d\varepsilon_{33} = -\nu d\varepsilon_{11}$ we have

$$(\sigma_{11} - 2\nu\sigma_{33})d\varepsilon_{11} = (\sigma_{11} - 2\nu_o\sigma_{33})d\varepsilon_{11}^{\,e} + dW_c \qquad (18)$$

If we again use eqn. (10) for $d\varepsilon_{11}^{\,e}$ and eqn (15) for dW_c, eqn. (18) can be written:

$$(\sigma_{11}^{i} - 2\nu\sigma_{33}^{i})d\varepsilon_{11}^{i} \geq \frac{(\sigma_{11}^{i} - 2\nu\sigma_{33}^{i})\left[\sigma_{11}^{i} - \sigma_{11}^{i-1}\right]}{E_o} + \frac{3D_o^{\frac{1}{3}}}{\alpha a}\frac{K_{Ic}^{\,2}}{E}\left\{\left[D^{i}\right]^{\frac{1}{3}} - \left[D^{i-1}\right]^{\frac{1}{3}}\right\} \qquad (19)$$

As in the uniaxial case, we relax σ_{11}^{i} and σ_{33}^{i} from their values predicted using the Budianski and O'Connell elastic constants. For each incremental reduction we recalculate the equilibrium damage D^i and then reevaluated equation (19) until it is satisfied. These stresses are then used in Procedure 1 to begin the i+1 step.

This triaxial case presents one problem that has not been discussed. Both σ_{11}^{i} and σ_{33}^{i} (σ_{rr} and $\sigma_{\theta\theta}$ for the spherical source) may be relaxed, and it is not clear how to do this in a non-arbitrary way. This problem, however, is not unique to the damage formulation and must be faced in any model which has a failure surface. One of two approaches is usually used: radial return or normal return. In the radial return scheme, each stress is reduced an amount proportional to its size. The stress is thus reduced along a radius in p-T space until the energy equation (19) is satisfied. In the normal return scheme, each stress is reduced in such a way that the return is normal to the failure surface and thus the reduction is along the shortest path in p-T space. The radial return is usually chosen since it is easier to implement and no physical argument has been made for either scheme.

CONCLUSIONS AND RECOMMENDATIONS

We are now implementing the above algorithm in HYDROX, a spherical one-dimensional Lagrangian source simulation code developed at Los Alamos National Laboratory and kindly supplied by Dr. Sam Shaw. We hope to have results by the September meeting. Three additional problems we are addressing are the effects of high loading rates on the stress intensity factor, the effects of water saturation on the fracture mechanics, and the effects of a spectrum of initial fracture sizes in the source rock. Solutions to all three exist in the literature - it is simply a matter of including them in the above algorithm.

REFERENCES

Ashby, M.F., and C.G. Sammis, The damage mechanics of brittle solids in compression, PAGEOPH, 133, 489-521, 1990.

Budianski, B., and R.J. O'Connell, Elastic moduli of a cracked solid, Int. J. Solids struct., 12, 81-97, 1976.

CHARACTERIZATION OF REGIONAL PHASE PROPAGATION IN EURASIA USING DATA FROM HISTORIC NUCLEAR EXPLOSIONS IN THE U.S.S.R.

Susan Y. Schwartz and Ron Mandel
University of California, Santa Cruz
Contract No. F29601-91-K-DB18

Objective

The use of regional phases to determine the yield of nuclear explosions and to discriminate them from earthquakes presently requires either the calibration of particular source receiver paths or improvement in our understanding of regional phase generation and propagation. To enhance our knowledge of path specific propagation and the nature of regional phases we have analyzed a new data set of hand digitized Soviet explosions and digitally recorded earthquakes in Eurasia. The objectives of this study are to empirically determine the combined geometrical spreading and attenuation relations for Lg and Pmax (maximum amplitude in the first 20 seconds of the P wave) using the large dataset of explosions, such that event averaged Pmax/Lg ratios for both explosions and earthquakes can be computed and evaluated as a source discriminant in Eurasia.

Research Accomplished

A remarkable correlation between amplitude and explosion yield has made the Lg phase extremely useful for determining the yield of nuclear explosions. An important caveat, however, has been the necessity of obtaining calibrated explosions for each site/station network. The calibration accounts for unknown differences in the efficiency of coupling explosion yield into Lg and for variations in Lg propagation along different paths. The amplitude ratio of P energy to Lg has also been shown to be useful in discrimination at regional and upper mantle distances, when source-receiver paths from both the earthquakes and explosions are similar. In the absence of calibration data, similar source-receiver geometries, or a history of previous nuclear testing, the usefulness of Lg amplitudes for yield estimation and source discrimination is questionable. Here we attempt to determine event averaged P/Lg ratios to assess their usefulness as a source discriminant. Our first year of work has focussed on an empirical study of the spectral properties of Lg and other regional phases using a new data set of hand digitized waveforms of nuclear explosions at Semipalatinsk and Matochkin Shar recorded at several Soviet stations. Our second year of effort has supplemented this data set with a smaller earthquake data set to determine the variability of one proposed discriminant (Pmax/Lg) in the explosion and earthquake populations and to assess its usefulness in non-proliferation monitoring.

The data set of hand digitized Soviet nuclear explosions consists primarily of explosions detonated at the Semipalatinsk and Matochkin Shar test sites between 1964 and 1988 and recorded at up to ten Soviet stations. The earthquake data set consists of digitally recorded events between 1988 and 1992 recorded at IRIS-IDA, CDSN and ASRO stations. Explosion, earthquake and station locations are indicated in Figure 1a. Figure 1b shows examples of the hand digitized waveforms recorded at seven stations from an explosion at the northeast Balapan subregion of the Semipalatinsk test site. We measured rms amplitudes of Pmax and Lg in the frequency band between 0.5-1.0 Hz after normalizing the data to a common instrument. Lg amplitude measurements were made in the group velocity window 3.1 to 3.7 km/s, following the procedure of Israelsson (1991). All amplitudes were corrected for background noise and maximum instrument magnification.

In order to empirically determine amplitude-distance relations for the Pmax and Lg phases, amplitudes must be normalized to a common magnitude. To accomplish this we determined Lg and Pmax amplitude-mb relations for the different source-receiver geometries. Plots of ISC mb versus Lg and Pmax amplitude, averaged for explosions with the same mb, at the Semipalatinsk and Matochkin Shar test sites are shown in Figures 2 and 3 respectively. These data are best fit by exponential relationships shown above the plot for each station. While the correlation between amplitude and mb is quite high at most stations, the exponential increase of amplitude with mb is different for the various stations and tends to be larger at the more distant stations. In addition, the increase in amplitude with mb is much smaller for explosions at Matochkin Shar than at

Semipalatinsk. It is well know that estimates of explosion yield using Lg amplitudes can be extremely precise; however, different propagation paths produce different explosion yield-scaling behavior (Ringdahl, 1990). The cause of the differences in Lg-yield scaling slopes between different paths is not understood. Our observation of increasing slope with increasing propagation distance, supports Lay's contention that variations in Lg-yield scaling may be due to frequency dependent source scaling effects (personal communication, 1993). The greater attenuation of Lg at farther distances will result in an apparent shift in the source spectra to longer periods were the spectra for different magnitude explosions are farther apart. The smaller slopes observed at Matochkin Shar may result from the same mechanism since this test site has only larger yield explosions which will have corner frequencies in the pass band of the data, resulting in smaller amplitude increases with increasing source size.

We use the derived amplitude-mb relations to normalize all amplitudes to a common magnitude of 5.9 to determine amplitude-distance relations for Lg and Pmax. Since all explosions at Matochkin Shar have a portion of their propagation path traversing an oceanic basin, which has a large effect on Lg propagation, we separate Lg from the two test sites into different groups (Figures 4b and c). A power law decay of amplitude with distance is fitted to the data yielding $r^{-2.0}$ and $r^{-3.3}$ falloffs with relatively high correlation coefficients for Lg from the Semipalatinsk and Matochkin Shar test sites respectively. The faster decay of Lg amplitude with distance for explosions at Matochkin Shar agrees with the stronger attenuation of Lg due to oceanic propagation reported by Zhang and Lay (1993). Since Pmax consists of diving P wave energy, Pn and possibly Pg, depending on the distance and crustal structure, we separated Pmax into two distance ranges: $\Delta<1500$ and $\Delta\geq1500$ km. For $\Delta<1500$ km, no Pmax amplitude decay was apparent, the amplitude decay for $\Delta\geq1500$ km is shown in Figure 4a. The decrease in Pmax amplitude with distance is poorly defined with a much lower correlation coefficient than Lg. Separation of the Pmax data from the two test sites did not result in higher correlation coefficients, therefore we combined the data to determine the best amplitude-distance relationship.

In the final stage of the analysis, we normalized explosion and earthquake Pmax and Lg amplitudes to a distance of 1000 km, and averaged values from several stations for each event. Figure 5 shows the distance normalized, average Pmax/Lg ratios versus ISC body wave magnitude. A separation between the earthquake and explosion populations is apparent with some overlap between sources. Additional amplitude corrections are presently being investigated in an attempt to further separate the amplitude ratios for the different sources.

Conclusions and Recommendations

As seismic discrimination efforts shift emphasis to parts of the world having no previous history of nuclear testing, comparison of phase ratios between earthquake and explosion populations will no longer be possible. To make advances in seismic monitoring of non-proliferation treaties, it will be important to establish the variability of proposed discriminants in earthquake populations. If earthquake sources alone show little variation in regional phase ratios, than ratios from unknown sources that differ dramatically from the earthquake population can be reliably identified as explosions. If, on the other hand, earthquakes reveal a large scatter in phase ratios, than that ratio will be useless for non-proliferation monitoring. Although we found a separation in Pmax/Lg for different source types in Eurasia, the present scatter in the earthquake population is unacceptable. Future work should concentrate on trying to reduce this scatter by exploring its origins.

References

Israelsson, H., (1992). RMS Lg as a yield estimator in Eurasia, Final Technical Report, Airforce Phillips Laboratory, Hanscom Air Force Base, MA, PL-TR-92-2117(I), ADA256692.

Ringdahl, F., (1990). NORSAR detection and yield estimation studies, Papers presented at 12th Annual DARPA/GL Seismic Research Symposium, Geophysics Laboratory, Hanscom AFB, MA 01731-5000, pp. 145-151, GL-TR-90-0212, ADA226635.

Zhang, T., and T. Lay (1993). Effects of crustal structure under the Barents and Kara Seas on short-period regional wave propagation for Novaya Zemlya explsions, in preparation.

a)

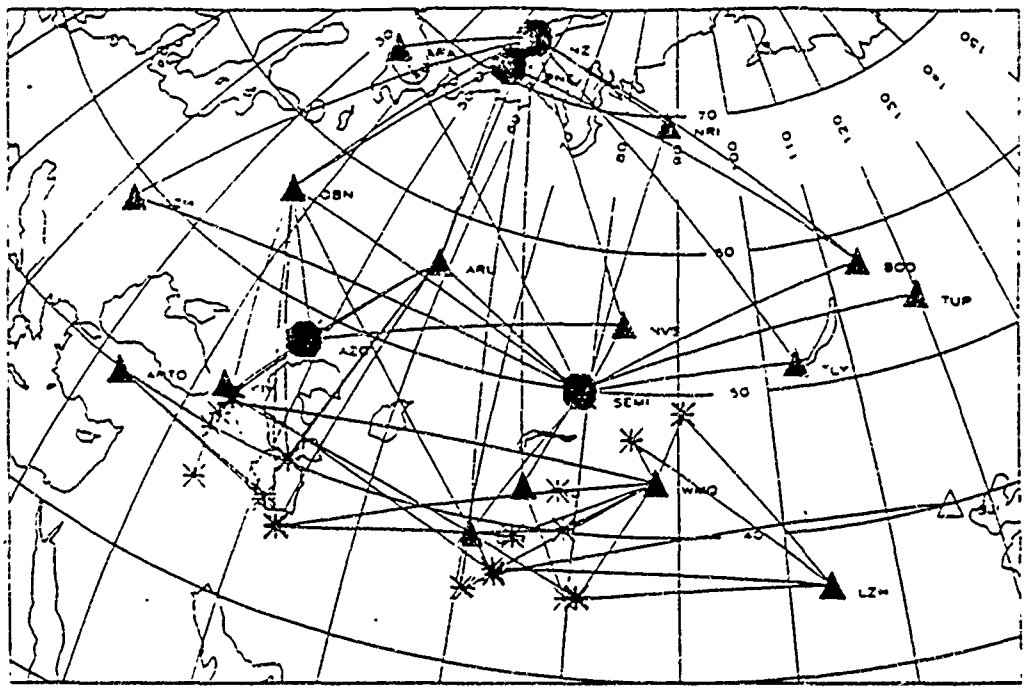

b)

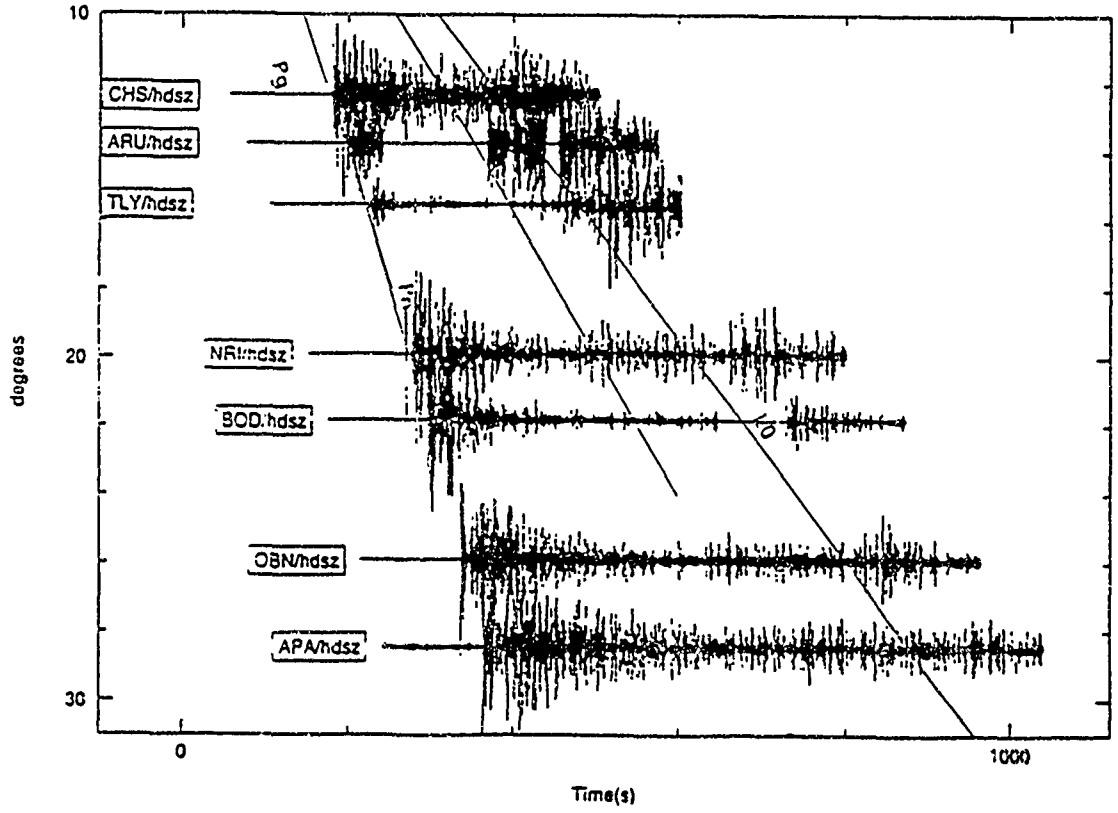

Figure 1 a) Map showing location of explosions (large circles), earthquakes (stars), and stations (triangles) with great circle paths showing source-station geometry. b) Hand digitized vertical component seismograms for an explosion at northeast Balapan recorded at different stations.

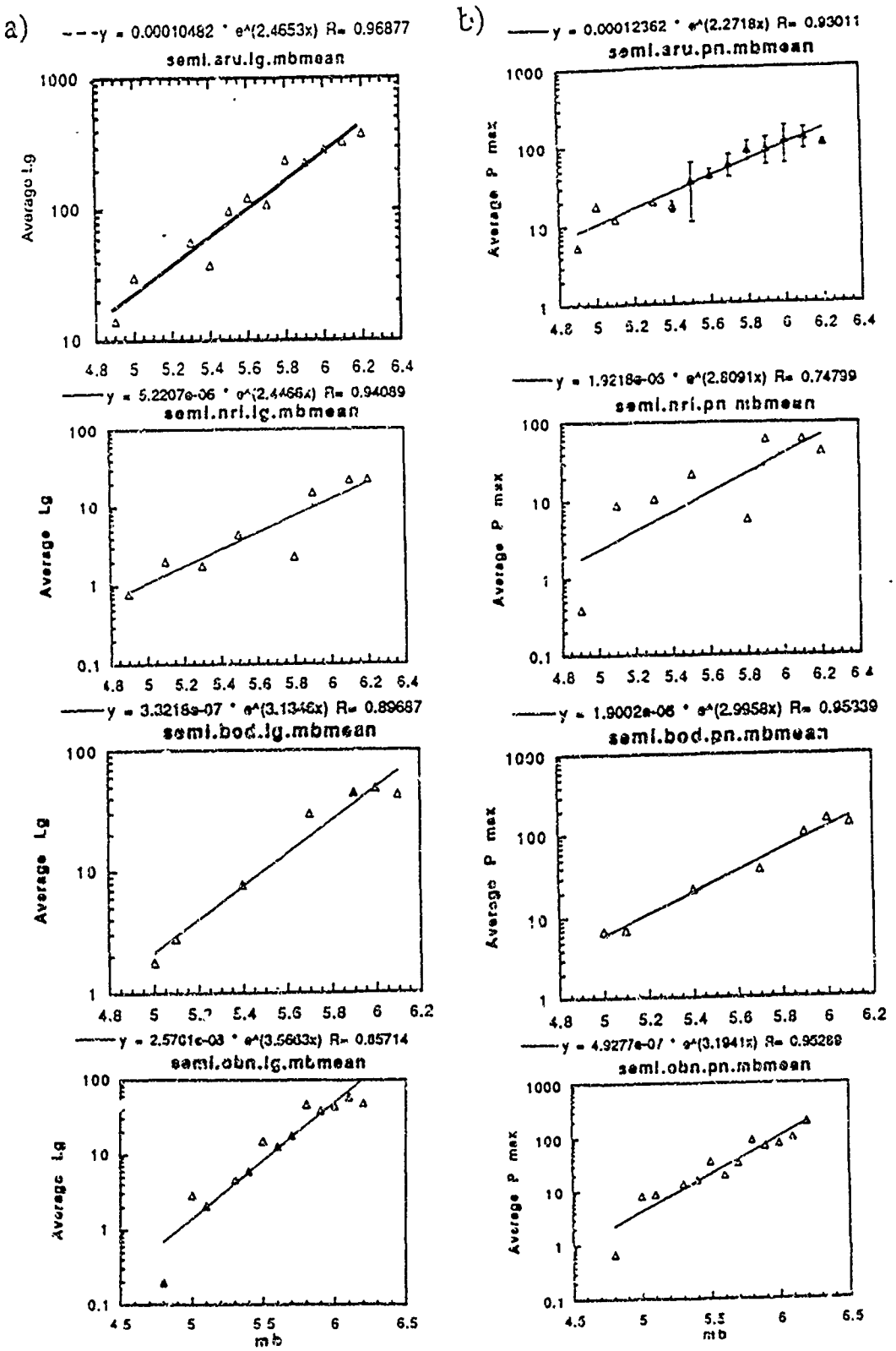

Figure 2 Averaged rms Lg (a) and rms Pmax (b) amplitude versus mb for all explosions at the Semipalatinsk test site recorded at different stations. The distance between the test site and the stations increases from the top to the bottom of the page. Best-fit exponential expressions and correlation coefficients are shown above each station.

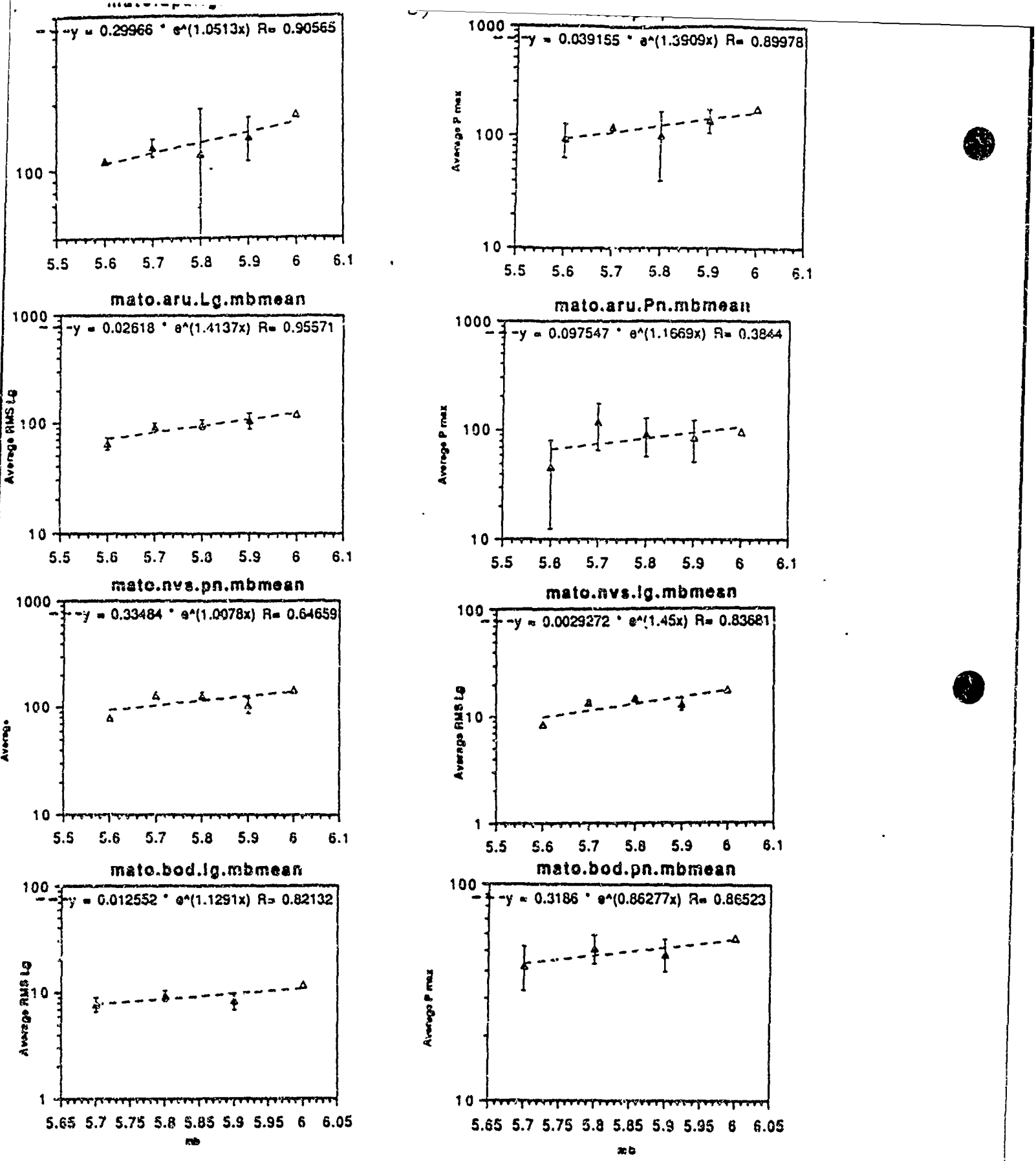

Figure 3 Averaged rms Lg (a) and rms Pmax (b) amplitude versus mb for all explosions at the Matochkin Shar test site recorded at different stations. The distance between the test site and the stations increases from the top to the bottom of the page. Best-fit exponential expressions and correlation coefficients are shown above each station. Note that the increase of both Lg and Pmax amplitudes with magnitude is smaller at Matochkin Shar than at Semipalatinsk.

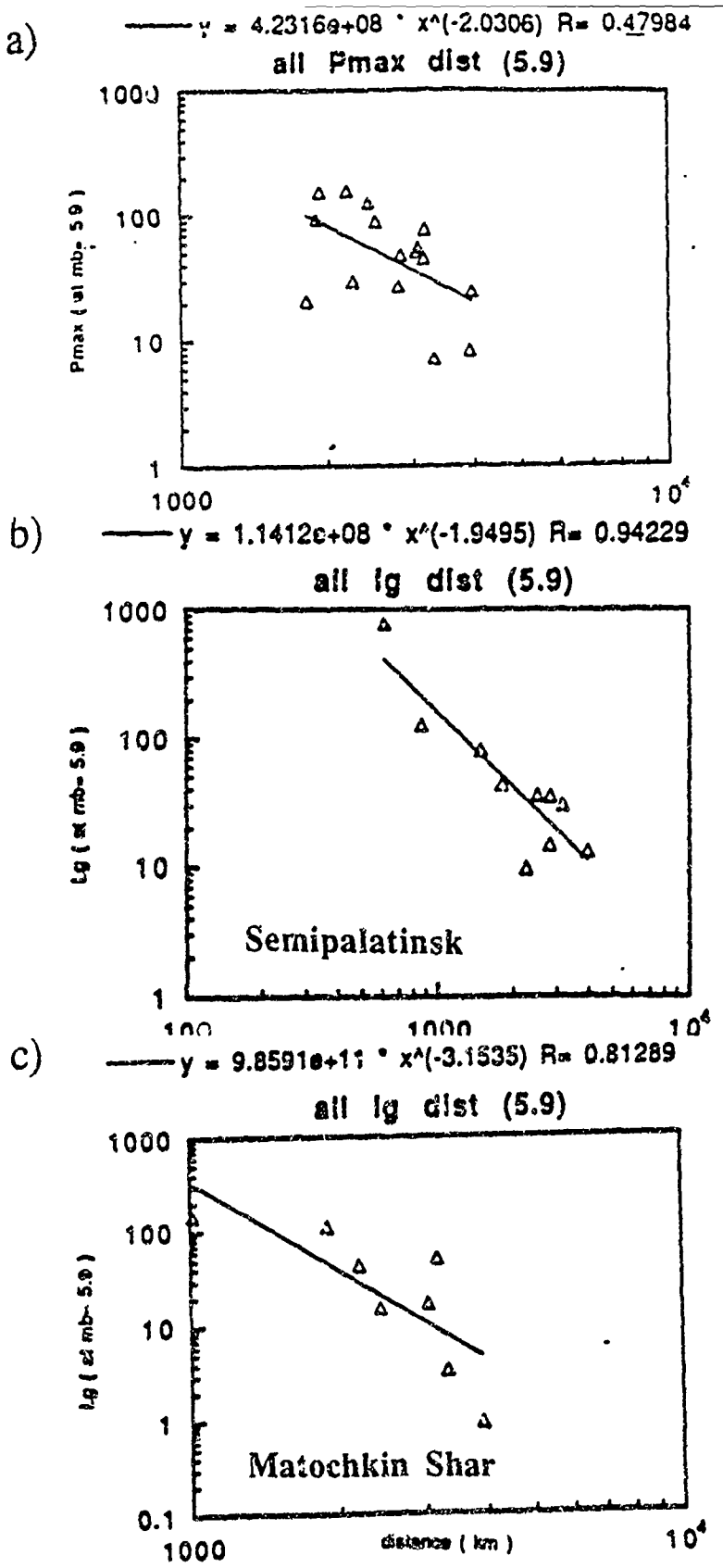

Figure 4. a) Rms Pmax amplitude, corrected to mb=5.9 using relations of figures 2 and 3, versus distance for explosions at both Semipalatinsk and Matochkin Shar test sites recorded at stations greater than 1500 km. Rms Lg amplitude versus distance normalized to mb=5.9 for explosions at b) Semipalatinsk and c) Matochkin Shar. The amplitude decay is faster from Matochkin Shar than Semipalatinsk.

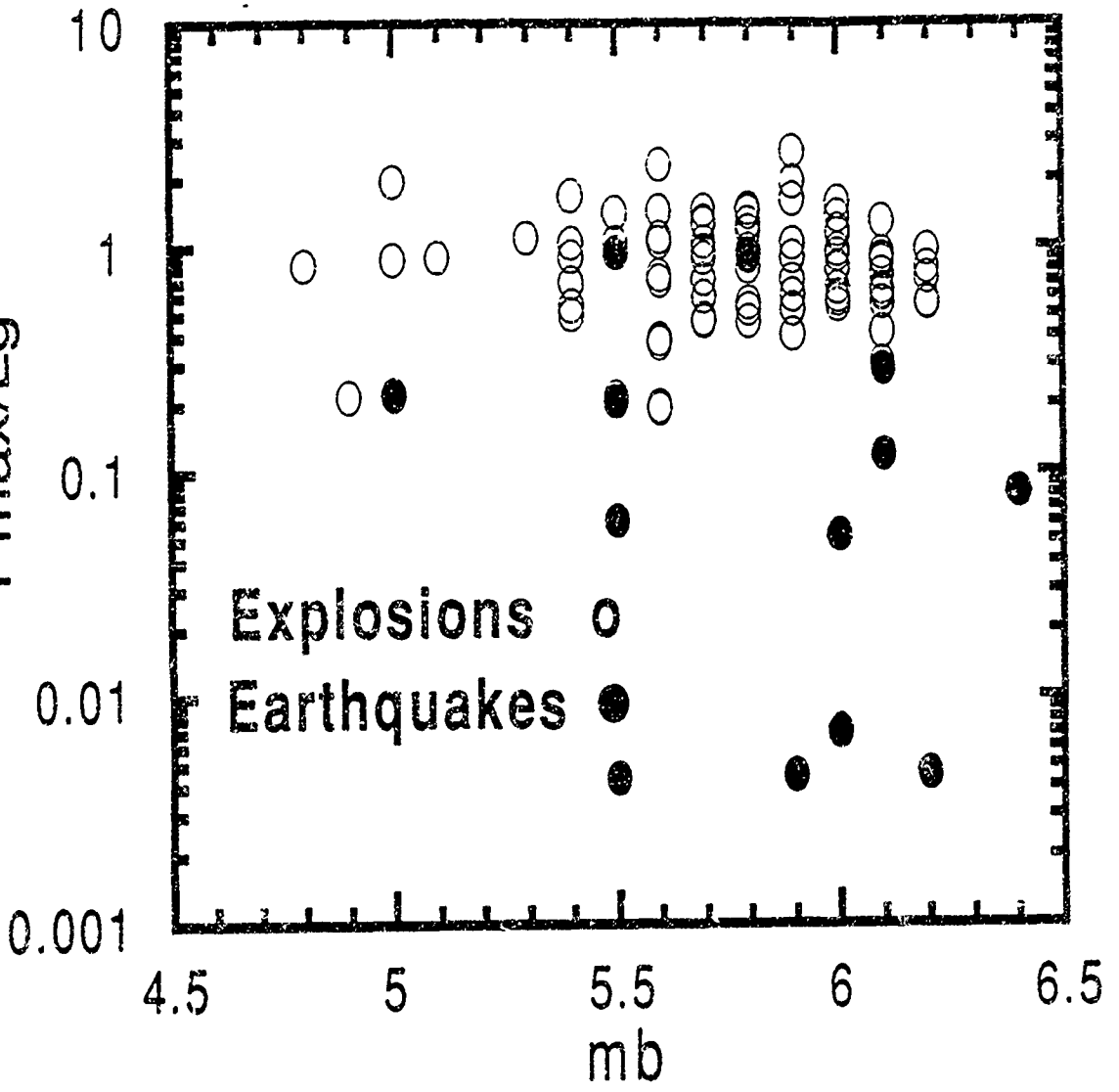

Figure 5 Average rms Pmax/Lg ratios versus ISC magnitudes for explosions (open circles) and earthquakes (closed circles). The explosions scatter about a ratio of 1 while the earthquakes show a much larger range in ratios. Even with the large scatter, the earthquake ratios are lower than the explosion ratios.

Progress in Automated Processing and Interpretation of Seismic Data

Thomas J. Sereno, Jr., Henry J. Swanger, and Thomas C. Bache

Science Applications International Corporation
10260 Campus Point Drive
San Diego, California 92121

Contract No. MDA972-92-C-0026

OBJECTIVE

The Intelligent Monitoring System (*IMS*) is one of several related systems that SAIC and its subcontractors (primarily Inference Corporation) have developed for automated and interactive analysis of data from a network of seismic stations to detect, locate and identify seismic events. It has been operating nearly continuously since 1989 while evolving through several increasingly capable versions. The main objective of our current contract is to improve the performance of *IMS* by extending the reasoning in our *Expert System for Association and Location* (**ESAL**), and adding the capability to collect, organize, and represent region-specific knowledge. We have focussed on adding data from new types of stations and developing techniques for rapid adaptation to data from stations in new areas.

RESEARCH ACCOMPLISHED

The first version of *IMS* was used to detect and locate regional events recorded by two 25-element arrays in Norway; NORESS and ARCESS. The second version was extended to detect and locate all seismic events recorded by an arbitrary network. This version was installed for operation in November, 1990, with data from NORESS, ARCESS, and a 16-element array in Finland (FINESA). In March 1991, data from a 25-element array in Germany (GERESS) was added to the *IMS*. This array is located in a different geologic and tectonic environment, and therefore addition of region-specific knowledge became important.

In the current contract, our focus has been on improving *IMS* for existing stations by adding region-specific knowledge, and extending *IMS* by adding data from new types of stations in new areas. We developed region-specific travel and azimuth corrections for paths to GERESS, and new station-specific tables for the Bayesian rules in *IMS* for final identification of regional phases. We enhanced the *IMS* to process and interpret data from 3-component stations, initially with data recorded by six *IRIS* stations in the CIS. Other station types being added to the *IMS* include 9-element mini-arrays (Apatity and Spitzbergen) and 4-element micro-arrays (Kislovodsk). Our most recent work emphasizes automated processing and interpretation of data from a global network to support new concepts being considered by the U.N. Conference on Disarmament's Group of Scientific Experts (GSE). This is motivating the development of new methods to represent and use relevant knowledge, such as the probability of detection at a station given estimates of the noise

level and an event location/magnitude hypothesis. Our progress for each of these new station types and networks are described in separate sections below. The first section describes our concept for acquiring new knowledge and our metrics for performance evaluation.

Knowledge Acquisition and Performance Analysis

Our objective is to minimize the number of events where ESAL makes serious errors. To improve ESAL at that level, we must incorporate more seismological knowledge, particularly about region-specific signal characteristics. We adopted the expert system approach to obtain the flexible framework needed for representing this knowledge. Our approach to acquiring new knowledge is sketched in Figure 1. As shown, ESAL does the automated interpretation and writes its results to the data management system, along with an audit trail which records the most important rules used in the reasoning process. An analyst then reviews the ESAL results, corrects them as necessary, and writes the edited results to the data management system. Performance analysis is then done by another expert system which compares the automated and analyst results. Data summarizing the results of this comparison are then written to the data management system. The Performance Analysis Expert System includes some deductive reasoning to decide which elements of the ESAL reasoning process have implicitly been rejected by the analyst, and the corresponding elements of the audit trail are marked accordingly.

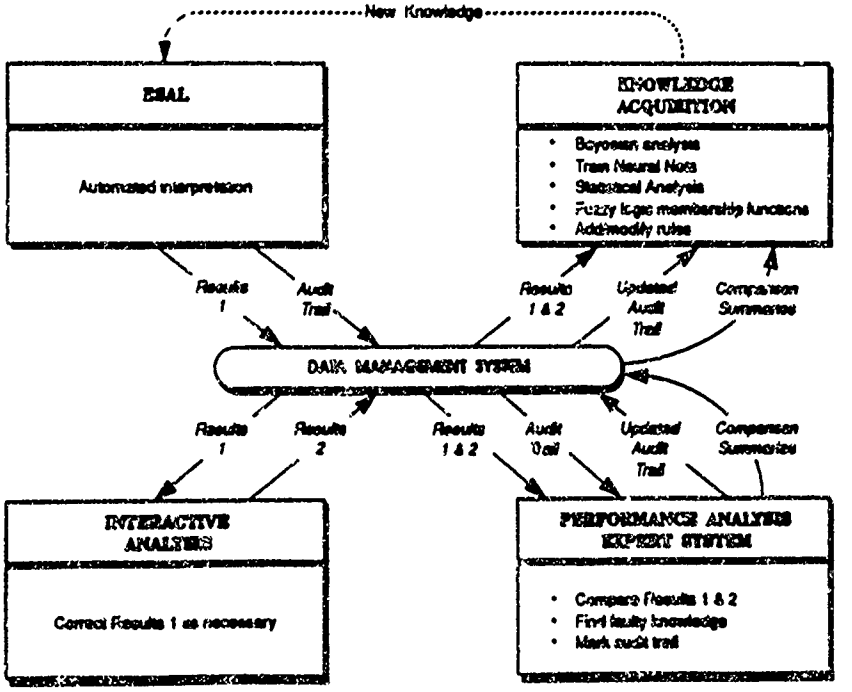

Figure 1. Knowledge acquisition in *IMS*.

The objectives of performance analysis are to measure progress in automated processing, and to focus attention on those elements of ESAL where improvement will be most effective. The knowledge contained in ESAL is represented in various forms, and the knowledge acquisition is done differently and with varying degrees of automation for each. As indicated in Figure 1, the

knowledge acquisition methods include Bayesian analysis, training of neural networks, statistical analysis, computing fuzzy-logic membership functions, and generation of new and modified rules. Examples of Bayesian analysis and neural networks are discussed later in this paper. Statistical analysis is used to estimate numerous parameters and thresholds that express the details of the knowledge represented in the rules. The fuzzy-logic technique is being used in the event identification portions of *IMS* [*Sereno and Wahl*, 1993], but this is outside the scope of this paper. The final step is to add the new knowledge to **ESAL**. Unless it requires additions or changes to the structure of the rules and fundamental reasoning process, the new knowledge is added as parameters and functions that are external to the **ESAL** source code.

We developed two metrics for evaluating the overall performance of the automated processing. The first is a measure of the quality, Q, of the automated bulletin with respect to the analyst's bulletin:

$$Q = (Pd)^n (1 - Pfa)^{(1-n)}$$

Pd represents the proportion of events in the analyst's bulletin that are detected by the automated system. It is a weighted sum of events that are accepted or corrected by the analyst, with the weight depending on the distance between the analyst's location and the location determined by the automated system. Pfa is the percentage of events in the automated bulletin that are subsequently rejected by the analyst (i.e., false-alarms). The exponent, n, is used to assign different weights to the detection of real events (i.e., events in the analyst's bulletin) and false-alarms. We are currently using n=0.75, which gives more weight to the detection of real events.

The other metric is a normalized estimate of the amount of effort required by an analyst to correct the automated bulletin. The analyst effort, E, is defined as:

$$E = (T - T_0) / (T_{max} - T_0)$$

where T is the time to analyze the automated bulletin, T_0 is the time to validate a perfect automated bulletin, and T_{max} is the time to produce the analyst bulletin without automated interpretation. E is zero if the automated bulletin is the same as the analyst's bulletin (T=T_0), and it is unity if automated interpretation is not done (T=T_{max}). The time estimates are based on the number of accepted, corrected, rejected, and added events; and on the number of analyst edits (e.g., retimed, associated or disassociated, renamed, and added phases).

High-frequency Regional Arrays

Most of our operational experience is with the high-frequency regional arrays in Norway, Finland, and Germany. Table 1 summarizes the performance of several versions of **ESAL** for data recorded by these arrays during a 15-day period in September, 1991. The column headings include the **ESAL** version dates. The first column lists the results for the version that was used in routine operation (*ESAL_8/91*). The results for two later versions appear in the next two columns. The first row is the number of analyst-verified events, and the second row is the number of events formed automatically by **ESAL**. The next two rows list the number of **ESAL** events whose location was moved by the analyst by <50 km and >50 km, respectively. The fifth row is the number of events that were added by the analyst (i.e., missed by **ESAL**), and the sixth row is the number

of events that were rejected by the analyst (i.e., false-alarms). The last two rows give the *analyst-effort* and *bulletin-quality* metrics described in the previous section.

Table 1: Performance Summary for High-Frequency Regional Arrays

	ESAL_8/91	*ESAL_2/92*	*ESAL_1/93*
Analyst Events	904	904	904
ESAL Events	1672	1422	1022
Moved < 50 km	599	586	599
Moved > 50 km	208	220	176
Added Events	97	98	129
Rejected Events	865	616	247
Effort	**0.46**	**0.38**	**0.27**
Quality	**0.73**	**0.76**	**0.80**

There has been clear and steady improvement in *IMS* for data from these high-frequency regional arrays since August, 1991. This is due to development of new and modified rules to reduce the number of false-alarms and to development of station-specific tables for the Bayesian rules used for final identification of regional phases [*Bache et al.*, 1993]. For example, the identification of regional *S* phases as *Sn*, *Lg*, or *Rg* is based on Bayesian rules using signal characteristics (e.g., phase velocity, a distance-normalized estimate of frequency, and horizontal-to-vertical amplitude ratio) and contextual characteristics (e.g., the phase is the only *S* phase, the first of two *S* phases, the first of many *S* phases, or the largest *S* phase). *Bache et al.* [1993] show that these characteristics are significantly different at GERESS than they are at the arrays in Scandinavia. The tables used in the Bayesian rules are a good example of compact knowledge representation in a form compatible with convenient acquisition of station-dependent knowledge. Station-specific tables for the Bayesian rules were introduced into the *IMS* in July, 1992.

Region-specific travel time and azimuth corrections were also developed for paths to GERESS [*Sereno et al.*, 1992]. This form of region-specific knowledge does not contribute to the performance metrics in Table 1 since both **ESAL** and the analyst use the same travel-time curves and azimuth corrections. However, these corrections significantly improve the accuracy of the event locations. For example, >200 single-station events recorded at GERESS were located with and without the region-specific corrections. On average, the locations are 38% closer to locations in the PDE bulletin when the region-specific corrections are used than when they are computed with the reference model for Scandinavia.

IMS Arrays and 3-Component IRIS Stations

We enhanced the *IMS* to process and interpret data from 3-component stations, initially with data recorded by six *IRIS* stations in the CIS. This motivated the development of neural networks

for interpreting a suite of signal features to identify initial wave type [*Patnaik and Sereno*, 1991], as well as the capability to add late-arriving data.

Table 2 summarizes ESAL's performance for a one-week set of *IMS+IRIS* data. The analyst's bulletin from the *IMS* arrays was used as a starting solution for the *IMS+IRIS* processing (i.e., the *IRIS* data provided an incremental addition to an existing bulletin). Table 2 gives the results for events that were detected by at least one of the *IRIS* stations (AAK, ARU, GAR, KIV, OBN, TLY). The major change between *ESAL_2/92* and *ESAL_12/92* is the incorporation of a neural network for identifying initial wave type (regional *P*, regional *S*, teleseism, noise). The earlier version did this task with rules based on rectilinearity and horizontal-to-vertical amplitude ratios. The neural network uses these and other polarization parameters plus context (e.g., number of arrivals before and after the arrival in question), and spectral content. ESAL_1/93 used improved station-specific neural network weights derived from a larger training data set.

Table 2: Performance Summary for the IMS+IRIS Network

	ESAL_2/92	*ESAL_12/92*	*ESAL_1/93*
Analyst Events	265	265	265
ESAL Events	1069	528	381
Moved < 50 km	118	139	129
Moved > 50 km	92	74	84
Added Events	55	52	52
Rejected Events	859	315	168
Effort	**1.03**	**0.55**	**0.46**
Quality	**0.52**	**0.64**	**0.70**

Like the Bayesian rules, the neural network weights are an example of compact knowledge representation that facilitates acquisition of station-dependent knowledge. Adding the neural network made a significant improvement in ESAL's performance for 3-component data (e.g., the *analyst-effort* was reduced by more than a factor of two). However, ESAL performs much better with data from high-frequency arrays than with data from 3-component stations. One of the main reasons is that the latter provide no estimates for regional *S*-wave azimuths, and these are important for grouping arrivals that belong to the same event. The result is a much higher false-alarm rate for 3-component data.

Micro-Array in Kislovodsk

Micro-arrays were originally suggested by *Kværna and Ringdal* [1990] as a less-costly alternative which still provided slowness and azimuth estimates accurate enough for reliably identifying initial wave-type and grouping arrivals that belong to the same event. In particular, they found that *f-k* analysis of NORESS A-ring data provided adequate resolution for an accuracy of 95% for automated identification of *P* and *S* phases, and azimuth uncertainties of about 30° for regional *P*

and *S* phases. Based on these results, Scripps Institution of Oceanography, the Center for Seismic Studies (CSS), and the Experimental Methodical Expedition (EME) in Obninsk collaborated on an experiment to establish and operate a 4-element micro-array in Kislovodsk [*Berger et al.*, 1992].

We analyzed a two-week data set from the micro-array in Kislovodsk (KIV0). While this data set is too small for definitive conclusions, our preliminary results suggest that the slowness estimates from this array are not accurate enough for reliable identification of initial wave type. For example, the accuracy is <50% for regional *P*, *S*, and teleseisms, and it is about 90% for noise. In contrast, our neural network applied to 3-component data identifies >95% of the regional *P*, *S*, and teleseisms correctly, and >90% of the noise detections. We added the *f-k* slowness estimate to our neural network, but this did not improve the accuracy of the KIV0 initial wave type identification very much. The main advantage of the micro-array over a 3-component station is that the array provides azimuth estimates for regional *S* waves to aid the grouping of arrivals from the same event. However, the KIV0 azimuth uncertainties are much larger than they are for NORESS-type arrays. For example, for typical regional signals the azimuth uncertainty is about 7° for NORESS-type arrays and about 35° for KIV0. While this uncertainty too large to be useful for location, it may be accurate enough to reduce the number of false events formed by **ESAL**. A much larger analyst-verified data set is needed to investigate this conjecture. Such a data set is being compiled at CSS for KIV0 and two 9-element mini-arrays (Apatity and Spitzbergen). We will use these data quantify the dependence of the false-alarm rate on the array geometry.

Global Network (GSETT-2)

Our most recent work emphasizes automated processing and interpretation of data from a global network to support new concepts being considered by the U.N. Conference on Disarmament's Group of Scientific Experts (GSE). Our most extensive experience with data from global networks stems from the GSE's second technical test (GSETT-2) in April-June, 1991. **ESAL**'s performance is summarized in Table 3 for the *GSETT* network (>50 stations) for a 5-day period that was carefully reanalyzed at CSS subsequent to the experiment.

The first column of Table 3 shows the results for *ESAL_12/91* which was run just prior to the reanalysis at CSS. The *analyst-effort* is higher for this network than it is for the regional arrays because a higher percentage of the events are at teleseismic distances, and these are more difficult to form correctly (e.g., they are detected by more stations and can have many more associated arrivals). On the other hand, the *analyst-effort* is less for the *GSETT* network than it is for the *IMS+IRIS* network because the station processing (initial wave type identification, event grouping, and final identification of regional phases) was done by seismologists rather than by **ESAL**. Many of the false (i.e., rejected) events produced by *ESAL_12/91* were formed using data from an unlikely combination of stations. We introduced the probability of detection at each station into the association process and event confirmation in *ESAL_6/93* to reduce the number of these false events. Our initial implementation was successful in this regard, but it was at the cost of missing more real events (i.e., added events in Table 3). The net result was only a slight improvement in **ESAL**'s performance as measured by our metrics. It is clear that probability of detection is new and valuable information for automated interpretation, but the **ESAL** implementation will require more tuning.

Table 3: Performance Summary for GSETT-2

	ESAL_12/91	*ESAL_6/93*
Analyst Events	412	412
AA Events	442	342
Moved < 50 km	121	123
Moved > 50 km	186	160
Added Events	105	129
Rejected Events	135	59
Effort	**0.38**	**0.36**
Quality	**0.62**	**0.64**

CONCLUSIONS AND RECOMMENDATIONS

New concepts are being considered by the GSE and ARPA/NMRO for global seismic monitoring at magnitude thresholds that are much lower than can be achieved by existing networks. There is no question that a high-degree of automation will be required to achieve this goal. The effectiveness of the automation will depend on how well region-specific knowledge can be represented, and how rapidly new stations can be added to the monitoring network. These issues have been the main focus of our work with data from regional networks. We are now extending this to data from a global network to support the new concepts that are emerging from the GSE.

REFERENCES

Bache, T., S. Bratt, H. Swanger, G. Beall, and F. Dashiell, Knowledge-based interpretation of seismic data in the Intelligent Monitoring System, *Bull. Seismol. Soc. Am.*, [in press], 1993.

Berger, J., D. Chavez, J. Given, and D. Williams, Kislovodsk mini-array experiment, October 7 through October 20, 1992, Final Report, Institute of Geophysics and Planetary Physics, La Jolla, California, 69 pp., 1992.

Kværna, T. and F. Ringdal, Real-time processing using a hybrid 3-component/small array station, Semiannual Tech. Summary, NORSAR Sci. Rep. No. 1-90/91, 96-109, 1990.

Patnaik, G. and T. Sereno, Neural computing for seismic phase identification, Sci. Rep., PL-TR-92-2110 (II), 42 pp., 1991, ADA252442.

Sereno, T., H. Swanger, R. Jenkins, W. Nagy, and D. Wahl, Attenuation and travel-time characteristics of regional phases recorded at GERESS, Proceedings of the GERESS Symposium, Waldkirchen, Germany, 22-24 June, 123-129, 1992.

Sereno, T. and D. Wahl, A fuzzy-logic approach to regional seismic event identification: application to the Novaya Zemlya event on 31 December 1992, [a paper to be included in an ARPA report on the 31 December 1992 Novaya Zemlya event], 24 pp., 1993.

RESOLUTION OF EXPLOSION SOURCE MODEL PARAMETERS BY THE NONLINEAR INVERSION OF NEAR-SOURCE DATA: SYNTHETIC TESTS AND OBSERVATIONAL APPLICATIONS

Brian Stump and Gyungsik Min
Department of Geological Sciences
Southern Methodist University
Dallas, TX 75275-0395
F29601-91-K-DB20

OBJECTIVE:

Near-source observations whether they are from nuclear or chemical explosions provide the opportunity for constraining the source model with minimal contamination from complex propagation path effects. These source models are in turn useful in understanding and interpreting seismic energy observed at regional and teleseismic distances. In the case of chemical explosions and particularly mining explosions these source characterizations can be used in understanding discriminants designed to separate event populations. The work reported in this paper is designed to improve our physical understanding of single, nuclear and chemical explosions.

The first part of this paper summarizes a nonlinear inversion procedure that utilizes near-source seismic data to determine the parameters of the explosion source model including moment, corner frequency, overshoot, high frequency decay and Q. Synthetic tests illustrate the utility of both prewhitening and damping in the procedure to speed convergence and maintain independence of parameters. A propagation path correction must be made in order to complete the source inversions. Path corrections as simple as an elastic whole space to as complex as a layered structure are investigated. Different portions of the near-source waveforms including body waves, surface waves and complete waveforms as well as different frequency bands are considered in the inversions. Trade-offs between inadequacies in the propagation path models and the source models are identified. These trade-offs are found to be source model dependent. Source models are divided into two parameterizations: a Sharpe/Blake type (includes the models of Mueller and Murphy,1971, and Denny and Goodman, 1990) and a Haskell type (includes models of von Seggern and Blandford,1972, Helmberger and Hadley, 1981, and Haskell, 1967).

The second part of this report describes empirical work designed to identify differences between chemical and nuclear explosions as well as quantify source scaling relations. A number of Rainier Mesa nuclear explosions have been instrumented in the near-source region for the purposes of source characterization. The explosions include MISTY ECHO, MINERAL QUARRY and HUNTERS TROPHY. Both free surface and free-field data have been recovered. A chemical explosion with a yield near 1 kt is planned for the Fall (CK, Chemical Kiloton). The same instrumentation array deployed on the previous nuclear explosions is planned for this event. In preparation for the large chemical

explosion, a 300 lb calibration shot (CK Cal) was detonated at the centroid of CK. The near-source seismic array was deployed for this calibration shot as well. Comparisons between the nuclear explosion and the CK Cal shot data are presented. This simple comparison suggests that scaling relations between chemical and nuclear explosions might be investigated with such data sets.

RESEARCH ACCOMPLISHED:

EXPLOSIONS SOURCE INVERSIONS: An inversion scheme is developed to recover explosion source model parameters from near-source data. The model is formulated in the frequency domain and is shown to be nonlinear in the source model parameters:

$$|u(\omega)| = P(\omega) \cdot \frac{\Psi_\infty \left[1+(1+n!B)^2 \frac{\omega^2}{k^2}\right]^{1/2}}{\left[1+\frac{\omega^2}{k^2}\right]^{\frac{1+n}{2}}} \cdot e^{-\frac{\pi f t}{Q}} \qquad (1)$$

where the first term on the right, $P(\omega)$, is the path model which could be as simple as that for a homogeneous full space or as complex as that for a layered structure. The second term on the right is the source model. It can represent a Brune model with n=2 and B=0, a von Seggern-Blandford model with n=2 or a Helmberger-Hadley model with n=3. The third term on the right is the simple attenuation model applied. The model parameters that will be determined by the inversion include Ψ_∞ or moment, the corner frequency k, the overshoot parameter B and attenuation operator Q. Trade-offs among these parameters in the nonlinear inversions are investigated as well as biases introduced by assumptions concerning the propagation path effects, $P(\omega)$.

A number of inversion schemes for source model parameters were tested against synthetic data sets. These included the simple Newton's iterative method:

$$m_{n+1} = m_n + \rho\,(G_n^T G_n)^{-1}\,(G_n^T(g(m_n)-d)) \qquad (2)$$

where equation 1 is represented as $d = g(m)$, m are the model parameters and $G = \frac{\partial g}{\partial m}$

Inversion with prewhitening using the data covariance matrix ($C_d = g^2(m_n)$);

$$m_{n+1} = m_n + \rho\,(G_n^T C_d^{-1} G_n)^{-1}\,(G_n^T C_d^{-1}(g(m_n)-d)) \qquad (3)$$

Inversion with damping (I) was introduced to minimize trade-offs among parameters:

$$m_{n+1} = m_n + \rho\,(G_n^T G_n + I)^{-1}\,(G_n^T(g(m_n)-d)) \qquad (4)$$

Finally a technique which includes both prewhitening and damping:

$$m_{n+1} = m_n + \rho\,(G_n^T C_d^{-1} G_n + I)^{-1}\,\{(G_n^T C_d^{-1}(g(m_n)-d)) + I(m_n - m_{n-1})\} \qquad (5)$$

An initial set of trial inversions were attempted in which the propagation path model (P(ω) in equation 1) was assumed known. These trials with different types of synthetic noise provided the opportunity to identify trade-offs among model parameters and investigate questions associated with uniqueness, stability, rate of convergence and residual analysis.

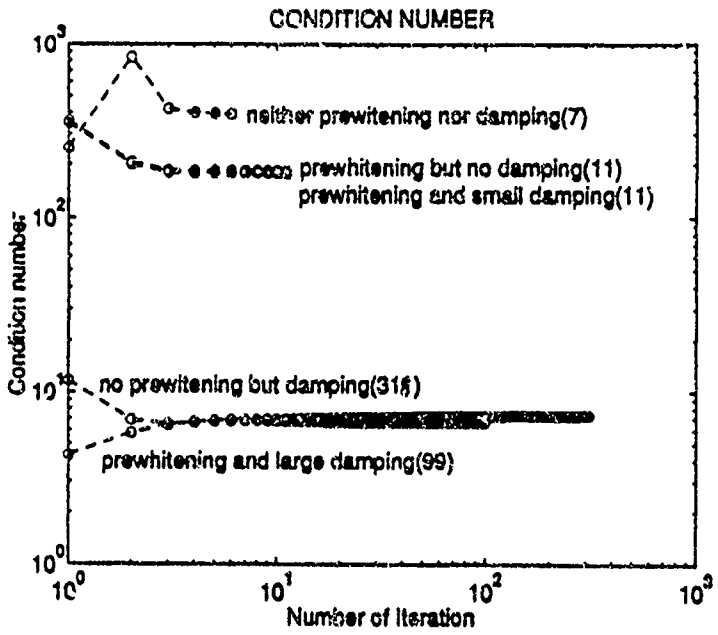

Figure 1: Condition number for source inversions using equation 2 (no prewhitening or damping), equation 3 (prewhitening only), equation 4 (damping only), and equation 5 (prewhitening and damping). The numbers in parenthesis are the total iterations required by each method.

These numerical experiments illustrated that in the case where there are trade-offs between model parameters, such as corner frequency, overshoot and long period spectral level in our case, that damping is necessary and prewhitening improves convergence (Figure 1). Equation 5 was found to be the preferred approach for source model determination. The trade-offs between model parameters was also shown to be dependent upon the bandwidth of the data. Equation 1 can be applied to frequencies high relative to the corner frequency ($f>>f_0$) and shown for a von Seggern-Blandford model (n=2) to be equivalent to:

$$|u(\omega)| \sim P(\omega) \cdot \frac{\Psi_\infty f_o^2 (1+2B)}{f^2} \cdot e^{-\frac{\pi f t}{Q}} \qquad (6)$$

This equation illustrates the inability to resolve the source parameters with only high frequency data and the need to include as broadband data as possible. Separation of Ψ_∞ and B is only possible with the longest period data well below the corner frequency. Unfortunately reliable long period strong motion data is difficult to recover in the field.

The next step in the study was the investigation of possible trade-offs between propagation path and source models. These trials were conducted by using equation 1 to generate synthetic data using a particular propagation path model and then completing inversions with a simplified propagation model. The purpose of this exercise was the identification of a simple operational procedure for recovery of stable source model estimates. Propagation path effects taken into account included the near-field term, amplitude partitioning at the free-surface, body and surface wave contributions, secondary source contributions such as those from spall, and near-receiver effects. In these trials, $u(\omega)$ was generated for an elastic half-space and then inversions were attempted retaining complete waveforms, body waves only, and surface waves only as data. In each of the inversions, different assumptions were made concerning the appropriate propagation path correction.

When the near-field term was not included in the propagation path correction, $P(\omega)$, although it remained in the data, it was found that the long period spectral level Ψ_∞ and overshoot B were strongly biased by data within 1-2 wavelengths of the source. As observations at farther ranges were included, inversions using Green's functions with no near-field contribution did not bias the source estimates.

Inversions were attempted with just the body wave component of the data. It was found that the major propagation path effect in this case was the interaction of the wavefield with the free surface. Whole space Green's functions in combination with waveform partitioning between vertical and horizontal components as predicted by Zoeppritz's equations were adequate for recovery of the original source parameters at high frequency. As equation 6 illustrates, the long period level, overshoot and corner frequency could only be determined in their combined form at high frequencies. The point here is that the propagation path effects could be simply taken into account at high frequencies.

The last set of numerical experiments used data that included both body and surface waves but the Green's functions, $P(\omega)$, in the inversions assumed that there were only body waves present. The purpose of this trial was to investigate source biases introduced by near-source surface waves. The synthetic data were generated by the ω^{-2} source model of von Seggern and Blandford (n=2). When inversions were completed using the ω^{-3} source model of Helmberger and Hadley (n=3 in equation 1), the high frequencies in the synthetic data were well matched. Near-source surface wave contributions produce a high frequency spectrum that decays more rapidly than that from the body waves and in this case the inversions misinterpreted this part of the data as a high frequency source decay. These

results emphasize the importance of including surface wave contributions in Green's functions used to interpret the near-source data from shallow explosions.

NUCLEAR/CHEMICAL SOURCE SCALING EXPERIMENTS: The second portion of our near-source studies is in progress. It involves free surface and free-field measurements at the same receivers for a number of nuclear explosions (MISTY ECHO, MINERAL QUARRY, HUNTERS TROPHY) and chemical explosions (CK and CK Cal) at Rainier Mesa. The purpose of this work is to establish scaling relations between these different sources minimizing local receiver effects. Figure 2 compares a vertical accelerogram from the nuclear explosion HUNTERS TROPHY with a vertical velocity record for the CK Cal at station 2 (approximate range of 1.4 km from each source).

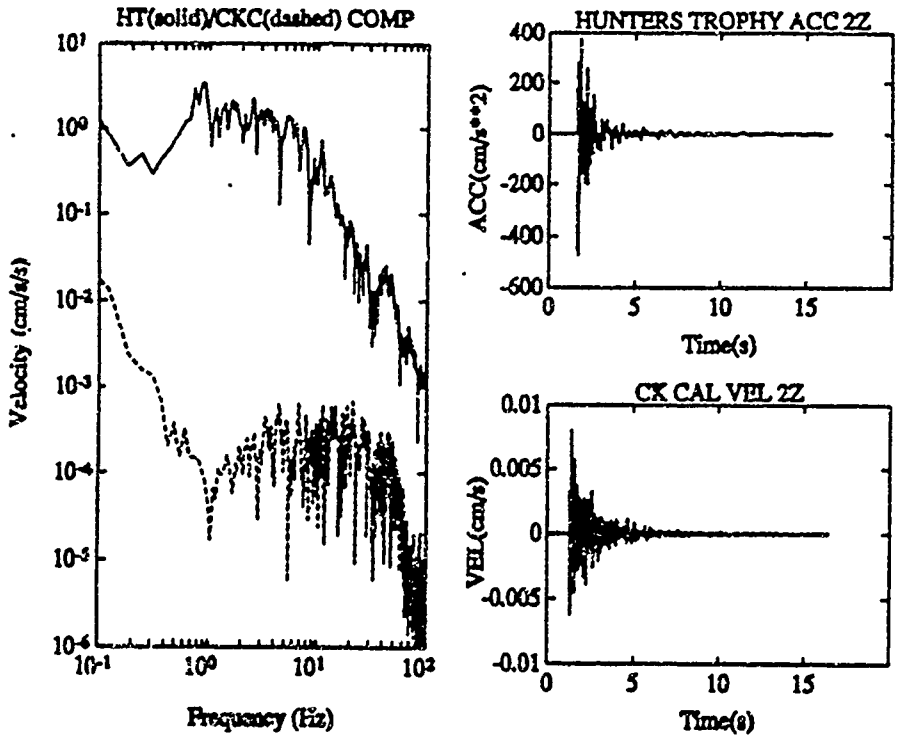

Figure 2: Vertical accelerogram from the nuclear explosion HUNTERS TROPHY and velocity waveform from the CK Cal (300 lbs) both observed at Station 2 on Rainier Mesa. The velocity spectra for the two waveforms are displayed to the left.

The observations are corrected for instrument response and compared in the frequency domain on the left hand side of Figure 2. The corner frequency of the nuclear explosion in the velocity is near 1 Hz while that for the small (300 lbs) calibration chemical shot is quite high, >30 Hz. In order to remove the receiver effect, a simple spectral ratio between the two observations was created. The nuclear and chemical explosions are close to one another and thus this procedure provides the opportunity to identify source differences

between the two shots within the data bandwidth (1-70 Hz). The ratio in Figure 3 indicates at the longest periods a source difference of $2x10^4$. The high frequency decay between the two source corner frequencies (1, 30 Hz) is no greater than ω^{-2}.

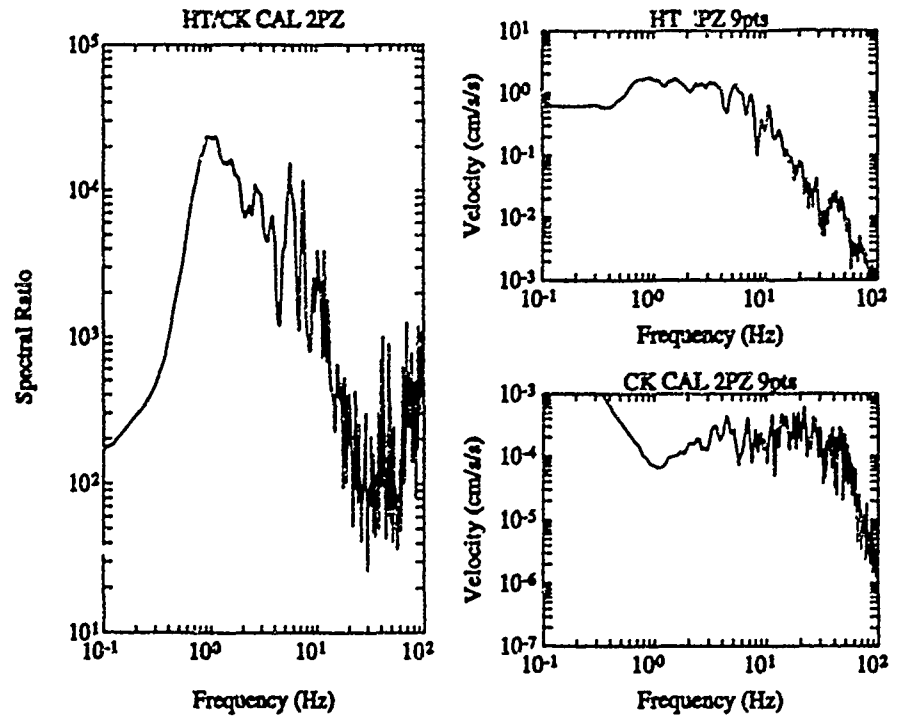

Figure 3: Vertical velocity spectra for the nuclear explosion HUNTERS TROPHY and CK Cal Shot (300 lbs) are displayed to the right. The ratio of the two spectra given to the left.

CONCLUSION AND RECOMMENDATIONS:

A source inversion procedure has been developed and tested. The testing of the procedure has been used to identify trade-offs between source model parameters and propagation path effects. The synthetic tests are now being used to identify an operational procedure that can be applied to the observational data from the nuclear explosions MISTY ECHO, MINERAL QUARRY and HUNTERS TROPHY. The procedure has been developed so that propagation path effects can be included and applied directly to the observational data. If the data has strong secondary source contributions such as spall or tectonic stress release, then the direct inversion of the observational data may provide a biased estimate even if propagation path effects are well known and modeled. An alternate procedure in this case would involve an initial moment tensor inversion in the frequency domain with complete synthetics. The isotropic moment tensor component could be used to extract the explosion source parameters using the proposed nonlinear inversion procedure.

The CK Cal data shows the results of an empirical study that is designed to investigate the relationship between chemical and nuclear explosion waveforms and possible identify a calibration technique for a test site. Local receiver effects can be eliminated when data from explosions with identical propagation path effects are compared. The CK and CK Cal experiments are designed to take advantage of such a geometry. The source comparison can be invalidated if in the case of the larger explosion, secondary source processes such as spall are initiated but remain absent from the small calibration shot. This effect can be investigated by careful analysis of the free surface data from the CK experiment prior to the spectral ratio procedure. The completion of this portion of the study awaits the detonation of the full scale chemical explosion at Rainier Mesa in the Fall.

In addition to recording the main explosion on the CK experiment, we plan to capture micro earthquakes following the event. Dual velocity and acceleration recording will be conducted at each site in order to accomplish this task. These events represent the redistribution of stress around the cavity and chimney. Their distribution in time and space offer a late time diagnostic of a large underground explosion. Several hundred events were recorded in a similar manner following the HUNTERS TROPHY nuclear explosion. A comparative study of these effects for nuclear and chemical explosions is planned.

REFERENCES:

Blake, F. G., Jr., Spherical Wave Production in Solid Media, *J. Acoust. Soc. Am., 24,* 211-215, 1952.

Denny, M. D. and D. M. Goodman, A Case Study of the Seismic Source Function: SALMON and STERLING Reevaluated, *J. Geophys. Res.,95,* 19705-19723, 1990.

Haskell, N. A., Analytic Approximation for the Elastic Radiation from a Contained Underground Explosion, *J. Geophys. Res., 72,* 2583, 1967.

Helmberger, D. V. and D. M. Hadley, Seismic Source Functions and Attenuation from Local and Teleseismic Observations of NTS Events Jorum and Handley, *Bull. Seism. Soc. Am., 71,* 51-67, 1981.

Mueller, R. A. and J. R. Murphy, Seismic Characterization of Underground Nuclear Detonations Part I. Seismic Spectrum Scaling, *Bull. Seism. Soc. Am., 61,* 1675-1692, 1971.

Sharpe, J. A., The Production of Elastic Waves by Explosion Pressures. I. Theory and Empirical Field Observations, *Geophys., 7,* 144, 1942.

von Seggern, D., and R. Blandford, Source Time Functions and Spectra for Underground Nuclear Explosions, *Geophys. J. Roy. astr. Soc., 31,* 83-97, 1972.

Station Evaluation and Accurate Event Locations for Global Monitoring

A. Suteau-Henson, V. Z. Ryaboy, H. Israelsson, and J. A. Carter

Science Applications International Corporation
Center for Seismic Studies
1300 N. 17th Street, Suite 1450
Arlington, VA 22209

Contract No. F29601-92-C-0005

OBJECTIVE

The GSE (*Group of Scientific Experts* of the Conference on Disarmament) has defined new goals for a future test of its concepts for global monitoring (GSETT-3). Among the new challenges are the need for more highly automated processing to handle large amounts of data and reduce the analysis load, and the requirement for rapid knowledge acquisition to efficiently monitor many regions of the globe. Our objectives address several aspects of these new challenges.

Correct phase identification and accurate azimuth estimation by arrays depend on their capabilities for estimating slowness, which vary with configuration and bandwidth. As part of a search for less costly alternatives to NORESS-type ("full") arrays, we have investigated the capabilities of various array configurations for estimating slowness. Another objective has been to develop methods for rapidly evaluating and selecting many three-component (3-C) and array candidate stations for GSETT-3 participation, and "tuning" their automated processing. The GSE has also recommended that any future network for global monitoring should employ regionally calibrated travel-time curves and amplitude-distance relations, since success in detecting nuclear proliferation is critically dependent on the accuracy of regional event locations. Therefore, one of our aims is to improve regional locations by correcting for the effect of lateral velocity inhomogeneities on the travel-times of the major regional phases. In addition, the depth estimation capability of the GSETT-3 global network has been addressed by performing computational experiments modelling detectability of *pP* and *sP*, and by investigating depth accuracy based on origin times from travel-time ratios of *P* and *S* waves.

RESEARCH ACCOMPLISHED

Station Evaluation

For four possible array configurations (derived from the NORESS geometry) the theoretical beam response to a plane-wave was calculated in the slowness space for various frequencies and slownesses. *Figure 1* compares the capabilities of these configurations in terms of slowness resolution and potential for spatial aliasing for various seismic phases. These results can be used to select the most appropriate configurations for specific monitoring targets. For example, the *expanded A0AB* configuration may become preferable to *A0AB* as dominant frequency decreases, since it keeps its high resolution, while its tendency for spatial aliasing decreases.

The following strategy for station evaluation and tuning was used for over 15 candidate stations for GSETT-3. Noise characteristics, background seismicity and station quality were investigated, and the results were used for station selection. Station-specific parameters were then derived to optimize the automated processing. A representative data set of noise and regional background seismicity was built for each station (typically from less than 10 days of continuous data), satisfying minimum requirements for reliable statistical analysis. A standardized set of processes for optimization was then run on these data, using results from analysis as the performance standard. These processes include: detector optimization, by seeking SNR (signal-to-noise ratio) thresholds for a standard set of beams that minimize an objective function with small positive contributions from noise detections and large negative contributions from real seismic phases (Ray Willemann, *personal communication*); selection of polarization processing parameters that optimize phase identification at 3-C stations; and ultimately the building of station-specific expert systems (Sereno *et al.*, 1993). As an illustration of the importance of individual station tuning, preliminary results show a significant variability of the optimum frequency band for polarization processing at stations of the *German Regional Seismic Network* (GRSN): it is 0.5-8.0 Hz at MOX and 0.5-4.0 Hz at BRG, 1.5° away. Processing parameters can be updated when more data have become available. For example, re-optimizing polarization parameters at MOX, after adding regional detections obtained during 15 days of IDC test operations to the two-day tuning data set, validated our initial tuning results with a significant increase in confidence.

Travel-Time Corrections

A method to estimate regional and local travel-time corrections for improving automatic event locations has been developed and is illustrated for *Pn*-waves recorded in Scandinavia. *Regional corrections* are the difference between the *Pn* travel-time curve derived from averaging DSS profile observations for the Baltic shield and neighboring areas (Ryaboy, 1993), and the standard travel-time curve for *Pn* based on the IASPEI-91 Seismological Tables and

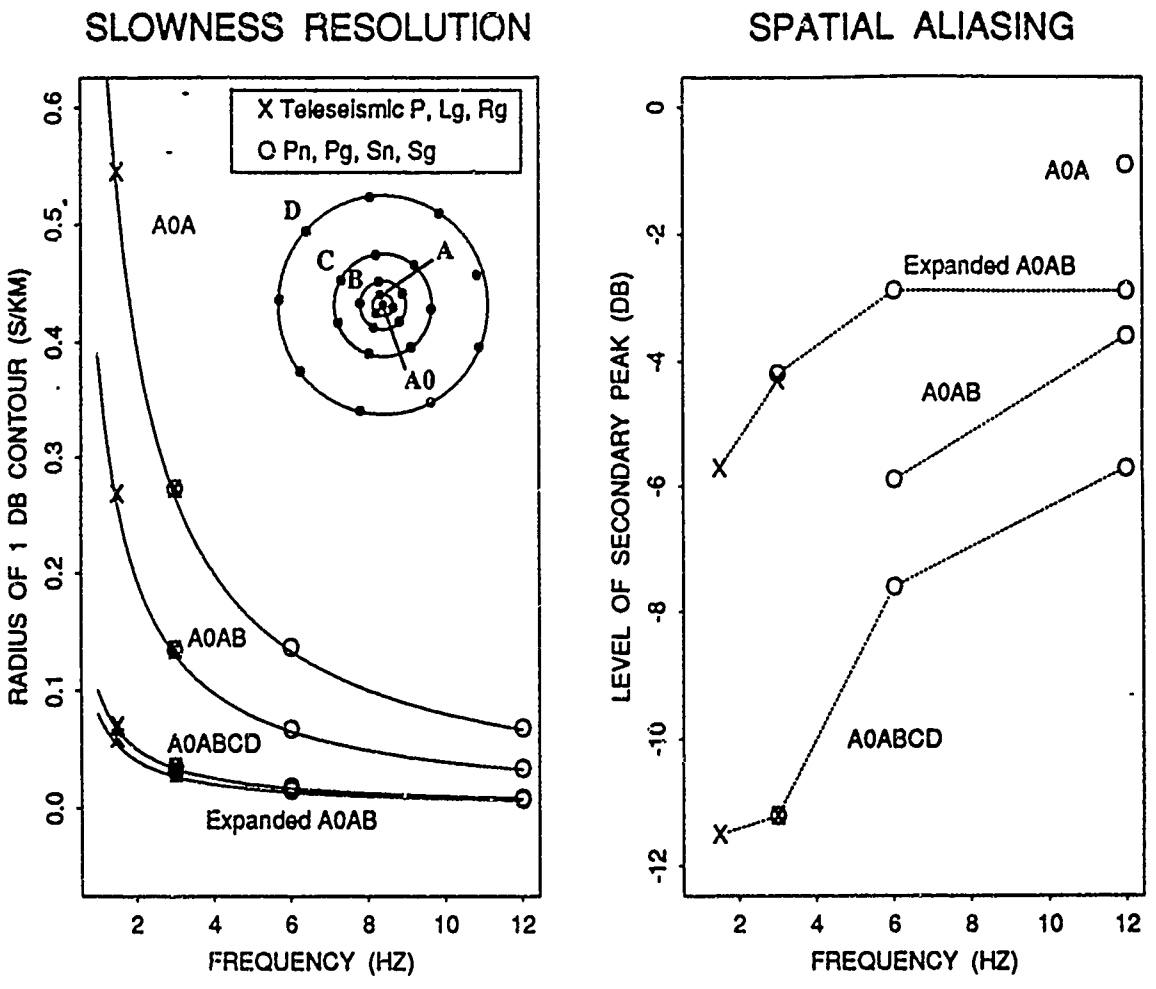

Figure 1: *The capabilities of four array geometries for estimating slowness are compared. "A0AB", for example, refers to the configuration including the center element A0, and the A and B rings. The outer ring radius is 1500 m. "Expanded A0AB" refers to nine-element A0AB scaled so that the outer ring has a D-ring radius. To the left, the radius of the 1 dB contour of the main peak of the f-k spectrum is plotted as a measure of slowness resolution. To the right, the level of the highest secondary lobe (if any within the slowness range of interest) is plotted in dB down from the main peak as a measure of spatial aliasing. Different symbols point to the main seismic phases of interest for a given frequency range.*

used as a global average (IASPEI, 1991). The *local corrections* were inferred from the residuals of the DSS observations with respect to the regional *Pn* travel-time curve and from variations of the Moho depth. A combination of these corrections can be used for improving event locations.

Previous work (Ryaboy, 1993) has shown that the difference between the Global IASPEI-91 and the Baltic shield travel-time curves for *Pn* ranges from 0.0 to 7.0 sec. A new Moho depth map of Scandinavia based on the most reliable published data has been compiled. The crustal thickness varies from approximately 30 km in southern Norway to 50-55 km in southern Finland and Sweden. The Moho depth map was digitized by researchers from Cornell University and included in a geophysical database (Fielding *et al.*, 1993).

The residuals of the observed *Pn* travel-times (TT_{res}) are highly correlated with variations of the Moho depth (the coefficient of linear correlation is 0.86 and the standard deviation is 0.39 sec):

$$TT_{res} = -4.802 + 0.058 * (M_{sp} + M_{rec}),$$

where M_{sp} and M_{rec} are the Moho depths in km beneath shot point and receiver, respectively, on the DSS profiles. This empirical relation and the new Moho depth map were used to calculate the ray-path dependent local corrections caused by lateral variations of the Moho depth. Maps of *Pn* local travel-time corrections were compiled for NORESS, ARCESS and FINESA. *Figure 2* shows the map of local corrections for FINESA. The maps for NORESS and ARCESS are similar, with differences caused by the variation of crustal thickness beneath these stations. The local corrections range from -1.5 to 1.5 sec.

Depth Estimation

An analysis of depth estimation was based on two kinds of secondary phases: (1) surface-reflected *pP* and *sP* recorded at teleseismic distances, and (2) *S* waves recorded primarily at regional distances.

(1) The modelling of depth accuracy from depth phases was based on two criteria: observability of moveout, and azimuthal coverage provided by the recording stations. We assumed a network of 50 stations similar to that planned for GSETT-3. Monte Carlo methods were used to estimate temporal fluctuations in noise and spatial fluctuations in signal. At about magnitude 4.0 the distance distribution was adequate to permit detection of moveout at almost the 100% level, assuming equal radiation of depth phases in all directions. The azimuthal coverage was defined, in percent, from the number of 45° sectors around the source that were covered by one or more detecting stations. Analysis of GSETT-2 data indicated that 50% azimuthal coverage improves the capabilities to detect and positively identify depth phases (Israelsson, 1993). The hypothetical GSETT-3 network reached this level a few tenths of a magnitude unit above its event detection threshold.

(2) Depth estimation based on *S* waves was evaluated from depth errors calculated at the 90% confidence level for events at 25 km depth. There was a clear gap between the depth estimation threshold (the magnitude at which the depth error equalled the event depth) and the 90%

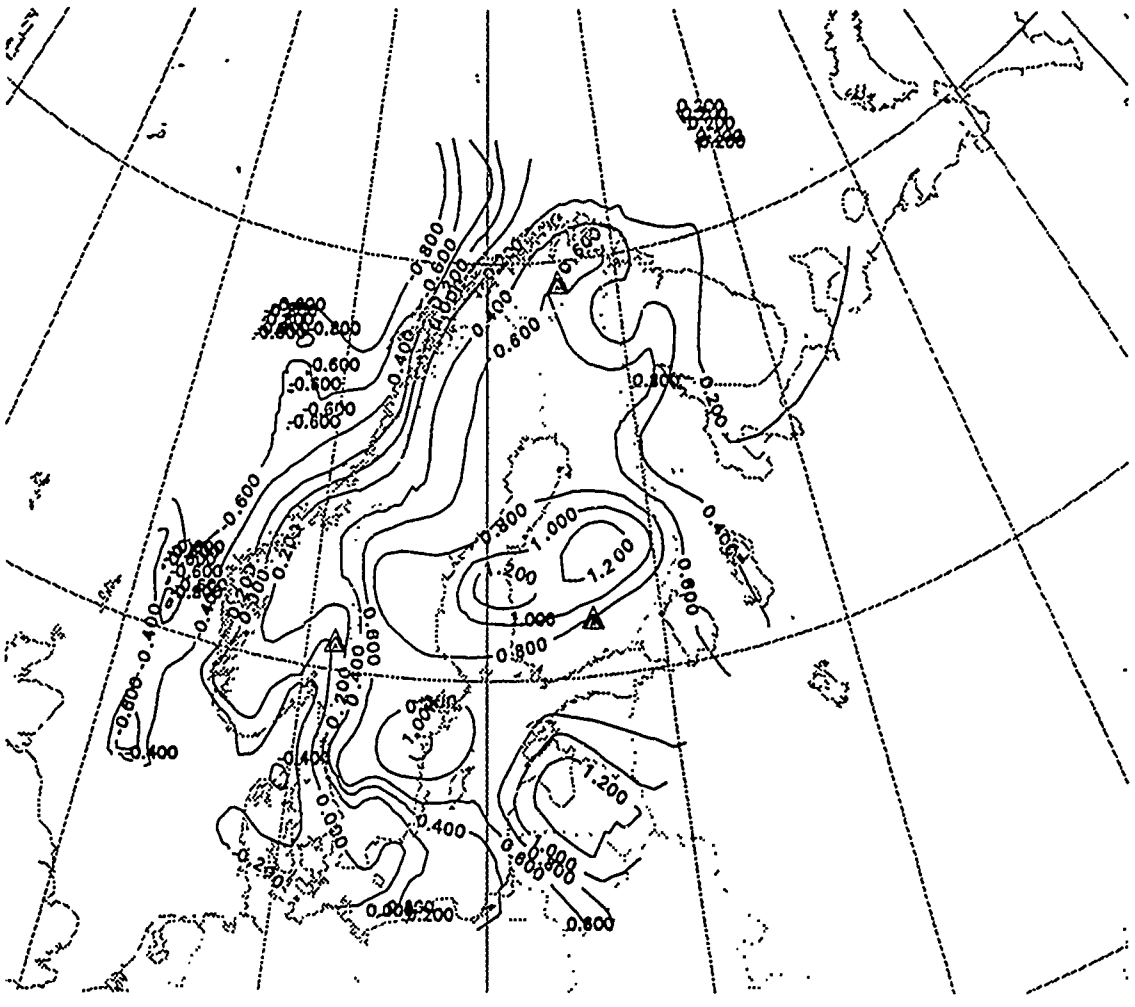

Figure 2: *Map of Pn local travel-time corrections for FINESA. Isolines represent the travel-time corrections in seconds. Triangles denote the NORESS (southern Norway), ARCESS (northern Norway), and FINESA (southern Finland) seismic stations.*

event detection threshold, implying that low-magnitude events will have poorly determined depths. In order to illustrate this effect we performed depth estimation simulations for the hypothetical GSETT-3 network. We generated a sample of earthquakes corresponding to 5 days of world-wide seismic activity using a program by North (1983) that models world-wide seismicity. The results are described in *Figure 3* .

Finally, simple simulations with synthetic data and calculations with actual data indicated that depth estimates based on origin times constrained with ratios of *S* and *P* arrival times might in

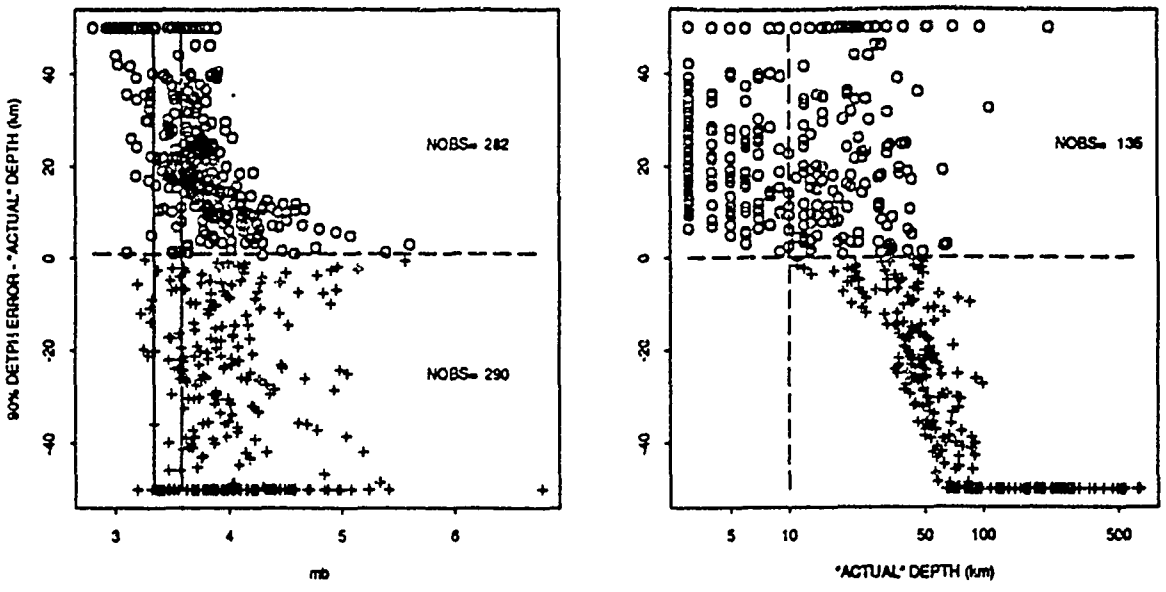

Figure 3: *The left frame shows the difference between calculated depth error and "actual" depth vs. m_b for 2997 synthetic events. Events with a negative difference (plus signs) would be identified as earthquakes, whereas those with a positive difference (open circles) would not be classified. The total number of events in each group is given in the left frame. The right frame shows that events with "actual" depths less than 10 km could not be identified as earthquakes, nor could a large fraction of events shallower than about 50 km. The left frame also indicates that these are primarily small events, mostly with m_b less than 4.0. The range of the m_b event detection threshold is indicated in the left frame with two vertical lines.*

some cases be superior to those obtained with standard algorithms for hypocenter determination.

CONCLUSIONS AND RECOMMENDATIONS

Modelling slowness estimation capabilities, as illustrated here, can be useful, among other criteria, for selecting array configurations tailored to specific monitoring targets. We have also demonstrated the feasibility of rapid station-specific knowledge acquisition for improving automated processing in the GSE systems.

The method presented for deriving travel-time corrections can be applied to different geological provinces and to other major regional phases, and implemented in the operational systems. Comparison of observed *Pn* travel-time curves for ancient Precambrian platforms and tectonically active regions shows variations of *Pn* travel-times up to approximately 10 sec. For Pre-

cambrian platforms, however, these variations are small, indicating that our results for Scandinavia could be transported to other similar geological provinces.

Although the observability of depth phases is difficult to model, it appears that the proposed GSETT-3 network is well distributed to observe such phases in the teleseismic window with regard to moveout and azimuthal coverage. However, near the detection threshold, there is a gap of about a few tenths of a magnitude unit with reduced chances to observe depth phases. For depth estimates based on *P*- and *S*-wave arrival times, there is a similar gap which is more pronounced for oceanic than for continental areas. Simulations indicate that this gap would be narrowed by enhanced detectability of *S* waves. One important function of the GSETT-3 regional stations would be to improve detection of *S* waves for depth determination.

Acknowlegments

The authors would like to thank Dr. Manfred Henger (BGR) for providing GRSN data used in station evaluation, and Flori Ryall for performing analysis. We are also grateful to Dr. Eric Fielding (Cornell University) for providing software and helping digitize maps used for travel-time corrections.

References

Fielding, E., M. Barazangi, and B. Isacks (1993). A network-accessible geological and geophysical database for Eurasia, North Africa, and the Middle East, *Paper to be presented at 15th Annual PL/ARPA Seismic Research Symposium*, 8-10 September 1993, Vail, Colorado.

IASPEI 1991 Seismological Tables (1991), *ed. B. L N. Kennett*, Australian National University, p. 167.

Israelsson, H. (1993). Stacking of waveforms for depth estimation, *EOS*, April 20 (*abstract*).

North, R.G. (1983). Synthetic Detection Generator - Program Package (*manuscript*).

Ryaboy, V. (1993). New regional travel-time tables for Scandinavia, *EOS*, April 20 (*abstract*).

Sereno, T., H. Swanger, and T. Bache (1993). Progress in automated processing and interpretation of seismic data, *Paper to be presented at 15th Annual PL/ARPA Seismic Research Symposium*, 8-10 September 1993, Vail, Colorado.

PARTIALLY DECOUPLED AND ENHANCED-COUPLED NUCLEAR EXPLOSIONS DETONATED IN CAVITIES AT AZGIR, KAZAKHSTAN: IMPLICATIONS FOR IDENTIFYING DECOUPLED NUCLEAR EXPLOSIONS IN SALT

Lynn R. Sykes

Lamont-Doherty Earth Observatory, Columbia University, Palisades NY 10964

CONTRACT NO. F19628-90-K-0059

Objectives

The detonation of nuclear explosions by Russia or any of the other countries of the former Soviet Union (FSU) in large underground cavities under a comprehensive test ban treaty (CTBT) constitutes the greatest challenge to U.S. verification efforts. That evasion scenario sets the limit on how low a yield can be verified effectively. The 1988 OTA Report found that between 1 to 2 and 10 kilotons (kt) the most critical method of evasion is that of nuclear testing in large cavities in salt domes. It concluded that no method of evading a monitoring network is credible above 10 kt and that several evasion scenarios, including testing in cavities in bedded salt and in hard rocks, are possible below 1 to 2 kt.

Our work address a number of aspects of the problem of clandestine nuclear testing in large cavities in salt domes, bedded salt and hard rock--what types of evasions scenarios are plausable based on geological and engineering constraints, which ones are likely to escape detection by the U.S. and which ones are likely to be identified. Particular attention is given to the critical yield regime from 1 to 10 kt, where scientific research over the next few years seems most likely to have a major impact on the verifiability of a CTBT and on the crucial question of how low in yield can we go in effective verification under various evasion scenarios.

Recently released information by the Russians (Adushkin et al., 1993) on their program of nuclear explosions conducted in cavities at Azgir (Fig. 1) indicates that a decoupled test of 8 kt was detonated in March 1976 within the air-filled cavity created in a salt dome by a tamped nuclear explosion eight times larger. The 1976 event was 20 times larger than the Sterling event, the only U.S. decoupled nuclear explosions detontated in salt. The Azgir explosion was recorded not only at local distances, like Sterling, but also at regional and teleseismic distances. Russian scientists have also released the dates of six very small nuclear explosions conducted in a water-filled cavity at Azgir. Those six events are all examples of enhanced seismic coupling at certain frequencies rather than of decoupled testing. Our work this year focused on past nuclear testing at Azgir, especially the magnitude and decoupling factor (DF) for the 8 kt partially decoupled event and the origin times, magnitudes and yields of the six events in the water-filled cavity.

Research Accomplished

Partially Decoupled Explosion of 1976

Adushkin et al. (1993) recently described an 8-kt partially decoupled nuclear explosion detonated on March 29, 1976 in a 1 km-deep cavity of 37 m radius that had been created within a salt

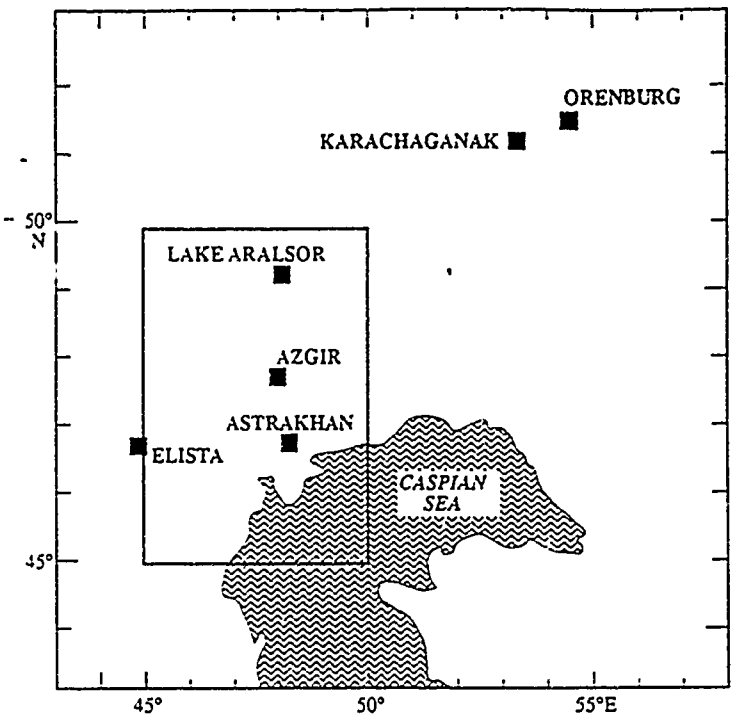

Fig. 1. North Caspian Region showing sites of nuclear explosions in and near thick salt deposts (squares) in Pre-Caspian depression and area of special study of small seismic events (boxed region).

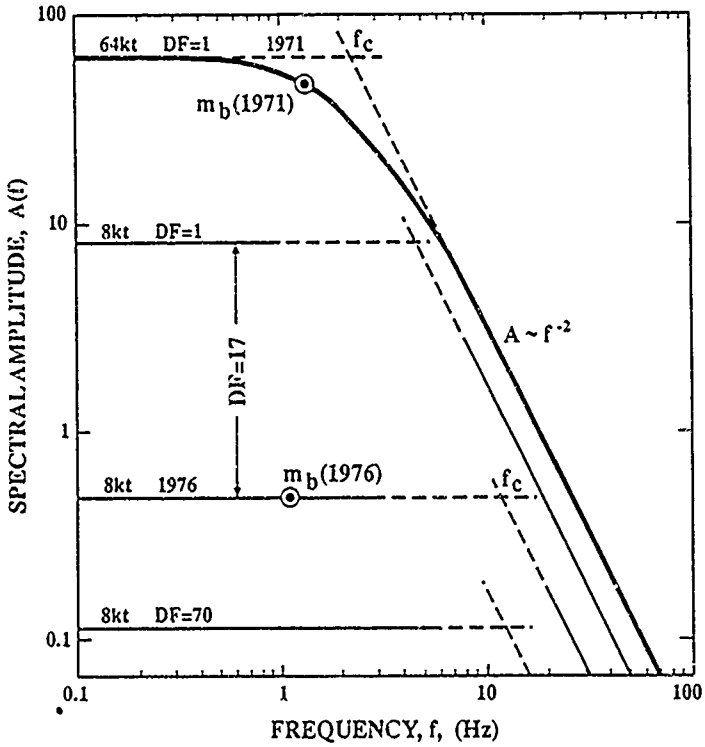

Fig. 2. Estimates of smoothed spectral amplitudes as a function of frequency, f, for tamped (de-coupling factor, DF, = 1) and decoupled nuclear explosions. f_c = corner frequency.

Table 1. Magnitudes and Decoupling Factors--1976Azgir Explosion

Station	Distance	(a^{71}/a^{76})	$\log(a^{71}/a^{76})$	m_b
KRV	785 km	670/8	1.923	4.14
BRV	1590	786/6	2.117	3.95
GAR	2205	470/5	1.973	4.09
TLG	2280	620/7	1.947	4.12
ELT	2690	650/5	2.114	3.95
BOD	4310	650/8.5	1.884	4.18
NAO	2760	--	--	3.98
Averages			1.993	4.06
± SEM			±0.041	±0.04

$m_b = A + B\log Y - \log(DF) \sim \log(a/T)$; $(m_b)^{1971} = 6.064 \pm 0.02$

$DF = (a^{71}/a^{76}) / (Y^{71}/Y^{76})^B = 12.3$ for $B = 1.0$

Table 2. Nuclear Explosions in Cavities in Salt at Azgir

Date	Hr.Min.	m_b ± SEM	n(m_b)	Yield (kt)
25 Apr. 1975	05 00	4.45 ±.13	7	1.1
*29 Mar. 1976	07 00	4.06 ±.04	7	8**
14 Oct. 1977	07 00	3.42	1	0.06
30 Oct. 1977	07 00	2.77	1	0.01
12 Sept 1978	05 00	3.02	1	0.02
30 Nov. 1978	08 00	3.07	1	0.02
10 Jan. 1979	08 00	4.36 ±.14	2	0.8

*In air-filled cavity created by 64 kt explosion of 1971; all other events in water-filled cavity created by 25 kt explosion of 1968.

**Yield of 1976 event from Adushkin et al.(1993); other yields, Y, from $m_b = 4.425 + 0.832\log Y$

dome by a tamped nuclear explosions 8 times larger in yield on Dec. 22, 1971. I derived station corrections for the magnitudes, m_b, of seven large explosions at Azgir (including the 1971 event) and applied them to all known events in the Azgir region including 10 tamped explosions from 1966 to 1979, the partially decoupled event of 1976 and the six very small nuclear explosions detonated in a water-filled cavity (Sykes, 1993). Those events must have occurred at Azgir (Sykes, 1993; Sykes et al., 1993).

The revised m_b's of the 1971 and 1976 events are 6.06 ± 0.02 and 4.06 ± 0.04. The 1976 value is based on data from Norsar (with its station correction of 0.48 m_b units applied) and six standard stations of the USSR network (Table 1). Amplitudes, a, used in calculating the m_b's and the decoupling factor (DF) were restricted to the narrow period range 0.6 to 1.1 s and to distances from 785 to 4310 km. The 1976 event was recorded by at least 15 stations in Eurasia.

Assuming the amplitudes used in Table 1 for the 1971 event with an average period of 0.73 s pertain to the flat, low-frequency portion of its source spectrum, DF = 12 is obtained for the 1976 explosion for B = 1.0. There is general agreement that low-frequency amplitudes scale as yield to the first power, i. e. B = 1.0, for explosions at the same depth (Denny and Johnson, 1991), as was the case for the 1971 and 1976 events. Adushkin et al. (1993) obtained an amplitude DF of about 20 for the 1976 shot using data at distances of about 1 to 100 km. The value of B that they used, 0.8, however, is more appropriate to explosions of various sizes fired at or near a given scale depth, such as the tamped explosions at Azgir that they used in deriving their value of B. The data in Table 1 give a very similar value, DF = 18.6, to theirs for B = 0.8. An approximate correction for the effect of corner frequency on the spectrum of the 1971 event (Fig. 2) gives DF = 17. It seems unlikely that the amplitudes used in Table 1 for the 1971 event were made close to a minimum in the spectrum, (as R. Blandford suggested to me), since analysts tend to pick the largest amplitude rather than the smallest in the vicinity of 1 Hz for teleseismic P waves. Also, the m_b of 6.06 for the 1971 explosion is already unusually large for events anywhere of yield near 64 kt (Fig. 3).

The revised values of m_b and the published yields for the tamped Azgir explosions of 1966, 1968 and 1971 and the Orenburg event of 1971, all of which are reported as having been detonated in salt, were used to obtain the following relationship: $m_b = 4.4250 + 0.832 \log Y$. For a tamped event of Y = 8 kt, $m_b = 5.18$. Subtracting $m_b = 4.06$ for the 1976 event from 5.18 gives DF = 13. The measured amplitudes for the 1976 event at an average period of 0.93 s are undoubtedly located on the flat portion of the spectrum as are those of a tamped event of similar yield. Thus, it seems likely that the DF for the 1976 event is closer to 12 than to 20 if its yield was 8 kt. If its yield was 11.5 kt as L. Glenn (written communication, 1993) has reported, DF = 18. In any case, the explosion was only partially decoupled. For either yield, however, $m_b = 3.40$ is obtained for a fully decoupled (DF = 70) event of 10 kt from those values and $m_b = 4.06$ for the 1976 explosion.

Stevens et al. (1991) used a finite difference scheme to calculate decoupling factors for explosions in cavities in salt. They conclude, taking an identification threshold of m_b 3.5 as described in the 1988 OTA Report, that "decoupled explosions with yields on the order of 20 to 30 kt could evade identification, even if it were only possible to construct a cavity large enough to fully decouple 5-kt." Their calculations, however, predict a DF of about 55 and an m_b of about 3.3 for the parameters of the 1976 event (Fig. 3). Their predicted m_b is about 0.75 units below that determined for the 1976 event. Calculations of DF by both Patterson (1966) and Stevens et al. (1991) for partially decoupled events are clearly well above the data points for the Azgir and Sterling nuclear explosions and for the Cowboy chemical explosions (Fig. 4).

Fig. 3. Magnitude, m_b, as a function of announced yield for five tamped and one partially decoupled nuclear explosions in salt. Solid symbols denote Azgir explosions. Four computed linear relatiionships are from Stevens et al. (1991).

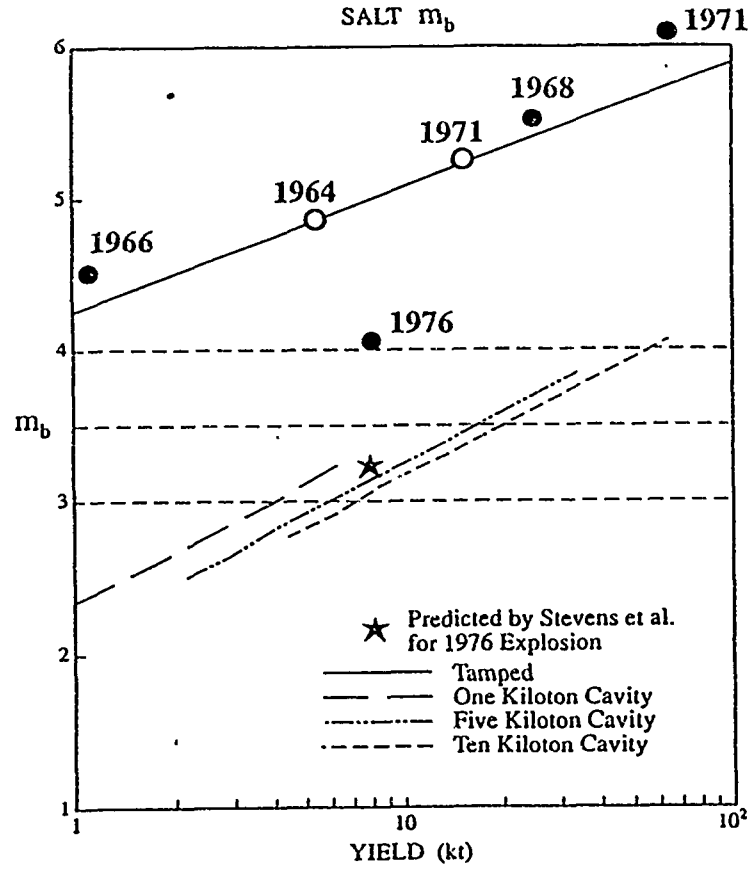

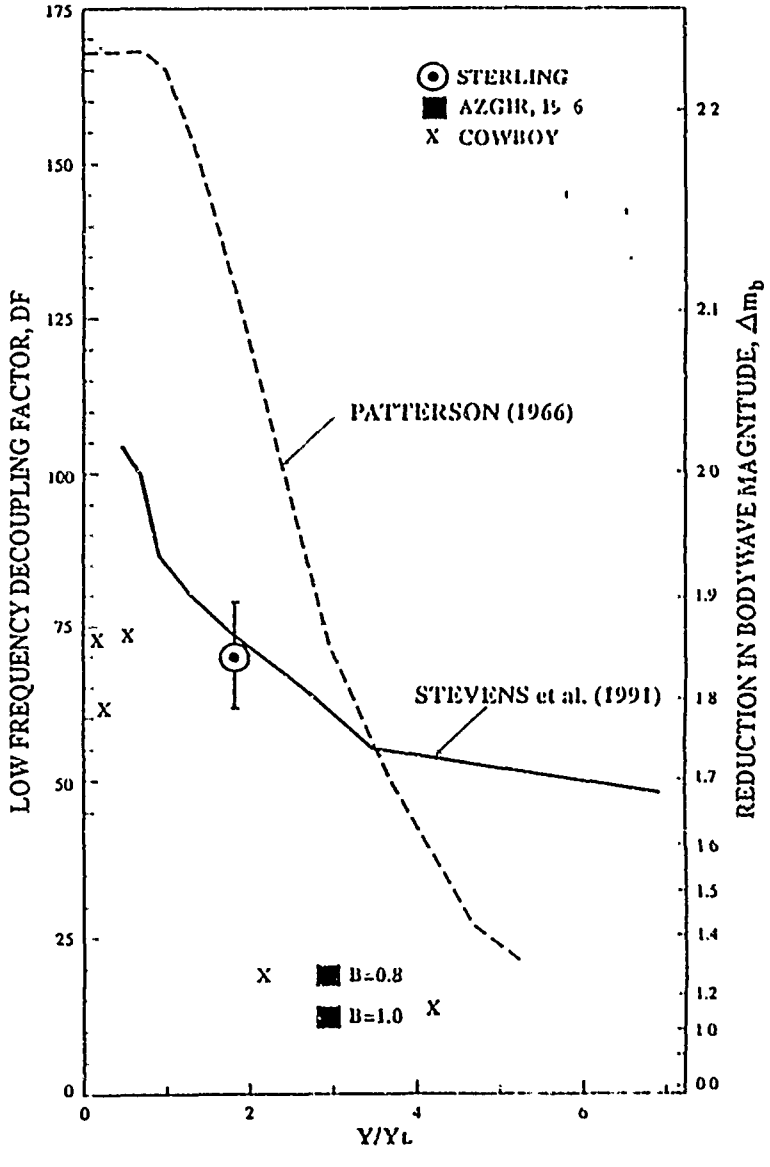

Fig. 4. Low-frequency decoupling factor, DF, as a function of ratio of yield, Y, of partially decoupled explosion to yield of a fully decoupled explosion, Y_L. Note that data points fall below both theoretical calculations.

Nuclear Explosions in Water-Filled Cavity at Azgir

The Norsar and Hagfors arrays and the ISC Bulletin have each located a number of small events in the general vicinity of Azgir, including the partially decoupled explosion of 1976. Sykes and Lyubomirskiy (1992) made a special study of small events reported by the ISC, Norsar and Lasa in the 5^0 by 5^0 box outlined in Fig. 1 that includes Azgir for the 23-year period 1969 through 1991. They compiled a catalog of chemical and nuclear explosions in that region that they show is complete down to m_b 3.1 since 1969. That m_b corresponds to a tamped nuclear explosion of about 0.02 kt and to yields of about 1 and 4 kt for decoupling factors of 20 and 70. This capability was made possible by recognizing that the Norsar, Hagfors and Lasa arrays recorded seismic waves from large events at Azgir that have m_b's about 0.5 units larger than the average. Thus, those arrays have (or for Lasa had) a detection capability for Azgir that extends down to a very small m_b and yield. The location capability of those arrays by themselves, however, is poor compared with that of either a local seismic network or data from several arrays well distributed in azimuth. Either those can be obtained by the installation of appropriate seismic monitoring equipment.

Sykes and Lyubomirskiy (1992) reported that seven small events of m_b 3.02 to 4.45 from their catalog fulfill an origin-time criterion (being detonated exactly on the hour within the uncertainty in estimating origin time) for being either very small tamped or small decoupled nuclear explosions, one of which is the 8-kt partially decoupled event of 1976. Of the 126 other small events in the area, most or all of which are taken to be chemical explosions from their concentration during the work day, the largest two in 23 years were of m_b 4.0. Chemical explosions of $m_b \geq 3.5$ and those of $m_b \geq 3.0$ occurred about 1.3 and 4.5 times per year in the entire study area. Thus, the number of chemical explosions per year in that area that would have to be discriminated as such from small decoupled nuclear events under a future test ban is small even at the m_b 3.0 level. A major uncertainty pointed out by the OTA Report is, in fact, how many chemical explosions must be contended with per year equal in m_b to that of decoupled explosions of various yields?

Russian scientists stated to me that besides the partially decoupled event of 1976 that four of the other events on the list of Sykes and Lyubomirskiy (1992) were very small nuclear explosions detonated in a water-filled cavity of radius 32m that was created in salt by a previous nuclear explosion. The earliest date of those small explosions, 1975, and the description of a cavity of that radius created by a 25 kt explosion in salt by Kedrovskiy (1970) indicate that the small explosions must have been detonated in the cavity created by the explosion of July 1, 1968 at Azgir. Those scientists indicated that two of the events on the list were not nuclear explosions but stated that two yet smaller nuclear explosions that were not on the list had been detonated in the same water-filled cavity on October 30, 1977 and November 30, 1978.

Since nearly all known or inferred Soviet nuclear explosions at Azgir and in the rest of the Pre-Caspian depression were detonated on the hour in a narrow range of local times from 0600 to 1100, I asked Dr. Frode Ringdal to search for possible small signals on those dates in 1977 and 1978 on Norsar recordings that would have been detonated exactly on the hour during that five-hour time window. He reported that Norsar was down for parts of those time intervals on those two days. He found, nevertheless, that the Hagfors array in Sweden did report P arrivals that were consistent to within a few seconds of events having occurred at Azgir on those two dates at 0700 and 0800 GMT respectively. Norsar was, in fact, down at the two expected arrival times. Hagfors recorded all of the seven events in Table 2; Norsar recorded five of the events and undoudtedly would have re-

corded and located the other two if that array had been in operation.

Station corrections for Norsar and Hagfors (and other stations that recorded the explosions in Table 2 of 1975, 1976 and 1979) were used in deriving magnitudes of the seven events. Approximate yields of the six events in the water-filled cavity were calculated assuming their m_b-yield relationship was like that of tamped exposions at Azgir. It can be seen that the calculated yields of the three smallest events in Table 2 are about 0.01 to 0.02 kt. Yield estimates based on one or two m_b values in Table 2 are understandably only approximate. Apparently the small explosions were tested to see if the fundamental frequency of a water-filled cavity surrounded by salt could be excited so as to produce larger than normal seismic waves near that frequency for use in deep seismic sounding. A simple calculation gives a fundamental resonance of about 11.7 Hz; Russian scientists report amplitudes up to five times those of tamped explosions in salt at frequencies of 7 to 9 Hz. Thus, the six events in the water-filled cavity were not tests of decoupling but of enhanced coupling at certain frequencies in the passband commonly used in deep seismic sounding.

Conclusions and Recommendations

Unlike the United States, the former Soviet Union detonated a number of nuclear explosions in salt including tamped events of about 1 to 100 kt, a partially decoupled nuclear explosion of about 8 kt in the cavity created by a tamped explosion 8 times larger, and six very small nuclear explosions in the water-filled cavity created by the 25 kt explosion of 1968. Clearly, the decoupled experiment of 1976 with a yield 20 times that of Sterling is crucial in ascertaining decoupling factors for overdriven (partially decoupled) nuclear weapons tests in the yield range from 1 to 10 kt. The release of additional data on that and other events in salt by the Russian Republic would go far in answering longstanding questions in the U.S.about detecting decoupled events under a CTBT.

References

Adushkin, V.V., I. O. Kitov, O. P. Kuznetsov and D. D. Sultanov (1993). Seismic efficiency of decoupled nuclear explosions, *Geophys. Res. Lett., 20*, issue of August 1, 1993.

Denny, M. D. and L. R. Johnson (1991). The explosion seismic source function: models and scaling laws reviewed, *Geophysical Mono., 65*, (American Geophysical Union), 1-33.

Kedrovshiy, O. L. (1970). Prospective applications of underground nuclear explosions in the national economy of the USSR, *UCRL- Trans-10477*, (Translation from Russian), Lawrence Radiation Laboratory, University of California, Livermore, CA, 1-47.

Paterson, D. W. (1966). Nuclear decoupling, full and partial, *J. Geophys. Res., 71*, 3427-3436.

Stevens, J. L., J. R. Murphy and N. Rimer (1991). Seismic source characteristics of cavity decoupled explosions in salt and tuff, *Bull. Seismol. Soc. Amer.* **81**, 1272-1291.

Sykes, L.R. (1993). Underground nuclear explosions in thick salt deposits of the Former Soviet Union: implications for identifying decoupled nuclear testing, *Bull. Seism. Soc. Am.*, submitted.

Sykes, L. R., J. Deng and P. Lyubomirskiy (1993). Accurate location of nuclear explosions at Azgir, Kazakhstan, from satellite images and seismic data: implications for monitoring decoupled explosions, *Geophys. Res. Lett., 20*, issue of August 1, 1993.

Sykes, L. R. and P. Lyubomirskiy (1992). Analysis of small seismic events near Azgir, Kazakhstan: implications for identifying chemical and decoupled nuclear explosions in a major salt dome province, in *Papers Presented at 14th Annual PL/DARPA Seismic Research Symposium*,Phillips Laboratory, Hanscom Air Force Base, MA, PL-TR-92-2210, ADA256711.

FINITE-ELEMENT MODELING OF THE BLOCKAGE AND SCATTERING OF Lg WAVE PROPAGATION

Yu-Chiung Teng and John T. Kuo

Aldridge Laboratory of Applied Geophysics

Henry Krumb School of Mines

Columbia University, New York, NY 10027

CONTRACT NO.: F49620-93-1-0073

OBJECTIVE

The objective of this research is to study numerically the effects of various basin widths and sediment velocities on the Lg wave propagation by modeling the Barents Basin. The final objective is finite-element modeling of the blockage and scattering of the Lg wave propagation through the entire propagation paths from Novaya Zemlya to ARCESS, NORESS and Graefenburg.

RESEARCH ACCOMPLISHED

Gramberg (1988) and Clarke and Rachlin (1990) provided fairly comprehensive geological maps of the Barents Sea and its vicinities, including Novaya Zemlya, the Kola Peninsula, Cheshkaya Bay, just above the Arctic Circle. Presumably, on the basis of the geological information given, Baumgardt (1990b) has constructed a NW-SE geological cross section (Figure 1) , showing (1) the absence of granitic layer under the southern Barents Sea Basin, contrary to the presence of a granitic layer under the Pechora Plate and the Central Barents Rise, (2) the thick accumulation of terrigenous sediments under the Barents Sea Basin, and the thin terrigenous sediments over the Plate and the Rise, (3) the variable thicknesses of basaltic layer present under the Plate, the Basin and the Rise, and (4) the bending of the Moho due to the loading of the thick accumulation of sediments in the Basin, and the irregularities of the depth of the Moho, ranging from about 30 km to 37 km under the Basin, 40 km under the Rise, and nearly 50 km under the Plate. Similar geological cross sections along the great-circle paths from Novaya Zemlya to ARCESS, NORESS and Graefenburg can be approximately constructed. It is thus expected that from Novaya Zemlya to the Scandinavian arrays, namely ARCESS and NORESS, and to Graefenburg, the great-circle paths of Lg essentially traverse major geological provinces, (1) the island margin with variable crust thicknesses (from Novaya Zemlya to the Barents Sea), (2) the basin with variable width, depth and sediments (the Barents Sea Basin), (3) the shield margin (from the Barents Sea to the Baltic shield), and finally (4) the shield and European continent with variable crustal thickness and lithology (from the Baltic shield to Graefenburg).

The Barents Sea Basin is characterized by variations of crustal thickness with sediment accumulation as large as 15 km, and by missing of granitic layer. This structure is based on low in magnetic anomalies caused by the missing of granitic layer and on high in gravity anomalies caused by the elevated Moho. As reported, the granitic layer in the adjacent province is characterized by P wave velocities on the order of 6.0 to 6.5 km/sec, and S wave velocities 3.46 to 3.75 km/sec (Clarke and Rachlin, 1990).

As a first step toward the final objective, we have investigated the effects of the blockage and scattering by basins with various width and sediments on Lg propagation by the following anti-plane strain finite-element models:

(A) The Island Margin Model

A line source with center frequency 0.5 Hz, with the first derivative of Gaussian type of forcing functions, is located on the island side of the model to simulate the test sites of Novaya Zemlya. (Figure 2). The S .wave velocities of the granitic/basaltic (averaged) layer and the upper mantle assumed to be 3.51 km/sec and 4.7 km/sec, respectively.

(B) The Basin and Crust-Pinch Models

The seismic waves, as shown in Figure 5, so generated near the left termination boundary BB' in Figure 2 have been used as the input waves at BB' in Figure 3 for the following twelve cases:

The basin models as shown in Figure 3-(a), with

(1) basin width = 150 km; shear velocities for
granitic/basaltic (averaged) = 3.51 km/sec;
sediments velocity = 3.51 km/sec (i.e., without basin);
upper mantle = 4.7 km.
(2) basin width = 150 km; shear velocities for
granitic/basaltic (averaged) = 3.51 km/sec;
sediments velocity = 2.75 km/sec;
upper mantle = 4.7 km.
(3) basin width = 150 km; shear velocities for
granitic/basaltic (averaged) = 3.51 km/sec;
sediments velocity = 2.2 km/sec;
upper mantle = 4.7 km.

The basin models with uplift of Moho as shown in Figure 3-(b), with

(4) the same parameters as case (1).
(5) the same parameters as case (2).
(6) the same parameters as case (3).

The basin models as shown in Figure 3-(a), with a different basin width, i.e.

(7) basin width = 250 km; shear velocities for
granitic/basaltic (averaged) = 3.51 km/sec;
sediments velocity = 3.51 km/sec (i.e., without basin);
upper mantle = 4.7 km.
(8) basin width = 250 km; shear velocities for
granitic/basaltic (averaged) = 3.51 km/sec;
sediments velocity = 2.75 km/sec;
upper mantle = 4.7 km.
(9) basin width = 250 km; shear velocities for
granitic/basaltic (averaged) = 3.51 km/sec;
sediments velocity = 2.2 km/sec;
upper mantle = 4.7 km.

The basin models with uplift of Moho as shown in Figure 3-(b), with

(10) the same parameters as case (7).

(11) the same parameters as case (8).

(12) the same parameters as case (9).

The synthetic seismograms obtained from Model A (as shown in Figure 4), and Model B (Figure 6-(a) corresponding to Case (1)), resemble the typical regional waveforms, with relatively sharp P_n onsets, an emergent arrival corresponding to the S_n onset, and strong Lg arrivals. The present finite element numerical results do not generate the P_n waves, since an anti-plane strain approach is adopted. Figure 6-(b) is the synthetic seismograms corresponding to Case (3) of Model B, in which the velocity contrast between the basin sediments (2.2 km/sec) and the surrounding granitic rocks is relatively large so that the scattering responses from the basin sides can be clearly identified. Figure 7 shows the synthetic seismograms corresponding to the above twelve cases observed at distance of 300 km from the source. The results show that: (1) the larger the velocity contrast between the basin sediments and the surrounding granitic rocks, or the longer the basins, the more delay and attenuated of the Lg waves; (2) the amplitude of the seismic responses for the cases with Moho-uplift is larger than those for the cases without Moho-uplift, the arriving times of the former cases are also earlier than those of the latter cases.

CONCLUSIONS AND RECOMMENDATIONS

The conclusion of this study is that heterogeneity in the granitic layer does show the effect in the blockage of Lg waves. Particularly, when the granitic layer contains a long basin with much lower velocity sediments, the Lg waves are delayed, diverted, scattered, and therefore blocked. In the future, we suggest the following: (1) the problem of the sensitivities (i) of the size of the basin (e.g. ratio of the depth to the width of the basin); (ii) of the dip angle of the basin sides, (iii) of the variation of thickness of the crust; (iv) of crustal-Q variations, to the variations of Lg amplitude must be systematically investigated. (2) extend this present study to the problem for the cases of elastodynamics or visco-elastodynamics.

References

Baumgardt, D.R., (1985). Comparative analysis of teleseismic P coda and Lg waves from underground nuclear explosions in Eurasia, Bull. Seism. Soc. Am., 75, 1413-1433.

Baumgardt, D.R., (1987). Spectral determination of regional and teleseismic Lg attenuation and source multiplicity in explosions, DARPA/AFGL Seismic Research Symposium, 15 - 18 June 1987, Harbor Hourse, Nantucket, MA.

Baumgardt, D.R., (1990a). Investigation of teleseismic Lg blockage and scattering using regional arrays, Bull. Seism. Soc. Am., 80, 2261-2281.

Baumgardt, D.R., (1990b). Causes of Lg amplitude variations and scattering in the Eurasian continental craton, Proceedings of the 12th Annual DARPA/AFGL Seismic Research Symposium, 18 - 20 Sept., 1990, 224-233, GL-TR-90-0212, ADA226635.

Clarke, J.W. and J. Rachlin (1990). Geology of the Barents Sea Structural Basin. U.S. Geological Survey, Military Geology Project, Open-File Report, July, 1990.

Gramberg,I.S.,(1988). The Barents Shelf Plate (in Russian), Volume 196, Nedra, Leningrad.

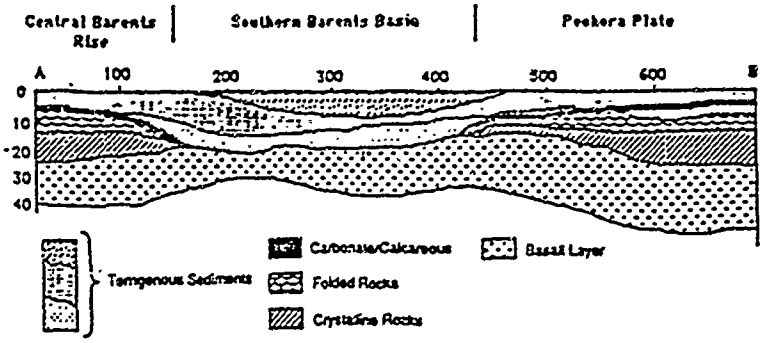

Figure 1. NW-SE cross section (AB) across the Barents basin. (After Baumgardt, 1900b)

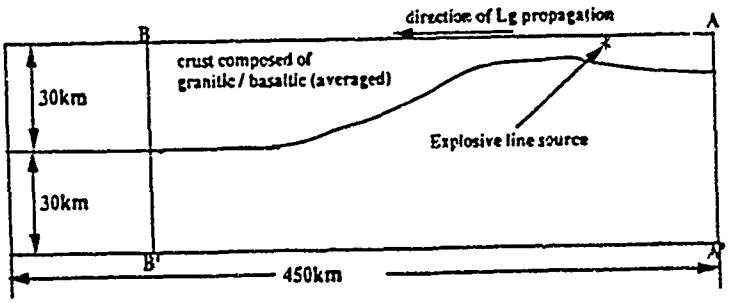

Figure 2. The Island Margin Model: the single crust with granite/basalt averaged.

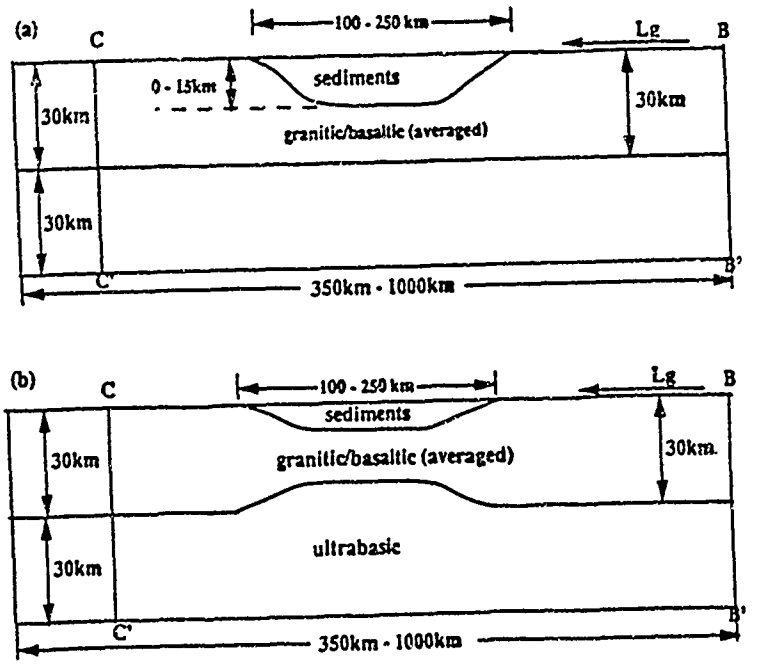

Figure 3. The Basin and Crust-Pinch Models:

(a) a sedimentary basin with a width of 120 -250 km, and a depth of 0 - 15 km, imbedded in the upper crust with a flat Moho.

(b) a sedimentary basin with an uplifted Moho.

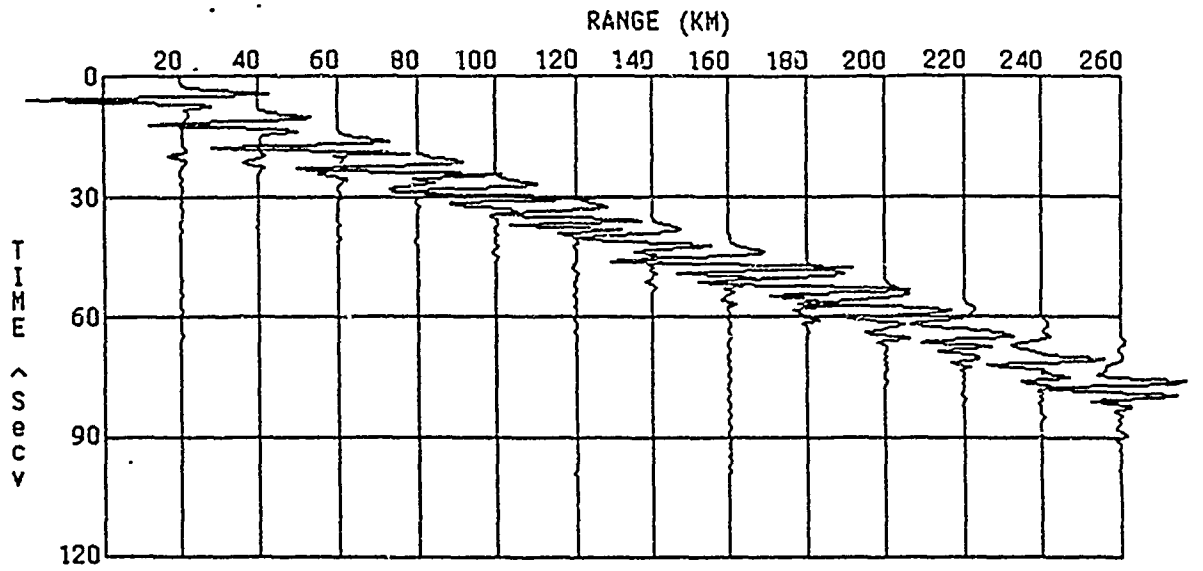

Figure 4. The finite element synthetic seismogram of Lg waves excited by an impulsive line source with a central frequncy of 0.5 Hz as observed at the distances from 20 km to 260 km from the source.

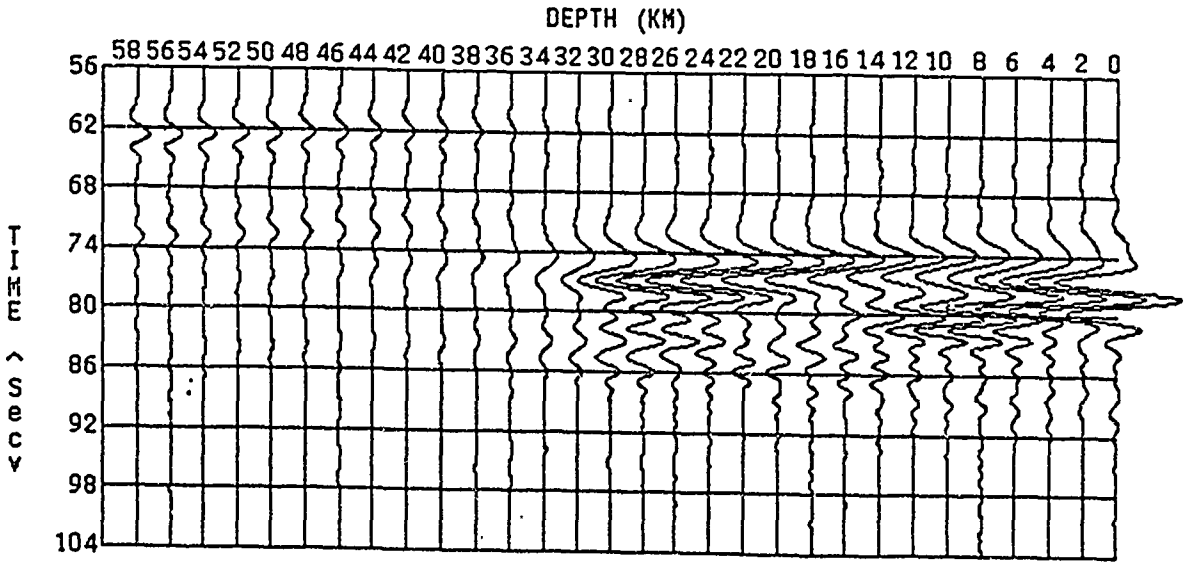

Figure 5. The seismic responses of Lg waves as observed along the vertical section BB'.

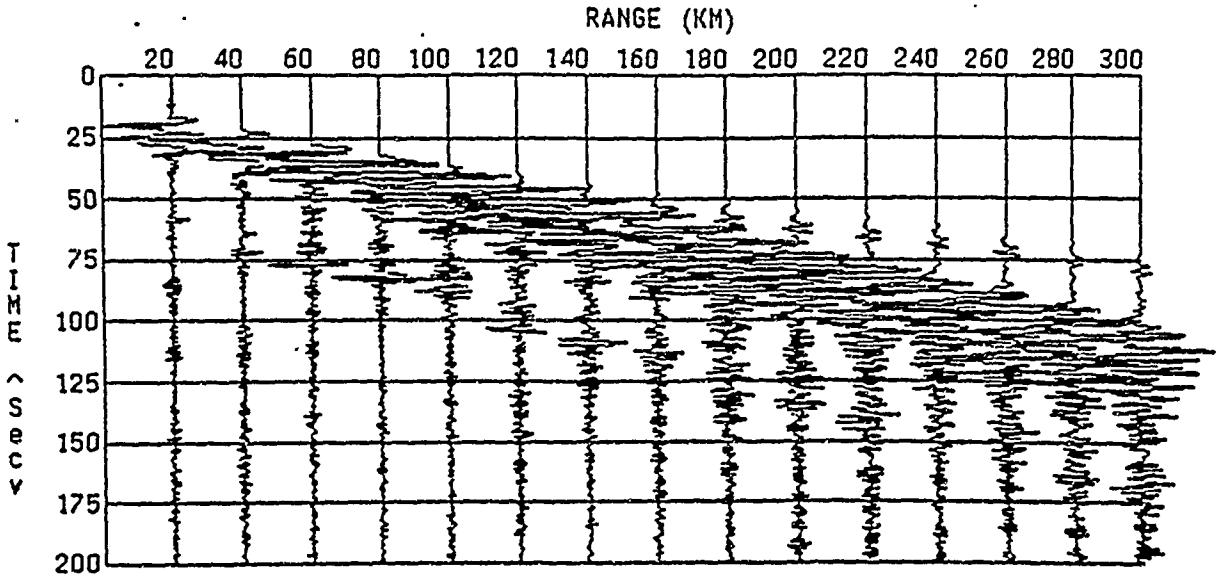

Figure 6(a). The finite-element synthetic seismogram of Lg waves for the structural model of Figure 3-(a) without a basin, i.e. the basin part is replaced by a velocity of 3.51 km/sec of the model, as observed at distances of 20 km to 300 km from the source.

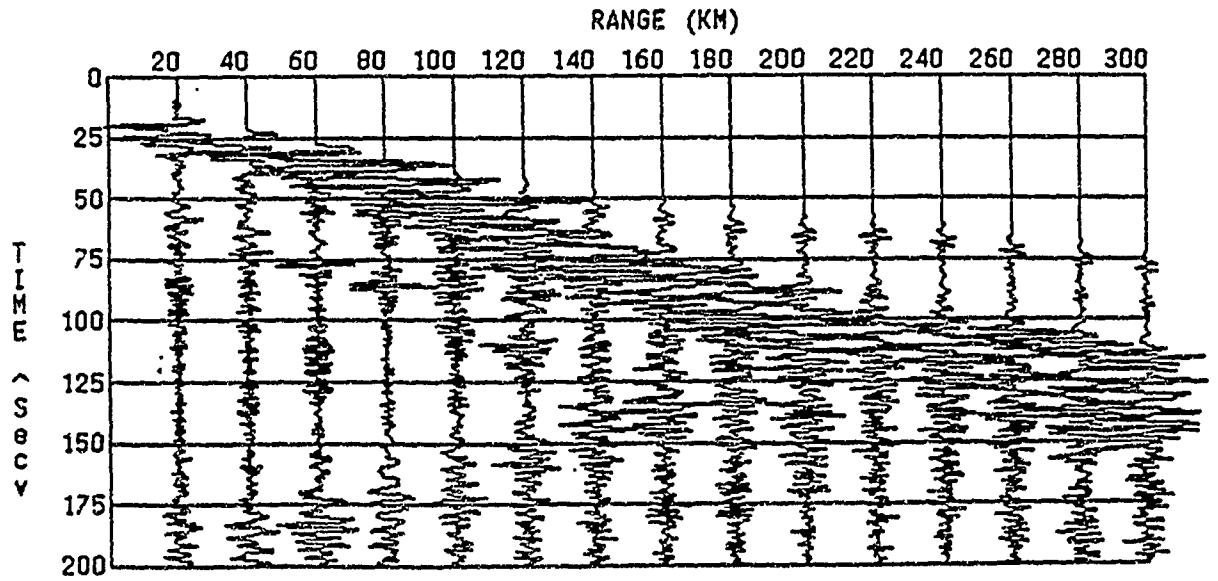

Figure 6-(b). The finite-element synthetic seismogram of Lg waves for the structural model of Figure 3-(a) with a basin velocity 2.2 km/sec, as observed at distances of 20 km to 300 km from the source.

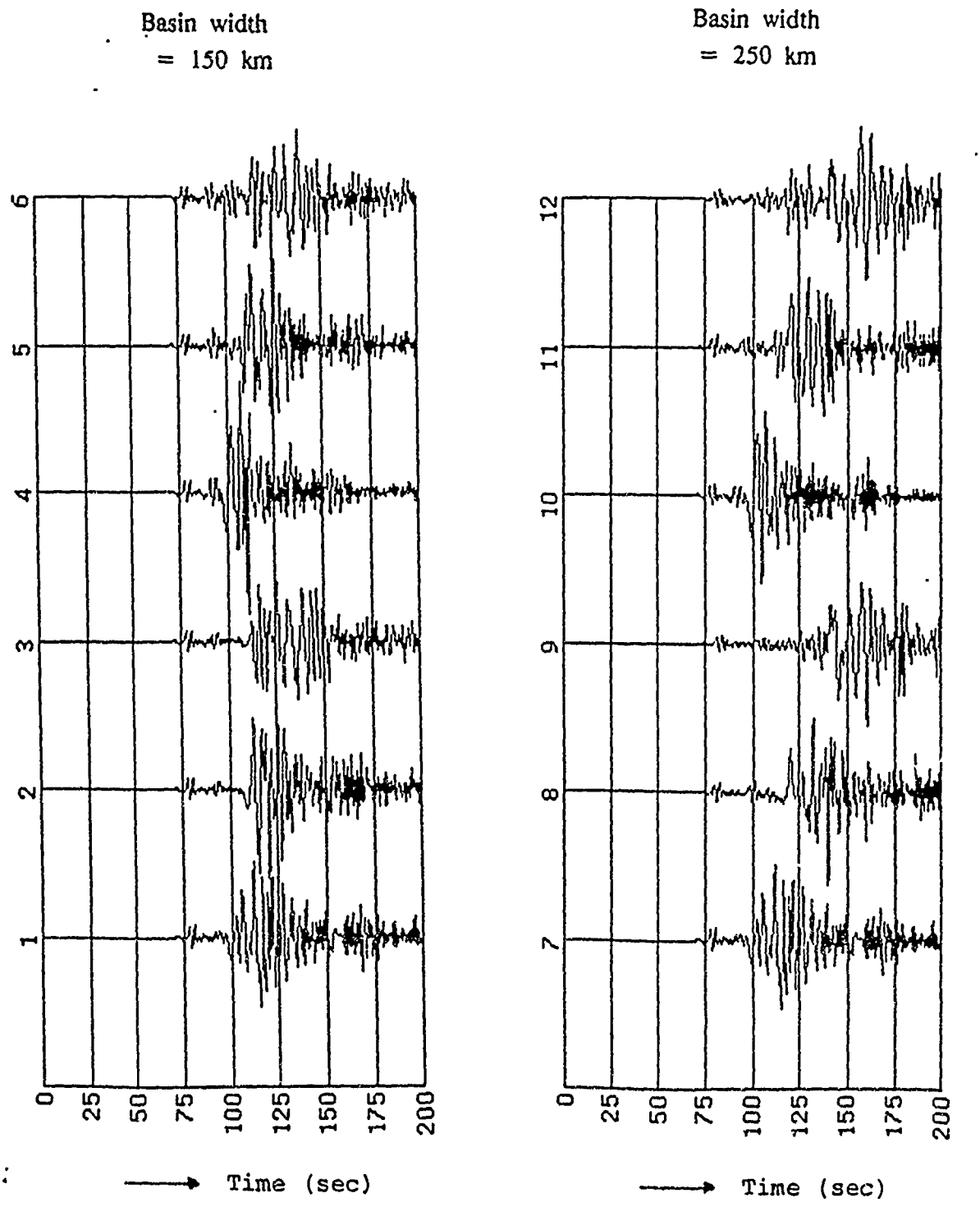

Figure 7. The synthetic seismograms for the twelve cases of Model B observed at a distance of 300 km from the source.

SEISMIC SOURCE CHARACTERIZATION WITH EMPIRICAL GREEN'S FUNCTION AND RELATIVE LOCATION TECHNIQUES

M. N. Toksöz, Y. Li and W. Rodi

Earth Resources Laboratory
Department of Earth, Atmospheric, and Planetary Sciences
Massachusetts Institute of Technology, Cambridge, MA 02139

Contract No. F29601-91-K-DB15

OBJECTIVE

The use of regional and teleseismic data to identify and characterize seismic events requires isolating source effects in observed seismograms from propagation effects. For event location using arrival time data, propagation effects are embodied in a traveltime model based on assumed seismic velocities, and errors in this model may bias the inferred locations. However, the relative locations amongst closely spaced events, inferred from arrival times differences between events, are much less affected by model errors (Jordan and Sverdrup, 1981). Moreover, it is possible to determine highly accurate arrival time differences between similar events using waveform correlation techniques (e.g., Pechmann and Kanamori, 1982).

For determining source time functions (STF) it is possible to account for propagation effects using empirical Green's functions (EGF). For two seismic events having a similar hypocenter and focal mechanism but different sizes (e.g., two explosions at the same test site, or an earthquake and one of its aftershocks) one can treat an observed seismogram from the smaller event as the EGF (Hartzell, 1978). Deconvolving the EGF from the corresponding seismogram of the larger event yields a relative source time function (Mueller, 1985) which is an estimate of the STF of the larger event. The EGF method has been very successful in estimating the source parameters of earthquakes (e.g., Lay *et al.*, 1992; Li and Toksöz, 1993).

In this paper we assess the usefulness of relative event location and empirical Green's function techniques in characterizing and discriminating seismic sources for nuclear monitoring, using earthquake, nuclear explosion and quarry blast data.

RESEARCH ACCOMPLISHED

Quarry Blasts in Estonia

Table 1 shows the hypocentral parameters of nine presumed quarry blasts located by DARPA's Intelligent Monitoring System (IMS) using data from the Scandinavian arrays (NORESS, ARCESS and FINESA). Applying waveform cross-correlation analysis to the identifiable regional phases at each array, we determined differential arrival times between event 7, selected as a reference event, and the remaining eight events. Using a multiple event location algorithm we have developed, we inverted these differential arrival times in combination with the absolute arrival times for the reference event. The event depths were constrained to the surface.

Our preliminary results showed that seven of the nine events defined a 1 by 3 km cluster but the remaining two were located several kilometers from this cluster. Given that all nine events were believed to be quarry blast and that the data residuals for the two outliers were large, we suspected and later confirmed that a one second clock error affected NORESS during

Table 1: Hypocentral Parameters of Nine Quarry Blasts in Estonia

No.	*Date*	*Time*	*Latitude*	*Longitude*	m_L
1	19910204	11:21:11.8	59.276558	27.050049	2.20
2	19910308	11:21:25.2	59.174534	27.171776	2.42
3	19910311	11:31:58.2	59.329784	27.002144	2.44
4	19911120	10:45:57.3	59.31406	27.04163	2.21
5	19920102	11:58:40.3	59.29866	27.18973	2.19
6	19920406	10:50:05.5	59.352058	27.013519	2.35
7	19920408	10:58:02.6	59.184971	27.145411	2.36
8	19910617	11:31:52.4	59.354	27.2066	2.41
9	19920703	11:13:30.8	59.234322	27.10408	2.22

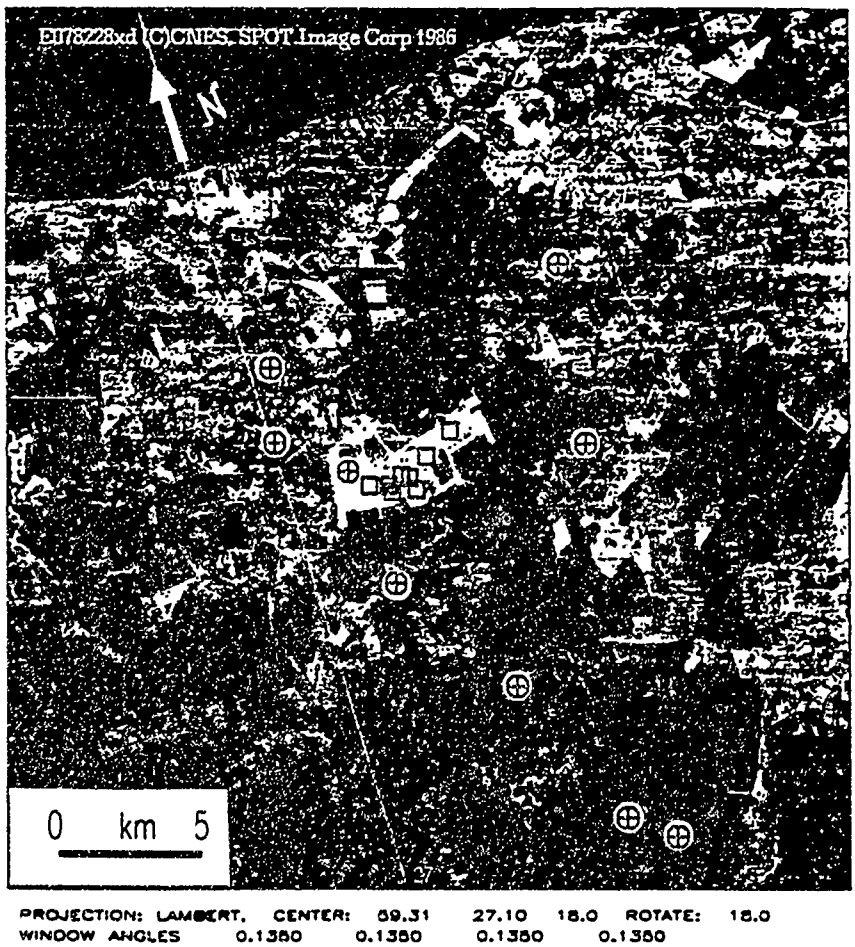

Figure 1: The initial IMS locations (crosses) of nine quarry blasts in Estonia, and our relocations (squares) determined with differential arrival times. The event locations are plotted on a SPOT satellite image of the area. The light area encompassing our new locations is presumed to be a quarry.

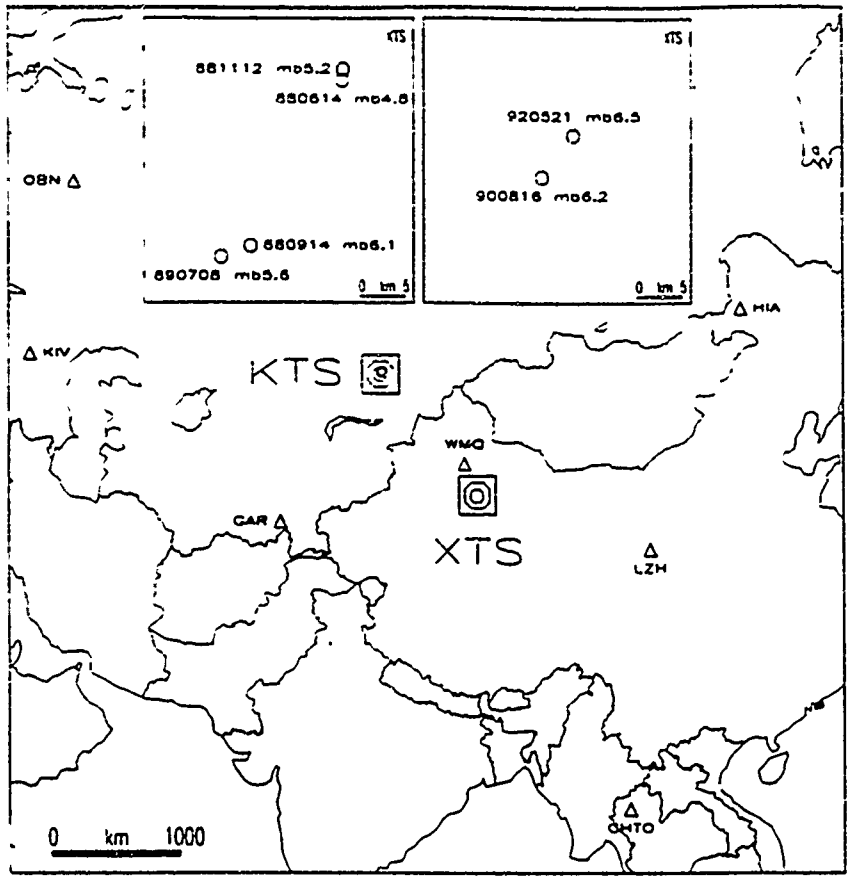

Figure 2: Map showing the Kazakhstan Test Site (KTS) and Xinjiang Test Site (XTS). The triangles represent seismic stations, and two insert maps show the relative locations of six nuclear explosions, used in this study.

late 1991 and early 1992. Figure 1 shows our results obtained by inverting the corrected data. Our new locations based on differential arrival times (squares) and the initial IMS locations (crosses) are superposed on a SPOT satellite image. Our locations fall within a white area of the image which we presume to be a quarry. Since the absolute locations we determined have errors of 5–10 km, the fact that they fall within the quarry is somewhat fortuitous and we certainly cannot be certain of their exact location within the quarry. The relative location errors, however, are only about one kilometer (the typical 90% confidence ellipse has semi-axes of 1.0 by 0.5 km) so the relative pattern of locations is reasonably well determined and we have confidence that the events are located in a small cluster as we have obtained. The initial IMS locations, in contrast, scatter over tens of kilometers (Figure 1).

Nuclear Explosions and Earthquakes

Using regional and teleseismic broadband waveform data of a pair of nuclear explosions in Lop Nor, Xinjiang, China and two pairs of nuclear explosions in Balapan, Kazakhstan (Figure 2), we retrieved the source time functions for the larger event in each pair. The hypocentral parameters and magnitudes for the three explosions under study (odd numbers) and their EGF counterparts (even numbers) are shown in Table 2.

Table 2: Hypocentral Parameters of Nuclear Explosions and Earthquakes

No.	*Date*	*Time*	*Latitude*	*Longitude*	*Depth*	m_b	M_s
1	19881112	03:30:03.7	50.047 N	78.969 E	0 km	5.2	—
2	19880614	02:27:06.4	50.036 N	78.968 E	0 km	4.8	4.1
3	19880914	03:59:57.4	49.878 N	79.824 E	0 km	6.1	4.5
4	19890708	03:46:57.6	49.868 N	78.779 E	0 km	5.6	4.1
5	19920521	04:59:57.5	41.604 N	88.813 E	0 km	6.5	5.0
6	19900816	04:59:57.6	41.564 N	88.770 E	0 km	6.2	—
7	19930513	11:59:47.2	54.972 N	160.396 W	34 km	6.4	6.9
8	19930525	23:16:43.1	55.086 N	160.421 W	33 km	6.2	5.8
9	19930608	13:03:34.1	51.243 N	157.806 E	51 km	6.5	7.2
10	19930612	20:33:26.4	51.256 N	157.744 E	49 km	6.0	5.8

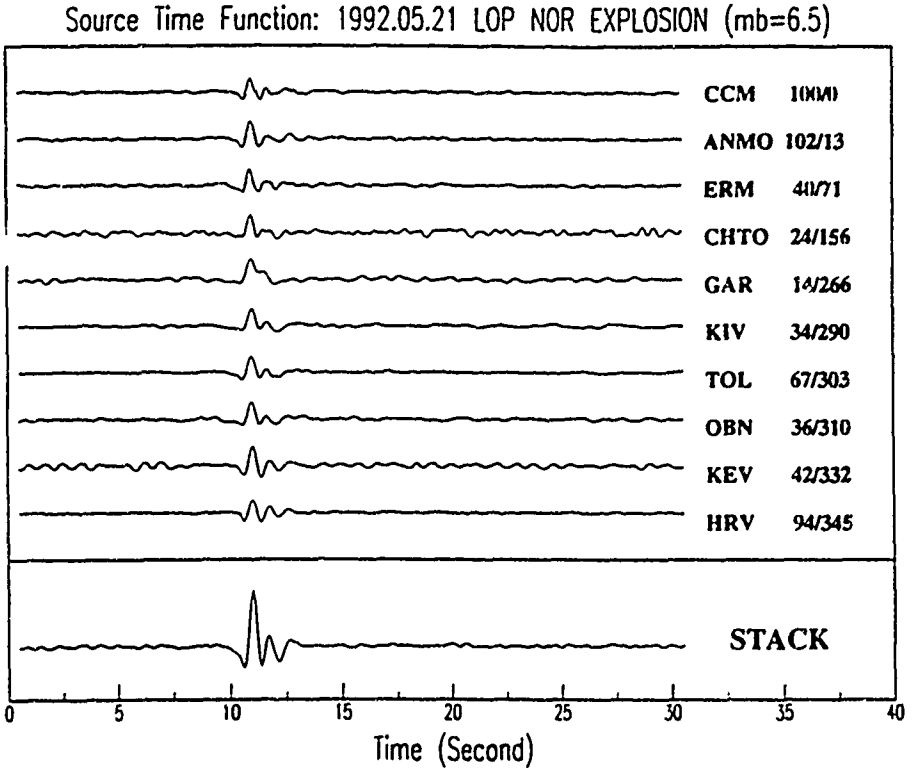

Figure 3: Source time functions of the m_b = 6.5 21 May 1992 Lop Nor explosion estimated with the empirical Green's function method. The top ten traces are the source time functions determined at ten teleseismic stations, while the bottom trace is a stack of these single station estimates. Numbers following station codes are distances and source-receiver azimuths.

We determined the source time function of the larger Lop Nor explosion (m_b = 6.5, 21 May 1992) by using the seismograms from the smaller explosion (m_b = 6.2) as empirical Green's functions. Based on the PDE bulletin the distance between the two Lop Nor explosions is less than 5 km. This is consisten. with a preliminary relative location we performed and which yielding a separation of about 4 km. We derived source time functions at ten stations and then stacked the results to obtain a final estimate (Figure 3). We see that the source time function of the 21 May 1992 Lop Nor explosion is dominated by a simple pulse with a duration of about 0.8 s. followed by a smaller secondary pulse. showing that the total source duration of the explosion is about 1.6 s. The secondary pulse may be due to spall or tectonic strain release.

For the explosion pairs in KTS. satellite image analysis (Thurber *et al.*. 1993) indicates the location difference between the large explosion and EGF event in each pair (Figure 2) ranges from 1 to 3 km. Broadband data from stations WMQ, LZH. HIA and COL were used to estimate the source time function (Figure 4a) of the 19880914 JEV2 explosion (m_b = 6.1) with a smaller explosion (19890817. m_b = 5.6) as the EGF event. With regional waveform data from only one station (WMQ). we estimated the source time function (Figure 4a) of 19881112 explosion (m_b = 5.2) using 19880614 explosion (m_b = 4.8) as the EGF event. Figure 4a shows source time functions of the three explosions (m_b = 5.2. m_b = 6.1. and m_b = 6.5) and source durations of the three explosions are measured to be 0.8. 1.1 and 1.6 s. respectively. These STF durations are indicative of the rapid energy release of nuclear explosions.

We also estimated source time functions for recent Alaska (19930513. m_b = 6.4) and Kamchatka (19930608. m_b = 6.4) earthquakes using their aftershocks as EGF events. (See Table 2 for their parameters.) Figure 4b shows that the Alaska event had a simple source time function with total duration of about 20 s and that the Kamchatka event was a complicated event with total duration of about 60 s. Comparing Figures 4a and 4b (note that the time scales for Figures 4a and 4b differ by a factor of ten) we see. as expected, a significant difference between the source time function estimated for an underground nuclear explosion and an earthquake of similar m_b magnitude. The earthquake source function generally shows a complex structure with a time duration of several tens of seconds. while the explosion source function is much simpler with a time duration of only 1–2 seconds.

CONCLUSIONS AND RECOMMENDATIONS

Methods for directly comparing the source parameters of seismic events appear to be of great ptoential value for nuclear monitoring. We have shown that relative locations determined from diferential arrival times measured directly from regional waveforms can be of useful accuracy (1 km) to help in event identification. Further. we have shown that source time functions estimated with the empirical Green's function method easily discriminate large explosions from earthquakes and also reveal information about the structure of complex events. A great advantage of these methods is that they do not require detailed knowledge of earth structure along the source-receiver propagation path. nor theoretical modeling of complex propagation effects to correct the data. We recommend further study of relative source estimation techiques to ascertain their usefulness on small events. focusing on regional broadband data. One interesting test is to compare source time functions of earthquakes occurring in the vicinity of the nuclear test site with those of the nuclear explosions.

REFERENCES

Hartzell. S.. 1978. Earthquake aftershocks as Green's functions. *Geophys. Res. Lett.*, 5, 1–4.

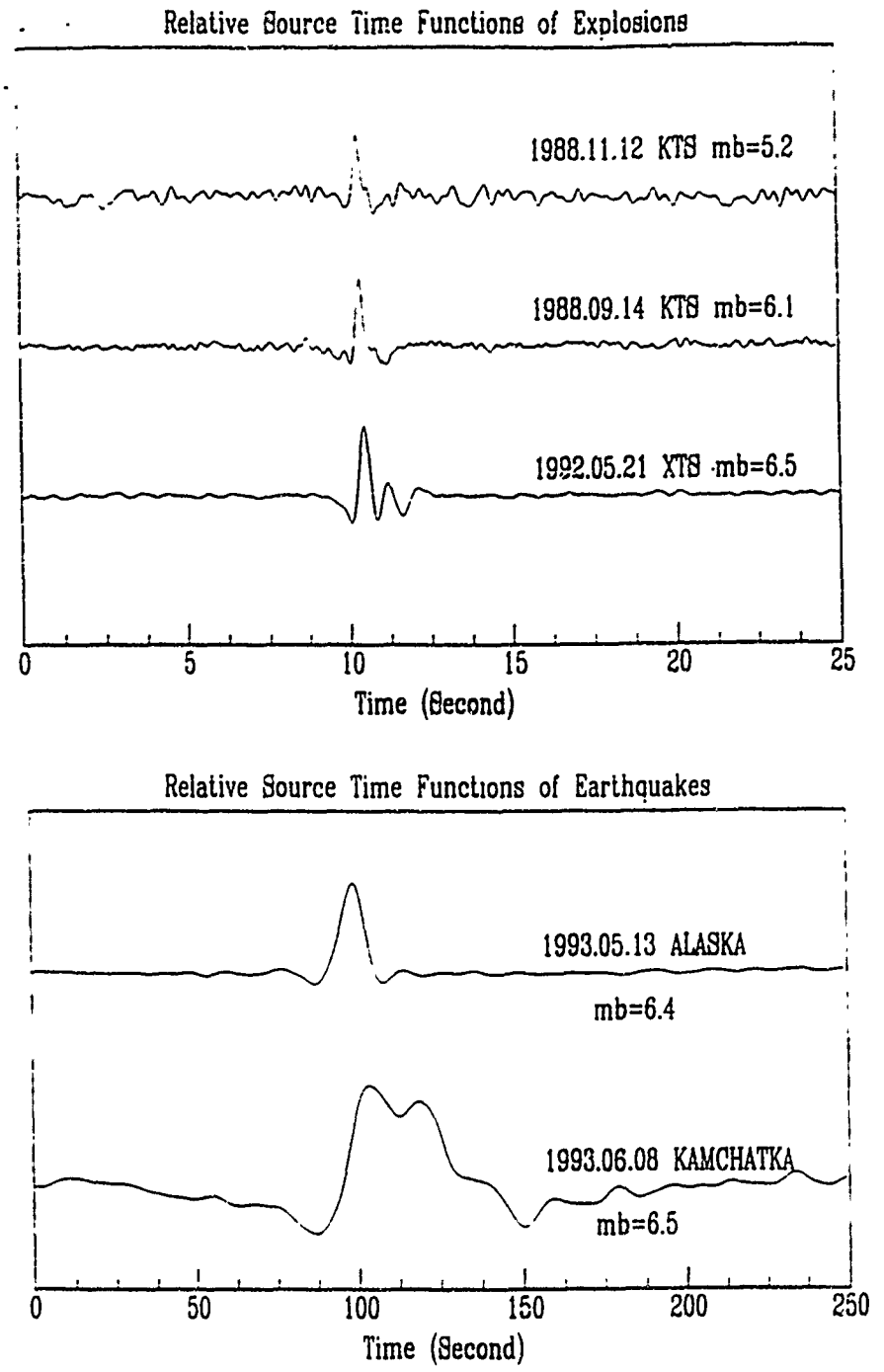

Figure 4: (a) Estimated source time functions of two explosions (19881112, m_b = 5.2 and 19880914, m_b = 6.1) in KTS and one explosion (19920521, m_b = 6.5) in XTS. The source durations for the three explosions range from 0.8 to 1.6 s. (b) Source time functions of the Alaska (19930513, m_b = 6.4) and Kamchatka (19930608, m_b = 6.5) earthquakes estimated with the EGF method. Note that the time scales in frames (a) and (b) differ by a factor of ten.

Jordan, T.H. and Sverdrup, K.A., 1981. Teleseismic location techniques and their application to earthquake clusters in the south-central Pacific. *Bull. Seism. Soc. Am.*, *71*, 1105–1130.

Lay, T., Velasco, A.A., and Ammon, C.J., 1992. Rupture directivity of the June 28, 1992, Landers, California, earthquake. *EOS, Trans. AGU*, *73*, 383.

Li, Y. and Toksöz, M.N., 1993. Study of the source process of the 1992 Colombia Ms= 5 earthquake with the Empirical Green's Function method. *Geophys. Res. Lett. 20*, 1087–1090.

Mueller, C., 1985. Source pulse enhancement by deconvolution of an empirical Green's function, *Geophys. Res. Lett.*, *12*, 33–36.

Pechmann, J. C. and Kanamori, H., 1982. Waveforms and spectra of preshocks and aftershocks of the 1979 Imperial Valley, California, earthquake: Evidence of fault heterogeneity? *J. Geophys. Res.*, *87*, 10579–10597.

Thurber, C.H., Quin, H.R., and Richards, P.G., 1993. Accurate locations of explosions in Balapan, Kazakhstan, 1987 to 1989. *Geophys. Res. Lett.*, *20*, 399–402.

SEISMIC SCATTERING FROM NON-SPHERICAL CAVITIES AND ROUGH INTERFACES

M. N. Toksöz, B. Mandal, W. Dong and C. Schultz

Earth Resources Laboratory
Department of Earth, Atmospheric, and Planetary Sciences
Massachusetts Institute of Technology, Cambridge, MA 02139

Contract No. F49620-92-J-0413

OBJECTIVE

The objective of this study is to examine seismic wave radiation from an explosive source in a cylindrical cavity and seismic scattering from highly irregular interfaces. Initial results indicate that the significant amount of shear energy could be generated from an explosion source placed in a semi-infinite cylindrical tunnel. Both P and S-wave radiation patterns do also change with the tunnel radius and the source position. As a second topic, enhanced backscattering of seismic waves from highly irregular interfaces has been studied theoretically for seismic waves and also compared with the laboratory data. Extensive study is necessary for further remarks of this relatively new phenomenon in seismic wave propagation.

RESEARCH ACCOMPLISHED

Introduction

Seismic radiation from a nuclear explosion is generally more complicated than that of simple isotropic point source. This has been shown by various observations (e.g., Wallace et al., 1983, 1985; Day et al., 1983, Priestley et al., 1990). The observations from nuclear explosions may be explained by one or more of the following physical mechanisms: (1) the nuclear explosion itself, (2) the tectonic release, (3) the spall, (4) the anisotropic and heterogeneous region near the source and (5) the asymmetry of the source. So far no single one of these mechanisms has proven sufficient to explain all of the observed data (Massé, 1981; Gupta and Blandford, 1983; Johnson, 1988). A purpose of this study is to investigate the seismic radiation from an explosive source placed in non-spherical cavity. Effect of spherical cavities on seismic explosions was studied in early sixties (e.g., Latter et al., 1961). Glenn et al. (1985) and Rial and Moran (1986) studied the coupling mechanism and the radiation pattern from an explosion in an ellipsoidal cavity in an unbounded medium. Helmberger et al. (1991) showed that correct modeling of near-field seismograms observed after nuclear explosions requires distinct source characteristics as well as the local crustal structure. They modeled the source characteristics by

using asymmetric sources inside ellipsoidal cavities. However, the common practice is to place the explosive sources in tunnels rather than in ellipsoidal cavities. In light of this fact, we have investigated the generation of compressional and shear waves from explosions in a cylindrical tunnels of different diameter.

In this study we also investigate the phenomenon known as enhanced backscattering, in which scattered energy preferentially travels back towards the source from highly irregular interfaces. This phenomenon has been observed in the field of optics (O'Donnell and Mendez 1987; Maradudin et al. 1990), and in this work we study enhanced backscattering for the seismic case. Specifically, we look at the scattering of acoustic waves from a highly irregular acoustic–elastic interface to determine whether the 'enhanced backscattering' which has been observed during forward modeling of SH and P-SV models (Schultz and Toksöz, 1993a,b) also occurs for acoustic waves.

Seismic Radiation from Tunnel

We have developed a frequency-domain hybrid boundary element and discrete wavenumber method for modeling waves radiated from various seismic sources; these sources are situated inside an infinite or semi-infinite cylindrical tunnel which is embedded in an infinite homogeneous isotropic or anisotropic medium. Using the assumption of axial symmetry, we can write the boundary integral equations for wavefields inside the tunnel and within the embedded elastic medium so that they yield an indirect boundary integral formulation. After discretizing the tunnel boundary into elements of uniform source distribution and imposing boundary conditions at each element, a system of matrix equations is obtained whose unknowns are the fictitious source distributions on each element. Elements of the resulting coefficient matrix are the integrals of displacement and stress Green's functions for the boundary elements. After the boundary sources are determined, wavefields inside and outside the tunnel can be easily calculated.

We performed numerical computations to estimate the P- and S-wave radiation patterns from an explosion source placed inside a semi-infinite tunnel in homogeneous elastic medium. The elastic medium has compressional and shear velocities of 4.0 km/s, 2.2 km/s respectively, and density of 2.2 g/cm^3. Figure 1 shows eight radiation patterns computed from four source positions measured from the end of the tunnel (1, 10, 20 and 30 meters) and two sizes of tunnel (5 and 10 meter radii). The results in Figure 1 clearly show that both the source position and the tunnel size affect the P- and S-wave radiation patterns.

For all the source positions and tunnel sizes, the linear elastic calculations show that the the shear wave amplitudes are greater higher than those of the compressional waves. This indicates that the tunnel is acting as a forcing system to generate a large shear wave. In the case of a analytic point force, the shear wave is nearly α^2/β^2 (e.g., 3 for Poisson's solid) times as large as the compressional wave (White, 1983). In our examples, the S-wave can be 3.3 times larger

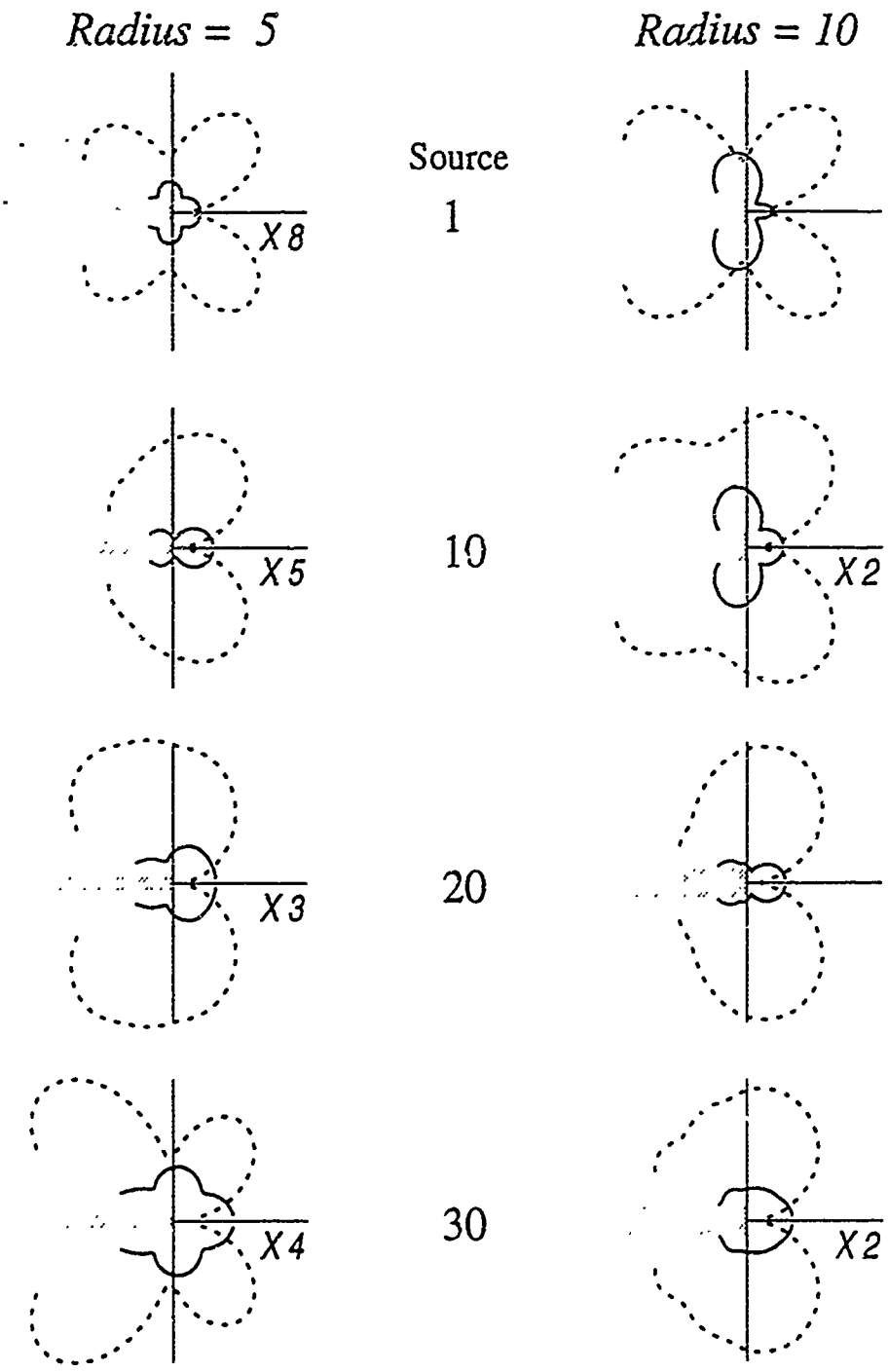

Figure 1: P (*solid*) and S (*dashed*) wave radiation from an explosive source (center frequency of 15 Hz) placed inside a horizontal tunnel which is embedded in a homogeneous elastic full space with an α of 4.0 km/s, β of 2.2 km/s and ρ of 2.2 g/cm^3. Results are shown for four positions of the source measured from the end of the tunnel (1, 10, 20 and 30 meters) and for two sizes of the tunnel (5 and 10 meter radii). Each radiation pattern is calculated at a semi-circular receiver array 250 meters in radius away from the source. Each pattern is drawn on the same scale, but with a separate magnification factor.

than P-wave. It is important to point out that neither the nonlinear effects nor the damping are considered in our calculations. The use of non-linear and hybrid techniques are required for realistic modeling in this area. .

Future studies will include more numerical experiments using realistic tunnel sizes (finite and irregular wall) and different surrounding media. The Nevada Test Site data will also be analyzed using this type of source and realistic propagation effects such as those included by Helmberger et al. (1991).

Enhanced Backscattering of Seismic Waves

We approach the problem of enhanced backscattering from both a numerical and experimental standpoint. We numerically combine the elastic representation theorem with the extinction theorem to develop a surface integral representation of the total scattered displacement. The scattered displacement is then expressed quantitatively in terms of a reflection coefficient which is similar to the reflection coefficient for a plane interface. After choosing an interface with specific statistical properties, we average over a full ensemble of realizations of this interface to determine the mean reflection coefficient for that interface. These 2-D mean reflection coefficients are then compared with 3-D ultrasonic water tank experiments obtained in our ultrasonic laboratory.

Comparisons between ultrasonic and numerical data have shown a number of distinctive features. Figure 2a shows numerical and experimental results found by placing the source at normal incidence to a rough interface; the 2-D numerical scattering results are very similar to the 3-D experimental scattering data. As the source position is moved to inclined angles, the 3-D experimental data (shown in Figure 2b) shows much more energy scattered in the forward direction and much less energy in the backward direction as compared to the 2-D numerical result. The phenomenon of enhanced backscattering is clearly seen in the numerical results and is supported by the experimental results. We note that the intensity of enhanced backscattering decreases as the incident angle deviates from normal incidence. It appears to finally disappear at an angle approximately equal to the *rms* slope of the interface. Referring again to Figure 2b, we see that enhanced backscattering is still detectable in the numerical results at a 30° incidence angle.

We have seen that the phenomenon of enhanced backscattering can be observed for seismic waves incident on an acoustic–elastic interface. In the future we want to use 3-D numerical techniques to study the complicated nature of energy scattered within the Earth's crust. This future work will include the study of unexplained forward and backscattered energy which is observed in both P and S codas.

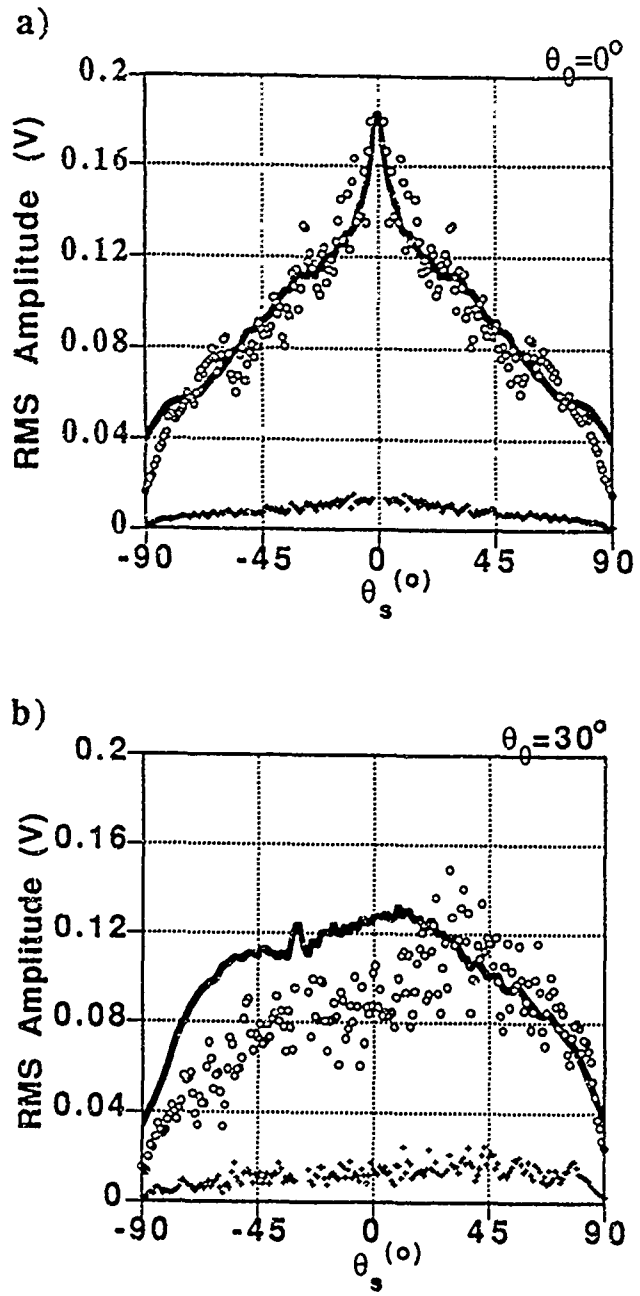

Figure 2: Comparison between numerical and laboratory data of RMS backscattered amplitudes from a rough interface for a source at (a) normal and (b) 30° incidence. θ_s is the angle of forward (positive) and backward (negative) scattering. The *solid line* is the result from the numerical calculations. The *circles* and $^+$s are the observational data with its standard deviation, respectively.

CONCLUSIONS AND RECOMMENDATIONS

We have studied two aspects of seismic wave scattering: seismic radiation resulting from explosions in non-spherical cavities and enhanced backscattering resulting from illumination of a rough interface. Preliminary study of the scattering of seismic waves from a semi-infinite tunnel shows that both *P*- and *S*-wave radiation patterns vary with the size of the tunnel and the position of the source position and that generation of the shear wave is significant. Enhanced backscattering is a relatively new phenomenon in the seismic community; we believe our research is the first to observe the effect in the laboratory (acoustic-elastic interface) and compare the experimental data with theoretical prediction. Further work is necessary before we apply these techniques to field observations. For future study we recommend the following:

1. Continuation of the theoretical investigation of scattering from non-spherical cavities with different surrounding media.

2. Determination of the *P*-to-*S* energy ratio with varying tunnel shape, source position and surrounding medium properties.

3. Comparison between 3-D modeling results of enhanced backscattering and 3-D experimental results (so far we have compared 2-D numerical results with 3-D experimental results).

4. Examination of array data, especially *P* and *S* codas, to observe the enhanced backscattering phenomenon.

REFERENCES

Day, S. M., N. Rimer, and J. T. Cherry, 1983. Surface waves from underground explosions with spall: analysis of elastic and nonlinear source models, *Bull. Seism. Soc. Am., 34*, 247-264.

Glenn, L. A., A. J. C. Ladd, B. Moran and K. A. Wilson, 1985. Elastic radiation from explosively-loaded ellipsoidal cavities in an unbounded medium, *Geophys. J. R. astr. Soc., 81*, 231-241.

Helmberger, D., L. Burdick and R. Stead, 1991. Modeling near-field data at NTS and Amchitka, *AGU Geophysical Monograph Series, 65*, 35-45.

Latter, A. L., R. E. LeLevier, E. A. Martinelli and W. G. McMillan, 1961. A Method of Concealing Underground Nuclear Explosions, *J. Geophys. Res., 66,* 3, 943-946.

Maradudin, A.A., Michel, & T., McGurn, A.R., & Méndez, E.R., 1990. Enhanced backscattering of light from a random grating, *Annals of Physics*, **203**, 255–307.

Massé, B. P., 1981. Review of seismic source models for underground nuclear explosions, *Bull. Seism. Soc. Am., 71*, 1249-1268.

O'Donnell, K.A. & Mendez, E.R., 1987. Experimental study of scattering from characterized random surfaces, *J. Opt. Soc. Am.*, 4 , 1194–1205.

Priestley, K. F., W. R. Walter, V. Martynov and M. V. Rozhkov, 1990. Regional seismic recordings of the Soviet nuclear explosion of the joint verification experiment, *Geophys. Res. Lett.*, *17*, 179-182.

Rial, J. A. and B. Moran, 1986. Radiation patterns for explosively-loaded axisymmetric cavities in an elastic medium: analytic approximations and numerical results, *Geophys. J. R. astr. Soc.*, *86*, 855-862.

Schultz, C. & Toksöz, M.N., 1993a. Enhanced backscattering of seismic waves from a highly irregular interface: SH case, *Geophy. J. Int.*, *114*, 91–102.

Schultz, C. & Toksöz, M.N., 1993b. Enhanced backscattering of seismic waves from a highly irregular interface: P–SV case, *Geophy. J. Int.*, (in press).

Wallace, T.C., D.V. Helmberger, and G.R. Engen, 1983. Evidence of tectonic release from underground nuclear explosions in long-period P waves, *Bull. Seism. Soc. Am.*, *73*, 593–613.

Wallace, T.C., D.V. Helmberger, and G.R. Engen, 1985. Evidence of tectonic release from underground nuclear explosions in long-period S waves, *Bull. Seism. Soc. Am.*, *75*, 157–174.

White, J. E., 1983. *Underground Sound: Application of Seismic Waves*, Elsevier, Amsterdm, 253p.

Characterization of broadband, regional distance seismograms in Eurasia and other regions of potential underground testing: preliminary results from the Arabian Shield, Kamchatka and South America

Terry C. Wallace
Susan L. Beck

Department of Geosciences
University of Arizona
Tucson, AZ 85721

Contract: F49601-92-J-0416

Objective:

The role of seismology in monitoring compliance with nuclear non-proliferation or comprehensive test ban treaties is one of detection and discrimination of low-yield devices in uncalibrated geologic environments. The low-yield condition requires that the backbone of the monitoring effort be at regional distances, where broadband seismic signals are a complex combination of both propagation and source effects. Given that we may be searching for a first and only nuclear explosion in a region, it is essential to calibrate suspect regions. We have focused on studying the regional seismic waves in three regions: (1) the Middle East, (2) Kamchatka, and (3) the South America.

Research Accomplished:

Regional distance seismic phases (Pn, Pg, Sn, Lg, and more collectively, P_{nl}) show great potential for discriminating low yield nuclear explosions from natural earthquakes and industrial explosions. In particular, utilizing the spectral characteristics of the regional distance seismograms has shown promise (Bennett et al., 1989; Lilwall, 1988; Taylor et al., 1989). Most spectral discriminates are based on two things: (1) given the same zero frequency moment, an earthquake witll be enriched in high frequencies as compared to an explosion, and (2) earthquakes excite more S-wave type energy than explosions. Typical spectral discriminates ratio the amplitude of a particular regional distance phase in narrow bands. Various phase-pair ratios, such as Pg/Lg and Pn/Lg show good separation of earthquake and explosion populations. Unfortunately, travel path has a strong influence on the "base line" of the trend of the line which separates the explosion

and earthquake populations (Lynnes, et al., 1990), and travel paths must be carefully calibrated for the spectral discriminates to work.

We have collected the regional distance seismograms from three regions which are of some interest to monitoring a comphrensive test ban, and begun analysis on the characteristics of regional seismic propagation. We are using the procedure of Wallace (1986) to invert the intermediate period regional distance body waves to determined crustal thickness and upper mantle velocities. Although analysis is preliminary, all three regions show dramatic travel path effects.

The crustal structure of the Middle East has been studied in detail only in a few places: Iran and the Zagros Collision region (Kadinsky-Cade et al., 1981; Cathcart and Wallace, 1990; Asudeh, 1983), and the southern Red Sea region. We have collected regional and upper mantle distance seismic waveforms from paths which cross the Arabian Shield and were recorded at WWSSN stations TAB, JER, HLW, SHI and EIL, and SRO station ANTO. Additionally, we have collected broadband digitial data recorded at GSN stations GNI, KIV (and a single record at ASH) and MEDNET station KEG. Figure 1 shows all the events, and their focal mechanisms, which produced at least one usable regional distance record.

Figure 2 shows the ray paths we used in our preliminary analysis of the Arabain plate. Using 15 paths we have divided the Shield into 4 blocks and inverted for average crustal thickness and Pn velocity. The blocks vary in thickness from 38 to 46 km. The variation in P_n velocity is from 7.8 to 8.1 km/sec. Most of the Pn phases which have traveled further than 1000 km require a well defined lid, which we have modeled as 40 km thick (although there is a strong tradeoff between depth and velocity gradient).

Numerous investigators have studied the characteristics of regional waveform propagation in the Eurasian continent in the last few years, but most have concentrated on the region around the Kazahkistan test sites and travel paths to NORESS, NORSAR and GERESS. The Kamchatka Peninsula is the most seismically active region of Russian, yet very little has been published on characteristics of propagation from Kamchatka events to seismic stations located in Eurasia. We have collected the regional waveforms from 31 events with shallow depth (< 10 km) and $m_b > 4.0$ recorded at CDSN stations MDJ and BJI, and IRIS/USGS station YSS. Travel paths across the northern part of the Sea of Okhotsk appear to have efficient Pg and Lg propagation; paths across the southern part of the Sea appear to exhibit blockage.

The crustal structure of South America is poorly characterized in large part due to the sparse station coverage. The best indications of crustal thickness for the Altiplano are from James (1971) who determined a crustal thickness of approximately 65-70 km from

analyzing surface waves. The crustal thickness probably decreases rapidly both east and west of the Altipiano, but there is apparently great variability in the crustal velocities and attenuation. These large variations in crustal thickness suggest the potential for Lg blockage. We have compiled a data set of shallow and intermediate depth earthquakes recorded at NNA, BDF and ZOBO (18 shallow and 6 intermediate depth events); the focal mechanisms and epicenters are shown in figure 3a. The ray paths from the events to the various stations is shown in figure 3b. Most of the shallow events occur in the Cordillera, and in general, the waveforms show strong travel path effects. We have just begun to invert each travel path for the best gross crustal structure, and then, regionalize the gross structure with a block tomography.

Conclusion and Recommendations:

The crustal thickness, layering and velocities has a strong effect on the character of short-period seismic phases. With the improved models which will be developed in this study (over the next year), blockage maps and various discrimination procedures will be tested. It is clear that to adequately calibrate a region considerible "empirical" work most be done (collection and processing of records, inversion for crustal structure models). At this stage of our research we are still analyzing the data base assembled over the last year.

References:

Asudeh, I. (1983). ISC mislocation of earthquakes in Iran and gemetrical residuals, *Tectonophysics, 95*, 61-74.

Bennet, T.J., B.W. Barker, K.L. McLaughlin and J.R. Murphy (1989). Regional discrimination of quarry blasts, earthquakes and underground explosions, S-Cubed Report, SSS-TR-89-10395.

James, D.E. (1971). Andean crustal and upper mantle structure, *J. Geophys. Res., 76*, 3246-3271.

Kadinsky-Cade, K., M. Barazangi, J. Oliver and B. Isacks (1981). Lateral variation of high frequency seismic wave propagation at regional distances across the Turkish and Iranian plateaus, *J. Geophys. Res, 86*, 9377-9396.

Lilwall, R.C. (1988). Regional m_b:Ms, Lg and Pg amplitude ratio and Lg spectral ratio as criteris for distinguishing between earthquakes and explisons: a theoretical study, *Geophys. J., 93*, 137-147.

Lyness, C.S., R. Baumstark, R.K. Cessaro and W.W. Chan (1990). Pg/Lg discrimination in the Western United States, in *12th Annual DARPA/GL Seismic Research Symposium*, J.F. Lewkowicz and J.M. McPhetres, editors, 123-129, GL-TR-90-0212, ADA226635.

Seber, D. and B.J. Mitchell (1992). Attenuation of surface waves across the Arabian peninsula, *preprint*.

Wallace, T.C. (1986). Inversion of long-period regional body waves for crustal structure, *Geophysc. Res. Let., 13*, 749-752.

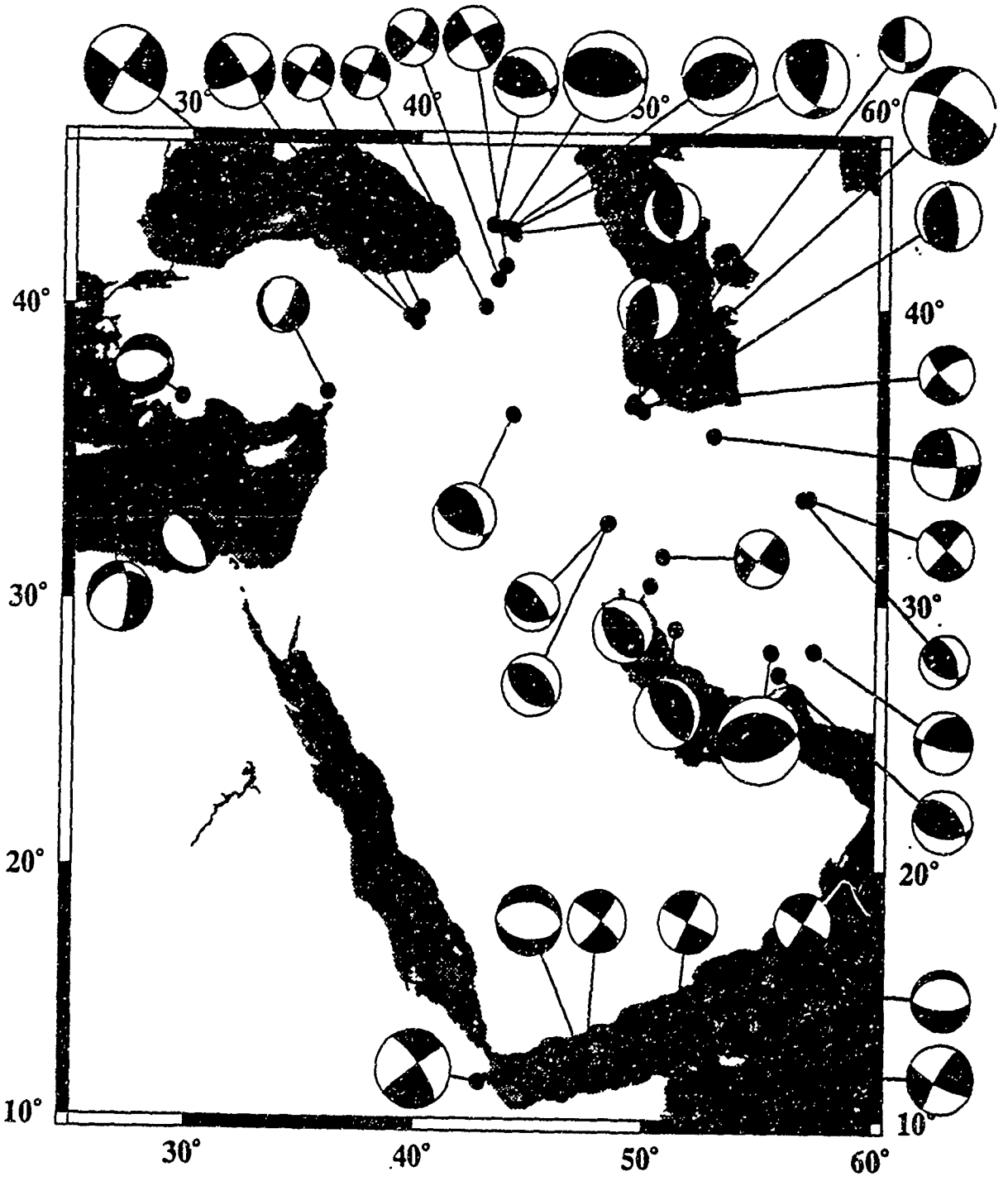

Figure 1: Focal mechanisms and epicenters of events in the middle east which produced at least one usable regional distance seismic record. Total number of records collected thus far: 68.

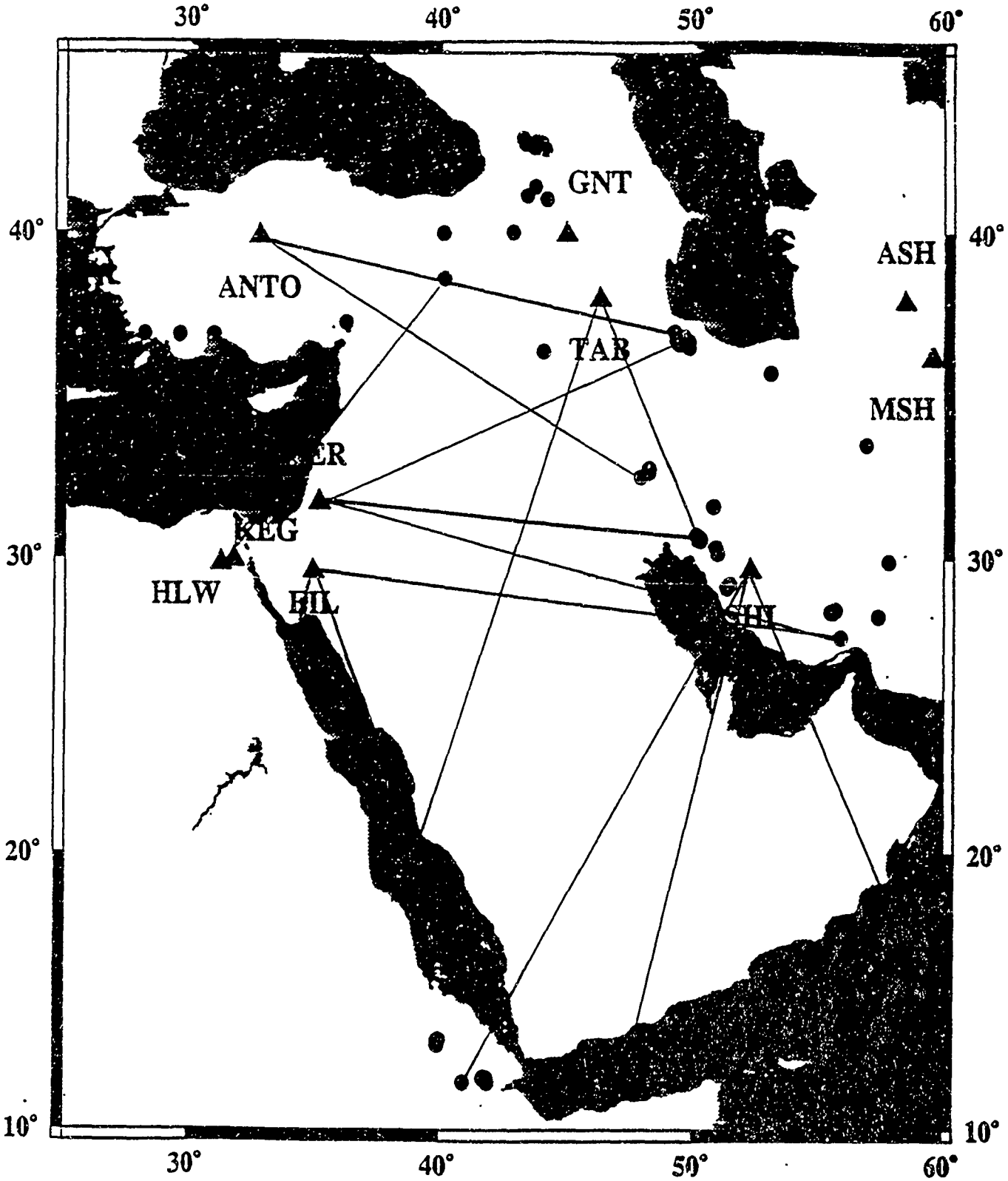

Figure 2: 15 ray paths available for preliminary inversion of Arabian shield.

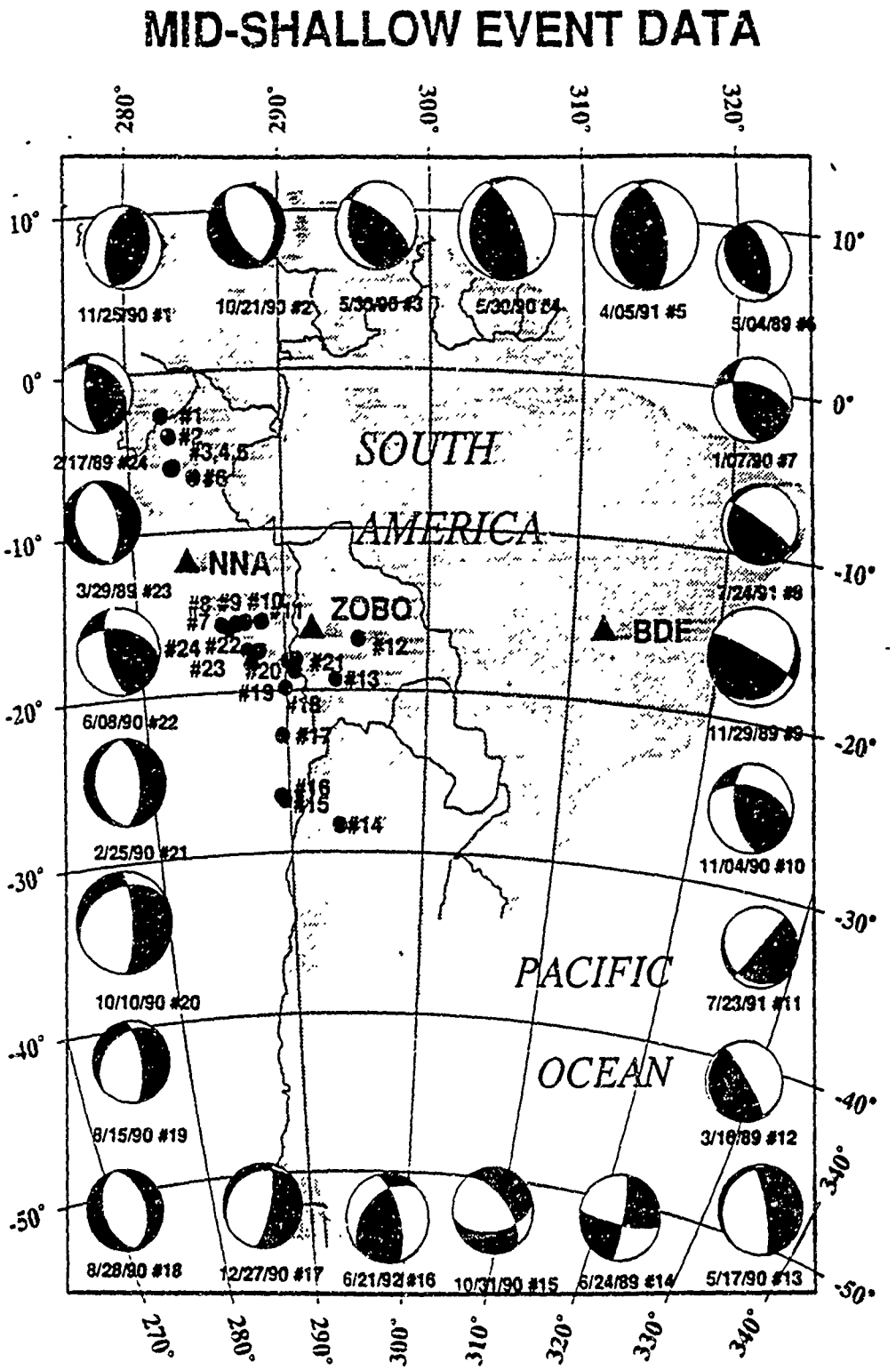

Figure 3a: Focal mechanisms and epicenters of events in South America which produced at least one usable regional distance seismic record.

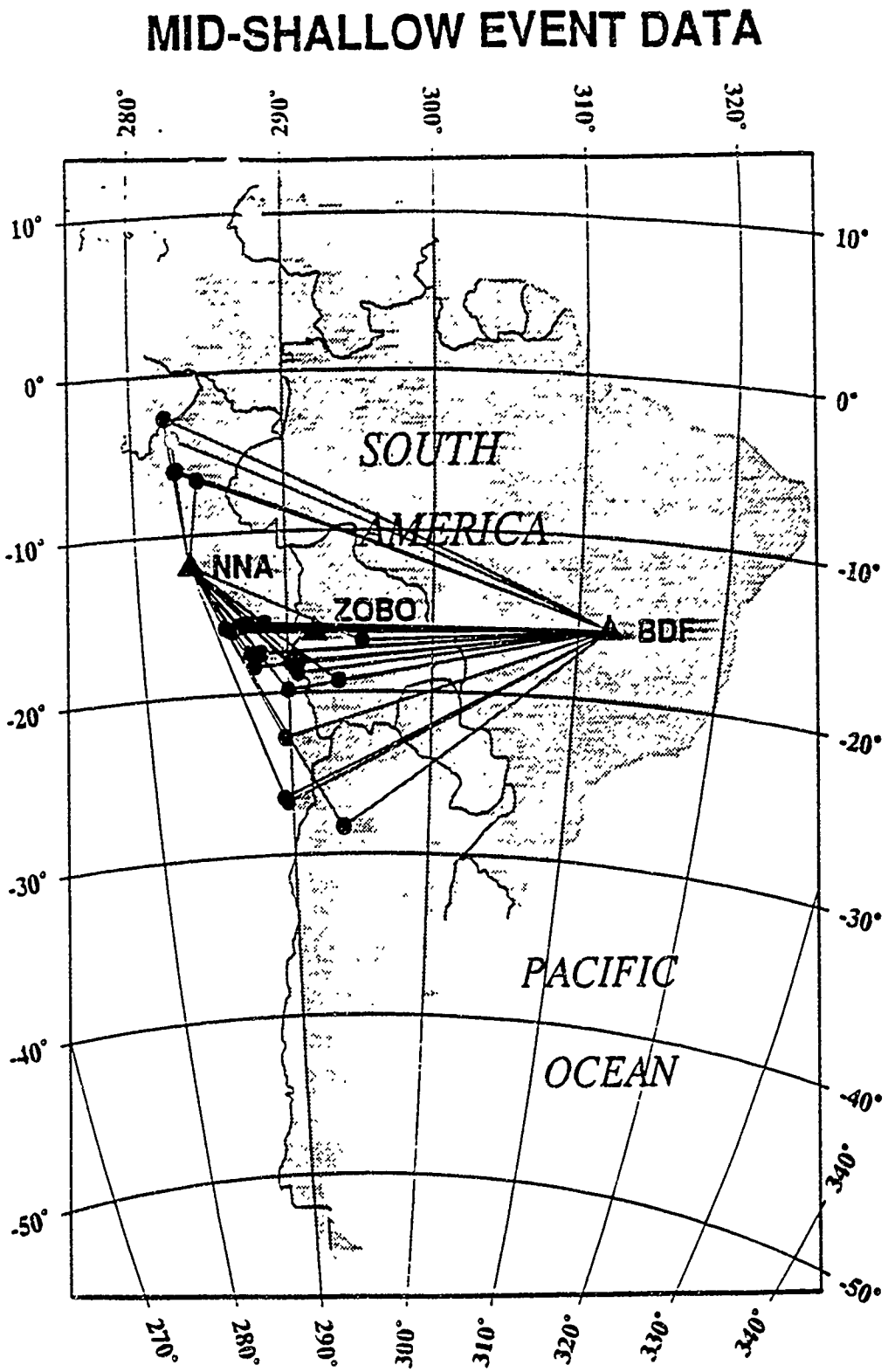

Figure 3b: Ray path for preliminary crustal structure inversion.

SEISMIC DISCRIMINATION STUDIES OF LITTLE SKULL MOUNTAIN EARTHQUAKES AND NTS EXPLOSIONS

William R. Walter, Howard J. Patton, Kevin Mayeda, Peter Goldstein,
Farid Dowla, and Albert T. Smith
Department of Earth Sciences, Lawrence Livermore National Laboratory

OBJECTIVE: The objective of this study is to evaluate both the potential of several regional discrimination methodologies, and their underlying physical basis. This study focuses on earthquake and explosion data from the Nevada Test Site (NTS). The m_b 5.5, June 29, 1992 Little Skull Mountain earthquake is the largest historical earthquake to occur at NTS. This event generated a rich series of aftershocks which were recorded at regional distances on the broadband seismometers of the Livermore NTS Network (LNN). Lawrence Livermore National Laboratory (LLNL) maintains a large database of NTS underground nuclear explosions which were also recorded on LNN. The proximity of the Little Skull mountain epicenters to sites of prior nuclear testing allows the opportunity to study small magnitude discrimination under the conditions of nearly common paths and common recording sites.

In this study we examine four potential regional discrimination methodologies. We seek to not only evaluate the performance of each potential regional discriminant, but to understand it's physical basis in order to make predictions for various source and receiver geologies. This predictive aspect is important in the present environment where the existing Non-Proliferation, and future Comprehensive Test Ban Treaties, are the principle concerns, and we are met with the challenge of monitoring many different areas around the world.

RESEARCH ACCOMPLISHED: We present the preliminary results of four potential discrimination methodologies using earthquakes and explosions that have occurred on NTS. The earthquakes are from the Little Skull Mountain sequence, which occurred between areas 25 and 28 near the southwestern perimeter of NTS. The sequence began with a M_L 5.6 main shock on June 29, 1992. By the end of 1992 there were more than 100 aftershocks with $M_L > 2$ and at least three with $M_L > 4$. Personnel from LLNL, in cooperation with the University of Nevada, Reno (UNR) and the United States Geological Survey (USGS), fielded portable instruments within a few days after the start of the sequence, and local recordings are available for many of the aftershocks. Excellent hypocentral control and many first motion focal mechanisms were available from the local Southern Great Basin Network, a short-period network operated by the USGS and UNR (S. C. Harmsen, written communication). The explosion data come from the LLNL database and includes events from Pahute Mesa, Rainier Mesa and Yucca Flats. At present only a subset of the data has been processed and the evaluation of the four potential discriminants described below must be considered preliminary.

The first potential discrimination method takes spectral ratios between regional phases, P_n/L_g and P_g/L_g. These discriminants are an outgrowth of general P/L_g amplitude studies (e.g. Pomeroy et al., 1982). These discriminants have given mixed results, for example showing strong overlap in a study P_g/L_g for western U.S. events (Taylor et al., 1989) and good discrimination at frequencies above two Hz in a study of regional P_n/Lg for central Eurasian events (Bennett et al., 1989). It has been suggested that differences in path and site effects have been the cause of the poor performance of the discriminant in some cases. In the present study we find that the ratios of P_n/L_g for earthquakes and explosions overlap in the 0.5 - 2.0 Hz frequency band, but the separation increases at frequencies above 2 Hz as shown in Figure 1. Explosions show significantly larger ratios than earthquakes in the 6-8 Hz range. The performance of this discriminant appears to be better at our Mina station than at Kanab for small magnitudes. On the other

hand, P_g/L_g ratios at Mina (not shown) have significant overlap even at high frequencies, indicating the significant influence of propagation on the P_g wave phases for this path.

The second method takes spectral ratios between two frequency bands, (1-2 Hz) to (6-8 Hz), for a single phase, either P_n, P_g, L_g or coda waves. Spectral ratios were found by Taylor et al. (1988) to be a useful discriminant for western U.S. events in the m_b range of 3 to about 4.5, with the spectral ratios of L_g giving the best performance. A focus of the present study is to compare the performance of various phases with coda wave measurements. Coda wave magnitudes in a narrow band (0.5-1.5 Hz) at a single station have been found to be more stable than magnitudes based on primary P_n or L_g amplitudes (Mayeda, 1993). Here we address the questions of the stability of the coda measurements at higher frequencies (6-8 Hz) and the potential to carry over this stability to discrimination measurements. Our preliminary results, shown in Figure 2, indicate that the single station spectral ratios based on coda waves show less scatter than the direct phase, particularly for the explosions. We have used more Rainier Mesa events than Taylor et al. (1988) and these appear to show the most overlap with the earthquake population.

For the third method, we follow up our previous studies of moment:magnitude relations (Patton and Walter, 1993). This potential discriminant is a variant of well known long-period to short-period ratio discriminants such as M_s:m_b. Here the seismic moment serves as the measure of long-period energy. We use the Little Skull earthquakes and some Rainier Mesa explosions to extend our previous results to smaller magnitudes. Seismic moments based on regional phases have been validated with measurements based on data recorded locally. Preliminary results for M_o:$m_b(P_n)$ are shown in Figure 3. A few events at very small magnitudes show large scatter on M_o:$m_b(P_n)$ plots which may be caused by difficulties with $m_b(P_n)$ measurement at low signal-to-noise levels. High background noise levels, related to the Landers earthquake sequence, hampered some measurements, particularly on the P_n phase. We are also investigating M_o:m_b relations for small events using magnitudes based on L_g waves and coda waves. It is important to state that the present results do not constitute a practical discriminant, since we have made use of isotropic moments for explosions and deviatoric moments for earthquakes. This was done for the purposes of researching the physical causes of the separation between earthquake and explosion populations. More work remains to be done to develop an operational discriminant based on M_o:m_b.

Finally, we are investigating the use of properties of the complete seismogram to estimate source depth. An unsupervised, self-organizing neural network is used to separate events into different clusters based on their spectrograms. The spectrograms use the same group velocity window, 7.5 to 2.0 km/s and the same frequency range, 0.8 to 6.8 Hz, for all events. A supervised learning neural network with output focal depth is trained on the derived spectrogram distributions. Preliminary results are encouraging for depth and event type classification. Examples of these spectrograms for a Little Skull earthquake and an NTS explosion are shown in Figure 4. The earthquake shows relatively more energy at higher frequencies than the explosion. Further work is needed to determine the relative contributions of source type and event depth to the differences between the earthquake and explosion spectrograms such as those observed in Figure 4. Toward this goal, we are applying the neural network approach to both synthetic and observed seismograms to improve our theoretical understanding of features identified by the network as important for the classifications.

CONCLUSIONS AND RECOMMENDATIONS: The preliminary results of this study are encouraging for regional discrimination at small magnitudes, with some caveats. Phase ratios, particularly P_n/L_g seem to be effective at high frequencies. However the uneven performance at different stations and for different P phases, P_n versus P_g, would appear to support arguments that such a discriminant is dependent on the particular propagation path. The use of coda does seem to reduce the scatter when compared to

spectral ratios of the direct L_g phase. There remain a number of questions about spectral ratios use as a discriminant including the physical basis and the transportability to other regions. The regional M_o:m_b results appear quite promising and there is a relatively simple theoretical explanation for the separation (Patton and Walter, 1993). However work remains to be done in order to make this an operational discriminant. The neural network results are very encouraging, but more work remains to be done on the relative contributions of source type and event depth to the observed differences in relative frequency content between the earthquakes and explosions. Examining the weights used by the neural net should help highlight the differences due to depth and those due to source type.

In the next stage of research we have started to include earthquakes from outside NTS but within the western U.S. to compare and contrast the effect of the common path on the discriminants. We have begun to make use of the local data to examine the relative frequency content of P and S energy close to the source. We have also begun to make use of the good hypocentral and focal mechanism control of the Little Skull Mountain events to determine whether these parameters can account for much of the scatter observed in the regional discriminants. Finally we hope to take advantage of outliers to shed light on the physical basis for the discriminants. A particularly interesting outlier, discussed extensively by Taylor (1993), is the May 14, 1981 mine collapse near Gentry Mountain, Utah. This event appears to fall in the earthquake population in the P_n/L_g in Figure 1, and close to the explosion population for both the Lg spectral ratios and the regional M_o:m_b as shown in Figures 2 and 3 respectively. The Gentry mountain event has some similarities to explosions since it occurred at a very shallow depth (200 m) and shows a large implosion component in its estimated moment tensor (Patton and Zandt, 1991). Further examination of the Gentry Mountain event and other outliers will be part of our future research. By combining information from all of the data we hope to determine the relative contributions of source, depth and path effects on each of the discriminants.

Acknowledgments. This work was performed under the auspices of the U. S. Department of Energy by the Lawrence Livermore National Laboratory under contract number W-7405-ENG-48.

References

Bennett, T. J., B. W. Barker, K. L. McLaughlin, and J. R. Murphy, Regional discrimination of quarry blasts, earthquakes and underground nuclear explosions, Final Report, GL-TR-89-0114, S-Cubed, La Jolla, California, 1989, ADA223148.

Mayeda, K., mb(LgCoda): a stable single station estimator of magnitude, *Bull. Seism. Soc. Am., 83*, 851-861, 1993.

Patton, H. J. and G. Zandt, Sesimic moment tensors of western U. S. earthquakes and implications for the tectonic stress field, *J. Geophys. Res., 96*, 18,245-18,259, 1991.

Patton, H. J., and W. R. Walter, Regional moment:magnitude relations for earthquakes and explosions, *Geophys. Res. Lett, 20*, 277-280, 1993.

Pomeroy, P. W., W. J. Best, and T. V. McEvilly, Test ban treaty verification with regional data - a review, *Bull. Seism. Soc. Am., 72*, S89-S129, 1982.

Taylor, S. R., N. W. Sherman, and M. D. Denny, Spectral discrimination between NTS explosions and western United States earthquakes at regional distances, *Bull. Seism. Soc. Am., 78*, 1563-1579, 1988.

Taylor, S. R., M. D. Denny, E. S. Vergino, and R. E. Glaser, Regional discrimination between NTS explosions and western U. S. earthquakes, *Bull. Seism. Soc. Am., 79*, 1142-1176, 1989.

Taylor, S. R., False alarms and mine seismicity: an example from the Gentry Mountain mining region, Utah, submitted to *Bull. Seism. Soc. Am.*, 1993.

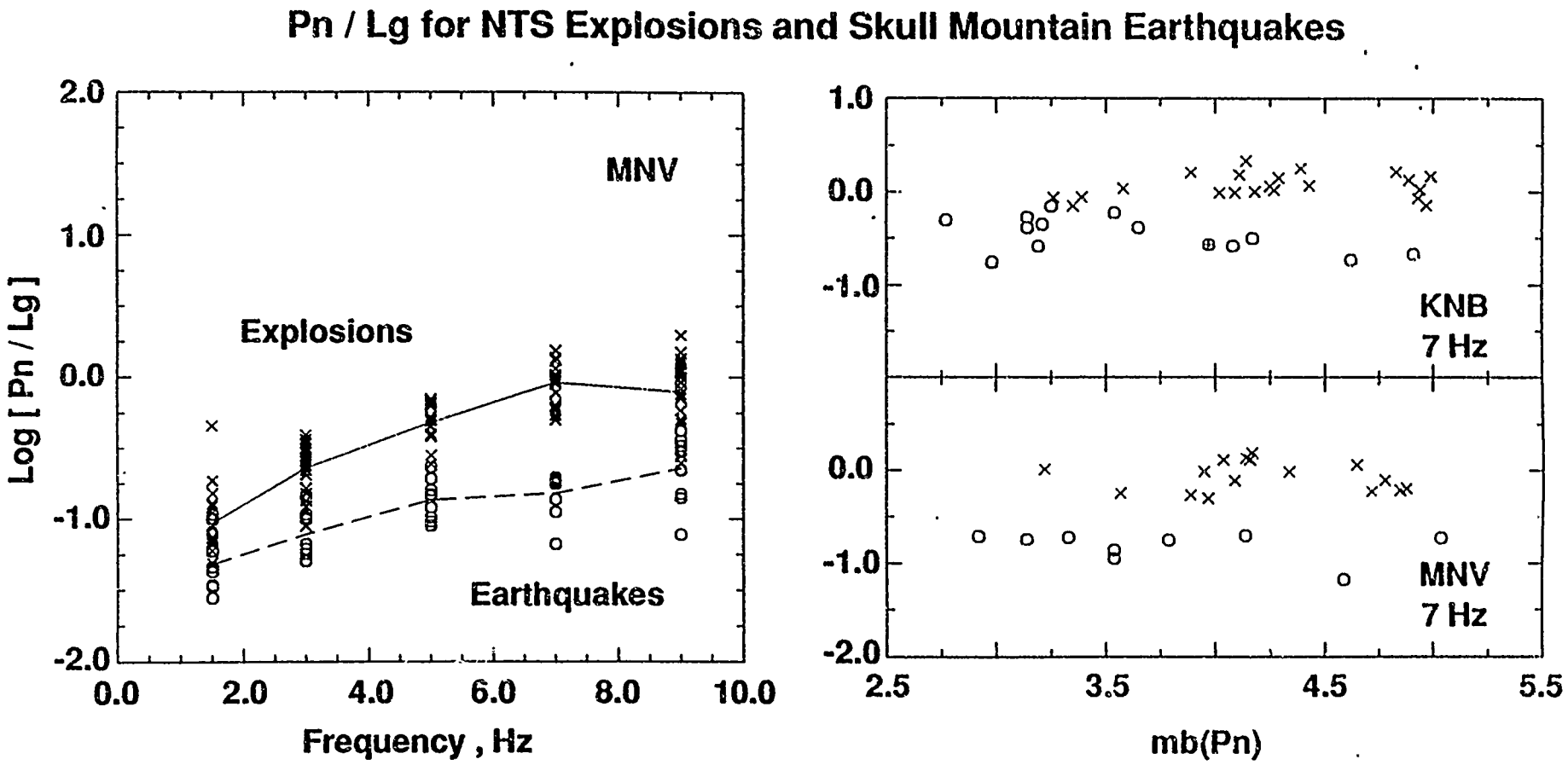

Fig. 1. Amplitude ratios between Pn and Lg phases as a function of frequency and magnitude. Explosions are shown by x's and Little Skull Mountain earthquakes are shown by o's. The o with a plus sign in the KNB plot on the right is the Gentry Mountain mine tremor discussed in the text. The measurements were obtained by taking ratios of spectral amplitudes for each phase in frequency bands 1 - 2 Hz, 2 - 4 Hz, 4 - 6 Hz,.6 - 8 Hz, and 8 - 10 Hz. Lines in the left panel connect means of the populations for each frequency band.

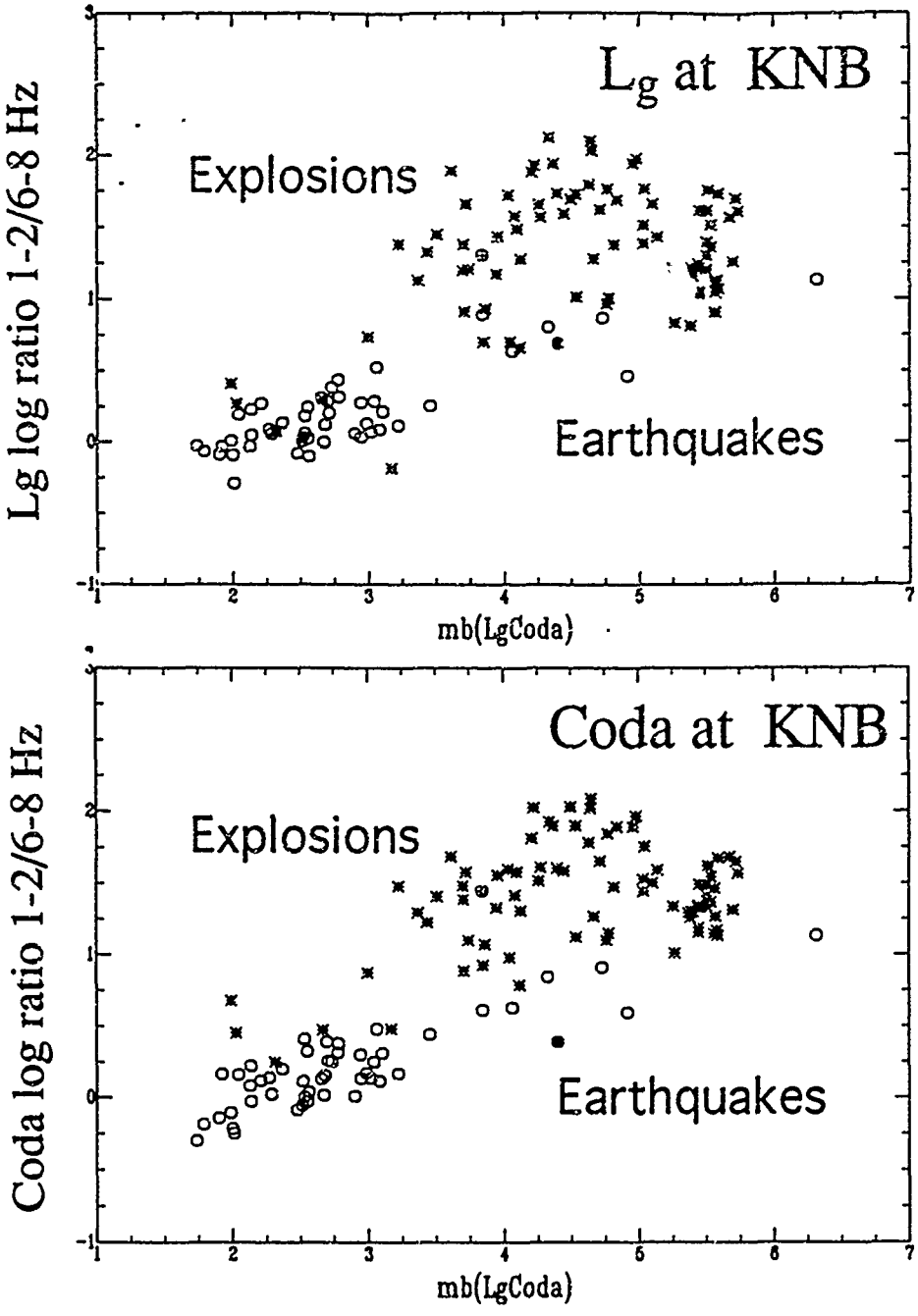

Fig. 2. Comparison of direct and coda Lg 1-2/6-8 Hz spectral ratios at KNB. Asterisks are NTS explosions and circles are Little Skull Mountain earthquakes. The circle with the cross is the Gentry Mountain mine collapse discussed in the text. The solid dot is a nearby Utah earthquake of similar magnitude. The spectral ratios are log averages of ratios measured on the two horizontal components.

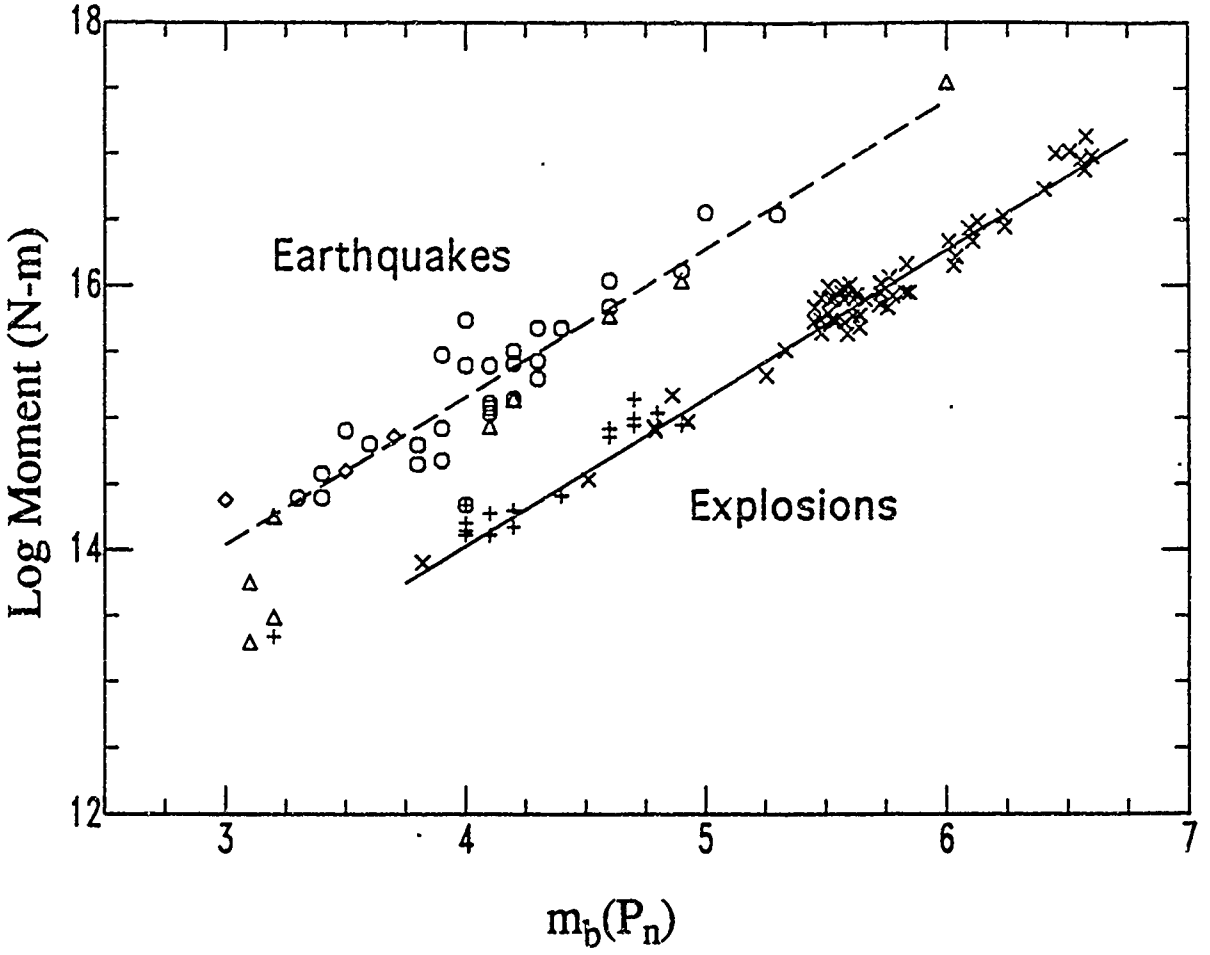

Fig. 3. Regional M_o:m_b relations for western U.S. earthquakes and explosions. The x's are NTS explosions used in the earlier study of Patton and Walter (1993), the pluses are additional NTS explosions. The circles are western U.S. earthquakes from the earlier study. The diamonds are additional western U.S. earthquakes, and the triangles are Little Skull Mountain earthquakes. The circle with the cross is the Gentry Mountain mine collapse. The lines are regression fits to the Patton and Walter (1993) data. Only the LNN station KNB was used to estimate $m_b(P_n)$ for the Little Skull Mountain events.

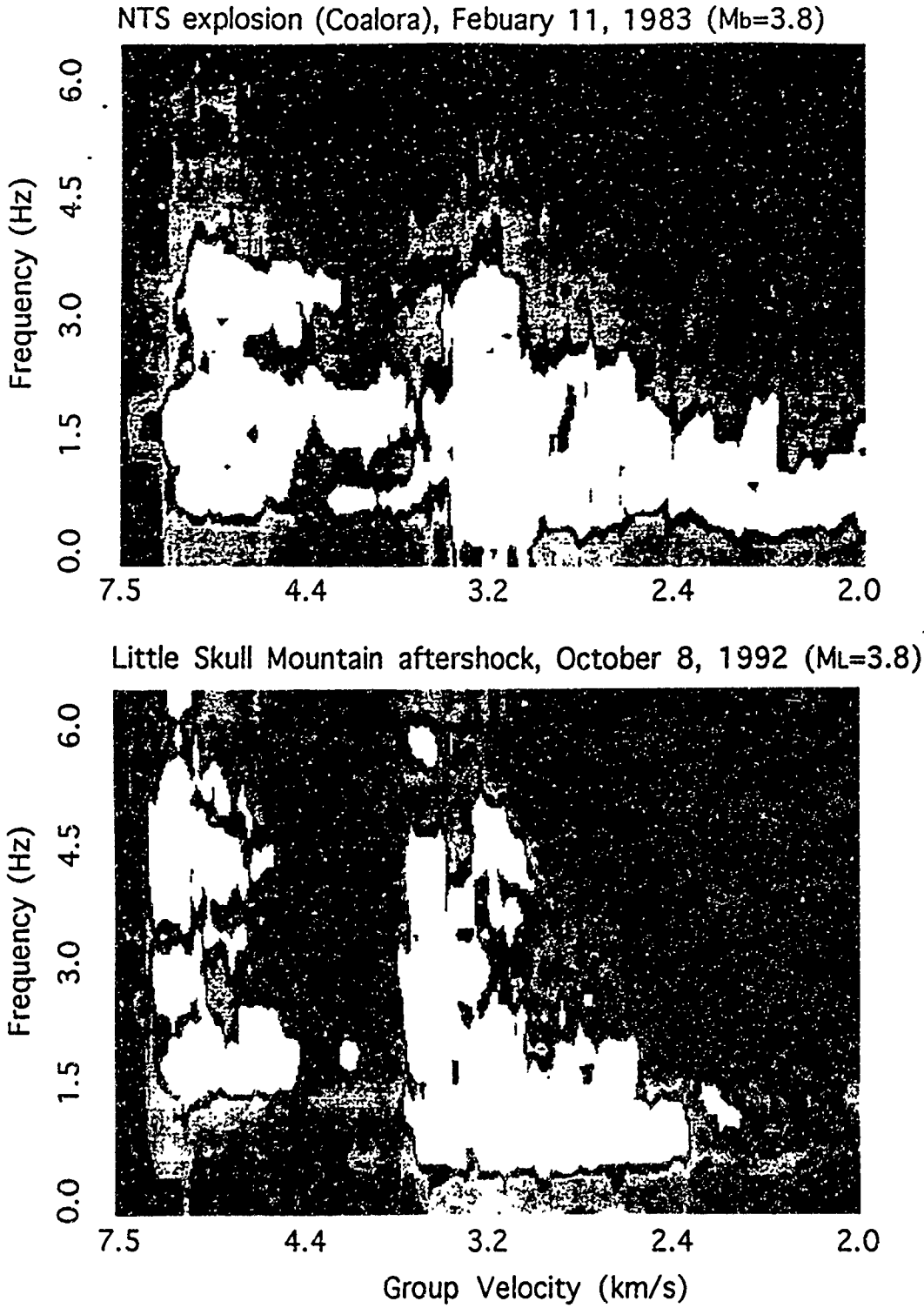

Fig 4. Spectrograms of an Mb=3.8, NTS explosion (Coalora) and an ML=3.8, Little Skull Mountain earthquake aftershock, recorded at the LLNL station KANAB. The largest spectral amplitudes are indicated by the white areas and have been normalized by peak amplitude. We are investigating the influence of event depth and source mechanism on differences in these distributions, such as the relative amounts of high and low frequency spectral amplitudes.

A PRELIMINARY MODEL FOR THE S WAVE VELOCITY BELOW CENTRAL ASIA

A. Zielhuis
Research School of Earth Sciences
Australian National University, Canberra ACT 0200, Australia

Grant: F49620-90-0352

OBJECTIVES

The objective of this study is to develop a three-dimensional (3-D) model of the shear wave velocity in the crust and upper mantle region below southeastern Eurasia. Such a velocity model will be useful for discriminating nuclear explosions from natural earthquakes through signal analysis techniques. Furthermore, it can provide insight in the tectonic history of the region.

During the last 10 years or so, more and more digitally recording broad-band and long-period stations from several networks (GSN, CDSN, Geoscope) have been installed in the region (see figure 1). The particular distribution of seismicity and stations provides a data set of seismograms that samples the region densely and that holds great possibilities for analysing the data in terms of a 3-D model.

In this study we apply a waveform analysis technique developed by Nolet [*J. Geophys. Res.*, 95, 8499-8512, 1990], the Partitioned Waveform Inversion (PWI). This approach is based on a path integral approximation and uses the time window from the S wave up to the fundamental mode of the Rayleigh wave to find, by methods of non-linear optimization, path integrals of the velocity along the particular source-station path. Synthetic seismograms are generated by mode summation and matched to the observations. The path integrals of velocity are transformed into a set of uncorrelated linear constraints on the velocity-depth profile. After inverting many seismograms associated to different wave paths, all linear constraints are combined in a linear inversion for a 3-D velocity model. A previous application of the method, in which a 3-D model of the S wave velocity below Europe was developed [Zielhuis and Nolet, submitted to *Geophys. J. Int.*, 1993], shows that body waves can be predicted accurately by the 3-D model for frequencies up to 60 mHz and the fundamental mode of the Rayleigh wave for frequencies up to 25 mHz.

RESEARCH ACCOMPLISHED

A complicating factor for the application of the PWI in southeast and central Asia is the large variation in crustal thickness across the region. A preliminary analysis of regional seismograms showed that such large differences in crustal thickness produce significant differences in waveforms. Fortunately, detailed maps of the crustal thickness in this regions are available [*Karta Glubinogo Rayonirovaniya Eurazii* , 1:15,000,000, Ministry of Geology, USSR, 1988]. In order to obtain satisfying initial predictions of the waveforms we constructed a range of starting models with crustal thickness varying from 30 to 70 km.

As an example of the influence of crustal thickness on the waveforms we discuss the observed waveforms on a seismogram from an event in the Kazakhstan-Xinjiang border region (47.97N, 84.97E), on 3 August 1990, recorded at station KMI and predictions for different starting models. The wave path crosses the Tibetan Plateau where the crustal thickness reaches 70 km, while the event and the station are located in regions with 45 km crustal thickness. Figure 2 shows the predicted waveform for a starting model with a 45 km thick crust (uppermost traces, no 3). The predicted waveform of the traces in the middle (no 2) has been computed allowing for perturbations in the excitation coefficients of the modes caused by variations in crustal structure on the wave path: we used a model with a 45 km thick crust for the source and station location and a model with a 60 km thick crust for the path. The latter prediction resembles the observed waveforms (and the observed travel time) much better than the first. The lowest trace shows the fit obtained after the nonlinear inversion for a 1-D model for the source-station minor arc.

With the set of starting models with different crustal thicknesses we obtained good initial predictions and fits for many regional seismograms. So far we inverted 66 seismograms of regional events, recorded at CDSN and GSN stations. The associated wave paths are shown in figure 1. For most wave paths crossing the Tibetan Plateau we inverted the fundamental mode bandpassed between 0.005 and 0.02 Hz. For higher frequencies the waveform of the fundamental mode sometimes was slightly distorted. The reason for this can be that for such high frequencies the fundamental mode is mainly sensitive to the upper 70 km, and thus to the more heterogeneous crust which can cause effects of scattering and multipathing. In addition, the transition from the extremely thick crust of the plateau to the thinner crust of the surrounding regions will cause mode conversion for such frequencies. For paths running completely within the regions with a thinner crust we fitted the the fundamental mode for frequencies up to 0.025 Hz. Usually the S body waves could be fitted for frequencies up to 0.05 or 0.06 Hz.

CONCLUSIONS AND RECOMMENDATIONS

We have applied the method of partitioned waveform inversion to a preliminary set of seismograms recorded at the long period and broad band stations of the GSN and CDSN network. Using starting models with crustal thicknesses that are representative for the particular source-receiver minor arcs, we generally obtained good predictions for the observed waveforms and produced good fits. In order to obtain a good resolution for the 3-D model, we need to analyse more data: in particular the records from the GEOSCOPE station HYB, as well as records from events east of the Tibetan Plateau (which are available through IRIS), will contribute to a higher azimuthal coverage by the wave paths. The data from the PASSCAL experiment on the Tibetan Plateau will also be useful.

Figure 1:
Map with wave paths associated to the events analysed. Triangles represent the digitally recording seismic stations of the CDSN, GSN, and GEOSCOPE networks.

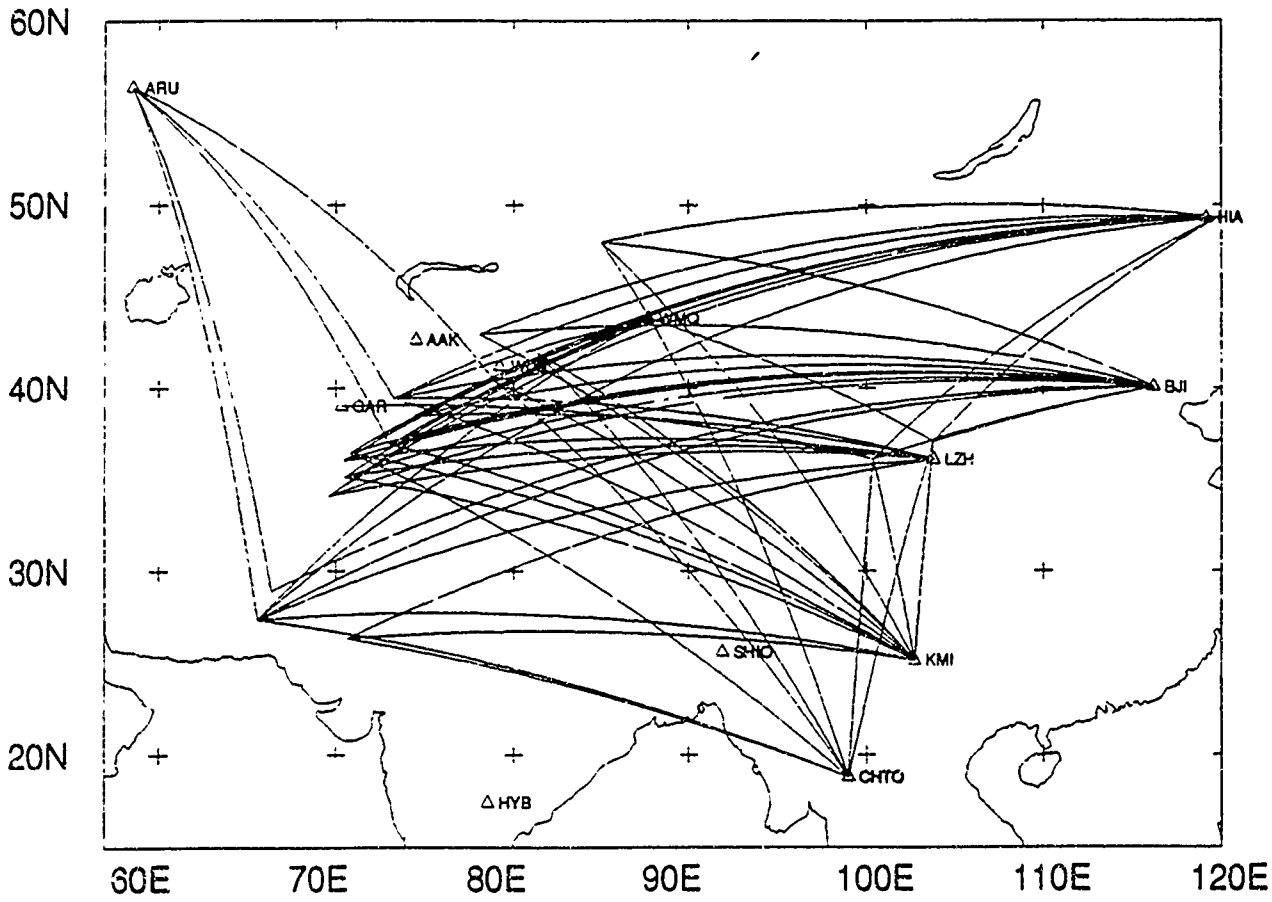

Figure 2:
Observed (solid) and predicted (dashed) waveforms for an event the Kazakhstan-Xinjiang border region (47.97N, 84.97E), on 3 August 1990.
A) Time window of observed seismogram that contains the S wave up to the fundamental mode of the Rayleigh wave (bandpass: 0.005-0.01).
B) Observed S wave and predictions for: a model with a 45 km thick crust for the station, path and source location (trace 3), a model with a 45 km thick crust for the source and station and a 60 km thick crust for the path (trace 2).
Trace 1 shows the fit after the nonlinear inversion using the starting models of trace 2.
C) Observed Rayleigh wave and predictions for: a model with a 45 km thick crust for the station, path and source location (trace 3), a model with a 45 km thick crust for the source and station and a 60 km thick crust for the path (trace 2). Trace 1 shows the fit after the nonlinear inversion using the starting models of trace 2.

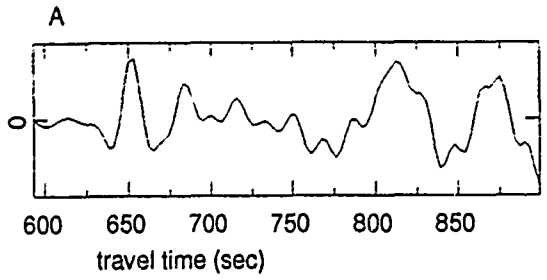

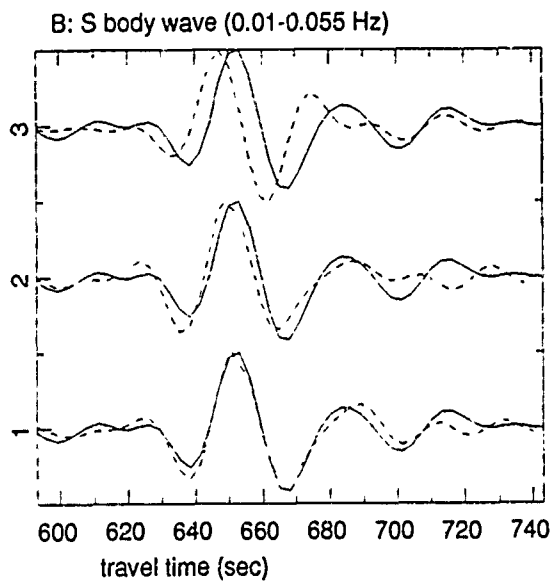

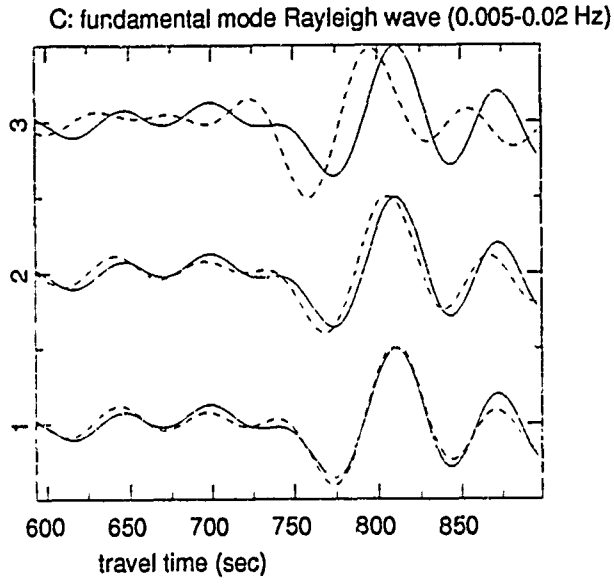

STATISTICAL INVERSION OF LAYERED MEDIA WITH PHYSICAL BOUNDARY CONDITIONS

Zhao-Qing Zhang[+], Benjamin White, and Ping Sheng
Exxon Research & Engineering Company, Annandale, New Jersey 08801

and

Raymond Jeanloz
[+]Department of Geology and Geophysics, University of California, Berkeley, California 94724

CONTRACT NO. : F49620-92-J-0544

I. OBJECTIVE

Random heterogeneities are a fact of nature. They exist in the atmosphere, in oceans, and in the Earth's subsurface. It is inevitable, therefore, that randomness would interfere with any detection or measurement process which involves wave propagation. Over short distances, the effect of randomness in the medium can generally be filtered out by various signal processing techniques. However, over long propagation distances random scattering can overwhelm the target or structural information that one intends to obtain from a probing wave. In fact, random multiple scattering is precisely the reason that many disordered materials appear "cloudy", and is a generic mathematical reason for the instability of classical inversion schemes.

Apart from multiple scattering, another generic inversion problem is the inability of a wave or a pulse to probe structures which vary on a scale much larger than its wavelength, or pulse width. Here the basic reason is that a wave is inherently a differential detector, i.e., it only scatters from and detects objects with material properties different from those of the background. When the material properties vary slowly, the scattering is weak and this can impose a severe constraint on the detection sensitivity.

Both problems described above can be resolved by a newly developed statistical inversion scheme for a randomly layered medium consisting of both small-scale fluctuations and large-scale inhomogeneities.[1-3] Although it is limited to one dimension, at present, this acoustic theory is capable of showing explicitly that a multiply-scattered wavefield has both wave-like and diffusive behavior. It is precisely the diffusive behavior that enables the multiply-scattered wave to detect the large-scale variations, although the wave-like part also has to be correctly treated in order to obtain the desired inversion results.[3-6] It has also been demonstrated that this theory can recover from a signal data set the slowly varying mean character of a medium with signal amplitude only 10^{-3} times the multiply-scattering noise.

In order to apply this new method to real seismic data, we have extended the inversion method to incorporate physical boundary conditions and attenuation. We consider here the mismatched and pressure-release boundary conditions, which are relevant to marine and land data, respectively. The main results of the theory are presented in Section II, where the equations governing the local power spectrum are given. The power spectrum contains all the multiple-scattering information resulting from small-scale fluctuations, and the equation depends explicitly

on the large-scale inhomogeneity only. The equation can be solved analytically when the medium is homogeneous.

Application of this statistical seismic inversion method is a new and unique approach to the determination of velocity and attenuation maps of the Eurasian crust and upper mantle, which is our main objective As explained below it is an approach that complements more traditional methods for inversion of seismic data when waves are reflected from large depths. Furthermore it addresses two other aspects of wave multiple scattering in these structures that may be important in monitoring underground nuclear explosions. (i) In addition to true attenuation the method produces estimates of a related but often-neglected phenomenon caused solely by sub-wavelength multiple scattering. This type of attenuation, which is related to the mathematical theory of localization, has frequency characteristics which differ from those of true attenuation. Thus neglect of this phenomenon in monitoring underground nulear explosions may adversely affect both yield estimation and the identification of source characteristics. (ii) While the method does not incorporate extraneous noise sources, it directly addresses the "cloudiness" that limits useful interpretation of waves that have been strongly multiply-scattered. The method optimally deals with cloudiness when constructing a velocity map from reflection seismic data, and also provides estimates of the relevant statistical parameters that quantify this effect.

II. RESEARCH ACCOMPLISHED

II A. THE STATISTICAL THEORY

We consider a slab of stratified medium, occupying $-L < z < 0$. A normal incident acoustic wave is governed by the following equations for pressure p and displacement velocity u along the z-direction,

$$\rho\frac{\partial u}{\partial t} + \sigma u + \frac{\partial P}{\partial z} = 0$$

$$\frac{1}{K}\frac{\partial P}{\partial t} + \frac{\partial u}{\partial z} = 0 \qquad (1)$$

where ρ is the density and K is the incompressibility. The factor σ describes the dissipation in the medium. In general, the dissipation effect depends on the frequency. Thus, the term σu in Eq.(1) is interpreted as the time convolution of σ and u. We assume that both the density and the incompressibility in the medium have a slowly varying backgrcund and a stochastic microstructure. To do this, let $\eta(z, z')$ and $\nu(z, z')$ be, for each fixed z, two zero-mean stationary random processes as functions of z'. If ε is a small parameter, $\eta(z, z/\varepsilon^2)$ or $\nu(z, z/\varepsilon^2)$ then has a microstructure to background length scale of ε^2.

In the case of the mismatched boundary condition, we embed the slab between two homogeneous half spaces and write ρ and K as

$$\rho(z)=\begin{cases}\rho_0 & \text{for } z>0\\ \rho_1(z)\left[1+\eta\left(z/\varepsilon^2\right)\right] & \text{for } -L<z<0\\ \rho_2 & \text{for } z<-L\end{cases} \tag{2}$$

and

$$\frac{1}{K(z)}=\begin{cases}\dfrac{1}{K_0} & \text{for } z>0\\ \dfrac{1}{K_1(z)}\left[1+v\left(z,z/\varepsilon^2\right)\right] & -L<z<0\\ \dfrac{1}{K_2} & \text{for } z<-L\end{cases} \tag{3}$$

The background speeds are

$$c_j=\sqrt{K_j/\rho_j} \qquad \text{for } j=0,1,2. \tag{4}$$

The dissipation factor σ could in general depend also on z and z/ε^2. However, here,we assume it to be z independent.

Now we consider a pulsed plane wave incident normally from $z>0$. If f(t) is the pulse shape the incident field can be written as

$$u^{inc}=\frac{-1}{\sqrt{\varepsilon}\rho_0 c_0}f\left[\frac{1}{\varepsilon}\left(t-\frac{z}{c_0}\right)\right]$$

$$p^{inc}=\frac{1}{\sqrt{\varepsilon}}f\left[\frac{1}{\varepsilon}\left(t-\frac{z}{c_0}\right)\right] \tag{5}$$

Note that the pulse width is of order ε, intermediate between the macroscale and microscale of the medium. The factor $\varepsilon^{-1/2}$ is inserted to preserve energy as ε is varied. The physical quantity of interest here is the reflected pressure at z=0, i.e. $p_{refl}=p(z=0,t)$. Now we define the autocorrelation of p_{refl}, I(t,t), and its local power spectrum, $S(t,\omega)$, as [6]

$$I(t,\bar{t})=\lim_{\varepsilon\to 0}E\left[P_{refl}\left(t+\frac{\varepsilon\bar{t}}{2}\right)P^{*}_{refl}\left(t-\frac{\varepsilon\bar{t}}{2}\right)\right]$$

$$=\frac{1}{2\pi}\int d\omega e^{-i\omega\bar{t}}S(t,\omega) \tag{6}$$

with

$$S(t,\omega)=\left|\hat{f}(\omega)\right|^2\Lambda(t,\omega) \tag{7}$$

where $\hat{f}(\omega)$ is the Fourier transform of the pulse shape f(t). Using a procedure similar to that described in Refs. [3,6], it can be shown that the renormalized power spectrum $\Lambda(t,\omega)$ is determined by the following equations

$$\frac{\partial V^N}{\partial \tau} - 2N\left(\frac{\partial V^N}{\partial t} + \frac{\hat{\sigma}}{\rho_1} V^N\right) = \frac{2w^2\alpha}{c_1}\left\{(N+1)^2 V^{N+1} - 2N^2 V^N + (N-1)^2 V^{N-1}\right\} \tag{8}$$

$$V^N(\tau = 0, t) = \left\{\delta_{N,0}\Gamma_I^2 + \left(\Gamma_I - \Gamma_I^{-1}\right)^2 \sum_{i=1}^{\infty} \Gamma_I^{2i}\delta_{N,i}\right\}\delta(t) \tag{9}$$

$$\Lambda(t,\omega) = V^0\left(\tau = \frac{-t}{2}, t, \omega\right) \tag{10}$$

where τ is the travel time and is defined as

$$\tau(z) = \int_0^z \frac{dz'}{c_1(z)} \tag{11}$$

and c_1 in Eq. (8) is now a function of τ. $\hat{\sigma}(\omega)$ is the Fourier transform of $\sigma(t)$. Γ_I is the reflection coefficient at z=0 and is defined as

$$\Gamma_I = (\xi_1(0) - \xi_0) \,/(\xi_1(0) + \xi_0) \tag{12}$$

where $\xi_1 = \rho_i c_i$ are the impedances in the regions j=0 and 1. α is defined as

$$\alpha = \frac{1}{4}\int_0^{\infty} E\left[n(z,z')n(z,z'+z'')\right]dz'' \tag{13}$$

with

$$n(z,z') = \left[\eta(z,z') - \nu(z,z')\right]$$

Here we have assumed that η and ν depend only on the microstructure (or z'), therefore, α is a constant.

In the case of the pressure-release boundary condition, the medium above z=0 has much small density than the medium below and the incident field becomes

$$p^{inc} = \frac{1}{\sqrt{\varepsilon}} f\left(\frac{t}{\varepsilon}\right) \tag{14}$$

The physical quantity measured here is the displacement velocity at z=0, i.e. $u_{refl}=u(z=0,t)$. The corresponding renormalized power spectrum $\Lambda(t, \omega)$ is still governed by Eq. (8) . However, Eqs.(9) and (10) should be replaced by

$$V^N(\tau = 0, t) = \left\{\sum_{i=1}^{\infty} \delta_{N,i}\right\}\delta(t) \tag{15}$$

$$\Lambda(t,\omega) = 4\xi_1^{-2}(0) V^0\left(\tau = \frac{-t}{z}, t, \omega\right), \qquad t > 0, \tag{16}$$

Eq.(8) depends explicitly on the large scale inhomogeneity only. All information resulting from multiple scattering by small-scale fluctuations are absorbed in the correlation functions V^N. When the medium is homogeneous, Eqs (8)-(13) and (15)-(16) can be solved exactly, yielding

$$\Lambda(t,\omega)=\frac{\omega^2\alpha\left[\Gamma_1^2-1\right]^2\exp(-\frac{\hat{\sigma}t}{\rho_1})}{c_1\left[1+\omega^2\alpha\left(1-\Gamma_1^2\right)t/c_1\right]^2} \tag{17}$$

for the mismatched boundary condition case, and

$$\Lambda(t,\omega)=4\exp(-\frac{\hat{\sigma}t}{\rho_1})\omega^2\ /\left(\xi_1^2c_1\right) \qquad (t>0) \tag{18}$$

for the pressure-release boundary condition case. These are the generalizations of the results found previously for a medium with matched boundary condition and without dissipation.[6,8] If the medium is inhomogeneous, one has to solve Eqs. (8)-(13) and (15)-(16) numerically.

II B NUMERICAL METHOD

In order to test the theory, we have developed a layere code to generate the local power spectrum numerically. The method of a layer code is described in detail in Ref. [3]. Here we only give the summary of the method. We consider a slab of N layers, each having the same thickness h. Let the surface of the first layer be at z=0, and the surface of the last layer be at z= -L= -hN. This slab is then connected to an infinite homogeneous medium at z=-hN. Write Eq.(1) in frequency space. Then, for any fixed frequency ω, we can always express the solution of Eq. (1) in each layer as a linear combination of up and down going waves. The amplitudes of these two waves in any two contiguous layers are related by the conditions of continuity of u and p at the interface of two layers. Thus, one can relate the wave function at any position to that at z=- χ by transfer matrices. Using the fact that there is only a down-going wave in the region z < -hN, we are able to obtain $\hat{p}_{refl}(\omega)$ or $\hat{u}_{refl}(\omega)$. For the case of the mismatched boundary condition, we also connect the system with another infinite homogeneous medium in the upper half space z > 0. The time sequence of $p_{refl}(t)$ or $u_{refl}(t)$ is then the Fourier transform of $\hat{p}_{refl}(\omega)$ or $\hat{u}_{refl}(\omega)$. The estimated power spectrum is then calculated by using the relation[4]

$$\hat{S}(t,\omega_j)=\left|\frac{1}{\sqrt{T}}\frac{T}{M}\sum_{\ell=0}^{M-1}\exp\left[-\frac{2\pi j\ell}{M}\right]P_{refl}\left(or\ u_{refl}\right)(t+s_\ell)\right|^2 \tag{19}$$

where T is the time window and M is the number of equally spaced data points of $p_{refl}(t)$ or $u_{refl}(t)$.

Numerically, we have chosen N=2500 and h=3m[9,10]. The number 3m is the correlation length obtained from the data analysis given in Ref. [9]. Thus, the thickness of the slab considered is 7500m. The slow variation of the mean sound speed has the form

$$C_1(z)=\left\{1-0.25\left[\tanh(5(z-750))-\tanh(5(z-5250))\right]\right\}x3000 \tag{20}$$

Here we have assumed that the mean density ρ_1 is constant and the slow variation comes from the variation in $1/K_1(z)$. Since the maximum speed here is 3km/sec, in a time domain of 0-5 sec, the reflected wave has not yet probed the region $z < -hN$, and the homogeneous region below it becomes irrelevant. In the case of mismatched boundary condition, we have deliberately set the value of c_0 at 1.5km/sec in order to test the theory in the high-mismatch limit. For the probing pulse, we use a Ricker pulse of the following form

$$f(t)=\left[\frac{\pi^2}{4\varepsilon^2}t^2-1\right]^2 e^{-\left(\frac{\pi^2 t^2}{8\varepsilon^2}\right)} \tag{21}$$

The width of the pulse ε is set to be 0.01, which provides a compact support of range 10-70 Hz to $\hat{f}(\omega)$. The time window T is chosen to be 1.6 sec.

In the case of no dissipation, $\hat{\sigma} = 0$, we have chosen the fast scale variations of ρ_1 and $1/K_1$ to be $\eta = \nu = 0.3$. The estimated power spectrum $\hat{S}(t,\omega)$ is simulated numerically for 500 different configurations. For both mismatched and pressure release boundary conditions, we have found that, at various values of t, the averaged $\hat{S}(t,\omega)$ agree excellently with the $S(t, \omega)$ obtained by solving Eqs. (8)-(13) and (15)-(16). This is also true for the case with dissipation. In this case we have chosen $\eta = 0$ and $\nu = 0.3$. The dependence of $\hat{\sigma}$ is modeled by a linear function of frequency[11], i.e. $\hat{\sigma}/\rho_1 = \omega/(2Q)$. The value of Q can be estimated from attenuation measurements of seismic waves.[11] We have chosen $Q=50\pi$ in our calculation. All the results we have obtained seem to indicate that the statistical theory does predict the correct local power spectrum. Based on Eq. (8), the inversion can be carried out, as shown in the next section. In the case of a homogeneous medium, this numerical method also reproduces excellently the analytic result shown in Eq. (17).

II C INVERSION RESULTS

Since Eq.(8) depends only on $\bar{\alpha}(\tau) = \alpha / c_1(\tau)$, the purpose of the inversion is to extract this information from a given set of estimated power spectra. If we assume that $p_{refl}(t)$ or $u_{refl}(t)$ is a Gaussian process,[12] a well-known theorem in signal-processing theory tells us that $S(t, \omega)$ of Eq.(7) follows an exponential distribution with $\hat{S}(t,\omega)$ as the mean.[4] If we further assume that each frequency ω is independent, a likelihood function $L[\tilde{\alpha}(\tau)]$ may therefore be written as

$$L\left[\tilde{\alpha}(t)\right]=\sum_{\omega_i}\frac{\hat{S}(t,\omega_i)}{S\left(t,\omega_i\middle|\tilde{\alpha}(\tau)\right)}+\ell n\left[S\left(t,\omega_i\middle|\tilde{\alpha}(\tau)\right)\right] \tag{22}$$

Maximization of L would yield the optimal $\tilde{\alpha}(\tau)$ consistent with the data $\hat{S}$. In the numerical inversion we have added a Bayesian term into L by assuming that $\tilde{\alpha}(\tau)$ is a slowly varying function as was done in Refs. [3,4]. The inversion results of $\tilde{\alpha}(\tau)$ are shown in Figs.1 and 2 for the cases without and with dissipation, respectively. Curve A represents the medium property. Curves B and C are the inversion results for mismatched and pressure release boundary conditions, respectively.

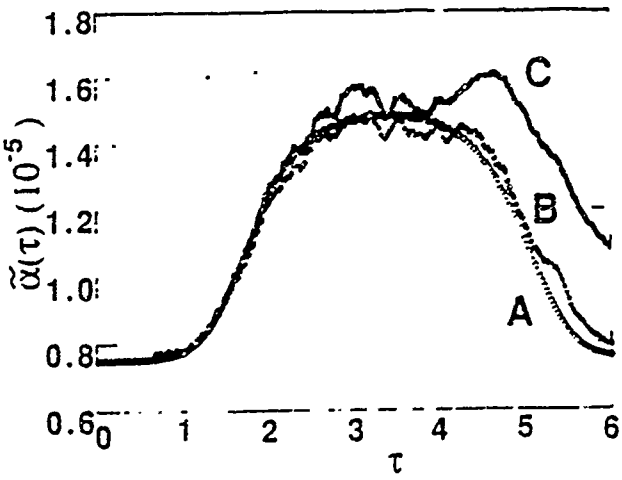

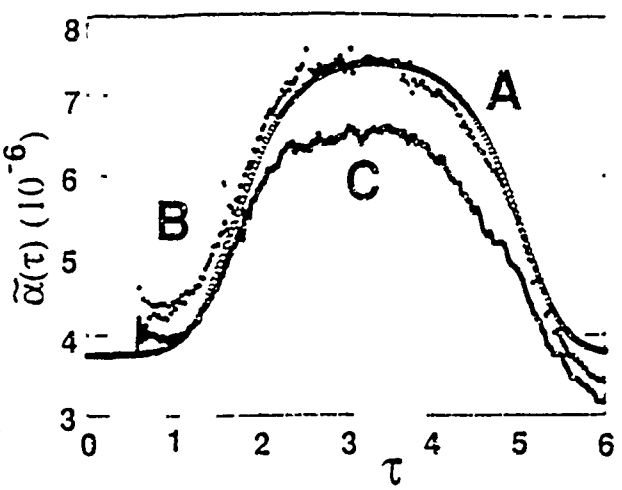

Fig. 1 Results of inversion with no dissipation. Fig. 2 Results of inversion with dissipation.

III. CONCLUSIONS AND RECOMMENDATIONS

Our new inversions resulis are generally good and in line with previous inversion work using no attenuation and matched medium boundary condition. There is some deviation in the case of the pressure-release boundary condition. More work is needed to track down the source of the difficulty. Our next step is to implement this method on real seismic data using normal incidence plane waves to avoid elastic effects. Work on elastic wave localization has already been carried out[13] and will be reported elsewhere. Our further projects include (1) Relate the correlation legths obtained from seismology to those derived from independent observations across geologically complex (heterogeneous) regions (e.g. heat flow and electromagnetic studies), and (2) Extend the present approach to take into account deviations from one dimensionality

REFERENCES

1. R. Burridge, G. Papanicolaou, P. Sheng, and B. White, SIAM J. Appl. Math. 49,582 (1989).
2. M. Asch, G. Papanicolaou, M. Postel, P. Sheng, and B. White, Wave Motion 12, 429 (1990).
3. M. Asch, W. Kohler, G. Papanicolaou, M. Postel, and B. White, SIAM Review 33, 519 (1991).
4. B. White, P. Sheng, M. Postel, and G. Papanicolaou, Phys. Rev. Lett. 63, 2228 (1989).
5. G. Papanicolaou, M. Postel, P. Sheng, and B. White, Wave Motion 12, 527 (1990).
6. M. Asch, W. Kohler, G. Papanicolaou, M. Postel, and B. White, 'Localization and Propagation of Classical Waves in Random and Periodic Structures', C. Soukoulis, ed., Plenum, New York.
7. P. Sheng, Z. Q. Zhang, B. White, and G. Papanicolaou, Phys. Rev. Lett. 57,1000 (1986).
8. B. White, P.Sheng, Z. Q. Zhang, and G. Papanicolaou, Phys. Rev. Lett. 59,1918 (1987).
9. B. White, P. Sheng, and B. Nair, Geophysics, 55, 1158 (1990).
10. L. R. Jannaud, P. M. Adler and C. G. Jacquin, Geophysics, 58,408 (1993).
11. M. B. Dobrin, *'Introduction to Geophysical Prospecting'*, (McGraw Hill, 3rd Edition 1976).
12. E. Parzen, Technometrics 3, 167 (1961).
13. W. Kohler, G. Papanicolaou, and B. White, (manuscript in preparation).

END

FILMED

DATE:
11-93

DTIC